

Understanding the Role of Androgen Receptor Signalling in Prostate Cancer: A Lipidomics Approach by MALDI Mass Spectrometry Imaging

SHADRACK MULINGE MUTUKU

BSc., MSc.,



THE UNIVERSITY
of ADELAIDE

Adelaide Medical School

Faculty of Health and Medical Sciences

The University of Adelaide and

South Australian Health and Medical Research Institute

Australia

© Shadrack Mulinge Mutuku

A thesis by combination of conventional narrative and publication formats
submitted to The University of Adelaide in fulfillment of the requirements for
the degree of Doctor of Philosophy

July 2020

TABLE OF CONTENTS

TABLE OF CONTENTS	I
ABSTRACT	VIII
DECLARATION	X
DEDICATION.....	XI
ACKNOWLEDGEMENTS.....	XIII
LIST OF PUBLICATIONS ARISING FROM THESIS	XVI
LIST OF CONFERENCE PRESENTATIONS	XVII
AWARDS AND ACHIEVEMENTS	XVIII
LIST OF FIGURES, TABLES AND APPENDICES	XX
ABBREVIATIONS	XXVII
CHAPTER 1: INTRODUCTION AND LITERATURE REVIEW.....	1
1.1. Human Prostate Gland	2
1.2. Prostate Cancer	5
1.2.1. Epidemiology of Prostate Cancer	5
1.2.2. Androgens Receptor Signalling in Prostate Cancer.....	6
1.2.3. Prostate Pathophysiology	8
1.2.4. Clinical Diagnosis of Prostate Cancer.....	12
1.2.5. Standard Care and Treatment of Prostate Cancer	16
1.2.6. Biomedical Challenges in Prostate Cancer Research	22
1.3. Lipid Biochemistry	24
1.3.1. Lipid Metabolism in Prostate Cancer	29
1.4. Introduction to Mass Spectrometry	34
1.4.1. Matrix-Assisted Laser Desorption/Ionisation (MALDI)	35
1.4.1.1. Ion Formation in MALDI	37
1.4.2. Electrospray Ionisation	39
1.4.2.1. Ion Formation in ESI	41
1.4.3. Desorption Electrospray Ionisation (DESI).....	42
1.4.4. Formation of Lipid Ions	43
1.5. Mass Spectrometry Instrumentation.....	46
1.5.1. Quadrupole Mass Analysers.....	46
1.5.1.1. API 4000 QTrap LC-MS/MS System.....	47
1.5.2. Time-of-flight (TOF) Mass Analysers	50
1.5.3. Quadrupole-TOF Systems.....	51

1.5.3.1.	SYNAPT HDMS Q-TOF	52
1.5.3.2.	timsTOF Flex.....	53
1.5.4.	Ion Mobility Separation	54
1.6.	Mass Spectrometry Imaging	56
1.6.1.	MALDI Mass Spectrometry Imaging	56
1.6.1.1.	MALDI MS Imaging Sample Preparation.....	59
1.6.1.2.	MALDI MS Imaging Matrix Selection.....	62
1.6.1.3.	MALDI MS Imaging Matrix Application	64
1.6.1.4.	MALDI Laser Selection.....	66
1.7.	Conventional Lipidomics	68
1.7.1.1.	Shotgun Lipidomics	68
1.7.1.2.	LC-MS/MS Lipidomics.....	69
1.8.	LC-MS/MS Drug Quantification.....	70
1.9.	Mass Spectrometry Imaging in Cancer.....	71
1.10.	Literature Review Article: Lipidomics in Prostate Cancer Research	73
1.11.	Project Summary.....	115
1.12.	Thesis Hypothesis and Project Rationale	116
1.13.	Research Aim and Objectives.....	117
CHAPTER 2:	MATERIALS AND METHODS	118
2.1.	Materials, Reagents and Equipment	119
2.1.1.	Commonly Used Reagents, Chemicals and Buffers	119
2.1.2.	Equipment.....	123
2.1.3.	Reagent and Buffer Preparation	124
2.2.	Chapter 3 Methods	125
2.2.1.	Tissue Sectioning.....	125
2.2.2.	Histological Staining.....	127
2.2.3.	Cell Counting	127
2.2.4.	Instrument Calibration.....	128
2.2.5.	Matrix Application by Sublimation	130
2.2.6.	MALDI MS Imaging Data Acquisition	132
2.2.7.	MSI Data Processing and Analysis	133
2.2.7.1.	Waters High Definition Imaging.....	133
2.2.7.2.	R Cardinal	134
2.2.7.3.	SCiLS Lab	135

2.2.8.	Lipidomics.....	135
2.2.8.1.	Total DNA Assay.....	135
2.2.8.2.	Lipid Extraction.....	137
2.2.8.3.	Mass Spectrometry	137
2.2.8.4.	Data Analysis	138
2.3.	Chapter 4 Methods	139
2.3.1.	Tissue Preparation for MALDI MS Imaging.....	139
2.3.2.	Matrix Application by Automated Spray Coating.....	140
2.3.3.	MALDI MS Imaging Data Acquisition.....	141
2.3.4.	Histology and Immunohistochemistry	141
2.3.5.	Lipidomics.....	142
2.4.	Chapter 5 and Chapter 6 Methods	143
2.4.1.	<i>Ex Vivo</i> Culture of Human Prostate Tissue.....	143
2.4.2.	Drug Extraction from Explant Culture System for Enzalutamide Quantification.....	145
2.4.2.1.	Explant Tissue Homogenisation.....	145
2.4.2.2.	Protein Precipitation/Crude Extraction Method for Tissue Homogenates	145
2.4.2.3.	Protein Precipitation for Culture Medium.....	146
2.4.2.4.	Standard Curve for Biological Matrices	146
2.4.2.5.	Quantitative Run Assay Set-Up.....	147
2.4.3.	Bicinchoninic Acid Total Protein Assay.....	147
2.5.	Chapter 7 Methods	149
2.5.1.	Tissue Preparation for MALDI MS Imaging.....	149
2.5.2.	Histological Staining	149
2.5.3.	Instrument Calibration.....	149
2.5.4.	Matrix Application	150
2.5.5.	MALDI MS Imaging Data Acquisition.....	150
2.5.6.	Drug MS/MS Imaging Data Acquisition.....	151
2.5.7.	Data Processing and Analysis	151
2.5.7.1.	SCiLS Lab	151
2.5.7.2.	Metabolomic feature annotations	152
2.5.7.3.	Statistical Analysis	153
2.5.8.	Cell Counting	153
2.5.9.	Immunohistochemistry.....	154

CHAPTER 3: MALDI MS IMAGING AND LIPIDOMICS PROFILING REVEAL HETEROGENEITY IN LIPID COMPOSITION OF CLINICAL PROSTATE TISSUES	156
3.1. Introduction	157
3.2. Experimental Approach	161
3.3. Results	162
3.3.1. Cellular Heterogeneity of Prostate Tissues Changes with Depth...	162
3.3.2. Relating Spatial Segmentation Analysis of MSI Data to Tissue Morphology	171
3.3.3. Component Analysis Reveals Lipid Signature of Prostate Epithelium	177
3.3.4. Validation of Lipid Species by MALDI MS/MS Imaging.....	179
3.3.5. Validation and Characterisation of Lipid Species in Prostate Tissue Homogenates by Conventional Lipidomics	186
3.4. Discussion	200
CHAPTER 4: MALDI MSI OF CLINICAL PROSTATE TISSUES REVEALS CELL-TYPE SPECIFIC LIPID COMPOSITIONS	205
4.1. Introduction	213
4.2. Materials and Methods	215
4.3. Results	221
4.3.1. Differential distribution of phospholipids between tissue stroma, malignant and non-malignant prostate epithelium.....	221
4.3.2. Prostate tissue morphology is reflected in spatial lipid distribution	226
4.4. Discussion	232
4.5. Conclusion	237
4.6. Supplementary	238
CHAPTER 5: DEVELOPMENT OF AN LC-MS/MS METHOD FOR QUANTIFICATION OF ENZALUTAMIDE UPTAKE IN PROSTATE EXPLANT CULTURE SYSTEM	250
5.1. Introduction	251
5.2. Experimental Approach	253
5.2.1. Set up of Mass Spectrometry Conditions.....	253
5.2.2. Set up of Liquid Chromatography Conditions	256
5.2.3. Establishment of Linear Range.....	257
5.2.4. Establishment of Drug Extraction.....	259
5.2.5. Preparation of Stock Solutions.....	260
5.2.6. Bioanalytical Method Validation Procedures.....	261

5.2.7. Data Analysis.....	264
5.3. Results.....	265
5.3.1. Mass spectrometry conditions	265
5.3.2. LC-MS/MS conditions	267
5.3.3. Establishment of Drug Extraction.....	268
5.3.4. Sample Handling of Prepared Calibration and QC Samples	271
5.3.5. Method Validation Parameters.....	273
5.3.5.1. Selectivity and Specificity	273
5.3.5.2. Calibration Curve in Neat Solution	274
5.3.5.3. Accuracy and Precision in Neat Solution.....	278
5.3.5.4. Extracted Calibration Curve in Biological Matrices.....	280
5.3.5.5. Accuracy and Precision in Biological Matrices	281
5.3.5.6. Matrix Effects	282
5.3.5.7. Stability in Biological Matrices	283
5.3.5.8. Stock Solution Stability.....	286
5.4. Discussion	287
CHAPTER 6 EVALUATION OF SMALL MOLECULE DRUG UPTAKE IN PATIENT-DERIVED PROSTATE CANCER EXPLANTS BY MASS SPECTROMETRY	291
6.1. Published Paper	295
6.2. Supplementary Information	306
CHAPTER 7: SPATIAL MAPPING OF THE LIPIDOMIC EFFECTS OF AR INHIBITION BY ENZALUTAMIDE IN PATIENT-DERIVED PROSTATE CANCER EXPLANTS.....	314
7.1. Introduction.....	315
7.2. Experimental Approach	321
7.3. Results.....	323
7.3.1. Enzalutamide Abrogates AR in PDE Tissues	323
7.3.2. Morphological Changes in Cultured and Drug-Treated PDE Tissues 326	
7.3.3. MALDI MS/MS Imaging of Enzalutamide.....	328
7.3.4. Molecular Annotations in MSI Data.....	330
7.3.5. Spatial Segmentation Maps Epithelium and Stroma Cells	332
7.3.6. Culture Effects on PDE Lipid Profiles	340
7.3.6.1. Negative Ion Mode MALDI	340
7.3.6.2. Positive Ion Mode MALDI.....	340

7.3.7.	Treatment Effects on PDE Lipid Profiles	344
7.3.7.1.	Negative Ion Mode MALDI	344
7.3.7.2.	Positive Ion Mode MALDI	344
7.3.8.	LC-ESI-MS/MS Lipidomics	348
7.3.9.	Co-registration of IHC and Spatial Lipid Profiles	349
7.4.	Discussion	351
7.5.	Supplementary Information	356
CHAPTER 8:	CONCLUSION AND FUTURE DIRECTIONS	357
8.1.	Introduction.....	358
8.2.	Thesis Findings	360
8.2.1.	MALDI MSI Offers Precise Tissue-Specific Lipid Profiles	360
8.2.2.	MALDI MSI Revealed Spatially Informative Lipid Changes in Prostate Tumours.....	361
8.2.3.	Robust Drug Quantification and Targeted Enzalutamide Imaging in Patient-Derived Explants (PDE) Culture System	362
8.2.4.	High Resolution MALDI Q-TOF Imaging Shows Refined Insights into Lipidomic Compositions of <i>Ex Vivo</i> Cultured Prostate Tissues	363
8.3.	Future Work.....	364
8.4.	Conclusion	370
9.	Appendices	371
9.1.	Appendix 1: Supplementary Information Chapter 3	372
9.2.	Appendix 2: Supplementary Information Chapter 5	379
9.3.	Appendix 3: Supplementary Information Chapter 7	382
9.4.	Appendix A: <i>Cardinal R</i> Markdown Script.....	403
9.5.	Appendix B: SYNAPT Q-TOF HDMS MALDI MSI Optimisation	426
B.1.	Optimisation of Solvent Composition and Matrix Concentration 426	
B.2.	Effect of Solvent and Matrix Content on Lipid Ion Signal	430
B.3.	Comparison of Matrix Deposition Techniques for Lipid Imaging 432	
9.6.	Appendix C: timsTOF Flex MALDI MSI Optimisation	437
C.1.	Optimisation of Solvent Composition and Matrix Concentration 437	
C.2.	Optimisation of Solvent Composition for Imaging	440
C.3.	High Resolution MALDI MS Imaging in Negative Ion Mode	444
C.4.	Method Transfer Between MALDI Q-TOF Systems	444

9.7. Appendix D: Experimental Optimisation for Frozen Section IHC Staining	447
D.1. Optimisation of Sample Fixation for IHC p63+AMACR Staining	447
D.2. Evaluation of IHC p63+AMACR Staining in Day 0 Tissues	449
10. References	453

ABSTRACT

Prostate cancer (PCa) remains one of the deadliest cancers globally and is primarily driven by aberrant androgen hormone signalling. Clinical blood-based biomarker testing which detects prostate specific antigen (PSA) and the Gleason grading system have been important diagnostic and prognostic tools to aid clinical management. However, a significant research challenge is the ability to stratify men according to their risk of tumour progression without having to overtreat many of them. Recent research has discovered that the androgen receptor (AR) regulates key lipid metabolic genes throughout PCa tumorigenesis. Advances in metabolomics/lipidomics technologies have further emphasised this unique hallmark of PCa with changes across the diversity of the lipid classes. The hypothesis of this thesis is that lipid composition of PCa has prognostic value.

Currently, conventional lipidomics, like other omics, is confounded by prostate tumour heterogeneity. This project utilised matrix-assisted laser desorption/ionisation mass spectrometry imaging (MALDI MSI) that has the advantage of *in situ* spatial information to histologically delineate tissue-type specific lipid profiles in prostate glands. Initial MALDI MSI experiments in 10 patients, achieved by sublimation of MALDI matrix on tissue sections collected at interspersed levels, revealed lipidomic profiles consistent with morphological and pathological features of PCa. These findings were further underpinned by validation using MALDI MS/MS imaging and lipidomics. A subsequent study in an independent cohort employed automated spray coating of matrix that afforded markedly improved lipid ion sensitivity in prostate epithelia and critically, the stroma which is the physiological milieu for the tumour microenvironment.

Crucially, it was demonstrated using a combination of clustering and multivariate analysis methods that benign glands are enriched in particular lysophospholipids compared to tumours. However, lipid metabolism appeared to be heterogenous in tumours which did not show sufficiently discriminative lipid species. MALDI MSI did also appear to indicate spatial changes in relative abundance for the common monounsaturated phosphatidylcholine species PC(34:1).

This project also assessed the uptake of the AR inhibitor, enzalutamide (ENZ), in a well-characterised *ex vivo* model of human PCa of patient-derived explants (PDE). An LC-MS/MS bioanalytical assay was developed and validated according to US FDA guidelines. Together with targeted drug imaging by MALDI MS/MS, these studies revealed a time-dependent uptake of ENZ and its enhanced localisation to AR-positive epithelial rich areas. The significance of this work is to better understand pharmacodynamic implications of experimental design in tissue culture models.

Finally, a more advanced high resolution MALDI Q-TOF system was applied to interrogate the lipid profiles of PDE samples. Explants from five patients' biopsies with high grade prostate tumours were cultured in DMSO or ENZ. Spatial characterisation in dual MALDI polarities was conducted at a lateral resolution of 20 μm that offered well-defined tissue segment lipidomic fingerprints. Negative ion mode imaging uncovered heterogenous abundance of cholesterol sulphate in multifocal tissues. Altered lipid composition in drug treated PDEs possibly because of pharmacological inhibition of AR was seen. This facet of the project has potential to unravel novel lipid biomarkers of treatment response and other metabolic susceptibilities of aggressive PCa and promises exciting investigations in the future.

DECLARATION

I, *Shadrack Mulinge Mutuku*, certify that this work contains no material which has been accepted for the award of any other degree or diploma in my name, in any university or other tertiary institution and, to the best of my knowledge and belief, contains no material previously published or written by another person, except where due reference has been made in the text. In addition, I certify that no part of this work will, in the future, be used in a submission in my name, for any other degree or diploma in any university or other tertiary institution without the prior approval of the University of Adelaide and where applicable, any partner institution responsible for the joint-award of this degree.

I acknowledge that copyright of published works contained within this thesis resides with the copyright holder(s) of those works.

I also give permission for the digital version of my thesis to be made available on the web, via the University's digital research repository, the Library Search and also through web search engines, unless permission has been granted by the University to restrict access for a period of time.

Shadrack Mulinge Mutuku

31 Jul 2020

DEDICATION

To my parents; John and Jane Mutuku

To my siblings: Mwendé, Sila and Munanie

To nephew and nieces: Collins, Alice, Abby, Ariana, and Amanda,

Mutheu and Baraka

For I can do everything through Christ, who gives me strength.

Philippians 4:13 (NLT)

ACKNOWLEDGEMENTS

First, I wish to thank my Supervisory Panel; Professor Lisa Butler, Dr. Marten Snel and Dr. Paul Trim for their guidance, support, and patience since I started my PhD. Their collective scientific input and advice has made it possible for me to come this far and moulded me into a proper researcher. I have learnt how to think, communicate, and approach challenges through their constant supervision. I have accomplished many goals in tough times through their hands.

I wish also to express my uttermost gratitude to the Adelaide Graduate Centre for awarding me an international scholarship to enable me to undertake my doctoral studies at the University of Adelaide and housed within the magnificent South Australian Health and Medical Research Institute (SAHMRI).

I wish to personally thank Prof. Lisa Butler for being an academic mentor with unwavering commitment and leadership . From that very first Skype call five years ago that gave me a shot that led to all of this wonderful scientific pursuit. The many times I knocked on her door and my professional interests and personal concerns listened to with wise counsel. I appreciate the countless opportunities she has awarded me to advance my all-round skill sets. It has also been wonderful being a Research Officer within the Prostate Cancer Research Group (PCRG) she heads.

I also wish to individually thank my co-supervisor Dr. Paul Trim. A fantastic trainer, devoted teacher always willing to help me. I appreciate all the technical help he has accorded me on various aspects of mass spectrometry and MALDI imaging throughout my project. An exceptional mention to Dr. Nicole Moore for her kindness and support. Her fantastic organisation allowed me to participate in many conferences, seminars and presentations.

It has also been a pleasure to work within the PCRG. I appreciate the support from Ms. Joanna Gillis and Ms. Natalie Ryan for their dedicated support which helps students' projects run smoothly. I also wish to thank my colleagues from Lipids and Prostate Cancer, Dr. Margaret Centenera, Dr. Zeyad Nassar, Ms. Chui Yan Mah and Ms. Ataa Hinnah, it's been fantastic to be surrounded with gifted and brilliant scientists and I have learned a lot from their work. I note all the academic and technical support staff from the University, Faculty of Health and Medical Sciences and SAHMRI Precision Medicine Theme - Cancer Program for facilitating a conducive working and research environment.

I also wish to express my sincere gratefulness to Dr. Adel Aref for being a good friend. Thanks for all the advice that would help any international PhD student survive and thrive. It was always been nice to have pairs of understanding ears and company from fellow PhD mates, Dr. Benjamin Leow and Mr. Andrew Shoubridge to share with the struggles, frustrations, and occasional victories. I recognise my "older mentors", high-flying postdoctoral fellows, Dr. Fredrick Mobegi and Dr. Krzysztof Mrozik for also being a good source of invaluable career advice and personal support.

I wish to officially acknowledge all the assistance I have received to enable execution of my PhD research project. I appreciate all the scientific contributions from fellow co-authors especially the critical review of my research work by my Supervisors; Professor Lisa Butler, Dr. Marten Snel and Dr. Paul Trim. My huge thanks to Ms. Swati Irani and Ms. Kayla Bremert for training me on human tissue culture. I am grateful to Dr. Johan Gustafsson for the data science insights on mass spectrometry imaging and help with bioinformatics in *R*. I wish to thank fellow collaborators from KU Leuven Professor Johan Swinnen, Dr. Jonas

Dehairs, Mr. Xander Spotbeen and Mr. Daan Van Den Bosch for productive engagements and lipidomics analysis within the wider Movember Revolutionary Team (MRTA) project working on Lipids and Prostate Cancer. Special thanks to Dr. Jessica Logan and Ms. Courtney Moore for their enthusiastic assistance with running automated immunostaining experiments at Prof. Doug Brooks' laboratory at the University of South Australia Cancer Research Institute. Not forgetting to mention Dr. Stephen Pederson and Mr. John Salmon for statistical analysis input.

Lastly, I want to acknowledge the emotional support of my beloved family back home. I cannot express enough from the bottom of my heart my appreciation to Dad, Mum and my siblings Mwende, Sila and Munanie. Their *Love, Thoughts and Prayers* after being a decade away from home has made me not only the person I am today, but also the scientist and made my dreams come true. They would remember me very well singing "*I will go to England when I finish Class Eight...*" And this desire became a reality when I attended the University of Nottingham, not only because I was smart, driven, and focused when I was growing up, but more so because of their sacrifice. A big warm thanks to Aunt Agnes and Uncle Ben as well, my second family who have also contributed tremendously to my journey. Finally, I wish to thank my partner, Jacinta, for being a good companion since I started my studies. Her encouragement kept me going despite the bumpy road. Her support has helped me achieve this milestone.

LIST OF PUBLICATIONS ARISING FROM THESIS

Mutuku, S. M., Trim, P. J., Snel, M. F., Butler, L. M. (2020). *MALDI MSI Of Lipids in Prostate Cancer: An Attractive Target for Spatially Resolved-Lipidomics Based Biomarker Discovery.*

Manuscript in preparation

Mutuku, S. M., Trim, P. J., Das, R., Salamon, J., Logan, J. M., Brooks, D.J., Dehairs, J., Swinnen, J. V., Lynn, D. J., Snel, M. F., Butler, L. M. (2020). *MALDI MSI Of Lipids in Clinical Prostate Tumors Reveals Cell-Type Specific Lipid Compositions.*

Manuscript in preparation

Mutuku, S. M., Trim, P. J., Prabhala, B. K., Irani, S., Bremert, K. L., Logan, J. M., Brooks, A.D., Stahl, J., Centenera, M. M., Snel, F.M., Butler, L. M. (2019). *Evaluation of small molecule drug uptake in patient-derived prostate cancer explants by mass spectrometry.* Scientific Reports, 9(1), 15008.

Published

Butler, L.M., Mah, C.Y., Machiels, J., Vincent, A.D., Irani, S., **Mutuku, S.M.**, Spotbeen, X., Bagadi, M., Waltregny, D., Moldovan, M., Dehairs, J., Vanderhoydonc, F., Bloch, K., Das R., Stahl, J., Krench, J., Gevaert, T., Derua, R., Waelkens, E., Nassar, Z.D., Selth, L.A., Trim, P.J., Snel, M.F., Lynn, D.J., Tilley, W.D., Hovarth, L.G., Centenera, M.M., Swinnen, J.V. (2020). *Lipidomic Profiling of Clinical Prostate Tissues Reveals Targetable Alterations in Lipid Composition. Preprinted in bioRxiv*

Submitted for publication

LIST OF CONFERENCE PRESENTATIONS

Mass Spectrometry Imaging: An Emerging Spatial Tool for Discovery Lipidomics of Prostate Cancer

Oral presentation: Australian Society for Molecular Imaging (ASMI) Meeting held on 08 Nov 2019, at the SAHMRI Auditorium North Terrace, Adelaide, Australia.

Understanding the Role of Androgen Receptor Signalling in Prostate Cancer: A Lipidomics Approach

Oral presentation: Cancer in SA Translation Research Meeting held on 28 Aug 2019, at the SAHMRI Auditorium North Terrace, Adelaide, Australia.

MALDI Imaging to Characterise the Lipid Signature of Clinical Prostate Tumours

Poster presentation: 67th American Society for Mass Spectrometry Conference and Allied Topics held on 02 - 06 Jun 2019, at the Georgia World Congress Centre, Atlanta, United States.

Evaluation of Small Molecule Drug Uptake in *Ex Vivo* Cultured Prostate Tumours by Mass Spectrometry

Poster presentation: 19th Asia-Pacific Prostate Cancer Conference held on 22 - 25 Aug 2018, at the Brisbane Convention Centre, Brisbane, Australia.

Evaluation of Small Molecule Drug Uptake in *Ex Vivo* Cultured Prostate Tumours by Mass Spectrometry

Poster presentation: 12th Annual Florey Postgraduate Research Conference held on 25 Sep 2018 at the National Wine Centre, University of Adelaide, South Australia.

One Molecular Picture, A Million Words – Improving Prostate Cancer Diagnosis

Oral presentation: A 3-Minute PhD thesis competition during the 4th SAHMRI Annual Scientific Meeting held on 30 - 31 Oct 2017 at SAHMRI, Adelaide, SA

A Mass Spectrometry Approach to Characterise Lipid Composition in Prostate Tumours

Poster presentation: 11th Annual Florey Postgraduate Research Conference held on 20 Sep 2017 at the National Wine Centre, University of Adelaide, South Australia.

Quantification of Enzalutamide in Cultured Prostate Tissue Using LC-MS/MS

Poster presentation: 26th Australian & New Zealand Society for Mass Spectrometry Conference (ANZSMS26) held on 16 - 20 Jul 2017 at Flinders University Victoria Square campus, Adelaide, South Australia.

AWARDS AND ACHIEVEMENTS

2020: Poster Session Judge

Florey Undergraduate Research Conference, University of Adelaide

2019: Australian Society for Molecular Imaging (ASMI) Award

Best PhD oral presentation 1st runner-up at SAHMRI Adelaide meeting
Value: AUD\$ 250

2019: Australian and New Zealand Society for Mass Spectrometry (ANZSMS) Student Travel Award

Awarded to present at the 67th ASMS Conference, Atlanta, Georgia, USA
Value: AUD\$ 1,000

2019: American Society for Mass Spectrometry (ASMS) Student Stipend

Awarded to present at the 67th ASMS Conference, Atlanta, Georgia, USA
Value: USD\$ 200

2018: Demonstrator for Third Year Research Placements

Tutored journal club sessions to Medical Sciences and Neurosciences students and assessed final year reports for three semesters

2018: Industry Mentoring in STEM (IMNIS) Mentee

Selected to participate in a yearlong mentorship connection with an industry expert in the MedTech Pharma program SA sponsored by the Adelaide Graduate Centre and Australian Academy of Technology and Engineering

2017: Research Business & Partnerships Prize

11th Annual Florey Postgraduate Research Conference, University of Adelaide. Awarded for a research project with translational potential to positively impact the community and received corporate nominee membership to AusBiotech

2016: University of Adelaide International Wildcard Scholarship

University of Adelaide (Adelaide Graduate Centre) full sponsorship towards four-year doctoral degree studies

LIST OF FIGURES, TABLES AND APPENDICES

Figures

<i>Figure 1.1. Anatomy of the prostate gland</i>	2
<i>Figure 1.2. Normal prostate physiology</i>	4
<i>Figure 1.3. Androgen signalling in prostate gland</i>	7
<i>Figure 1.4. Prostate cancer pathophysiology</i>	11
<i>Figure 1.5. Gleason grading of prostate cancer</i>	16
<i>Figure 1.6. Clinical strategies for targeting AR signalling pathway in prostate cancer</i>	20
<i>Figure 1.7. Phospholipid building blocks</i>	24
<i>Figure 1.8. Overview of phospholipid metabolism in eukaryotic systems</i>	27
<i>Figure 1.9. Overview of androgen regulated lipid metabolism in prostate cancer</i>	31
<i>Figure 1.10. Novel genomic mechanism of aberrant lipid metabolism in prostate cancer</i>	33
<i>Figure 1.11: Principle of the MALDI process</i>	37
<i>Figure 1.12. Photoexcitation and energy pooling model</i>	38
<i>Figure 1.13. Cluster ionisation model</i>	39
<i>Figure 1.14. Schematic of an ESI source</i>	40
<i>Figure 1.15. Models of the ESI process</i>	41
<i>Figure 1.16. DESI instrumentation process</i>	42
<i>Figure 1.17. Lipid ion isomers and mass resolution</i>	45
<i>Figure 1.18. Simplified schematic of quadrupole mass analyser</i>	47
<i>Figure 1.19. Schematic layout of the API4000 LC-MS/MS system</i>	49
<i>Figure 1.20. Schematic of the Waters MALDI SNYAPT HDMS hybrid Q-orthogonal acceleration-TOF system</i>	52
<i>Figure 1.21. Schematic of the Bruker timsTOF Flex optics and ion transmission</i>	53
<i>Figure 1.22. Types of ion mobility platforms</i>	55
<i>Figure 1.23. Schematic representation of a MALDI MSI experiment workflow</i>	58
<i>Figure 1.24. Laser fluence of Nd:YAG lasers</i>	67
<i>Figure 2.1. Image of embedded fresh-frozen prostate biopsy tissue</i>	126

<i>Figure 2.2. Calibration report for MALDI imaging on Waters SYNAPT</i>	<i>130</i>
<i>Figure 2.3. Sublimation apparatus for matrix application</i>	<i>131</i>
<i>Figure 2.4. Image of mounted fresh-frozen prostate biopsy core</i>	<i>139</i>
<i>Figure 2.5. MALDI matrix automated spray coating set-up</i>	<i>140</i>
<i>Figure 2.6. Prostate patient-derived explant (PDE) culture set-up workflow ...</i>	<i>144</i>
<i>Figure 3.1. Experimental workflow for MALDI MSI, histology and lipidomics. 161</i>	
<i>Figure 3.2. Representative example of PC headgroup in cohort.....</i>	<i>166</i>
<i>Figure 3.3A. Lipid mass spectra of multiple pathological regions.....</i>	<i>168</i>
<i>Figure 3.3B. Lipid mass spectra of multiple pathological regions.....</i>	<i>169</i>
<i>Figure 3.3C. Lipid mass spectra of multiple pathological regions.....</i>	<i>170</i>
<i>Figure 3.4. Comparison of segmentation analysis approaches.....</i>	<i>173</i>
<i>Figure 3.5. Comparison of molecular ion clustering analyses of prostate tissue with histopathology scans.....</i>	<i>176</i>
<i>Figure 3.6. Lipid signature of clinical prostate tumours.</i>	<i>178</i>
<i>Figure 3.7. Validation of PC lipid species in epithelium by targeted imaging. 180</i>	
<i>Figure 3.8. Validation of Cer lipid species in epithelium by targeted imaging. 182</i>	
<i>Figure 3.9. Validation of lipid ions in stromal regions of prostate tissue.</i>	<i>184</i>
<i>Figure 3.10. Validation of lipid ions in stromal regions of prostate tissue.</i>	<i>185</i>
<i>Figure 3.11. Quantification of fatty acid composition in PC in prostate tissue homogenates.....</i>	<i>188</i>
<i>Figure 3.12. Quantification of PC lipids by sum notation in prostate tissue homogenates.....</i>	<i>189</i>
<i>Figure 3.13. Quantification of LPC in prostate tissue homogenates.....</i>	<i>190</i>
<i>Figure 3.14. Quantification of Cer species in prostate tissue homogenates... 191</i>	
<i>Figure 3.15. Quantification of Cer species in prostate tissue homogenates... 192</i>	
<i>Figure 3.16. Quantification of SM species in prostate tissue homogenates. ... 193</i>	
<i>Figure 3.17. Quantification of SM species in prostate tissue homogenates... 194</i>	
<i>Figure 3.18. Dimensionality reduction of comprehensive lipidomics analyses.</i>	<i>196</i>
<i>Figure 3.19. Lipid profile in multifocal prostate cancer – 32926R.....</i>	<i>197</i>
<i>Figure 3.20. Lipid profile in multifocal prostate cancer – 33042R.....</i>	<i>198</i>
<i>Figure 5.1. Graphical profile of the chromatographic elution conditions.....</i>	<i>256</i>
<i>Figure 5.2. Linearity of instrument response.</i>	<i>258</i>

<i>Figure 5.3. Chemical structures of analyte and internal standard ions.</i>	266
<i>Figure 5.4. Chromatogram of enzalutamide and internal standards.</i>	267
<i>Figure 5.5. Method development for drug extraction from cultured medium and explant tissue.</i>	270
<i>Figure 5.6. Calibration curve in neat solution.</i>	275
<i>Figure 5.7. Assessment of enzalutamide carryover.</i>	276
<i>Figure 5.8. Validation of calibration curve in neat solution.</i>	278
<i>Figure 5.9. Validation of calibration curve in extracted M4 culture medium.</i>	280
<i>Figure 5.10. Validation of calibration curve in extracted tissue homogenate.</i>	280
<i>Figure 7.1. Mechanism of action of enzalutamide in prostate cancer.</i>	319
<i>Figure 7.2. Ki67 proliferative index to enzalutamide in individual patients.</i>	319
<i>Figure 7.3. Comprehensive molecular imaging workflow.</i>	321
<i>Figure 7.4. IHC staining of AR in a PDEs.</i>	324
<i>Figure 7.5. MALDI MSI of lipids in ENZ uptake in PDEs over a time course.</i>	325
<i>Figure 7.6. Tissue morphology of fresh-frozen and PDE cultured samples.</i>	327
<i>Figure 7.7B. Drug-related morphological changes in PDE samples.</i>	328
<i>Figure 7.7A. MALDI MS/MS imaging of enzalutamide in PDE.</i>	329
<i>Figure 7.8. Molecular annotation by ion deconvolution.</i>	331
<i>Figure 7.9. Spatial segmentation in negative ion mode.</i>	334
<i>Figure 7.10. Spatial segmentation in positive ion mode.</i>	335
<i>Figure 7.11A. MALDI MSI in negative ion mode in PDE tumours.</i>	337
<i>Figure 7.11B. Co-registration of serial H&E scan with MALDI MSI ion map.</i>	338
<i>Figure 7.12. Culture effect in prostate tissue segments of negative ion MALDI data.</i>	342
<i>Figure 7.13. Culture effect in prostate tissue segments of positive ion MALDI data.</i>	343
<i>Figure 7.14. Treatment effect in prostate tissue segments of negative ion MALDI data.</i>	346
<i>Figure 7.15. Treatment effect in prostate tissue segments of positive ion MALDI data.</i>	347
<i>Figure 7.16. Conventional lipidomics analysis of culture effects.</i>	348
<i>Figure 7.17. Comparison of histopathological H&E and p63+AMACR IHC staining to spatial lipid ion maps.</i>	350

<i>Supplementary Figure 3.1. Determination of number of segments for SSCG clustering.</i>	372
<i>Supplementary Figure 3.2. Comparison of different segmentation metrics of the bisecting k-means algorithm.</i>	373
<i>Supplementary Figure 3.3. Validation of lipid ions in stromal regions of prostate tissue.</i>	374
<i>Supplementary Figure 3.4. Correlation of distribution of lipid fragment ions in stromal regions of prostate tissue.</i>	375
<i>Supplementary Figure 3.5. Sum notation of PC species.</i>	376
<i>Supplementary Figure 7.1. MALDI MS/MS imaging of enzalutamide in PDE.</i>	399
<i>Supplementary Figure 7.2. Fatty acid distribution in PDE tissues.</i>	401
<i>Supplementary Figure 7.3. Phospholipid distribution in PDE tissue.</i>	402
<i>Figure B1. SunCollect SunChrom spray settings.</i>	427
<i>Figure B2. Optimization of lipid imaging in positive ion mode.</i>	429
<i>Figure B3. Comparison of automated spray coating at varying solvent composition and matrix concentration.</i>	431
<i>Figure B4. Matrix deposition on consecutive section of a single prostate tissue.</i>	432
<i>Figure B5. Spatial ion maps of different matrix deposition protocols.</i>	434
<i>Figure B6. Importation data quality in SCiLS Lab between different matrix application technologies.</i>	436
<i>Figure C1. Optimisation of the solvent composition and matrix concentration.</i>	439
<i>Figure C2. Optimisation of the solvent composition for imaging.</i>	441
<i>Figure C3. Optimisation of the solvent composition for MALDI MSI.</i>	442
<i>Figure C4. Comparison of the solvent composition for MALDI MSI.</i>	443
<i>Figure C5. Comparison of histology and MALDI MSI ion maps.</i>	445
<i>Figure C6. Comparison of two MALDI Q-TOF MS imaging data sets.</i>	446
<i>Figure D1. Optimisation of sample preparation for IHC staining.</i>	448
<i>Figure D2. Comparison of histological staining to p63+AMACR IHC staining.</i>	450
<i>Figure D3. Higher magnification images of co-registered histological staining and p63+AMACR IHC staining scans.</i>	451

Tables

Table 1.1. TNM classification system of prostate cancer.	13
Table 1.2. Drugs approved for the treatment of prostate cancer.	21
Table 1.3. Lipid synthesis expressed as a percent composition of different organelles.	29
Table 1.4. Lipid ion isomerism and isobarism.	44
Table 1.5. Examples of popular MALDI matrices.	63
Table 1.6. Parameters of lasers used in MALDI imaging.	66
Table 1.7. Key studies exploiting the application of MALDI technology to cancers.	73
Table 2.1. Commonly used reagents and chemicals for project.	122
Table 2.2. Equipment and instruments for project.	123
Table 2.3. Preparation of commonly used reagent and buffers.	124
Table 2.4. Instrument settings for MALDI imaging on Waters SYNAPT.	129
Table 2.5. Hoechst DNA assay standard curve set-up.	136
Table 2.6. Micro BCA assay for protein determination set-up.	148
Table 3.1. Popular statistical approaches for clustering in MSI data analysis.	159
Table 3.2. Pathological assessment of prostate depth profiling tissue sections.	164
Table 3.3. Clustering parameters in R Cardinal.	174
Table 3.4. Main list of tentatively identified lipids.	199
Table 5.1. Key physicochemical descriptors of enzalutamide.	251
Table 5.2. Shows the established MS method for the analyte - enzalutamide.	255
Table 5.3. Standard concentration for testing the linear range of instrument response – lower end.	257
Table 5.4. Standard concentration for testing the linear range of instrument response – upper end.	257
Table 5.5. Method development for drug extraction from cultured medium.	268
Table 5.6. Stability of enzalutamide at post-preparative (autosampler) conditions.	272
Table 5.7. Cross talk between a neat solution of zero IS with the analyte MRM channel.	274

Table 5.8. Calibration curve preparation sheet for enzalutamide.	277
Table 5.9. Accuracy and precision of the LC-MS/MS assay for neat solution standards.....	279
Table 5.10. Accuracy and precision of the LC-MS/MS assay for culture medium samples.....	281
Table 5.11. Accuracy and precision of the LC-MS/MS assay for tissue homogenate samples.....	281
Table 5.12. Matrix effects assay M4 AR antagonist medium IS reconstituted in DMSO.....	282
Table 5.13. Matrix effects assay tissue homogenate IS reconstituted in acetonitrile.....	282
Table 5.14. Short-term and post preparative stability of enzalutamide in M4 AR antagonist medium.....	284
Table 5.15. Freeze-thaw and long-term stability of enzalutamide in M4 AR antagonist medium.....	284
Table 5.16. Short-term and post preparative stability of enzalutamide in tissue homogenate.....	285
Table 5.17. Freeze-thaw and long-term stability of enzalutamide in tissue homogenate.....	285
Table 5.18. Stock solution stability testing of enzalutamide.....	286
Table 7.1. Negative MALDI data ANOVA of tissue types between treatment groups.....	336
Table 7.2. Estimated lipidomic composition changes in PDE tissues.....	339
Supplementary Table 7.1. Clinical pathology of PDE tissues used for HR-MALDI MSI.....	356
Supplementary Table 3.1. Total DNA measurement results for lipidomics analyses.....	378
Supplementary Table 5.1. Summary procedure for assessment of matrix effects and recovery efficiency parameters.....	379
Supplementary Table 7.2. Bucket list for annotation for negative ion mode data.....	382
Supplementary Table 7.3. Bucket list for annotation for positive ion mode data.....	386

<i>Supplementary Table 7.4. Culture effects in MALDI negative ion mode data – epithelium.</i>	391
<i>Supplementary Table 7.5. Treatment effects in MALDI negative ion mode data – epithelium for volcano plot analyses.</i>	392
<i>Supplementary Table 7.6. Culture effects in MALDI negative ion mode data – stroma for volcano plot analyses.</i>	393
<i>Supplementary Table 7.7. Treatment effects in MALDI negative ion mode data – stroma for volcano plot analyses.</i>	394
<i>Supplementary Table 7.8. Culture effects in MALDI positive ion mode data – epithelium for volcano plot analyses.</i>	395
<i>Supplementary Table 7.9. Treatment effects in MALDI positive ion mode data – epithelium for volcano plot analyses.</i>	396
<i>Supplementary Table 7.10. Culture effects in MALDI positive ion mode data – stroma for volcano plot analyses.</i>	397
<i>Supplementary Table 7.11. Treatment effects in MALDI positive ion mode data – stroma for volcano plot analyses.</i>	398
<i>Table B1. Total ion chromatograms of matrix and lipid masses.</i>	430

ABBREVIATIONS

°C	degree Celsius
ADT	androgen deprivation therapy
AR	androgen receptor
BPH	benign prostatic hyperplasia
Cer	ceramide
CHCA	α -cyano-hydroxycinnamic acid
Da	Dalton
DESI	desorption electrospray ionisation
DNA	deoxyribonucleic acid
ENZ	enzalutamide (MDV3100)
ESI	electrospray ionisation
eV	electron volt (V)
FA	fatty acids
FASN	fatty acid synthetase
FT-ICR	Fourier transform ion cyclotron resonance
FWHM	full width half maximum
GG	Gleason grade
GS	Gleason score
h	hour
H&E	haematoxylin and eosin
HMDB	human metabolome database
HQC	high quality control
Hz	Hertz
IHC	immunohistochemistry
IMS	ion mobility separation
LC-MS/MS	liquid chromatography tandem mass spectrometry
LLOQ	low limit of quantification
LMSD	LIPID MAPS® Structure Database
LOD	limit of detection
LPA	lysophosphatidic acid
LPC	lysophosphatidylcholine

LQC	low quality control
<i>m/z</i>	mass-to-charge ratio
MALDI	matrix-assisted laser desorption/ionisation
min	minutes
MQC	medium quality control
MRM	multiple reaction monitoring
MS	mass spectrometry
MS/MS	tandem mass spectrometry
MSI	mass spectrometry imaging
MUFA	monounsaturated fatty acids
PC	phosphatidylcholine
PCA	principal component analysis
PCa	prostate cancer
PDE	patient-derived explant
PE	phosphatidylethanolamine
PG	phosphatidylglycerol
PI	phosphatidylinositol
PIN	prostatic intraepithelial neoplasia
PLSA	probabilistic latent semantic analysis
PLS-DA	partial least squares discriminant analysis
ppm	part per million
PS	phosphatidylserine
PSA	prostate specific antigen
PUFA	polyunsaturated fatty acids
QC	quality control
Q-TOF	quadrupole time-of-flight
<i>rcf</i>	relative centrifugal force
RNA	ribonucleic acid
RP	radical prostatectomy
sec	second
SM	sphingomyelin
SREBP	sterol regulatory element binding protein
TOF	time-of-flight

CHAPTER 1:

Introduction and Literature Review

1.1. Human Prostate Gland

The prostate gland is composed of four main zones; peripheral, central, transition and fibromuscular stroma all secured in a capsule^{1,2}. The peripheral zone is the largest and constitutes at least two-thirds of the prostate mass with the central zone constituting a significant part of the remaining gland. Together, these zones are comprised of epithelial secretory cells adjoined to basal cells arranged in a layer that anchor to the stroma to form the luminal duct system^{1,2}. This luminal space varies in distribution throughout the zonal architecture of the prostate making it highly heterogenous at the tissue level. The fibromuscular stroma is a dense arbitrary aggregation of smooth muscle cells that is usually permeated by bands of dense fibrous tissue. Other important morphological features of the prostate are blood vessels and nerves^{1,2}.

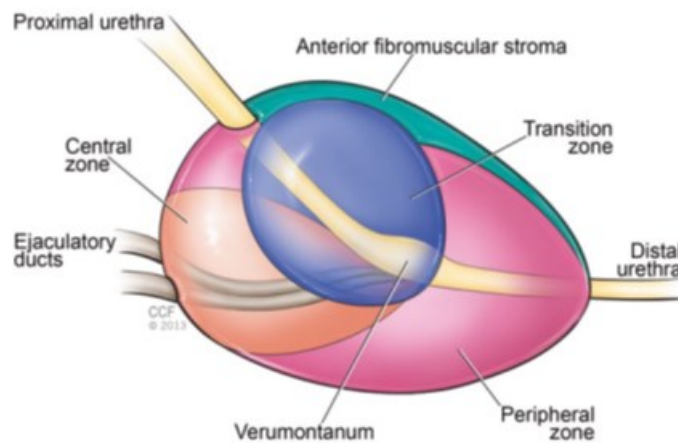


Figure 1.1. Anatomy of the prostate gland. Reprinted with permission from Cleveland Clinic Center for Medical Art & Photography © 2020. All Rights Reserved. Image from Springer Nature: Fine S., Mehra R. (2015) Anatomy of the Prostate Revisited: Implications for the Prostate Biopsy and Zonal Origins of Prostate Cancer³.

The glandular epithelium plays the role of secreting a fluid that together with fluid from seminal vesicles forms semen which is important for sperm health and necessary for normal male reproductive function. The prostatic fluid is rich in proteolytic enzymes and metabolites (lipids and citric acid)². A key proteolytic enzyme is the kallikrein related peptidase 3 (KLK3), clinically referred to as the prostate specific antigen (PSA), which is believed to be important for maintenance of normal semen properties for sperm function². KLK3 is a serine protease implicated in prostate carcinogenesis, leading to its wide use for early detection, diagnosis and staging of prostate cancer (PCa) in the form of the PSA blood test^{2,4}. However, its level is also increased in other prostate disorders, reducing its effectiveness as a precise biomarker of PCa. PSA can be elevated in non-cancer pathologies such as bacterial prostatitis or inflammation that are discussed further herein.

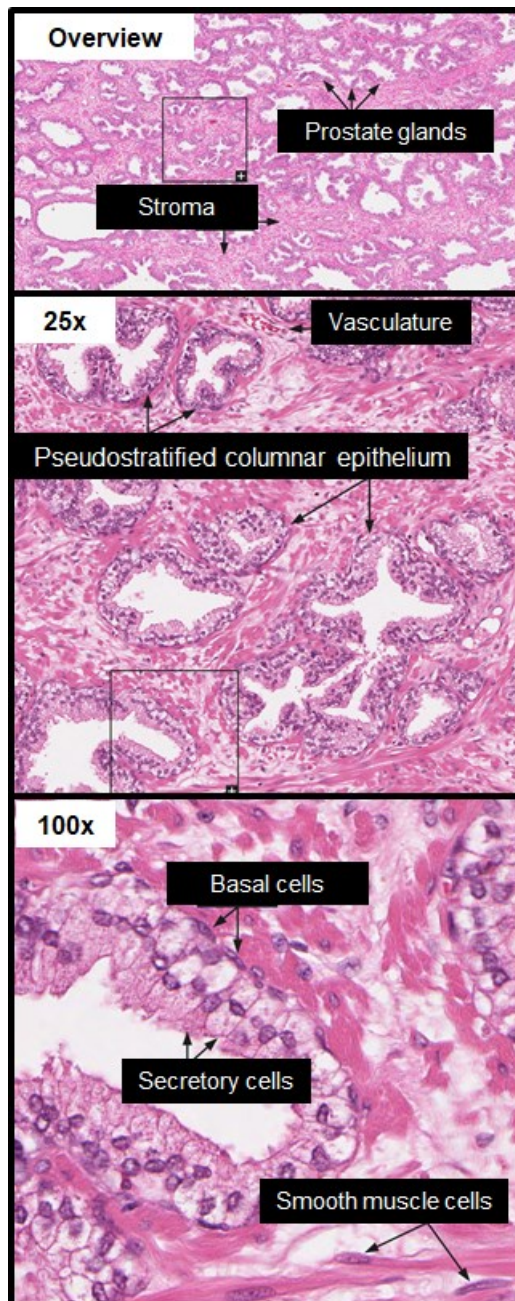


Figure 1.2. Normal prostate physiology. Top image, stroma and prostate glands depicted. Middle image, 25X magnification shows secretory cells and blood vessel. Bottom image, 100X magnification shows basal cell layer supporting secretory cells and smooth muscles cells.

Images credited to and adapted from Human Protein Atlas.

Uhlén M *et al.*, 2015. Tissue-based map of the human proteome. *Science*
<https://www.proteinatlas.org/learn/dictionary/normal/prostate>

1.2. Prostate Cancer

1.2.1. Epidemiology of Prostate Cancer

Prostate cancer is the second most common malignancy in men and the sixth leading cause of cancer death among men globally⁵. Expectedly with population growth and ageing, majority of men are increasingly being diagnosed with localised PCa^{5,6}. The 10-year survival rate can be predicted by disease grade dependent on the type of treatment intervention^{7,8}. One long-term observational study reported that expected mortality rates varied widely with respect to risk category⁹. In high-income countries, the five-year survival rate of prostate cancer is high. The United States has nearly 100% survival rate, 90% in Australia and 85% in the UK, but the mortality rates in Australia and New Zealand are poor in comparison to their Western world counterparts with the latest data from GLOBOCAN indicating that age-standardised mortality rate is 10.2% versus 7.7% in North America⁵. Despite, the survival rates being particularly higher in these developed countries including the greater Western Europe, the mortality rates are lower among non-Caucasian ethnic minority groups, particularly men of African descent. Pettaway et al conducted a prospective cohort follow-up study of men with benign prostatic hyperplasia (BPH) where it was established that the risk of prostate cancer diagnosis was 2.2 times in African American than Caucasian men (95% CI 1.48 – 3.35, $p < 0.001$) after adjusting for serum PSA levels¹⁰. In addition, the mortality rates in Africa are reportedly understood to be poor although there are inadequate cancer registries in these countries.

1.2.2. Androgens Receptor Signalling in Prostate Cancer

Androgens are a group of male sex hormones crucial for sexual, reproductive function and development of male primary and secondary sexual characteristics¹¹. Importantly, androgens promote the maturation and function of the prostate. Systemically, androgens are essential for bone and muscle anabolism in men¹². Testosterone is the main sex hormone largely produced by Leydig cells of the testes and adrenal glands through a tightly regulated hypothalamus-pituitary-adrenal (HPA) axis. Testosterone and its more potent, metabolite, dihydrotestosterone (DHT) collectively exert their effects through the androgen receptor (AR)¹³.

AR belongs to the nuclear hormone super-family class of receptors¹¹. AR is a 110-KDa protein composed of four main domains. The N-terminal domain interacts with several co-regulators to effect transcription, DNA-binding domain with two zinc finger motifs to bind to AR target genes promoter regions (androgen response elements (ARE)), the hinge region is important for AR nuclear translocation through microtubules, and ligand-binding domain binds androgens. When androgens bind to AR, they induce a conformational change that causes AR dimerization. The androgen-AR complex then translocates to the nucleus following dissociation of chaperone heat shock proteins (HSP) 90,70¹⁴. AR co-regulators (co-activators or co-repressors) regulate AR function by influencing DNA binding, subcellular localisation, and stability of AR either in its active form or inactive form¹⁵.

Huggins was the first to show overproduction androgens promotes prostate cell proliferation and tumour development¹⁶. Subsequently, initial studies

revealed elimination of androgens decreases the viability of prostate cells, cause cell death and extend patient survival^{17,18}. Even in the absence of androgens, abnormalities in AR structure and function are predisposing contributors to PCa progression at a molecular level which mostly arise following hormonal therapy. These are embodied as gene mutations^{19,20}, overexpression, and amplification²¹ and how they support aggressive forms of PCa has been previously extensively reviewed^{15,22,23}.

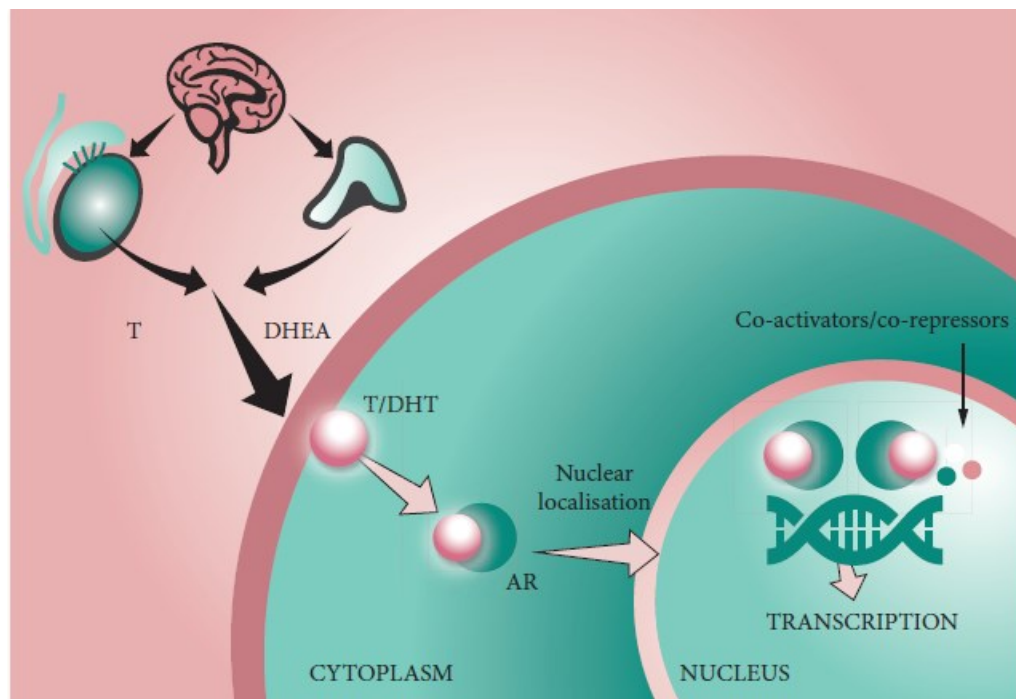


Figure 1.3. Androgen signalling in prostate gland.

Reproduced with permission from John Wiley and Sons: Schalken *et al.*, 2016 Enzalutamide: targeting the androgen signalling pathway in metastatic castration-resistant prostate cancer BJU International²⁴. T- testosterone, DHT – dihydrotestosterone , DHEA – dehydroepiandesterone.

1.2.3. Prostate Pathophysiology

Prostate cancer is a highly heterogeneous disease with the occurrence of multiple lesions at different tumorigenic stages within one gland. Although, these varied lesions are principally driven by dysregulated AR signalling, other different molecular mechanisms such as those mediated by PI3K-AKT-mTOR pathway can accompany, succeed or coordinate with the predominant AR phenotype and lead rise to other more aggressive tumours^{25,26}. PCa is clinically referred to as adenocarcinoma. There are multiple forms of non-neoplastic conditions that can precede tumorigenesis at the macroscopic level. These are inflammation, atrophy, adenosis, hyperplasia and metaplasia²⁷.

Inflammation is generally characterised by the appearance of numerous leukocytes bearing dark nuclei within the stroma as an immune response to the presence of cancerous cells or injury. There are three subtypes of inflammation, acute, chronic and granulomatous inflammation. The presentation of acute inflammation takes the form of neutrophil invasion between epithelial and luminal layers. Chronic inflammation presents with lymphoblastic infiltration at the periglandular and stromal niches and in some cases can be associated with atrophic and squamous changes. Granulomatous inflammation can be caused by viral, bacterial or fungal pathogens, prevailing systemic diseases, post-surgical procedures, or idiopathic (non-specific). Post-procedural granulomatous inflammation is often observed following transurethral resection of the prostate (TURP) or needle core biopsies and may result in tissue necrosis^{28,29}. Acute, chronic and non-specific granulomatous inflammation can be attributed to reduced intraductal drainage capacity or blocked acini and may lead to elevation

of serum PSA levels. The term prostatitis is sometimes used to describe acute or chronic inflammation if it is because of a known prior disease or injury (clinical sequelae)^{27,29}. Atrophy is defined as the reduction of cytoplasmic volume in acini luminal cells and is often reported to accompany prostatitis. It frequently affects the peripheral zone. The proportion of atrophic changes is positively correlated with a rise in serum PSA levels. However, the association of atrophy with increased PSA levels has little association with finding adenocarcinoma or high-grade prostatic intraepithelial neoplasia (PIN) within the same or separate biopsies²⁷. Atrophy can be confused with prostatic adenocarcinoma due to similar appearance of nucleoli and infiltration pattern³⁰. Adenosis is the crowding of non-cancerous glands imitating low-grade PIN. It is uncommon and present mostly in the transition zone and regularly observed in TURPs²⁷.

Metaplasia refers to the transformation of terminally differentiated cells to another mature cell type mostly in epithelial tissues^{31,32}. In prostate, it is a frequent auxiliary clinical observation in prostate examinations. There are three types of metaplasia. Transitional and squamous cell metaplasia are challenging to be distinguished from a morphological feature or pathological process observed as mild to moderate nuclear enlargement and nucleoli prominence³⁰. Mucinous metaplasia is characterised by apical cells rich in mucin, a glycosylated protein complex. Both these forms of metaplasia are often secondary findings. The third type, nephrogenic metaplasia, is characterised by expression of renal tubular cells along the epithelium of the urothelial tract. This type is linked with chronic or acute inflammation with frequent oedema of the stroma²⁹. All forms of metaplasia can be mistaken for prostate adenocarcinoma due to the similar differentiation pattern of epithelium. Ganglia and peripheral nerves are normal

structures that can permeate the prostate gland. Interestingly, the collection of these cells/tissue within the gland as part of the parasympathetic/sympathetic nervous system can mimic prostate adenocarcinoma²⁷.

Benign prostatic hyperplasia (BPH) is a non-cancerous increase in the quantity of cells in the prostatic epithelium or stroma, an early stage of prostate carcinogenesis. It is the most prevalent urologic condition in men³³, and it is more frequent with age³⁴. Hence, BPH is widespread in majority of elderly men. Importantly, it is the most common non-cancer related cause of elevated serum PSA levels. BPH has been strongly histologically associated with chronic inflammation in several population diverse studies³⁵. Basal cell hyperplasia (BCH) is the proliferation of basal cells within nodular glands and cells are described as basophilic because of minor cytoplasm. It is reported to be more common in the transition zone and linked with anti-androgen therapy in non-neoplastic and normal prostate^{36,37}. Leuprolide is known to induce marked atrophy in prostate carcinoma^{38,39}, while a study by Yang and colleagues found no significant histological changes induced by finasteride including BCH⁴⁰. Collectively, pathologists and clinicians are recommended to be aware of these wide-ranging morphological changes effected by hormonal therapy as they can be confusing with treatment-naïve biopsies for better disease management. The current clinical practice is that prostate biopsies following neoadjuvant therapy are not clinically graded.

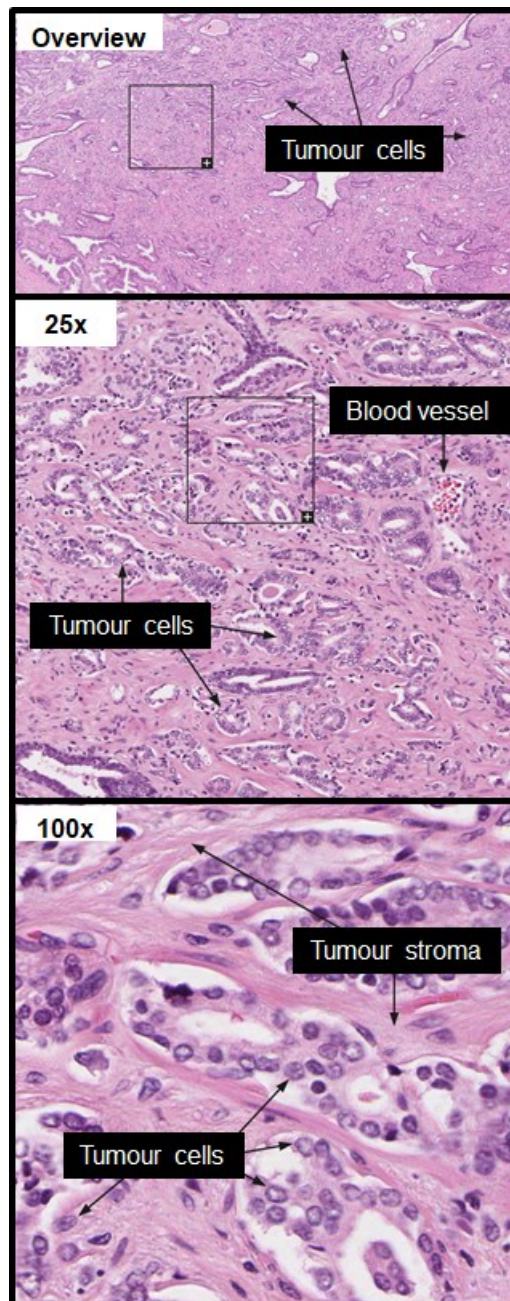


Figure 1.4. Prostate cancer pathophysiology. Top image, tumour cells in prostate gland. Middle image, 25X magnification shows tumour cells and blood vessel. Bottom image, 100X magnification shows stroma adjoining tumour cells. Images credited to and adapted from Human Protein Atlas. Uhlen M *et al.*, 2017. A pathology atlas of the human cancer transcriptome. *Science* and Thul *et al.*, 2017. A subcellular map of the human proteome. *Science*. <https://www.proteinatlas.org/learn/dictionary/pathology/prostate+cancer>

1.2.4. Clinical Diagnosis of Prostate Cancer

Concomitant with the Gleason scoring system, the clinical diagnosis of PCa relies on digital rectal examination (DRE), serum PSA, trans-rectal ultrasound (TRUS) and pelvic nuclear magnetic resonance imaging (MRI) scan⁴¹. Incepted in the late 1980's, a blood test for PSA test has greatly enhanced PCa detection⁴². Despite being also elevated in prostatitis and other non-malignant conditions, a key clinical trial by Catalona and colleagues concluded that PSA remains as the single most important independent predictor of PCa occurrence than either DRE or TRUS and measuring PSA metrics also aids diagnosis of indolent disease⁴³. A commonly accepted threshold value for diagnosis is 3.0 ng/ml⁴⁴ but this is not an agreed standard. There is no global guideline for PSA screening and there are different PSA testing recommendations for various geographical regions^{45,46}. American, European and Australian guidelines have various specifications with age being the biggest question as to which men will benefit from screening⁴⁷⁻⁴⁹. Following initial screening that shows above threshold PSA values, and in consideration of patient's physical symptoms, the physician may perform a DRE. If nodules are detected, TRUS is used to guide biopsy sampling and a multiparametric MRI may be required to rule out PCa or check if it's contained. While many patients cannot access multiparametric MRI due to cost limitations, the prostate-specific membrane antigen (PSMA) is probed by PET scanning as an additional clinical staging tool^{41,50}. PSMA is a glycoprotein overexpressed in PCa cells and is highly specific to PCa often associated with high Gleason scores²⁸.

Diagnosis of PCa means subsequent staging of the disease. PCa staging is done by assessing the size and extent of tumour, lymph node involvement, spread to other organs or bone using the TNM (tumour, node, metastasis) classification system. T (Tumour) signifies the level of cancer invasion (1-4) – the higher the number the further the tumour has spread checked by DRE. N (Nodes) indicates whether lymph node are affected (0-3) to describe how much the tumour has spread to lymph nodes in the bladder region and M (Metastasis) denotes whether the cancer has spread to other body parts, M0 no distant metastasis, M1 distant metastasis⁵¹. **Table 1.1** below summarise the TNM system in conjunction with other clinical parameters such as PSA at diagnosis and Gleason score of biopsies.

T	N	M	PSA (ng/ml)	Gleason Grade	AJCC Stage
cT1a-c, cT2a	N0	M0	<10	1	I
pT2a	N0	M0	<10	1	I
cT1a-c, cT2a	N0	M0	≥ 10 < 20	1	IIA
pT2	N0	M0	≥ 10 < 20	1	IIA
cT2b-c	N0	M0	< 20	1	IIA
T1-2	N0	M0	< 20	2	IIB
T1-2	N0	M0	< 20	3	IIC
T1-2	N0	M0	< 20	4	IIC
T1-2	N0	M0	≥ 20	1-4	IIIA
T3-4	N0	M0	Any	1-4	IIIB
Any T	N0	M0	Any	5	IIIC
Any T	N1	M0	Any	Any	IVA
Any T	Any	M1	Any	Any	IVB

Table 1.1. TNM classification system of prostate cancer. Buyyounouski M *et al.*, 2017. Prostate cancer – major changes in the American Joint Committee on Cancer 8th Edition Cancer Staging Manual. *CA: a cancer journal for clinicians*⁵⁰.

PCa may have no signs or symptoms in its early stages. Symptoms may include nocturnal frequent urination, painful urination, blood in semen or urine, pelvic discomfort, erectile dysfunction and overall physical lethargy. However, these symptoms may be caused by a myriad of conditions, including BPH. With the onset of prostate adenocarcinoma, tissue morphology remarkably changes according to the disease continuum concept proposed by Bostwick⁵². It starts with normal glands. BPH is not linked to and does not increase the risk of PCa carcinogenesis, but both may be accompanied with inflammation or atrophy²⁸. Proliferative inflammatory atrophy (PIA) can degenerate to prostatic intraepithelial neoplasia (PIN) characterised by increasing in-budding of epithelial cells and poor basal cell differentiation. PIN can further be categorised and classified as either low grade- or high grade-PIN depending on cellular abnormality. There is growing acceptance that high-grade PIN is a precursor of adenocarcinoma in spite of little evidence^{52,53}. Adenocarcinoma is characterised by overcrowding and disarrangement of epithelial cells with complete loss of glandular structure. The disappearance of basal cells is a strong immunohistological indicator of malignancy and metastatic potential of the disease, where the tumour cells can grow substantially to infiltrate seminal vesicles or rectum or undergo angiogenesis and intrude into the surrounding vasculature or lymph nodes. This is the most severe form of PCa.

The pathological diagnosis of PCa is reliant on three main properties, architectural, nuclear and luminal features²⁸. Architectural features pertain to the level of differentiation of tumour cells within glands which can be described as either poor or well-differentiated and sharpness of the luminal borders. Nuclear features include the enlargement, prominence and hyperchromatic appearance

of nuclei. Luminal features comprise the exhibition of a blue-tinged intraluminal mucin, sharp rhomboid crystalloids together with eosinophilic secretions and lack of corpora amylacea⁵⁴. Presently, PCa is scored using the 2005 ISUP modified Gleason grading system⁵⁵ where the two most predominant grades, histologically observed features using haematoxylin and eosin (H&E) staining in the biopsied tissue are summed to give a score⁵³. The pathological use of the Gleason Grading system has been extensively reviewed before³. For instance, Gleason Score (GS) 7 cancer can be constituted of a Gleason grade 4 tumour in either core of the prostate followed by the second dominant tumour pattern, Gleason grade 3, and denoted as GS 4+3 or vice versa⁵⁶. The 2014 ISUP Gleason Grading conference adopted the amalgamation of Gleason scores to be in line with other carcinomas, where Grade Group (GG) 1 is comprised of GS (3+3 or 3+2 or 2+3 or 2+2). This reduced the oddity that GS 6 prostate tumours are the most differentiated and further resolve the ambiguity of GS 7 tumours^{47,57}. In current practice, adenocarcinoma is only classified from GS 6 up to GS 10^{53,55}. The Gleason Grade Groups are used to give a prognosis whereby GG1 (GS ≤6) patients have low risk PCa, GG2 (GS7) have intermediate risk and both GG4 (GS 8) and GG5 (GS 9 or GS10) have high risk disease. The ISUP pathological grading is used together with the TNM classification system for disease management^{47,50}.

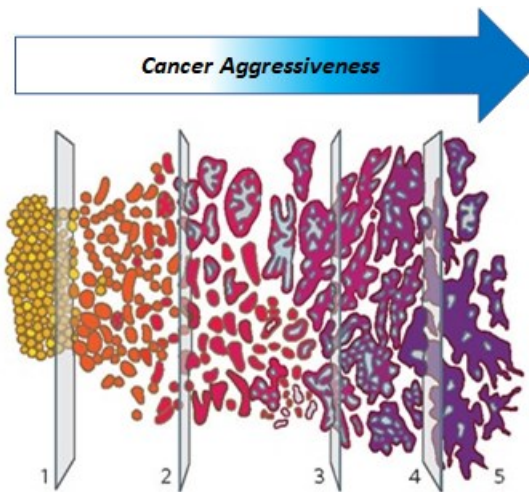


Figure 1.5. Gleason grading of prostate cancer. Pathological scale ranging from Gleason grade 1 to Gleason grade 5 depicting well differentiated to poorly differentiated glands. Adapted with permission from <https://www.prostate.org.au/>

1.2.5. Standard Care and Treatment of Prostate Cancer

The decision-making process for PCa treatment is complex for urologists, oncologist and patients and is dependent on several factors like physical wellbeing, age and stage of disease at diagnosis. Selection of treatment options can vary by country, region and often influenced socio-economic backgrounds^{44,58}. Radiation works by using radiation to kill prostate tumour cells. There are two types of radiotherapy: external beam radiation therapy (ERBT) and prostate brachytherapy (PB). ERBT employs high energy X-ray beams focused on the prostate gland from outside the body whereas brachytherapy utilises either low or high dose radioactive material placed within the prostate. Low-dose rate PB is a standard for low-risk localised disease (LRLD)^{47,59} and has been reported to effectively control disease in men at a high risk of relapse as monotherapy⁶⁰.

Radical prostatectomy (RP) is a surgical procedure that purposes to remove all the prostate gland and cancer. There are three main forms of RP, open, laparoscopic or robotic assisted^{6,61}.

LRLD is managed using the so-called active surveillance strategy which primarily has a curative intent in men with a life expectancy of more than 10 years^{47,62}. It entails careful PSA testing every 3-6 months. If the PSA trajectory rises, DRE and needle core biopsies are additional measures used to track cancer progression⁶². Application of definitive treatments is guided by minimisation of treatment-related side effects⁴⁷. Many low risk patients prefer surgery and/or radiation to arrest disease progression. The watchful waiting approach can be applied to all patients irrespective of risk level⁴⁴. This method refrains from using any treatment and regular monitoring the patient's status and medical intervention happens if symptoms worsen. Hence, it is opted in advanced disease and palliative settings, and in some men with other prevailing health conditions and with life expectancy of less than 10 years may find it amenable. High-risk localised disease (HRLD) is treatable with radiation and surgery and are employed as curative measures especially in younger men⁷.

Despite a combination of the abovementioned curative-driven approaches, these measures are not always successful in durably treating patients with more aggressive PCa⁶³. Within continued increment of PSA levels, androgen deprivation therapy (ADT) is commenced. ADT works by reducing circulating levels of androgens by medical (chemical) or physical castration⁶⁴. Historically, orchiectomy (the surgical removal of testicles) was common but quickly became psychologically unbearable for many men^{16,65}. Conventional ADT comprises of agonists and antagonists of the hypothalamus-pituitary-adrenal

(HPA) axis to achieve chemical castration. Luteinising hormone releasing hormone (LHRH) agonists work by stimulating the positive feedback loop of the HPA axis, upregulating LHRH synthesis by the hypothalamus to stimulate LH release by the pituitary gland⁶⁵. LH then acts on Leydig cells of the testes to release androgens that bind to AR on glandular prostate epithelia. This initially leads to a flare up of testosterone production that causes pituitary LH release but a longer-term blockade of further LH release (**Figure 1.6**). On the other hand, LHRH antagonists competitively block LH binding to its receptors and do not cause increase testosterone production²².

Initially, PCa is responsive to anti-hormonal therapies such as LHRH agonists and is termed as hormone-sensitive PCa²⁴. If ADT stops working, revealed as progressive increase in PSA levels, the disease is designated as castration-resistant prostate cancer (CRPC)^{66,67}. When this happens targeted anti-hormonal therapies that block androgen production or inhibit AR signalling activity are incorporated into the regimen an approach called complete androgen blockade⁶⁵. In addition, docetaxel and cabazitaxel⁶⁸, from the taxane class of chemotherapeutic drugs are used in combination with ADT to improve treatment response in metastatic CRPC (previously termed hormone-refractory) disease⁶⁹. Taxanes and their derivatives exhibit cytotoxicity in tumour cells by stabilizing proteins that mediate mitosis⁷⁰. However, a recent systematic review highlighted that ADT potentially diminishes taxane efficacy leading to the questioning of the optimal sequencing of taxane and ADT therapy in managing metastatic CRPC in clinical practice⁷¹.

Anti-androgens work to slow down tumour growth (**Figure 1.6**). Androgen production blockers include abiraterone acetate and ketoconazole⁷². Abiraterone

acetate (Zytiga®, Yonsa®) is a second-generation AR inhibitor that is an analogue of testosterone that disrupts testicular androgen biosynthesis and acts as an AR antagonist. It is administered with prednisolone in men with metastatic CRPC⁷³. Bicalutamide (Casodex®) is a first-generation AR inhibitor that competitively inhibits androgen-AR interaction but suffered from low binding affinity and partial agonist activity upon cessation^{74,75}. It was replaced by enzalutamide (Xtandi®, MDV3100) with additional modes of action. Enzalutamide acts on the AR signalling pathway by first disrupting androgen binding, interrupting nuclear translocation of androgen-AR complex and its DNA binding to induce expression of AR regulated genes, including PSA⁷⁵. However, even with highly potent anti-AR drugs such as enzalutamide, durable disease control remains unattainable and survival is prolonged only by around 18 months^{76,77}. mCRPC manifests as secondary neoplasms of the bone and liver which is unfortunately lethal⁷⁸. Recently, other efficacious second-generation AR antagonists have demonstrated a conferral of greater survival benefit to patients at a high-risk of metastatic PCa^{79,80}. Darolutamide and apalutamide have been evaluated with men with non-metastatic CRPC and now clinically approved in USA, Canada and Australia⁷⁹⁻⁸¹.

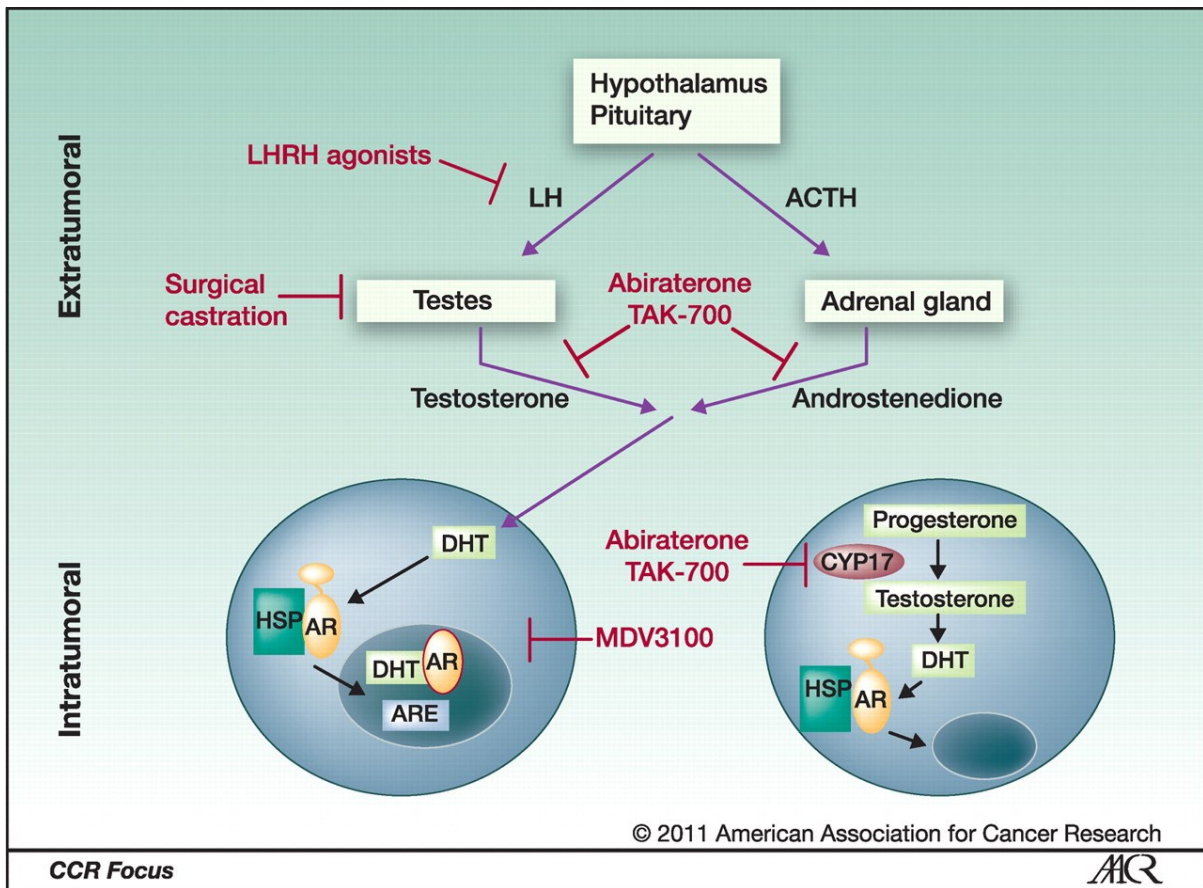


Figure 1.6. Clinical strategies for targeting AR signalling pathway in prostate cancer. Reproduced with permission from AACR: Massard *et al.*, 2011. Targeting continued androgen receptor signalling in prostate Cancer. *Clinical Cancer Research*⁸².

Agent	Classification	Potency	Usage	Year of release
Finasteride	5 α -reductase 2 inhibitor	pIC ₅₀ 7.8	BPH	1992
Leuprolide	GnRH ₁ agonist	pIC ₅₀ 9.1	Advanced PCa	1985
Goserelin acetate	GnRH ₁ agonist	–	Hormone sensitive PCa	1989
Degarelix	GnRH ₁ antagonist	pK _i 8.8	Hormone sensitive PCa	2008
Abiraterone acetate	17 α -monooxygenase inhibitor	–	Refractory PCa along with prednisolone	2011
Flutamide	AR antagonist	pK _i 5.4	local metastatic PCa	1989
Bicalutamide	AR antagonist	pK _i 7.7	metastatic PCa along with LHRH agonists	1995
Nilutamide	AR antagonist	pIC ₅₀ 7.1	local PCa	1996
Enzalutamide	AR antagonist	pK _i 7.1	Advanced, mCRPC	2012
Apalutamide	AR antagonist	pK _i 7.0	Advanced, m/CR(S)PC	2018
Darolutamide	AR antagonist	pK _i 8.0	CRPC with resistance F876L mutation	2019
Docetaxel	β -tubulin class 1 inhibitor	–	Advanced mCRPC along with ADT	1996
Cabazitaxel	β -tubulin class 1 inhibitor	–	Advanced mCRPC along with ADT + prednisolone in docetaxel failure	2010

Table 1.2. Drugs approved for the treatment of prostate cancer. Pharmacological agents used in current clinical practice approved by the Food and Drug Administration (FDA) and/or European Medicines Agency (EMA). <https://www.guidetopharmacology.org/>

1.2.6. Biomedical Challenges in Prostate Cancer Research

Recent research shows that the PSA test is highly sensitive but not specific for prostate carcinomas⁸³. PSA levels are often elevated in most men with advancing age who have benign enlargement of the prostate (BPH) and also in men with bacterial prostatitis⁸⁴. Therefore, the PSA test can indicate levels that meet the threshold for diagnosis even in such men with well differentiated, non-cancerous tissue thereby resulting in wide “over-diagnosis and over-treatment”⁸⁵. In contrast, there have been cases of advanced grade tumours with below cut-off PSA levels⁸³. Two large clinical studies, the European Randomized Study for Prostate Cancer (ERPSC) trial^{86,87} and the United States Prostate Lung Colorectal and Ovarian Cancer (PLCO)^{88,89} screening trial, are not in agreement that annual PSA testing does not confer significant survival benefit⁹⁰. Moreover, PCa cannot be definitively ruled out at any PSA threshold⁹¹. Its use remains controversial as a conventional test for PCa diagnosis, hence representing an important clinical challenge^{92,93}. This has necessitated new guidelines that recommend less frequent PSA screening as exemplified by the U.S. Preventive Services Task Force⁴⁶. Case detections of generally low Gleason grade prostatic carcinomas previously required onset of standard therapy which was recommended for such patients instead of careful monitoring⁴². Importantly, it is hard to predict if low Gleason grade carcinomas will remain indolent or progress to active disease⁹². This predicament makes oncologists resort to treating PCa as the “safest option” and leading to over-treatment of many tumours that were unlikely to progress or become life-threatening. Hence, this challenge is being addressed by the search for molecular biomarkers to amplify the prognostic

power of the Gleason grade and PSA test^{94,95}. Yet, available molecular markers have not been able to truly improve the sensitivity of these methods.

Since altered metabolism has been widely accepted as an emerging hall mark of cancer⁹⁶, the past 20 years have seen a strategic change in focus of PCa research. In addition, increased obesity⁹⁷ and high dietary fat⁹⁸ are also acknowledged as correlated factors to the risk of developing the disease⁹⁹. Herein, the role of lipids in prostate tumorigenesis is explored in detail and this research project aimed to investigate the potential of lipid molecules as biomarkers of PCa aggressiveness and treatment response utilising mass spectrometry imaging. To begin with, the following section offers an insightful look into lipid biochemistry.

1.3. Lipid Biochemistry

Lipids are important constituents of cell and organelle membranes¹⁰⁰, energy storage macromolecules¹⁰¹ and function as intracellular signalling molecules¹⁰². Lipids are an interesting class of biomolecules because of their rich diversity in eukaryotic systems. For instance, phospholipids (PL) structure is based on a glycerol backbone which can combine with any of six headgroups at the *sn*-3 position (unsubstituted phosphate, choline, ethanolamine, serine, inositol or glycerol) and different conformers of esterified fatty acyl chains at the *sn*-1 and *sn*-2 positions precedes the existence of species numbering in their hundreds for each subclass^{103,104} as depicted in **Figure 1.7**. Another important template that increases lipid diversity is the sphingoid base for ceramides (Cer) and sphingomyelins (SM) classes. Fatty acids (FA) are composed of carboxylate group with long hydrocarbon (acyl) chain.

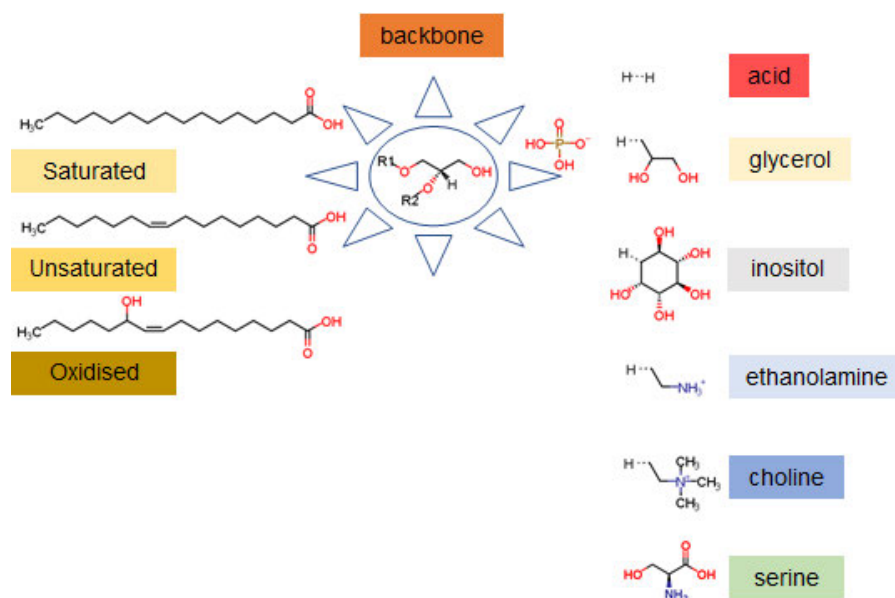


Figure 1.7. Phospholipid building blocks. Diversity of glycerophospholipids arising from a simple glycerol backbone leads to different subclasses dependent on degree of fatty acyl saturation, oxidation and headgroup substitution at the phosphate ion.

FA are key constituent and intermediates of lipid haemostasis involved in glycerophospholipid, glycerolipids and sphingolipid metabolism. FA synthesis begins with citrate conversion to acetyl-CoA in the cytoplasm by ATP-citrate lyase (ACLY)¹⁰⁵. Acetyl-CoA carboxylase (ACC) then incorporates a carboxylate ion into acetyl-CoA generating malonyl-CoA which is then converted to an acetoacetyl group all held by an acyl carrier protein¹⁰⁶. Fatty acid synthase (FASN) performs 7 more iterations of acetyl-CoA condensation yielding palmitic acid, the simplest fatty acid composed of 16 hydrophobic carbons that are fully saturated (C16:0)^{107,108}. Palmitic acid can undergo series of anabolic reactions that lead to the synthesis of more complex FA that are elongated (ethylation reaction) and/or desaturated (double bond insertion) to produce divergent saturated fatty acid (SFA) and monounsaturated fatty acids (MUFAs)¹⁰⁹. In mammals, desaturation occurs at the Δ^9 carbon of almost exclusively even numbered FAs which results in *cis*-configured MUFAs^{110,111}. Examples of common MUFAs are palmitoleic acid (9 *cis*-C16:1) and oleic acid (9 *cis*-C18:1). Polyunsaturated fatty acids (PUFAs) like linoleic acid (C18:2) and α -linolenic acid (C18:3) are found in plants thus rendered essential and only obtained from the diet. They respectively serve as precursors for arachidonic acid (AA) and eicosapentaenoic acid (EPA) that can be incorporated into PL¹¹². Conversely, AA (C20:4) and EPA (C20:5) are released from the plasma membrane by phospholipase A₂ to serve as substrates for synthesis of prostaglandins that acts as intracellular signal transducers in mediation of complex inflammatory responses¹¹².

The major pathways of PL synthesis begin with diacylglycerol (DAG) or phosphatidic acid (PA) templates ([Figure 1.8](#)). Glycerol-3-phosphate, an

intermediate of glycolysis provides the glycerol core for PA synthesis that undergoes interconversion to DAGs via the Kennedy pathway¹¹³. DAGs are key substrates for the major *de novo* synthesis pathway of phosphatidylcholine (PC), phosphatidylethanolamine (PE) and phosphatidylserine (PS). The DAG route involves the activation of the respective headgroups of PC and PE covalently anchored to cytidine diphosphate (CDP) by cytidyltransferase¹¹³. PS is synthesised by a headgroup reversibly exchanged of the serine moiety with ethanolamine. PS, PE and PC can be interconverted by an intricate mechanism in the mitochondria and endoplasmic reticulum (ER). However, the trimethylation of PE to PC is not reversible^{114,115}.

In the CDP-diacylglycerol pathway, phosphatidylglycerol (PG) and phosphatidylinositol (PI) synthesis begins with a PA template that attacks a cytidine triphosphate (CTP) to yield a CDP-diacylglycerol¹¹⁶. CDP-diacylglycerol can then react with inositol to yield PI catalysed by a PI synthetase. CDP-diacylglycerol can also undergo a synthetase reaction with glycerol-3-phosphate, a reduction product of dihydroxyacetone phosphate (DHAP) from aerobic glycolysis, to yield phosphatidylglycerol-3-phosphate which in turn undergoes hydrolysis to yield PG. Two molecules of PG undergo condensation to yield cardiolipin (CL)¹¹⁴. A proportion of DAGs are used for synthesis of TAGs which form lipid droplets that acts as intercellular energy stores. Palmitoyl-CoA and other activated FAs together with serine are be coupled into sphinganine for Cer synthesis via synthases reactions in the ER¹¹⁷. Importantly, a cellular nexus of lipid metabolic relationship is mediated by sphingomyelin synthase where phosphorylcholine from PC is transferred Cer to yield SM and DAGs in the Golgi and plasma membrane¹¹⁷.

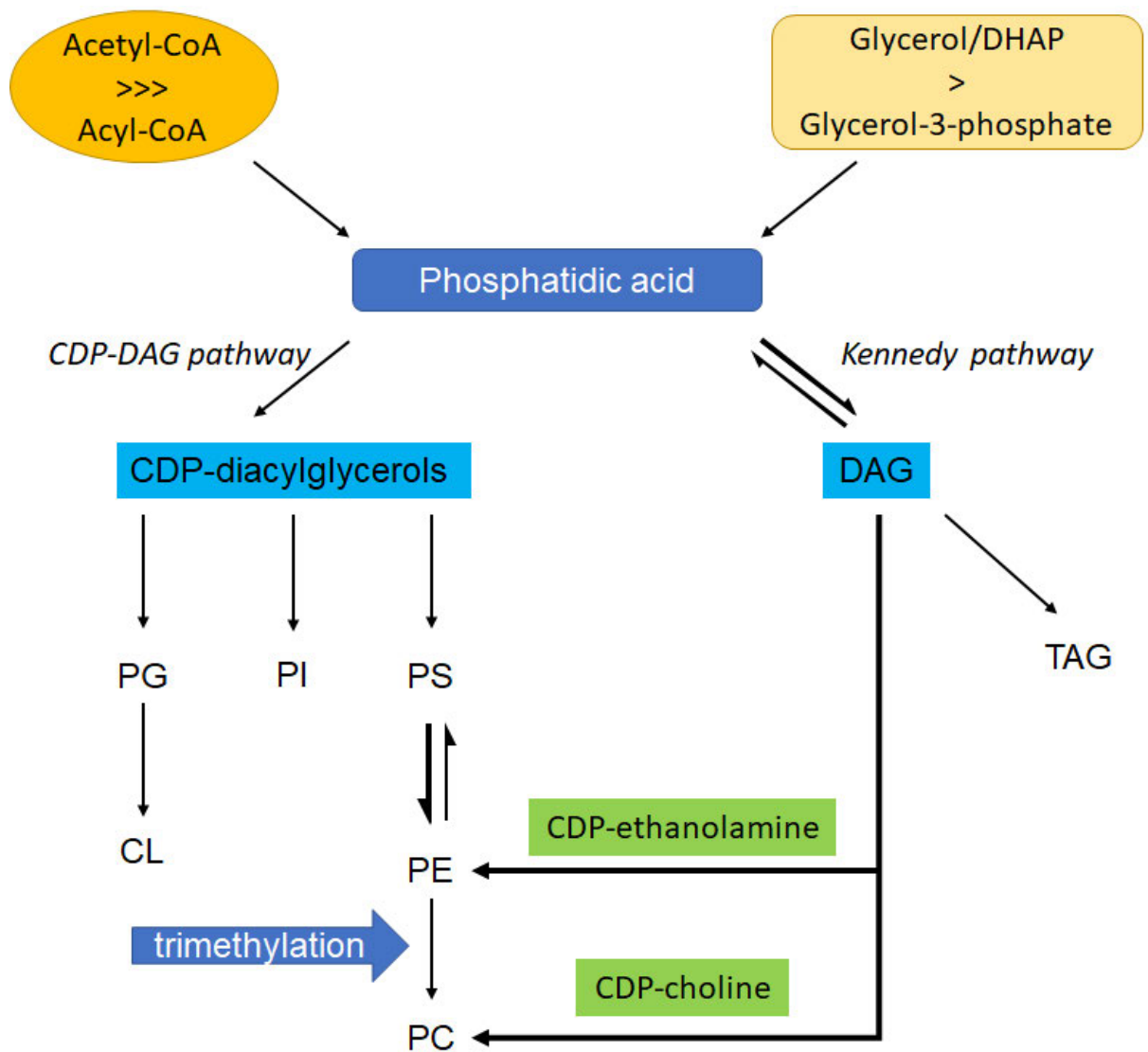


Figure 1.8. Overview of phospholipid metabolism in eukaryotic systems.
 Adapted with permission from author. <https://lipidmaps.org/resources/lipidweb>

Lysophospholipids (LPL) are an important subclass of glycerophospholipids that impact on PL content. LPL contain a monoacylglycerol and their metabolic balance with PL maintained by the Lands cycle¹¹⁸. LPL are acted upon by headgroup-specific lysophospholipase enzymes to generate lysophosphatidic acid (LPA) with lysophosphatidylcholine (LPC) as the main extracellular source¹¹⁹. Lysophospholipase D is abundant in serum and has been detected in seminal fluid. Intracellular autacoid action by phospholipase A₁/A₂ produces LPA from PA, which can also be produced by freeing choline from PC mediated by phospholipase D¹²⁰.

Around 60% of total lipids in most mammalian cells are PL and approximately 10% are sphingolipids. 0.1% - 40% are neutral sterol lipids depending on cell type and organelle¹²¹. Generally, PL are major constituents of cell and organelle membranes of the ER, mitochondria, Golgi apparatus and endosomes. PC are the most prominent lipids in the plasma membrane, followed by PE, PS, SM and PI as outlined in **Table 1.3**. Overall, lipids represent a structurally diverse class of compounds that are highly abundant in an assortment of human tissues¹¹⁵. In the prostate gland, sterols such as androgens regulate transcription of key genes, glycerophospholipids such as PC are critical structural components and glycerolipids such as TAG are energy storage molecules that can fuel cell growth and proliferation¹⁰⁹. Androgens are a class of steroid hormones that play critical roles in the prostate gland and their genomic and metabolic roles in PCa is the focus of the next section.

Lipid	Plasma membrane	Endoplasmic reticulum	Mitochondrion	Golgi	Late endosomes
PC	45%	55%	50%	45%	50%
PE	23%	30%	25%	15%	20%
PI	5%	15%	10%	10%	2%
PS	10%	5%	2%	5%	1%
SM	17%	—	—	12%	—
CL	—	—	12%	—	—
Cholesterol:PC molar ratio	1.0	0.15	0.1	0.2	0.5

Table 1.3. Lipid synthesis expressed as a percent composition of different organelles. The tabular data of major lipid categories was read from graphical representation; van Meer, G, Voelker, DR & Feigenson, GW 2008, 'Membrane lipids: where they are and how they behave', *Nat Rev Mol Cell Biol*, 9:112-124.

1.3.1. Lipid Metabolism in Prostate Cancer

Lipid metabolism ultimately begins with the provision of glycolytic pathway products and intermediates of tricarboxylic acid cycle (TCA)¹²². Indeed, PCa cells adapt to alternate metabolic pathways including isoform switching and non-canonical enzymes of the pentose phosphate pathway to promote fatty acid synthesis¹²³. PCa cells require exogenous and *de novo* FAs to support their highly proliferative phenotype for new membrane biogenesis¹²⁴. Within the lipid bilayer, preferential localisation of cholesterol and glycosphingolipids in the form of lipid rafts initiates membrane signalling and in association with membrane proteins, supports cell multiplication¹²⁵⁻¹²⁷. Deregulated lipid metabolism is orchestrated by androgens characterised by two main mechanisms - heightened enzyme mediated lipid oxidation and anabolism¹²⁸.

First, cancerous cells show increased *de novo* lipogenesis, uptake and metabolism. FASN is regarded a key oncogenic enzyme¹²⁹. It is overexpressed in many cancer types including prostate cancer¹³⁰ and its expression is regulated

by the AR signalling pathway¹³¹. Similarly, under metabolic stress, acetate is greatly recruited for acetyl-CoA synthesis¹³² which may potentially provide more substrate for FASN activity. Acetyl-CoA synthetase (ACS) expression has been correlated with PCa progression¹³³. Additionally, cholesterol biosynthesis enzymes, 3-hydroxy-3-methylglutaryl-CoA (HMG-CoA) synthase and farnesyl-diphosphate -farnesyltransferase and -synthase, are concomitantly over expressed in PCa^{134,135}. Notably, restoration of effects of lipogenic enzymes following testosterone treatment in an orchidectomy rat model has been reported¹³⁵.

Second, PCa cells accumulate lipids in hypoxic conditions from adipose tissue by increased lipase activity¹³⁶ and store them as droplets for supplying energy to meet proliferation requirements¹³⁷. Assimilated exogenous lipids are processed to generate mainly SFAs and MUFAs¹³⁸, thus its plausible for glands in BPH to have markedly varied membrane lipid composition compared to normal stroma and epithelium. Actually, as a tumour grows the centre becomes denser as the oxygen gradient relatively declines inside the malignant tissue, evidenced by increased levels of mitochondrial β -oxidation¹³⁹. Prostate tumours express higher levels of hypoxia inducible factor-1 α (HIF1 α), an oxygen-sensitive protein^{140,141}. Under normoxic conditions, HIF1 α is polyubiquitinated by the action of prolyl hydroxylase and tagged for proteasomal degradation¹³⁶. Interestingly, HIF1 α has also been implicated in the upregulation of FASN via the Akt/mTORc pathway¹⁴². Another facet of hormonal control of aberrant lipid metabolism involves the cholesterol transporter ATP-binding cassette in androgen dependent cells¹⁴³.

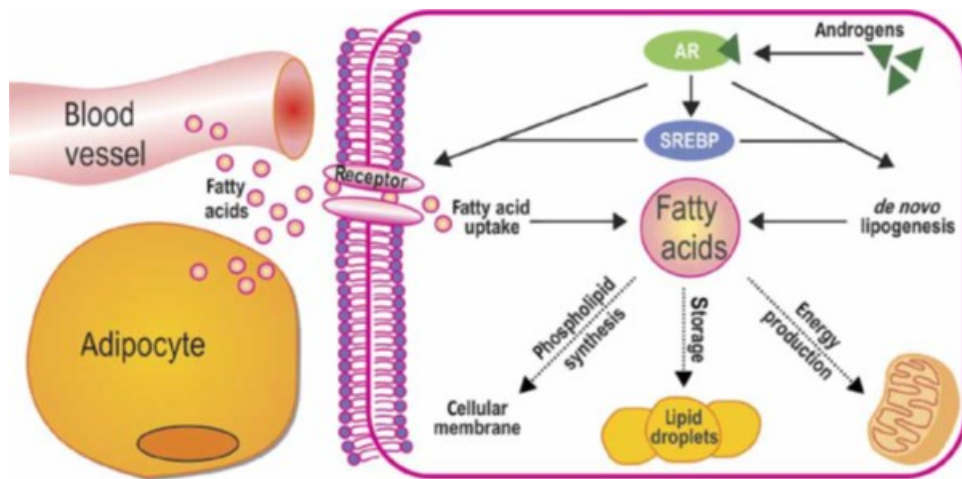


Figure 1.9. Overview of androgen regulated lipid metabolism in prostate cancer. Reproduced with permission from Bioscientifica Limited: Butler *et al.*, 2016. Androgen control of lipid metabolism in prostate cancer: novel insights and future applications. *Endocrine-Related Cancer*¹³⁸.

In a classic study, Swinnen *et al.*, demonstrated using PCa cell lines that androgens drive an organised gene program of lipogenesis^{131,144} but the link between lipid metabolism and PCa progression remains unclear. One mechanism by which the AR signalling axis induces transcriptional regulation is via activation of sterol regulatory element-binding proteins (SREBP) which bind sterol response elements (SRE) on DNA to activate the expression of various enzymes that modulate lipid homeostasis as shown in **Figure 1.9**. SREBP has three major isoforms -1a, 1c and 2¹⁴³. Dormant SREBP is bound to the ER by SREBP cleavage activating protein (SCAP) and insulin induced genes (INSIG) which is controlled by intracellular sterol levels¹⁴⁵. Another mechanism is direct AR regulation of lipid metabolism genes with AR as a transcription factor that induces androgen response elements (ARE) in the DNA. This results in SCAP transcriptional activity on the Golgi apparatus leading to expression of lipogenesis and FA uptake enzymes^{138,146}. Remarkably, immunohistochemical

staining of positive SREBP-1 expression has been associated with increase in pathological Gleason grades compared to benign tissues¹⁴⁷, which implicates SREBP-1 dysfunction promotes tumour progression. A more recent review by Pouluse *et al.*, paints a clearer picture of aberrant lipid metabolism with novel insights of genomic drivers of tumour growth and metastasis in PCa in PTEN-null mouse studies¹⁴⁸. PTEN is a critical tumour suppressor gene. First, overexpression of pyruvate dehydrogenase complex regulated by PDHA1 provides added acetyl-CoA that facilitates histone deacetylation of SREBP. Second, hyper activation of MAPK signalling by co-deletion of another tumour suppressor gene PML also promotes SREBP activity. Collectively, both mechanisms support epigenetic regulation of SREBP-target genes which regulate key *de novo* lipogenesis genes as indicated in **Figure 1.10.** below.

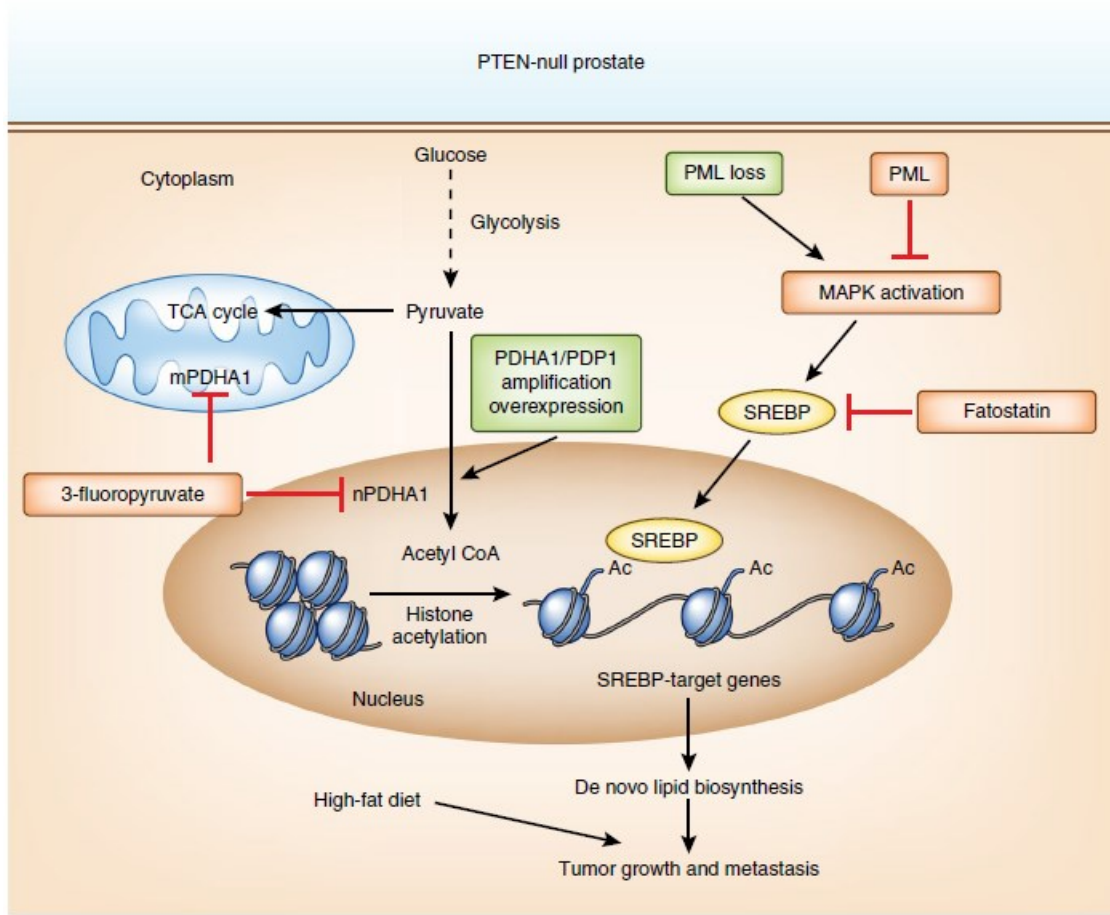


Figure 1.10. Novel genomic mechanism of aberrant lipid metabolism in prostate cancer. Reprinted with permission from Springer Nature: Poulose *et al.*, 2019. Genetics of lipid metabolism in prostate cancer *Nature Genetics*¹⁴⁸.

This aforementioned literature exposition establishes a critical research gap where lipidomics analysis by mass spectrometry has the capability to identify novel lipid biomarkers of prostate cancer aggressiveness with respect to pathological tumour grades.

1.4. Introduction to Mass Spectrometry

Lipid abundancies are reflective of different metabolic functions in cells and pathophysiological changes due to cancer or other diseases¹⁴⁹⁻¹⁵². The detection and measurement of lipids is largely conducted by mass spectrometry which is undoubtedly the most powerful technique to match up to their multiplicity.

Mass spectrometry (MS) is the production of gas-phase charged ions from molecules, these ions are measured in the form a mass-to-charge (m/z) ratio using a mass analyser (spectrometer)¹⁵³. The ions are detected as analogue electrical signals for example using a microchannel plate or fast secondary emission multiplier^{154,155}. The analogue signal is converted into a digital output using an oscilloscope coupled to a computer that further processes the signal into graphical data. A single mass spectrum is composed of multiple types of ions visualised in form of peaks, their area corresponding to the intensity or abundance of the detected signal. MS is at least a four step process: sample preparation, ionisation, mass separation and detection¹⁵⁶. Additionally, samples may be fractionated prior or post ionisation for examples using chromatography.

Sample preparation is determined by the application of the MS technology. For biological applications, ultra/high performance liquid chromatography (U/HPLC) is the most common technique prior to MS analysis of lipids. Ionisation sources include matrix-assisted laser desorption/ionisation (MALDI), electrospray ionisation (ESI) and desorption electrospray ionisation (DESI) which are increasingly being adopted for metabolomics and lipidomics studies. Sample preparation for LC-MS/MS aims at reducing sample complexity by extraction and isolation of lipids from the biological medium and removing contaminants¹⁵⁷. On the contrary, ESI-based shotgun lipidomics require little sample preparation -

specimens are pulverised by homogenisation and/or sonication in an appropriate solvent prior to direct infusion into the inlet of the mass spectrometer¹¹⁶. Similarly, MALDI and DESI samples do not necessitate extensive preparation as specimens are analysed with the aim of retaining their architecture. The second step involves generation of gas phase ions in an ion source which can be achieved by chemical and/or physical means i.e. atmospheric pressure chemical ionisation (APCI) using buffered salts or laser irradiation to analyte coupled to a chemical matrix^{158,159}. In the final step, the mass analyser separates ions based on their m/z values which are finally recorded by a detector.

The principles of MALDI, LC-MS/MS, DESI, and ESI-shotgun lipidomics are discussed in greater detail in the ensuing sections.

1.4.1. Matrix-Assisted Laser Desorption/Ionisation (MALDI)

The development of MALDI took decades. Early spectroscopists and physicists precepted that it was difficult to separate bioorganic molecules from their physiological environments and convert them to charged particles. Beckley pioneered field desorption. In this technique, analytes (D-ribose and D-glucose) were desorbed and ionised using a wetted wire filament, which upon gradual heating, generated parent ion peaks¹⁶⁰. He observed that very little formations of fragment ions and termed a “soft ionization” method suitable to substances of low volatility. After that, laser desorption was developed in large part by Kistemaker who evaluated the mass spectrum of digitonin using an infrared (IR) CO₂ laser¹⁶¹. The first commercial form of laser desorption was the laser microprobe mass analyser (LAMMA) invented by Hillenkamp and Kaufmann. The instrument used

a 347 nm frequency-doubled ruby ultraviolet (UV) laser or 266 nm frequency-quadrupled Nd:YAG-laser and yielded spectra of inorganic metal ions from 1 μm spots on very thin epoxy resin sections¹⁶²

The term MALDI was devised by Michael Karas and Franz Hillenkamp in the late 1980s¹⁶³. They described a metastable decay of matrices that exhibited formation of quasimolecular ions with fewer spectra at the low range after application of UV laser energy using a LAMMA instrument¹⁶⁴. Shortly after, Tanaka developed a laser ionisation time-of-flight (TOF) system capable of detecting spectra of high mass protein and polymers such as the 34 kDa carboxypeptidase-A¹⁶⁵. Tanaka was awarded a share of the 2002 Nobel Prize for Chemistry for this work. Presently, MALDI is achieved by coating or mixing a sample with a matrix. Interaction of the samples analytes and matrix is key to the desorption and ionisation process. The matrix absorbs radiation energy at the wavelength of the laser. The matrix is typically a small molecule organic compound that transfers thermal energy to the solid mixture causing instantaneous desorption/ionisation of both the matrix and analyte molecules into the gas phase¹⁶⁶. The matrix donates or abstracts a proton from the analyte to generate charged molecules (ions) (**Figure 1.11**). Conventionally, matrices are applied in molar excess of the analyte up to 5,000 fold but better signal intensity of analytes can be achieved using lower matrix concentrations¹⁶⁷.

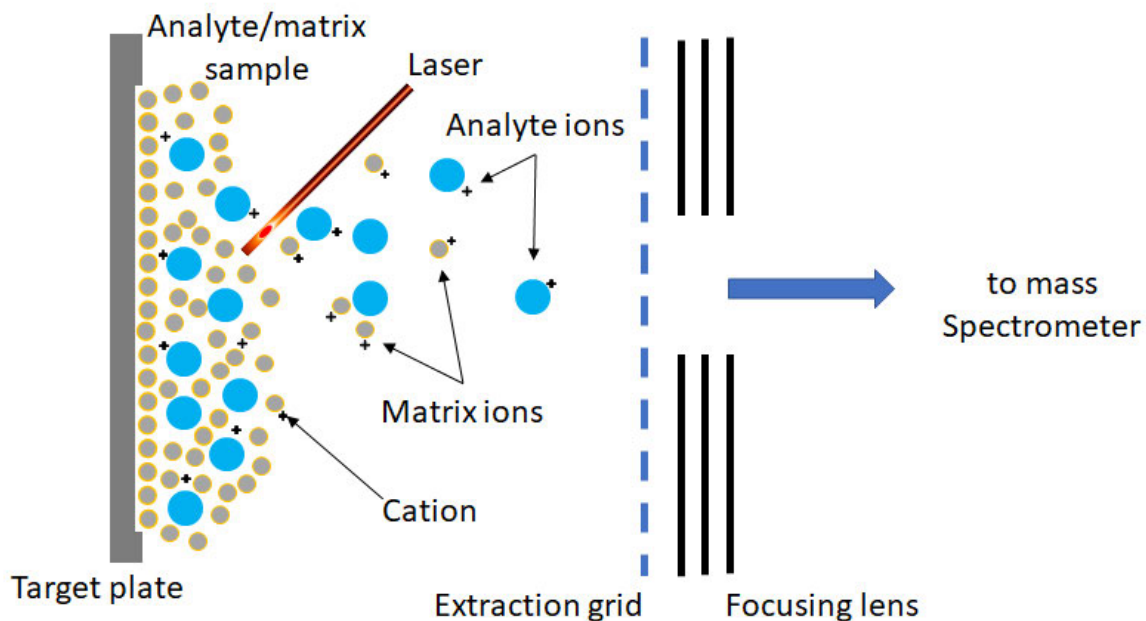


Figure 1.11: Principle of the MALDI process.

1.4.1.1. Ion Formation in MALDI

Despite MALDI technology existing for 30 years, the mechanism of ion formation in MALDI process is still poorly understood and debate is still active within the MALDI community¹⁶⁸. The primary model for understanding UV-MALDI ionisation begins with ionisation of the matrix molecules themselves. As illustrated earlier on, almost all MALDI matrices are organic molecules with aromatic structure and their crystals form stacked π electron systems. In the photoionisation model, ablation of matrix by a laser at a wavelength (λ) creates a plume of photons each with single energy ($h\nu = \frac{hc}{\lambda}$). At least two photons are needed for the photoionisation of a free matrix (M) molecule. During the photoionisation, the matrix molecules become excited with high energy and they are termed excitons. In the case of two excitons, one matrix molecule loses

photon energy, moving to the ground state while its counterpart shifts to a higher excited energy state. In the process, a photoelectron is released by neutral matrix molecule to yield complementary negative and positive radical ions. This model is also known as energy pooling of excited states¹⁶⁹. The process is as follows:

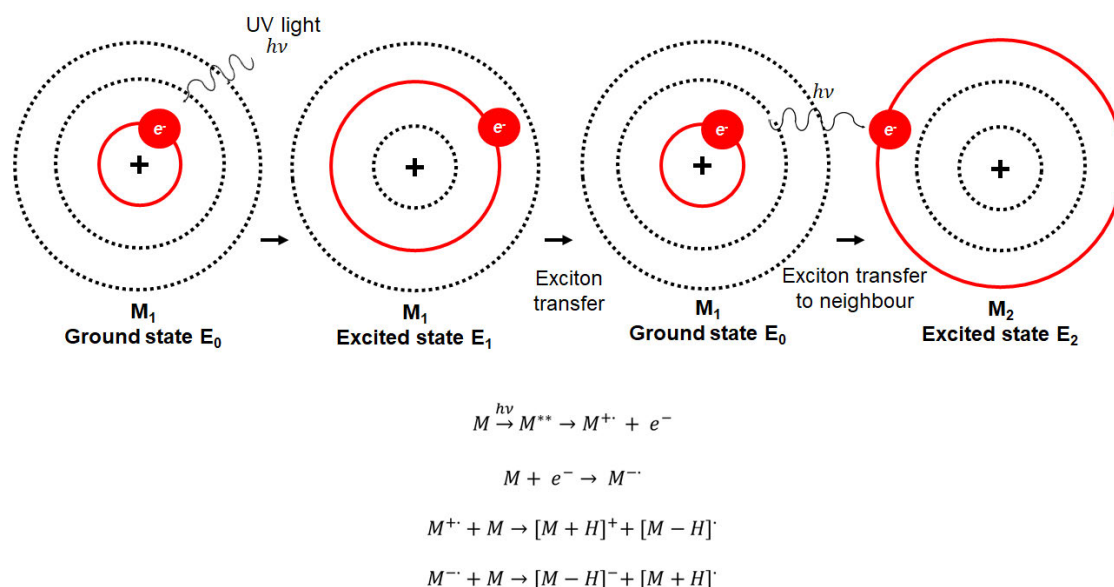


Figure 1.12. Photoexcitation and energy pooling model.

Another, primary ionisation mechanism is the cluster ionisation model proposed by Karas¹⁷⁰. Its precepts are on photoionisation and photochemical reactions but aims to explain why only singly charged ions are mostly formed during MALDI. It assumes that analyte ions are formed in the solid matrix crystals during co-crystallisation and upon irradiation undergo extensive neutralisation by counterions either by neutral loss of the matrix ion or solvent molecules in the expanding plume containing small and large lattices. In the case of basic analytes, by electrons or acidic analytes, by protons, leaving only a few useful ions, initially termed “lucky survivors”, that make it into the vacuum and are consequently detected¹⁷¹.

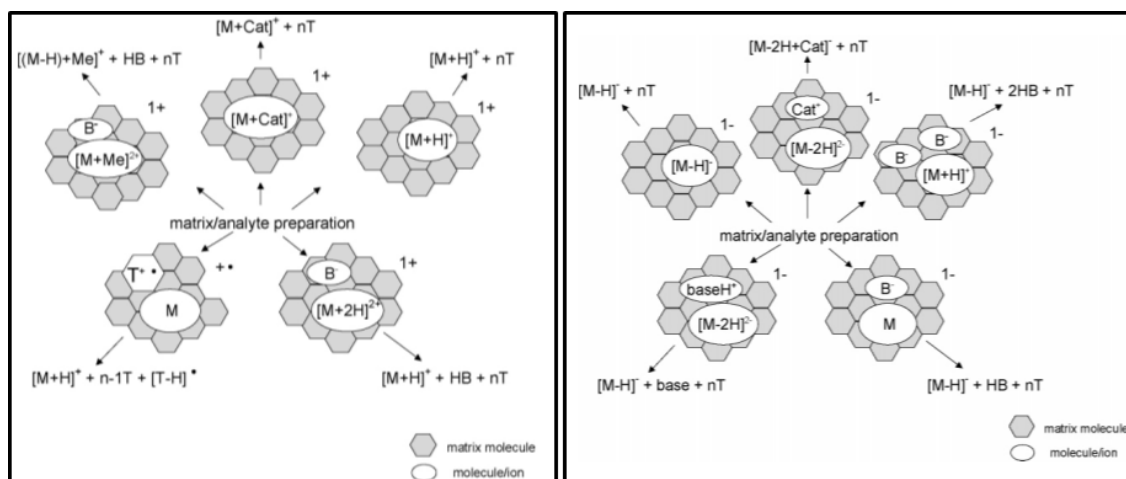


Figure 1.13. Cluster ionisation model. Left panel. Positive ions. Right panel. Negative ions. Adapted with permission from John Wiley and Sons: Karas *et al.*, 2000. Ionization in matrix-assisted laser desorption/ionization: singly charged molecular ions are the lucky survivors. *Journal of Mass Spectrometry*¹⁷⁰.

These two divergent mechanisms of initial primary ion formation are the most widely accepted. Other opposing models include direct-multiphoton ionisation of matrix or matrix-analyte complexes, polar fluid model, excited state proton transfer and pneumatic assistance. However, secondary ionisation models where subsequent reaction follow in the plume are in more agreement¹⁷².

1.4.2. Electrospray Ionisation

Electrospray ionisation (ESI) is another common soft-ionisation technique like MALDI. ESI is the production of gas-phase ion from solution in an electric field¹⁷³. The field was pioneered by John Fenn in 1984 where mass spectra were generated from large biomolecules^{173,174}. First, in the ESI process, charged droplets are formed at the capillary spray tip supplied with high voltage usually between 2 -5 kilo Volts (Kv). This is known as the Taylor cone. Second, the mist of charged droplets shrinks with solvent evaporation using a nebulising carrier

gas (N_2) and recurring droplet disintegration yielding more smaller highly charged droplets. Last, very small droplets produce gas-phase ions (desolvation) with the aid of counter flowing heated drying gas around the transfer capillary (**Figure 1.14**). All three steps take place at atmospheric pressure hence the process is called atmospheric pressure ionisation (API)¹⁷⁵

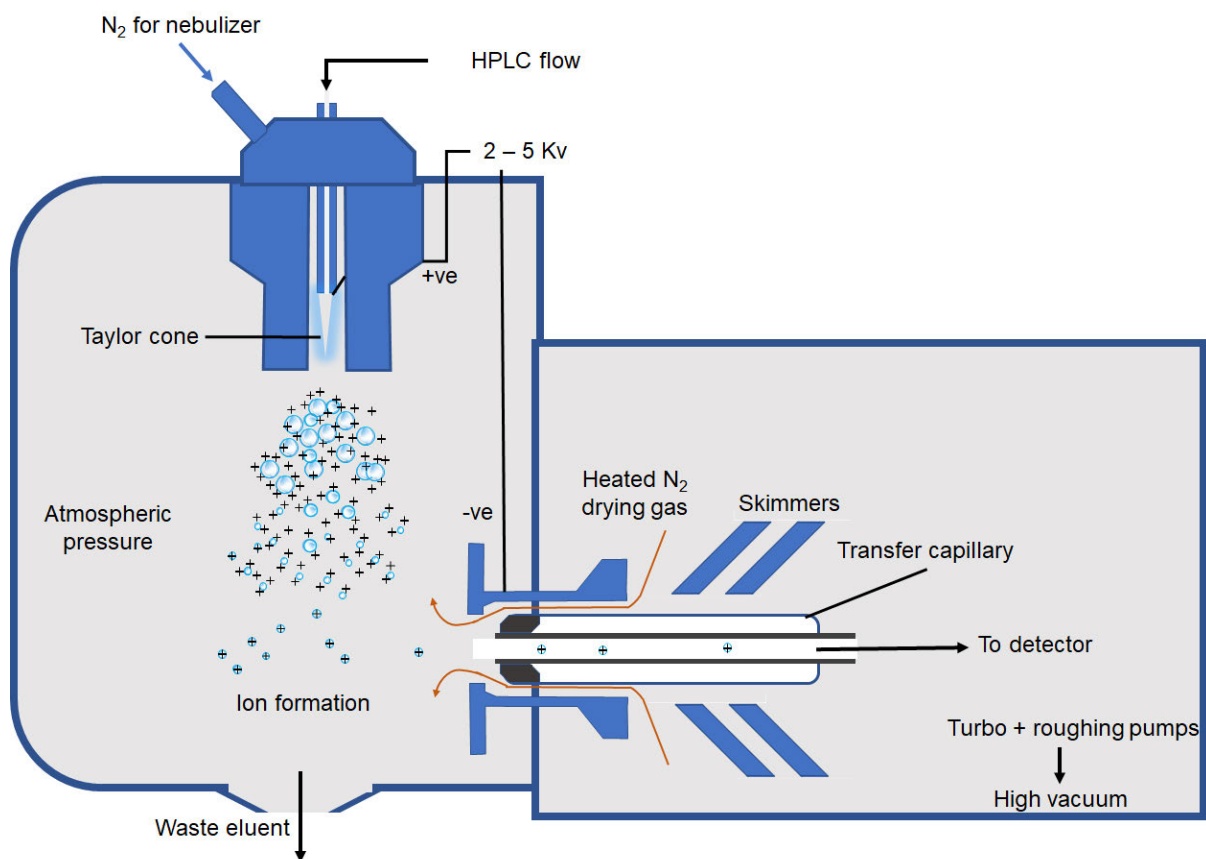


Figure 1.14. Schematic of an ESI source.

1.4.2.1. Ion Formation in ESI

The charge residue model (CRM) and ion evaporation model (IEM) have been proposed for the formation of gas-phase ions from very tiny highly charged droplets. The CRM, recommended by Dole *et al.*, predicts extremely small droplets form that contain a single analyte molecule with few ionic charges. Upon solvent evaporation, a gas-phase analyte ion forms with charges from the surface of the departed charged droplet¹⁷⁶. Oppositely, the IEM put forward by Iribane and Thomson, postulates that when the radii of droplets shrink to a given size, it becomes possible for ions to directly discharge from the droplet overcoming Coulombic fission, known as Rayleigh limit¹⁷⁷. **Figure 1.15** provides a simplified schematic of these models of ion formation in ESI.

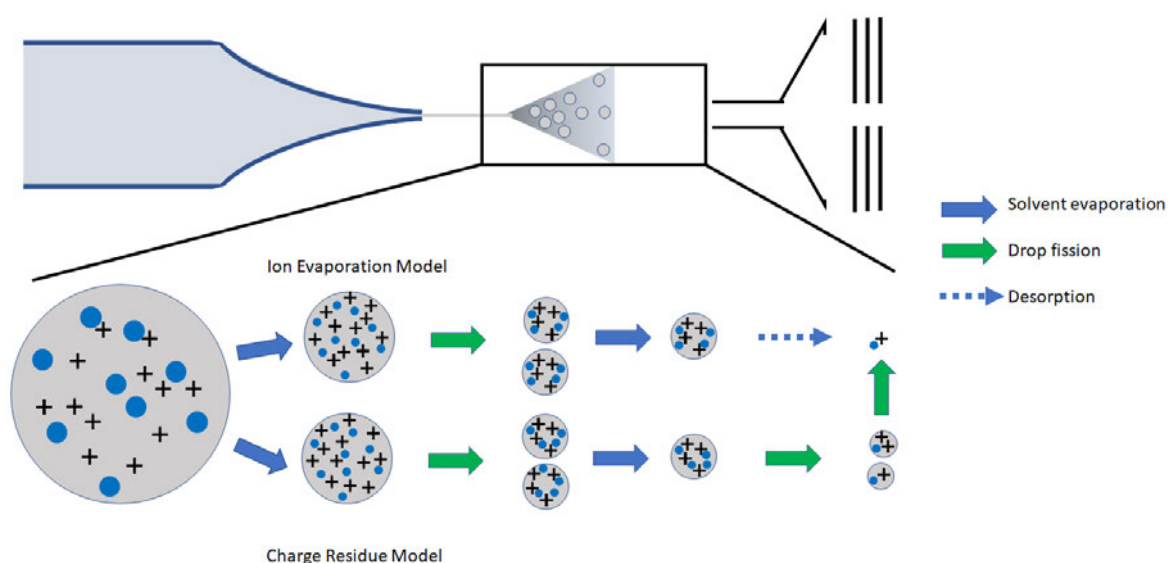


Figure 1.15. Models of the ESI process.

1.4.3. Desorption Electrospray Ionisation (DESI)

The process of ESI was incorporated into DESI by Zoltan Takáts¹⁷⁸. The DESI process involves desorbing ions from a flat surface using a sprayer. The tissue is bombarded by charged droplets and ions form in the electronic mist (**Figure 1.16**). DESI mass spectra are like ESI with single and multiply charged ions. DESI sources can be coupled to MS analysers for imaging. However, the benefit of conducting MSI directly on tissue at ordinary conditions can be the techniques' Achilles heel. Feider and colleagues has shown that DESI in negative ion mode may be prone to variations in relative humidity that disturbs the spray's electrical discharge leading to inferior image quality¹⁷⁹.

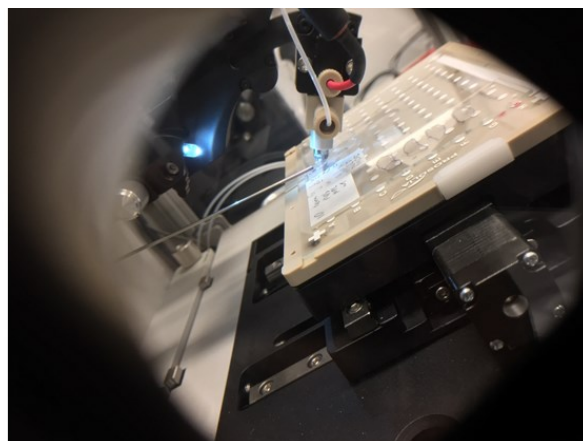
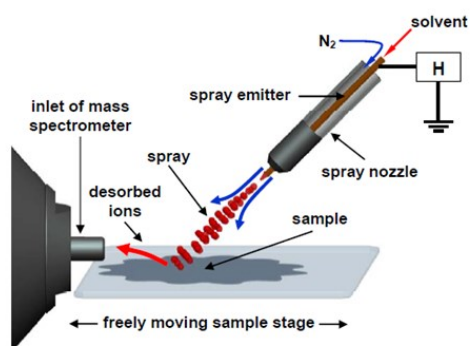


Figure 1.16. DESI instrumentation process. Right. A simple schematic of the DESI process. The solvent impacts the tissue at an angle creating electrically charged droplets that are drawn into the mass spectrometer inlet. **Left.** Photograph of Prosolia source in action showing an illuminated glass slide (white diode), nebulizing gas (grey tube) and high voltage supply (red tube).

1.4.4. Formation of Lipid Ions

PC species are the predominant lipid component on the extracellular membrane and other organelles¹⁸⁰. This makes PC the most readily detectable species using a combination of mass spectrometry approaches such as electrospray ionisation (ESI) mass spectrometry and mass spectrometry imaging (MSI) in positive ion mode^{115,181}. Moreover, the ionisation efficiency of PC compared to PE may be easier due to the different electronegativity properties of the two headgroups, the greater inductive effect of trimethylazanium of PC compared to single ammonium of PE. PS like PE, only moderately form cations due to the basicity of the primary amine and in the presence of equimolar concentrations with PC and SM suffer from ion suppression¹⁸².

During MALDI MS imaging of biological tissues, alkali metal adducts of lipids are formed due to their intrinsic enrichment as electrolytes in physiological systems¹¹⁵. Depending on the matrix, lipid cations of sodium and potassium adducts are often in higher proportion to proton adducts whereas dehydrated adducts may result from the de-solvation and ionisation process^{115,183,184}. Noteworthy, is that the glycerol backbone and fatty acid double bond position isomerism produces many structurally diverse lipids. These can lead to the generation of isobaric lipid ions during MSI experiments as exemplified in **Table 1.4**. For mass spectrometry literature and reporting, M denotes the neutral mass with common positive ion adducts that are either proton (H^+), sodium (Na^+), protonated with loss of water ($H-H_2O^+$) and potassium (K^+). Negative ions frequently occur as loss of proton (H^-) or (Cl^-)¹⁸⁵. Acetate (CH_3COO^-) or formate ($CHOO^-$) are observed when using buffered mobile washes in chromatography-based methods¹⁸⁵.

Lipid Species	M	[M+H] ⁺	[M+Na] ⁺	[M+H-H ₂ O] ⁺	[M+K] ⁺	[M-H] ⁻
PC(32:0)	733.5622	734.5695	756.5514	716.5589	772.5254	732.5549
PC(34:0)	761.5935	762.6008	784.5827	744.5902	800.5567	760.5862
PC(34:3)	755.5465	756.5538	778.5357	738.5432	794.5097	754.5392
PC(36:3)	783.5778	784.5851	806.5671	766.5745	822.5410	782.5705
PE(38:1)	773.5935	774.6008	796.5827	756.5902	812.5567	772.5862
PE(40:1)	801.6248	802.6321	824.6140	784.6215	840.5880	800.6175

Table 1.4. Lipid ion isomerism and isobarism. *m/z* values of protonated, sodiated, dehydrated and potassiated adducts for respective neutral molecules. The bright green isomers of PC species have ± 0.0024 Da within class fractional mass difference compared to the PE species $\pm 0.0364 - 0.0388$ Da.

Two important considerations in MS measurements are mass accuracy and mass resolution. Mass resolution or resolving power is the *m/z* value divided by peak full width at half maximum (FWHM). Mass accuracy is the difference between measured and actual *m/z* values. Overlapping of peaks due to isomeric *m/z* values makes it challenging to confidently identify lipid precursors and their corresponding fragments ions. This can be addressed by using MALDI-TOF systems with high mass accuracy and mass resolution. Another option is combining MS with ion mobility separation which is discussed in **Section 1.5.4**.

Figure 1.17 shows how mass resolution influences lipid ion measurements.

Increasing mass resolution

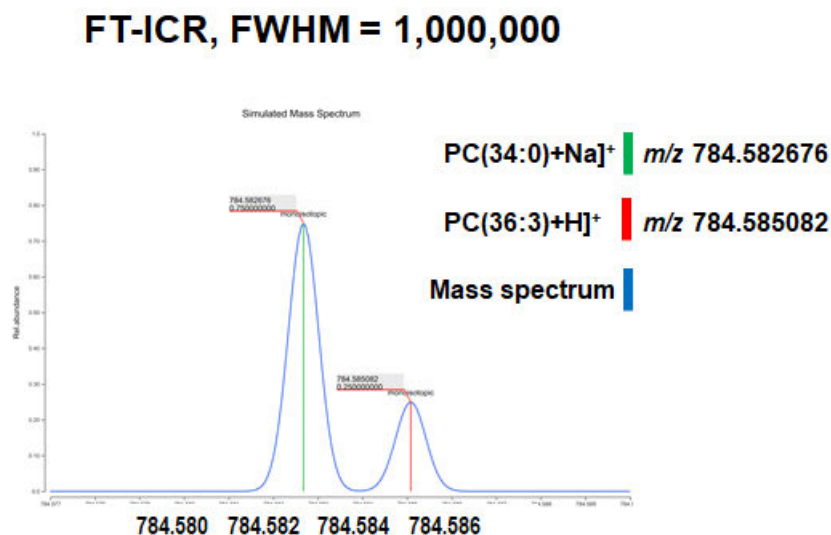
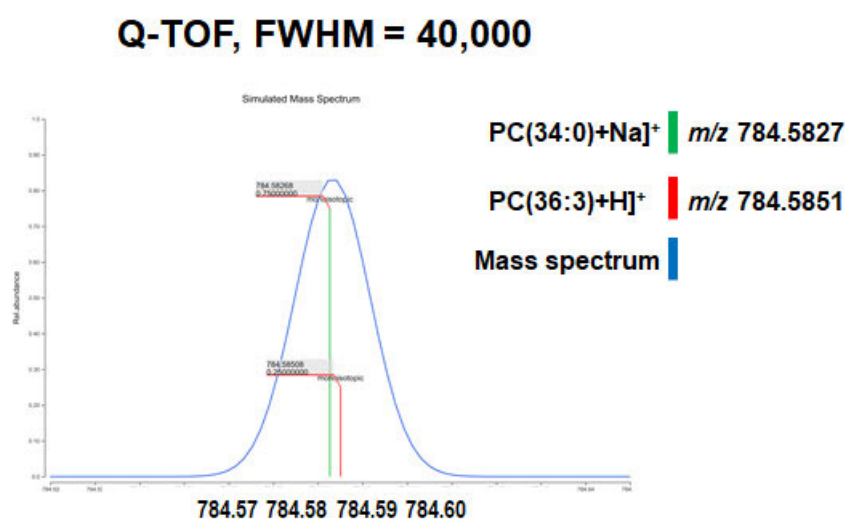
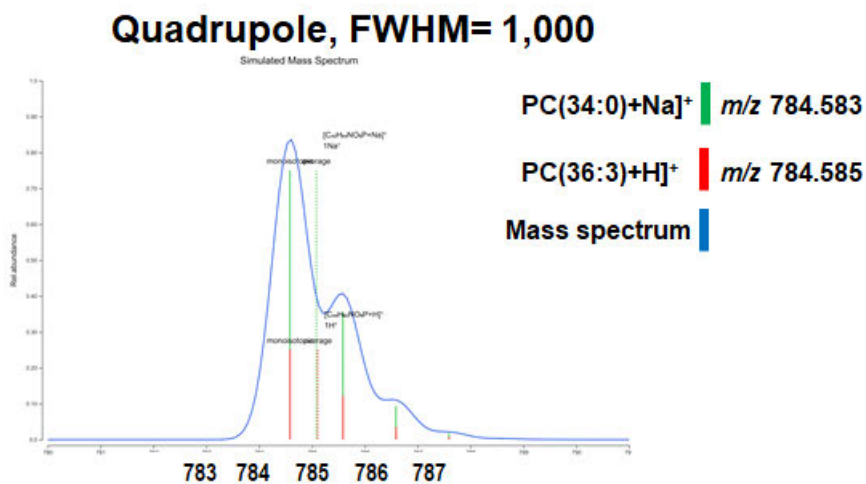


Figure 1.17. Lipid ion isomers and mass resolution. Separation of isobaric peaks of PC(34:0) sodiated adduct; $[C_{42}H_{84}NO_8P+Na]^+$ and PC(36:3) protonated adduct; $[C_{44}H_{82}NO_8P+H]^+$. The mass spectrum is better resolved from quadrupole to Q-TOF to FT-ICR instruments.

1.5. Mass Spectrometry Instrumentation

1.5.1. Quadrupole Mass Analysers

Quadrupoles consists of four parallel identical metal rods that guide ions based on the ratio of radiofrequency (RF) to direct current (DC) voltages alternately applied to pairs of oppositely arranged rods (**Figure 1.18**). The superimposition of RF and DC potential causes ions to oscillate as they travel along the axial plane of the rods:

$$\phi_o = U + V\cos\Omega t$$

where ϕ_o the electric potential applied to the rods, is either an RF potential $V\cos\Omega t$ or a combination of DC potential, U , and Ω is the angular frequency of the RF field¹⁸⁶.

Ions of certain m/z that have stable trajectories based on the DC potential and frequency of the RF field are transmitted whereas ions with unstable trajectories will collide into the rods and be lost¹⁸⁷.

By keeping the RF (U) potential constant and varying RF (V) potential across a preselected mass range, ions of preferred m/z values with stable trajectories can be separated. This is known as RF-only mode and allow the quadrupole to act as an ion-transmission guide.

In tandem (MS/MS) mass spectrometry experiments, an RF-only quadrupole functioning as a collision cell is used to fragment ions, when an inert buffer gas is introduced. This is described as collision induced dissociation (CID). Product ions are formed when the RF energy is increased from a few eV to up to 100 eV.

Combining three sets of quadrupoles mass analysers in a straight sequence creates a triple quadrupole (QqQ) mass spectrometer. The first analyser is called Q1, second, Q2 and third, Q3. Q1 is can be employed as a mass filter scanning or selecting ions of a selected m/z range. Q2 is almost exclusively used as a collision cell to dissociate ions allowed to enter from Q1. Q3 is used to scan the fragment ions to create a mass spectrum or set to monitor a specific ion. Blending, Q1 and Q3 in different modes can lead five main types of experiments, product ion scan (MS^2), precursor ion scan, neutral loss scan and selected/multiple reaction monitoring which have been extensively described before¹⁰³.

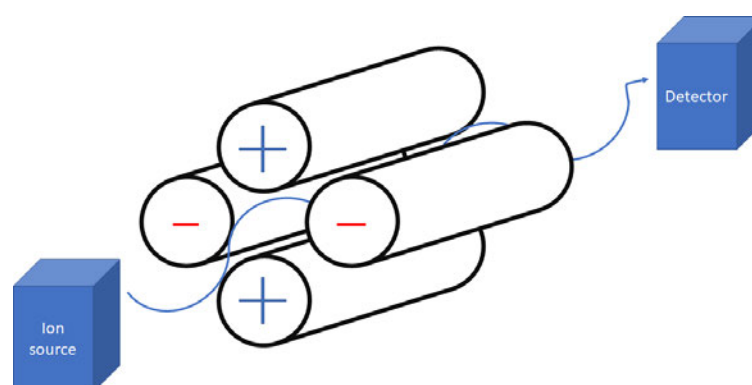


Figure 1.18. Simplified schematic of quadrupole mass analyser.

1.5.1.1. API 4000 QTrap LC-MS/MS System

The API 4000 QTrap is a hybrid instrument that can be operated as a standard quadrupole or linear ion trap mass spectrometer¹⁸⁸. The principle of the standard triple quadrupole mode is to use two identical mass filters, Q1 and Q3 linked by a collision cell denoted Q2, where a neutral gas fragments ion by CID.

Q1 separates the precursor ions in a mixture based on their m/z ratios, Q2 fragments the precursor ion and Q3 separates the product (fragment) ions of their precursors. This scan type is known as multiple reaction monitoring (MRM) and used for quantitative analysis of small molecules. In QTrap mode, the Q3 region is used as a linear ion trap (LIT)¹⁸⁶. Ions are first collected by applying main RF voltage and holding them with an exit lens with DC voltage. After a pre-defined time, another DC barrier voltage is applied to an entrance lens which confines ions in the Q3. Ions are then scanned out by concurrent ramping of the voltages at the exit lens and auxiliary RF to the main RF voltage¹⁸⁶. Full spectrum data are produced with increased resolution and sensitivity. The LIT mode has additional scan types; enhanced MS, enhanced product ion and MS³ (MS/MS/MS) which are designed for qualitative analysis of small molecules. Hence, delivering improved quantitative performance and specificity¹⁸⁸.

Coupling to HPLC elution is a common utility of triple quadrupole mass analysers yielding an LC-MS/MS system. The key parts of the API 4000 system are shown in the **Figure 1.19**. The AB SCIEX API 4000 QTrap system is one of the most robust commercial instruments purposefully developed for high throughput analysis and with high sensitivity and specificity for quantification of small molecules (drugs, lipids, and their metabolites). This platform and its subsequent generations continue to be the work horse in many analytical laboratories and has featured in countless drug development pipelines across the globe^{189,190}.

NOTE:

This figure/table/image has been removed to comply with copyright regulations.

API 4000™ system components with pump

Figure 1.19. Schematic layout of the API4000 LC-MS/MS system.

Adapted from instrument manufacturer's manual.

1.5.2. Time-of-flight (TOF) Mass Analysers

TOF analysers accelerate ions given the same kinetic energy in an electric field in a flight tube and the smallest ions with higher velocity move quickly and reach the detector first¹⁹¹.

The principle of TOF instruments is all ions of charge q are initially accelerated by a potential difference U , from the sample target to a kinetic energy, Ek , before they travel down a field-free path (flight tube)¹⁹². Hence,

$$Ek = zeU$$

where z is the charge state and e is the elemental charge.

Ions with identical kinetic energy, Ek , will have different velocities, v , according to their mass, m , following the equation

$$Ek = \frac{1}{2}mv^2 \text{ or } v = \sqrt{\frac{2Ek}{m}} = \sqrt{\frac{2zeU}{m}}$$

Ions will travel at a constant velocity, taking time, t , to travel distance L of the flight tube to arrive at the detector

$$t = \frac{L}{v}$$

By substituting v for the value shown above, this equation can be rearranged to

$$\frac{m}{z} = 2eU \left(\frac{t}{L}\right)^2$$

A calibration equation is used to correctly assign the mass to its corresponding time-of-flight, t . Thus, the relationship between m/z and t is given by

$$\frac{m}{z} = At^2 + B$$

Where A and B are constants that account for known arrival times of accelerated ions and initial velocity of the plume¹⁹¹.

A pusher, a voltage deflector, is included in fundamentally axial-TOF instruments to create an orthogonal flight path, where the ion beam path is re-directed perpendicularly to the initial direction of motion from the source. This serves to remove the high initial axial velocity from the cloud of ion distribution. Additionally, it helps to improve calibration and mass accuracy, thus orthogonal TOF instruments have a mass error of <10 ppm compared to axial TOF instrument ~ 20 ppm. TOF instruments are the most popular for MALDI MS imaging as its suited to generation of ions by short laser pulses¹⁹³.

1.5.3. Quadrupole-TOF Systems

Lipidomics studies often employ hybrid mass spectrometer systems to achieve the suitable characterisation of analytes with high reproducibility, wide dynamic coverage, good signal-to-noise ratio and isotopic deconvolution. A prime example is the quadrupole-TOF systems. By substituting the Q3 with a TOF, such instruments leverage the agility, robustness of triple quadrupoles and high mass accuracy and resolution of TOF to attain higher quality tandem mass spectra as first conceptualised by Morris *et al.*,¹⁵⁴. In this project, two MALDI Q-TOF systems were utilised and described in subsequent sections.

1.5.3.1. SYNAPT HDMS Q-TOF

The Waters MALDI SYNAPT HDMS Q-TOF is equipped with a source consisting of a 200 Hz solid-state frequency-tripled Nd:YAG laser ($\lambda = 355$ nm) and a hybrid quadrupole-TWIMS with orthogonal geometry to the TOF analyser. It was used in standard duty cycle for data acquisition in MS and MS/MS modes. In MS only mode ions were accelerated by the hexapole ion guide and focused through to the quadrupoles. In tandem experiments quadrupoles were focused to select precursor ion at appropriate windows, CID fragmentation was achieved by Argon using the “Triwave” IMS trap region as a collision cell. The TOF component was operated in “V reflectron mode before ion arrival at the microchannel plate detector. **Figure 1.20** shows the layout of MALDI SYNAPT HDMS system used for imaging in [Chapter 3](#), [Chapter 4](#), [Chapters 5](#) and [6](#).

NOTE:

This figure/table/image has been removed to comply with copyright regulations.

Figure 1.20. Schematic of the Waters MALDI SYNAPT HDMS hybrid Q-orthogonal acceleration-TOF system. <https://waters.com>

1.5.3.2. timsTOF Flex

The Bruker timsTOF Flex is equipped with a Smartbeam™ 3D laser source with repetition rate of 10,000 Hz. In MS only mode, ions are transmitted through the Dual TIMS funnel and quadrupole mass filter tuned to the selected range. The software allowed a flexible “TIMS ON/OFF” mode with adjustable IMS functionality to achieve desired selectivity. Ejected ions are pushed forward with a unidirectional buffer gas flow proportionate to their unique collisional cross-section areas then held back on the first funnel based on their electric charge and then separated in the second funnel as new ions enter the TIMS cartridge. This allows almost complete duty cycle. Subsequent ions (or fragmented in the collision cell after IMS) follow a reflectron flight path for detection in the TOF analyser. **Figure 1.21** shows the ion optics Bruker timsTOF Flex used for high resolution mass accuracy lipid imaging in [Chapter 7](#).

NOTE:

This figure/table/image has been removed to comply with copyright regulations.

Figure 1.21. Schematic of the Bruker timsTOF Flex optics and ion transmission. <https://www.bruker.com/products/>

1.5.4. Ion Mobility Separation

Ion mobility separation (IMS) is perhaps the most important technological advancement for improved measurement of lipids when paired with MSI. Principally, IMS is the movement of charged molecules in a neutral buffer gas under the influence of an electric field (inside an electric cell). Each ion moves with a characteristic drift velocity in the direction of the electric field and measured as drift time. The contact between ions and buffer gas is described by the property, collision-cross section (CCS) area, which can be related to its drift time (mobility) using the Mason-Champ equation¹⁹⁴. There various types of IMS devices that separate ions based on their mobility in space or time; drift tube (DTIMS), travelling wave (TWIMS), trapped (TIMS), field asymmetric (FAIMS) and differential mobility analyser (DMA)¹⁹⁴. Their primary differences are illustrated in **Figure 1.22**. DTIMS devices have no gas flow and ions movement is achieved by a weak electric field¹⁹⁵. TWIMS devices too have no gas flow and composed of stacked electrode rings that create an oscillating electric field at reduced pressure that push ions towards the analyser¹⁹⁶. TIMS devices have unidirectional gas flow through three electrodes regions where ions are separated in opposition to electric field strength¹⁹⁷. FAIMS devices have periodic electrical fields to isolate ions using a parallel gas flow with alternating high and low voltages. DMA devices have a constant electric field, operate at atmospheric pressure, have a unidirectional gas flow and scan for selected ions.

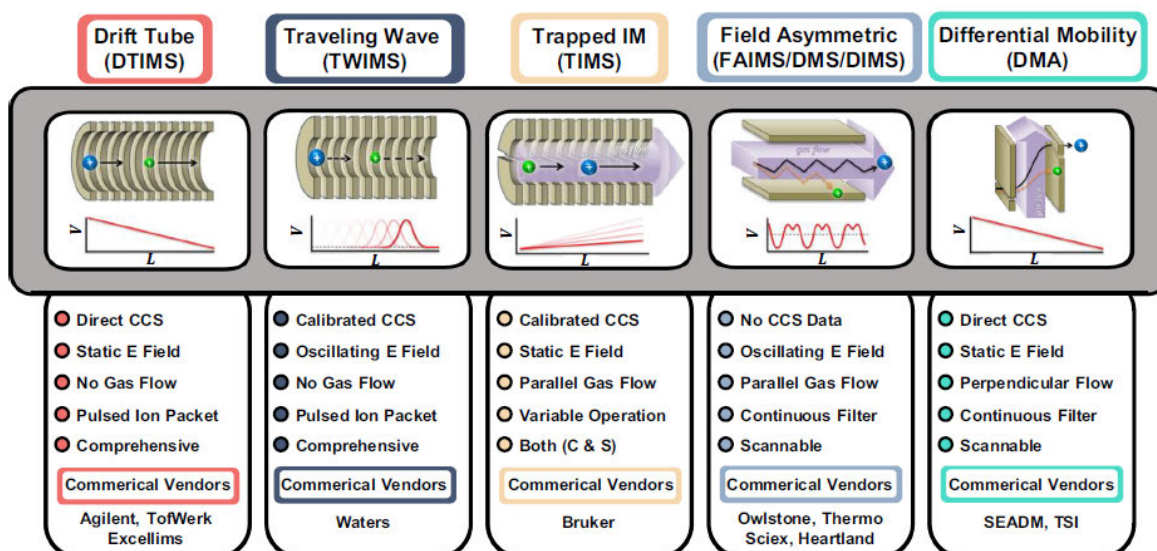


Figure 1.22. Types of ion mobility platforms. Reprinted with permission from American Chemical Society: Dodds *et al.*, 2019. Ion mobility spectrometry: fundamental concepts, instrumentation, applications, and the road ahead. *Journal of the American Society for Mass Spectrometry*¹⁹⁴.

Drift times and CCS values are highly unique to different groups of biomolecular ions. Thus depending on the IMS experiment, mobility and CCS measurements can identify isobaric metabolite and lipid ions¹⁹⁸. For instance, the PC isomers of PC(16:0/18:1)+Ag]⁺ and PC(18:1/6:0)+Ag]⁺ have been relatively quantitated with differential mobility mass spectrometry with unambiguous assignment of the fatty acyl chain sn-positions¹⁹⁹.

1.6. Mass Spectrometry Imaging

Mass spectrometry imaging (MSI) is a term that encompasses the generation of ions at known locations across a flat surface with inorganic or biological material. The main technical modes of MSI are MALDI, DESI and secondary ion mass spectrometry (SIMS). DESI and SIMS are covered in the review article. This section pays dedicated attention to MALDI MSI.

1.6.1. MALDI Mass Spectrometry Imaging

MALDI MSI involves the coating of a thin tissue section with an energy absorbent small molecule acid or base, known as matrix. Data is acquired by ablating the tissue sample at discrete coordinate positions to obtain a mass spectrum^{200,201}. With the knowledge of the spatial co-ordinates of each spectrum (pixel), the mass spectra are combined to create a molecular ion map that can display a selected m/z using a false-colour scale depicting its relative intensity. This technique is powerful as it yields label-free *in situ* chemical information of the tissue in question as exemplified in **Figure 1.23**. By co-registering ion maps with histopathology scans, MALDI MSI is a spatially informative tool for the characterisation of biochemical profiles of morphological or anatomical features²⁰². This is a key strength of MALDI MS imaging compared to other lipidomics strategies employing ESI and LC-MS/MS²⁰³.

The earliest work of adopting MALDI for imaging was described by Bernhard Spengler in 1994²⁰⁴. Subsequently, a proof-of-principle study by Richard Caprioli showcased the application of MALDI imaging to biological samples²⁰⁵. Here, they showed peptide ion signals of rat pituitary and pancreas cut at 50-100 μm thickness. Later, the group automated the process of MALDI

imaging on a TOF system paving the way for graphical user instrument control²⁰⁶. Stoeckli developed one of the earliest imaging processing programs known as “Biomap” which allowed visualisation of a selected ion peaks at defined mass range as molecular images^{200,207}. Subsequent years have seen the enhancement of imaging software by adding clustering and multivariate statistical analysis tools to delineate key m/z features in tissues i.e. segmentation based on histological appearance and comparison of segments by principal component analysis^{208,209}. Now current MS imaging tools such as SCiLS Lab are equipped with more amenable user interfaces seemingly making MALDI imaging more convenient²¹⁰.

There are two type of operation for MALDI MSI²¹¹. The first is microscope MALDI that pertains irradiating the whole area that is to be imaged. This yields ions from the specimen which retain their spatial location and, arrival times and impact position measured on a 2-dimensional (2D) position-sensitive detector²¹². The second and most common mode in commercial instruments is microprobe MALDI²⁰⁶. A laser ablates a user defined area of pixels and recording the resulting spectra for each location. After data acquisition is complete, a 2D ion intensity map is reconstructed for each ion based on its density at particular locations. In this project, the MALDI SYNAPT HDMS instrument employed an oversampling raster pattern technique²¹³. The estimated spot of the laser beam was approximately 100 μm . The step size was set at 60 μm , therefore an extra 40 μm at each incremental step was always ablated as the stage moved. This way the spatial (lateral) resolution was maintained with sufficient lipid ion signal intensity²¹⁴. Alternatively, the timsTOF Flex utilises pixel-to-pixel irradiation with each MALDI spectrum acquired from a discrete grid position without oversampling²¹⁵.

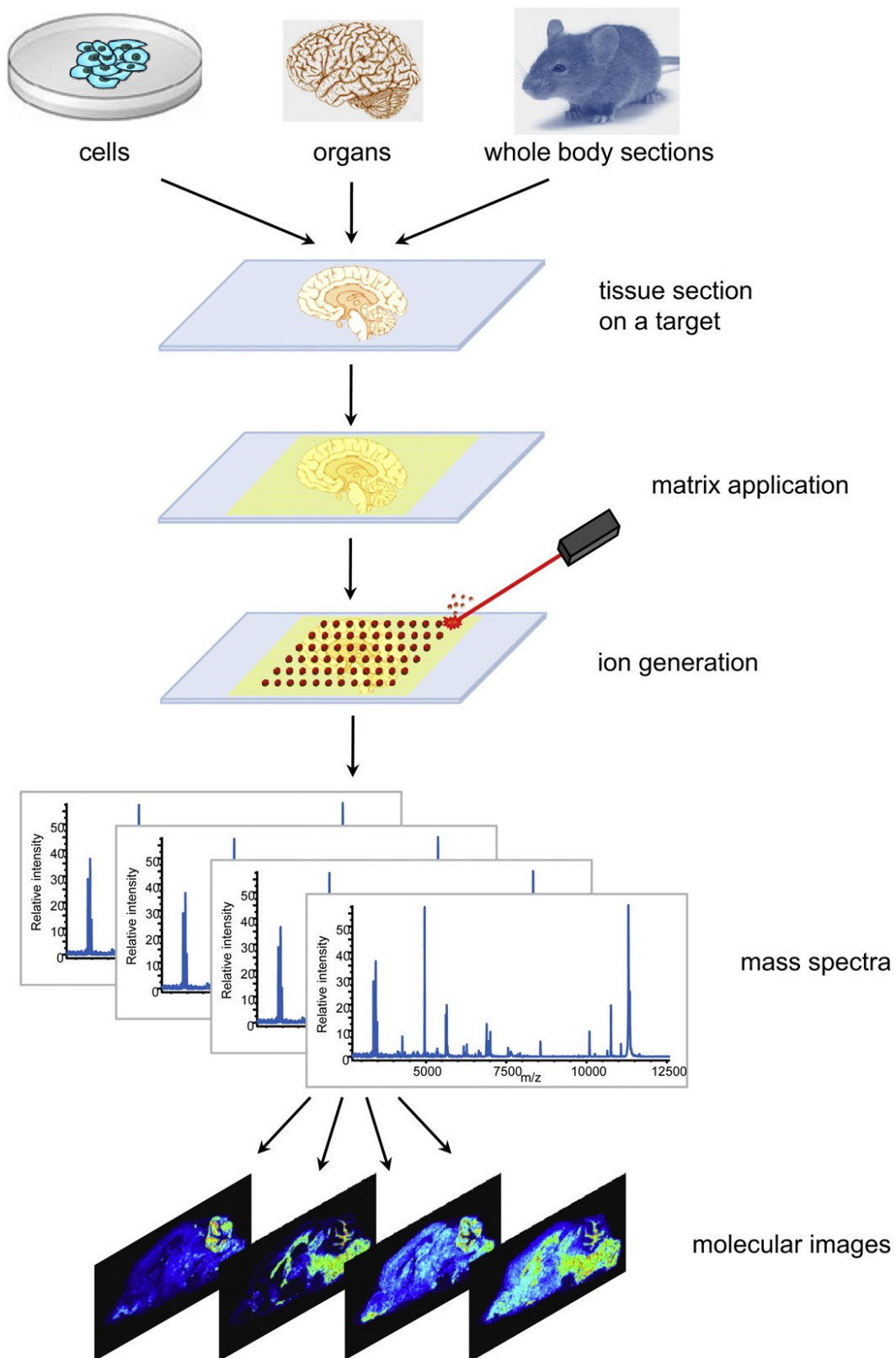


Figure 1.23. Schematic representation of a MALDI MSI experiment workflow. Reprinted with permission from Schwamborn *et al.*, 2010. MALDI imaging mass spectrometry – painting molecular pictures. *Molecular Oncology*²¹⁶.

1.6.1.1. MALDI MS Imaging Sample Preparation

Sample preparation is critical to the quality of the acquired MALDI image. It is paramount to have procedures that preserve tissue integrity and limit delocalization and degradation of *in situ* biomolecules. Traditionally, formalin-fixed paraffin embedded (FFPE) tissues have been the gold standard in pathology for tissue preservation after surgical resection as morphology is retained long term. Globally, many biobanks have extensive libraries of archived FFPE blocks that can be harnessed for large scale biomarker research projects²¹⁷. However, paraffin hinders to some degree the desorption and ionisation of MALDI due to protein cross-linking induced by formaldehyde. Nonetheless, some protocols entail tryptic digestion and antigen retrieval of FFPE tissue to be compatible with MALDI MSI and immunohistochemical labelling, respectively²¹⁸. Organic solvents used in the tissue processing of FFPE blocks leach out many lipids but solvent-resistant membrane lipids like PAs and PIs are said to remain trapped in protein networks. A MALDI MSI study showed large differences between FFPE and fresh-frozen tissue in m/z 600 – 1,000 the lipid range with comparable metabolite peaks in the m/z 50-400²¹⁹. The lower mass range metabolites are hydrophilic and ostensibly preserved due to dehydration step.

Fresh-frozen tissues are the most suitable for MALDI MSI analysis^{202,220}. Post-surgical biospecimens can be transported in cold ischemia (buffered solution at 4°C) or immediately after excision placed in cryovials and snap-frozen in liquid nitrogen (-180°C) Dewar, liquid-nitrogen cooled isopentane or placed with cryoprotectants^{221,222}. Snap-freezing reduces ice crystal formation in

mammalian tissues. Frozen samples are then stored at -80°C for long term storage for up to 5 years²²³. Fresh-frozen samples can also be stored in gelatin capsules or embedded in a temperature-sensitive polymer such as carboxymethyl cellulose (CMC) or optimal cutting temperature (OCT) that stabilises the tissue as it quickly freezes. CMC and OCT also aid the visibility of cryosectioning small specimens. However, if OCT smears across the tissue repeating peaks of 44 Da are observed in the m/z spectrum which cause ion suppression of endogenous biomolecules by competing for free radicals²²⁴. On the contrary 2% CMC aqueous has little interference on the 100 – 1,000 Da range and is recommended²²⁵.

Cutting of fresh-frozen tissues is done inside a cryostat (cryotome) maintained between -5°C and -25°C . MSI cryosections are normally 8 – 12 μm thick. This depth of cutting is affected by the diameter of the type of cell. A good case is of neurons where in the transverse plane they measure as little as 4 μm whereas in the coronal plane they measure hundreds of millimetres²²⁶. For prostate tissue, a typical size epithelium cell is $\sim 8 \mu\text{m}$ diameter is regardless of the cutting plane. The thickness of tissue has been reported to spectral quality and image quality of analytes²²⁷. Low molecular weight molecules are better ionised between 5 and 20 whereas high molecular weight molecules ($>9,000 \text{ Da}$) like proteins $<5 \mu\text{m}$ is recommended²²⁸. Parallel sections can be obtained for imaging and histopathological staining. In real terms, the same post-imaging section can be used for H&E staining as the MALDI laser ablation causes minimal damage to the tissue, thus offering ideal co-registration of images¹⁵⁹. Nevertheless, adjacent stained fresh sections offer more vivid scans despite a small level of variability due to tissue heterogeneity.

Tissue sections are thaw-mounted onto glass slides. This is achieved by placing the glass slide into the chamber and pressing onto the section. Poly-L-lysine coated glass slides are suitable for this as the positive charge of the slide allows the frozen tissue to adhere as it thaws. Slides can be briefly allowed to air-dry at room temperature. Additionally, it is common to use a vacuum desiccator to completely dry sections before and/or after matrix application which minimises condensation²²⁹⁻²³¹. Interestingly, one study has shown the delocalization of ATP up to 200 μm away off-tissue with desiccation compared to without desiccation¹⁵². A second type of glass slides is the indium-tin-oxide (ITO) made by Bruker²¹⁰. Whereas, normal glass slides are compatible with orthogonal-TOF MALDI systems, ITO slides are electrically conductive and designed for axial-TOF (linear or reflectron mode) instruments¹⁵¹. Modification of ITO slides to improve tissue adhesion afforded by poly-L-lysine coating with a solution of the same or corona discharge²²⁵.

The final aspect of sample preparation is matrix application.

1.6.1.2. MALDI MS Imaging Matrix Selection

The choice of matrix for MALDI MS imaging experiments is governed by the analytes of interest and polarity of detection. Traditionally, MALDI matrices such as α -cyano-hydroxycinnamic acid (CHCA), sinapinic acid and dihydroxybenzoic acid (DHB) were developed for proteomic profiling^{232,233}. However, some matrices used for peptide analysis have become applicable to lipids, sugars, complex carbohydrates and glycoproteins. Common to all matrices is a conjugated π electron system of fused benzene rings and functional groups that facilitate the absorption of energy in the form of UV light¹⁹². The most important considerations in using a matrix for MALDI MSI are its solvent solubility, molar absorptivity at the laser wavelength, and the in-source vacuum stability¹⁹². A summary of popular matrices in MALDI literature is provided in **Table 1.5**.

Numerous matrices have been used in MALDI MS imaging of lipids as showcased in a review by Leopold *et al.*,¹⁸¹ and each can affect the sensitivity of different lipid sub-classes²³⁴. Anionic lipids (PI, PS and PA) are better measured in negative mode MALDI using basic matrices whilst cationic lipids (PC, LPC, SM, Cer) are robustly detected with acidic matrices. Edwards reported that 9-AA exhibited far better signal intensity for analysis of anionic metabolites in comparison to CHCA, DHB, DHAP and 3-hydroxypicolinic acid²³⁵. Solvents have been demonstrated to considerably affect the production analyte-matrix interactions. Sun and colleagues discovered that using a combination of acetonitrile and isopropanol gave a more robust signal than either solvent alone or methanol alone, when analysing 1,2-distearoyl-snglycero-3-phosphocholine standard¹⁸³.

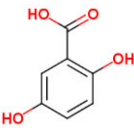
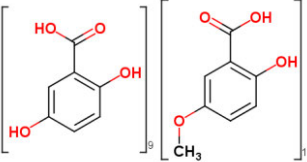
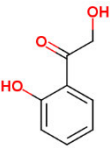
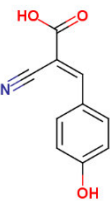
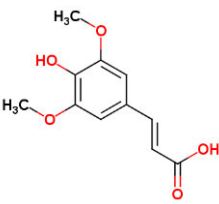
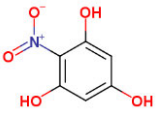
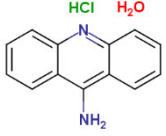
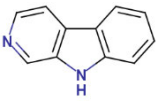
Matrix	Structure	Analyte
2, 5-dihydroxybenzoic acid (DHB)		Sugars, oligosaccharides (Harvey 1993) ¹⁶⁷ , peptides (Billeci <i>et al.</i> , 1993) ²³⁶ , nucleotides (Billeci <i>et al.</i> , 1993) ²³⁶ , polymers, lipids
Super DHB		Peptides, proteins (Tsarbopoulous <i>et al.</i> , 1994) ²³⁷ , glycolipids (Guo <i>et al.</i> , 1997) ²³⁸
2, 6-dihydroxyacetophenone (DHAP)		Sugars, peptides (Gorman <i>et al.</i> , 1996) ²³⁹ , nucleotides (Lichtenwalter <i>et al.</i> , 2000) ²⁴⁰ , polymers
α -cyano-4-hydroxy cinnamic acid (CHCA)		Peptides (Zhou <i>et al.</i> , 1995) ²³² , proteins, polymers, lipids
Sinapinic acid		Proteins (Fischer <i>et al.</i> , 1993) ²⁴¹ , peptides, polymers (Castro <i>et al.</i> , 1992) ²³³
2-Nitrophenol		Proteins (Inutan <i>et al.</i> , 2012), (Trimpin <i>et al.</i> , 2012) ^{242,243}
9-aminoacridine hydrochloride hydrate (9-AA)		Nucleotides (Edwards <i>et al.</i> , 2005) ²³⁵ , lipids (Sun <i>et al.</i> , 2008) ¹⁸³ , polymers (Heudt <i>et al.</i> , 2012) ²⁴⁴
Norhamane (beta-Carboline)		Oligosaccharides (Yamagaki <i>et al.</i> , 1999) ²⁴⁵ , lipids (Scott <i>et al.</i> , 2016) ²⁴⁶ , proteins (Nonami <i>et al.</i> , 1998) ²⁴⁷

Table 1.5. Examples of popular MALDI matrices. Red functional groups indicate acidic (conjugate base) and blue functional groups are basic (conjugate acid).

1.6.1.3. MALDI MS Imaging Matrix Application

Once a suitable matrix is chosen the next step in MALDI is applying the matrix on the biological samples. The deposition technique affects how the well matrix forms crystal on the sample surface which is crucial to the success of the experiment. A study has shown for any given matrix, smaller matrix-analyte co-crystals is important for creating high lateral resolution images²⁴⁸.

There are several methods for depositing the matrix. These include spotting, airbrush, inkjet printing, sublimation and automatic sprayer^{237,249}. Spotting is done by applying a droplet of the matrix solution on top of the tissue or tissue extract-matrix mixture onto a target surface. It is more suited to MALDI MS profiling experiments rather than imaging, where using a ground or polished stainless-steel target plate with wells to quickly check the mass spectra of a compound, calibration prior to MALDI MS imaging or development of fragmentation methods for certain analytes. For this thesis, sublimation and automatic spray coating were employed for MALDI imaging.

Sublimation is based on the principle of solid-gas phase conversion following a decrease in the temperature gradient induced by vacuum in a closed system¹⁵². The sublimation apparatus consists of a hot plate that sits under a glass chamber with an internal cold finger at the top²⁵⁰. An absolute organic matrix solution dries to form a powder which gradually vaporises as the pressure drops to form a homogenous layer of very minute crystals on the samples. This method is solvent-free, and analytes are unlikely to delocalise but some compounds may go undetected because of insufficient interaction with the

matrix²⁵¹. Thus, the usefulness of sublimation is confined to certain small molecules and lipids.

Automatic spray coating systems use a computer interface to control a robotic controlled spray head nozzle coupled to a pneumatic syringe pump that deliver the solvent matrix formulation. Mounfield and Garret reported the utility of spray coating using an in-house built programmable logic controller combined to an enclosed chamber resulting customizable spray options²⁵². They demonstrated that their spray device attained well resolved rat brain lipid images in comparison to the inkjet deposition method²⁵³. Typically in automated spray coating, the parameters to be considered are nebulizing gas pressure, spray velocity, solvent flow rate, spray head-sample (Z) distance, in-between pass distance (X, Y), time between passes and number of passes (layers). Examples of routinely used commercial automatic spray coating systems are the TM-Sprayer (HTX Technologies, Carrboro, NC, USA)^{254,255} and Suncollect (SunChrom, Friedrichsdorf, Germany)^{256,257}. Automated spray coating achieves better MS signals peak intensity and reproducibility, compared to other matrix deposition methods as tissues are covered with a highly homogenous matrix layer in which analytes form co-crystal with the matrix. Nonetheless, the functionality of these devices can be impeded by high matrix concentration which can block the nozzle.

A matrix optimisation protocol comparing sublimation versus automated spray coating is presented in [Appendix B](#) of this thesis.

1.6.1.4. MALDI Laser Selection

Lasers are defined by their emission and beam parameters²⁵⁸. MALDI systems work best with pulsed lasers because the energy for desorption and ionisation must be transferred to the sample before the internal thermal energy rises^{164,259}.

Conventionally, N₂ lasers have been the most widely used in early MALDI work²⁴¹. N₂ lasers are simple, compact and cheap²⁶⁰. They emit at a wavelength of 337 nm which is compatible for numerous UV-MALDI matrices¹⁶⁷. However, they suffer from a limited average repetition rate of utmost 60 Hz and the total lifetime is $\leq 10^8$ laser shots²⁶¹. For this reason, diode laser-pumped solid-state frequency tripled lasers based on Neodymium (Nd) were developed^{262,263}. This include Nd:YAG, Nd:YLF and Nd:YVO₄. These emit at a wavelength of 349-355 nm in the UV region with a durability of $\leq 10^9$ shots. They offer the advantage of higher repetition rates facilitating reduced acquisition times for comparable data collection. The parameters for lasers available in commercial MALDI instruments are summarised in **Table 1.6** below.

Laser	N ₂	Nd:YAG	Nd:YLF	Nd:YVO ₄
Wavelength λ (nm)	337	[^] 266 / 355	349	355
Pulse width nanoseconds (ns)	0.3 – 10	<0.25	10 - 20	1.5
Pulse energy (μ J)	1 - 10,000	120 - 300	36.0 – 63.7	5
Repetition rate	1 - 60 Hz	200 Hz – 10 kHz	200 Hz – 5 kHz	1 - 20 kHz
Beam profile	Multiple maxima	Gaussian-Multiple maxima	Gaussian-Multiple maxima	Gaussian-Multiple maxima

Table 1.6. Parameters of lasers used in MALDI imaging. [^]frequency-quadrupled laser. Information sourced from <https://ms-imaging.org/wp/overview-of-commercial-instruments> and Prentice *et al.*, 2015. High-speed MALDI MS/MS imaging using continuous raster sampling. *Journal of Mass Spectrometry*²⁶⁴.

An important factor in the yield of ions from MALDI is fluence – distribution of photon energy incident upon the target²⁶⁵. The beam profile in Nd:YAG lasers is Gaussian, meaning, there a “hot spot” in the middle of the raster. Analytes at the centre of the laser are irradiated in greater proportion than towards the edge. Commercially instruments, use fibreoptic cabling or a fundamental beam shaper to improve divergence of unsmooth laser fluence to create a flat-top /“top hat” beam profile²⁴⁸. This also can be corrected by oversampling whereby the laser is fired to generate ions from sequentially smaller unablated areas²¹³.

The two MALDI MS imaging instruments used in this project only used Nd:YAG UV lasers (**Figure 1.24**). The MALDI SYNAPT HDMS (Waters Corporation, Manchester, UK) laser had a Gaussian beam profile²⁶⁶ whereas timsTOF Flex (Bruker Daltonics, Bremen, Germany) currently have designed arguably better ion source optics denoted “Smartbeam 3D” that generates a structured beam profile with multiple maxima in the laser spot^{234,267}.

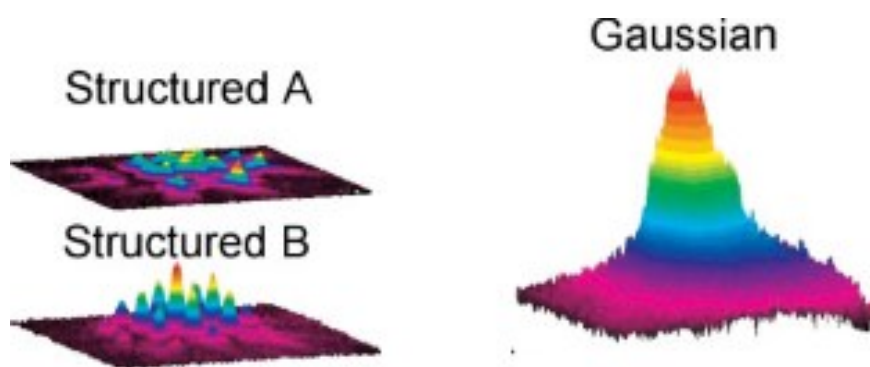


Figure 1.24. Laser fluence of Nd:YAG lasers. The structured beam profile of the Bruker timsTOF Flex smartbeam 3D laser compared to the Gaussian profile representative of the Waters SYNAPT G2 HDMS instrument laser. Reprinted with permission from John Wiley and Sons: Holle *et al.*, 2006. Optimizing UV laser focus profiles for improved MALDI performance. *Journal of Mass Spectrometry*²⁶⁷.

1.7. Conventional Lipidomics

The invention of the ESI source has undeniably been essential for application of MS to lipid analysis¹¹⁶. This has led to the emergence of shotgun lipidomics and LC-MS/MS lipidomics as the most popular approaches in modern lipidomics cancer research^{268,269}. Both techniques offer high sensitivity and specificity, dynamic coverage, and comprehensive structural characterisation of lipids. Internal standard mixtures that mimic the physicochemical properties (functional groups, charge state) of the lipid subclass are included for quantitation²⁷⁰. However, the biggest disadvantage with liquid phase lipidomics is that all spatial information of lipids in anatomical foci of interest in the biological tissue is lost. Hence, it becomes challenging to accurately relate identified lipid species back to disease biology.

1.7.1.1. Shotgun Lipidomics

Shotgun lipidomics is the direct infusion of an extracted sample into the ESI inlet of a MS analyser¹⁰³. Lipids are isolated by liquid-liquid extraction using a high organic mixture (chloroform/methanol) that disaggregate hydrophobic lipid from the complex biological tissue. The most popular methods of lipids extraction are the Folch extraction²⁷¹ or Bligh-Dyer methods²⁷² with minor modifications. Partitioning is achieved using a small volume of water followed by centrifugation to separate the lipid-containing bottom layer from the upper-aqueous layer by carefully pipetting through the protein interphase. Derivatization or salt addition steps are optionally included to improve signal detection depending on functional group moieties and fatty acyl double bond position of interest. Shotgun lipidomics

is offers straightforward and simple quantification. A unique feature is lipid class are sampled at a constant concentration of the solution during infusion paving way for multiple fragmentation strategies^{103,269}. So, one internal standard per class is sufficient because ionisation depends on headgroup not the differing acyl chains making shotgun lipidomics more quantitative than LC-MS/MS^{103,269}. With the inclusion of an analytical column between the pneumatic sample outlet and mass analyser source, shotgun lipidomics essentially becomes LC-MS/MS.

1.7.1.2. LC-MS/MS Lipidomics

LC-MS/MS has the added advantage of an additional dimension of separation – retention time. Separation is achieved by elution of compounds based on their physiochemical properties and interaction with the stationary phase. This also improves sensitivity of lowly abundant lipids²⁶⁸. Reverse phase chromatography usually employs a hydrophobic stationary phase column constituted of C18 alkyl groups. Typically, an increasing gradient of organic mobile phase impels elution, thereby retention of lipids is dictated by the lipophilicity of the fatty acyl groups. Contrary, hydrophilic interaction chromatography (HILIC) uses a hydrophilic stationary phase such as amide with increasing polar mobile phase to elute lipids based on their headgroup chemistry²⁷⁰. The merits of both techniques in isolating lipids have been extensively reviewed before¹⁰³. Normalisation approaches are important to robustly quantify the lipids of interest. Measurement of total weight, total DNA or protein is ordinarily performed prior to analysis to establish the appropriate injection volume for statistical comparison of different samples in the batches.

1.8. LC-MS/MS Drug Quantification

Besides its wide application in lipidomics, ESI-based quantitative mass spectrometry is one of the principal techniques for targeted analysis of pharmaceuticals (synthetic drug) and biopharmaceuticals. Exogenous drugs and their metabolites are regarded as small molecules like lipids. Biopharmaceuticals include vaccines, recombinant proteins and monoclonal antibodies are considered large molecules²³⁸. Multiple body sites are used for sampling test drug²⁷³. Typically, plasma and urine are the most common but cerebrospinal fluid, saliva can also be tested to capture a complete physiological profile of the compound^{273,274}.

A critical juncture in any drug development pipeline is in the pharmacokinetic (PK) studies²⁷⁵. Regulatory authorities such as the FDA and EMA have put forward guidelines for the establishment, testing and validation of bioanalytical methods. During regulatory approval, investigational new drug applications (NDA) are scrutinised, part of this, is a requirement for sponsors to have robust and defensible assays in place. PK parameters focus on absorption, distribution, metabolism and excretion (ADME) both at Phase I and Phase II studies²⁷⁶. Post-marketing surveillance studies and current clinical practice also require robust LC-MS/MS analytical methods to personalise treatment dosage especially in cancer²⁷⁷. This is driving forward the areas of precision medicine, therapeutic drug monitoring and pharmacogenomics^{274,278}.

1.9. Mass Spectrometry Imaging in Cancer

The following **Table 1.7** gives an overview of key studies in the literature where MSI has addressed knowledge gaps in lipidomics composition of solid tumours.

Author	Method	Matrix/Solvent	Instrument	Disease	Main Findings
Eberlin <i>et al.</i> , 2010 279	DESI MSI	50:50 acetonitrile water	LTQ linear ion trap mass spectrometer, Thermo Fisher Scientific	Prostate cancer	Cholesterol sulfate differential abundant in cancer compared to normal tissue in n=68 patients
Cimino <i>et al.</i> , 2013 280	MALDI MSI	1,5 DAN sublimation	SolariX FTICR, Bruker	Breast cancer tumour mouse xenografts	Various low abundant PL species detected with high mass accuracy and mass resolution differentially distributed between necrosis, inflammation, and tumour
Pirman <i>et al.</i> , 2013 281	MALDI-MS profiling	DHB (20 mg/ml chloroform: ethanol (9:1 v/v)	SYNAPT G1 Q-TOF, Waters	Non-small cell lung cancer (NLSC)	EPA incorporation into PL was 4 times higher in H596 cells than A549 cells due to low expression in cytosolic PLA ₂
Mirnezami <i>et al.</i> , 2014 282	MALDI MSI	CHCA	SYNAPT G2 HDMS Q-TOF, Waters	Colorectal cancer	PC(16:0/18:1), LPC(16:0) and LPC(18:1) significantly higher in tumour adjacent mucosa compared to tumour remote regions in n=12 patients
Goto <i>et al.</i> , 2014 283	MALDI MSI	9-AA sublimation	IMScope, Shimadzu	Prostate cancer	Three species; PI(18:0/18:1), PI(18:0/20:3) and PI(18:0/20:2) higher in cancer epithelium compared to benign in n=14 patient samples

Goto <i>et al.</i> , 2015 284	MALDI MSI			Prostate cancer	LPC(16:0)+H] ⁺ , LPC(16:0)+Na] ⁺ , LPC(16:0)+K] ⁺ , LPC(16:0)+matrix+H] ⁺ and SM(d18:1/16:0)+H] ⁺ significantly lower in cancer than in benign tissue in n=31 patients <ul style="list-style-type: none"> LPC(16:0)+H]⁺ predicted biochemical recurrence after radical prostatectomy
Hall <i>et al.</i> , 2016 285	MALDI MSI	DHB or DHAP 10 mg/ml	MALDI LTQ Orbitrap Elite, Thermo Fisher Scientific	MYC-driven lung cancer mouse model	<ul style="list-style-type: none"> Increased signalling precursor lipids in normal compared to tumour (saturated PC and PG) Increased PI and AA containing PL in tumours Deactivation of MYC decreased AA and eicosanoid metabolites with reduced activity of high cPLA₂ expression
	LESA-MS	1:2:4 chloroform: methanol: isopropanol with 10 mmol/L ammonium formate	LTQ Orbitrap Elite, Thermo Fisher Scientific		
Sans <i>et al.</i> , 2017 286	DESI MSI	Dimethylformamide: acetonitrile 1:1 (v/v) for negative ion mode 100% acetonitrile for positive ion mode	LTQ Orbitrap Elite, Thermo Fisher Scientific	Serous ovarian cancer	<ul style="list-style-type: none"> Molecular characterisation of normal, borderline ovarian tumours and high-grade serous carcinoma based on altered metabolite signatures in n=78 patient samples Classification model identified predictive markers of aggressiveness FAs, Cer, PL, cardiolipins and TAGs
Sun <i>et al.</i> , 2010 287	DESI MSI	Acetonitrile:water 8:2 (v/v) in positive and negative ion mode	Q-Exactive mass spectrometer	Esophageal squamous cell carcinoma	<ul style="list-style-type: none"> FA biosynthesis was altered in 256 cases of cancer versus matched normal tissue FASN implicated in carcinogenesis

Table 1.7. Key studies exploiting the application of MALDI technology to cancers.

A concise review of spatially resolved lipidomics in prostate cancer is presented in the next section.

1.10. Literature Review Article: Lipidomics in Prostate Cancer Research

The following review article summarises previous work that has been done on mass spectrometry lipidomics profiling analysis in prostate cancer with a focus on studies that exploited MSI as a spatial tool for the discovery of lipid biomarkers with clinical translational potential.

Statement of Authorship

Title of Paper	Prostate Cancer: An Attractive Target for Spatially Resolved-Lipidomics Based Biomarker Discovery
Publication Status	<input type="checkbox"/> Published <input type="checkbox"/> Accepted for Publication <input type="checkbox"/> Submitted for Publication <input checked="" type="checkbox"/> Unpublished and Unsubmitted work written in manuscript style
Publication Details	Manuscript in preparation and planned for submission to an invitational request to Cancers (Basel) on behalf of Prof. Johan Swinnen

Principal Author

Name of Principal Author (Candidate)	Shadrack Mulinge Mutuku		
Contribution to the Paper	Conceptualized the article, Writing, editing, and reviewing of the manuscript		
Overall percentage (%)	80%		
Certification:	This paper reports on original research I conducted during the period of my Higher Degree by Research candidature and is not subject to any obligations or contractual agreements with a third party that would constrain its inclusion in his thesis. I am the primary author of this paper.		
Signature		Date	14 Jul 2020

Co-Author Contributions

By signing the Statement of Authorship, each author certifies that:

- i. the candidate's stated contribution to the publication is accurate (as detailed above);
- ii. permission is granted for the candidate to include the publication in the thesis; and
- iii. the sum of all co-author contributions is equal to 100% less the candidate's stated contribution.

Name of Co-Author	Paul J. Trim		
Contribution to the Paper	Provision of ion mobility data and participated in editing and reviewing of draft manuscript		
Signature		Date	20/07/20

Name of Co-Author	Marten F. Snel		
Contribution to the Paper	Participated in editing and reviewing of draft manuscript		
Signature		Date	21/7/2020

Name of Co-Author	Lisa M. Butler		
Contribution to the Paper	Participated in editing and reviewing of draft manuscript		
Signature		Date	14/7/2020

Prostate Cancer: An Attractive Target for Spatially Resolved-Lipidomics Based Biomarker Discovery

Shadrack M Mutuku^{1,2}, Paul J. Trim^{1,3}, Marten F. Snel^{1,3}, Lisa M Butler^{1,2,4}

¹Adelaide Medical School, University of Adelaide, Adelaide, South Australia 5005, Australia.

²Prostate Cancer Research Group, South Australian Health and Medical Research Institute (SAHMRI), South Australia 5000, Australia

³Proteomics, Metabolomics and MS-Imaging Core Facility, SAHMRI, Adelaide, SA 5000, Australia.

⁴Freemasons Foundation Centre for Men's Health, University of Adelaide, Adelaide, SA 5005, Australia.

Key words: Prostate Cancer, Biomarkers, Mass Spectrometry Imaging, Lipidomics, Metabolomics.

Total word count: 8,210 (excluding references)

Background

The conundrum in biomedical research of prostate cancer (PCa) is the inability of current prostate specific antigen (PSA) diagnostics to delineate the more indolent, low-risk localised disease (LRLD) from the more aggressive, high-risk localised disease (HRLD) cases. There is a critical deficiency of prognostic markers to aid treatment selection and response to standard therapy. However, intensive research over the past decade has revealed PCa to generate energy from intracellularly synthesised fatty acids (FA) and extracellular lipids from the circulation or adjacent, periprostatic adipose tissue^{109,124,134,288,289}. This understanding, coupled with advances in technologies to assay lipids by quantitative and qualitative mass spectrometry (MS) lipidomics platforms and mass spectrometry imaging (MSI), has led to considerable interest in lipidomics as a tool for discovery of lipid-based biomarkers for PCa^{290,291}.

Prostate cancer (PCa) is a leading cause of cancer mortality and is the second most common cancer among men in developed countries^{5,292,293}. By binding to the androgen receptor (AR), androgens promote the development and growth of the prostate gland in human males^{127,294} and are established regulators of lipid metabolism²⁹⁵. PCa cells often exhibit deregulated AR signalling that enhances lipid metabolism through the overexpression of key lipid synthetic enzymes²⁹⁶ and mobilisation of fatty acid uptake from adipose tissue in the tumour microenvironment by lipolysis¹³⁷. This metabolic reprogramming component is regarded as a hallmark of many other solid tumours like lung and prostate cancer²⁹⁷.

In this review, PubMed and Scopus, were queried for all publications pertaining to applying mass spectrometry analytical strategies (MS and MSI) in PCa. With the aim of evaluating the utility of lipidomics and metabolomics in diagnosis and prognostication of PCa, studies are included that describe lipids and lipid metabolites that are associated with prostate tumours compared to benign tissue and increased risk of PCa progression. In addition, articles that discuss the metabolome of PCa, principles of MS analytical procedures and their application to PCa biomarker discovery and advancement of MSI technologies are included. The main articles that explored the utility of MSI techniques to detect PCa and categorise severity of PCa based on clinical pathological features of human prostate tissue specimens are summarised in [Table 1](#). and examined in text.

The Role of Androgens and Lipids in Prostate Cancer

Lipid play a wide array of physiological functions in health and disease in eukaryotic systems¹⁸⁰. Glycerophospholipids (PC, PE, PS, PI and PG) are important structural components for extracellular plasma membrane and organelles¹¹⁵. Specifically, PC and PE species are major constituents of the lipid bilayer domain that form barriers to regulate cellular homeostasis, transmembrane protein transporters and receptors for signal transduction¹⁸⁰. The rich incorporation of cholesterol and sphingomyelin form lipid rafts for membrane signalling where lipids act as second messengers¹²⁶. Phospholipase C (PLC) hydrolysis of phosphatidylinositol 4,5-bisphosphate (PIP₂) releases inositol trisphosphate (IP₃) and diacylglycerol (DAG) that activate intracellular calcium signalling and protein kinase C activation, respectively^{102,298,299}. Fatty acyls not only provide substrates for aliphatic chain of glycerolipids but participate in mitochondrial β -oxidation that provides energy for cell multiplication^{124,149}. Triacylglycerols are cellular reserves of energy in the form of lipid droplets. Several categories of lipids play important roles not only in the normal prostate gland but also in PCa ([Figure 1](#)). These include but not limited to sterols, fatty acyls glycerophospholipids and glycerolipids.

Steroid hormones are critical for the normal development and maturation of the prostate. The growth, progression and metastasis of PCa is hormonally regulated by the actions of androgens at the androgen receptor (AR)^{300,301}. Once in the nucleus, AR directly binds to androgen response elements or indirectly activates steroid response element binding protein (SREBP) to modulate lipogenic genes. Thus AR initiates the expression of the fatty acid synthetase

(FASN), ATP-citrate lyase (ALCY) and acetyl-CoA carboxylase (ACC) and these enzymes also harbour SREBP binding sites³⁰⁰. ACLY converts cytosolic citrate to acetyl-CoA while ACC produces malonyl-CoA from carboxylation of acetyl-CoA. FASN is responsible for palmitate C16:0 synthesis from acetyl-CoA that is a central template for synthesis of other fatty acids and lipids with varied specialised roles in prostate epithelial cells. Complexity of phospholipid class variety is realised by insertion of double bonds at C9 of palmitate and propagation of fatty acyl chain length catalysed by desaturation and elongation enzymes, stearoyl-CoA desaturase (SCD)³⁰² and ELOVL2-7³⁰³, respectively.

Androgens support *de novo* lipid biosynthesis by promoting anabolic gene pathways in PCa where cancer cells have been shown to overexpress FASN, ACC and ACLY^{131,296,304}. There is accumulating evidence that SCD and ELOVL5 and ELOVL6 are under transcriptional control of AR^{147,305} and upregulated in PCa. Hence, current research strategies are informed by exploitation of lipid metabolic pathways to provide key therapeutic vulnerabilities of PCa. Rysman and colleagues described targeting of the lipogenesis program by pharmacological and siRNA inhibition of ACC. This resulted in decreased phospholipids containing saturated and mono-unsaturated fatty acids and increase in polyunsaturated species which enhanced PCa cell susceptibility to peroxidation leading to oxidative stress and cell death³⁰⁶. Likewise other studies have shown counteraction of AR driven lipogenesis in PCa, by development of novel inhibitors of FASN that demonstrate suppression of growth, migration and invasion of PCa cells³⁰⁷ and reduction in cellular FA and lipid turnover³⁰⁸. Moreover, androgens have been recently reported to regulate the expression of

lipid transporters LDLR³⁰⁹ and SCARB1 which is reversed with enzalutamide inhibition²⁸⁸.

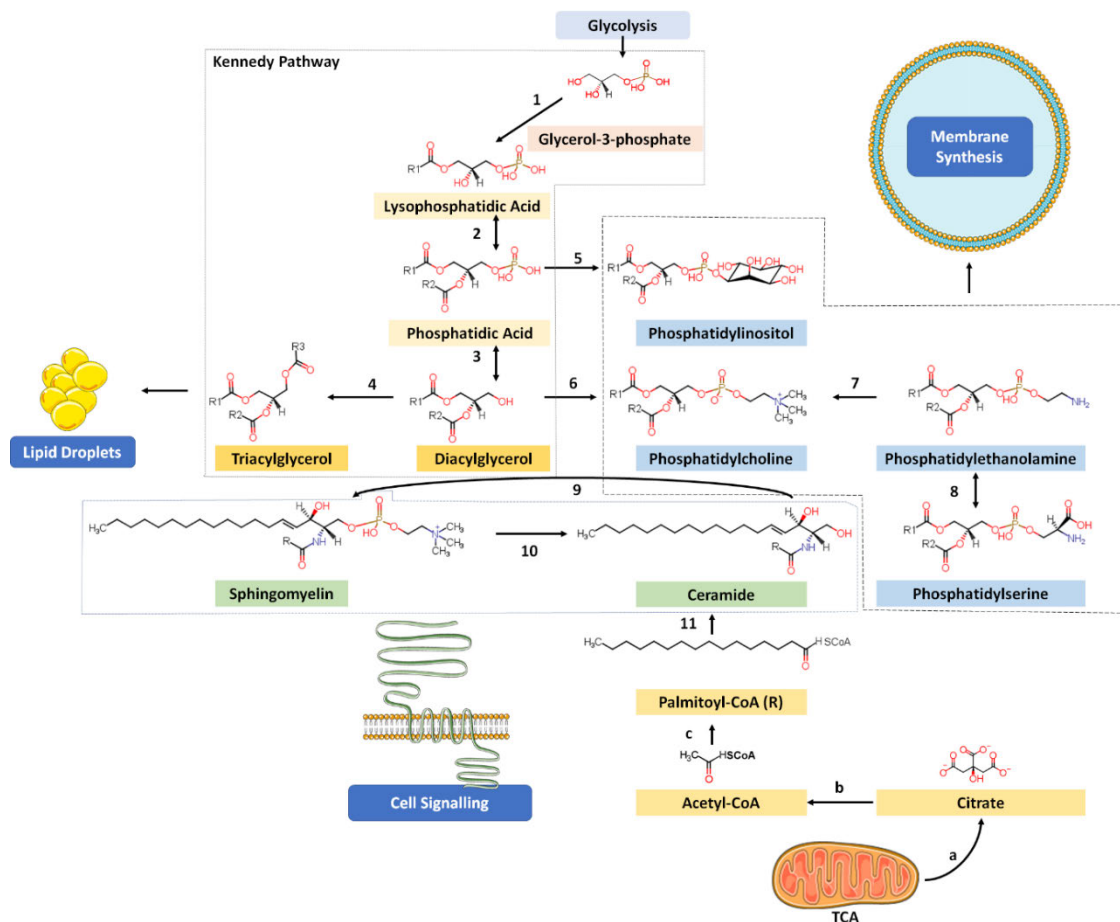


Figure 1. Schematic representation of lipid metabolism in prostate cancer.

Glycolytic pathway provides glycerol-3-phosphate a key substrate for lysophosphatidic acid (LPA), phosphatidic acid (LPA) and diacylglycerol (DAG) synthesis in the Kennedy pathway. DAG and PA are precursor for phospholipid (PL) synthesis that ultimately function as cellular membrane components. DAG is converted to triacylglycerol (TAG) that form lipid droplets that serve as cellular energy stores. Sphingolipids (ceramides and sphingomyelin) from autocrine enzymes participate in cell signalling. Mitochondrial TCA cycle provides citrate that precedes synthesis of fatty acids that are incorporated in TAG, DAG, PL and sphingolipid metabolism. **1.** Acyltransferase reacts with fatty acyl CoA generated from **a** TCA cycle **b.** ATP-citrate lyase (ACLY) **c.** Fatty acid synthase (FASN) **2.** Acyltransferase, phospholipase, **3.** Phosphatidic acid phosphatase **4.** Acyltransferase. **5** CDP-diacylglycerol inositol phosphatidyltransferase **6.** CTP-phosphocholine cytidyltransferase and CDP-choline;1,2 diacylglycerol choline phosphotransferase **7.** Methyltransferase using S-adenosylmethionine as a donor. **8.** Decarboxylase and serine transferase. **9.** Sphingomyelin synthase. **10** Sphingomyelinase. **11.** β -oxidation and Δ^4 desaturation reactions with serine.

Author	Research	Method	Findings
Randall <i>et al.</i> , 2019	Molecular characterisation of PCa	MALDI FT-ICR MSI, MALDI TOF MSI	Prostate tumours can be differentiated using different Gleason grades based on metabolomic differences
Morse <i>et al.</i> , 2019	Identification of PCa	DESI MSI	Logistic regression and PCA/LDA model of lipid and metabolite classifiers can reliably identify cancer and distinguish Gleason grade groups
Banerjee <i>et al.</i> , 2017	Diagnosis of PCa	DESI MSI	LASSO model identified glucose and citrate as predictors of PCa and normal tissue
Wang <i>et al.</i> , 2017	Metabolite profiling of PCa	MALDI FT-ICR	Increased energy charge and low abundance of neutral triacylglycerols in cancerous tissue
Goto <i>et al.</i> , 2015	Molecular characterisation and diagnosis of PCa	MALDI MSI	LPC(16:0) and SM(d18:1/16:0) were lower in tumour compared to benign epithelium. LPA(16:0) was an independent predictor of biochemical recurrence after radical prostatectomy
Goto <i>et al.</i> , 2014	Molecular characterisation and diagnosis of PCa	MALDI MSI	PI species highly abundant in cancer compared to benign epithelium <ul style="list-style-type: none"> • PI(18:0/18:1) • PI(18:0/20:3) • PI(18:0/20:2)

Table 1. Main studies using MSI as a spatial tool for prostate cancer metabolomics and lipidomics.

Experimental Approaches in Metabolomics and Lipidomics

The lipidome is the comprehensive composition of all lipid classes found in a cell and/or its subcellular compartments and biological fluids (plasma, serum, saliva). Lipidomics is a subset of the field of metabolomics. Early lipidomics studies used fast atom bombardment mass spectrometry (FAB-MS)³¹⁰. Electrospray ionisation (ESI) technology was invented in 1984 by John Fenn¹⁷³. Later, Han and Gross were the first to report the use of ESI-MS in a lipid analytical context, where they profiled erythrocytes for structural determination and quantitation of important plasma membrane phospholipids³¹¹. This technological advancement enabled measurement of phospholipids with at least 1,000-fold increase in signal sensitivity and improvement in lipid coverage compared to FAB-MS³¹¹. This heralded the development of shotgun lipidomics where ESI sources coupled to mass analysers were applied for the direct analysis of lipids from biological samples³¹².

Conventional ESI-MS methods utilise triple quadrupole (QqQ) instruments which are tuned for lipid quantitation. This involves using low energy collision induced dissociation/collision activated dissociation (CID/CAD), where selected precursor masses are fragmented to yield constituent product ions. This approach has the advantage of covering a wide variety of moderately abundant lipids with a high accuracy of quantitation²⁶⁸. However, ambiguities of the structural fragment ions can remain for the elucidation of fatty acyl chain positional isomers. Furthermore, ESI-MS/MS QqQ platforms are reported to exhibit ion suppression which affects the sensitivity of capturing naturally abundant lipids^{313,314}. For instance, choline containing lipids form cations more

efficiently at the expense of PE or LPE species. Hence, other types of enhancements to improve confidence of annotation have been formulated. These include using high resolution accurate mass (HRAM) measurements and different chemical modifications of the aliphatic side chains or headgroups.

HRAM platforms such as quadrupole time-of-flight (Q-TOF), Orbitraps and magnetic Fourier transform-ion cyclotron resonance (FT-ICR) have transformed ESI-MS/MS by improving the selectivity of precursors and assignment of MS/MS fragments^{315,316}. In Q-TOF, the m/z values of ions are calculated from their flight times in an electric field with suitable mass accuracy and coverage³¹³. Orbitraps and FT-ICR instruments principally measure the frequency of focused, accumulated or stored ions to accurately record their exact m/z . Because mass resolution is proportionate to the acquisition time, there is some loss of high throughput analysis and sensitivity³¹³. Chemical modification includes charge-switch derivatization techniques for poorly ionisable compounds, alkaline hydrolysis for sphingolipids and plasmalogens and isotopologue analysis of double anionic lipids^{182,317,318}. A major drawback of exact mass measurements or conventional tandem MS methods is that it remains difficult to obtain detailed information on aliphatic chain double bond (C=C) positions and stereochemistry. Yet in recent years, three techniques have made it possible to gather detailed chemical information on C=C positions beyond the CID tandem MS products. Firstly, ultraviolet photodissociation (UVPD), which uses photons emitted at 193 nm cleave double bonds³¹⁹. Secondly, the Paternò-Büchi reaction, which employs an UV irradiated acetone infusion which forms an oxetane ring that is then CID reacted³²⁰. Lastly, gas-phase ozonolysis (OzID) which resolves both double bond and regiospecific isomers³²¹.

LC-MS/MS is employed for the separation of different subclasses of lipids based on lipophilicity with each species having a unique retention time³²². This added level of confidence overcomes the inability of shotgun lipidomics to resolve isobaric precursor compounds³²³. LC-MS/MS methods are often targeted experiments to begin with, based on established chromatographic methods. Each unique lipid species has the same peak (retention time), meaning lipids from a certain subclass have the same elution window in different samples in a single experiment. Lipid measurements can be processed by either untargeted or targeted data processing methods, but downstream untargeted processing should be able to mitigate “correspondence determination” as reviewed by Richard Gross²⁶⁸. As mentioned earlier, QqQ instruments are sensitive but lack enough selectivity. This challenge can be ameliorated by using Q-TOF systems which have a mass resolving power of 8,000 up to ~40,000 FWHM which can afford the resolution and identification of more unknown lipid species. LC-MS/MS Q-TOF systems are more suited for qualitative analysis and relative quantification of statistical highly abundant lipids leading to hypothesis generation¹⁵⁴. LC-MS/MS QqQ systems are suitable for absolute quantification of many lipids from a pre-formulated research question.

Mass Spectrometry Imaging

Mass spectrometry imaging (MSI) is a newer approach to metabolomics and lipidomics developed to address the lack of spatial knowledge of cellular and compartmental source altered metabolites in tissues that is classical to shotgun and LC-MS/MS lipidomics methods. Similarly, traditional lipid imaging techniques such as Oil Red O staining have been used to visualise neutral acyl glycerides, cholesterol esters and lipid droplets in fresh(-frozen) samples³²⁴. The major limitation of this technique is lack of specificity in differentiation of these neutral lipids and inability to stain hydrophilic lipid classes³²⁵. Now MSI has become an increasingly popular tool for lipidomics, appreciably due to its power to depict pathology and probe pathophysiological perturbations in heterogenous and complex biological samples^{152,287}. MSI is commonly used as an untargeted tool for discovery systems biology lipidomics. MSI sources are coupled to time-of-flight (TOF), Q-TOF, Orbitrap, magnetic Fourier transform-ion cyclotron resonance (FT-ICR) mass analysers (in order of increasing mass resolution and mass accuracy).

MSI is the generation of ions at definite co-ordinate loci across a tissue or inorganic surface²⁰⁸. Molecular information from multiple mass spectra are combined to create an ion map akin to chemical histology³²⁶. There are multiple modes of MSI. The first is matrix-assisted laser desorption/ionisation (MALDI) which uses a laser to fire at a small molecule base or acid known as matrix, that is uniformly applied on top of the tissue^{162,200}. In 1985, Michael Karas demonstrated that the application of UV radiation for desorption of non-volatile and organic molecules at a wavelength for the frequency-quadrupled Nd-YAG

(266 nm) or tripled (355 nm) laser, which was regarded as a soft-ionisation technique^{163,164}. Separately, Tanaka and Spengler then reported the laser ionisation of high mass protein and polymers to generate spectra around m/z 100,000 by UV-pulsed ion extraction on TOF MS systems^{165,327}. Initial MALDI MSI studies were focused for proteomics discovery. Caprioli and colleagues have showed the utility of MALDI-TOF MS for the detection of insulin and hormonal peptides in biological tissue samples in enzyme digested fresh-frozen sections of rat pancreas and pituitary glands, respectively²⁰⁵. They have also detected intact proteins in alcohol-fixed lung specimens by MALDI MSI²²⁰. Sun *et al* was the first to measure cellular phospholipids by MALDI-TOF profiling of cellular lipids extracted from murine heart in which they described the formation of lipid ions and associated alkali adducts using various matrices¹⁸³. 9-aminoacridine matrix enabled the detection of anionic lipids (PI, PG, PS, PE and PA and CL) in negative ion mode and PC in positive ion mode¹⁸³. Another useful application of MALDI MSI is the characterisation of small molecule drug distributions in solid tumours. Trim *et al* visualised the uptake of the anti-glioblastoma agent vinblastine in whole body rat sections by MALDI MSI with ion mobility separation³²⁸. Recently, using both MALDI MS/MS imaging and LC-MS/MS, kinetics of enzalutamide uptake were demonstrated in a time course dose study in patient-derived prostate explants with the drug ion signal spatially localised to heterogenous epithelial regions³²⁹.

The Cooks group pioneered another MSI method called desorption electrospray ionisation (DESI)^{178,330}. It employs a charged solvent stream that scans across the tissue surface to deflect particles into an angular positioned inlet that propagates ions towards the detector¹⁷⁸. DESI imaging results in less

complex spectra which make lipid assignments easier in absence of chemical noise from matrix ions. There is also the advantage of doping derivatives such Li^+ for tandem MS or Ag^+ for improved detection of unsaturated olefins and cholesterol esters³³¹, but the lateral resolution with DESI is typically 100 μm – 200 μm resulting in average quality ion maps compared to high definition MALDI imaging. Another imaging technique is laser ablation electrospray ionisation (LAESI), a hybrid of MALDI and DESI. In LAESI, a laser ablates particles from the surface that are charged by a perpendicular stream of electro-sprayed charged solvents³³². Secondary ion mass spectrometry (SIMS) is an ionisation method for the analysis of solid surfaces by sputtering of the sample with a focused primary ion beam and collecting the ejected secondary ions^{155,333}. SIMS like DESI is a matrix-free approach but achieves an extraordinary spatial resolution of 100 nm which generate spectra from sub-cellular lipidomes. However, SIMS yields a lot of in-source fragment ions making it less suitable for lipid imaging but rather fit for analysis of elements, metabolites and small molecule drugs with an m/z less than 200 m/z Da.

The choice of the analytical method to unravel lipidomic profiles is guided by type of sample, availability of instrument, expertise and intended biological interpretation. Each of the different lipidomics approaches discussed herein have their share of distinct advantages and disadvantages for different experimental considerations as highlighted in [Table 2](#). However, with proper designing of experiments, shotgun lipidomics, LC-MS/MS and MSI can be used in combination for structural characterisation, compound annotation together with other “omics” information of samples to be appropriately applied to elucidate lipid biomarkers of disease. Shotgun lipidomics and LC-MS/MS have been

extensively employed to study cell lines, plasma and tissue homogenates. Their application to analysis of tissues and patient derived xenografts relies on histological information for effective group-wise (treatment or disease vs control) comparisons.

	Shotgun Lipidomics	LC-MS/MS Lipidomics	Spatial Metabolomics
Speed	Very high throughput	High throughput	Low to medium throughput
Separation	Exact mass (<i>m/z</i>)	Exact mass (<i>m/z</i>)	Mass accuracy
	Ion Mobility Separation	Retention time <ul style="list-style-type: none"> • Hydrophobic • Head group chemistry • Chiral • Stereochemistry 	Spatial location
		Ion Mobility Separation	Ion Mobility Separation
Identification	Internal standards	Internal standards	Limited internal standards
	MRM	MRM	MS/MS
	MS/MS	MS/MS	Isotopic pattern
	Isotopic pattern	Isotopic pattern	CCS
	CCS values	CCS values	
Quantification	Relative	Relative	Relative
	Absolute	Absolute	Semi-quantitative

Table 2. Comparison of experimental platforms employed in lipidomics analysis in prostate cancer.

The Case of High Mass Accuracy, High Resolution, and Ion Mobility Separation

PCa is recognised as a highly heterogenous and multifocal disease at patient, tumour, cell, genetic and epigenetic levels³³⁴. The first three types of heterogeneity have the potential to be exploited to unravel accurate novel lipid markers of disease aggressiveness by leveraging the *in situ* modalities of MSI. This holds true especially with recent advances in MALDI MSI imaging technologies touching upon virtually all mass spectrometer components. However, the high diversity and structural complexity of lipids in a limited small chemical space and mass range gives rise to several isobaric species³¹⁴. This necessitates high resolution and accurate mass (HRAM) lipidomics approaches for confident identification and annotation of lipid and metabolites and structural fragments^{269,323} ([Figure 2](#)). It is important to describe two parameters in MS experiments. Mass resolution refers to the ability of an instrument to distinguish two peaks with similar m/z values and measured as full width half maximum (FWHM, $m/\Delta m$)¹⁹¹. Mass accuracy is the difference between observed mass and theoretical mass expressed often as parts per million (ppm). Therefore, it is desirable to have “high mass accuracy” and “high mass resolution” MS platforms for spatial lipidomics.

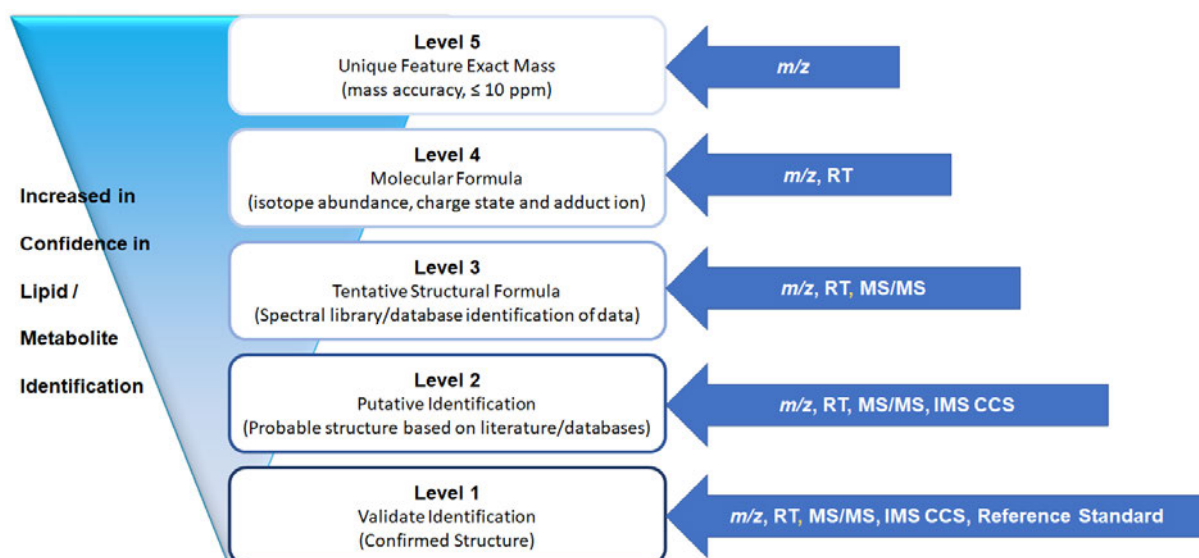


Figure 2. Levels of confidence of metabolite annotation and identification. Adapted with permission from American Chemical Society: Schrimpe-Rutledge *et al.*, 2016. Untargeted metabolomics strategies-challenges and emerging directions. *Journal of the American Society for Mass Spectrometry*³³⁵.

The most common commercial mass spectrometer for imaging are MALDI time-of-flight (TOF) systems because of pulsed ion sources, with quadrupole-TOF instruments offering higher resolution and faster scan speed for imaging¹⁸⁷. Recent improvements include advance laser sources, ion guides and detectors for such systems. Advanced laser sources and focal parameters result in enhanced lateral resolution, focal scanning area and acquisition speeds as exemplified by the 3rd generation Bruker Smartbeam laser^{255,336}. Ion guide rods have been optimised to minimise ion loss and maximise transmission. The analogue-to-digital converters (ADC) in analysers also have improved sensitivity and in spectral dynamic range. Ultra-high mass resolution and accuracy instruments like Orbitrap and FT-ICR instruments offer much better resolving power compared to Q-TOF systems (FWHM 40,000 at m/z 782) but can be less

throughput for imaging since the gain in resolution is a trade-off for acquisition scan time and sensitivity³¹³. The typical resolving power of an Orbitrap is 240,000 FWHM at m/z 400 and 21-T FT-ICR is 1,000,000 FWHM at m/z 400^{337,338}. In recent years ion mobility separation (IMS) has been integrated into imaging mass spectrometers offering a unique orthogonal, gas-phase dimension of separation that can add greater specificity to imaging experiments³³⁹. Separation is described by the collision-cross section (CCS) area – the contact between ions moving at a specific drift velocity through a buffer gas. Dodds *et al* has recently documented summary of the concepts of various IMS systems¹⁹⁴. Just like a mass spectrum, the delineation of two close peaks in an ion mobility spectrum are expressed by resolving power (R_p)¹⁹⁵. The resolving power on the latest commercial instruments are 70 - 300 which still leaves some lipid isomers barely resolved. Ongoing efforts aim to come up with better IMS devices and so far, non-commercial devices have reached R_p of 400¹⁹⁴. A graphical example of the application of MALDI MSI-IMS in prostate tissue is given in [Figure 3](#).

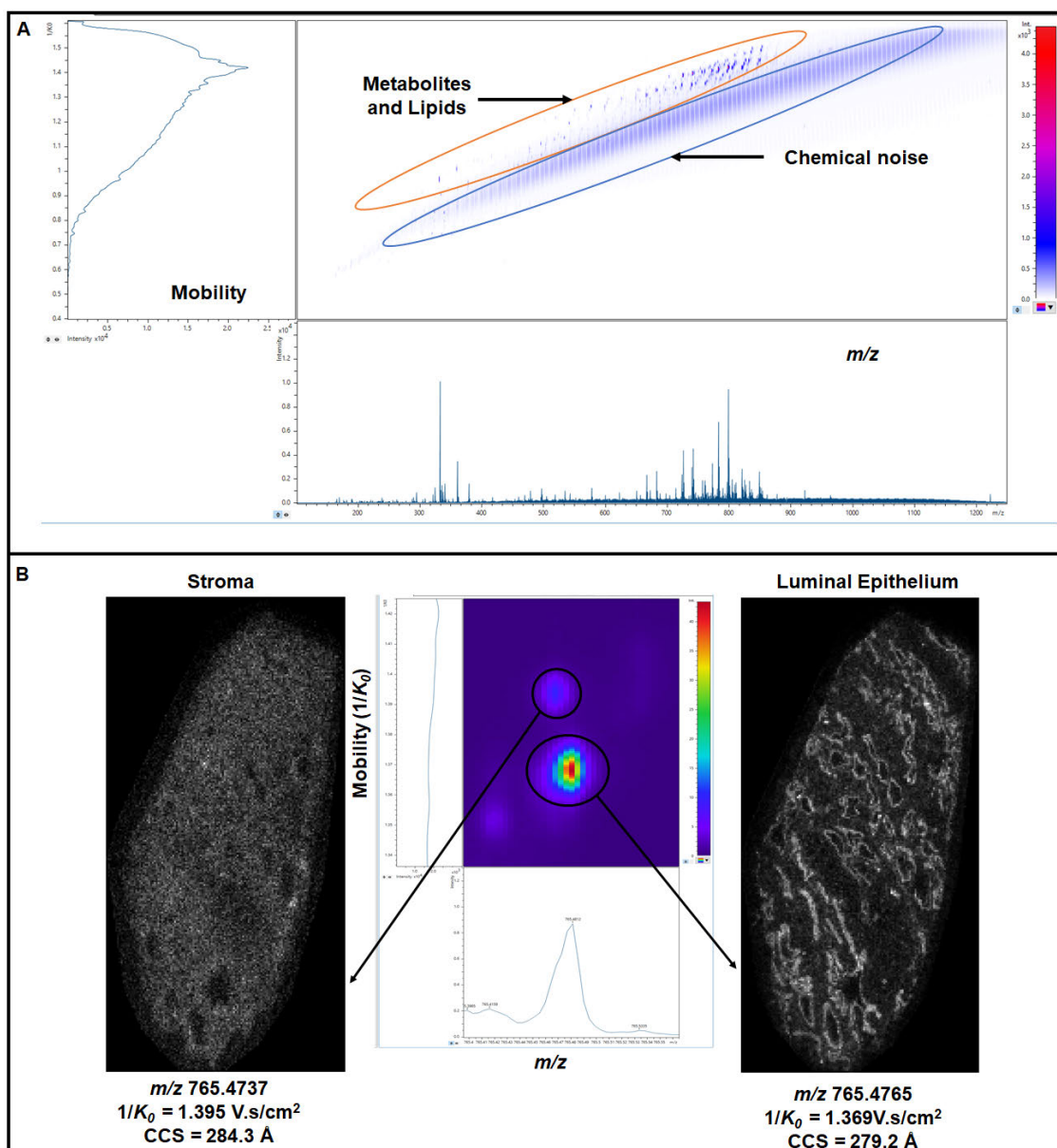


Figure 3. MALDI MSI couple to ion mobility separation. Prostate tissue collected at 10 μm cryosection thickness and CHCA matrix applied with SunCollect Sunchrom sprayer for MALDI positive ion mode imaging with trapped ion mobility on a timsTOF Flex mass spectrometer (Bruker GmbH, Bremen, Germany). **A.** Combined mass spectrum and ion mobility spectrum data shows separation of endogenous metabolites and lipids from chemical noise, with IMS offering more specificity. **B.** An isobaric lipid with a mass accuracy of ± 0.03 Da that is spatially distributed between stroma and epithelium separated based on unique mobilities. The calculation of inverse mobility ($1/K_0$) – CCS area values achieved using the Mason-Champ equation.

Lipidomics in Prostate Cancer

Cell Line Models

The majority of preclinical PCa biology research has been performed using immortalised cell culture³⁴⁰. Androgen-dependent cell lines include the LNCaP which positively express AR^{341,342}. C4-2B is an androgen independent LNCAP lineage cell³⁴³. Androgen-independent cell lines include the 22Rv1 and PC-3 which express mutated AR or lack the receptor, respectively, hence unresponsive to androgen treatment *in vitro*³⁴⁴. Cell lines are easily manipulated, readily available and experimentally predictable³⁴⁵.

Numerous studies probing lipid metabolism in PCa have shown using shotgun lipidomics, and other confirmatory approaches such as spectroscopy and transcriptomics, that PCa cells have a marked enrichment of specific lipid classes. PTEN deletion or loss in PCa has been shown to contribute to metabolic reprogramming involving fatty acid metabolism³⁴⁶. DU-145 cells transfected with siRNA resulted in increased acylcarnitine synthesis and fatty acid β -oxidation compared to controls³⁴⁶. Comparative metabolomic profiling of normal RWPE-1 and metastatic MDAPCa2 AR positive cell lines showed significant increase of PE(18:1/22:4) and PI(16:0/20:4)³⁴⁷. Lipid profiling of normal cell lines, PNT1a, compared to PCa cell lines (LNCaP, DU145 and 22Rv1) showed an increased abundance of PE(18:1/16:0), PE(18:1/18:1) and cholesterol esters (CE) species³⁴⁸. Early studies on the effects of anti-tumoral agents on cancer cell metabolism showed dynamic drug-related lipidomic changes. In the PC-3 cell line, Ouabain induced profound alterations in lipid content in phosphatidylinositol and sphingomyelin lipids as analysed by both FTIR spectroscopy and shotgun mass spectrometry using a nano ESI capillary³⁴⁹. Another study by Jeong and

colleagues assessed the impact of D-allose treatment cell growth in normal prostate epithelial cells (PrEC), LNCaP and DU145 by nano flow LC-ESI-MS/MS. It showed induction of increased abundance of PE(14;0/14:0), PG(16:2/16:0) and PA(20:6) in PrEC with no observable changes compared to LNCaP and DU145³⁵⁰.

Lipogenesis in PCa cells has also been demonstrated by live cell imaging. Using Raman scattering monitoring of deuterated glucose incorporation, Li *et al* showed *de novo* lipogenesis in LNCaP cells and PC3 cells was much higher compared to normal epithelial RWPE1 cells³⁵¹. They also showed level of exogenous FA uptake of deuterated palmitic acid was higher in PC3 cells³⁵¹. A gas chromatography study showed treatment of LNCaP and PC3 cells with linoleic acid (C18:3) induced cell growth³⁵². Intracellular androgens and their active metabolites have also been detected in LNCaP cells using atmospheric pressure photochemical ionisation³⁵³. Untargeted lipidomic analysis of epithelial to mesenchymal transition (EMT) in DU145 PCa cell line, a phenotypic metastatic development showed increase in several polyunsaturated TAG species following TNF α induction³⁵⁴. On the contrary, Cer16:0 levels were revealed to be downregulated presumably to aid membrane fluidity and cell motility going against pro-apoptotic signalling and promoting cancer progression³⁵⁴.

Additional to probing the lipidomics of cell lines, exosomes released by PCa cells have witnessed increasing research interest as non-invasive circulating biomarkers. Exosomes are extracellular vehicles constituted of closed membrane structures that carry lipids and other biomolecules to undergo endocytic fusion with other organelles thereby being recognised as mediators of intracellular communication³⁵⁵. Lipidomic profiling of exosomes secreted by

normal, tumour and metastatic PCa cell lines has shown differential abundance of lipid composition with sterols, sphingolipids and phospholipids being enriched in both NB26 and PC-3 cell lines³⁵⁶. Difference in lipid species of urinary exosomes have also been described, with PS (18:1/18:1) and lactosylCer (d18:1/16:0) levels being significantly higher PCa patients compared to healthy controls³⁵⁷.

Although performing lipidomics analysis on cell line models is amenable to most lipidomics platforms, can be executed in high throughput fashion and can offer insights into deregulated lipid metabolism in PCa, cells lines do not factor in tumour heterogeneity. PCa is heterogenous at the patient, tumour and population level^{2,4,334}. Specifically, at the macroscopic tissue level where the tumour microenvironment has a multitude of cell types such fibroblast, stem cells, immune cells, inflammatory cells, adipocytes, and endothelial cells²⁹⁷. For instance, fibroblasts in the stroma are recognised as implicated in playing either a cancer promoting or suppressing role in solid tumours including the prostate³⁵⁸.

Xenografts, Patient-Derived Models and Human Tissues

Despite cell culture being the most convenient platform to initiate PCa biomarker discovery, they suffer from the distinct disadvantage, of inadequately and inaccurately simulating the physiological architecture of prostate tissue³⁴⁵. Importantly, they do not represent systemic intracellular communication and hormonal signalling³⁵⁹. *In vivo* model systems are generated using cell lines that are engrafted by subcutaneous injection into the flank of immunocompromised mice. These are termed as xenografts and are regarded more clinically relevant systems, as they allow evaluation of drug efficacy and predict human pharmacokinetics. Although, as tumour implants are within a closed whole body environment, the murine host must also be either immunocompromised or non-obese diabetic for successful implantation of malignant cells, which therefore excludes the important role of the immune system^{345,360}. This technique has been advanced by using primary human tumour cells termed patient-derived cancer tissue xenografts (PDX). They retain key physiological properties of the original tumour such as heterogeneity, androgen ablation response and metastasis³⁶¹. Nonetheless, this approach still lacks consideration of the immune microenvironment of the tumour and has significant variability in engraftment rate in the host³⁶⁰. Another approach is *ex vivo* culture of human tissue called patient derived explants (PDE)³⁵⁹. This still has the advantage of PDX model but in addition a level of immune system activity is retained with cells present from the resected tissue^{359,362}. Moreover, PCa is difficult to establish as PDX models due to unknown intrinsic factors³⁶³ making PDE more ideal for therapeutic screening and precision medicine.

In a PTEN/PML null mouse model to mimic metastatic PCa, overactivated lipogenesis mediated by SREBP showed that 72% of 1,743 identifiable lipids had a log₂ fold change values greater than zero in comparison of *Pten^{pc-/-}; Pml^{pc-/-}* to wild type. There was overabundance of usually low-level membrane phospholipids LPE, LPG and PG which the researchers postulated could provide metastatic promoting lipid messengers³⁰⁹. Moreover, elevation of the 30 most common fatty acyl chains, showed that saturated (14:0, 16:0, 18:0) and monounsaturated (16:1, 18:1 and 24:1) were upregulated in PTEN and PML knockout of prostate epithelium in simulation of aggressive PCa³⁰⁹. Pharmacological inhibition of SREBP by fatostatin has been shown to reduce expression of lipid and cholesterol synthesis genes, FASN and HMGCR, respectively, to decrease AR-mediated PSA levels³⁰⁵ and suppress primary tumour growth and distant bone metastasis³⁰⁹. However, not all prostate tumours have equal therapeutic responsiveness to statins, owing to the reciprocal feedback loop whereby sterol depletion reactivates SREBP that propagate the mevalonate pathway of cholesterol synthesis. A recent study showed additional targeting of SREBP by dipyrindamole, enhanced sensitivity to Fluvastatin, resulting in delayed tumour growth in LNCaP derived mouse xenografts³⁶⁴.

Clinical tumour tissues show similar abnormalities in lipid metabolism compared to their *in vivo* model counterparts. Yue *et al* revealed using Raman spectroscopy that esterified cholesterol was abnormally accumulated in advanced PCa. This study involved 19 PCa patients, 10 benign prostatic hyperplasia (BPH), 3 prostatitis, 3 prostatic intraepithelial neoplasia (PIN), 12 Gleason 3 and 12 >Gleason 4. This was corroborated with ESI-MS of lipid extracts that showed the cholesterol ester (CE), cholesteryl oleate (CE 18:1) was

more abundant in high-grade PCa compared to normal tissue. Mechanistically, the researchers showed PTEN loss and subsequent PI3K-AKT-mTOR signalling³⁶⁵ caused CE accumulation in aggressive PCa and that blocking CE metabolism impaired tumour cell proliferation by reduction of essential FA uptake and reduction of CE stores impaired invasiveness³⁶⁶. In a comparison of PCa tumour with adjacent non-tumour tissue from 76 PCa and 18 BPH patients using non-targeted lipidomics, Li and colleagues identified accumulation of cholesterol ester (CE) species as potential biomarkers that distinguished adenocarcinoma from BPH with greater sensitivity compared to PSA with an AUC of 0.9-0.96³⁶⁷. Consistent with the Yue study, CE(18:1) was more abundant in cancerous tissue and had the highest discriminant capacity, being able to classify prostate tumour from normal tissue and BPH with AUC of 0.91 and 0.96 respectively³⁶⁷.

The more complex condensation products of PG, cardiolipins (CL), have been implicated in promoting tumour cell behaviour. CL composition has been reported to be higher in cancer compared to normal tissue in 5 out of 6 patients at individual level although this was a small study. The content of palmitoleic acid (16:1) in CL was found to be higher in tumour tissues which indicates that free fatty acids play an important assimilatory roles in PCa cells³⁶⁸.

Plasma Based Lipidomics

Plasma based lipidomics in PCa is a compatible strategy to develop a non-invasive blood-based biomarker such as PSA²⁹. Together with urine, plasma or serum based lipidomics are considered liquid biopsies and in practice they are more tolerable by patients since they are minimally invasive techniques. Screening of metabolite markers relies on the premise that lipids released from the prostate into systemic circulation or patient metabolic changes in response to the disease or hormonal therapy can be monitored just like PSA.

Secreted lipids involved in endocrine and/or paracrine signalling can be found in the blood stream. An example of the source of bioactive lipids is the conversion of plasma membrane bound sphingomyelins to ceramides³⁶⁹. In a recent shotgun lipidomics study of two population cohorts in Australia of men undergoing PCa treatment and management with docetaxel and prednisone³⁷⁰, Cer(d18:1/24:1), SM(d18:2/16:0) and PC(16:0/16:0) species were significantly prognostic of a shorter cumulative overall survival. Hormone sensitive CRPC was characterised by the abundance of 16:0/18:0 acyl chains that constitute the majority of the plasma ceramides (~60%). In contrast, hormone insensitive CRPC was characterised by the enrichment of 22:0/22:4 acyl chains that are highly uncommon, representing less than 2%. The complexity of the fatty acyl chain appeared to have a specific relationship with emergence of the hormone-independent disease phenotype. This study raises the promise of measuring fatty acyl chain length in translational PCa diagnostics via a plasma-based assay, but authors recommended mechanistic studies to identify the functional enzymes underpinning altered sphingolipid metabolism in CRPC. A possible explanation

is the translocation of sphingosine kinase 2 to the plasma membrane to shunt sphingosine toward Cer metabolism³⁷¹. Glycerophospholipids (PC and PE) are substrates for sphingomyelin by the action of sphingomyelinase. Ceramides are produced during cellular stress³⁷² and long considered as bioactive lipids in many cancers³⁷³. Although ceramide metabolism has been implicated in propagating autophagy and resistance to apoptosis in PCa³⁷⁴, their associations with survival have only been recently expounded in CRPC.

In a recent report, Kiebish and colleagues analysed the sera of an ethnically diverse cohort (n=382) in a 20-year longitudinal follow-up study of biochemical recurrence (BCR) of localised PCa³⁷⁵. They used a multi-platform proteomics, metabolomics and lipidomics strategy encompassing global proteomics, tandem shotgun lipidomics, RP-LC-MS/MS and HILIC-MS/MS as well as GC-TOF-MS/MS, respectively. They showed that a four panel biomarker set comprised of Tenascin C, Apolipoprotein A1V, 1-methyladenosine and PA(18:0/22:0) was a predictor of BCR with an AUC = 0.78, OR = 6.56 (CI 2.98 - 14.40) $p \leq 0.0001$. With incorporation of pathological T-stage and Gleason score as clinical co-variables, the sensitivity and specificity improved with an AUC = 0.89, OR =12.47 (CI 4.85 -32.05) $p \leq 0.0001$. They did not find significant associations with signalling lipids³⁷⁵. In another study involving 18 PCa patients with equivalent control samples, PC(39:6) and FA(22:3) were identified as possible serum markers of PCa with 77% specificity. However, the investigators proposed the two lipid species needed to be validated complimentary with PSA in a larger cohort³⁵².

Cholesterol has long been implicated in promoting PCa aggressiveness³⁷⁶. 3-hydroxy-3-methylglutaryl-CoA reductase (HMGCR) is yet

another SREBP regulated lipogenic gene responsible for the rate-limiting step in cholesterol biosynthesis via mevalonate pathway³⁷⁷. HMGCR expression by immunohistochemistry has been reported to be higher in primary tumour compared to matched normal tissues in 149 patients³⁶⁴. Hypercholesteremia (HCE) has been associated with enhanced intratumoural steroidogenesis, increased inflammation, increased epithelial proliferation and altered formation of lipid rafts³⁷⁶. From a molecular standpoint, cholesterol-rich lipid raft enhance androgen signalling by promoting AR-Akt interaction within extracellular membrane domains^{127,378}. Statins conventionally used to counteract cardiovascular disease have been shown to offer benefit in men at risk of developing CRPC by reversing these phenotypes. Pre-operative HCE was shown to be associated with post-operative advanced disease and tumour aggressiveness (tumour stage ≥ 7 pT3 and Gleason score ≥ 7) in men with localised PCa (OR 2.01, $p < 0.0001$)³⁷⁹ and statin use decreased risk of aggressive disease by HCE (OR 0.49, $p = 0.005$)³⁷⁹.

Mass Spectrometry Imaging of Lipids in Prostate Cancer

Current strategies for exploring the lipidomic phenotype of PCa have one major drawback – the lack of spatial information to relate the localisation of specific lipids to their potential pathophysiological function in PCa. With the inception of MSI in the past 20 years^{164,200} and the augmentation of it by different types of mass analysers^{380,381}, it has become possible to obtain *in situ* information on metabolites and lipids in many solid malignancies¹⁵⁹ including the prostate. MALDI MSI offers a powerful label free semiquantitative technique to interrogate deregulated lipids in prostate tissue ([Figure 4](#)). Co-registration or overlay of MALDI ion maps with histological scan of tissue can reveal the association of biomolecules to key anatomical and morphological features, hence offering more information about disease aggressiveness, monitor disease progression and effect of pharmacological agents²⁸⁰.

So why is a spatial approach to metabolomics or lipidomics of PCa critical? There are several important factors that arise from the heterogenous nature of prostate gland¹ and its tumours^{2,4}. First, normal glandular epithelium can transform into multifocal lesions (benign or low/high-grade PIN or malignant)²⁸. Second, the stroma that anchors secretory lumen is also composed of muscular cells physiologically distinct from basal epithelium¹. Third, is the tumour microenvironment, where there is interplay of tumour cell migration, fibroblast activation and macrophage recruitment within the stroma and neoplastic cells. Baenke and colleagues have presented an excellent review of the role of lipids in the tumour microenvironment³⁸². Hence, in these three facets the lipid profiles can be dynamic and follow a tissue or cell-type specific composition.

MSI has the advantage of identifying lipidomic and metabolomic phenotypes related with severity of tumour-grade. Overexpression of multiple phospholipid classes in PCa has been described using MALDI MSI in negative ion mode with 9 amino acridine (9-AA) matrix in a discovery patient set (n=14)²⁸³. Fourteen PI, 3 PE and 3 PA species were highly abundant in cancer, specifically PI(18:0/18:1), PI (18:0/20:3) and PI(18:0/20:2) as significantly abundant lipids (p value ≤ 0.05). A validation set (n=24) was built using an orthogonal partial least squares discriminant analysis (OPLS-DA) model that established PI species to have 87.5% sensitivity and 91.7% specificity for PCa diagnosis²⁸³. The authors postulated that PI distribution may be related to changes in acyltransferase activity and PI3K signalling²⁸³. Following this report, Goto and colleagues showed using positive ion mode MALDI-IT-TOF imaging, decreased levels LPC(16:0) in benign epithelium compared to cancer, which they associated with biochemical recurrence (increasing serum PSA levels) after radical prostatectomy²⁸⁴. They proposed that enhanced LPC levels in normal tissue was attributable to lysophospholipase D activity and PC remodelling pathways. Wang and colleagues conducted metabolomic imaging of prostate tissue (n=3 patients) by MALDI FT-ICR³⁸³. In this HRAM approach, they combined quercetin and 9-AA for positive and negative ion mode imaging and claimed to have identified 565 compounds with quercetin only and 698 compounds using both matrices. LC-MS/MS was used as a structural validation tool. However, they employed an uncommon normalisation approach for MALDI imaging data of normalising lipid peak intensities to reference calibration masses instead of the more widely used total ion count (TIC) method or even root means square error (RMS). In the study *m/z* 534.296 PC(16:0) and *m/z* 740.520 PE(34:1) were abundant in cancerous

regions whilst neutral lipids, m/z 633.485 DG(34:1), m/z 895.716 TG(52:3) and m/z 951.778 TG(56:3) and m/z 769.562 SM(d36:1) were distributed in non-cancerous regions, although this might actually have encompassed stromal adiposity. 9-AA afforded the detection of nucleotide anions in which they argued m/z 505.989 ATP was enhanced in cancerous regions while m/z 346.056 AMP and m/z 426.022 ADP were diminished consistent with energetic hallmark that increased ATP flux is critical for tumour cell proliferation³⁸³.

In 2019, Randall and colleagues reported a study of 10 specimens, 2 GS 6, 3 GS (3+4), 3 GS (4+3) and 1 GS 9 for analysis by MALDI FT-ICR MSI with α -CHCA matrix in positive ion mode³³⁶. Three additional specimens were used for MALDI TOF MSI and 4 additional samples for liquid extraction surface analysis (LESA). They identified 481 m/z features that discriminated between GS (3+4) and GS (4+3) with sensitivity and specificity analysis ROC values above a threshold of 0.75. Of 56 ions that were searched against LIPID MAPS[®], four PC, four PA, eight PS and four cardiolipins and five PIs were identified. However, none of the ions were classifiers of either the two grades, albeit, CL were detected more frequently in higher GS disease consistent with a previous report³⁶⁸. Five additional specimens with consistent tumour grades to the first data set were used in a validation set by MALDI FT-ICR MSI which resulted in similar variation in distribution of lipid m/z features. Despite, the seemingly small sample size employed in this study, the investigators demonstrated the ability of MALDI MSI to identify tumour-specific lipid markers, palmitoylcarnitine and stearyl carnitine that were detected as discriminant features with high intensity in particular regions of GS 9 and G7 tumours, an indication that PCa cells have upregulated mitochondrial uptake of long chain FA to support ATP-generation by β -

oxidation³³⁶. Moreover, overexpression of carnitine transporter (CPT2) has been reported in primary PCa to support mitochondrial oxidative phosphorylation³⁸⁴.

DESI imaging has also been applied to compare the relationship between multifocal prostate cancer lipid fingerprints and pathological grade. A recent DESI MSI study assessed metabolite markers in prostate needle core biopsies in 35 samples from 18 patients³⁸⁵. 289 metabolite ions were selected from ROIs created 289 benign cases and 675 PCa cases. First, a univariate statistical analysis by Mann – Whitney test of all 289 ions was evaluated to identify metabolites that enriched in cancer compared to benign ROIs which exhibited significant changes in FA, PE, PI, and PC between the two conditions. Second, metabolites that were differentially abundant between Gleason grade groups were evaluated. Here, they compared GG2 and GG3 ROIs and showed that lyso-PEs (16:0 and 18:0) were more abundant in benign tissue whereas dephosphorylated monounsaturated PLs (P-38:1 and P-40:1) and reduced polyunsaturated PLs (O-38:2 and O-40:2), were more prominent with increasing tumour grade. Physiologically, it can be theorised that lysophospholipid enrichment in benign or normal glands compared to over-abundance of phospholipids composed of polyunsaturated FA is due to the provision of anabolic substrates to support the need for cellular growth and proliferation. Last, a logistic regression-based classification model was built to identify highly sensitive and specific features in which, 376/161 cancer-benign ROIs constituted the testing/training set and 302/128 cancer-benign ROIs the validation set. The classification model achieved overall balanced accuracies of 97% and 85% in the training and validation sets, respectively.

Another DESI MSI study investigated the metabolite and lipid composition of 54 fresh-frozen prostate tissue specimens³⁸⁶. This work particularly focused on metabolite ions between m/z 50-200 range found in the Krebs's cycle. A least absolute shrinkage and selection operator (Lasso) was used to identifier classifiers in 36 tissue samples (18 normal vs 18 PCa) in a training set and the top 54 peaks were further evaluated in a validation set of 18 samples (10 normal vs 8 PCa). Interestingly, the Lasso tool showed inferior performance for ions on the lipid m/z 50-1000 range but with better accuracy with inclusion of the Krebs's cycle metabolite ions - 89% vs 94% overall agreement. Glucose/citrate ratio was found to be a biomarker that spatially distinguished BPH from PCa when ion maps were compared to corresponding histopathological scans³⁸⁶. Normal prostatic fluid is rich in citrate³⁸⁷ and normal prostate cells ostensibly derive citrate from glucose metabolism³⁸⁸. The oxidation rate of citrate for ATP production increases as PCa transitions from a Warburg-state glycolysis to FA oxidation¹²⁴.

Although exploiting spatial lipidomics and metabolomics is arguably the most histologically accurate way to develop diagnostic or prognostic markers of PCa, there significant challenges that remain to adopt MSI in population-centric systems biology driven approach. First, MSI is not a high throughput technique compared to conventional metabolomics. Second, MSI generates highly complex multidimensional data sets that require advanced computational bioinformatics systems and considerable computing power³²⁶. Furthermore, multiple commercial platforms do not have all the needed statistical tools being contained in a single program^{389,390}. Even though recently, a new program called Lipostar has sought to provide users with all necessary features for spatial metabolomics data analysis³⁹¹.

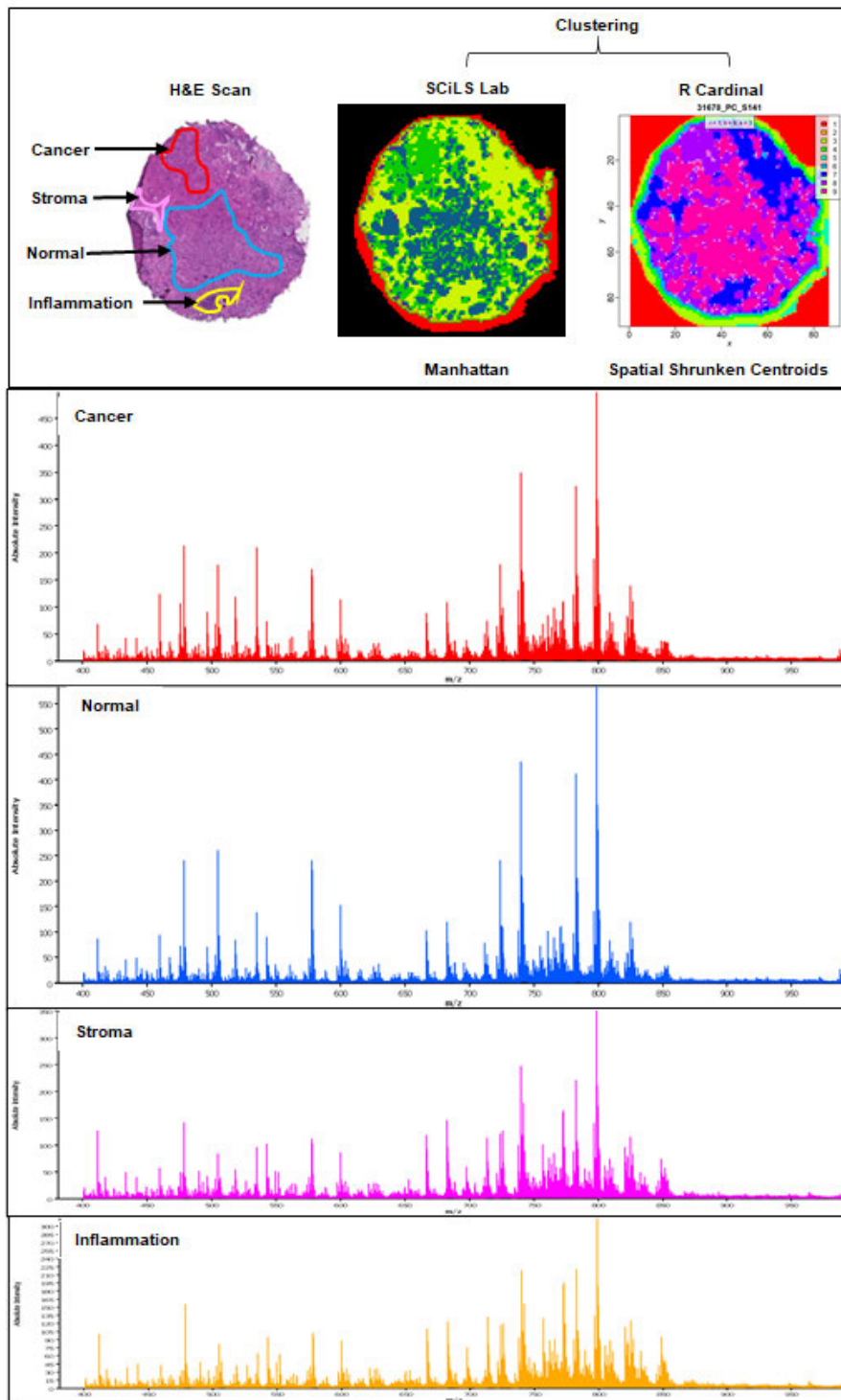


Figure 4. MALDI MSI of prostate tumours. Tissue morphology (H&E scan) of multifocal disease in prostate tissue and spatial segmentation using clustering in SCiLS Lab and R *Cardinal* from a serial imaged section. The associated mass spectra show different m/z features for cancer – red, normal – blue spectra, stroma – pink and inflammation – yellow.

Towards Implementation of Translational and Clinical Lipidomics in Prostate Cancer

Untargeted metabolomics platforms based on high resolution MS and IMS are being touted as potential screening tools PCa clinical biomarkers using liquid biopsies (serum and urine samples). Such specimens are patient-friendly and easily obtainable. Even though thin sections from solid biopsies recapitulate well disease heterogeneity, they may incompletely represent tumours, making fluid samples attractive for translational research. Chromatographic based lipidomics methods typically have run times ranging 20-30 min and tedious sample extraction procedures not ideal for high capacity biomarker screening^{280,392}. To attain efficient biomarker screening platforms, more rapid methods have been developed for clinical settings.

A flow-injection TWIM-MS metabolomic serum profiling method has been reported for prostate cancer with an analysis time of 6 min including a 3 min wash step¹⁹⁶. This method was evaluated with an OPLS-DA model resulting in 89% average accuracy, distinguished PCa patient and control samples with 90% sensitivity and 81% specificity. Discriminant metabolites were assessed by accurate mass, CCS values, MS/MS fragments in comparison to database or reference standards¹⁹⁶. Another study reports the development of a segmented flow approach, where urine sample volumes are interspersed with an immiscible solvent emitted in front of a custom ESI source. The acquisition time is 1.5 min and results validated against LC-HRMS were more reproducible³⁹³.

MSI in clinical diagnostics has been tested and can be most effective in identification of surgical resection in organ confined PCa. Cook's group have used DESI MSI and touch spray mass spectrometry (TS-MS) ionisation to

determine surgical margins in men undergoing radical prostatectomy (n=18). DESI MSI and TS-MSI data had prediction of 97.5% and 96% in discriminating cancer from normal tissue. TS-MS was further validated with accuracy of 92.5% of tumour from normal tissue relative to histopathology and they proposed the technique to be useful for rapid detection of surgical margins³⁹⁴.

Future Perspectives

This review expounds on key work within metabolomics and spatial lipidomic spheres (MALDI and DESI) in facilitating improved delineation of tumour and normal tissue and utilisation of lipidomics fingerprints in prognostication of PCa with more precise biomarkers. New imaging technologies composite with shotgun lipidomics and chromatography-based mass spectrometry modalities have become available within the last year that will provide the deeper coverage of cancer lipid metabolism. The following are avenues where application of MSI lipidomics to PCa research has exciting future potential:

MALDI-2 for Enhanced Resolution of Small Molecule Imaging

A critical technical need in MALDI MSI is the need to image lowly abundant metabolites and lipids without loss of sensitivity and maintaining appreciable spatial resolution. MALDI-2 is the generation of ion beam from a second pulsed UV laser orthogonally to the direction of the plume created by a first laser. Already one study has shown high resolutions lipid images of up to 6 μm in comparison to conventional MALDI on Orbitrap Elite (Thermo Fisher)³⁹⁵. Using an identical instrument, the detection of small molecule pharmaceutical agents triamcinolone acetonide in human cartilage and dog liver with two orders of magnitude intensity compared to MALDI was also reported³⁹⁶. A recent report further exemplified the advantage of improved signal sensitivity with transmission mode MALDI-2. By using a custom modified source MALDI-2 source, lipid ion intensities at sub-cellular resolution for mouse cerebellum were achieved³⁹⁷.

Combining MS with Ion Mobility Separation for Multidimensional Separation

The Bruker timsTOF Flex launched in June 2019 has a source equipped with latest generation smartbeam 3D laser technology for high throughput pixel acquisition. The new trapped ion mobility (TIMS) device has 100% duty cycle. i.e. all ions generated from a single laser shot are accumulated, trapped, and eluted without any loss. This is attained by three electrode regions; an entrance funnel, TIMS mobility region and exit funnel. The entrance and exit funnels regulate ion deflection while the TIMS compartment is used to gather, catch, and release ion as a function of the interaction of between the parallel gas glow and opposing electric fields. Coupling TIMS with a technique parallel accumulation serial fragmentation (PASEF), 15 precursors were fragmented every 100 ms of a TIMS scan¹⁹⁷. Impressively, the researchers showed three-fold increase in identified lipid yield from 1 μ L plasma compared to TIMS-MS/MS¹⁹⁷, which would be at least several orders of magnitude by conventional lipidomics.

Another new instrument from Waters Corporation, Q-cyclic ion mobility (CIM) TOF MS was launched in April 2019³⁹⁸. The CIM is an advancement of TWIMS where the cell functions as a “racetrack” that separates travelling ions. Smaller ions loop the cell faster compared to larger ions and they can be separated by temporarily directing ions to a “pit stops” known as pre- and post-arrays, before passaging them back to the cell. After multiple passes in the CIM cell, the mobility resolution of ions increases allowing ions to be selected for detection. So far, this technology has been applied to separate three distinct isomeric pentasaccharides each with different anomeric configurations (glycosidic linkages)³⁹⁸.

Both TIMS and CIM devices greatly improve the confidence of metabolomics identification when coupled to HRAM MS analysers. This portends unprecedented scales of lipidomics data where ion identity can be ascertained based on retention time, m/z , MS/MS structural fragments and CCS values. Matched together with the latest processing PCs, software and bioinformatics tools, these new MS capabilities are promising to contribute to the discovery of accurate metabolomics markers of PCa and supplement traditional and recent PCa screening and prognosis platforms.

Lipids as Biomarkers of Treatment Response

Evaluation of therapeutic response markers in hormone-driven cancers using MSI is understudied, except for breast cancer. MALDI MSI has been used to predict treatment response in a patient-derived xenograft (PDX) model of triple-negative breast cancer, using proteomic classifiers³⁹⁹, while in colorectal cancer liver metastasis lipidomic signatures were determined⁴⁰⁰. Possibly, MSI can also be adopted to interrogate the utility of lipids as treatment response markers in prostate cancer models that reflect patient and tumour heterogeneity such as PDX and patient-derived explants (PDEs).

MSI Potential to Reveal Lipids as Biomedical Imaging Probes

The biochemical and biophysical nature of lipids and other metabolites involved in lipid biosynthetic pathways have led to intense investigation into their potential and suitability as imaging probes for PCa disease staging, diagnosis, and response to treatment. These imaging probes are either substrates of fatty acid synthesis that form secondary products of membrane lipid synthesis that can be incorporated into cell membranes or end-products of lipid metabolism that can be assimilated into these structural components. Such metabolic probes are augmented with contemporary medical imaging technologies such as positron imaging tomography (PET) and computed tomography (CT).

The switch from sugar-based to lipid-based probes has improved diagnostic molecular imaging of prostate cancer in clinical settings. Multiple studies have reported improved uptake and sensitivity of ^{11}C -acetate⁴⁰¹, ^{11}C -choline⁴⁰² and ^{18}F -choline^{403,404} in characterising prostate malignancies compared to the commercial ^{18}F -fluoro-deoxyglucose (FDG)^{405,406}, which is mainly limited to Warburg cancers^{407,408}. MSI studies can thus generate PCa metabolomic and lipidomic signatures that can offer new compounds to facilitate the development of more novel radiolabelled lipid molecules following the success of PET/CT imaging probes like FDG as a multimodal tool in PCa management⁴⁰⁹.

1.11. Project Summary

Current literature has expounded that the lipidome of prostate cells is modulated by metabolic reprogramming during oncogenesis and throughout disease progression. These alterations emanate from androgen receptor dysregulation that exact downstream effects either by direct or indirect regulation of lipid metabolic genes and associated fatty acid metabolism enzymes. Majority of metabolomics studies in prostate cancer have been by shotgun lipidomics and LC-MS/MS and only a handful of mass spectrometry imaging studies by DESI^{385,386} and MALDI³³⁶ have been conducted on patient prostate biopsies with the aim of correlating fatty acid metabolites and lipid profiles to Gleason grading. Indeed, these MSI studies have highlighted key lipid changes in benign epithelium and tumour tissues with prognostic significance. MALDI MSI is an emerging lipidomics platform and more studies are warranted to explore the lipid composition of the multitude of cell-types in prostate tissue. Therefore, MALDI MSI was utilised in this PhD project as a proof-of-concept to spatially delineate the lipid profiles in different prostate tissue compartments with pathologically driven-data analysis approaches. This was supplemented with conventional lipidomics on matched specimens to obtain annotated lipid species and improve the confidence in identification of lipid *m/z* signatures in the MSI data.

While cell line studies have demonstrated prostate cancer anti-hormonal therapies abrogate androgen receptor activity to reduce tumour cell viability, proliferation and metastasis, lipidomic profiling of clinical prostate tissues demonstrates that tumours have targetable alterations in membrane lipid composition. Preclinical assessment using clinically relevant model systems is probably the most appropriate approach to understand the pharmacodynamics

effects of novel therapeutics and discover biomarkers of treatment response or drug resistance. Our laboratory employs an *ex vivo* tissue culture model of human prostate tumours with enzalutamide, a clinical agent approved for high-risk and metastatic castration-resistant prostate cancer as one of the treatments. However, key to this pharmacodynamic understanding is the level of drug concentrations achieved and ascertaining whether the drug interacts with the desired target. This PhD thesis showcases mass spectrometry studies involving LC-MS/MS and MALDI MS/MS imaging used in complement to assess the uptake of enzalutamide, during culture of patient-derived prostate cancer explants (PDEs), together with immunohistochemical staining of the androgen receptor. Further to this, state-of-the-art high resolution MALDI MSI was employed as a spatial tool to illustrate cell-type specific lipidomic composition in fresh-frozen biopsies relative to PDEs cultured in enzalutamide treated medium.

1.12. Thesis Hypothesis and Project Rationale

The hypothesis of this thesis is that MALDI MSI can accurately identify lipids that correlate with PCa features and aggressiveness. The rationale for this project was to highlight the importance of lipids as novel biomarkers of PCa and MALDI MSI is a powerful approach to profile lipids in clinical tissues. The outstanding issues to be resolved are;

1. Heterogeneity of lipid composition throughout different cell types in prostate tissues.
2. Spatial analysis of drug penetration into *ex vivo* cultured prostate tissues.
3. Dynamics of changes in lipid composition in *ex vivo* cultured prostate tissues due to pharmacological ADT therapy.

1.13. Research Aim and Objectives

The overall aim of this research project was to exploit the utility of mass spectrometry imaging to characterise lipid changes in prostate tissue tumourigenesis and during AR inhibition therapy, consequently identifying lipids as potential biomarkers that correlate to PCa aggressiveness and treatment response. This was addressed through the following objectives:

1. To determine the spatial location of lipid species across prostate tissue using MALDI MSI and correlate to histopathological evaluation in individual PCa patients, including the use of LC-MS/MS and MALDI MS/MS to validate lipid species.
2. To quantitate the uptake of enzalutamide in human prostate patient-derived explant cultures using LC-MS/MS and evaluate enzalutamide penetration in prostate tissues by MALDI MS/MS imaging together with AR immunohistochemistry.
3. To explore the lipidomic changes in patient-derived explant cultures following enzalutamide antagonism of AR using high resolution MALDI MSI.

The methodological approaches to achieve the above objectives are expounded on in **Chapter 2 Materials and Methods**.

CHAPTER 2:

Materials and Methods

2.1. Materials, Reagents and Equipment

2.1.1. Commonly Used Reagents, Chemicals and Buffers

Category	Solvent/Chemical Name	Product Code/ Number	Company/Country
Haematoxylin and Eosin Staining (manual)	DPx Mountant for Histology	101572495	Sigma Life Science
	Eosin Phloxine Alcoholic, 1%	AEPA 1.0L	Australian Biostain P/L, Australia
	Ethanol, Undenatured 100%	CHE52603	Chem Supply, Australia
	Haematoxylin, Lillie Mayer's	AHMA 2.5L	Australian Biostain P/L, Australia
	Hydrochloric acid, 32%	RP1104-P2.5L	RCL Labscan Limited, Thailand
	Water, reverse osmosis (RO)	–	SAHMRI, Australia
	Xylene, sulphur free	CHE52603	Chem Supply, Australia
Immunohistochemistry (semi-automated)	Sodium chloride	S9888-2.5KG	Sigma
	Tris Base Ultra-Pure	TRIS01	Formedium Ltd., England
	4% paraformaldehyde	158127	Sigma-Aldrich, NSW Australia
	4% formaldehyde	FB002	Invitrogen, Life Technologies, USA
	AR Ab, monoclonal	Ab108341	Abcam, Cambridge, UK
	Anti-Rabbit HQ antibody	760-4815	Roche, Basel, Switzerland
	Anti-HQ HRP antibody	760-4820	Roche, Basel, Switzerland
	ChromoMap DAB kit	760-159	Roche, Basel, Switzerland
	Haematoxylin	760-2011	Roche, Basel, Switzerland

Immunohistochemistry continued	Bluing reagent	760-2037	Roche, Basel, Switzerland
	Optiview DAB IHC Detection kit	760-700	Roche, Basel, Switzerland
	Ultraview Red kit	760-501	Roche, Basel, Switzerland
	34 β E12+p63	790-4538	Roche, Basel, Switzerland
	p504s (SP-118)	790-6011	Roche, Basel, Switzerland
Tissue Culture	RPMI 1640 1X, phenol free medium	1185-030	Life Technologies, USA
	Fetal bovine serum (FBS)	12003C- 500ML	Sigma
	α -antimycotic	A5955-5ml	Sigma
	Gelatin sponge		Johnson and Johnson, NC, USA
	Gelfoam	09-0342-04- 015	Pharmacia, Upjohn USA
	Gelatin capsules	RL040	ProSciTech, Australia
	Dimethyl sulfoxide (DMSO)	D2650-100ML	Sigma
	Enzalutamide (ENZ), MDV3100	S1250 000- 09083	Selleckchem, Houston, TX, USA
	Carboxymethylcellulose, (CMC) sodium salt	C4888-500G	Sigma, USA
	Tissue-Tek OCT Compound	IA018	ProSciTech, Australia
Consumables	Indium tin oxide (ITO) slides	8237001	Bruker Daltonik, GmbH, Germany
	Superfrost ultraplus slides	J3800AMNZ	Thermo Scientific, Hungary
	Graduated microcentrifuge tubes 0.6ml	508-GRD-Q 19161544	QSP, Mexico Thermo Fisher
	Microcentrifuge tubes 2.0 ml, RNAse/DNAse free	508-GRD-Q 18250032	QSP, Mexico, Thermo Fisher

Consumables	Zirconium oxide, 1.4 mm beads	03961-1-103	Bertin Technologies, France
	Tough tubes, 2.0 ml	13119-1000	Mo Bio Laboratories, CA, USA
	Plate, 24-well	3524	Corning Incorporated, USA
	Plate, 96-well	651201	Greiner Bio-One International GmbH, Germany
	Surgical steel blades	REF0508	Swan-Morton, Sheffield, England
	Cryotube vials	377267	Thermo Scientific, Denmark
	Slide mailers	92205	ProScitech Pty Ltd, Australia

Mass Spectrometry Reagents	Argon	262	BOC, NSW, Australia
	Reverse osmosis (RO)-water (H ₂ O)	Milli-Q 0.22 µm filter, Advantage A10	SAHMRI, Australia
	2,6-di-tert-butyl-4-methylphenol	B1378	Sigma-Aldrich, Belgium
	Ethanol	111727	Merck, Belgium
	Chloroform (CHCl ₃)	102444	Merck, Belgium
	Hydrochloric acid (HCl)	VWRC30024.290	VWR, Belgium
	Methanol	CAS-No67-56-1	Lichroslov, Merck, VIC, Australia
	Methanol (CH ₃ OH)	106035	Merck, Belgium
	Acetonitrile		Lichroslov, Merck, VIC, Australia
	Acetonitrile	A955-4	Fisher Chemical, NJ, USA
	Formic acid	A117-50	Fisher Chemical, Czech Republic
	Trifluoroacetic acid (TFA)	1001988462	Sigma-Aldrich, USA

Mass Spectrometry reagents	α -cyano-hydroxycinnamic acid (CHCA)	1002096313	Sigma-Aldrich, USA
	Norhamane	102038142	Sigma-Aldrich, Switzerland
	Polyethylene glycol (PEG), 200	1002300575	Sigma-Aldrich, USA
	PEG, 600	06518AJ	Sigma-Aldrich, USA
	PEG, 1000	018K0124	Sigma-Aldrich, USA
	PEG, 1500	101820903	Sigma-Aldrich, Germany
	Sodium iodide	186007090-3	Waters Corporation, MA, USA
	[² H ₆]-(<i>d</i> ₆)-Enzalutamide	C4527	Strasbourg, Alsachim, France
	[² H ₆]- (<i>d</i> ₆)-Desmethyl-enzalutamide	C4556	Strasbourg, Alsachim, France
	BEH C18 1.7 μ m 2.1 \times 50 mm column	186002350	Waters Corporation, Ireland
	XBridge amide column 150 mm \times 4.6 mm, 3.5 μ m	–	Waters Corporation, Ireland
Other	Hoechst 33258, Pentahydrate (bis-Benzimide), 100 mg	LTSH1398	Thermo Fisher
	Herring Sperm DNA, 10mg	D1811	Promega Australia
	Micro Bicinchoninic acid (BCA) kit	232235	Thermo Scientific, Rockford, IL, USA

Table 2.1. Commonly used reagents and chemicals for project.

2.1.2. Equipment

Instrument/Equipment Name	Company/Country
Christ RVC 2.33 CD-Christ Alpha 2.4 LD	John Morris Scientific, Germany
Centrifuge, Biofuge Pico	Heraeus, Thermo Scientific, Australia
Centrifuge, Megafuge 40R	Heraeus, Thermo Scientific, Australia
Centrifuge, 5424R	Eppendorf, Germany
Precellys 24 homogeniser	Bertin Technologies, Australia
Rotator SB3 Stuart	Adelab Scientific, Australia
Microscope Olympus BX41	Olympus Corporation, Japan
Shandon Cryotome E	Thermo Fisher Scientific, Germany
SunCollect automated sprayer	SunChrom GmbH, Friedrichsdorf, Germany
Acuity ultra-performance liquid chromatography (UPLC) System	Waters Corporation, MA, USA
API 4000 QTrap	Applied Biosystems MDS Sciex, Ontario, Canada
MALDI SYNAPT HMDS Mass Spectrometer	Waters Corporation, Manchester, UK
Bruker timsTOF Flex	Bruker Daltonik GmbH, Bremen, Germany
Nexera X2 UHPLC system	Shimadzu, UK
API 6500+ QTRAP system	Applied Biosystems MDS Sciex, Ontario, Canada
Victor3 1420 Multichannel Counter	Perkin Elmer, Finland

Table 2.2. Equipment and instruments for project.

2.1.3. Reagent and Buffer Preparation

Reagent Name	Preparation
M4 media	In a tissue culture Biosafety cabinet, sterile 45 ml RPMI 1640, 5 ml FBS and 500 μ L α -mycotic were added to a 50 ml centrifuge tube. The tube was gently rotated, and media kept at 4°C.
Tris buffered saline, 1X, pH 7.6	1000 ml 10X Tris pH 7.6, 1000 ml 10X NaCl, 8 L RO-H ₂ O and 5 mL Tween 20 were combined
Tris buffered saline, 20X, pH 8.4	122 g Tris Base Ultra-Pure and 180 g NaCl were gradually added to 1,000 mL RO-H ₂ O in a beaker. The solution was gently stirred at room temperature on top of a magnetic stirrer. The pH was adjusted with concentrated HCl. The stock solution was diluted with RO-H ₂ O to make 1X tris buffered saline.
Homogenisation buffer, (0.05 M Na ₂ HPO ₄ /NaH ₂ PO ₄ buffer, 2.0 M NaCl, 2.10 ⁻³ M EDTA, pH 7.4)	58 g NaCl and 0.372 g EDTA was dissolved by stirring with approximately 300 ml Milli-Q H ₂ O to make 0.5 M phosphate buffer. Milli-Q H ₂ O was added to 50 ml of this solution up till 500 ml to make (10X phosphate buffer will be diluted to make 1X working solution). The buffer solution was passed through a Millipore filter and autoclaved.

Table 2.3. Preparation of commonly used reagent and buffers.

2.2. Chapter 3 Methods

2.2.1. Tissue Sectioning

Human prostate tissue was obtained following radical prostatectomy from written informed participants under the South Australian Prostate Cancer BioResource. Biopsy cores (n=10) were delivered to the laboratory under cold chain storage and snap-frozen upon receipt. Small pieces of biopsy core were cut and embedded in 2% CMC (98:02 H₂O-CMC v/v) in gelatin capsules, put into cryotubes then quickly transferred to liquid nitrogen and subsequently put in 80°C freezer storage. Prior to sectioning, samples were removed from capsules and mounted with minimal OCT whilst frozen using dry ice. The mounted tissue was then transferred to Shandon Cryotome E (Thermo Scientific, Germany) with chamber cutting temperature maintained at -20°C (**Figure 2.1**). Cryosections were affixed on Superfrost Ultra Plus glass slides by thaw mounting. For each individual patient biopsy core, 10 µm tissue sections for MALDI MSI were collected at four interspersed depths. Four triplicate sections (n=12 sections) were also collected for validation by MALDI MS/MS imaging and three triplicate 30 µm sections collected for lipidomics by LC-ESI-MS/MS.

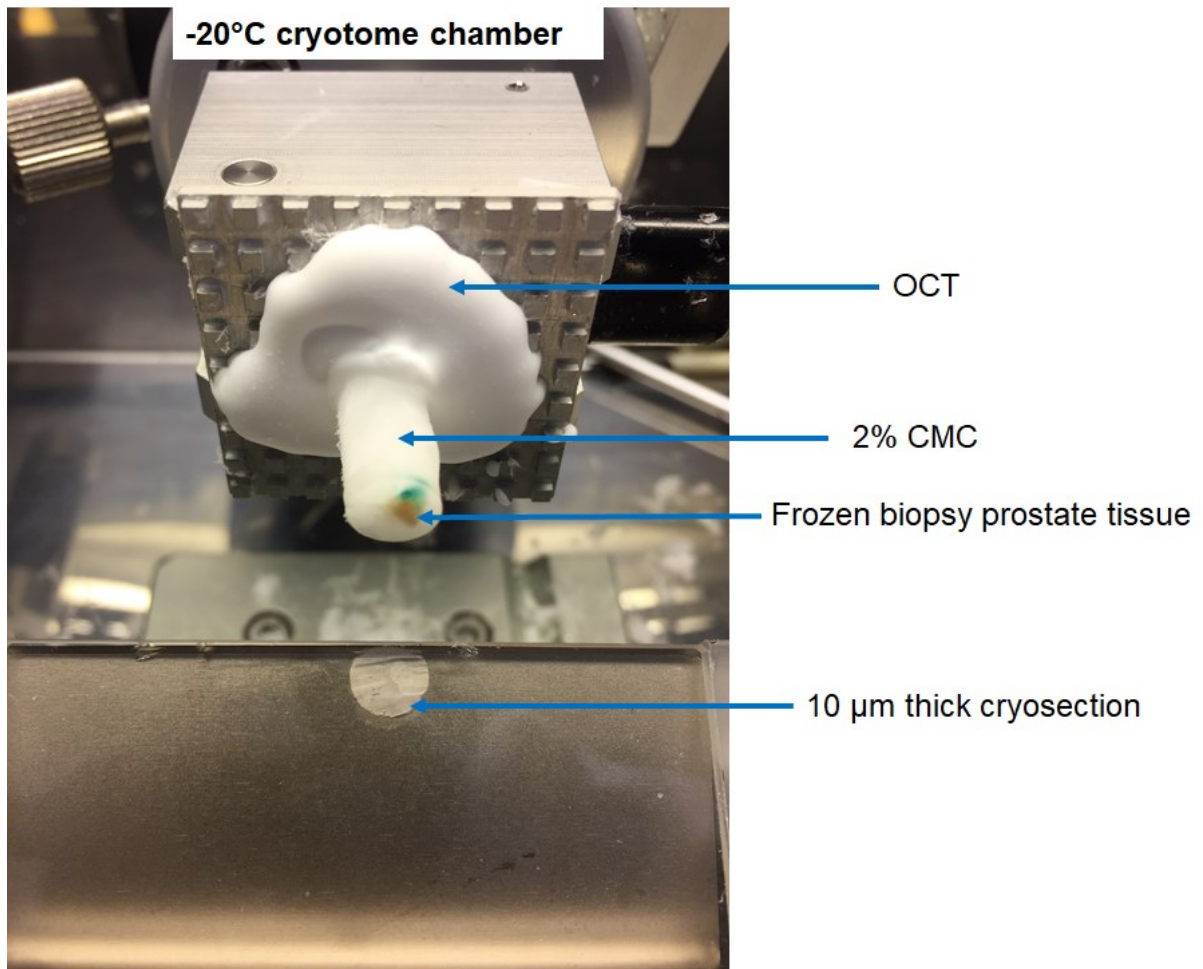


Figure 2.1. Image of embedded fresh-frozen prostate biopsy tissue. Sample embedded in 2% CMC and mounted onto mould with OCT for cryosectioning.

2.2.2. Histological Staining

Tissue sections adjacent to MALDI MSI section were stained by haematoxylin and eosin (H&E). Slides were heat-fixed at 65°C for 2 h. Slides held in racks were twice dipped in 95% ethanol pots until clear and rinsed in RO-H₂O for 1 min. Slides were then dipped in filtered haematoxylin for 4 min then rinsed in running RO-H₂O until clear. Slides were blued by dipping twice in 0.3% acid alcohol solution. The rack was then transferred to 95% ethanol and dipped twice and stained in eosin for 20-30 sec. Slides were then dehydrated by 2 changes in 10 dips of 95% ethanol and 3 changes of 10 dips in 100% ethanol. Alcohol was removed by 2 changes in 10 dips in xylene. removed and cover-slipped using DPx and allowed to completely dry inside the chemical hood. Slides were scanned with a NanoZoomer Digital Slide Scanner 2.0-HT (Hamamatsu, Japan) using a 40X objective and images were captured using NDP.view.27.25 (Hamamatsu Photonics K.K., Japan).

2.2.3. Cell Counting

Cell counting for epithelial cells in H&E scans was done in ImageJ 1.52a (National Institutes of Health, USA). Coloured bitmap files as .png format were opened and any folded edges were cut out using free drawing tool. The new colour file was then converted to a 16-bit greyscale image. The adjust threshold tool was set at maximum entropy (red) between 1 – 100. Applying this threshold created a black mosaic image from red highlighted purple stained regions. The analyse particle tool was then used to estimate number of cells by counting black

pixels representative of individual cells. Area of histological stained tissues was calculated using NanoZoomer Digital Slide Scanner 2.0-HT (Hamamatsu, Japan).

2.2.4. Instrument Calibration

The MALDI SYNAPT HDMS hybrid quadrupole orthogonal acceleration Time-of-Flight Mass Spectrometer (Q-oa-TOF) (Waters Corporation, Manchester, UK) was calibrated prior to data acquisition. Stock solutions of calibrant were prepared by dissolving PEG (Sigma-Aldrich, USA) 200 (20 mg/ml), PEG 600 (10 mg/ml), PEG 1000 (10 mg/ml) and PEG 1500 (10 mg/ml) in 1:1 acetonitrile-water (V/V) in 12 ml glass tubes. Tubes were vortexed for 30 sec. MALDI matrix was prepared by weighing out 10 mg α -CHCA (Sigma-Aldrich, USA) into a glass tube and adding 1,500 μ L acetonitrile, 1,500 μ L water and 3 μ L TFA. The mixture was sonicated for 2 min and vortexed for 30 sec to obtain 3.3 mg/ml matrix solution. A PEG mix solution was prepared by combining 5 μ L PEG 200 and 2.5 μ L each of PEG 600, PEG 1000 and PEG 1500 in a 600 μ L microcentrifuge tube. 1 μ L of sodium iodide was spiked and briefly vortexed. To this mixture 87 μ L of matrix solution was added. 1 μ L of this calibration solution was spotted on a clean MALDI target plate and allowed to air dry. The target plate was then loaded into MALDI source. The instrument settings are shown in **Table 2.4**.

Mode	+ve ion V mode MALDI
Laser Energy	150
Step rate	2
Source Gas (ml/min)	10.0
Trap Gas (ml/min)	1.5
IMS Gas (ml/min)	Off
Detector voltage (V)	1950
Mass range (<i>m/z</i>)	50 – 1,990
LM resolution	4.7
HM resolution	15
Quad profile	Auto

Table 2.4. Instrument settings for MALDI imaging on Waters SYNAPT.

Calibration data was acquired using the Octagonal_mkII pattern file. The instrument mass accuracy was checked using a dominant calibrant ion if the mass error was >0.1 Da the V_{eff} was adjusted using the equation below.

$$V_{eff} \text{ factor} = \frac{\textit{theoretical mass}}{\textit{observed mass}}$$

Calibration was performed by acquiring data until a minimum ion intensity of 1,000 counts was achieved for the lowest intensity calibration ion. The data was summed, smoothed using Savitky Golay method, base line subtracted, centroided and saved. The reference calibration file contained theoretical sodiated PEG masses. The calibration data was checked against the reference file. Calibration was accepted if the mass accuracy was <3 ppm. An acceptable calibration setting for imaging experiments is exemplified in **Figure 2.2**.

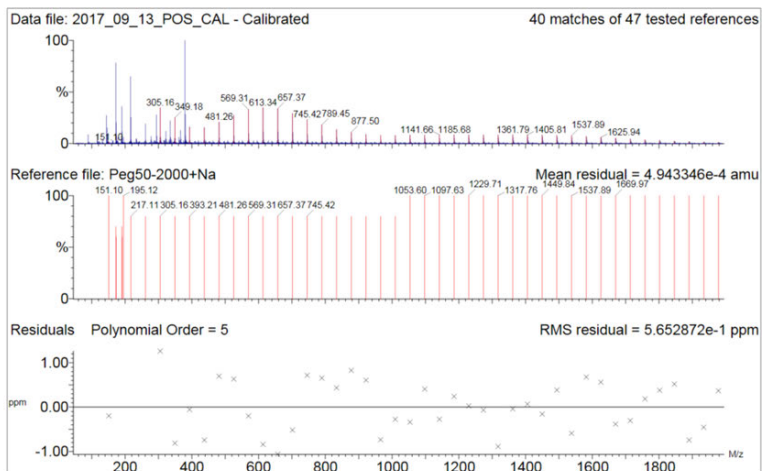


Figure 2.2. Calibration report for MALDI imaging on Waters SYNAPT. Left panel. Calibration based on a sodiated PEG reference with 40 out of 47 masses matched with a root mean square residual (RMS) of 5.6 e-1 ppm. **Right panel.** Mass difference report shows that the calibration mass accuracy passes at 1.52 ppm.

2.2.5. Matrix Application by Sublimation

MALDI MSI slides from sectioning were air-dried, further desiccated by blowing with dry high-pressure nitrogen gas while placed in slide mailers before being tightly sealed and wrapped with parafilm. Before matrix deposition, slides stored at -80°C were fully equilibrated to room temperature in a dry atmosphere to avoid condensation before processing began. Sublimation entailed depositing 300 µL of 10 mg/ml α-CHCA in methanol, with the solution limited using circular aluminium foil, on the bottom of the glass chamber of the sublimation apparatus. The solvent was allowed to evaporate at room temperature to achieve a final dry weight of approximately 3 mg of MALDI matrix. The sublimation device was

connected to a vacuum pump (Christ, John Morris Scientific, Germany), placed in an oil bath on a heating block and evacuated to a set pressure of 0.03 mbar. 100 ml of water was added to cool the sublimation apparatus, and a cylindrical ice block was suspended in the water without touching the bottom of the chamber and allowed to cool down for 10 min. The heating block was set to 145°C for at least 45 min. The matrix was gradually coated on the glass slide through a solid-gas phase state change because of the low pressure and high temperature difference in the closed system. The sublimation apparatus set up is shown in **Figure 2.3**.

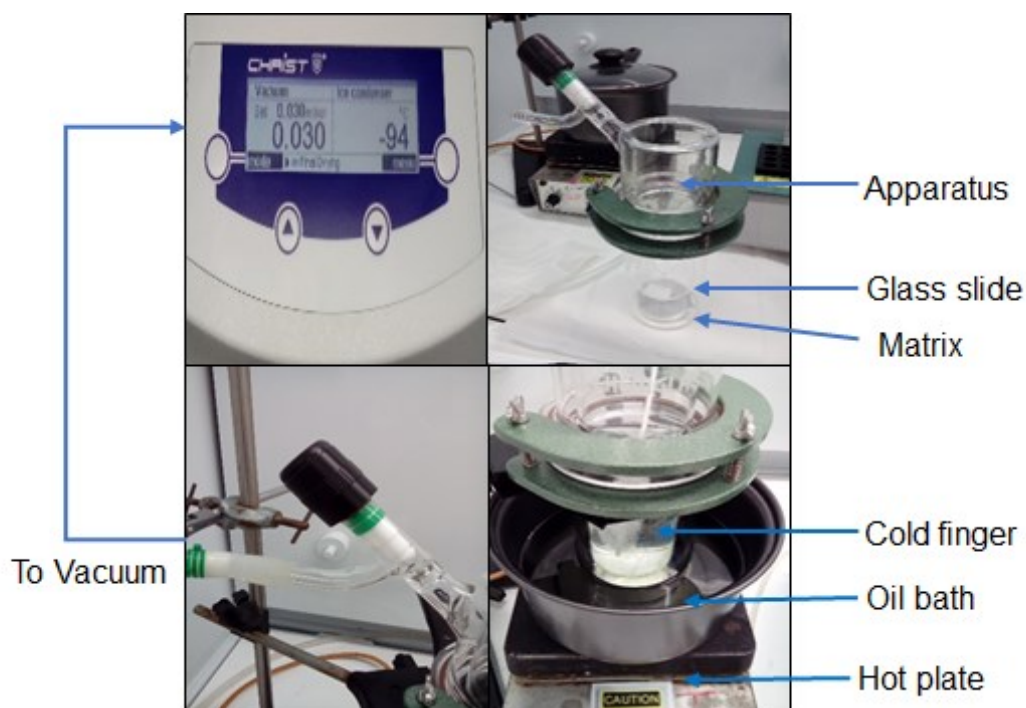


Figure 2.3. Sublimation apparatus for matrix application. A glass slide is cut and adhered with tape at the bottom of the glass chamber above a dried matrix deposition on aluminium foil. The green clamps are tightly fastened to hold the glass device before being emerged in an oil bath evacuated to 0.03 mBar and heated to 145°C.

2.2.6. MALDI MS Imaging Data Acquisition

After successful instrument calibration, data acquisition was performed. The matrix coated glass slide was attached onto the MALDI glass slide holder plate using double sided adhesive tape. The process of loading the normal slide was as follows. First, the laser was fired at an area coated with matrix away from the tissue. If the ablated spot was not aligned with cross hairs, the image was switched from live to static and cross hairs adjusted. Second, the glass slide holder was ejected, and a 384-well plate loaded. The laser fire position was not changed rather the target plate was moved so the cross hairs were aligned to the centre of well A1 in the source settings. The accuracy of the laser firing position was ascertained by switching between small to medium frame sizes. Last, the glass slide holder was re-loaded.

Using Mass Lynx pattern creator, the free-handing drawing tool was used to sketch out the outline of tissues to be imaged based on a high-resolution scan of the glass slide holder with slide. Four corners of the glass slide holder were marked. The sampling (lateral) resolution of the image was set at 60 μm step size for both X and Y. The file was saved as a pattern definition metafile (.pdm). Whereas each pattern was saved individually as a pattern file (.pat). The acquisition method parameters of each tissue section were set up, scan rate set at 1 sec, user defined pattern files assigned, time per pixel set at 1 scan, firing rate at 200 Hz and laser energy attenuated by neutral density filter set at 150 a.u. The trap and transfer collision energy were set at 6 eV and 4 eV, respectively, these settings were saved as an experiment (.exp) file. An over sampling technique was used where subsequent laser spots eclipsed the previous laser

ablation area²¹³. Quality control (QC) check involved ablating two separate 1-2 mm² of areas on the glass slide before and after the tissue sections to check for homogeneity of matrix coating and instrument sensitivity. These matrix distribution QC areas were acquired as MALDI MS imaging experiments within the instrument calibration mass range.

2.2.7. MSI Data Processing and Analysis

The imaging data .raw files were converted into Biomap format using Waters imaging converter. The data were binned at 0.03 Da. The Biomap format is also known as Analyse 7.5 and is compatible for the command-line bioinformatics software program *R*.

2.2.7.1. Waters High Definition Imaging

The .raw files were imported into HDI software which translated the pixel coordinate position of the raw spectra. Data processing import settings were resolution of 8,000 full-width half-height (FWHM), mass window of 0.02 Da and top 1,000 mass (*m/z*) features. After processing, the .raw files folders were written with an “imaging” folder with a text (.txt) files or MSI data files which could then be opened in the analysis window. The HDI program afforded the conversion of the MSI data files into the universal file sharing format .imzML compatible for analysis in SCiLS Lab MVS Pro (Bruker Daltoniks GmbH, Germany). Regions of interest (ROIs) in the MSI data were selected by comparison to the adjacent histological stained tissue. Each single pixel (0.0036 mm²) encompassed several cells. 9 pixels (~0.0324 mm²) were selected for each

morphological area annotated by a pathologist. The ROIs mass spectra were exported as .csv files for multivariate analysis in MetaboAnalyst⁴¹⁰.

2.2.7.2. R Cardinal

The data was imported at a range of m/z 400 – 990. The Analyze 7.5 data was first pre-processed prior to analyses to improve computational power efficiency. First, the mean spectra per pixel for each section was visualised at an appropriate scale intensity (0 - 5000) to ensure good signal was present throughout the data. Second, the data was batched and multi-processed by normalisation to total ion count (TIC), signal smoothing, baseline reduction, peak picking and peak alignment. Batch processing virtually condenses large raw data (0.5 GB - 2 GB) stored in the hard drive into smaller packets (>10-20 MB) to allow easier loading into RAM memory for downstream processing. Then the data was subjected to unsupervised clustering analysis using the *R* package Cardinal. Essentially, this approach employs a segmentation algorithm that groups mass spectra into distinct clusters across the spatial data enabling the delineation of areas within tissue with similar morphological or anatomical properties. Spatial shrunken clustering Gaussian (SSCG) algorithm ranked the significance of the m/z features based on t-statistics. The SSCG method parameters set at $r = 1$, $s = 3$, $k = 9$ to reduce sparsity of the data and computational times. Briefly, r , is the neighbouring smoothing radius, k , is the initial number of segments and s , is the shrinkage parameter. As s expands, fewer mass features are built into the spatial segmentation and only useful mass features are preserved. Normally, the number of segments (k) decrease as s increases, hence if only some mass

features are used, the fewer cluster there will be to describe⁴¹¹. The determination of the number of segments is exhibited in [Supplementary Figure 3.1](#).

2.2.7.3. SCiLS Lab

imzML MSI data were saved as .slx and .sbd files. Baseline removal was by convolution method set at 20 Da. The imzML data for each patient were imported for intra-patient analysis to create a single data analysis file. Data processing was conducted following the manufacturer's software manual (SCiLS Lab Help Version 2018/Release 6.01). Using the "Find Peaks" tool, peak picking was performed on 100 maximum peaks per spectra on every 16th spectrum at a maximum interval processing mode across all spectra in the multiple tissue sections. This identified several m/z intervals for a single spectrum and data was normalised to total ion count (TIC). The bisecting k-means segmentation method was employed based on the "Find Peaks" m/z intervals, where clustering was evaluated using three metrics approaches – Correlation distance, Euclidean and Manhattan. The number of PLSA components was set to 5 and derived either by random or deterministic initialisation. The PLSA object were then exported as .csv files for external visualisation in *R*.

2.2.8. Lipidomics

2.2.8.1. Total DNA Assay

DNA in tissue homogenate was measure by the Hoechst staining method. Working stock solutions comprised of 1 $\mu\text{g}/\mu\text{L}$ Herring Sperm DNA and 1 mg/ml Hoechst dye. A standard curve was constructed on a 96-well plate as displayed

in **Table 2.5**. 900 μL of Milli-Q H_2O was added to 100 μL of Herring Sperm DNA to achieve 100 $\text{ng}/\mu\text{L}$. 200 μL of homogenisation buffer (HB) was added to 50 μL of Herring Sperm DNA to well H1-H2 to achieve 2,500 $\text{ng DNA}/125 \mu\text{L}$ (20 $\text{ng}/\mu\text{L}$ DNA). 125 μL of HB was added to wells G1-G2 and up to B1-B2. Serial dilution was done by transferring 125 μL from H1-H2 to wells G1-G2 and so forth up to C1-C2. 125 μL was removed from C1-C2. A blank was constructed with 125 μL RO- H_2O added to wells B1-B2.

		ng DNA/125 μL	μL HB	μL DNA	μL of previous well
	1	2			
A					
B	Blank	0 (Blank)	125	-	-
C	1	78.125	125	-	125
D	2	156.25	125	-	125
E	3	312.5	125	-	125
F	4	625	125	-	125
G	5	1250	125	-	125
H	6	2500	250	-	-

Table 2.5. Hoechst DNA assay standard curve set-up.

Triplicate 30 μm cryosections of tissue adjacent to MALDI MS imaging slides were pooled into a single glass vial. Tissue sections were homogenised in 500 μL of H_2O with a UP50H sonicator (Hielscher, Germany). Samples were freeze-thawed to achieve better lysis then sonicated at 80% power cycle 5 sec for 3 times to release DNA from homogenate. A resuspension volume of 30 μL was used. Measurements were carried out in duplicate. The plate was sealed and incubated at 37°C for at least 1 h. Hoechst working solution was prepared by diluting 100 times with HB to a concentration of 2 $\mu\text{g}/\text{ml}$. 125 μL of diluted Hoechst dye was added per well. The plate was read on the Fluostar at 355 (excitation)/460 (emission) nm wavelength. The concentrations were calculated

using the standard curve linear response equation in an MS spreadsheet Excel and normalised sample volumes used for lipid extraction.

2.2.8.2. Lipid Extraction

Tissue homogenate equivalent to 0.5 µg DNA was diluted to 700 µL and mixed with 800 µL 1 N HCl:CH₃OH 1:8 (v/v), 900 µL CHCl₃ and 200 µg/ml of the antioxidant 2,6-di-tert-butyl-4-methylphenol (BHT; Sigma Aldrich). 3 µL of SPLASH® LIPIDOMIX® MS Standard (#330707, Avanti Polar Lipids) was spiked into the extract mix. The organic fraction was evaporated using a Savant Speedvac spd111v (Thermo Fisher Scientific) at room temperature and the remaining lipid pellet was stored at -20°C under argon.

2.2.8.3. Mass Spectrometry

Lipid pellets were reconstituted in 100% ethanol. Lipid species were analyzed by liquid chromatography electrospray ionisation tandem mass spectrometry (LC-ESI-MS/MS) on a Nexera X2 UHPLC system (Shimadzu) coupled with hybrid triple quadrupole/linear ion trap mass spectrometer (6500+ QTRAP system; AB SCIEX). Chromatographic separation was performed on a XBridge amide column (150 mm × 4.6 mm, 3.5 µm; Waters) maintained at 35°C using mobile phase A [1 mM ammonium acetate in water-acetonitrile 5:95 (v/v)] and mobile phase B [1 mM ammonium acetate in water-acetonitrile 50:50 (v/v)] in the following gradient: (0-6 min: 0% B → 6% B; 6-10 min: 6% B → 25% B; 10-11 min: 25% B → 98% B; 11-13 min: 98% B → 100% B; 13-19 min: 100% B; 19-24 min: 0% B) at a flow rate of 0.7 ml/min which was increased to 1.5 ml/min from 13 minutes onwards. SM, CE, CER, DCER, HCER, LCER were measured in

positive ion mode with a precursor scan of 184.1, 369.4, 264.4, 266.4, 264.4 and 264.4 respectively. TAG, DAG and MAG were measured in positive ion mode with a neutral loss scan for one of the fatty acyl moieties. PC, LPC, PE, LPE, PG, LPG, PI, LPI, PS and LPS were measured in negative ion mode with a neutral loss scan for the fatty acyl moieties. Lipid quantification was performed by scheduled multiple reactions monitoring (MRM), the transitions being based on the neutral losses or the typical product ions as described above. The instrument parameters were as follows: Curtain Gas = 35 psi; Collision Gas = 8 a.u. (medium); Ion Spray Voltage = 5500 V and -4,500 V; Temperature 550°C and Ion Source Gas 1 = 50 psi; Ion Source Gas 2 = 60 psi; Declustering Potential = 60 V and -80 V; Entrance Potential = 10 V and -10 V; Collision Cell Exit Potential = 15 V and -15 V. The following fatty acyl moieties were taken into account for the lipidomic analysis: 14:0, 14:1, 16:0, 16:1, 16:2, 18:0, 18:1, 18:2, 18:3, 20:0, 20:1, 20:2, 20:3, 20:4, 20:5, 22:0, 22:1, 22:2, 22:3, 22:4, 22:5 and 22:6 except for TGs which considered: 16:0, 16:1, 18:0, 18:1, 18:2, 18:3, 20:3, 20:4, 20:5, 22:2, 22:3, 22:4, 22:5, 22:6.

2.2.8.4. Data Analysis

Peak integration was performed with the MultiQuant™ software version 3.0.3. Lipid species signals were corrected for isotopic contributions (calculated with Python Molmass 2019.1.1) and were normalised to internal standard signals. Unpaired T-test p-values and FDR corrected p-values (using the Benjamini/Hochberg procedure) were calculated in Python StatsModels version 0.10.1.

2.3. Chapter 4 Methods

2.3.1. Tissue Preparation for MALDI MS Imaging

Human prostate biopsy cores were obtained as described in [Section 2.2.1](#). In this study, larger cryosections (6 – 8 mm diameter) were collected as shown in **Figure. 2.4**.

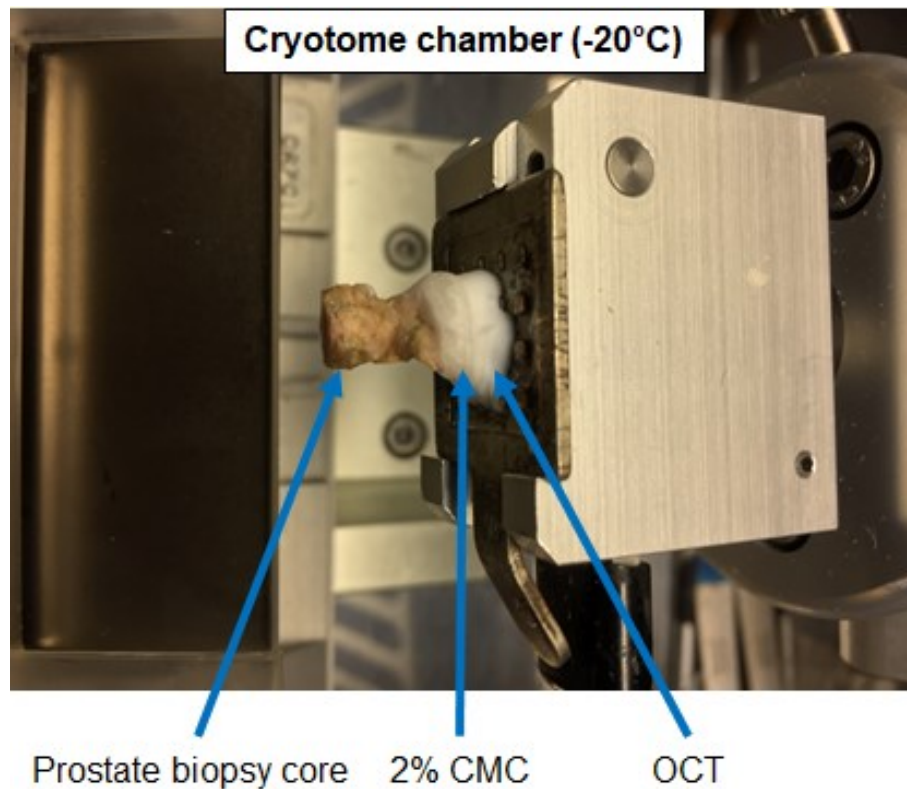


Figure 2.4. Image of mounted fresh-frozen prostate biopsy core.

2.3.2. Matrix Application by Automated Spray Coating

Automated spray coating of the matrix was achieved by deposition of 7.0 mg/ml (80% methanol-0.1% TFA v/v) α -CHCA using a SunCollect MALDI sprayer (SunChrom GmbH, Friedrichsdorf, Germany) as depicted in **Figure 2.5**. This technique forms the basis of the works described in [Chapter 4](#).

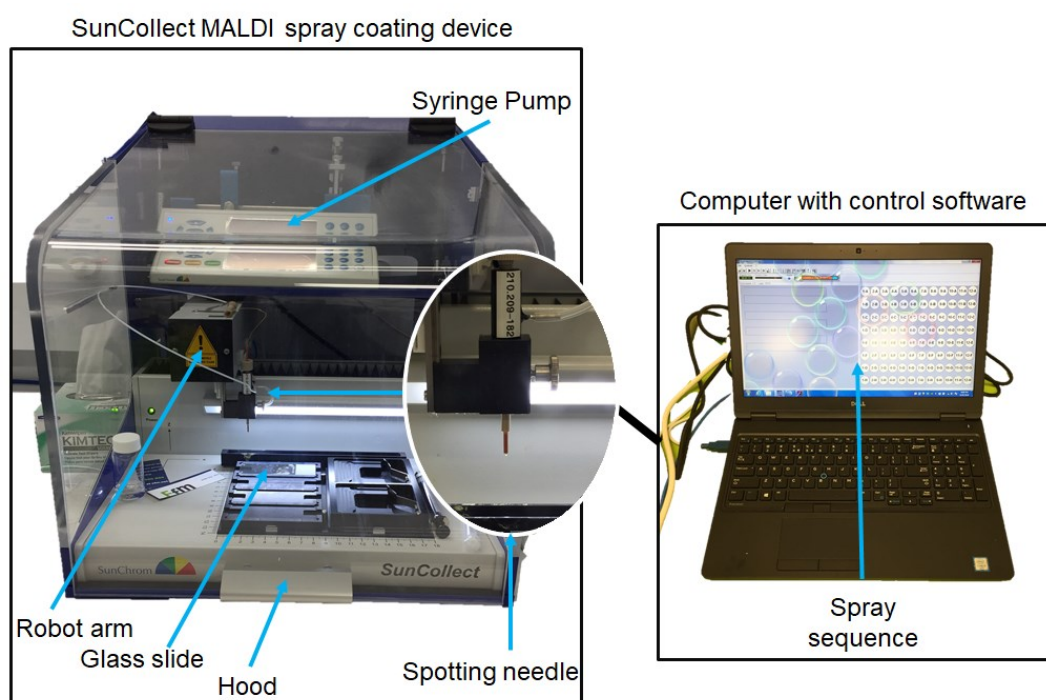


Figure 2.5. MALDI matrix automated spray coating set-up.

2.3.3. MALDI MS Imaging Data Acquisition

Tissue sections were analysed on a MALDI SYNAPT HDMS hybrid quadrupole Q-oo-TOF Mass Spectrometer as described in [Section 2.2.6](#). MSI data was recorded between 400-990 Da a lipid rich *m/z* range.

2.3.4. Histology and Immunohistochemistry

Before histological staining, post-MALDI acquisition glass slides were rinsed with 100% methanol to remove CHCA. H&E staining was then performed stained as described in [Section 2.2.2](#). The procedure for immunohistochemistry (IHC) for AR as previously described is fully outlined here⁴¹². Prior to staining, consecutive serial cryosections to the H&Es for IHC kept at -80°C were equilibrated to room temperature. Slides were briefly rinsed with RO-H₂O and 1X Tris Buffered saline (TBS) pH 7.6 for 2 min and fixed in 4% paraformaldehyde (Sigma-Aldrich, NSW, Australia) at room temperature for 10 min. Slides were again washed with TBS for 5 minutes before they were loaded on to the Discovery Ultra staining platform (Roche, Basel, Switzerland). Routine IHC was performed using the androgen receptor antibody (ab10831, Abcam Cambridge, UK) 200-fold dilution in antibody diluent buffer (Roche, Basel Switzerland), anti-rabbit HQ antibody (760-4815 Roche, Basel, Switzerland), and anti-HQ HRP antibody (760-4820, Roche, Basel, Switzerland) and ChromoMap DAB kit according to manufacturer's instructions. Slides were counterstained with haematoxylin (760-2011, Roche, Basel, Switzerland) and bluing reagent (760-2037, Roche, Basel), dehydrated and mounted in DPX (LabChem, Zelineople, PA). Slides were scanned with a

NanoZoomer Digital Slide Scanner 2.0-HT (Hamamatsu, Japan) using a 40X objective and images were capture using NDP.view.27.25 (Hamamatsu Photonics K.K., Japan).

2.3.5. Lipidomics

LC-MS/MS analysis of fresh-frozen cryosections was performed as outlined in [Section 2.2.8](#).

2.4. Chapter 5 and Chapter 6 Methods

2.4.1. *Ex Vivo* Culture of Human Prostate Tissue

Following radical prostatectomy, 6–8 mm tissue cores from the left and/or right sides of the prostate were dissected into approximately 1–3 mm³ (~3–5 mg) pieces and cultured in quadruplicate. An illustrative workflow is depicted in **Figure 2.6**.

Explant culture set-up for drug quantification was as follows. 2,000 μ l of M4 AR antagonist media was added to two sterile containers, for DMSO (vehicle) and enzalutamide (ENZ). 2 μ L of 10 mM ENZ stock was added in each container to attain a final concentration of 10 μ M. Cuboid shape gelatin sponges were then placed in each container to soak treatments and transferred to 24-well plates. 500 μ L of media was then added in to each well. 1 sponge was added per well using forceps carefully to avoid deformation and placed such that the top was a flat surface. Pre-weighed fresh-cut biopsy tissues were placed on top of the sponge with a total of two explant pieces per sponge. Wells with tissue were denoted as drug quantitation (DQ) wells. 510 μ L of the remaining media was transferred to a cryotubes and denoted as time 0 h. The 24-well plate was then incubated at 37°C for 48 h. Drug stability (DS) was assessed by aliquoting 2,000 μ L of treatment in separate wells with gelatin sponges but without tissue (**Figure 2.6**). Following the incubation period, media was harvested in cryovials, snap-frozen and transferred to -80°C freezer. Explant tissues were transferred to 2.0 ml tough tubes.

Explant culture set up for MALDI MSI was as follows. In addition to the 10 μ M dose, 10 μ L of 10 mM ENZ stock in the same 2,000 μ L volume attained 50

μM ENZ. After the incubation period, explant tissues were picked by carefully holding along the edges and place in a capsule with 2.0% CMC. The orientation of the tissue as it sat during culture was maintained. Capsules were then carefully placed in appropriately labelled cryovial and immediately snap-frozen in liquid nitrogen (LN_2) dry shipper. Samples were then shortly transferred to a -80.0°C freezer.

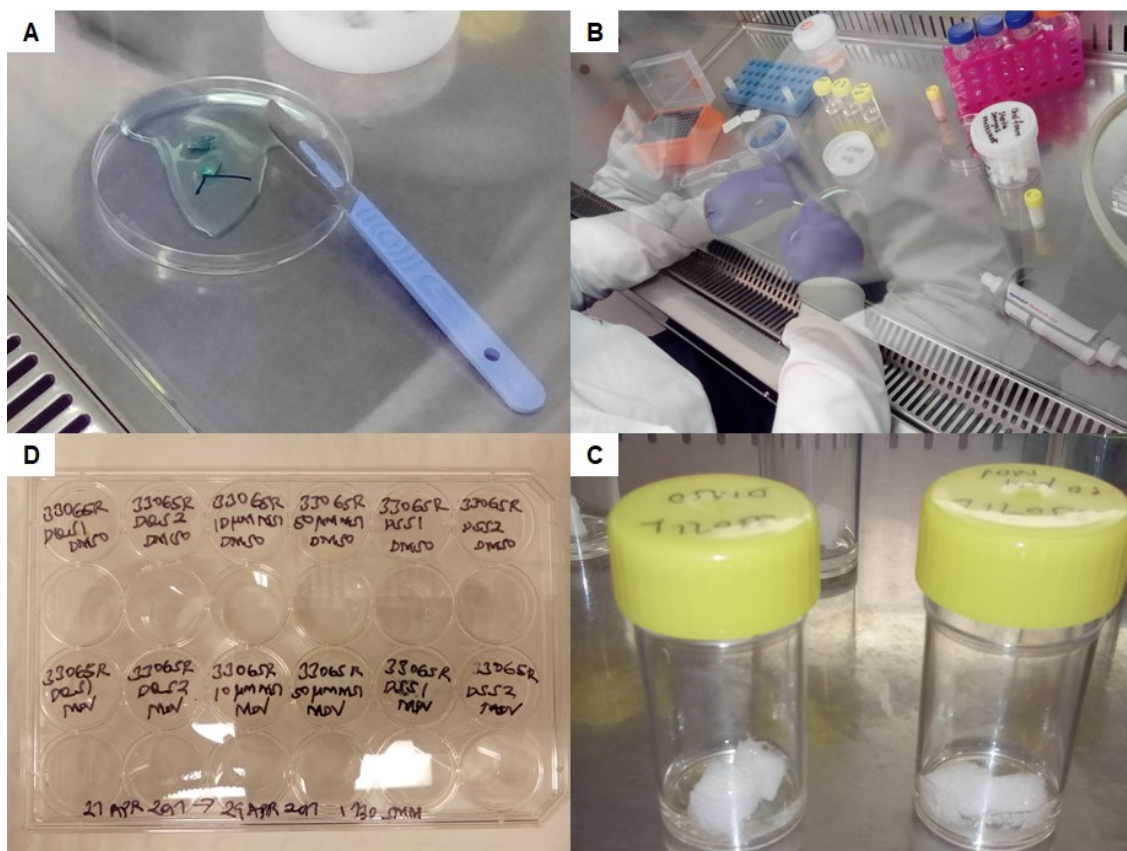


Figure 2.6. Prostate patent-derived explant (PDE) culture set-up workflow. **A.** Prostate core stored in PBS from surgery is placed on sterile petri dish. **B** 6-8 mm core is cut into smaller pieces to be used as explants. **C.** Sterile gelatin sponges are pre-soaked in treatments. **D.** Treatment wells are loaded with 500 μL M4 media and 2 explant pieces are placed per sponge per well in duplicate.

2.4.2. Drug Extraction from Explant Culture System for Enzalutamide Quantification

2.4.2.1. Explant Tissue Homogenisation

Following 48 h culture treatment, PDE tissues were gently picked by forceps from gelatine sponges and blotted on lint free paper for 30 sec. Samples were then transferred to 2.0 ml tough tubes containing 0.6 g Precellys 1.4 mm Zirconium oxide beads. 1,000 μ L of solvent blank (50:50 CH₃OH-H₂O (Milli-Q)) was then added. Tissues were homogenised using a Precellys 24 at 4.0°C at 6,500 rounds per minute (rpm), two times 60 sec with equivalent rest period in between. The lysate was then pelleted down by using a refrigerated centrifuge (Eppendorf 5424R, Germany) set at 4.0°C for 10 min at 10,000 rpm (9,391 *rcf*). Samples were then stored -80.0°C.

2.4.2.2. Protein Precipitation/Crude Extraction Method for Tissue Homogenates

Volumes of 250 μ L tissue homogenate supernatant from above were transferred to appropriately labelled 2.0 ml Microcentrifuge tubes. 100 μ L of internal standards (IS) mix (50 μ L d₆-enzalutamide 1,000 nM and 50 μ L d₆-desmethylenzalutamide 1,000 nM) was added. Samples were vortexed for 30 sec followed by a short centrifuge spin. 100% pre-chilled/ice-cold acetonitrile was added to sample in a ratio of 4:1 (V/V) ~ 1.4 ml. Tubes were briefly vortexed and incubated in -20.0°C for 1 h. Tubes were centrifuged at 13,000 rpm (15,871 *rcf*) for 20 min at 4.0°C to obtain a protein precipitate at the bottom. The rack with

tubes was maintained on dry ice to prevent pellets from resuspending. The supernatant was transferred to clean appropriately labelled tubes. Samples then underwent freeze-drying in a rotational vacuum concentrator (RVC) overnight. Later, tubes were reconstituted with 400 μL of $\text{CH}_3\text{OH-H}_2\text{O}$ 1:1 (v/v), vortex for 30 sec and contents spun down at 13,000 rpm (16,060 *rcf*) for 5 min using a centrifuge (Biofuge Pico, Heraeus, ThermoScientific, Australia). 300 μL of reconstituted volume was then pipetted into a 96-well plate. For each sample, 5 μL of was injected into the LC-MS/MS system.

2.4.2.3. Protein Precipitation for Culture Medium

Briefly, 250 μL of M4 medium was subjected to protein precipitation. A 100-fold dilution of patient M4 medium sample was made by taking 2.5 μL of cryopreserved media to 247.5 μL of freshly made medium. Triplicate dilution QC samples were made by making 1:100 dilution of 10 μM or 50 μM ENZ freshly spiked. IS was added and protein precipitation performed as described in **Section 2.4.2.2.**

2.4.2.4. Standard Curve for Biological Matrices

For method validation and sample analysis the following standards were required in fresh M4 medium and in pooled tissue homogenates from 10 separate patient biopsy samples (prepared using the method above **2.4.2.1**): blank sample – matrix only, zero sample – matrix and internal standard mixture, enzalutamide “standards” spiked with IS (10, 9, 8, 7, 6, 5, 4, 3 and 2) and QC samples spiked with IS LLOQ, LQC, MQC and HQC, both extracted and unextracted. QC

samples were individually extracted as three technical replicates. The standard curve preparation sheet is outlined in [Chapter 5 Table 5.8](#). Protein precipitation was performed as described in **2.4.2.2**

2.4.2.5. Quantitative Run Assay Set-Up

The analytical run was programmed from least to most concentrated standards. Adequate solvent blanks were placed between samples across the run to minimise carry over and test samples were bracketed by QC samples and standards i.e. lay in the middle of the programmed run. The run sequence was set as follows: solvent blank, blank sample, zero sample, standard 10, 9, LLOQ, LQC, 8, 7, 6, MQC, DQC (medium only), DMSO (M4 medium/explants) ENZ (M4 medium/explants) standard 5, 4, DQC (medium only), 3, HQC and standard 2. Calibration curve samples required a single injection. QC samples required single injections of independent triplicate extracts.

2.4.3. Bicinchoninic Acid Total Protein Assay

Protein determination was attained by the Micro BCA assay kit (23235 Thermo Scientific, IL, USA). Tissue homogenates were removed from the freezer and thawed on ice for. A standard curve was constructed using a stock of 2 mg/ml bovine serum albumin (BSA). 100 μ L of this stock was diluted with 900 μ L of Milli-Q H₂O to achieve a final concentration of 200 μ g/ml. Samples were plated in duplicate one column at a time as illustrated in **Table 2.6**. The volume of the tests samples was governed by the weight of PDE tissues to obtain readings within the calibration curves. For 10 μ M ENZ dose, tissues weighed 0.5 - 1.5 mg hence 100 μ L of tissue homogenate volume was used. For the 50 μ M dose time course

study, 10 μL of tissue homogenate was used since explants were larger. Volumes were made up to 100 μL with Milli-Q H_2O . 5 ml of Micro BCA Reagent A, 4.8 ml of Micro BCA Reagent B and 200 μL of Micro Reagent C were aliquoted into a 10 ml yellow top tube and thoroughly mixed by inversion. This made colour reagent for detection. A multichannel pipette was used to add 100 μL of the colour reagent into each well and mix the samples. Plates were sealed with an adhesive back plastic sealer and incubated at 37°C for 2 h. The plate was read on VICTOR3 plate reader (Perkin Elmer, Finland) with absorbance at 560 nm. Drug (analyte) responses measured as ng/ml were normalised to total protein expressed as ng/ μg .

	Standards	Volumes		
	$\mu\text{g}/\text{well}$	200 $\mu\text{g}/\text{mL}$ stock	Milli-Q water	Total volume/well
A	0 μg	0 μL	100 μL	100 μL
B	1 μg	5 μL	95 μL	100 μL
C	2 μg	10 μL	90 μL	100 μL
D	4 μg	20 μL	80 μL	100 μL
E	8 μg	40 μL	60 μL	100 μL
F	12 μg	60 μL	40 μL	100 μL
G	16 μg	80 μL	20 μL	100 μL
H	20 μg	100 μL	0 μL	100 μL

Table 2.6. Micro BCA assay for protein determination set-up.

2.5. Chapter 7 Methods

2.5.1. Tissue Preparation for MALDI MS Imaging

Patient-derived cultured explants were harvested and stored as previously described in [Section 2.4.1](#). Tissue sectioning was conducted as previously described in [Section 2.2.1](#).

2.5.2. Histological Staining

H&E staining was conducted as previously described in [Section 2.2.2](#).

2.5.3. Instrument Calibration

The Bruker timsTOF Flex instrument (Bruker Daltoniks, Bremen, Germany) was calibrated in “ESI” mode using tuning mix (Agilent) using the timsControl program. The tune settings were optimised to achieve balanced detection of ions across the desired mass range m/z 50 -1250 for analysis of lipids. This involved optimising the transfer, quadrupole, collision cell and TOF parameters. Calibration used four reference masses, for negative polarity; m/z 112.9856, m/z 301.9981, m/z 601.9790, m/z 1033.9881, for positive polarity; m/z 118.0863, m/z 322.0481, m/z 622.0290, m/z 922.0098, in “enhanced quadratic” mode. The calibrant for drug imaging was sodium formate made by mixing 0.2 μ L 10 M NaOH, 2 μ L formic acid into 1,997 μ L H₂O. Sodium formate suitable for the small m/z 50 - 500 range. A calibration accuracy score of 99.9-100.0% corresponding to standard deviation (error) of <0.02 ppm was acceptable. The instrument source was set back to “MALDI” mode for subsequent imaging.

2.5.4. Matrix Application

Automated spray coating of the matrix was achieved by deposition of either 10 mg/ml (80% aqueous methanol) norhamane for negative ion mode lipid imaging or 7 mg/ml (80% aqueous methanol-0.1% TFA v/v) CHCA for positive ion mode lipid and drug imaging using a SunCollect MALDI sprayer (SunChrom GmbH, Friedrichsdorf, Germany) as illustrated in [Section 2.3.2](#). 15 passes of matrix were used at an increasing flow rate of 10-40 $\mu\text{L}/\text{min}$ and 30 sec pause between passes. The first four layers are important for formation of very minute “seeding” matrix crystals; 1st pass 10 $\mu\text{L}/\text{min}$, 2nd pass 20 $\mu\text{L}/\text{min}$, 3rd pass 30 $\mu\text{L}/\text{min}$ and 4th pass 40 $\mu\text{L}/\text{min}$. The horizontal track (X) speed was 350 mm/min, line distance of 2.00 mm, Z-position of 1.00 mm, and nitrogen gas at room temperature set to a nebulizing pressure of 2.0 Bar. Fiducials were covered with blank microscope slides so that only the ITO glass area with tissue was coated with matrix.

2.5.5. MALDI MS Imaging Data Acquisition

Using a diamond marker, an “L” shaped fiducial was inscribed to denote the top left of the ITO slide and three “X” crosses were etched around the tissue sections. One or two ITO slides were then attached on the MTP target plate and scanned with a flatbed scanner. ITO slides were then removed, and matrix coated as described above in **Section 2.5.4**. Coated slides were then returned to the target plate and loaded into the source. The scanned image was imported into Flex Imaging. In the imaging run experiment set up, three “X” fiducials were used to co-align the image and slide position. The “L” fiducial confirmed crosshair position accuracy by selecting it with the cursor on Flex Imaging and observing the movement of the target plate to the corresponding location on the camera window

in timsTOF control. Imaging patterns were drawn around tissue sections and saved as a region for imaging with the lateral resolution (raster size) specified for the x and y direction. The baseline subtraction and peak smoothing were activated, and data acquired. For lipid imaging, data was acquired at 20 μm pixels. The 10,000 Hz smartbeam 3D laser was set to 60% laser power attenuation and 250 shots per pixel. Data was acquired over a mass range m/z 50 – 1250.

2.5.6. Drug MS/MS Imaging Data Acquisition

For targeted drug imaging, data was acquired at 60 μm pixels unless specified otherwise. The acquisition settings were set in timsTOF control. The 10,000 Hz smartbeam 3D laser was set to 100% laser power attenuation and 250 shots per pixel. Data was acquired over a mass range m/z 50 – 500 in MRM mode for the m/z 465.45 to m/z 209.10 transition. The collision induced dissociation energy (CID) for precursor ion fragmentation was set at 32 eV.

2.5.7. Data Processing and Analysis

2.5.7.1. SCiLS Lab

MSI data from Flex Imaging were imported into SCiLS Lab either as “Bruker TOF instruments Flex series format” or as “vendor-neutral imzML format”. Baseline removal was not performed as the files were in reduced format (.dat) or as .imzML data. Typical MSI data file sizes for three tissues, each 4-6 mm^2 , on a single ITO slide ranged from 8 – 12 GB at a spatial resolution of 20 μm . Thresholding was done to select the top 500 – 1000 peaks per spectrum creating a list of m/z features. Peak picking used mean spectra of peak list and identified m/z intervals

moved to local maxima with total ion count (TIC) normalisation. Segmentation was performed on combined data sets with weak denoising where bisecting k-means segmentation method by Correlation Distance, Euclidean and Manhattan metrics. Clusters were named according to tissue types based on adjacent H&E stained scans with the regions denoted as either epithelium or stroma. The segmented clusters of Day 0, DMSO and ENZ regions were stratified as epithelium and stroma groups. The peak list data from these regions were exported to MetaboScape 5.0 for feature annotation.

2.5.7.2. Metabolomic feature annotations

SCiLS Lab was used to create MetaboScape 5.0 .srd files which were imported using the create experiment tool which linked with the .msi experiment files made by FlexImaging. The T-Rex² algorithm for MALDI Q-TOF imaging data was used for detection and combination of isotope peaks and adducts. ROI subsampling was performed by combining spectra from 3 x 3-pixel blocks called speckles. A maximum of 50 speckles for each region were used for average spectral sampling. The next processing step was ion deisotoping. In negative ion mode, [M-H]⁻ was the primary adduct and [M+Cl]⁻ and [M-H₂O-H]⁻ as seed ions. In positive ion mode, ion deconvolution parameters were set as [M+H]⁺ as the primary adduct and [M+Na]⁺, [M+K]⁺ and [M-H₂O+H]⁺ as seed ions. The HMDB⁴¹³ and LMSD⁴¹⁴ detected metabolites were used to annotate matched *m/z* features. The criteria for identification was accurate mass (3 - 10 mDa) and mSigma (0-20). mSigma is annotation quality score that factors distribution of isotopic ions. The annotated files were then exported and re-imported into SCiLS Lab which was then set to display the *m/z* features with metabolite/lipid species names.

2.5.7.3. Statistical Analysis

Univariate analysis was performed to look for changes between groups (epithelium and stroma categorised as Day 0, DMSO and ENZ). A volcano plot is a combination of fold-change and t-tests. The group variance was deemed unequal, p-value set at a threshold of 0.05 with adjustment for false-discovery rate (FDR) and the \log_2 fold change (FC) >1 . t-test was performed between two groups. ANOVA analysis was performed for three groups and the reported parameters included p-value and p-value for Anderson-Darling (AD-test to check if sample of data comes from a population with a specific distribution). According to the manufacturer's software manual (SCiLS Lab Help Version 2019c/ Release 7.02), for a given m/z feature, if p-value t-test/ANOVA ≤ 0.05 and p-value AD > 0.05 then a peak is considered "interesting" and this relationship was summarised by p-value (rank). MetaboScape 5.0 and MetaboAnalyst 4.0 volcano plots were identically constructed.

2.5.8. Cell Counting

Cell counting for positively labelled cells in IHC scans was done in ImageJ Fiji 1.52p (National Institutes of Health, USA). This procedure was suited where the primary antibody was stained for AR. Coloured bitmap files as .png format were opened and any folded edges were cut out using free drawing tool. The colour deconvolution tool was set at "H DAB" suited for IHC slides. This split the image into three colour channels (green, purple and brown). The adjust threshold tool was set at black and white for the brown channel. The analyse particle tool was then used to estimate number of cells by counting the black pixels representative of individual cells.

2.5.9. Immunohistochemistry

IHC for p63+AMACR was as follows. Slides stored at -80°C were transferred to 4°C and allowed to thaw for 30 min before being allowed to equilibrate at room temperature for 1 h. Slides were then placed on a heat block, at 45°C for 2 min to enhance tissue adhesion and then allowed to return to room temperature (RT). Sections were placed in RO-H₂O for 2 min to allow 2% CMC to dissolve and rinsed in 1X TBS pH 8.4 for 2 min. Sections were then fixed in 4% formaldehyde solution (Invitrogen, Life Technologies, USA) at RT for 10 min. Slides were again rinsed in 1X TBS pH 8.4 for 5 min. Slides were immunolabelled with p63-AMACR using the Benchmark Ultra IHC platform (Roche, Basel, Switzerland)⁴¹⁵. Detection of p63 immunolabelling was achieved using the Optiview DAB kit (760-700 F18342, Roche Diagnostics, Australia) while the AMACR immunolabelling was detected using the Ultraview Red kit (760-501 F10132, Roche Diagnostics Australia). Slides were wet mounted from 1X TBS pH 8.4 into the machine. Antigen retrieval was performed using cell conditioning solution 1 (CC 1) (950-224 Roche) at 95°C for 4 min. Slides were then washed in with reaction buffer (950-300 Roche) twice at 36°C. Endogenous peroxidase was blocked using the Optiview peroxidase inhibitor (760-700 Roche) applied at 36°C for 4 min. Slides were then washed with reaction buffer twice. The **first antibody, 34βE12+p63** (790-4536 Roche), was applied (100μL) and incubated at 36°C for 20 min. Slides were again washed with reaction buffer thrice. 100 μL of the secondary antibody, Optiview HQ universal linker (760-700 Roche) was applied and incubated for 8 min. Slides were again rinsed as with the preceding step. 100 μL of Optiview HRP multimer (760-700 Roche) was applied and incubated for 8 min. Sides were then rinsed with reaction buffer thrice. 100 μL each of H₂O₂ (760-700 Roche) and

DAB (760-700 Roche) was then applied and incubated for 8 min. Slides were then washed with reaction buffer once. 100 µL of Optiview copper (760-700 Roche) was applied to differentiate the background.

Slide heaters were then disabled, and samples rinsed with reaction buffer. 900 µL of reaction buffer was applied and slides warmed to 90°C for 4 min twice, before being rinsed again at 36°C for 4 min, for a total 6 wash cycles. Slides were then rinsed with reaction buffer at 37°C. 100 µL of **second antibody, p504s SP116** (790-6011 Roche) was applied and incubated at 37°C for 32 min. Slides were rinsed with reaction buffer once. One drop of the secondary antibody, UV red universal multimer (760-501 Roche) was then applied and incubated at 36°C for 12 min. Slides were then rinsed with reaction buffer and one drop of a series of UV red cocktail (760-501 Roche) applied. Red Enhancer for 4 min, Fast Red A-Naphthol for 8 min and Fast Red B applied for 8 min. Slides were then rinsed with reaction buffer. Slides were counterstained by applying one drop of Haematoxylin (760-2021 F03787 Roche) and incubating for 4 min. Slides were then washed with reaction buffer twice. This was followed by applying a single drop of bluing reagent (760-2037 Roche) and incubating for 4 min. Liquid cover slip was removed by dipping slides in a gently running pot of RO-H₂O with mild liquid dishwashing detergent for 5 min, twice. Slides were dehydrated in an oven set at 45°C for 15 min. Slides were transferred to a pot with xylene for 15 sec. Cover slipping was done with DPx mountant and slides allowed to dry.

CHAPTER 3:

MALDI MS Imaging and Lipidomics Profiling Reveal Heterogeneity in Lipid Composition of Clinical Prostate Tissues

Context

This Chapter reports on a collaborative project involving researchers funded by the Movember revolutionary Team Award (MRTA) 3 grant. Tissue sectioning, histopathological staining, MALDI MS imaging and data analysis and collection of samples for validation by MS/MS imaging and lipidomics were performed by the author. Dr. Rajdeep Das performed expert pathological assessment. MALDI MS/MS imaging of selected epithelial lipids was performed by Daan Van den Bosch (KU Leuven) based on data analysis of the prior MSI only data. Lipidomics analysis was performed using the Lipometrix platform (Dr. Jonas Dehairs, Prof. Johan Swinnen) at the Laboratory of Lipid Metabolism and Cancer at KU Leuven, Belgium. Some of the results of this Chapter were incorporated into a manuscript detailing tumour-related changes in lipid profile (Butler LM et al, submitted), which is included in this thesis.

3.1. Introduction

The plethora of lipid metabolic reactions are under tight hormonal control (both insulin and androgens) through many enzymes which have been studied as mediators of altered lipid metabolism of PCa. Deregulated expression of lipid metabolic genes that encode for FASN, ACLY and ACC are frequently reported to be altered in PCa development and progression²⁹⁶. The prostate gland is composed of heterogenous tissue characterised by contrasting proportions of various cell types such as secretory epithelial cells, basal cells and fibromuscular stromal cells. Oncogenesis in prostate tissue primarily afflicts the epithelium²⁷ and can lead the development of primary tumours with different growth rates. Therefore, this gives prostate cancer (PCa) a multifocal nature, where within one patient different grades of tumours can arise and different patients can bear multiple primary and metastatic tumours³³⁴. MALDI MSI is an ideal approach define the chemical fingerprint of heterogeneous tumours and to take into account the lipid composition of the tumour microenvironment, compromising stromal, vascular and immune cells, all of which can support the growth and progression of cancer.

The challenge with lipidomics experiments is that thousands of variables (lipid masses) can be measured in each sample for MALDI MS imaging hundreds within a single pixel in a sample. To rationalise such multi-parametric data sets, dimensionality reduction techniques such as principal component analysis (PCA) and t-distributed stochastic neighbour embedding (t-SNE) are commonly used. PCA is an unsupervised way to summarise numerous variables and look for object groupings. A score plot represents the best possible two-dimensional window of the original data and the loadings plot shows the contribution of each variable to the objects. PCA is suitable for data sets with high variance. Transformation

approaches such as logging, cube root and scaling by mean, auto, pareto and range methods are applied depending on the nature of the data⁴¹⁰. On the contrary, t-SNE is a non-linear algorithm that models related objects to close points and unrelated objects are by distant points based on probability. t-SNE was first applied to MSI data sets by Fonville and colleagues to describe the morphology of rat brain⁴¹⁶. Partial least square discriminant analysis (PLS-DA) is an extension of PCA. It is a supervised approach where known variables are used to predict the behaviours of unknown several variables using regression. Thus PLS-DA is widely used in untargeted metabolomics and lipidomics to identify metabolites which best correlate with phenotypes⁴¹⁷.

Probabilistic latent semantic analyses (PLSA) is an emerging approach for concise interpretation of MALDI imaging data⁴¹⁸. It has the unique advantage of detecting changes where different cell types are present in tissue and in varying proportions and may therefore be more informative than the more conventionally used PCA. The other benefit of PLSA is that both scores and loadings can be interpreted as mass intensities. Nonetheless, PCA is still useful for exploratory data analyses either by visual inspection of spatial differences or exporting regions of interest from the MALDI data for external statistical analysis. Another advanced approach to understanding the spectral composition of the MSI data sets in context of tissue morphology is clustering analysis by spatial segmentation. This computational method was pioneered by Alexandrov and colleagues to explore the proteome on a mouse kidney section and neuroendocrine tumour²¹⁰. It has since been successfully applied to interrogate the lipidome of head and neck cancer among other solid tumours⁴¹⁹. This method of data mining is less cumbersome than scrolling through individual ion images

among hundreds in a signal MALDI experiment and more informative than PCA⁴²⁰. The essence of segmentation is to statistically group or divide spectra according to their likeness as they occur across the tissue. Spectra that are related are denoted with a unique single colour and clusters follow a colour-coded map. In this project, bisecting-k-means was opted for, as its more efficient than hierarchical clustering, where the algorithm recursively portioned the data into two segments at each level and it was possible to interact with the clustering tree.

Clustering	Approach	Method	Interactivity	Reference
Hierarchical	Bottom-up (Agglomerative)	Correlation Distance	Yes	Frank <i>et al.</i> , 2013 ⁴²¹
Bisecting k-means	Top-down (Divisive)	Correlation Distance Manhattan Euclidean	Yes	Krasny <i>et al.</i> , 2015 ⁴¹⁹
k-means	Classical	–	No	McCombie <i>et al.</i> , 2005 ²⁰⁴ , Konicek <i>et al.</i> , 2012 ^{208,422}
Shrunken spatial centroids	-	Adaptive Gaussian	Limited	Bemis <i>et al.</i> , 2016 ⁴¹¹

Table 3.1. Popular statistical approaches for clustering in MSI data analysis.

MALDI MSI has been applied in the study of proteomics, metabolomics and lipidomics in various solid tumours⁴²³ and there is a growing body of evidence that it slowly has the potential to be applied to clinical diagnostics and prognostics biomarker discovery. Herein, MALDI MSI was applied to probe the *in situ* chemical profile of clinical prostate biopsies. A subclass of lipids detectable in positive ion mode MALDI MSI – phosphatidylcholine (PC), Ceramides (Cer), and sphingomyelin (SM) are reported. Following a database search to identify which *m/z* features are tentative lipids and utilising several bioinformatics applications in an unsupervised analysis approach, presented herein are the visualisation of distinct lipid *m/z* features and comparison of lipid ion signals in selected tissues containing multifocal prostate adenocarcinomas. It was hypothesised MALDI MSI would unravel cell type-specific lipid profiles within heterogenous tissues. The objective of this Chapter is to evaluate the different spatial clustering methods offered by *R* Cardinal and SCiLS Lab and determine the most suitable segmentation approach for subsequent studies of lipidomics-based prostate tissue morphology and PCa pathology in the project.

3.2. Experimental Approach

The figure below summarises the procedures from the **Chapter 2 Materials and Methods Section 2.2** for data generation in this Chapter.

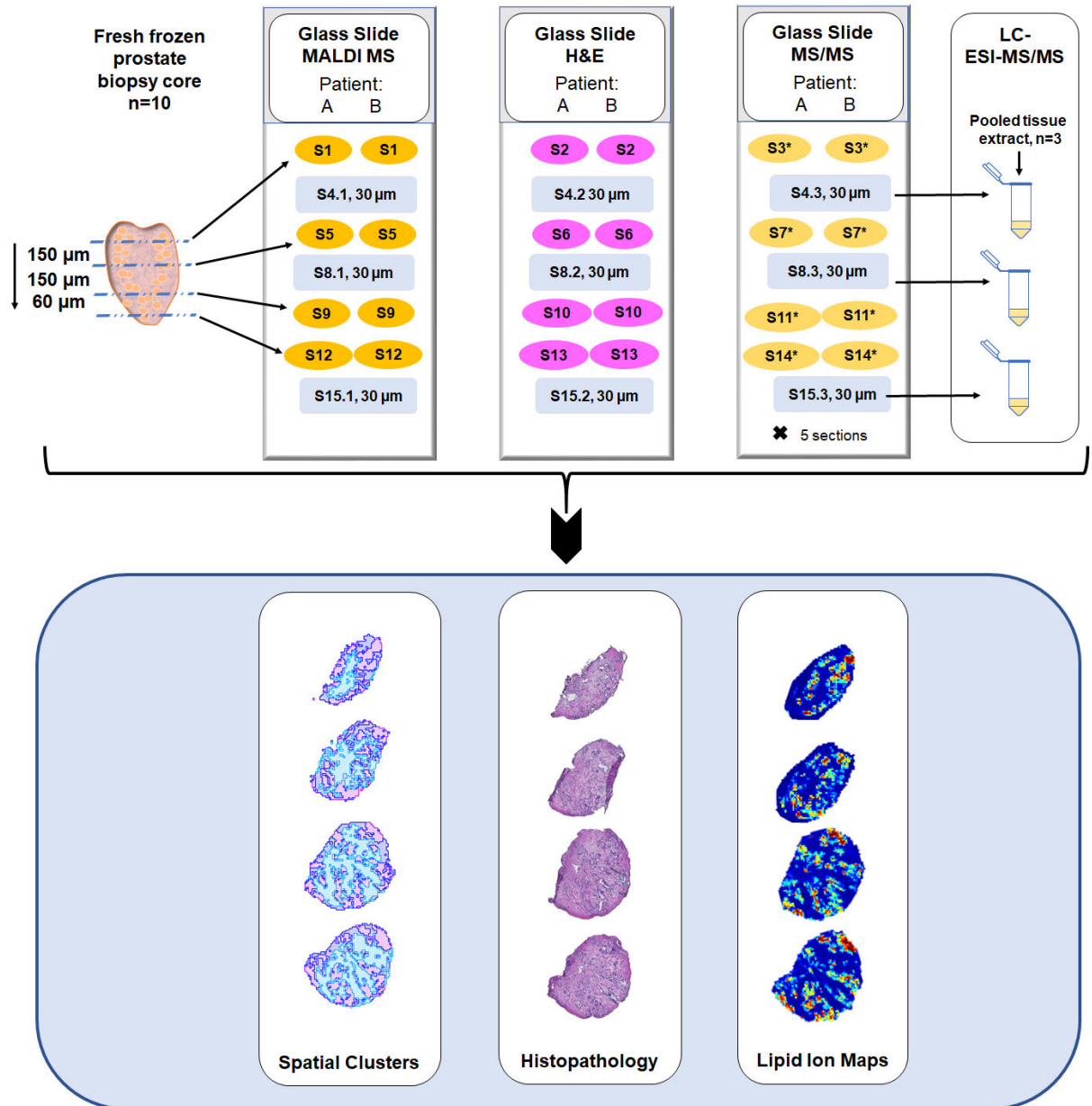


Figure 3.1. Experimental workflow for MALDI MSI, histology and lipidomics.

3.3. Results

3.3.1. Cellular Heterogeneity of Prostate Tissues Changes with Depth

In this study the morphology of prostate tissue was assessed to describe the cellular heterogeneity, to detect suitable sections with tumour and to describe the depth profile of lipid signatures in prostate tissue. Prostate biopsy cores from 10 patients were assessed for prostate cancer based on the Gleason grading system, of which, two were (Gleason 6), seven (Gleason 7) and one (Gleason 9) at the time of RP. Tissue sections were obtained at interspersed depths through each biopsy core as depicted in **Figure 3.1**. Each section used for MALDI imaging was similar but not identical. Pathological assessment of all the tissue sections confirmed presence or absence of specific cell types within the tissue. Multiple cancer phenotypes were present in varying degree in each section, regardless of having the same Gleason score. Hyperplasia, adenocarcinoma, tumour, malignant cells were identified across the patient cohort and these phenotypes varied with each level of sectioning as shown in **Table 3.2**.

	Patient	Section Number	Section Area (mm²)	Epithelial Cell Estimate	Total Area	Pathology comments
1	32770L	S2 - S3.5	3.45	486	1426	No glandular structures / normal
		S6 - S7.5	5.35	822	3439	Normal
		S10 - S11.5	4.97	1792	11971	Normal / transformation
		S13 - S14.5	4.66	1805	9522	Normal mild atrophy / near-normal transformation
2	32831R	S2 - S3.5	8.44	858	7196	Normal/ normal processing effect
		S6 - S7.5	9.64	757	3525	Normal papillary / near-normal, tumour cells
		S10 - S11.5	10.20	1154	8112	Normal moderate atrophy tumour*/ NN tumour
		S13 - S14.5	7.01	1323	12137	Near-normal/normal
3	32820R	S2 - S3.5	7.01	158	575	No glandular structures
		S6 - S7.5	11.60	381	1323	No glandular structures
		S10 - S11.5	11.50	569	2052	No glandular structures, normal
		S13 - S14.5	11.70	1114	5128	No glandular structures, normal
4	32926R	S2 - S3.5	3.03	8256	56535	Benign, atrophy, inflammatory cells (IC) / normal, stromal IC
		S6 - S7.5	4.93	6600	104482	Benign, atrophy, IC dense stroma / malignant, non-malignant
		S10 - S11.5	4.10	6351	69857	LGPIN, malignant lacuna/ HGPIN, dense stroma, atrophy
		S13 - S14.5	3.55	5322	65247	Malignant lacuna formation / non-malignant, LGPIN
5	32928R	S2 - S3.5	1.92	310	15776	Atrophy, near normal, folded
		S6 - S7.5	4.19	1268	15714	Normal, folded
		S10 - S11.5	4.97	1887	18570	Normal, folded, tumour cells, LGPIN with IC, folded
		S13 - S14.5	5.27	1734	15858	Atrophy, normal, folded / hyperplasia, HGPIN, tumour cells*,
6	32950R	S2 - S3.5	3.09	816	3728	LGPIN, normal, folded
		S6 - S7.5	5.12	880	3785	30% atrophy, normal, folded
		S10 - S11.5	6.60	2077	13888	Normal atrophy / HGPIN, tumour cells*
		S13 - S14.5	6.54	1931	16121	LGPIN, HGPIN, normal
7	33015R	S2 - S3.5	8.33	349	1536	Normal /atrophy*, normal
		S6 - S7.5	8.94	377	1796	Normal / LGPIN*, normal
		S10 - S11.5	8.82	267	932	Normal, folded / normal

		S13 - S14.5	8.81	279	1154	Normal, folded / normal with atrophy
8	33020L	S2 - S3.5	7.11	130	769	Normal with moderate atrophy
		S6 - S7.5	8.96	162	653	Normal
		S10 - S11.5	7.98	199	982	Normal, atrophy / normal
		S13 - S14.5	7.84	177	408	Normal
9	33042R	S2 - S3.5	7.42	51	145	Normal, folded / hyperplasia, processing effect
		S6 - S7.5	7.27	142	320	Tumour cells treatment effect, folded / folded [^]
		S10 - S11.5	4.04	136	488	Hyperplasia, malignant area (tumour cells) / folded [^]
		S13 - S14.5	3.84	123	468	Tumour cells, folded, hyperplasia
10	33036R	S2 - S3.5	10.70	153	775	Cancer cells*, normal
		S6 - S7.5	11.60	200	636	Normal / hyperplasia
		S10 - S11.5	11.50	312	1317	Tumour cells*, normal
		S13 - S14.5	9.20	583	4651	Normal / hyperplasia

Table 3.2. Pathological assessment of prostate depth profiling tissue sections. S2 and S 3.5 were collected for H&E staining, where ‘ - ’ indicates a gap of 50 μ m. S3.1, S7.1, S11.1 and 14.1 were collected for lipid imaging analysis on the MALDI HDMS SYNAPT Q-TOF. A summary of descriptive morphological features in prostate tissue annotated by Dr. Rajdeep Das, UCLA are collated. *denotes a pocket of tumour cells, atrophy. [^]marked sections were deemed unsuitable for pathological review. Section area denotes area of tissue section calculated in NanoZoomer. ImageJ threshold tool was used to estimate epithelial cells count in H&E images and total area corresponded to number of square pixels in analysed image. 30 μ m triplicate cryosections after S3.5, 7.5 and 14.5 were collected for lipidomics analysis in KU Leuven on the Nexera -API 6500 UPHLC-MS system.

Initial MALDI MSI experiments showed there was little signal in the higher molecular weight range from m/z 990 – 1990 in the first six patients analysed in the study. Consequently, subsequent analysis in four patients was restricted to m/z 50 – 990 (**Table 3.2**), which improved instrument sensitivity and enhanced lipid ion signal intensity as the quadrupoles were focused on monitoring ions at a smaller window. Visualisation of the data in HDI software (Waters Corporation, Manchester) showed that the PC headgroup m/z 184.07 was ubiquitous in $n=9$ patient samples, particularly abundantly in glandular areas of the tissue, but in $n=1$ patient (32820R) with sections generally composed of stroma, m/z 184.07 was barely detectable. This indicated that majority of PCs are largely distributed in epithelial areas of prostate tissue among them m/z 782.56 which was highly abundant and common to many samples. The detection of m/z 184.07 can be attributed to in-source fragmentation during the desorption/ionisation process. A representative example of key ions in the MS only spectrum is shown in **Figure 3.2**. Accordingly, these masses corresponded to putative fatty acyl chain loss m/z 577.57 and m/z 599.5, representing lipids tentatively identified as $\text{PC}(34:1)[\text{M}+\text{Na}]^+$ and $\text{PC}(36:4)[\text{M}+\text{H}]^+$, respectively, using LMSD consistently dominated the spectra. Moreover, these identities were confirmed subsequently by LC-ESI-MS/MS lipidomics and previous reports in literature show the same MALDI fragment ions of PCs^{103,181}.

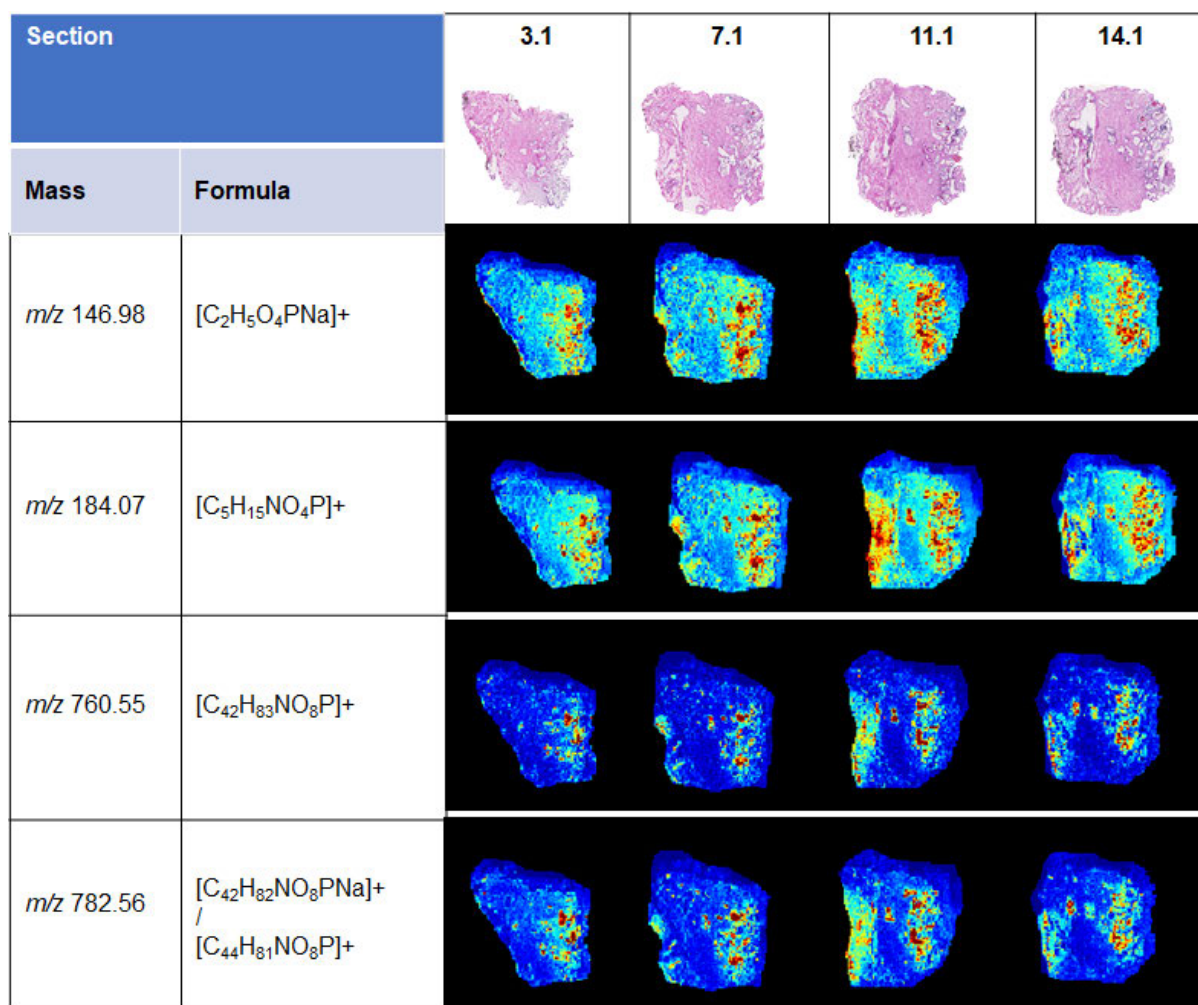


Figure 3.2. Representative example of PC headgroup in cohort. MALDI mass spectra of four interspersed sections from a single patient prostate core imaged in a single experiment. Data is normalised by total ion count (TIC) method.

An inspection of the (phospho)-lipid rich mass spectra was carried out by selection of pathological regions of interest (ROI) in adjacent imaged sections. The number of pixels (data points) was equivalent between the multiple annotated ROIs to check for differences in their relative abundance. Three representative examples are shown in **Figure 3.3**. These results suggest tissue-type specific alterations in lipid composition that accompany cellular and tumorigenic changes in prostate epithelium. Considering these observations, clustering analysis was performed to identify epithelial and stromal lipid ions.

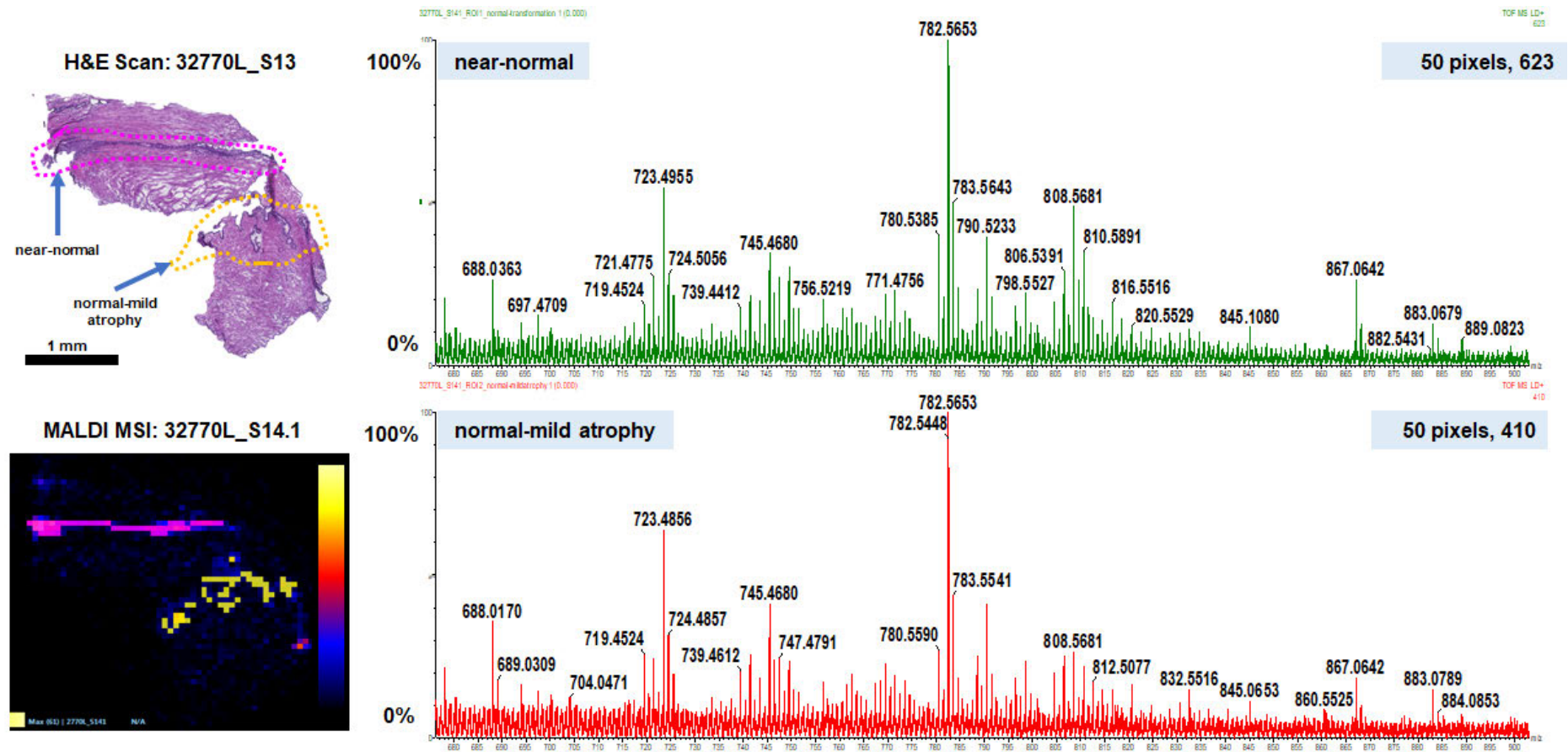


Figure 3.3A. Lipid mass spectra of multiple pathological regions. Comparison of spectra from pathology-guided ROI selection between near-normal epithelium (pink outline) and normal with mild atrophy (orange outline) within the same patient section. The sum of 50 pixels for each tissue type was taken to give the relative abundance.

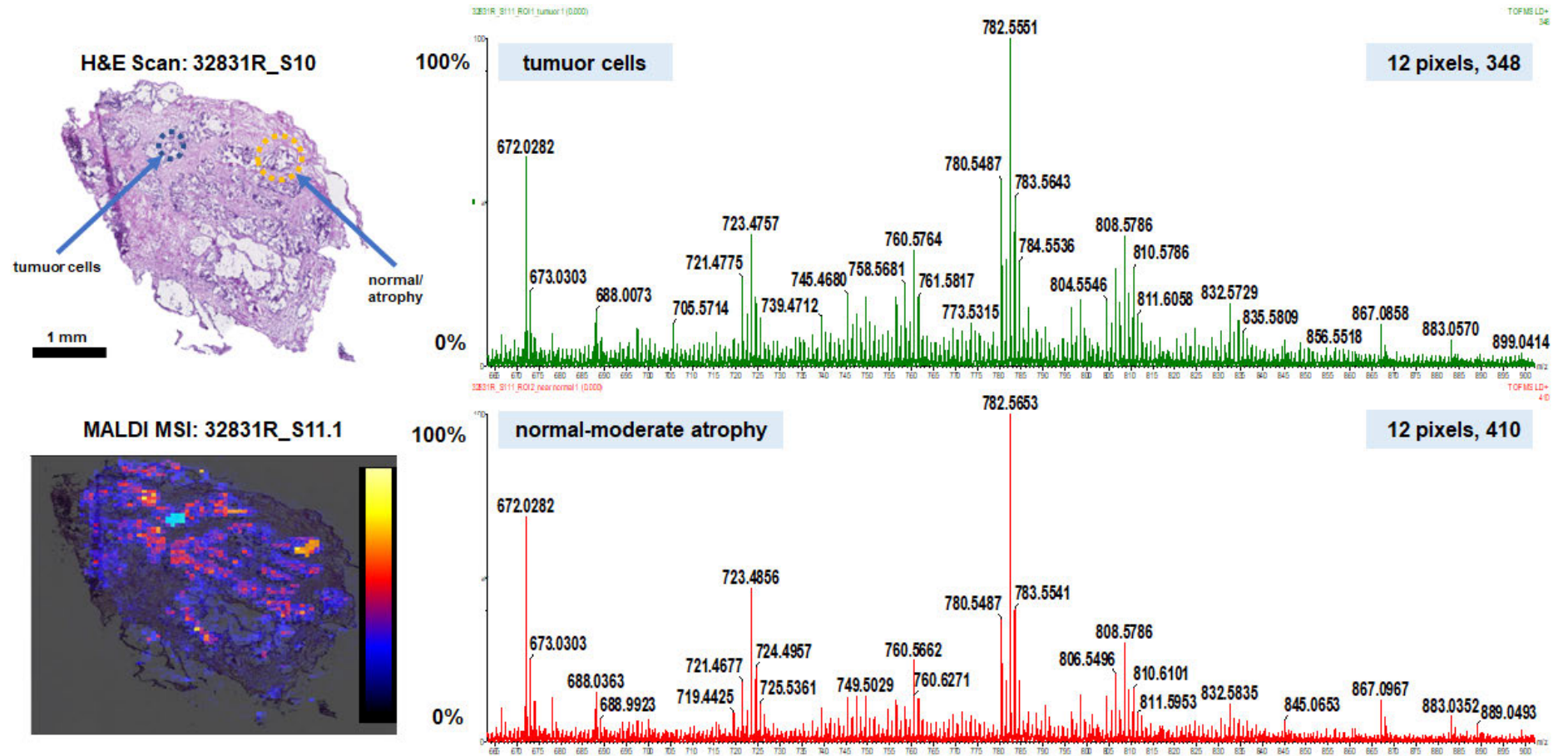


Figure 3.3B. Lipid mass spectra of multiple pathological regions. Comparison of spectra from pathology-guided ROI selection between tumour cells (blue circle) and normal with moderate atrophy (yellow circle) within the same patient section. The sum of 12 pixels for each tissue type was taken to give the relative abundance.

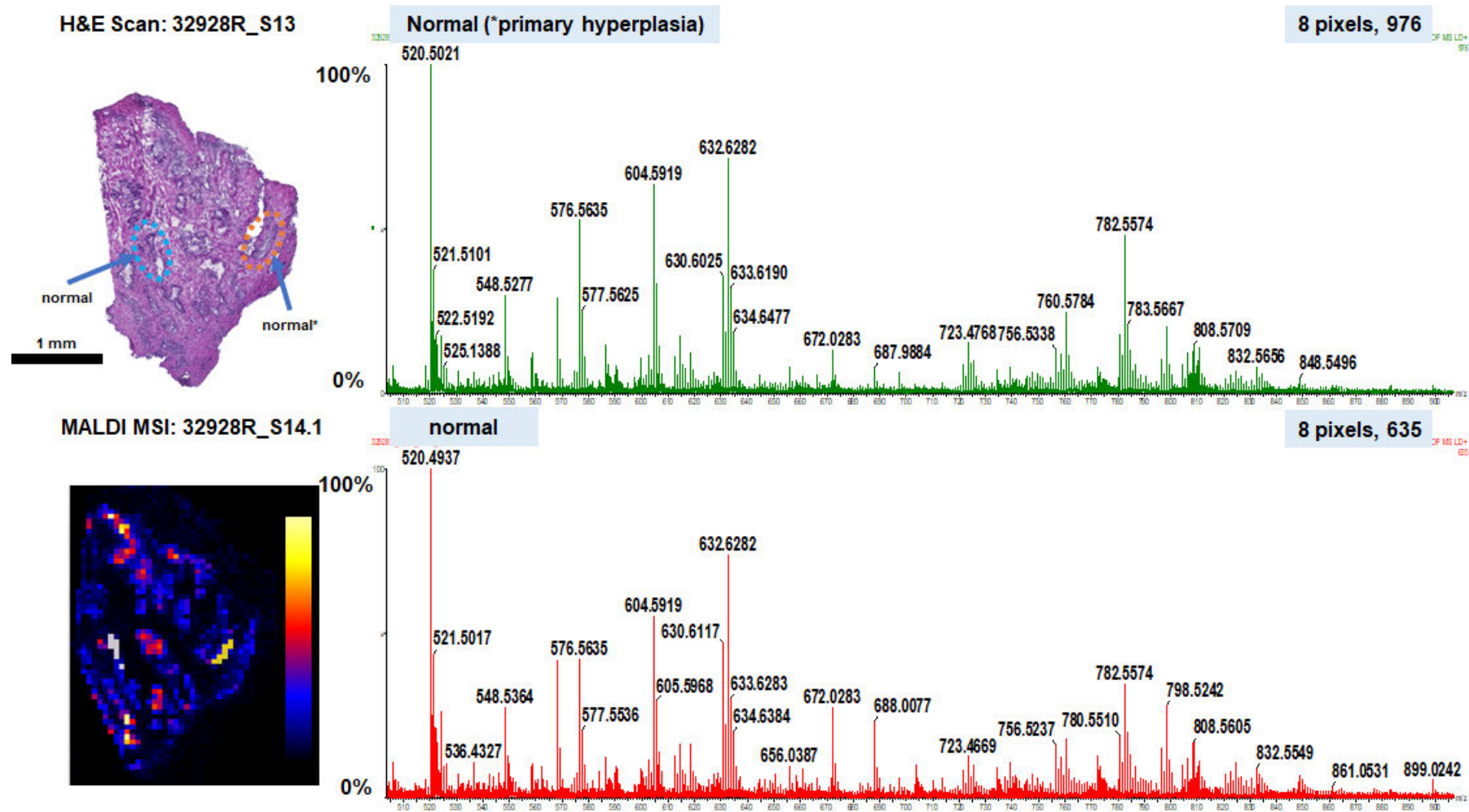


Figure 3.3C. Lipid mass spectra of multiple pathological regions. Comparison of spectra pathology-guided ROI selection between normal areas within the same patient section. Normal region in orange circle* progressed to primary hyperplasia in a serial section 30 μm away. The sum of 8 pixels for each tissue type was taken to give the relative abundance.

3.3.2. Relating Spatial Segmentation Analysis of MSI Data to Tissue Morphology

Subsequent data analysis focused on a narrower range of m/z range 400-990, chiefly to reduce computational times and cut off the noise detected at the lower mass range. In R *Cardinal*, four patient sets were imported and individually subjected for spatial segmentation by the SSCG algorithm. Patient 32928R serves as an example. Each cluster (segment) denotes a single type of tissue compartment or noise. Performing intra-patient analysis of each section/data set it would be expected that each respective cell/tissue type at each level would bear identically coloured clusters, but this was not always the case. However, by inter-patient analysis, combination of each individual patient data set after data importation as a merged multi-dimensional data array for downstream pre-processing, yielded more pathologically consistent segmentation maps. Clustering by this approach resulted in segmentation of identically coloured clusters across the four tissue levels as indicated in **Figure 3.5**. The top mass features by intra-patient analyses in the epithelia consistently picked the same masses with slight variations in peak parameters (centres and t-statistics) probably indicating differences in cellularity but which were comparable to the combined inter-patient segmentation as shown in **Table 3.3**. The code for creating **Figure 3.4** is shown in the [Appendix A](#) at the end of this thesis.

R Cardinal

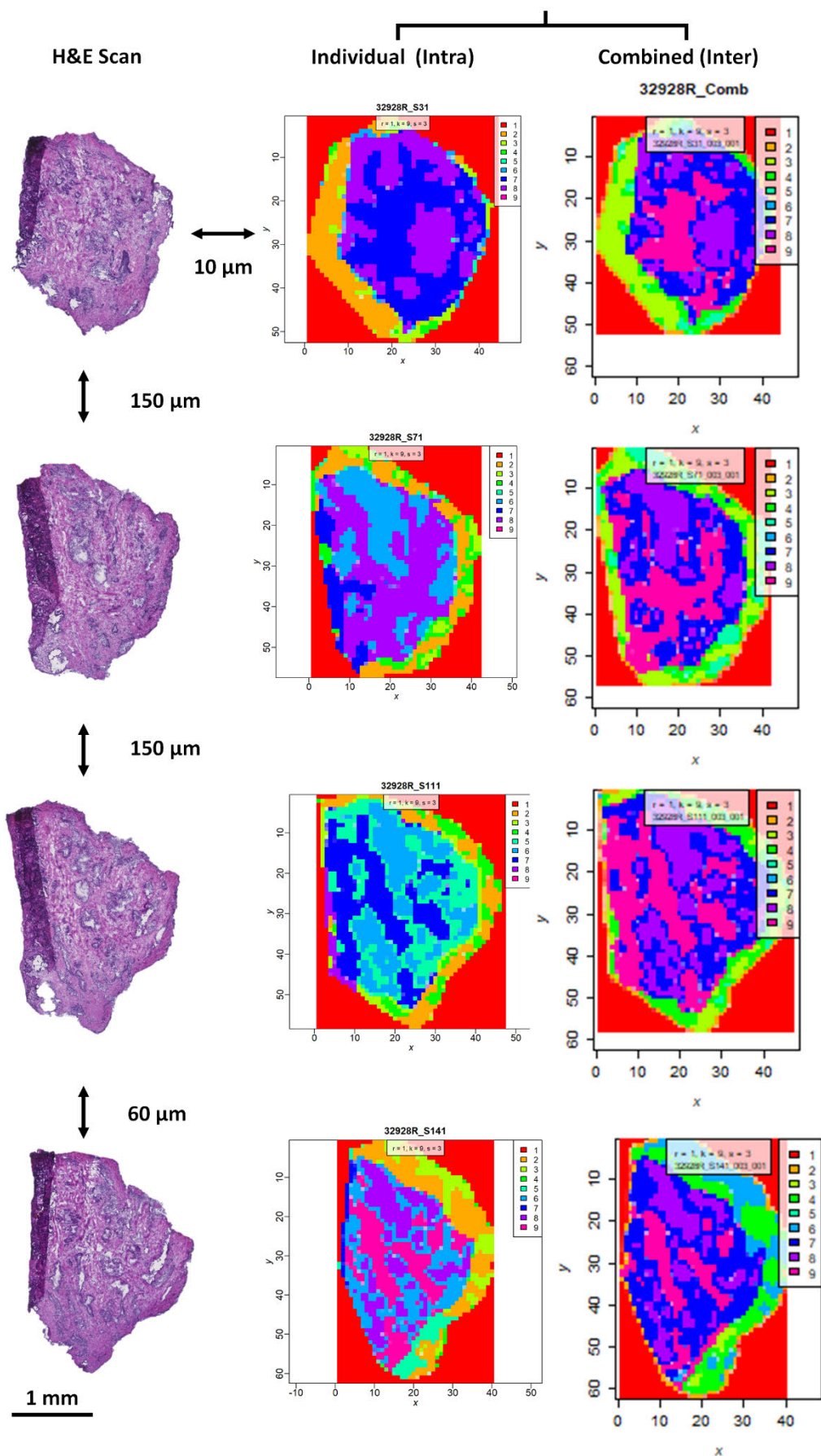


Figure 3.4. Comparison of segmentation analysis approaches. Four interspersed data sets were imported into R *Cardinal*. Intra-patient analysis of each separate section results in different coloured segments. Inter-patient analysis by combining each data set into a single intersected array shows identical coloured segments. Combined analysis shows dark blue is stroma, purple epithelium and pink is sub-stromal noise when matched to adjacent H&E scan.

	Epithelial cluster		<i>m/z</i>	centres	t-statistics
32928R_S31	Intra	K9c8	520.49	69.2	32.8
			632.63	40.2	32.5
			604.58	30.7	30.7
			630.62	29.9	29.8
			782.54	25.3	25.3
32928R_S71	Intra	K9c6	520.49	75.9	34.3
			632.60	43.0	34.8
			604.58	32.8	33.5
			782.54	24.1	32.4
32928R_S111	Intra	K9c6	520.49	78.0	32.9
			632.6	48.6	35.2
			604.58	37.7	34.5
			782.54	27.5	34.6
32928R_S141	Intra	K9c8	520.49	75.3	30.0
			632.60	48.9	34.3
			604.58	39.8	33.1
			576.56	29.3	32.6
			782.54	28.5	32.4
32928R_Combined	Inter	K9c8	520.49	78.7	58.9
			632.60	49.2	64.1
			604.58	38.9	63.6
			630.59	32.3	57.3
			782.54	30.2	66.7

Table 3.3. Clustering parameters in R *Cardinal*. Top five lipid ions in clusters corresponding to epithelial regions of tissue by intra-patient analysis and combined analysis from **Figure 3.5**. *k* denotes number of segmentation clusters and *c* is cluster number. Centres indicate number of peaks calculated for each ion's respective cluster membership. t-statistics is used to rank important mass features in the segmentation.

The top 20 m/z features were established for the epithelial and stromal clusters across the entire cohort. Cluster membership of ions was ranked based on t-statistics resulting in only the most informative m/z features. These provided a candidate list for subsequent lipid validation by MS/MS imaging. A list of the most important tentatively identified lipids is presented in [Table 3.4](#).

The inter-patient heterogeneity chemical profiles of the interspersed sections were compared using two different clustering algorithms in R *Cardinal* and SCiLS Lab. Essentially, these algorithms were tested for their ability to group the mass spectra into three main histological areas of interest: chemical matrix, epithelium and stroma as shown in **Figure 3.5**. SSCG made it possible to delineate distinct areas of the MSI data that corresponded with histopathological assessments of prostate tissue across all 10 patients in the sublimation cohort. It was able to yield segments that matched with biological areas of interest, namely the glandular (epithelial) and stromal regions of the tissue. Importantly, areas of tissue with predominant matrix ions were denoted in most cases as a single area on the outer edges of the MSI data indicating that they were off-tissue regions. SCiLS Lab was similarly capable of defining regions of data which matched with adjacent histological stained sections. The bisecting k-means segmentation patterns between the three-distance metrics (Correlation Distance, Euclidean and Manhattan) varied but were consistent with histopathological images ([Supplementary Figure 3.2](#)). The Manhattan metric was slightly better with deconvoluted segments corresponding well to tissue morphology (**Figure 3.5**). If cancer was present, the glandular compartments could be further segmented to reveal normal glands and tumour.

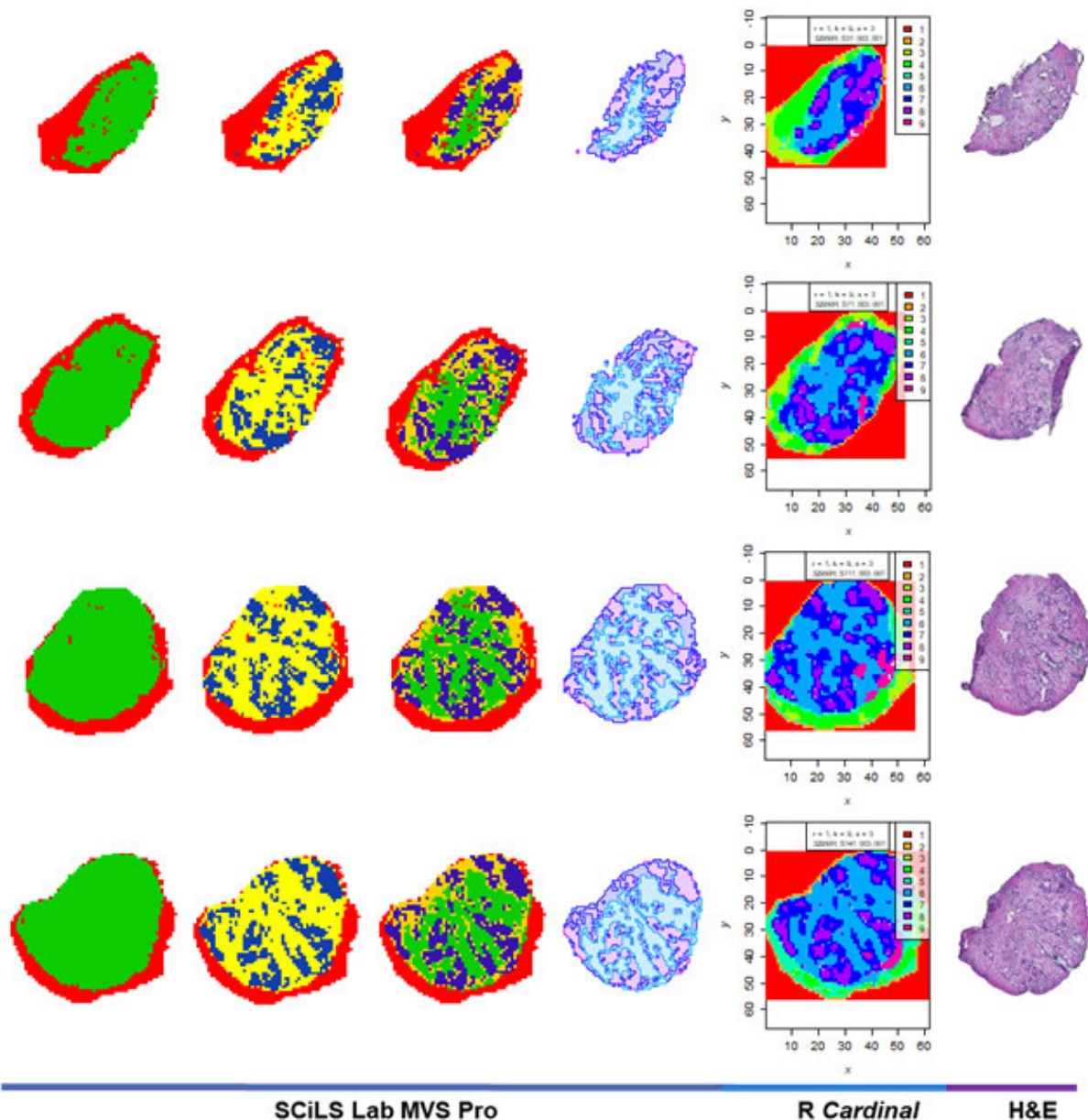


Figure 3.5. Comparison of molecular ion clustering analyses of prostate tissue with histopathology scans. Segmentation clustering using the bisecting k-means method using the Manhattan metric where the MSI files were split into coloured regions. Left panel, red depicts matrix ions and green main tissue area. The “main tissue area” further subdivides into yellow (stroma) and blue (epithelium) segments. Subdividing the “main stroma” area further, creates a green subregion, of mostly matrix ions and orange region (stroma) and blue region (epithelial tissue). The segmentation in SCiLS is highly comparable to SSCG method in R *Cardinal* and both correspond well to adjacent H&E morphology.

3.3.3. Component Analysis Reveals Lipid Signature of Prostate Epithelium

Next, component analyses using the PLSA method was performed using picked peaks as described in **Chapter 2 Materials and Methods [Section 2.2.7.3](#)**. The main advantage of application of pLSA in spatial analysis is the ability to factor in tissue heterogeneity – differences and population of cell types. PLSA components split the mass features into respective tissue compartments and the level of membership of a mass feature to a component is based on its maximum loading score of 1. This improved the association of an m/z value with either off-tissue regions or tissue segments (clusters), thus determining whether it is likely to represent an endogenous biomolecule. The naming of the PLSA components was histologically guided. This made it possible to check the molecular specificity of ions to their morphological regions. Epithelium and stromal components were readily discernible. The ratios for the respective components for each patient data set were then exported as .csv files imported and visualised in *R*. Epithelium and stromal components are shown in **Figure 3.6**. A common band is noticeable in the phospholipid range across the cohort except for two patients. 32820R sections had very little glandular structures being chiefly constituted of fibromuscular tissue whilst 32770L had a fainter band intensity owing to little epithelial cellularity.

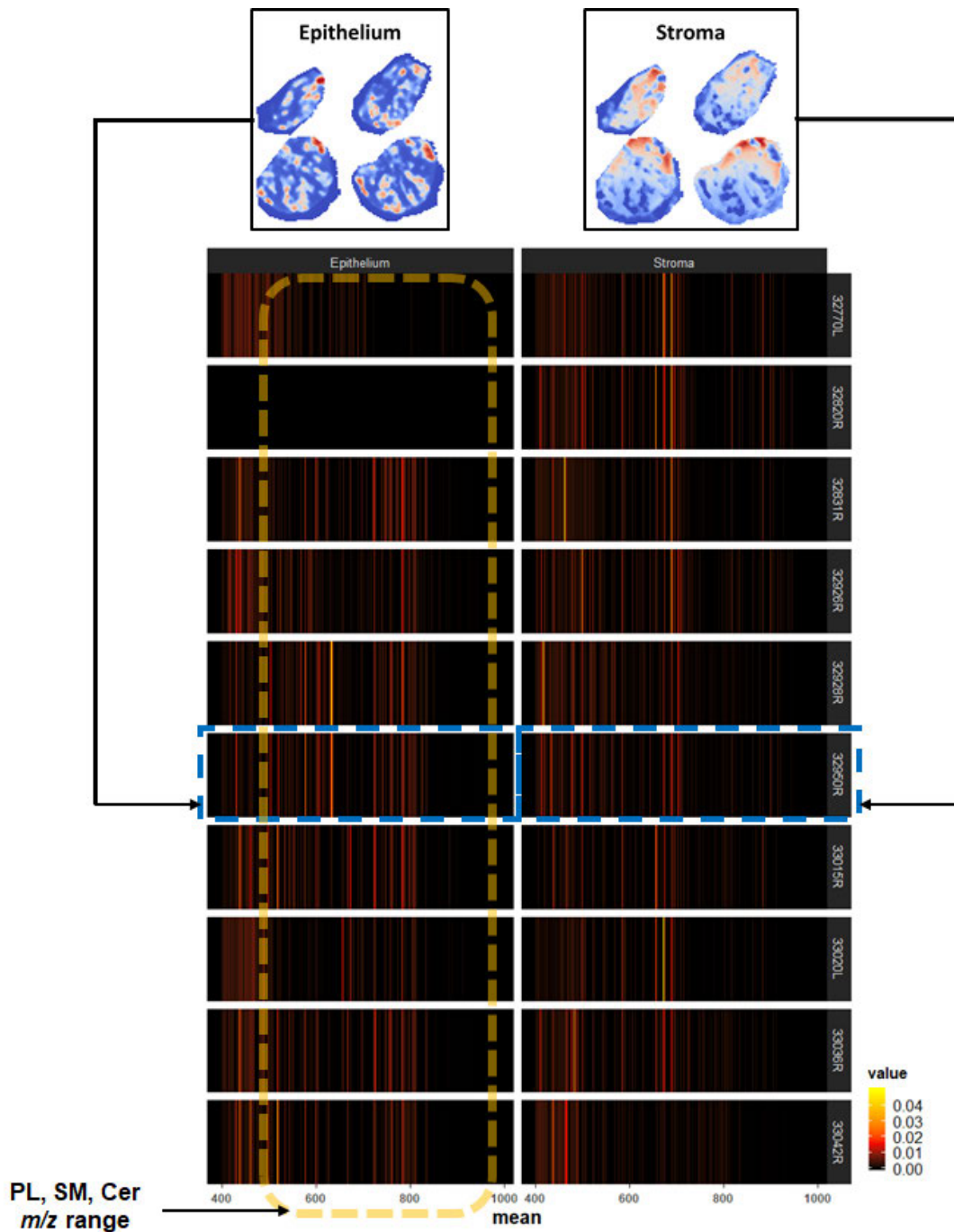


Figure 3.6. Lipid signature of clinical prostate tumours. PLSA loading scores of features based on their component membership are shown within the m/z 400 – 990 range. Appearance of characteristic band (highlighted in yellow) on the epithelium component compared to stromal component indicates presence of phospholipids (PL), sphingomyelin (SM) and Ceramide (Cer) species. The value on the intensity false colour scale indicates the contribution of each ion to a PLSA component for $n=10$ patients. Plot created using *ggrepel*, *reshape2* and *ggplot2* packages in *R*.

3.3.4. Validation of Lipid Species by MALDI MS/MS Imaging

Targeted lipid imaging was performed for the most predominant ions in the epithelial and stroma regions of tissue from the prior spatial segmentation in *R* Cardinal with the aim of establishing precursor ion structures and identity assignment to probable lipid subclasses. Ten separate epithelium-enriched lipid ions were selected for imaging in eight patients.

Validation of PC subclass was performed for six ions: *m/z* 782.56, *m/z* 808.55, *m/z* 780.53, *m/z* 806.54, *m/z* 760.55 and *m/z* 798.53. *m/z* 782.56 is an isomeric species of PC(34:1)[M+Na]⁺ and PC(36:4)[M+H]⁺ given the theoretical - observed fractional mass differences cannot be distinguished at the mass resolution of this instrument (resolving power of 8,000 full-width half maximum). This complexity is further exacerbated because *m/z* 760.55 is potentially PC(34:1)[M+H]⁺. The fragmentation behaviour of *m/z* 782.56 in six patients is exemplified in **Figure 3.7**. It is observable that two patients have differential distribution of protonated headgroup, *m/z* 184.07 and sodiated headgroup, *m/z* 146.98. Patient 32770L and 32820R had smaller glandular areas showing little abundance of the precursor and fragments. Patient 33015R with normal tissue had an enrichment of PC(34:1) compared to PC(36:4). By contrast, 32926R bearing multifocal tumours has an opposite distribution whereas 33020L appears to have an enrichment of PC(36:4) in epithelium with pronounced atrophy. Altogether, the spatial information suggests the identity of *m/z* 782.56 cannot be fully determined and the structural MS/MS fragments point to presence of both PC(34:1) and PC(36:4). This is further underpinned by the lipidomics analyses in **Section 3.3.5**.

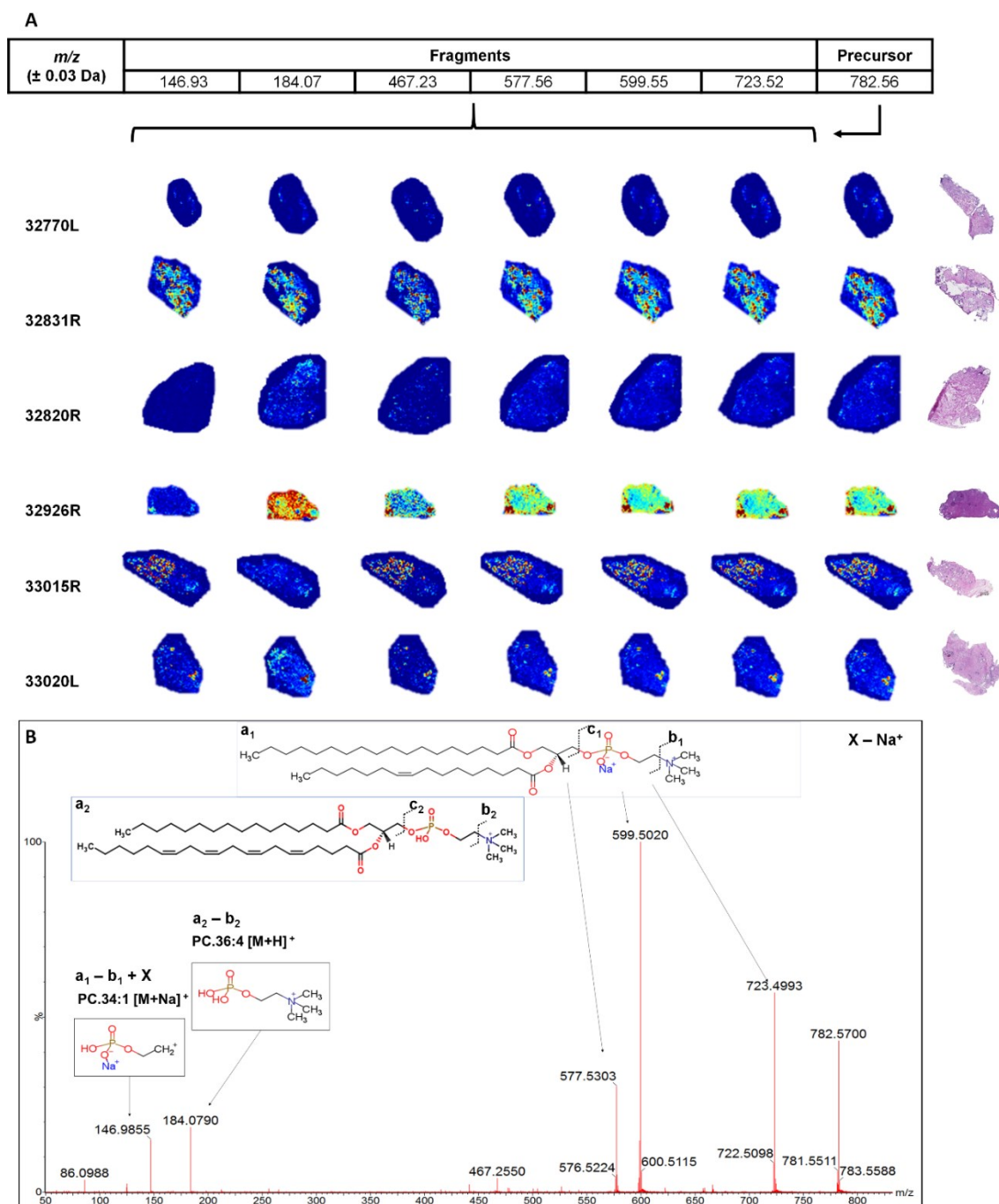


Figure 3.7. Validation of PC lipid species in epithelium by targeted imaging.
A. Combined MS/MS images of m/z 782.56 as a single processed object of $n=6$ patient MSI files. **B.** Spectrum of m/z 782.56 the tentative PC(34:1)[M+Na]⁺ or PC(36:4)[M+H]⁺ with the distribution of the fragment ions, including the characteristic m/z 184.07 [M+H]⁺ phosphorylcholine headgroup, shows the localisation of the lipid within the secretory glandular epithelium of prostate tissue.

Validation of the ceramide (Cer) subclass was conducted for four ions, m/z 520.49, m/z 604.58, m/z 632.60 and m/z 576.56. The fragmentation profile of m/z 520.49 is shown for two patients in **Figure 3.8**. m/z 520.49 was identified as Cer(d18:1/16:0) with a loss of water $[M+H-H_2O]^+$ using LMSD. This identity was further confirmed based on the characteristic m/z 264.27 fragment indicated in the Mass Bank of North America (MoNA) database. Consequently, an identical validation approach search of the other tentative Cer species indicated that they are related metabolites of m/z 520.49, with chain elongation at *N*-acyl moiety, detected as dehydrated and/or protonated adducts. m/z 576.56 was Cer(d18:1/20:0) $[M+H-H_2O]^+$, m/z 604.58 was Cer(d18:1/22:0) $[M+H-H_2O]^+$ whereas 632.60 was isobaric species Cer(d18:1/24:0) $[M+H-H_2O]^+$ or Cer(d18:1/24:1) $[M+H]^+$. Although, sodiated and some dehydrated adducts had formulas close to the calculated mass, these are less likely to be the observed species since they contain odd numbered saturated sphingoid bases and/or fatty acyl substituents.

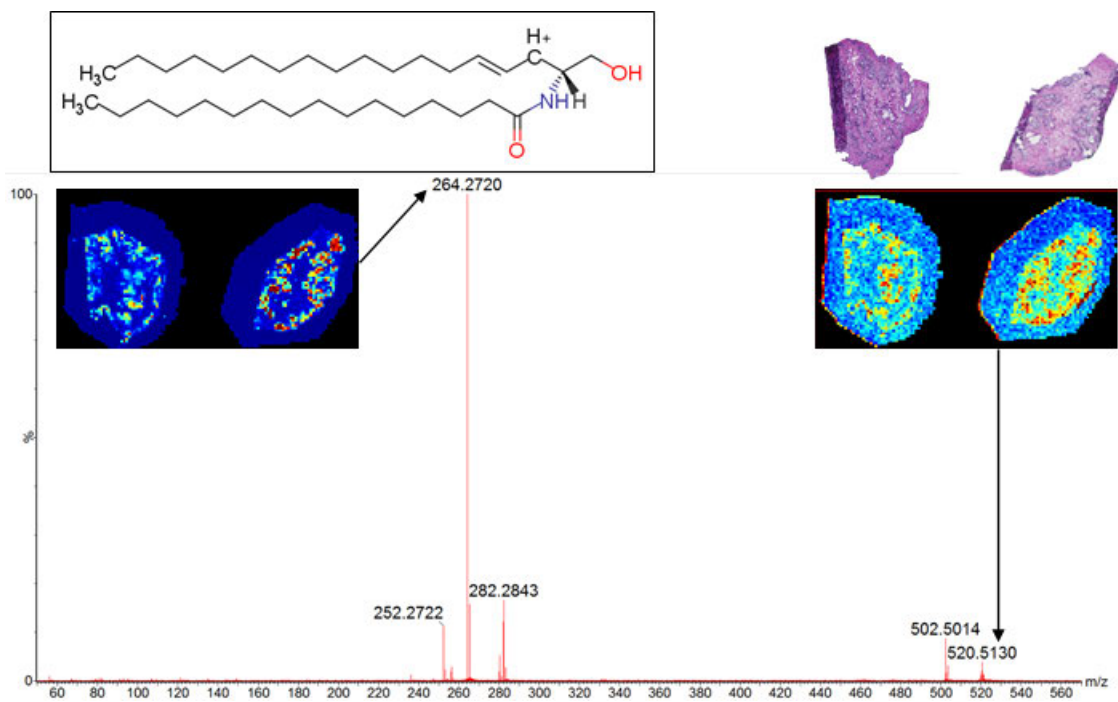


Figure 3.8. Validation of Cer lipid species in epithelium by targeted imaging. MS/MS imaging spectra of m/z 520.51 with a characteristic fragment ion m/z 264.27 had a matched exact mass for Cer(d18:1/16:0) [M+H-H₂O]⁺ in LMSD. CID bond breakage position not shown but species identity further confirmed in the MoNA database.

<https://mona.fiehnlab.ucdavis.edu/spectra/display/LipidBlast014209>.

To confirm the presence and identity of lipid ions predominant in the stroma as elucidated by SSCG segmentation, targeted lipid imaging was performed on two patients (33042R and 33036R). Establishment of precursor ion structures and assignment to probable lipid subclasses was done based tandem spectrum. m/z 756.55 (**Figure 3.9**), m/z 725.55 (**Figure 3.10**) and m/z 666.43 ([Supplementary Figure 3.3](#)) and were imaged in to create six lipid precursor ion images and associated single fragment ion maps. Based on the MS/MS imaging spectrum corroborated with LMSD and HMDB, m/z 756.55 was tentatively identified as PC(32:0)[M+Na]⁺ and m/z 725.55 is identified as SM(d34:1)[M+Na]⁺. m/z 666.46 appeared to an in source of fragment SM(d34:1)[M+Na]⁺. It is also possibly HexCer(d30:1). The spatial distribution of the dominant fragment ions m/z 697.47 and m/z 573.48 was also correlated which further reinforces that these fragments are indeed products of their selected precursors as plotted in [Supplementary Figure 3.4](#). However, given the varying distribution of protonated headgroup, m/z 184.07 and sodiated headgroup, m/z 146.98, represents a mixture of isobaric lipid species and its appears m/z 756.54 PC(32:0)[M+Na]⁺ is mainly abundant in the glandular epithelium (**Figure 3.9**). Contrarily, m/z 725.55 SM(d34:1)[M+Na]⁺ is quite evidently largely localised to the stroma (**Figure 3.10**).

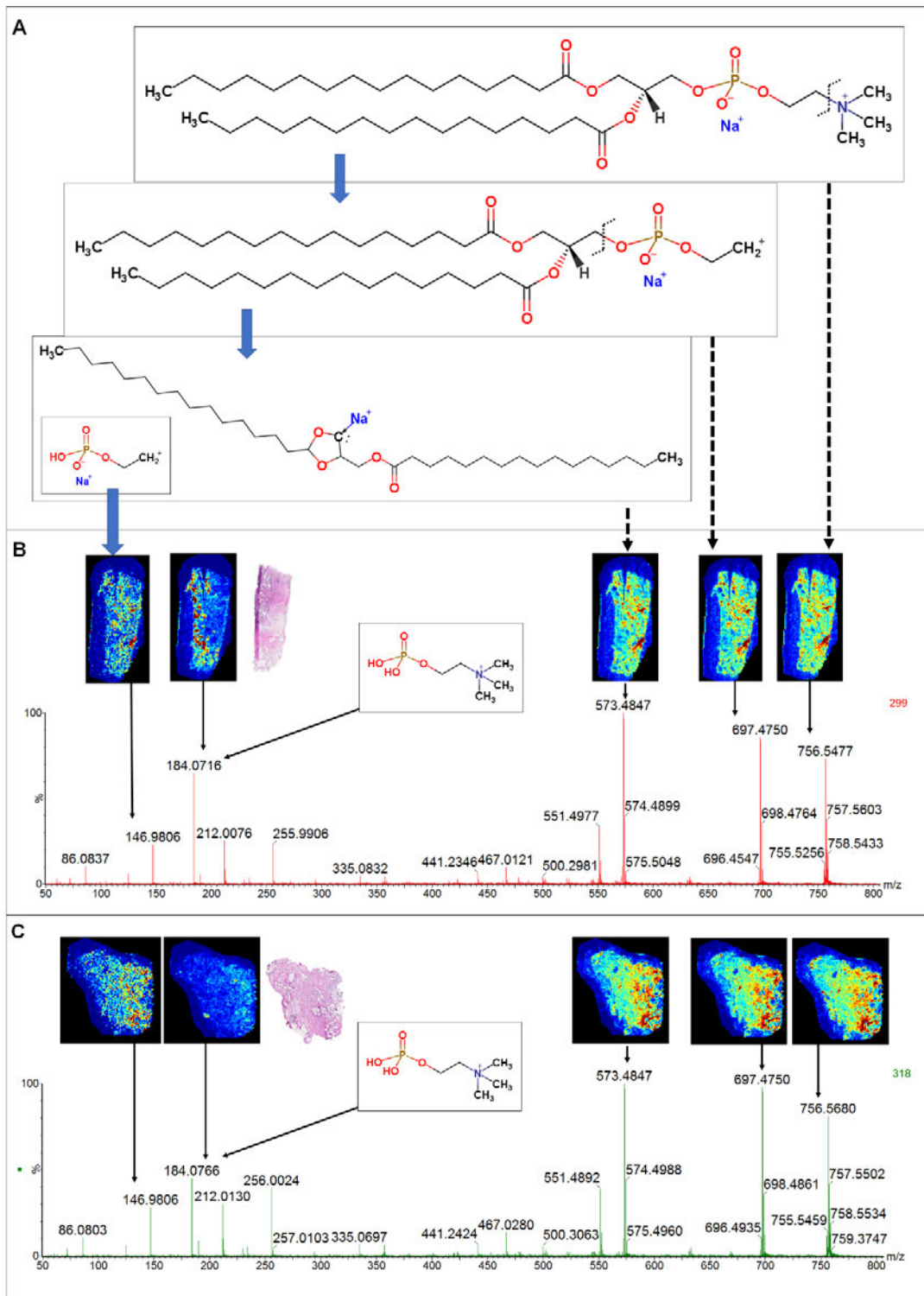


Figure 3.9. Validation of lipid ions in stromal regions of prostate tissue. A. Chemical structures **B.** MS/MS spectrum of PC(32:0)[M+Na]⁺ *m/z* 756.55 in patient 33042R shows co-localised distribution of predominant fragment ions *m/z* 697.47, *m/z* 573.47 and *m/z* 146.98. whereas *m/z* 184.07 indicates a phospholipid species outside stroma **C.** MS/MS spectrum of PC(32:0)[M+Na]⁺ *m/z* 756.55 in patient 33032R also bearing a similar spatial profile.

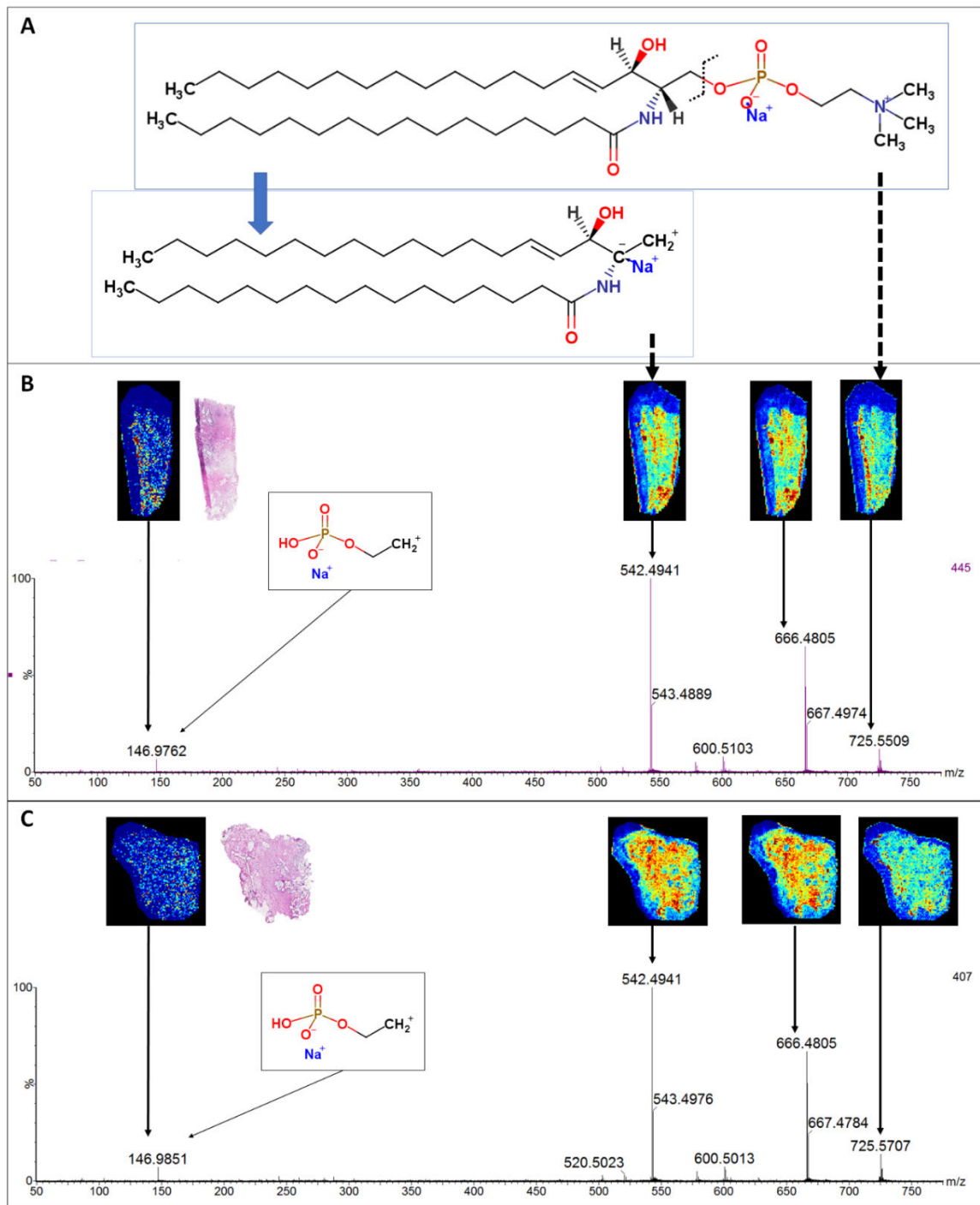


Figure 3.10. Validation of lipid ions in stromal regions of prostate tissue. A. Chemical structures. **B.** MS/MS spectrum of SM(d34:1)[M+Na]⁺ m/z 725.56 in patient 33042R shows co-localised distribution of predominant fragment ions m/z 697.47 and m/z 542.49 **C.** MS/MS spectrum of SM(d34:1)[M+Na]⁺ m/z 725.56 in patient 33036R also bearing a similar spatial profile.

3.3.5. Validation and Characterisation of Lipid Species in Prostate Tissue Homogenates by Conventional Lipidomics

LC-ESI-MS/MS lipidomics analyses was conducted on cryosections samples adjacent to the MALDI imaging samples from the same patient cohort. This resulted in multitude of lipid species being characterised in comparison to spatial lipidomics analysis. Importantly, it allowed further confidence in the annotation of the species analysed by the targeted MS/MS imaging. The PC, SM and Cer are highlighted herein as they are comparable with the positive ion mode MALDI MSI data. Three cryosections, individual slice being 30 μm thick, collected at three interspersed depths within the biopsy were pooled for lipid extraction. Analysis of the triplicate pooled samples showed variation of the PC, LPC, Cer and SM content within the block. The heatmap data is arranged according to increasing fatty acid composition complexity. The total DNA measurements of these samples is provided in [Supplementary Table 3.1](#). Since lipidomics analysis of the PC category encompassed virtually all possible acyl chain length compositions resulting in 203 different species, for simplicity the sum notation of the PC representative of 69 lipids is shown ([Supplementary Figure 3.5](#)).

Quantitative analysis of the fatty acid composition of the PC species is shown in **Figure 3.11** and **Figure 3.12**. m/z 734.56, PC(16:0/16:0)[M+H]⁺, m/z 760.56, PC(16:0/18:1)[M+H]⁺ or m/z 782.56 PC(16:0/18:1)[M+Na]⁺ and m/z 758.56, PC(16:0/18:2)[M+H]⁺ or m/z 780.55 PC(16:0/18:2)[M+Na]⁺ were the most abundant lipid species detected. Out of the 30 pooled samples across the 10-patient cohort, only patient sample 33042R_SGL_S8, had comparably much higher amounts of total lipids species. Interestingly the high total PC content matched with the pathological annotation of hyperplasia in that sample. Analysis

of the LPC lipids, showed that FA(16:0) was the most common. LPC(18:0) was also highly expressed together with MUFA substituent LPC(18:1) and PUFA substituent LPC(18:2). LPC(20:4) and LPC(20:1) were present at comparatively lower concentrations (**Figure 3.13**).

Quantitative analyses of Cer species are depicted in **Figure 3.14** and **Figure 3.15**. Two out of three samples for Patient 33036R and 32950R exhibited elevated levels of Cer consistent with their greater hyperplasia/tumour cells and PIN content, respectively as noted in **Table 3.2**. Interestingly, the highly expressed Cer species were different between these two patients as plotted in the heatmap (**Figure 3.15**). On the other hand, the rest of the samples in the cohort had lower Cer levels which can be possibly attributed to their predominantly benign status.

The quantitative examination of SM is summarised in **Figure 3.16** and **Figure 3.17**. The most abundant SM species detected in the tissue lipidomics was SM(d18:1/16:0) which makes the lipidomics data consistent with the imaging data on two accounts. First, a subset of SM appear to be abundant in stroma as normal constituents of muscular cells, given the elevated levels witnessed in 32820R_SGL_S4 and 32820R_SGL_15 which had greater proportion of stromal tissue compared to the other samples in the cohort as shown in the heatmap plot (**Figure 3.17**). Second, the same species were elevated as seen in 33042R_SGL_S15 which markedly was a smaller section with hyperplastic glands in comparison to others in the cohort.

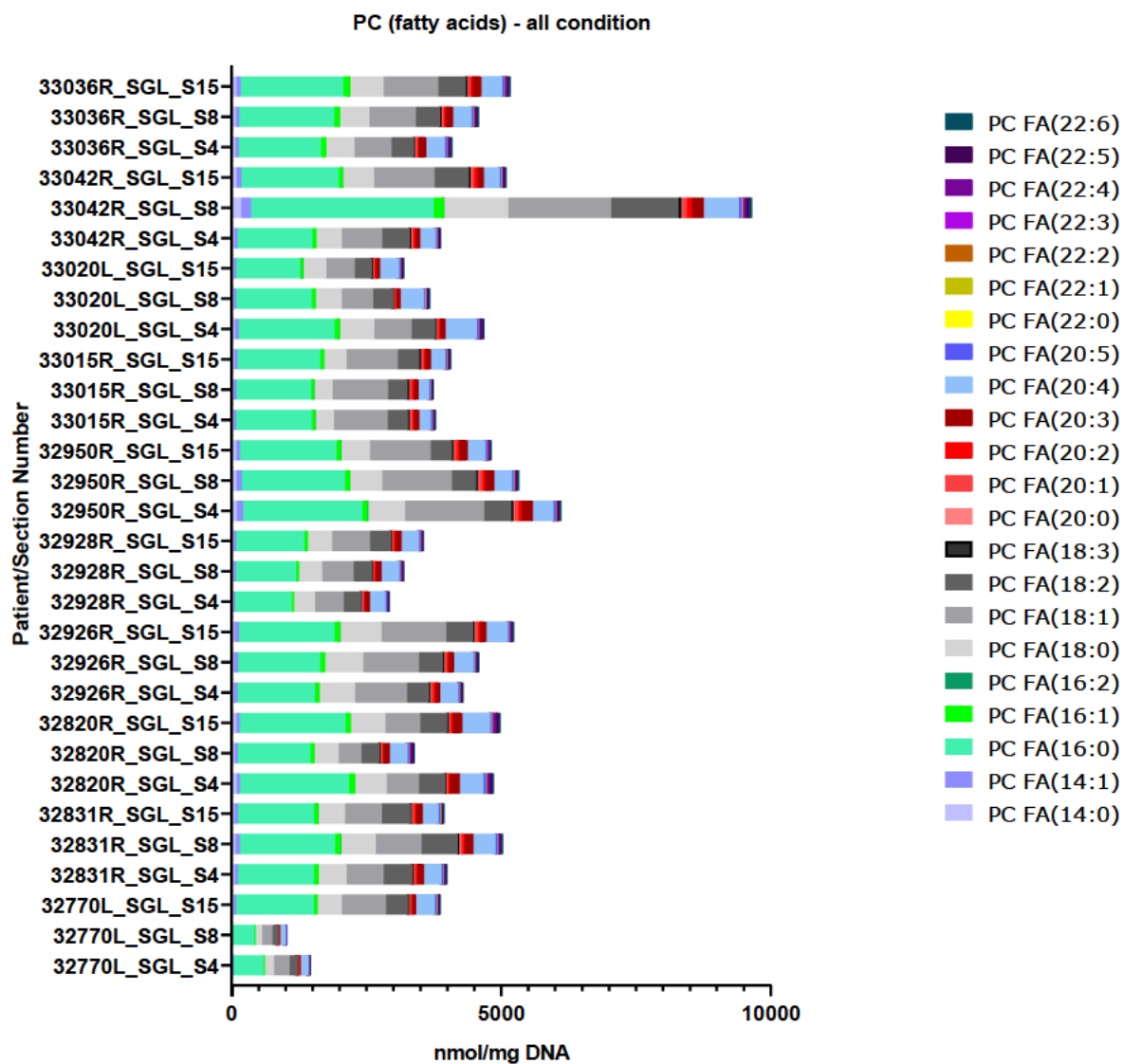


Figure 3.11. Quantification of fatty acid composition in PC in prostate tissue homogenates. 22 fatty acyl moieties were measured in 30 samples in n=10 patients (3 triplicates per sample). Measured lipid content is normalised to total DNA expressed as nmol/mg DNA.

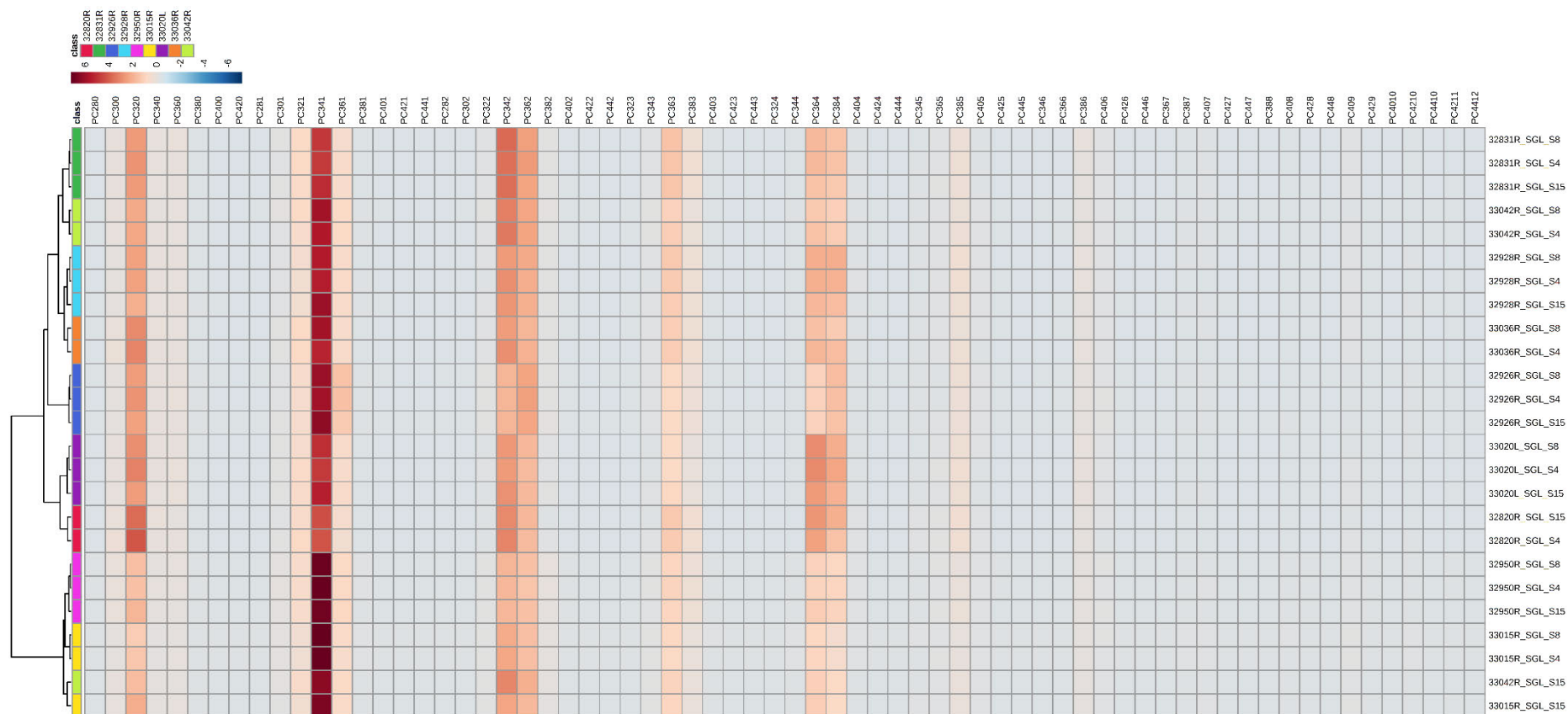


Figure 3.12. Quantification of PC lipids by sum notation in prostate tissue homogenates. 22 fatty acyl moieties were measured in 30 samples in n=10 patients (3 triplicates per sample) resulting in 69 PC species. Measured lipid content is normalised to total DNA expressed as nmol/mg DNA.

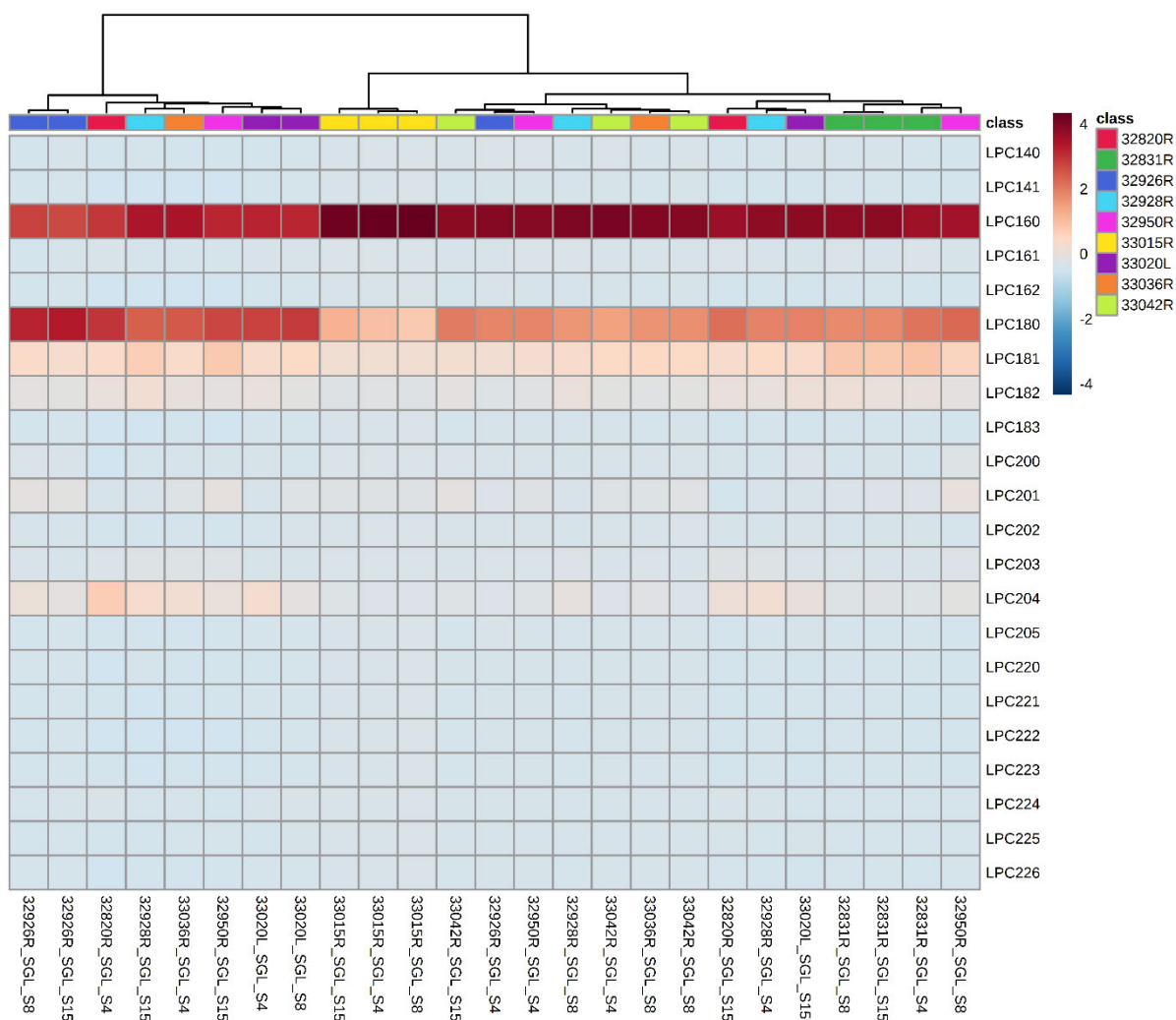


Figure 3.13. Quantification of LPC in prostate tissue homogenates. 22 fatty acyl moieties were measured in 30 samples in n=10 patients (3 triplicates per sample). Measured lipid content is normalised to total DNA expressed as nmol/mg DNA.

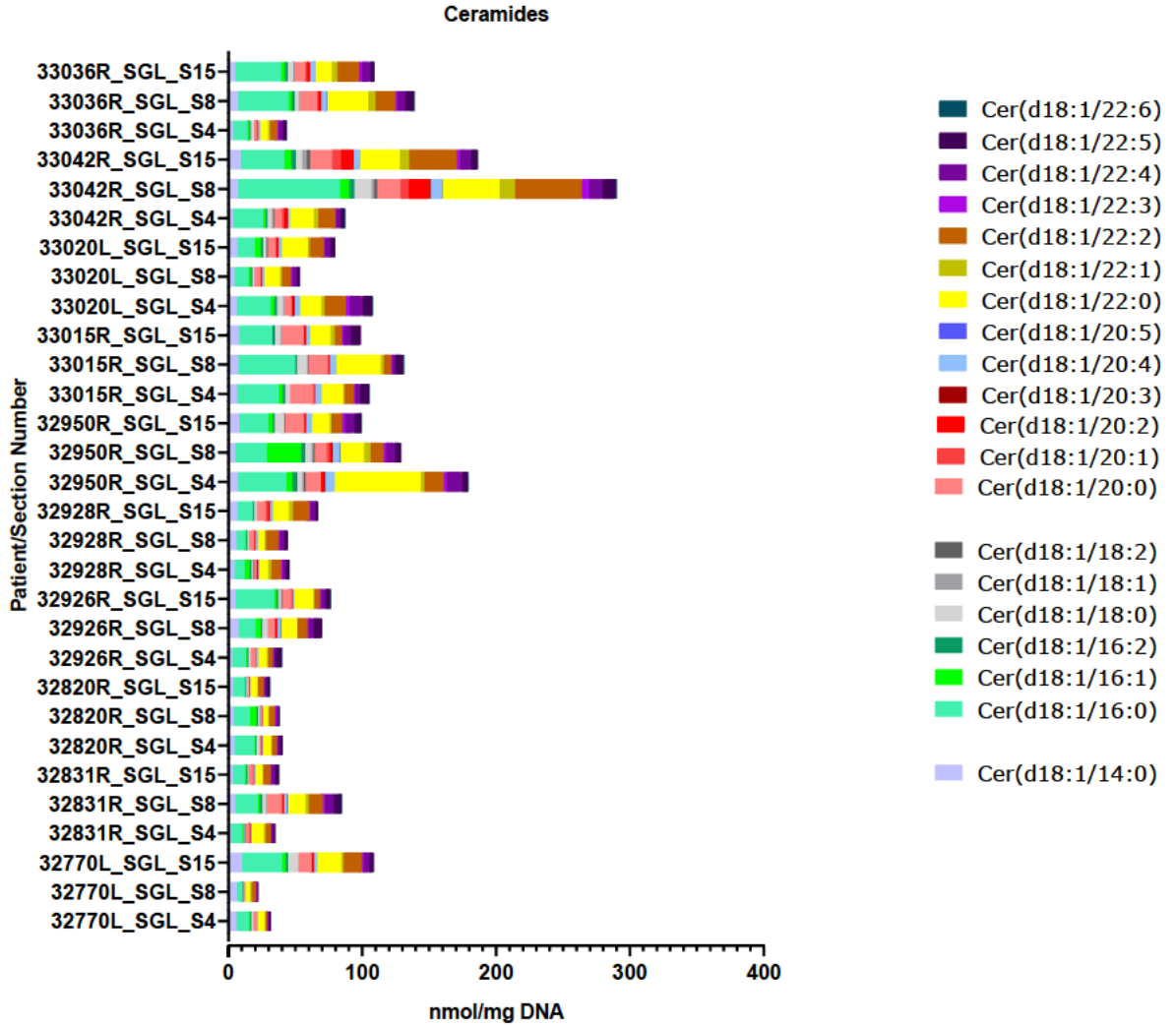


Figure 3.14. Quantification of Cer species in prostate tissue homogenates. *sn*-2 fatty acyl moieties of d18:1 unsubstituted sphingoid bases were measured in 30 samples in n=10 patients (3 triplicates per sample). Measured lipid content is normalised to total DNA expressed as nmol/mg DNA.

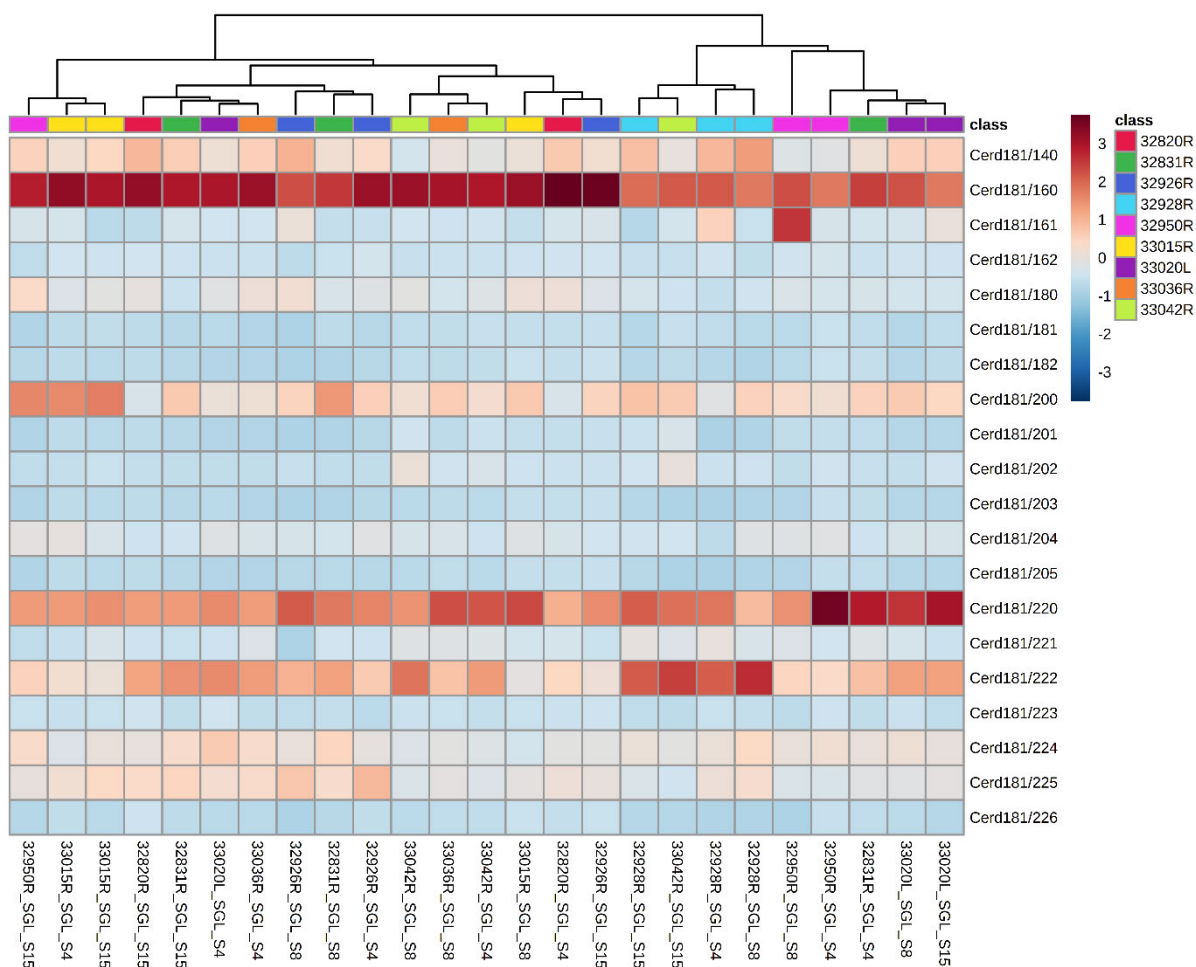


Figure 3.15. Quantification of Cer species in prostate tissue homogenates. *sn-2* fatty acyl moieties of d18:1 unsubstituted sphingoid bases were measured in 30 samples in n=10 patients (3 triplicates per sample). Measured lipid content is normalised to total DNA expressed as nmol/mg DNA.

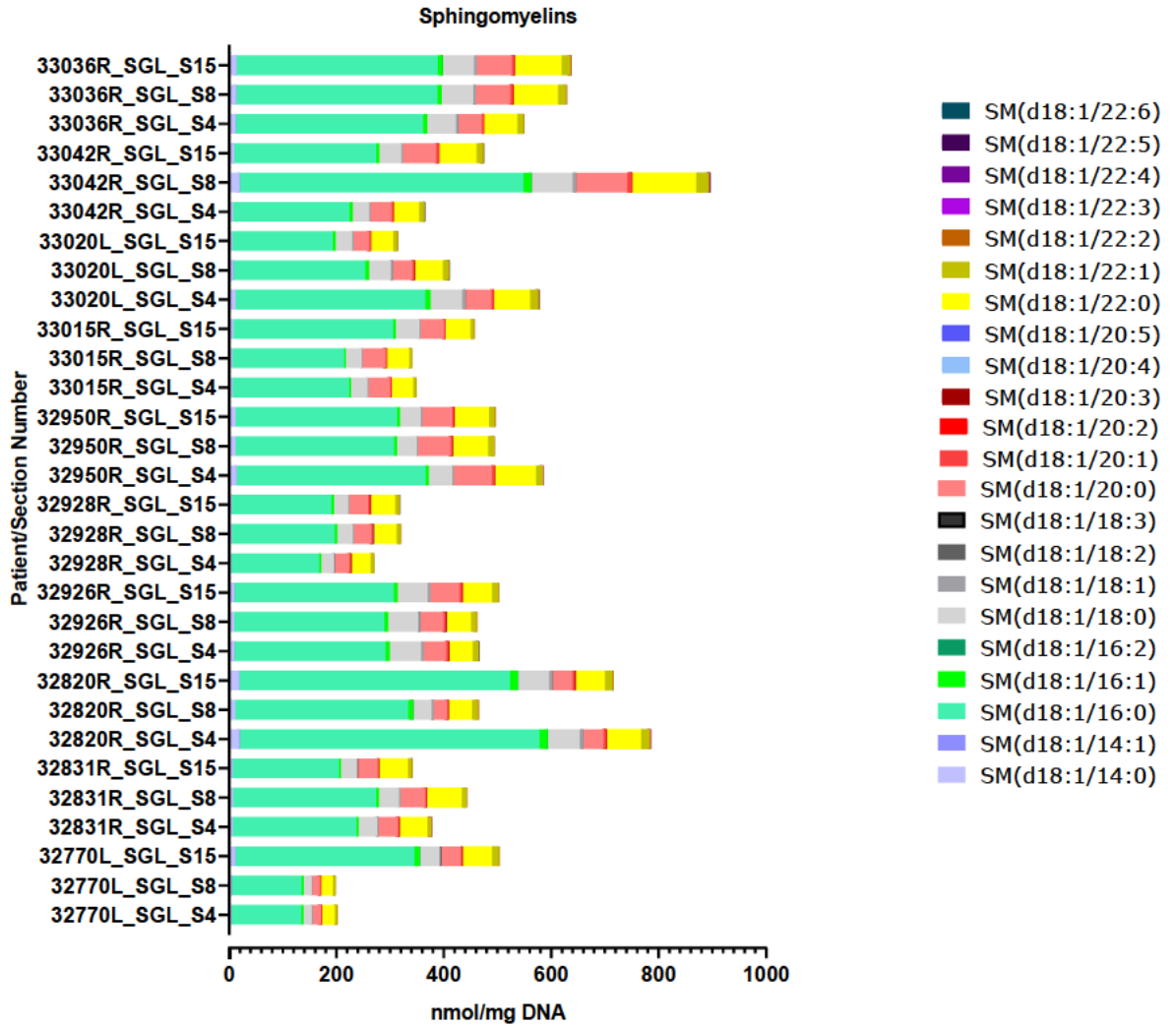


Figure 3.16. Quantification of SM species in prostate tissue homogenates. *sn*-2 fatty acyl moieties of d18:1 sphingoid bases were measured in 30 samples in n=10 patients (3 triplicates per sample). Measured lipid content is normalised to total DNA expressed as nmol/mg DNA.

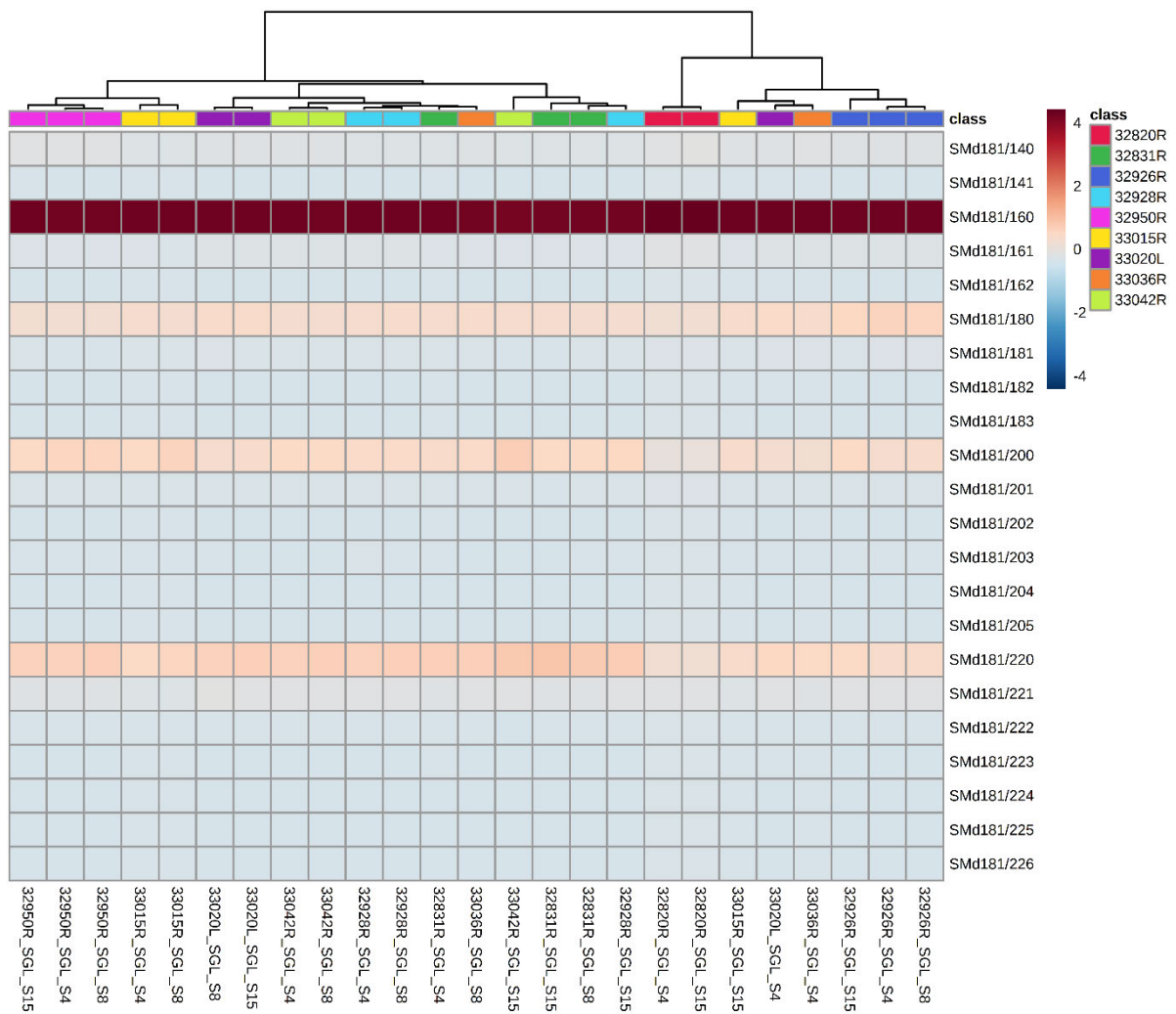


Figure 3.17. Quantification of SM species in prostate tissue homogenates. *sn*-2 fatty acyl moieties of d18:1 sphingoid bases were measured in 30 samples in n=10 patients (3 triplicates per sample). Measured lipid content is normalised to total DNA expressed as nmol/mg DNA.

Dimensionality reduction of the tissue homogenate lipidomics data was achieved by PCA and t-SNE. Analysis based on all the measured lipids species across all classes showed that ten samples separated from the rest of the cohort (n=30) as shown in **Figure 3.18**. In the context of the pathological annotation (**Table 3.2**), these samples exhibited morphological features towards cancer progression whereas the rest were benign or normal tissue. Consequently, ANOVA and hierarchical clustering analysis of the MALDI MSI data from individual patients was performed. Pathological ROIs corresponding to benign, LGPIN and malignant areas showed separation based on their lipid profiles in Patient 32926R as shown in **Figure 3.19**. Similarly, benign and malignant foci split according to their lipid composition in 33042R (**Figure 3.20**). Collectively, these data show that LPCs (m/z 518.31) are more predominant in benign tissue compared to malignant tissue. However, PC(16:0/18:1) did not appear to be enriched in benign epithelium of 32926R compared to 33042R.

The purpose of the conventional lipidomics was to support the identification of species from the MALDI MS/MS imaging. The prominent identified lipid species included two LPCs, four Cer, one SM and nine PCs as outlined in [Table 3.4](#). It is evident from the MALDI MSI data, lipid species with significant spatial intensity and commonly distributed across different patient samples were also reliably detected from the quantitative lipidomics analysis. An important difference is that conventional lipidomics achieved better lipid coverage and captured lowly abundant species compared to MALDI MSI, which however, offered precise location of pathology-related differences in lipid abundance. Overall, these results highlight both *in situ* and homogenate lipidomics analyses of prostate tissues can be used as highly complementary tools.

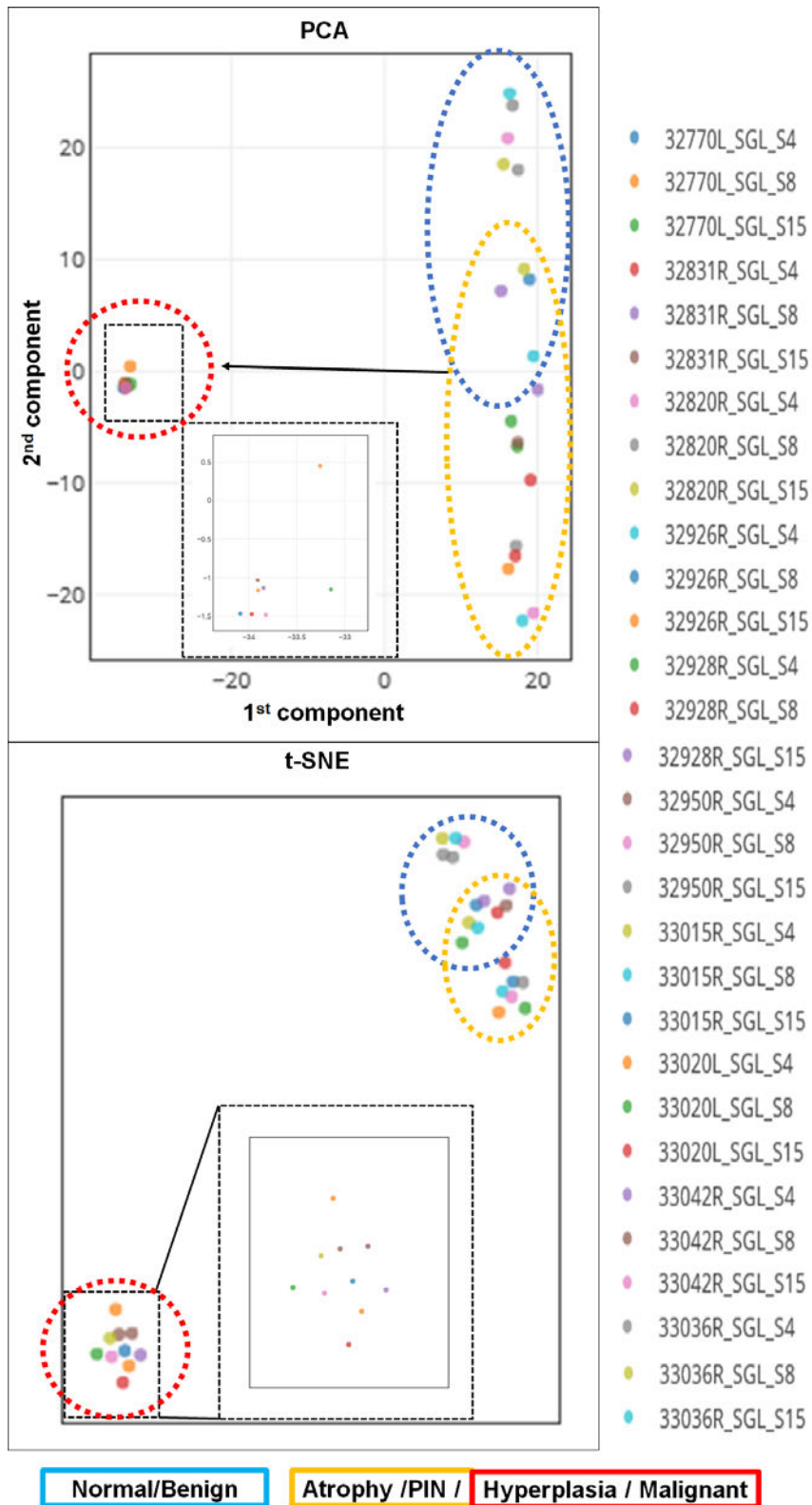


Figure 3.18. Dimensionality reduction of comprehensive lipidomics analyses. Top. PCA scatter plot. Bottom t-SNE plot. Separation of prostate tissue homogenate samples based on global lipidomics data is dependent on severity of PCa.

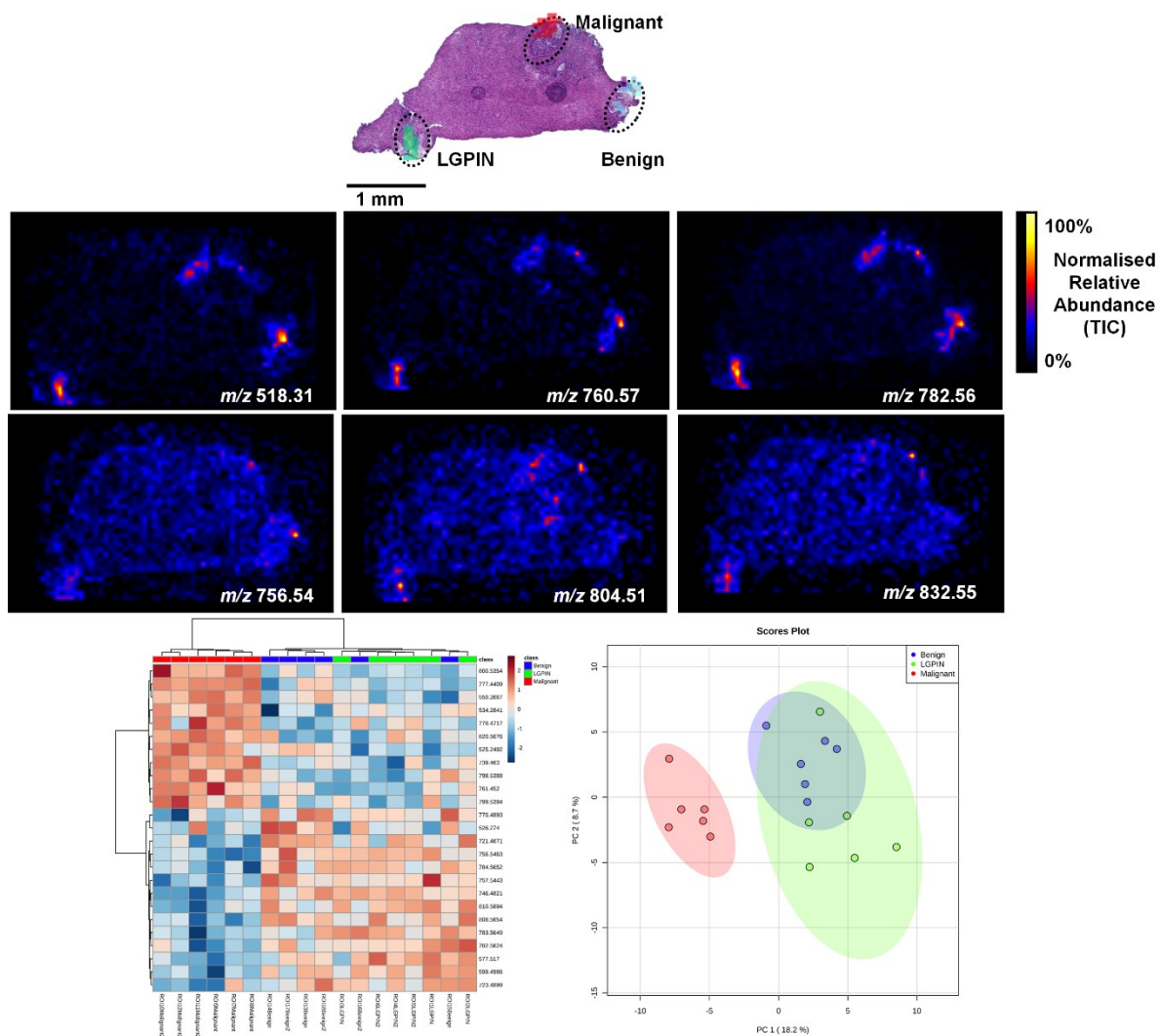


Figure 3.19. Lipid profile in multifocal prostate cancer – 32926R. Top panel. H&E scan showing benign, LGPIN and malignant regions. **Middle panel.** Maps of key ions from multivariate analysis. **Bottom panel.** Hierarchical clustering heatmap and PCA score plot for respective tissue types.

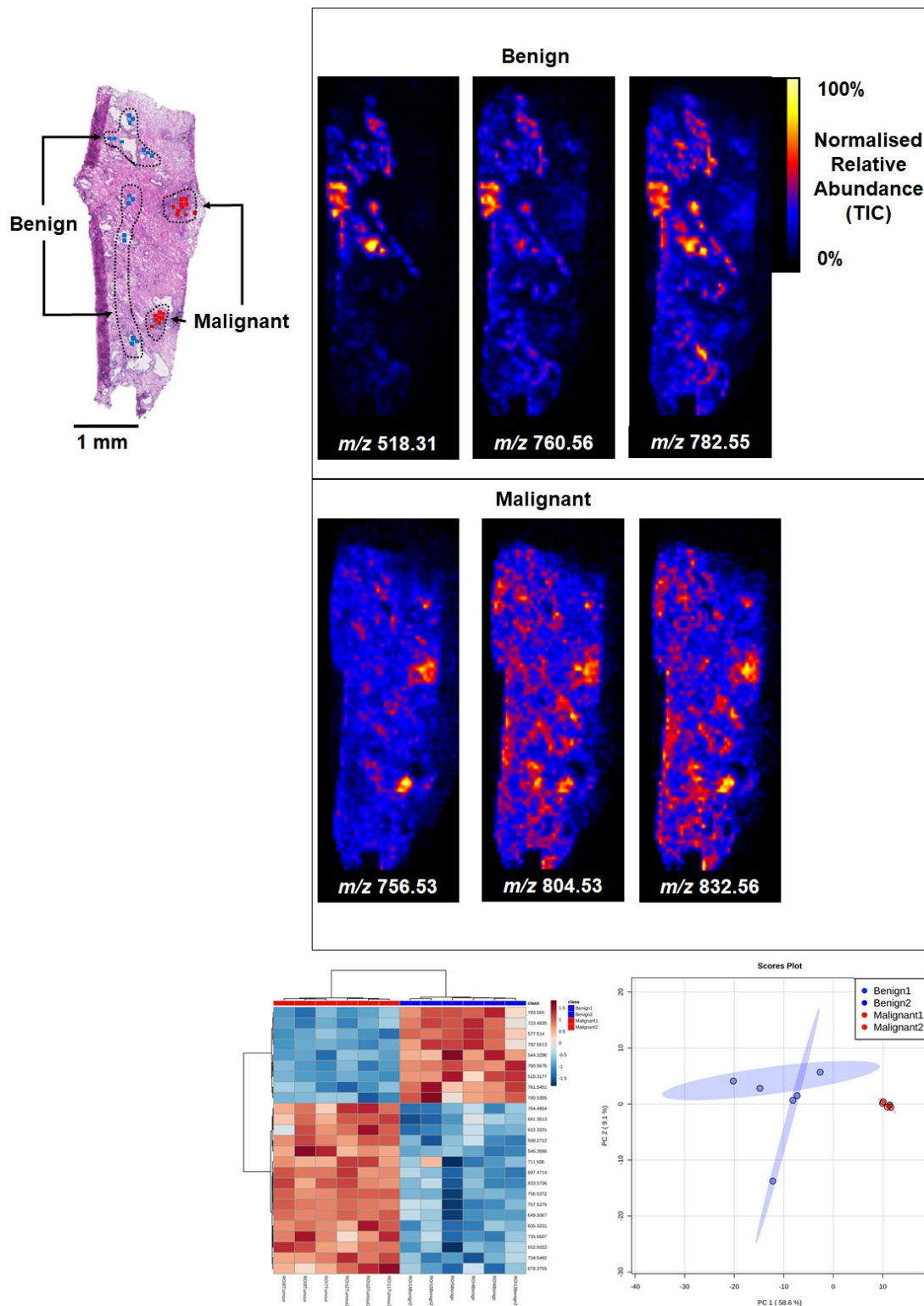


Figure 3.20. Lipid profile in multifocal prostate cancer – 33042R. Left panel. H&E image showing benign and malignant areas in which two groups of ROIs were subjected for analysis **Right panel** Shows maps of key ions found in benign tissue compared to tumour areas. **Bottom panel.** Hierarchical clustering heatmap and PCA score plot for respective tissue types.

Theoretical <i>m/z</i>	Observed <i>m/z</i>	Error PPM	MALDI Ion Species	MS/MS Validation	LC-ESI-MS/MS Identification
496.3398	496.3348	-10.07	[M+H] ⁺	Profiling	LPC(16:0)
504.3448	504.3379	-13.68	[M+H-H ₂ O] ⁺	Profiling	LPC(18:1)
518.3217	518.3181	-6.95	[M+Na] ⁺	–	LPC(16:0)
520.5088	520.5009	-15.18	[M+H-H ₂ O] ⁺	Imaging	Cer(d18:1/16:0)
576.5714	576.5656	-10.06	[M+H-H ₂ O] ⁺	Imaging	Cer(d18:1/20:0)
604.6027	604.5925	-16.87	[M+H-H ₂ O] ⁺	Imaging	Cer(d18:1/22:0)
632.6340	632.6347	1.11	[M+H-H ₂ O] ⁺	Imaging	*Cer(d18:1/24:0)
698.4731	698.4700	-4.44	[M+Na] ⁺	Imaging	PC(28:1)
725.5568	725.5514	-7.44	[M+Na] ⁺	Imaging	SM(d18:0/16:1)
754.5357	754.5351	-0.80	[M+Na] ⁺	Profiling	PC(32:1)
756.5514	756.5502	-1.59	[M+Na] ⁺	Imaging	PC(32:0)
760.5851	760.5726	-16.43	[M+H] ⁺	Imaging	PC(34:1)
780.5514	780.5422	-11.79	[M+Na] ⁺	Imaging	PC(34:2)
782.5670	782.5665	-0.64	[M+Na] ⁺	Imaging	PC(34:1)
798.5410	798.5406	-0.50	[M+K] ⁺	Imaging	PC(34:1)
804.5514	804.5313	-24.98	[M+Na] ⁺	Profiling	PC(36:4)
806.5670	806.5620	-6.20	[M+Na] ⁺	Imaging	PC(36:3)
808.5827	808.5776	-6.31	[M+Na] ⁺	Imaging	PC(36:2)
832.5827	832.5865	4.56	[M+Na] ⁺	Profiling	PC(38:4)

Table 3.4. Main list of tentatively identified lipids. Observed *m/z* indicate the average centroided mass spectra from selected whole patient MSI data sets compared against the theoretical monoisotopic *m/z* from a search hit on the LMSD. Mass error calculated as parts per million (ppm) expressed to 2 d.p. Lipid species validation was achieved by MS/MS imaging or target plate profiling using Folch extract of tissue homogenate mixed in equal amounts with 3.3 mg/ml CHCA matrix (methanol-water 1:1 (v/v)). *Mass transition not covered by method.

All other supplementary data for Chapter 3 is provided in [Appendix 1](#).

3.4. Discussion

In this Chapter, comprehensive analyses of patient prostate tissue sections by MALDI MSI, tandem MS/MS imaging and lipidomics analysis supplemented with pathological annotation revealed histology-related differences in the lipidomic landscape of prostate tissues. Cryosections from individual patients' biopsies were collected at four depths, to effectively describe heterogeneity in multiple tissue areas for each patient, locate small tumour regions within the core and gain insight into their lipid signatures. The positive ion mode MALDI data generated by sublimation of tissue sections with CHCA was primarily able to measure cations of PC, LPC, SM and Cer species. The most statistically enriched ions in the MALDI MS only data resulting from spatial segmentation analyses in *R Cardinal* were validated by MS/MS imaging. This was to gain structural insight and confirm the lipid species identity. Lipidomics analyses underpinned the identity of the observed lipid species and further reflected pathology-related changes in lipid profile, confirming that integration of spatial techniques with orthogonal approaches to lipid measurement enhances the amount and accuracy of information gained.

Initial exploratory analyses of the MALDI MSI data focused on assessment of various spatial segmentation methods to determine regions of spectral data with discrete chemical profiles and the most informative masses from these regions. Both *R Cardinal* and SCiLS Lab clustering algorithms achieved highly similar lipid m/z cluster regions which closely reflected the morphology of heterogeneous prostate tissues. Additionally, PLSA also provided another approach to investigate tissue heterogeneity ultimately resulting in clear representation of the lipid signature of the stroma and epithelium. The bisecting

k-means method in SCiLS Lab was found to be more practical compared to R Cardinal because of its user-friendly interface. Within the different bisecting k-means options, the Manhattan metric was superior in deconvolution of tissue segments in closeness to histopathological features of the sublimated cohort.

Within the phospholipid class, MALDI MSI analyses of the tissue primarily detected PC species, even though PE species can theoretically form cations. This is attributable to better ionisation efficiency of choline rather than ethanolamine because of differences in basicity of the head group¹⁰³ or affinity to react with other ions in the desorption plume¹⁸³, meaning they are better measured in negative ion mode. Moreover, as described in the introduction ([Chapter 1 Section 1.3](#)) PCs are present greater proportion than PEs (~45% vs ~25%) in cell and organelles membranes and therefore cause ion suppression of other lipids during laser desorption/ionisation process as observed in wider MALDI lipid imaging literature^{115,181}. Lipidomics analyses, on the other hand, were performed in negative ion mode as this results in better fragmentation efficiency to show fatty acid chain lengths and number of double bonds^{306,424}. Betancourt *et al* demonstrated separation of PC and PE cations via charge inversion by reacting with 1,4-phenylenedipropionic acid (PDPA) forming corresponding anions³¹⁷. Deciphering the MALDI *m/z* values with their MS/MS fragments and LC-ESI-MS/MS fatty acyl chain composition and degree of unsaturation information, the lipid identities were mostly resolved.

The phosphorylcholine headgroup fragment *m/z* 184.07 dominated the spectra from the lipid imaging indicative of PC, LPC and SM lipids. The detection of this fragment could be from in source decay which is common in MALDI with fairly “hot lasers”, such as the one present in the MALDI SYNAPT HDMS Q-TOF.

Another explanation for the rich spectral intensity of m/z 184.07, could be that it is a copious intracellular metabolite produced from constant flux activity of PC remodelling pathways, either from *de novo* synthesis via CDP-choline pathway or breakdown from phospholipase to yield DAG.

MALDI lipid imaging has been extensively used in numerous biological tissues, such as glioblastoma murine models^{257,425}, rat brain³³⁷ and breast cancer xenografts²⁸⁰. Phospholipid profiling is of great interest in solid tumour biomarker discovery and MALDI MS imaging approaches have been previously applied in lung and prostate cancer. Marien and colleagues showed that increased acyl chain elongation in PC, PE, PI and PS in clinical human squamous cell lung cancer was mediated by ELOVL6 using a combination of transcriptomics, ESI-MS/MS and MALDI imaging³⁰³. Goto *et al* identified twenty PL species to be enriched in prostate tissues including 14 LPI and PI, three PEs and three PAs with the most common fatty acid substituents being 16:0, 18:0, 18:1, 18:2, 20:2, 20:4 and 22:6²⁸³. In this study, PC(34:1) was prevalent in prostate tissue irrespective of disease condition. MALDI imaging data in a subset of patients with multifocal disease showed that m/z 518.318 LPC(16:0)[M+Na]⁺ was the most enriched species in benign and normal tissue. Oppositely, these spatial profiling results demonstrated m/z 756.53 PC(32:0)[M+Na]⁺, m/z 804.53 PC(36:4)[M+Na]⁺ and m/z 832.56 PC(38:4)[M+Na]⁺ were more abundant in tumours., From a structural standpoint it may be inferred from these findings, benign glands do not require as much PC content in comparison to tumourigenic glands with high cell membrane production and cell proliferations needs. It has been posited that cancer cells exhibiting increased *de novo* lipogenesis produce

saturated phospholipids which promotes membrane rigidity and these saturated membranes withstand chemotherapy induced oxidative stress⁴²⁶.

Physiologically, SM have been reported to constitute myelin sheaths of nerve cells and to be rich in cellular membranes. SM synthesis is precisely regulated and disturbances in its metabolism may impact normal physiological function⁴²⁷. Sphingomyelin synthase 1/2 enzymes are involved in maintenance of lipid equilibrium, in that they mediate the reversible condensation of PC and Cer to yield SM and DAG⁴²⁷. Cer serve key functions as pro-apoptotic second messengers in response to cancer initiation³⁷⁰. MALDI imaging showed that SM(d18:1/16:0) was largely localised in the stroma whilst a host of elongated Cer species (d18:1/16:0-18:0-20:0-24:0) were mapped to glandular epithelium. Abundance of SM expression was more consistent across all the patient samples with most abundant species, SM(d18:1/16:0), previously linked to the cellular apoptotic pathway in HMDB. This makes sense given that patient 33042R tissue had more advanced pathological tumorigenic phenotypes compared to the rest of the cohort, had the highest levels of SM(d18:1/16:0). Contrastingly, across the patient cohort, Cer species amounts were more heterogenous. This diversity in lipid profile is likely indicative of complex metabolic roles of Cer in prostate disease progression. Whether Cer expression is higher during onset of neoplastic activity is not fully conclusive from these data.

In conclusion, assessment of different clustering approaches of MSI data identified bisecting k-means method (Manhattan metric) as the most effective spatial segmentation tool for analysis of lipid *m/z* features of prostate tissues generated on a Waters MALDI SYNAPT HDMS. Consequently, this approach was preferred and is presented in the subsequent study in **Chapter 4**. PLSA

analyses described components of the main tissue types consistent with the spatial segmentation and could potentially be useful in revealing the tumour microenvironment in a cohort with high grade Gleason tumours. MALDI MSI uncovered tissue/cell-type specific lipid species with conventional lipidomics applied to confirm their identities.

CHAPTER 4:

MALDI MSI of Clinical Prostate Tissues Reveal Cell Type Specific Lipid Compositions

Context

This Chapter describes MALDI MS imaging data acquired using an alternative matrix deposition technology. To maximise on the powerful *in situ* capability of MALDI MSI, an automated spray coating protocol was subsequently developed and applied. The details of the experimental optimisation of the automated spray coating method is included at the end of this thesis in [Appendix B](#). This new approach enabled the detection of various lipid classes with markedly improved sensitivity to ultimately enable more robust analyses of the lipidomic composition of prostate tissue. The coverage of lipid classes was similar between sublimation and automated spray coating of CHCA matrix for positive ion mode MSI on the Waters MALDI SYNAPT HDMS. Another advantage was reproducibility of MALDI MSI data generation, meaning that multiple data sets from different patients could be combined without loss of data quality.

Statement of Authorship

Title of Paper	MALDI MSI of Lipids in Clinical Prostate Tumours Reveals Cell-Type Specific Lipid Compositions
Publication Status	<input type="checkbox"/> Published <input type="checkbox"/> Accepted for Publication <input type="checkbox"/> Submitted for Publication <input checked="" type="checkbox"/> Unpublished and Unsubmitted work written in manuscript style
Publication Details	Manuscript in preparation and planned for imminent submission to an invited collection at <i>Frontiers Endocrinology (Spatial Intracrinology)</i>

Principal Author

Name of Principal Author (Candidate)	Shadrack Mulinge Mutuku		
Contribution to the Paper	Research design Generation of data (tissue sectioning, lipid imaging MS data and validation) Performed data analysis and interpretation (spatial segmentation and unsupervised models) Development, writing and editing of manuscript		
Overall percentage (%)	70%		
Certification:	This paper reports on original research I conducted during the period of my Higher Degree by Research candidature and is not subject to any obligations or contractual agreements with a third party that would constrain its inclusion in this thesis. I am the primary author of this paper.		
Signature		Date	10 Jun 2020

Co-Author Contributions

By signing the Statement of Authorship, each author certifies that:

- i. the candidate's stated contribution to the publication is accurate (as detailed above);
- ii. permission is granted for the candidate to include the publication in the thesis; and
- iii. the sum of all co-author contributions is equal to 100% less the candidate's stated contribution.

Name of Co-Author	Paul J. Trim		
Contribution to the Paper	Supervised the research work, analysis and interpretation of data, writing and editing of manuscript		
Signature		Date	12/06/2020

Name of Co-Author	Rajdeep Das		
Contribution to the Paper	Analysis and interpretation of data (pathological expertise)		
Signature		Date	07/15/2020

Please cut and paste additional co-author panels here as required.

July

Name of Co-Author	John Salamon		
Contribution to the Paper	Data analysis and supervised statistical modelling		
Signature		Date	10/6/2020

Name of Co-Author	Jessica M. Logan		
Contribution to the Paper	Provided technical input on experimental design (immunohistochemistry)		
Signature		Date	10.06.2020

Name of Co-Author	Douglas A. Brooks		
Contribution to the Paper	Provided technical input on experimental design (immunohistochemistry)		
Signature		Date	10.06.2020

Name of Co-Author	Jonas Dehairs		
Contribution to the Paper	Performed experiments (lipidomics), Data analysis and interpretation		
Signature		Date	10/06/2020

Name of Co-Author	Johannes V. Swinnen		
Contribution to the Paper	Editing and critical review of manuscript Grant project funding		
Signature		Date	22/06/2020

Name of Co-Author	David J. Lynn		
Contribution to the Paper	Data analysis and interpretation		
Signature		Date	10/6/2020

Name of Co-Author	Marten F. Snel		
Contribution to the Paper	Supervised the research work, interpretation of data, writing and editing of manuscript		

Name of Co-Author	Lisa M. Butler		
Contribution to the Paper	Conceptualization of study, experimental design, supervised the research, interpretation of data, writing, editing and critical review of manuscript, project funding and acted as corresponding author		
Signature		Date	15/7/2020

MALDI MSI of Lipids in Clinical Prostate Tumors Reveals Cell-Type Specific Lipid Compositions

Shadrack M Mutuku^{1,2}, Paul J. Trim^{1,3}, Rajdeep Das⁴, John Salamon⁵, Jessica M. Logan⁶, Douglas A. Brooks⁶, Jonas Dehairs⁷, Johannes V. Swinnen⁷, David J. Lynn⁵, Marten F. Snel^{1,3}, Lisa M. Butler^{1,2,8}

¹Adelaide Medical School, University of Adelaide, Adelaide, South Australia 5005, Australia.

²Prostate Cancer Research Group, South Australian Health and Medical Research Institute (SAHMRI), South Australia 5000, Australia

³Proteomics, Metabolomics and MS-Imaging Core Facility, SAHMRI, Adelaide, SA 5000, Australia.

⁴Helen Diller Family Comprehensive Cancer Center, University of California, San Francisco, CA, USA

⁵Computational & Systems Biology Program, Precision Medicine Theme, SAHMRI, South Australia 5000, Australia

⁶Mechanisms in Cell Biology and Disease Research Group, School of Pharmacy and Medical Sciences, Cancer Research Institute, University of South Australia, Adelaide, SA 5000, Australia

⁷Laboratory of Lipid Metabolism and Cancer, LKI – Leuven Cancer Institute, KU Leuven, B-3000 Leuven, Belgium

⁸Freemasons Foundation Centre for Men's Health, University of Adelaide, Adelaide, SA 5005, Australia.

Correspondence:

Lisa Butler: lisa.butler@adelaide.edu.au

Keywords: spatial lipidomics, androgens, mass spectrometry imaging, prostate cancer.

Abstract

Prostate cancer (PCa) cells have a uniquely altered lipidome that supports the requirements of enhanced cell proliferation, intracellular signalling and energy storage. With recent increases in sensitivity of mass spectrometry (MS)-based lipidomics platforms, it has become possible to accurately measure lipids in clinical samples as novel biomarkers and for drug discovery. However, as clinical prostate tumours are highly heterogeneous, mass spectrometry imaging (MSI) provides the valuable opportunity to assess lipid composition in the multiple cell types and pathological features of the tumour microenvironment. Herein, we utilised matrix-assisted laser desorption/ionisation (MALDI)-MSI to measure and spatially characterise the lipid composition of clinical prostate tissues (n=10 patients) using a histology-guided approach coupled with immunohistochemical staining of the androgen receptor (AR). Parallel segments of each tissue were homogenised and subjected to quantitative MS lipidomics analysis and on-tissue MALDI MS/MS profiling to guide annotation of lipid masses identified by MSI. The MSI data was subjected to multivariate analyses at an individual patient level where spatial segmentation approaches revealed consistent evidence of cell type-specific lipid fingerprints, including from the immune infiltrate. Receiver operator characteristic curves were generated from sensitivity and specificity analyses of the different spatial clusters and the discriminant capability of a given mass spectra (m/z) feature was represented by its area under the curve (AUC) value. A PLS-DA classification model was subsequently built from the mass spectra of the entire cohort to delineate lipid features for benign epithelium, tumour and stroma. We identified the lysophospholipid species m/z 518.318, LPC(16:0)[M+Na]⁺ as characteristic of normal-benign epithelium compared to

stromal tissue (AUC = 0.80). Tumour-associated lipids were less discriminative but the tentative phosphatidylcholine species, m/z 826.562 PC(36:1)[M+K]⁺, was more abundant in cancerous areas (AUC = 0.74). The sphingomyelin species, m/z 835.654 SM(d42:2)[M+Na]⁺ was more enriched in stroma compared to glandular regions (benign epithelium and tumour); AUC = 0.88). The 10-fold cross-validated PLS-DA model indicated very good classification performance for benign, tumour and stroma lipid m/z features with AUC \geq 0.95, R² of 0.603 and mean squared error of 0.054. Our findings confirm the cell type-specificity of lipid profiles and reinforce the need to apply spatial techniques such as MALDI MSI to study the metabolomic and lipidomic features that extend beyond cancer cells and foci to the complex tumour microenvironment.

4.1. Introduction

Characterising the spatially resolved prostate cancer (PCa) lipidome is an important step towards a better understanding of the heterogeneity of PCa biology, identification of potential disease markers and subtypes, and development of novel drug targets. Unlike many cancers, which favour glycolytic metabolism, PCa has a uniquely dysregulated metabolome that is subject to androgenic regulation^{294,388}, where there is increased *de novo* lipogenesis³⁰⁸ and exogenous fatty acid uptake^{124,428}. Lipid metabolism in the prostate is at least partly under transcriptional regulation by the androgen receptor (AR)^{288,300}, which is also the primary driver of prostate tumorigenesis and treatment resistance. AR induces expression of the fatty acid synthetase (FASN) complex of enzymes^{13,429}, and FASN is increasingly being regarded as a prostate cancer oncogene and promising therapeutic target³⁰⁰. Acting either directly or indirectly via activation of sterol response binding protein (SREBP-1), AR is now known to regulate the expression of a wide range of lipogenic genes beyond FASN. This lipogenic phenotype of PCa cells grants them necessary lipid substrates to support their uncontrolled cell proliferation⁴³⁰, tumour growth and metastasis⁶⁵. Moreover, prostate cancer cells often feature mutated tumour suppressor genes such as p53 that can cooperate with dysfunctional AR signalling through the PI3K-AKT/mTOR axis to promote an aberrant lipid metabolic program⁴³¹.

The highly heterogenous nature of clinical PCa^{1,4} presents its most significant biomedical research challenge⁴³². Many bioanalytical techniques rely on the use of tissue homogenates which inevitably are a composite mixture of multiple cell types at different ratios, and potentially contain distinct tumour foci depending on tissue sampling. With the advent of mass spectrometry imaging

(MSI), cell type-specific lipidomic and metabolomic profiles of small clusters or even individual cells can be obtained *in situ*. This allows not only a more precise analysis of lipid composition in tumour cells, but also allows consideration of the tumour microenvironment, which plays a critical role in promoting tumour survival and metastasis³⁵⁸. MSI typically involves acquiring mass spectra from material ablated from a surface e.g. tissue using either a laser, particle beam or solvent spray. The x-, y-coordinates of each data point are recorded, thus the spatial and mass spectral data can be used to build up a distribution map of a molecular ion of choice^{200,201}.

Matrix-assisted laser desorption/ionisation (MALDI) is a popular method of soft ionisation for tissue imaging^{233,327}. MALDI MSI has been applied in the study of metabolomics and lipidomics³³⁸ in various forms of solid tumours²⁸¹ and there is a growing body of evidence that it has the potential to be applied for clinical diagnostics⁴²⁵ and prognostics biomarker discovery. Here, we applied MALDI MSI to probe the chemical profile of clinical prostate biopsies *in situ* with the view of characterising distinct *m/z* features of the different tissue types/cell populations present. We focused on lipids detectable in positive ion mode and present the comparison and visualisation of tissue-specific lipid profiles in tissues with multifocal prostate cancer.

4.2. Materials and Methods

Chemicals

Methanol and acetonitrile (all LC-MS hyper grade, Lichrosolv) were purchased from Merck (VIC, Australia). Trifluoroacetic acid (TFA) was from Sigma-Aldrich (USA). Argon for mass spectrometry application was purchased from BOC (Australia). α -cyano-hydroxycinnamic acid (CHCA) and polyethylene glycol (PEG) standards (200, 600, 1000 g/mol) were obtained from Sigma-Aldrich (NSW, Australia). Carboxymethyl cellulose (CMC) sodium salt was purchased from Sigma, USA and Tissue-Tek Optimum cutting temperature (OCT) compound was from ProSciTech (Australia).

Tissue Preparation for MALDI MS Imaging

Human prostate tissue was obtained with written consent from informed participants under the South Australian Prostate Cancer BioResource collection protocol. Collection was approved by the Human Research Ethics Committees of the University of Adelaide and St Andrew's Hospital, Adelaide, South Australia (**Supplementary Table 1**). Frozen tissue cores from n=10 patients were slightly embedded on 98:02 H₂O-CMC (V/V) then placed onto minimal OCT whilst frozen using dry ice. The mounted tissue was then transferred to Shandon Cryotome E (Thermo Scientific, Germany) with cutting temperature maintained at -20°C. In the present study, serial consecutive tissue sections were collected for haematoxylin and eosin (H&E) staining, MALDI MS imaging, immunohistochemistry (IHC), and shotgun lipidomics. H&E and MALDI imaging

sections were cut at 10 μm and thaw mounted onto Superfrost Ultra Plus slides (Thermo Scientific, Hungary). Each glass slide was able to fit 3-4 separate patient sections which ensured consistent data acquisition in each experiment. For lipidomics, 30 μm serial sections in triplicate were collected in cryotubes and stored -80°C prior to analyses.

Matrix Application on Tissue Sections

Automated spray coating was used to deposit 7.0 mg/ml (80% aqueous methanol-0.1%TFA v/v) of α -CHCA matrix using a SunCollect MALDI sprayer (Sunchrom GmbH, Friedrichsdorf, Germany). 15 passes of matrix were used at an increasing flow rate of 10-40 $\mu\text{L}/\text{min}$ and 30 sec pause between passes, horizontal track (X) speed of 350 mm/min, line distance of 2.00 mm, Z-position of 1.00 mm, and nitrogen gas at room temperature set and nebulizing pressure at 2.0 Bar.

MALDI MS Imaging

Tissue sections were analysed on a Waters SYNAPT HDMS hybrid quadrupole orthogonal acceleration Time-of-Flight Mass Spectrometer (Q-oa-TOF). The scan rate was set at 1 sec and 1 scan was acquired per pixel. Laser repetition rate 200 Hz and laser energy was attenuated by a variable neutral density filter set to 150 a.u. Prior to analyses, the mass spectrometer was calibrated using a calibration solution of PEG and α -CHCA to 3 parts per million (ppm) over the acquisition range. MSI data was recorded between 400-990 Da window that is rich in the lipid m/z range. The spatial resolution was set at 60 μm

(x, y) with an over sampling technique where subsequent laser spots eclipsed the previous laser ablation area²¹³. Quality control (QC) checks involved ablating two separate 1-2-mm² of areas on the glass slide before and after the tissue sections to check for homogeneity of matrix coating. These matrix distribution QC spots were acquired as MALDI MS imaging experiments within the instrument calibration mass range.

Histology and Immunohistochemistry

Separate tissue sections adjacent to those for MALDI imaging were stained for H&E and immunohistochemistry for AR as previously described⁴¹².

Lipidomics

Tissue sections were homogenised in 500 µL of water with a UP50H sonicator (Hielscher, Germany) and a volume that contained 0.5 µg DNA was diluted to 700 µL and was mixed with 800 µL 1 N HCl:CH₃OH 1:8 (v/v), 900 µL CHCl₃ and 200 µg/ml of the antioxidant 2,6-di-tert-butyl-4-methylphenol (BHT; Sigma Aldrich). 3 µL of SPLASH® LIPIDOMIX® Mass Spec Standard (#330707, Avanti Polar Lipids) was spiked into the extract mix. The organic fraction was evaporated using a Savant Speedvac spd111v (Thermo Fisher Scientific) at room temperature and the remaining lipid pellet was stored at -20°C under argon. Just before mass spectrometry analysis, lipid pellets were reconstituted in 100% ethanol. Lipid species were analysed by liquid chromatography electrospray ionisation tandem mass spectrometry (LC-ESI-MS/MS) on a Nexera X2 UHPLC system (Shimadzu) coupled with hybrid triple quadrupole/linear ion trap mass

spectrometer (6500+ QTRAP system; AB SCIEX). Chromatographic separation was performed on a XBridge amide column (150 mm × 4.6 mm, 3.5 μm; Waters) maintained at 35°C using mobile phase A [1 mM ammonium acetate in water-acetonitrile 5:95 (v/v)] and mobile phase B [1 mM ammonium acetate in water-acetonitrile 50:50 (v/v)] in the following gradient: (0-6 min: 0% B → 6% B; 6-10 min: 6% B → 25% B; 10-11 min: 25% B → 98% B; 11-13 min: 98% B → 100% B; 13-19 min: 100% B; 19-24 min: 0% B) at a flow rate of 0.7 ml/min which was increased to 1.5 ml/min from 13 minutes onwards. SM, CE, CER, DCER, HCER, LCER were measured in positive ion mode with a precursor scan of 184.1, 369.4, 264.4, 266.4, 264.4 and 264.4 respectively. TAG, DAG and MAG were measured in positive ion mode with a neutral loss scan for one of the fatty acyl moieties. PC, LPC, PE, LPE, PG, LPG, PI, LPI, PS and LPS were measured in negative ion mode by fatty acyl fragment ions. Lipid quantification was performed by scheduled multiple reactions monitoring (MRM), the transitions being based on the neutral losses or the typical product ions as described above. The instrument parameters were as follows: Curtain Gas = 35 psi; Collision Gas = 8 a.u. (medium); IonSpray Voltage = 5500 V and -4,500 V; Temperature = 550°C; Ion Source Gas 1 = 50 psi; Ion Source Gas 2 = 60 psi; Declustering Potential = 60 V and -80 V; Entrance Potential = 10 V and -10 V; Collision Cell Exit Potential = 15 V and -15 V. The following fatty acyl moieties were taken into account for the lipidomic analysis: 14:0, 14:1, 16:0, 16:1, 16:2, 18:0, 18:1, 18:2, 18:3, 20:0, 20:1, 20:2, 20:3, 20:4, 20:5, 22:0, 22:1, 22:2, 22:4, 22:5 and 22:6 except for TGs which considered: 16:0, 16:1, 18:0, 18:1, 18:2, 18:3, 20:3, 20:4, 20:5, 22:2, 22:3, 22:4, 22:5, 22:6. Peak integration was performed with the MultiQuant™ software version 3.0.3. Lipid species signals were corrected for isotopic contributions

(calculated with Python Molmass 2019.1.1) and were normalised to internal standard signals. Unpaired T-test p-values and FDR corrected p-values (using the Benjamini/Hochberg procedure) were calculated in Python StatsModels version 0.10.1.

Data Processing and Analysis

The MALDI Waters SYNAPT .raw spectrum files were converted to MSI data files by Waters high definition imaging (HDI) software which translated pixel coordinate positions of the raw spectra. The data processing settings were resolution 8,000 full-width half-height (FWHM) at mass window of 0.02 Da. The HDI imaging data was further exported in continuum mode to the universal MSI file-sharing format- imzML. The imzML data was compatible for analysis on SCiLS Lab MVS Pro (Bruker Daltoniks GmbH, Germany) which has versatile multivariate statistical analysis options. Baseline reduction was by convolution set at 20 Da. Peak picking was performed on 200 maximum peaks per spectra. The identified *m/z* intervals were moved to the local maxima to align the mean spectra of one *m/z* interval to the centre of a single peak by its maximum intensity according to the manufacturer's manual (SCiLS Lab Help MvS 2019c).

The imzML data were imported separately, for intra-patient analysis, or combined to create a single data analysis file, inter-patient analysis. The combined multi-image set of the confirmation cohort of 11 MSI files had reasonable average data point accuracy ($m/z \pm 9.661$ mDa) with a peak list of 199 *m/z* values. The bisecting k-means segmentation method was employed, and clustering was evaluated using three metrics approaches – Correlation distance, Euclidean and Manhattan. Regions of interest (ROIs) in the MSI data

were selected by comparison to the adjacent histological stained tissue. Each single pixel (0.0036 mm²) encompassed several cells. 9 pixels (~0.0324 mm²) were selected for each morphological area annotated by a pathologist. The ROIs mass spectra were exported as normalised to TIC in excel format (.csv) for external statistical analysis.

Statistical Analysis

Using an ANOVA p-value <0.05 revealed that 132 out of 199 *m/z* features (variables) were significantly different between ROIs. Consequently, spectra .csv files were then imported into web-based version of the *R* package MetaboAnalyst for multivariate analysis⁴¹⁰. Data was uploaded in the format of spectral bins; data filtering was done by inter-quantile range. Data normalisation steps composed of log transformation and pareto scaling. Heatmaps were generated using hierarchical clustering analysis and top 25-50 *m/z* features were ranked by ANOVA/t-test. Principal component analysis (PCA) score plots indicated the relative variation of groups of ROIs' based on distribution of lipid species. Additionally, partial least square discriminant analysis (PLS-DA) for classification testing of lipid *m/z* features for the different prostate tissue types was performed.

4.3. Results

4.3.1. Differential distribution of phospholipids between tissue stroma, malignant and non-malignant prostate epithelium

Frozen cores of prostate tissue from benign (n=1) and malignant (n=9) specimens were analysed in the study and the clinical features of the patients are detailed in [Supplementary Table 1](#). Histological annotation of the varying cell types and pathological features was performed by a pathologist for freshly obtained cryosections of each specimen since tissue morphology would vary from the clinical RP samples at the time of diagnosis due to sampling.

We analysed the distribution of lipid masses across patients with non-malignant prostate glands and with multifocal regions of PCa. The MALDI MSI spatial information was over-laid and co-registered with histology scans of post-MALDI and serial sections. Morphological regions of interest (ROI) from pathologically assessed adjacent H&E sections were used to guide selection of mass spectra for statistical analyses. Initially, exported ROI's from individual patients underwent multivariate unsupervised analysis using a principal component analysis (PCA) model and score plots were generated for each patient.

In tissue sections containing non-malignant glands, there were generally no marked differences in the profile of lipid masses from multiple sampled glandular regions within the same section. However, clear separation in lipid profile was evident between stroma and non-malignant glandular epithelium as depicted in [Figure 1A](#), ([Supplementary Figure 1](#)). By contrast, patients with malignant foci exhibited differential distribution of lipid masses in epithelial regions within the same tissue section. An example of clear separation of the lipid

m/z features of normal, near-normal with invagination, potential cancerous areas and contiguous inflammatory cells is shown in [Figure 1B](#). This pattern was replicated in another patient with benign, PIN and hyperproliferating cells accompanied with influx of inflammatory cells ([Supplementary Figure 2](#)).

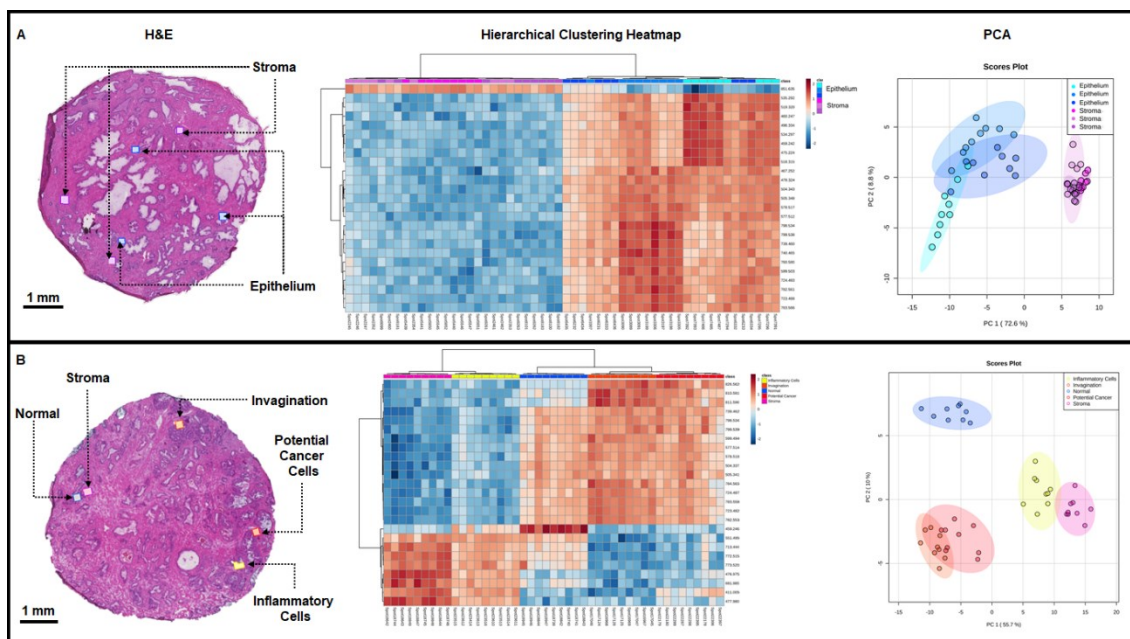


Figure 1: Histopathological guided ROI subsampling of prostate tissue. Clustering heatmaps and PCA score plots were generated using *m/z* features from regions depicted in H&E scans. **A.** Patient section with non-malignant glands exhibited different lipid profiles with strong similarity between individual ROIs for each cell type; stroma (pink shades) and epithelium (blue shades) . **B.** Patient section with malignant foci tissue exhibited variation on lipid profiles between non-malignant epithelium (blue shades), epithelium with features indicative of malignancy (orange) and inflammatory cells (yellow) in proximity.

In order to identify lipid masses associated with histological features across patients, we combined the individual tissue MSI files into a single multi-image file in SCiLS Lab. The ROI's selected from this individual patient MSI regions files were re-imported and co-registered to exactly match with their respective coordinates in the larger combined data set. This allowed the single multi-images ROIs to be exported with uniform m/z intervals across all the patients and facilitated multivariate analyses using principal component analysis (PCA). To reduce redundancy, ROIs were grouped such that normal and near-normal glandular tissue areas were combined and denoted as benign and hyper-proliferative and malignant areas were categorised as tumour.

Initially, a PCA model was built using 891 spectra derived from 315 benign, 63 inflammation, 261 stroma, 90 tumour margin (stroma adjacent to tumour areas), 126 PIN and 126 tumour ROI spectra selected from the annotated regions. As with the hierarchical clustering ([Supplementary Figure 3](#)), a PCA score plot revealed that the epithelial tissue types, comprising benign, tumour and PIN areas, grouped together and separated from stroma, inflammation and tumour areas, which collectively overlapped (**data not shown**). Using only benign, stroma and tumour ROIs, a distinct separation of benign and tumour areas is observed from the simplified PCA score plot ([Figure 2](#)).

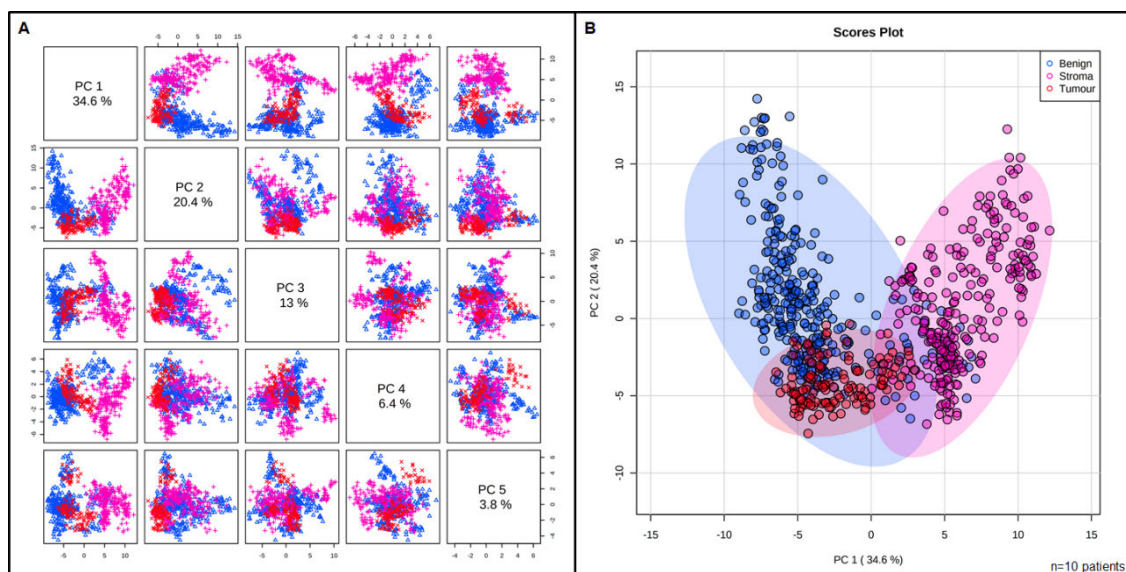


Figure 2. Unsupervised modelling of lipid masses from combined multi-patient pathological ROIs. A. Pairwise score plots between selected PC. The explained variance of each PC is depicted in the corresponding diagonal cell. **B.** Score plots of PC1 and PC2, explaining 34.6% and 13% of observed variances, respectively, demonstrating separation of lipid m/z features from benign (blue), stroma (pink) and tumour (red) ROIs selected across a combined MSI data set of $n=10$ patients.

Visualization of the top 50 m/z features in the hierarchical clustering analysis heatmap ([Supplementary Figure 3](#)) showed increased abundance of distinct masses in the phospholipid (PL) mass range in glandular epithelial tissue (benign and tumour) compared to stroma. Examples of these are tentative phosphatidylcholines (PC) m/z 782.554, m/z 798.543, m/z 760.574 and their potential in-source fragment ions m/z 599.495 and m/z 577.514 corresponding to fatty acyl chain loss. An increased abundance of lipid masses in tumour compared to benign glands was also apparent. These were m/z 826.563 and m/z 767.491. A unique subset of PL masses were characteristic of stroma and

inflammation regions, these were m/z 792.554, m/z 551.496, m/z 772.515 and with a tentative SM m/z 713.444 ([Supplementary Figure 3](#)).

Accordingly, Random Forest Classification (RF) was tested on this subset of combined ROI data. The RF model had an out-of-bag (OOB) error of 10.3% ([Supplementary Table 2](#), [Supplementary Figure 4](#)). The variable importance (in projection scores) showed the characteristic masses of benign epithelium to be m/z 459.24, m/z 518.318. PIN tended to be classified better by m/z 782.55 and m/z 723.482. Tumour classifiers were not distinct except for m/z 478.328 and m/z 496.337 which were only more marginally indicative compared to benign glands. Inflammation was classified by m/z 713.44, m/z 772.51 whereas m/z 792.55 accurately classified normal stroma. PIN, tumour-margin and inflammation had higher error rates of 31%, 28% and 16% respectively.

Therefore, subsequent supervised classification only focused on benign, tumour and stroma with a greater number of spectra to improve performance of the model. Hence, all spectra from the segmentation clusters from only three tissue types were combined to yield 11,969 benign, 22,573 stroma and 2,416 tumour data points.

4.3.2. Prostate tissue morphology is reflected in spatial lipid distribution

The MALDI MSI spatial information was overlaid and co-registered with histology scans of post-MALDI and serial pathology annotated sections. Immunohistochemical staining also offered additional morphology information of the sections and AR-positive cells were highly co-localised with spatial clusters as displayed in [Figure 3](#).

We analysed the chemical profile throughout the tissue sections from each patient using a multivariate statistical platform designed for MSI data, SCiLS Lab. Essentially, a clustering algorithm was applied to group the mass spectra into three main areas of interest: chemical matrix, epithelium and stroma which could generally be deconvoluted. If cancer was present, the glandular compartments could be further segmented to reveal benign glands and tumour. With increased steps top-down clustering, the stromal compartment could be further sub-divided to reveal areas of inflammation in some patients. The automated image segmentation of MSI data was used for delineation of three main tissue types – benign epithelium, stroma and tumour ([Figure 3](#)).

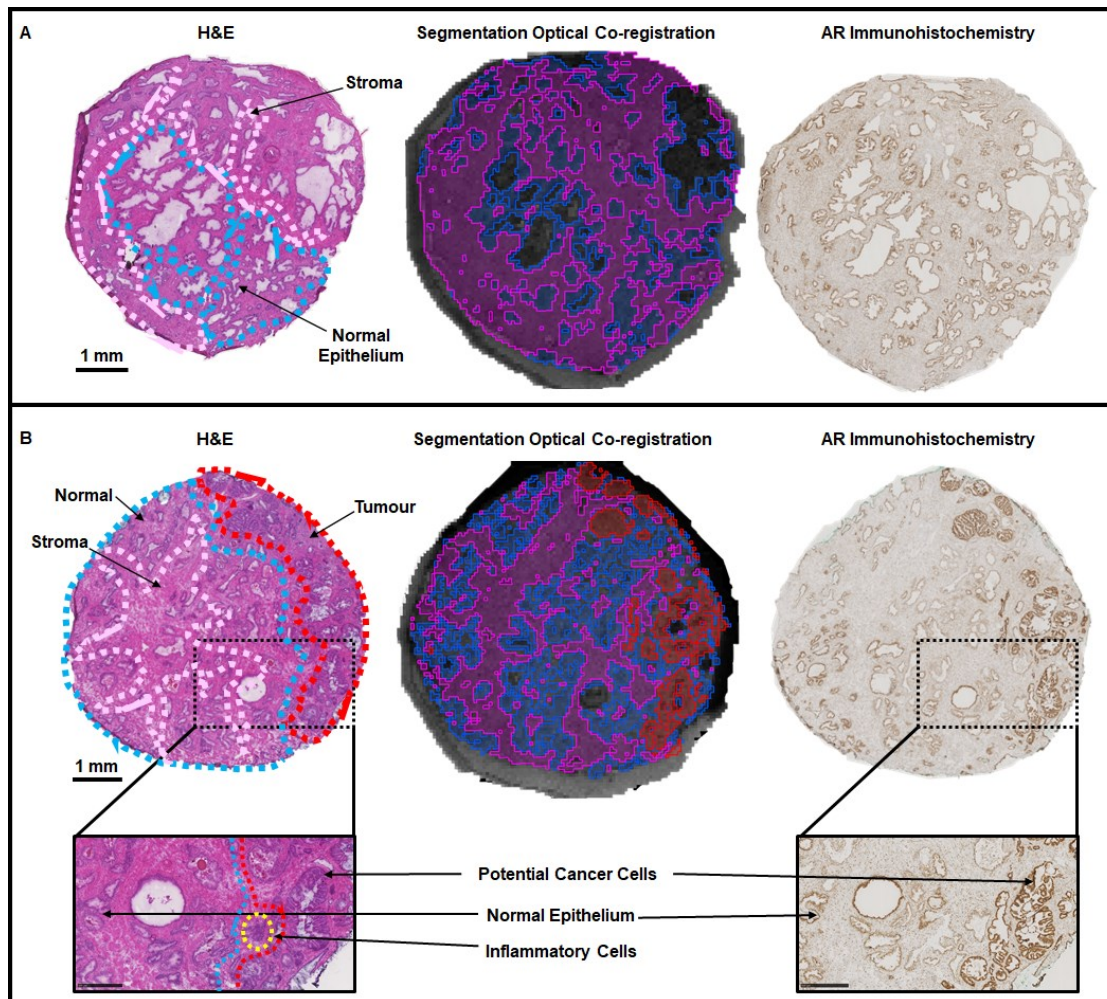


Figure 3. Co-registration of histopathological features to spatially defined lipid cluster segments. Comparison of serial H&E, MALDI MSI and AR IHC scans. MALDI MSI clustering of lipid-rich m/z features achieved with Bisecting k-means algorithm Manhattan metric. **A.** Patient prostate tissue section with non-malignant glands. **B.** Patient prostate tissue with heterogeneous pathological foci, showing inflammatory cells infiltrate between normal and cancerous epithelial cells overexpressing AR.

Afterwards, discriminant m/z values determined by receiver operator characteristic (ROC) curves or sensitivity/specificity analysis were calculated in SCiLS Lab. ROC analysis of benign vs tumour regions identified m/z 459.246 and m/z 518.318 whereas lipids masses m/z 768.506 and m/z 826.563 with highly similar distribution profiles were more localised to tumour glands as illustrated in [Figure 4 \(Table 1\)](#). Certain lipid masses were more specific to stroma in comparison to glandular areas (benign and tumour) ([Figure 4, Supplementary Table 3](#)). Results of these expanded multivariate analyses were consistent with the observations of the RF model and hierarchical clustering on the prior small data subset.

m/z	Tentative ID	ROC	
		Benign vs Tumour	Tumour vs Benign
459.246	LPA(18:1)[M+Na] ⁺	0.83	0.17
	LPA(20:4)[M+H] ⁺		
518.318	LPC(16:0)[M+Na] ⁺	0.80	0.20
	LPC(18:3)[M+H] ⁺		
496.337	LPC(16:0)[M+H] ⁺	0.76	0.24
	PC(O-16:O) [M+H] ⁺		
475.217	LPA(18:1)[M+K] ⁺	0.75	0.25
	LPA(18:4)[M+2Na-H] ⁺		
711.444	PA(34:2) [M+K] ⁺	0.26	0.74
	PE-Cer(34:3;O3) [M+K] ⁺		
770.515	PC(32:1) [M+K] ⁺	0.26	0.74
	HexCer(34:1;O4) [M+K] ⁺		
826.562	PC(36:1) [M+K] ⁺	0.26	0.74

Table 1. Discriminant (ROC) values of masses in benign vs tumour regions.

Spectra from benign and tumour clusters were used in receiver operator characteristic (ROC) analysis using local maximum peaks in SCiLS Lab. ROC values >0.75 are discriminative of different tissue types. Tentative IDs are based on LIPID MAPS® Structure Database search of bulk structures with a mass tolerance of ± 0.01 Da and quantitative lipidomics analysis.

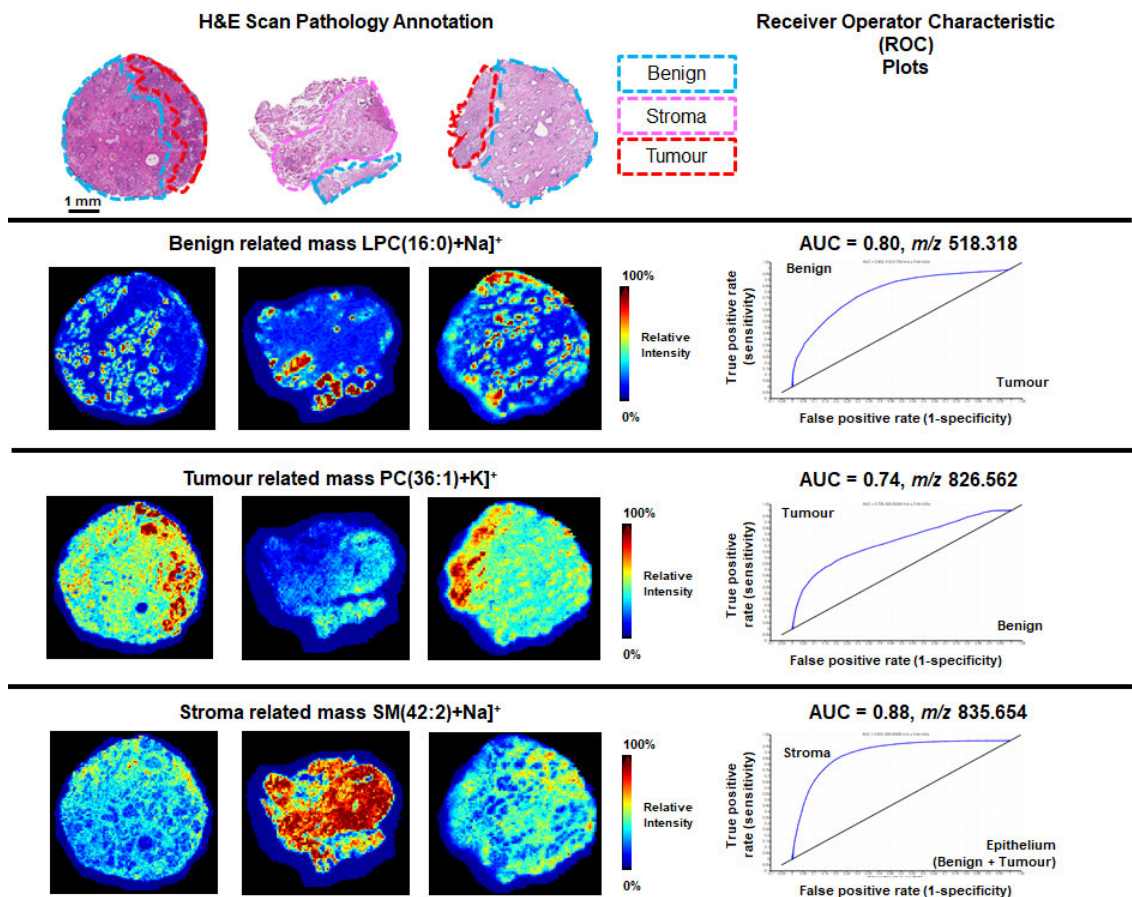


Figure 4. Visualization of discriminative lipids of multifocal heterogeneous prostate tissue. Representative ROC analysis of spatial segments matched to pathologically annotated H&E scans is shown for three separate patients. m/z 518.318 $\text{LPC}(16:0)+\text{Na}]^+$, m/z 826.562 $\text{PC}(36:1)+\text{K}]^+$ and m/z 835.654 $\text{SM}(d42:2)+\text{Na}]^+$ demonstrated high abundance in benign, tumour and stromal regions, respectively, in prostate tissue in combined MSI data set of $n=10$ patients.

Subsequently, a supervised model was built using partial least squares-discriminant analysis (PLS-DA) which included 132 *m/z* features (excluding masses from the CHCA matrix noise) as depicted in [Figure 5](#). So that no limits would be placed on the number of spectra used, the model was constructed locally using the Python-based Scikit-learn package⁴³³. Order of spectra was randomised and submitted to a 10-fold cross-validation procedure to fit an optimal model. Cross-validated AUC scores indicated very good classification performance ([Figure 5A](#)). The final model chosen had an R^2 of 0.603 and a mean squared error of 0.054 and displayed strong clustering of groups when PLS-DA scores were plotted ([Figure 5B](#)). Majority of the masses that were revealed to be highly discriminative from the spatial AUC analysis were also reflected in the top 10 contributing masses of the PLS-DA modelled variance ([Supplementary Figure 5](#), [Supplementary Table 4](#)). Tumour and benign spectra were associated with masses that contributed more strongly to the modelled variance than those associated with stroma spectra ([Supplementary Figure 6](#)). Stroma spectra had overall weaker correlations with specific masses than tumour or benign spectra ([Supplementary Figure 6](#), [Supplementary Table 5](#), [Supplementary Table 6](#) and [Supplementary Table 7](#)). The PLS-DA classifier was finally applied to full tissue sections ([Supplementary Figure 7](#)) to demonstrate the predictive ability of the model.

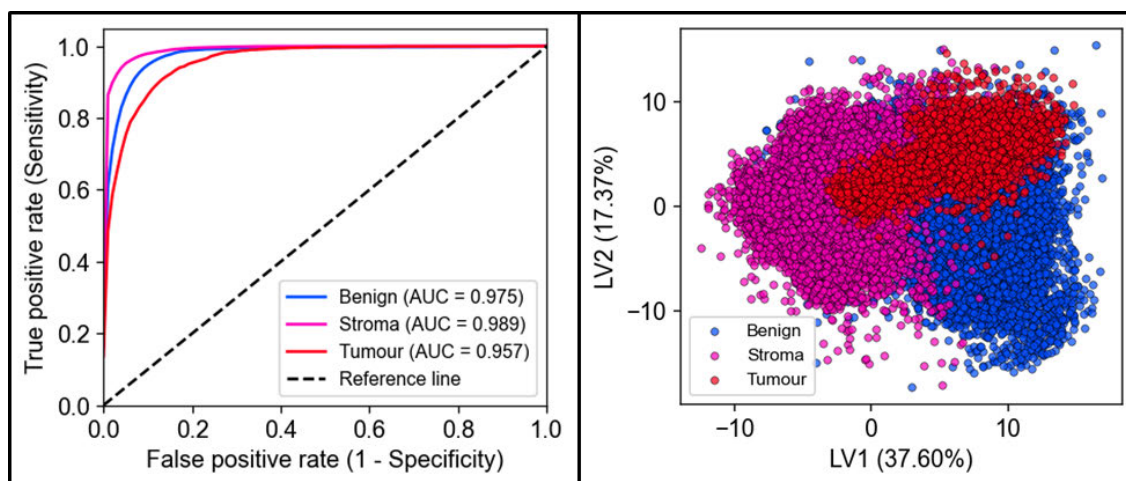


Figure 5. Specificity and sensitivity analyses of prostate tissue lipid mass features. ROC curves for cross-validated data in PLS-DA model. A. ROC curves for each label were determined for each cross-validation fold, from which the mean ROC curves and AUC values were calculated. **B.** PLS-DA model scores for all benign, stroma and tumour spectra on the first two latent variables (LVs). LV1 and LV2 respectively explain 37.6% and 17.37% of observed variance.

Lipidomics analyses of major lipid classes detected in MALDI mode are illustrated in [Supplementary Figure 8](#). In the case of PC, species with sum fatty acyl chain composition 32:0, 32:1, 34:0, 34:1, 34:2 and 36:4 were the most abundant. Interestingly, the spatial intensity of the putative salt adducts of common lipid PC(34:1) appeared to be tissue dependent. m/z 798.534 $[M+K]^+$ tended to be higher in three cancerous tissues whereas m/z 782.554 $[M+Na]^+$ (which is isobaric m/z 782.554 PC(36:4) $[M+H]^+$) was low in the TURP specimens and patients with more well differentiated glands. PC(34:1) was confirmed to be the most abundant species based on sum notation within this class from the lipidomics analyses.

4.4. Discussion

There is an increasing appreciation of the rapidly advancing spatial metabolomics and lipidomics platforms to discover more accurate biomarkers of disease aggressiveness in solid tumours^{257,286}. Such imaging technologies offer the advantage of direct analysis of tissue pathophysiology with minimal sample preparation and retention of tissue architecture³⁹¹. Although conventional metabolomics and/or lipidomics in PCa³⁶⁷ provide robust, quantitative and high throughput data, there is critical loss of spatial information during tissue preparation, hence a lack of precision in relating cellular disease processes to the metabolites found in different cells². Here we report the unique diversity of lipid composition in the various cell types of the clinical prostate tumour microenvironment, particularly between epithelial and stromal cell populations, and provide evidence for tumour-specific lipid profiles.

Utilising a combination of spatial MSI bioinformatic approaches, we showed that the MSI platform SCiLS Lab and subsequent analysis pipelines were capable of isolating chemical noise from genuine biological signal present on tissue surfaces to allow detailed interrogation of the MALDI MSI data sets. Clustering algorithms were able to divide the tissue regions consistently morphologically into benign epithelium, stroma, tumour and matrix. Intriguingly, segmentation analysis was able to further deconvolute chemical profiles of the main tissue areas, to reveal other potential tissue components that were not related to specific pathological features. These may represent a complex biological mixture of the major discernible tissue types and further investigation using advanced higher resolution MALDI imaging techniques such as the

recently reported MALDI-2³⁹⁷ coupled with other immunohistochemical markers is warranted.

Initially, the ROI data at individual patient level showed that the lipid profile from sections of normal tissue in PCa patients is largely identical whilst the patient tissues containing multiple areas of heterogenous adenocarcinoma had clear disparities in lipidomic composition. This observation necessitated the integration of all respective ROIs from multiple patients into a single combined MSI file where lipid masses could be uniformly compared with suitable mass accuracy. A PCA model showed a separation of benign regions from stroma and tumour-margins with a proportion of spectra having overlapping component scores. A subsequent random forest classification model revealed the most important lipid masses for each prostate tissue type. Although the sample size is relatively small, it leverages our well annotated pathological features, each containing multiple individual spectra. Moreover, expansion of this selection by merging 36,958 spectra from cluster regions of benign, tumour and stroma regions afforded supervised PLS-DA analysis.

An important outcome of the study is that our data shows that the lipid signature of the glandular epithelium is highly consistent across patients. Generally, higher molecular weight lipid masses were abundant in epithelium whereas a minor subset of these bearing different masses were unique to stroma. We detected certain lower masses in the lysophospholipid mass range to be distinctly localised in non-malignant glands. One potential reason for this diminished presence of lysophospholipids in cancer areas suggests that they may be depleted due to their roles as structural substrates for *de novo* lipogenesis of phospholipids to support cell growth and proliferation. This finding

is consistent with other MSI studies using desorption electrospray ionisation that have shown enhanced abundance of lyso PL/PC and their associated metabolic genes in benign prostate tissue^{134,385}. Lyso PL homeostasis is maintained by the Lands' cycle¹¹⁸. LPCs are converted to LPA by lysophospholipase D (LPD) whereas phospholipase A₂ (PLA₂) converts phospholipids to their corresponding lysophospholipids. LPC acyltransferases (LPCATS) incorporate fatty acids into LPC to yield PCs. Lyso PLs are second messenger ligands for G protein coupled-receptors that mediate lipid signalling to cause cell proliferation, migration and survival⁴³⁴. Overexpression of PLA₂ and two isoforms of LPCAT2 in prostate tumours has been shown in a prior lipidomics/transcriptomics study but only significant key disruptions in phospholipid metabolism not LPC³⁶⁷.

Interestingly, several diverse lipids characteristic of stroma also exhibited increased relative abundance in inflammation. Sphingomyelins (SM) constitute the myelin sheath of nerve cells and are abundant in plasma membrane, where they play important roles in regulating signalling from membrane-bound receptors. SM are commonly observed in MALDI spectra of biological tissues as alkali adducts³⁹⁵. For instance, the tentatively identified SM(d34:1) m/z 725.540[M+Na]⁺ / m/z 741.521[M+K]⁺ was pronounced in stromal tissue in this study. There was also an observable increase relative abundance of SM(d34:1) in higher tumour grade samples marked with inflammatory cell infiltrate in stroma, which suggests a potential role of SM in intracellular signal transduction at a macroscopic level for macrophage recruitment to combat active neoplastic transformation. Randall *et al* reported that SM(d34:1) discriminatively classified GS(3+4) from GS(4+3) prostate tumours³³⁶. Sphingolipids, together with cholesterol are major components of lipid rafts in extracellular vehicles and

membranous organelles where they mediate oncogenic signalling in primary tumours^{356,426}. SMs are converted to ceramides by sphingomyelinase³⁶⁹. Ceramides have been implicated to function as pro-apoptotic molecules during onset of tumorigenesis³⁷⁰. Collectively, our spatial lipidomic profiling data highlights that lipids have specific functional roles in different cells in prostate tissue.

Across all the patient cohort, m/z 782.56 a tentative PC(34:1)[M+Na]⁺ was ubiquitous. PC(34:1) has been observed in numerous MALDI imaging studies in different tissue types and perhaps an integral structural phospholipid in cell membranes^{285,286}. A lung cancer model of MYC-driven oncogenesis driving deregulated lipid metabolism, MALDI MSI revealed that PC(34:1) was distributed in tumour tissue²⁸⁵. In the present study, a rich spatial intensity of the potassium adducts of PC(34:1) was observed in patients with high tumour volume. This may be speculated to be an imbalance of Na⁺/K⁺ flux concomitant with induction of hypoxia as PCa develops¹⁴². Given that transforming PCa cells increasingly generate ATP by decoupling from glycolytic metabolism to fatty acid oxidation^{304,382}, this warrants further investigation. Previous MALDI MSI studies have reported the dysregulation of the Na⁺/K⁺ ATPase in ischaemic brain injury⁴³⁵. Furthermore, Hall and colleagues demonstrated the ratio of Na⁺/K⁺ adducts of PC(32:0) and PC(36:4) have been reported to be higher in tumour tissue compared to normal in a murine model of lung cancer²⁸⁵.

There are limited previous studies that have analysed prostate tissue using MSI. Randall *et al* employed MALDI Fourier transform ion cyclotron resonance (FT-ICR) for lipid imaging in 10 prostate specimens, a similar sample size to our study. Their research similarly employed automated spray coating

with CHCA as matrix in positive ion mode. They observed enrichment of 31 lipids spanning phosphatidylcholine (PC), phosphatidic acid (PA), phosphatidylserine (PS) and phosphatidylinositol (PI) and cardiolipins (CL) in GS (4+3) tumour compared to GS (3+4). Some of the lipids identified are consistent with the masses we identified, such as PC(32:0) and PC(34:1) and SM(d34:1). Interestingly, PC(34:2) with isobaric mass to CL(80:9) was observed to be enhanced in tumour glands similarly to their report³³⁶. Stearoyl-CoA desaturase mediates insertion of double bonds during fatty acyl synthesis³⁰² and has been shown to be overexpressed in PCa^{367,436}, which may explain enrichment of *m/z* 780.554, PC(34:2) in tumour regions compared to benign in some patients in this report. Another, study using MALDI-IT-TOF by Goto and colleagues similarly linked higher lysophosphatidylcholines (LPC) abundance in benign tissue compared to cancer tissue²⁸⁴. They used sublimation of 9-aminoacridine matrix and employed tandem MS/MS experiments to confirm structural identity of lipids. They identified the LPC(16.0) *m/z* 496.3 [M+H-H₂O]⁺ and *m/z* 518.3 [M+Na]⁺²⁸⁴. Their results are comparable to this study. Importantly, we demonstrate a novel *m/z* 459.246, a potential LPA(18.1)/LPA(20:4) to be enriched in benign glands compared to cancer. Overall, our results suggest metabolic flux of LPC/LPA to PC is characteristic of the tumourigenic phenotype. In tumour glands, there were not sufficiently discriminative lipid species, likely reflecting the heterogeneity between individual tumours and limited sample size, but *m/z* 826.562 PC(36:1) tended to be distributed with high spatial intensity in cancerous areas. PC(36:1) can be speculated to be an elongation product of PC(34:1). Elongase enzymes have been shown to be overexpressed via AR regulation in PCa³⁰⁹. More so, cancer cells have increased *de novo* synthesis of phospholipids with saturated

and monounsaturated fatty acids which determines membrane fluidity^{149,288,300,426}. Desaturated membranes with low cholesterol are thought to increase the migratory and invasive potential of tumour cells⁴²⁶. Further spatial systems biology studies are needed to ascertain associated changes in expression of enzymes involved in phospholipid remodelling pathways in PCa.

This study has a few limitations. First, the sample size potentially makes the PLS-DA model susceptible to overfitting. Given the highly heterogenous nature of PCa, analysis of a much larger cohort is necessary to validate the current findings and identify further characteristic lipidomic profiles of the various tissue types. Nonetheless, some of the identified lipids abundant in non-malignant glands were very consistent across patients and are supported by the literature. Second, the differential distribution of salt adducts of monounsaturated fatty acids constituents of PCs is interesting but MALDI MSI cannot fully experimentally account for their quantitative amounts. Additional techniques such as inductively coupled plasma mass spectrometry would be useful to map out the precise localisation of single Na⁺ and K⁺ ions in prostate tissue.

4.5. Conclusion

Our results highlight the importance of MALDI mass spectrometry imaging as a powerful *in situ* tool for characterisation of the unique deregulated lipidome of prostate cancer. Recent insights into the importance of the “metabolic microenvironment” of cancer underscore¹⁵⁰ the need to consider cell types beyond the tumour cells themselves for both biomarker discovery and design of therapeutic strategies targeting multiple features of the microenvironment.

4.6. Supplementary

Patient ID	Age at RP	PSA at RP	1° GS	2° GS	3° GS	GS Score	Stage	Cancerous cores	Cancer core used for the cohort
31678	63.8	3.75	4	3	5	7	PT3A	Left	Left 4+3
31684	67.3	6.43	4	3		7	PT3A	Left	Left 4+3
31713	68.6	7.54	4	3	5	7	PT3A	Left	Left 4+3
31728	61.5	10	4	3		7	PT3A	Left	Left 3+4
31772	62.8	6.1	3	4		7	PT2C	Left	Left 3+4
32036	58.9	8.5	4	3	5	7	PT2C	Left	Left 3+4
31697	60.5	13.2	4	5		9	PT3A	Right	Right 4+5
31743	69.2	2.93	4	5		9	PT3B	Both	Both 4+5
31865	63.2	12	4	5		9	PT2B	Left	Left 4+5
31852	70.3	2							Non-cancerous

Supplementary Table 1. Patient clinical pathological information of prostate fresh-frozen biopsies. GS - Gleason scoring, PSA – prostate specific antigen, Stage corresponds to TNM classification system^{50,53}.

	Benign	Inflammation	PIN	Stroma	Tumour	Tumour margin	Error (%)
Benign	307	1	5	2	1	0	3.0
Inflammation	0	53	0	6	3	1	16.0
PIN	32	1	87	2	4	0	31.0
Stroma	4	2	0	253	0	2	3.0
Tumour	0	1	8	1	116	0	8.0
Tumour margin	0	1	0	24	1	65	28.0

Supplementary Table 2. Random forest model classification performance of six prostate tissue types. Pathological ROIs were used to construct a model using 132 variables from n=10 patients. Confusion matrix of random forest classification with a total cumulative error rate of 10.3%.

<i>m/z</i>	ROC Stroma vs Glandular (Benign +Tumour)	ROC Glandular (Benign +Tumour) vs Stroma
652.595	0.89	0.11
835.654	0.88	0.12
773.52	0.87	0.13
851.635	0.87	0.13
772.515	0.85	0.15
756.545	0.85	0.15
697.473	0.85	0.15
757.54	0.84	0.16
551.496	0.84	0.16
713.444	0.84	0.16
792.554	0.83	0.17
518.318	0.08	0.92
799.539	0.08	0.92
459.246	0.08	0.92
505.342	0.05	0.95
783.559	0.04	0.96
782.554	0.04	0.96
600.499	0.04	0.96
724.487	0.04	0.96
599.495	0.03	0.97
723.483	0.03	0.97
504.337	0.03	0.97
578.519	0.03	0.97
577.514	0.02	0.98

Supplementary Table 3. Discriminant (ROC) values of masses in stroma vs glandular regions.

	% variance
459.246	1.388617
518.318	1.297824
812.544	1.267905
826.563	1.262446
827.567	1.254170
768.506	1.167059
828.524	1.146677
475.217	1.146652
496.337	1.146174
767.491	1.141051

Supplementary Table 4. Percentage of model variance explained by the top 10 most contributing *m/z* features.

	Benign
603.533	0.032351
475.217	0.029677
504.337	0.027994
505.342	0.026788
534.288	0.025888
765.472	0.024070
824.553	0.023686
811.597	-0.022574
535.293	0.022494
796.525	-0.022357

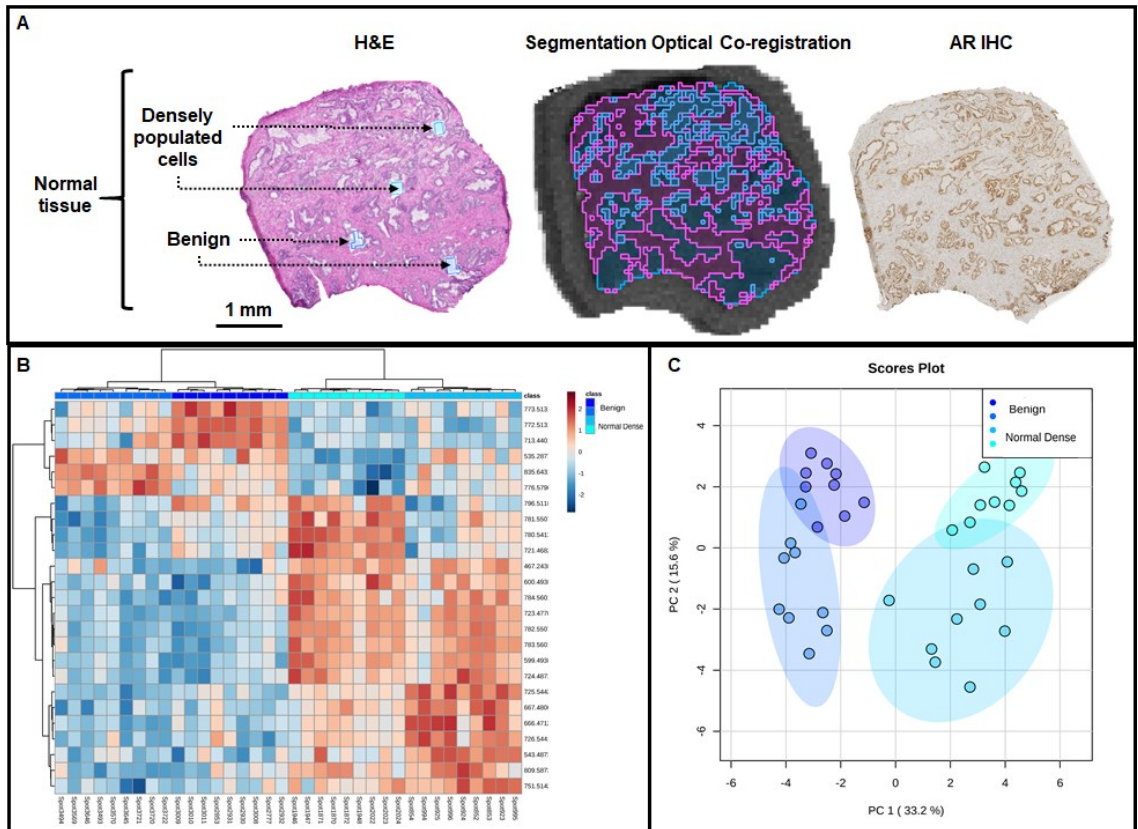
Supplementary Table 5. Top 10 masses correlated with benign spectra.

	Stroma
652.595	0.017675
475.217	-0.016774
798.534	-0.016525
792.554	0.016086
739.463	-0.016055
799.539	-0.016003
534.288	-0.015963
851.635	0.015561
800.544	-0.015232
562.317	-0.014866

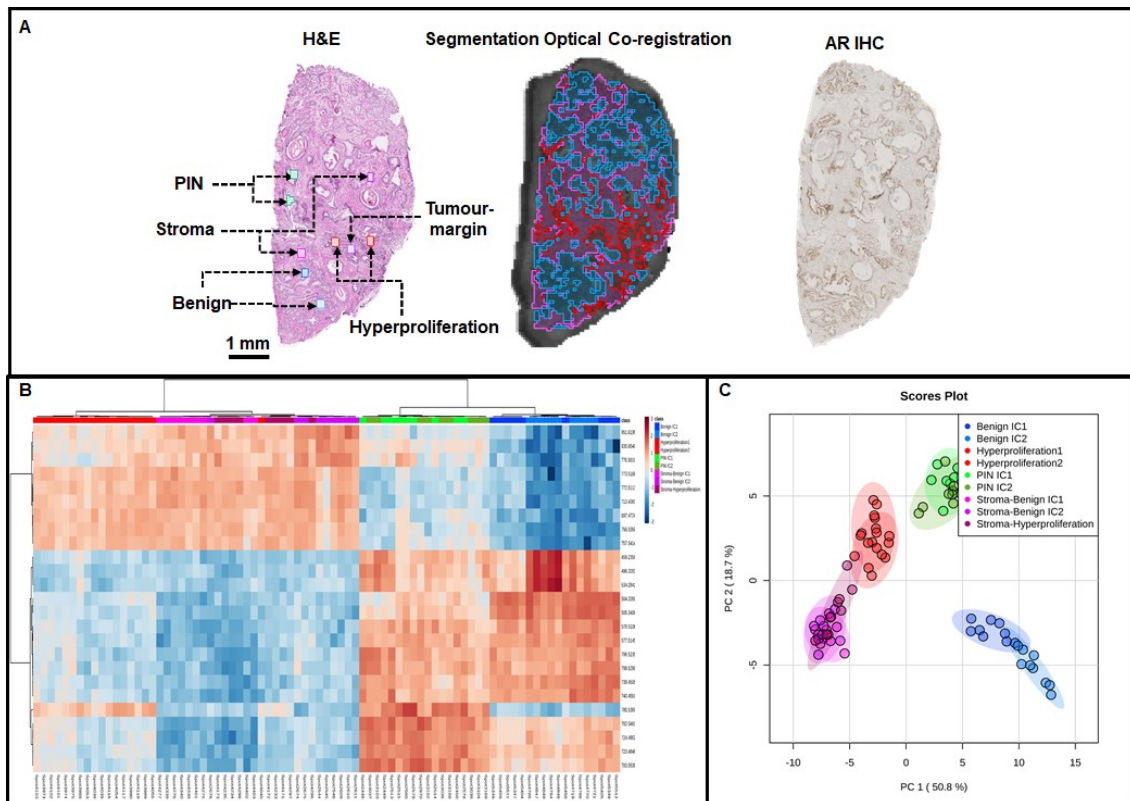
Supplementary Table 6. Top 10 masses correlated with stroma spectra.

	Tumour
603.533	-0.031234
811.597	0.027204
812.544	0.026610
765.472	-0.026533
824.553	-0.025216
827.567	0.022801
749.501	-0.022520
826.563	0.020792
808.573	-0.020168
506.356	0.019403

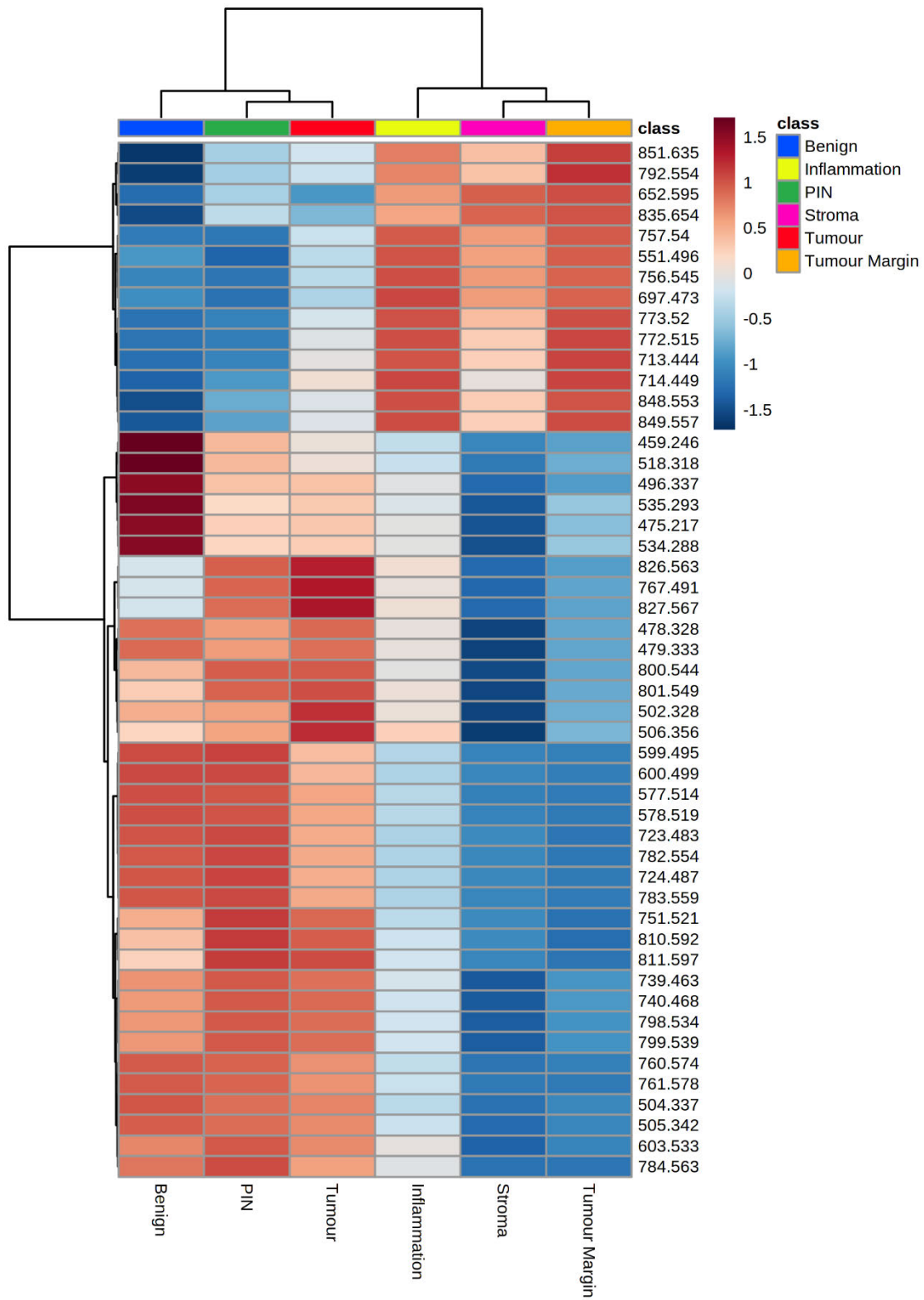
Supplementary Table 7. Top 10 masses correlated with tumour spectra.



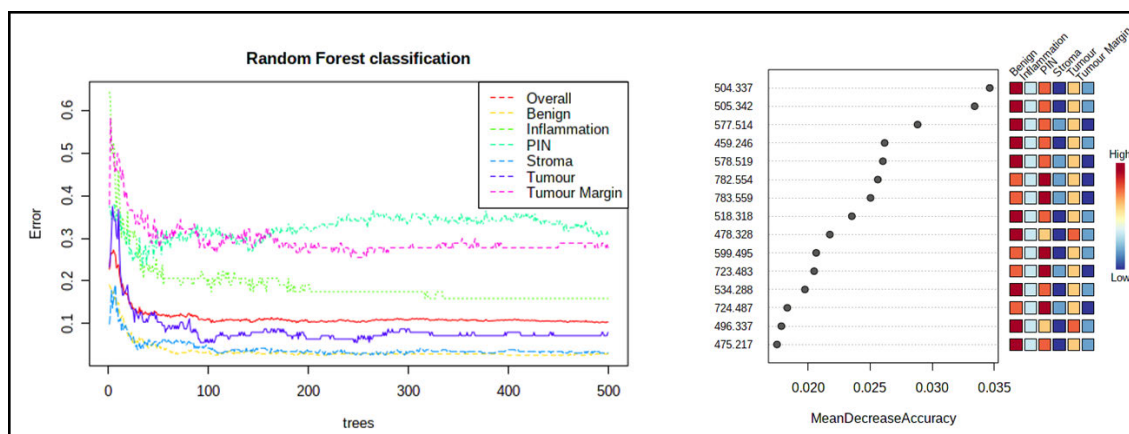
Supplementary Figure 1. Multivariate analysis in pathological ROI's in normal prostate tissue. Tissue section with a dense population of normal cells appears to have different lipid profiles between the upper and lower areas of the epithelium.



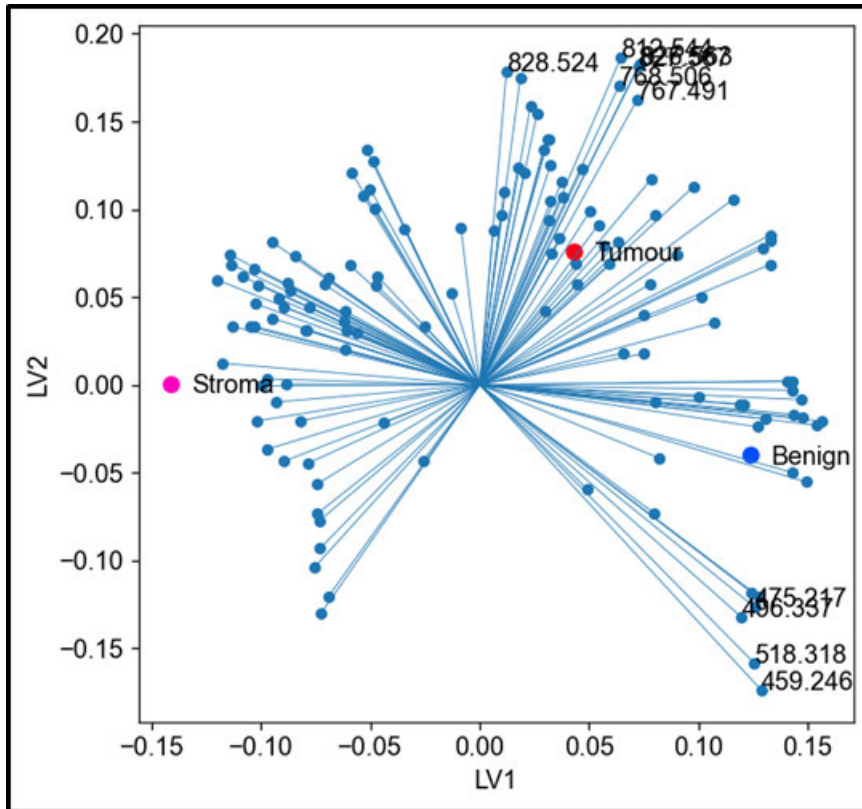
Supplementary Figure 2. Multivariate analysis in pathological ROI's in multifocal PCa tissue. Tissue section exhibits distinct pattern of separation of lipid ion spectra from benign (blue), PIN (green) with inflammatory cells and hyperproliferative epithelium (red) and stroma; stroma near benign tissue (pink) and stroma near malignant hyperproliferative epithelium (magenta).



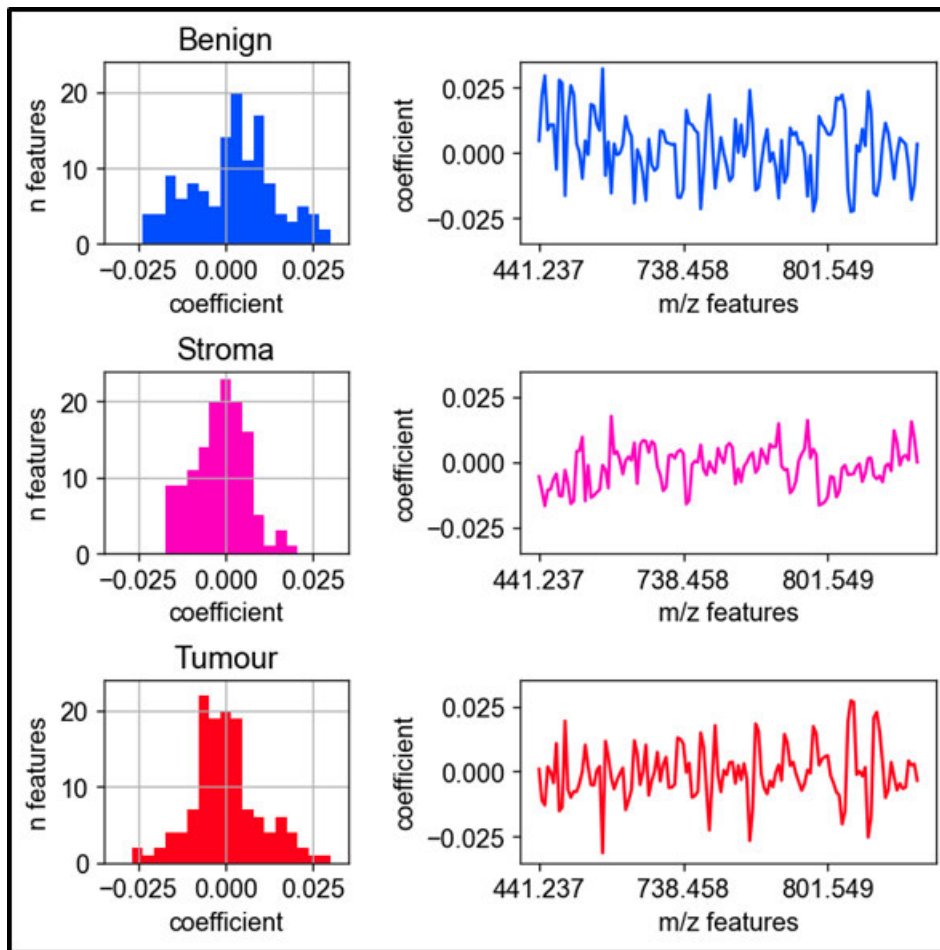
Supplementary Figure 3. Hierarchical clustering heatmap. Top 50 averaged group features across benign, inflammation, PIN, stroma, tumour and tumour margin are shown.



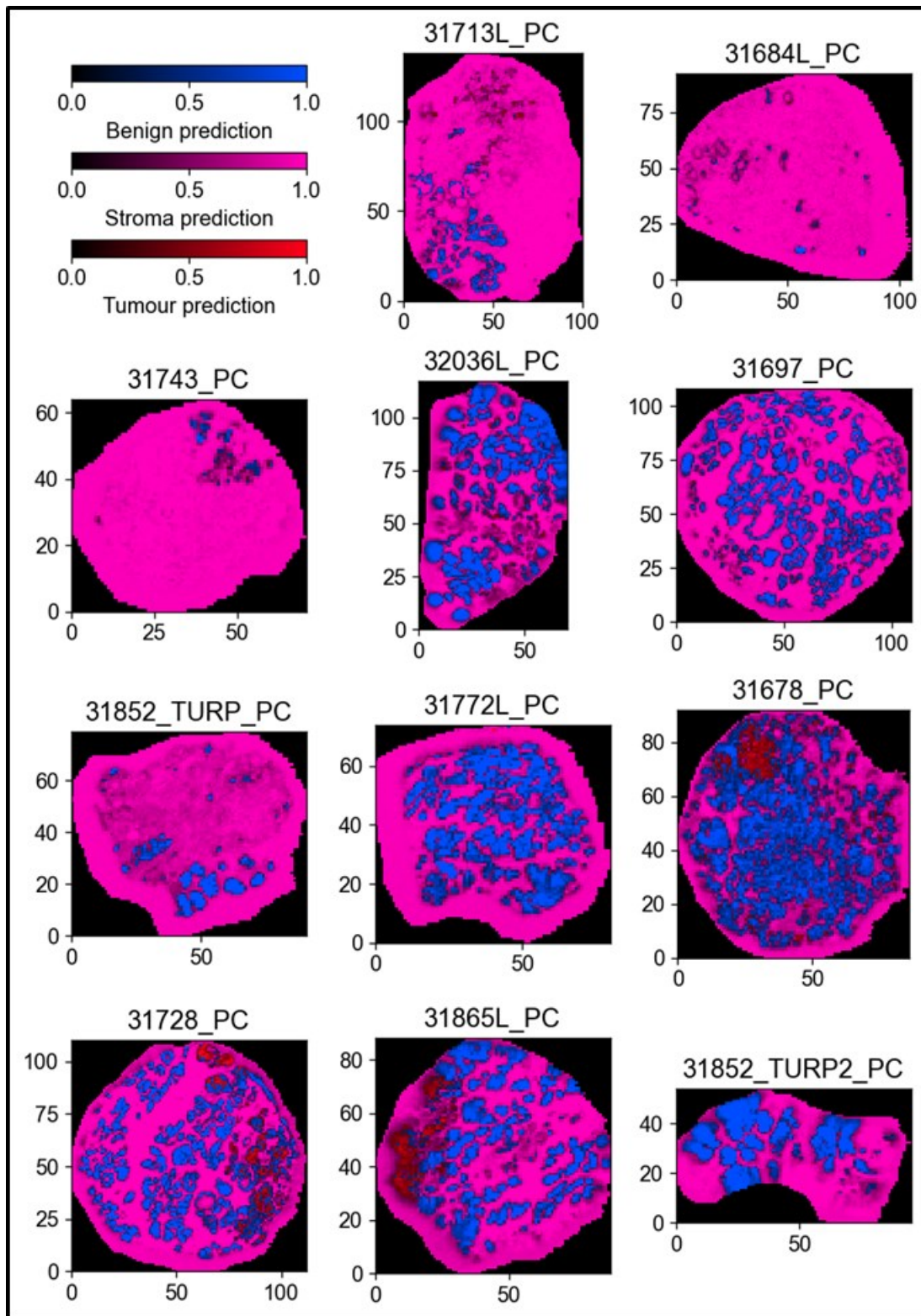
Supplementary Figure 4. Left. Supervised analysis by Random Forest classification trees of benign, inflammation, PIN, stroma, tumour and tumour margin are shown. **Right.** Top *m/z* classifiers across the six prostate tissue types ranked by mean decrease accuracy shows tentative lysophospholipids to be more prominent in benign tissue compared to tumour.



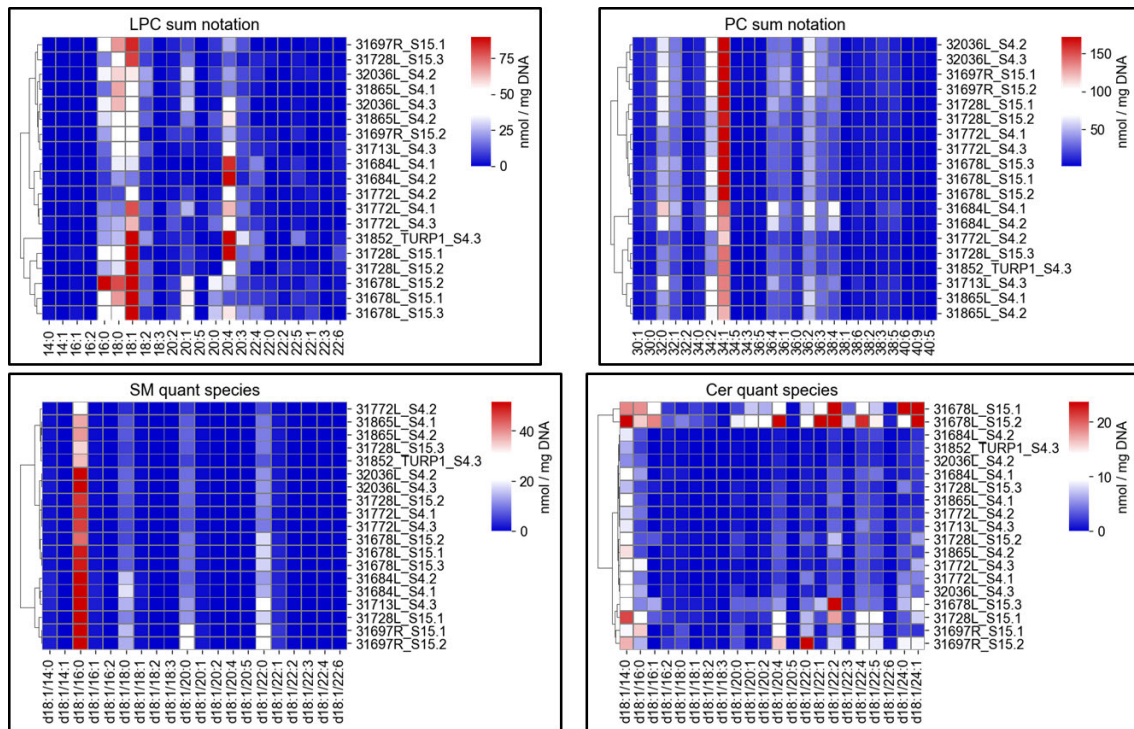
Supplementary Figure 5. PLS-DA model biplot, including feature weights (contribution to variance by mass) on the first two latent variables, and benign, stroma and tumour classes. The top 10 masses by total contribution to model variance are labeled.



Supplementary Figure 6. Visualization of strength of m/z feature correlation with benign, stroma, and tumour classes through PLS regression coefficients. Negative and positive coefficients indicate negatively or positively correlated m/z features. **Left.** Histograms of coefficient distributions for each class. **Right.** Per-feature correlation with each class.



Supplementary Figure 7. Visualization of all PLS-DA classifier predictions on 11 different tissue sections. Each pixel is coloured with a gradient corresponding to whichever class (benign, stroma or tumour) has the greatest prediction score.



Supplementary Figure 8. Lipidomics data analysis. Matched cryosections (n=3) adjacent to MALDI MSI tissue sections were analysed by LC-ESI-MS/MS across 10 patients. Heatmap plots of lysophosphatidylcholines (LPC), phosphatidylcholine (PC), sphingomyelins (SM) and Ceramide (Cer) classes of lipid species are shown. LPCs are denoted by fatty acyl chain composition and total number of unsaturated carbons. PCs presented as total fatty acid composition of the 2 acyl chains at *sn-1* and *sn-2* and total number double bonds. SM and Cer lipids are presented as a sphingoid base of d18:1 at *sn-1* position with varying fatty acyl composition at N-acyl group that is either saturated or unsaturated. Only quantitative values expressed as nmol/mg DNA based on total DNA assay my Hoechst staining are considered.

CHAPTER 5:

Development of an LC-MS/MS Method for Quantification of Enzalutamide Uptake in Prostate Explant Culture System

Context

This Chapter describes the development and validation of a bioanalytical LC-MS/MS method for the quantification of the second-generation androgen receptor (AR) inhibitor, enzalutamide, in patient-derived explant (PDE) tissue homogenates and tissue culture medium. For the spatial distribution of enzalutamide in prostate tissue work described in [Chapter 6](#) of this thesis, it was critical to have an accurate and independent overall concentration of the drug not only in explant tissue, but also the dosed culture medium.

5.1. Introduction

Enzalutamide action *in vivo* stems cancer cell proliferation ultimately effecting apoptosis and reduced tumour volume⁴³⁷. Enzalutamide is metabolised by hepatic enzymes CYP3A4 and CYP2C8 to *N*-desmethylenzalutamide which remove a methyl group^{15,438}. Moreover, the major route of elimination is via hepatic metabolism. Systemically, both enzalutamide and *N*-desmethylenzalutamide exhibit high plasma protein binding at 97.5% and 95% , respectively. The drug is also known as MDV-3100 and marketed as Xtandi® (Table 5.1). <https://www.drugbank.ca/drugs/DB08899>.

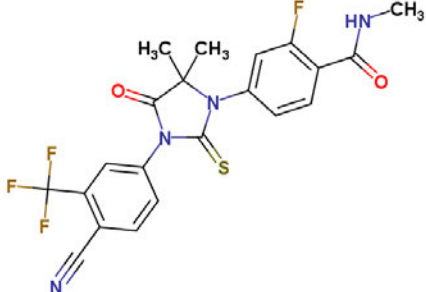
Structure	Property	Value
	Molecular weight	464.0930
	Water solubility	0.00136 mg/ml (insoluble)
	LogP (lipophilicity)	4.16
	Hydrogen Bond Acceptors	3
	Hydrogen Bond Donors	1
	Polar surface area	76.44 Å ²
	No. of Lipinski's rules broken	0

Table 5.1. Key physicochemical descriptors of enzalutamide. Properties simulated using MarvinSkecth 18.19.0 (ChemAxon Ld)

Validation of enzalutamide and *N*-desmethylenzalutamide, and other androgen targeting agents, abiraterone and bicalutamide has been performed previously human plasma⁴³⁹. They used an Agilent 1200 SL autosampler with Synergi Polar-RP column coupled to ABI SCIEX 4000 QTrap system with a gradient method. Uncommonly, their experimental method monitored C₁₃ isotopes of the enzalutamide and its metabolite due to efficient ionisation of their protonated adducts which were found too sensitive for the detector. Others have also described the quantitation of multiple androgen analogues in human

serum⁴⁴⁰. A method has also been reported in literature for quantification of enzalutamide in rat plasma also using an Agilent 1200 HPLC system⁴⁴¹. More recently, enzalutamide has been validated alongside its subsequent analogue successors, apalutamide and darolutamide together with its active systemic metabolite, ORM-15341, and applied to a pharmacokinetic study in mice⁴⁴². The key principles of the bioanalytical assay parameters following US FDA guidelines⁴⁴³ are outlined accordingly in the methods and results of this method development and validation report.

An LC-MS/MS quantification method was developed to assess the uptake and penetration of enzalutamide (ENZ) in the explant culture system of our laboratory. To the best of my knowledge is the first time a quantitative ENZ assay has been developed for measuring drug concentration in medium and tissues in *ex vivo* or *in vitro* experimental settings.

5.2. Experimental Approach

5.2.1. Set up of Mass Spectrometry Conditions

The AB SCIEX 4000 QTrap turbo spray ion source had the following settings: curtain gas, 10 psi; ion spray voltage, 5500 V; temperature, 450.0°C, ion source gas 1, 12 psi, ion source gas 2, 0 psi and heater interface on. The identification of characteristic enzalutamide ion was carried out by direct infusion into the ESI source. 10 nM ENZ was made in CH₃OH-H₂O 1:1 (v/v) from a stock solution of 10 mM ENZ. 500 µL was aspirated into Hamilton syringe with a diameter of 3.26 mm and flow rate set at 10 µL/min. The procedure for optimisation of analyte and internal standards in positive ion mode was based on an established SAHMRI internal protocol/instrument manufacturer's guideline.

Briefly, the scanning of ions was conducted in manual tuning mode. First, Q1 scan mode, ions were passed through the Q1 mass filter with a mass window covering the theoretical precursor ion. The most prominent ions were recorded. A multiple channel acquisition of the ions of interest was performed within ± 10 amu at 1 sec. Second, in Q1 multiple ion mode, once a stable signal was established, the declustering potential (DP) was then optimised by ramping the voltage from 1 V to 200 V with a step of 2 V and the signal smoothed twice before proceeding. Then, the exit potential (EP) was optimised at a range of 1 V – 15 V. Third, in Q1 product ion mode, product ions were identified by monitoring the precursor ion of interest at a scan range of 50 up to and 50 amu higher than the precursor mass with a single incremental step of collision energy (CE) voltage ranging from 1 V to 130 V using the edit ramp feature. The loss of the most prominent product ions was observed between 25 V and 80 V and the most

suitable CE setting was chosen. The most dominant product ion was designated quantitation ion and secondary ions as confirmation ions. Fourth, in multiple reaction monitoring (MRM) mode, the optimisation of the identified precursor/product ions transitions were conducted. Here, the mass transition of the precursor and products were entered as exact masses and monitored for 200 msec. The CE readings were taken at least five times and average taken. Finally, with the optimisation of the CE values, the collision exit potential (CXP) energy for each individual product ion transition was optimised. The CXP ramp ranged from 0 V to 55 V at step of 2 V, with two times signal smoothing. CXP readings were taken at least 5 times. A summary of the results of the established mass spectrometry conditions is shown in **Table 5.2**.

Enzalutamide Ion								
Q1 Mass (Da)	Q3 Mass (Da)	Time (msec)	Fragment Ion ID	Declustering Potential (volts)	Exit Potential (volts)	Collision Energy (volts)	Collision Exit Potential (volts)	
465.1	380.2	50	Confirmation 1	130.0	13.0	36.0	10.0	
465.1	209.2	50	Quantitation	130.0	13.0	39.0	13.0	
<i>465.1</i>	<i>178.2</i>	<i>50</i>	<i>Confirmation 2</i>	<i>130.0</i>	<i>13.0</i>	<i>55.0</i>	<i>10.0</i>	
Deuterated [² H ₆]-enzalutamide								
Q1 Mass (Da)	Q3 Mass (Da)	Time (msec)	Fragment Ion ID	Declustering Potential (volts)	Exit Potential (volts)	Collision Energy (volts)	Collision Exit Potential (volts)	
471.1	380.0	50	Confirmation 1	130.0	11.0	37.0	25.0	
471.1	215.1	50	Quantitation	130.0	11.0	41.0	14.0	
<i>471.1</i>	<i>184.0</i>	<i>50</i>	<i>Confirmation 2</i>	<i>130.0</i>	<i>11.0</i>	<i>53.0</i>	<i>11.0</i>	
N-desmethylenzalutamide								
Q1 Mass (Da)	Q3 Mass (Da)	Time (msec)	Fragment Ion ID	Declustering Potential (volts)	Exit Potential (volts)	Collision Energy (volts)	Collision Exit Potential (volts)	
451.1	178.1	50	Confirmation 1	130.0	10.0	54.0	12.0	
451.1	195.1	50	Quantitation	130.0	10.0	40.0	13.0	
[² H ₆] - desmethylenzalutamide								
Q1 Mass (Da)	Q3 Mass (Da)	Time (msec)	Fragment Ion ID	Declustering Potential (volts)	Exit Potential (volts)	Collision Energy (volts)	Collision Exit Potential (volts)	
457.1	184.0	50	Confirmation 1	130.0	10.0	54.0	12.0	
457.1	201.1	50	Quantitation	130.0	10.0	40.0	13.0	
<i>457.1</i>	<i>158.1</i>	<i>50</i>	<i>Confirmation 2</i>	<i>130.0</i>	<i>10.0</i>	<i>58.0</i>	<i>10.0</i>	

Table 5.2. Shows the established MS method for the analyte - enzalutamide.
m/z transition values in italics not included in final MRM method.

5.2.2. Set up of Liquid Chromatography Conditions

Once the MS conditions were established, the chromatography conditions were developed using An Acquity UPLC BEH C18 column (1.7 μm particle size 2.5 mm ID and 50 mm length). The column temperature was set at 30°C, solvent A 0.1% aqueous formic acid and solvent B 99.9% acetonitrile-0.1% formic acid.

To select the most appropriate elution method the peak shape of the eluted drug on the chromatogram was considered. An isocratic elution was not preferred because it would not have yielded sharp peaks (broad base of lower intensity indicating compound/drug elutes gradually). Moreover, carry over effects were more likely with isocratic elution. A gradient elution with up to a 10 min run-time was developed. The final linear gradient had a run time of 7.4 min. Elution of ENZ was observed approximately at 3.03 min. **Figure 5.1** shows the flow rate and solvent composition during the run time in for the selected liner gradient method.

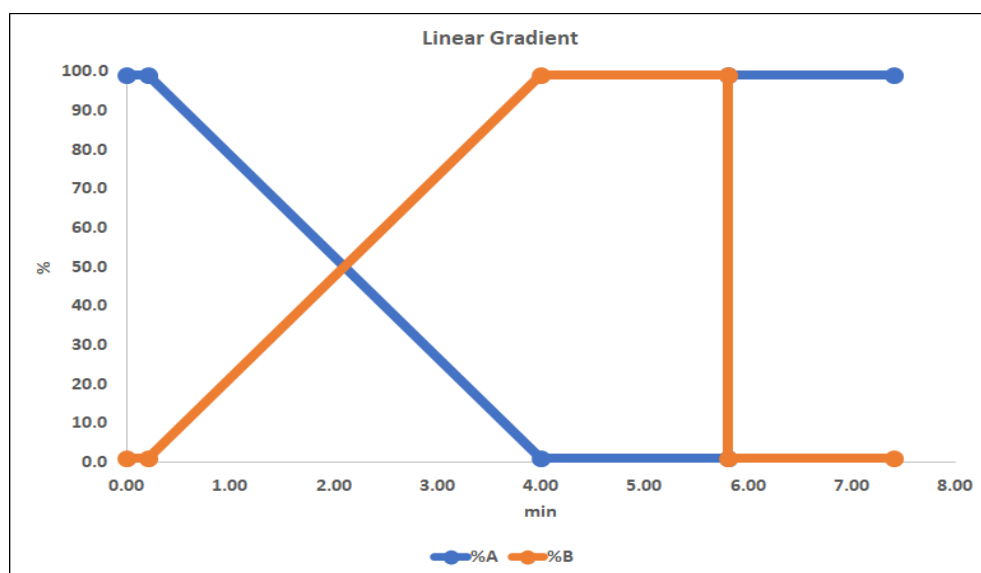


Figure 5.1. Graphical profile of the chromatographic elution conditions.

5.2.3. Establishment of Linear Range

Initially, the primary stock of ENZ in 50 μL of 10 mM in DMSO was diluted to a concentration of 10 μM (10,000 nM) in methanol-water 1:1 (v/v). The linear range of the method was determined by making a 10-fold dilution series with 1,000 nM solution as the highest starting concentration as shown in **Table 5.3**. Additionally, another dilution series starting with 1,080,000 nM as the highest “standard” was checked and the response is shown in **Table 5.4**.

	Concentration (nM)	Response (Peak Area)	%CV
MDV Standard 01	1.00e+03	1.08e+06	8.5
MDV Standard 02	1.00e+02	1.38e+05	5.1
MDV Standard 03	1.00e+01	1.43e+04	5.8
MDV Standard 04	1.00e+00	1.53e+03	2.1
MDV Standard 05	1.00e-01	3.03e+02	9.9
MDV Standard 06	1.00e-02	1.93e+02	20.6
MDV Standard 07	1.00e-03	2.24e+02	5.6
MDV Standard 08	1.00e-04	2.15e+02	15.4
MDV Standard 09	1.00e-05	4.30e+02	11.2

Table 5.3. Standard concentration for testing the linear range of instrument response – lower end. Means of three replicate injection is shown for each concentration.

	Concentration (nM)	Response (Peak Area)	%CV
MDV Standard 01	1.08e+06	5.55e+07	0.5
MDV Standard 02	1.08e+05	3.56e+07	2.8
MDV Standard 03	1.08e+04	1.22e+07	2.2
MDV Standard 04	1.08e+03	1.76e+06	0.3
MDV Standard 05	1.08e+02	2.39e+05	2.2
MDV Standard 06	1.08e+01	9.05e+04	2.4
MDV Standard 07	1.08e+00	1.88e+03	2.2
MDV Standard 08	1.10e-01	6.48e+03	4.7

Table 5.4. Standard concentration for testing the linear range of instrument response – upper end. Means of three replicate injection is shown for each concentration.

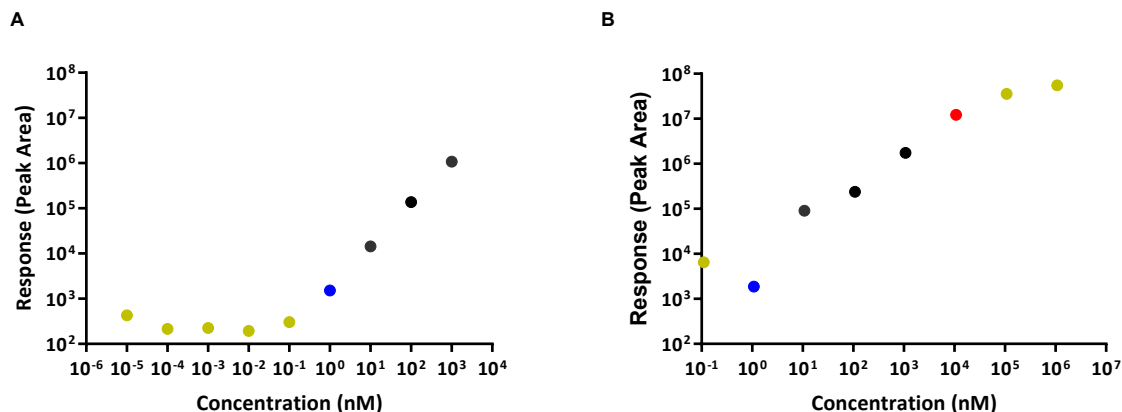


Figure 5.2. Linearity of instrument response. Analyte signal measured by peak area as a function of concentrations. Ten-fold dilutions of ENZ with a starting concentration of **A.** 1.0×10^3 nM **B.** 1.08×10^6 nM.

The linear range of the instrument was projected to lie between 1 nM (**Figure 5.2A**, blue dot) and 10,800 nM (**Figure 5.2B**, red dot). Loss of linearity of instrument response as a function of standards was caused by saturation of the detector at the higher concentrations or insufficient ions at the lower concentrations. Considering this, the calibration curve was carefully validated as described in section **5.3.5.1** and **5.3.5.2**.

5.2.4. Establishment of Drug Extraction

Originally, two sample preparation methods of drug extraction were evaluated, crude extraction by protein precipitation and a modified Folch extraction²⁷¹. Both methods, in theory aimed to isolate and concentrate the moderately lipophilic enzalutamide (predicted LogP = 4.16) from a protic solution, such as culture medium or tissue homogenate, to a hydrophobic phase. An explant culture was simulated by incubating a 24-well treatment plate without actual human prostate *ex vivo* specimens. The treatment dose used was 50 μ M. 510 μ L out of 2,000 μ L sample volume in each well was transferred to an Eppendorf tube after 48 h.

For the protein precipitation approach, 100% acetonitrile was added to 250 μ L M4 media 4:1 (v/v). The sample tubes were vortexed at 1,000 rpm/min for 10 min and centrifuged at 16,060 *rcf* for 16 min. Supernatant was then transferred to clean pre-labelled 10 ml glass tubes and precipitate discarded. Samples were then dried under nitrogen at 38°C overnight. The dried phase of the supernatant was reconstituted with 200 μ L of methanol-water 1:1 (v/v) (solvent blank).

For the Folch extraction approach, 125 μ L of spiked medium was transferred to a 10 ml glass tube. 2 ml CHCl₃-CH₃OH 2:1 (v/v) was added to each sample. Tubes were briefly inverted to check for leaks, mixed on a tube rotator for 10 min at 40 rpm and left to stand on the bench for 50 min. Samples were partitioned with addition of 0.2 volumes of MilliQ water (0.4ml) and mixed on a tube rotator for 10 min at 40 rpm. Tubes were then centrifuged at 2,689 *rcf* (3,500 rpm) for 5 min using a centrifuge (Megafuge 40R, Heraeus, ThermoScientific, Australia). A glass Pasteur pipette was used to transfer the upper aqueous layer to a clean glass tube. The lower hydrophobic phase was also transferred to a

clean glass tube whilst carefully avoiding the protein interphase. In a fume hood, both these phases were dried overnight under nitrogen gas at 38°C. Samples were then reconstituted with 100 µL solvent blank. 5 µL of a 1:100 dilution reconstituted samples were injected for LC-MS/MS analysis.

After, an explant culture with human tissue specimens was set up with 10 µM ENZ treatment dose. Protein precipitation and Folch extraction were evaluated as described.

5.2.5. Preparation of Stock Solutions

Working solutions of ENZ were prepared from 10 mM 50 µL aliquots in DMSO. Internal standards (IS) were prepared from standard commercially weighed powder stocks ~1 mg. 10 µM aliquots of the IS were made in DMSO kept at -20°C. Working solution was prepared by thawing out 1 ml of 10 µM IS stock solution and adding 9 ml of absolute solvent (DMSO or acetonitrile) to achieve a concentration of 1.0 µM. 500 µL aliquots of these were kept at -20°C and used on the day of the assay.

To design the protocol, it was important to check the integrity of the drug at laboratory working conditions. The stability of ENZ at working QC concentrations was initially pre-evaluated at autosampler conditions, 4°C - 6°C.

5.2.6. Bioanalytical Method Validation Procedures

The validation of LC-MS/MS method was performed according to USA FDA guidelines for bioanalytical method validation⁴⁴³. The primary objective was to establish the robustness of the accuracy and precision of the method. The secondary objectives were to test the recovery efficiency of the method and perform drug stability testing. The rationale was to assess stability of enzalutamide in M4 culture (AR antagonist) medium and explant homogenates during the processing and storage container conditions.

The validation parameters tested were selectivity, matrix effect, accuracy and precision, recovery, calibration curve linearity and stability. **Selectivity** was tested by analysis of six blank samples of the biological matrix from independent sources. The tissue homogenate was a combined pool from 10 different patients' biopsies, where 1-2 mm³ pieces were pulverised in solvent blank in Precellys tubes. Each blank was required to be tested for interference and selectivity demonstrated at the lower limit of quantification (LLOQ). **Specificity** was assessed by observing the crosstalk between MRM MS/MS channels of the ENZ and [²H₆]-ENZ at the LLOQ. **Calibration curve** for ENZ consisted of blank samples (biological matrix processed without internal standard), a zero unextracted sample (solvent blank with IS) or a zero sample (matrix processed with IS), eight neat or spiked standard samples for extraction including the LLOQ), four neat or extracted quality control (QC) samples - LLOQ, low QC (LQC), medium QC (MQC) and high QC (HQC). The calibration curve was described by linear regression equation where the concentration (x) was weighted by 1/concentration (x²) to achieve a good fit – concentration-detector response.

Accuracy and **precision** were measured using six replicates per concentration and with four QC concentrations in the expected range. The deviation of the mean from the true value serves as the measure of accuracy and was expressed as a percentage. The mean value should be within 15% of the actual value except at the LLOQ, where it may deviate up to 20%. Intra-batch precision (within-run or repeatability) and inter-batch precision (between run) were determined at each concentration which should not have exceeded 15% of the coefficient of variation (CV) except for the LLOQ, at 20% CV.

The assessment of **matrix effects**, **recovery efficiency** and **process efficiency** parameters were assessed at four QC levels in a manner analogous to described by Matuszewski *et al*⁴⁴. A full outline is provided in [Appendix 2 Supplementary Table 5.1](#). Matrix effect is the ratio of analyte/IS spiked after extraction to neat, recovery efficiency is the ratio of analyte/IS spiked after extraction to analyte/IS spiked before extraction and process efficiency is the ratio of analyte spiked before extraction relative to neat, which is identical to the product of matrix effect and recovery efficiency expressed as a percentage. The recovery parameters of ENZ using the extraction method included the internal standard mix of 50 μ L [²H₆]-ENZ and 50 μ L [²H₆]-desmethylENZ) at a concentration of 100 ng/ml, where absolute DMSO or 100% acetonitrile were the IS diluents for the M4 medium and TH samples extraction experiments, respectively.

Stability testing used defined QC concentrations of spiked biological matrices (M4 medium and TH samples) and readings were gauged against fresh-extracted QC samples in the same analytical run. Multiple parameters of stability testing were evaluated. A full outline is provided in [Appendix 2 Supplementary](#)

Information. For, **short-term stability**, three aliquots of each of the LLOQ, LQC, MQC and HQC concentrations were prepared at room temperature and kept at ambient conditions on top of the laboratory working bench for 18 - 20 h and analysed. For, **post-preparative stability**, the stability of processed samples, including the resident time in the autosampler was determined. Three aliquots of each of the LLOQ, LQC, MQC and HQC concentrations were placed in the Acquity UPLC autosampler and kept a temperature of 6°C for at least 20 h in separate sealed wells. For, **freeze-thaw cycle stability**, three aliquots of each of the LLOQ, LQC, MQC and HQC concentrations were prepared and kept at -20°C and -80°C until the day of the assay. Samples were thawed unassisted at room temperature for 12 h until completely thawed and refrozen for 12 h under the same conditions. The freeze–thaw cycle was repeated two more times and tested on the third cycle. For, **long-term stability**, three aliquots of each of the LLOQ, LQC, MQC and HQC concentrations were stored under the same conditions as the study samples which were kept at -80°C.

In **stock-solution stability**, a new powder stock of ENZ was weighed out. The balance was calibrated prior to use using Mettler Toledo (Serial No. B807438294) standard weights covering the measurement range (10 mg). The new ENZ stock was reconstituted in DMSO identical to the old stock. New stock QC samples were analysed on the day of drug reconstitution together with old QC samples prepared from 10mM stocks in -20°C and -80°C conditions.

5.2.7. Data Analysis

The LC-MS/MS data were processed using Analyst (Analyst 1.62, AB Sciex). The datafiles (.wiff and .scan files) were processed using a quantitation method tuned to measure the peak intensities at the expected elution times. The analytes, enzalutamide (ENZ) and *N*-desmethylENZ and IS ($[^2\text{H}_6]$ -ENZ, $[^2\text{H}_6]$ -desmethylENZ) peaks were checked for appropriate retention times, 3.0 min and 2.8 min +/- 30 sec, respectively. Next, the peak integration parameters were configured to a smoothing radius of 2 and bunching factor of 1-3. Automatic peak integration of all the peaks was manually checked and adjusted when necessary. The run criteria included checking if each IS responses was within 30% of the mean extracted response of all samples. The tabulated concentration for each QC samples was within 15% threshold (except for the LLOQ which is 20%). Interferences were assessed by including a biological matrix blank, unextracted IS solution and a spiked biological matrix of IS solution.

5.3. Results

5.3.1. Mass spectrometry conditions

The fragmentation pattern of deuterated analogue ought to be identical to the analyte for it to be a reliable analytical internal standard. The results of the positive ion mode optimisation from the CE values unique to the drug and IS in **Table 5.1** are described. The structural configuration of the fragment ions of the drug and internal standard precursor ions were created in MarvinSketch version 18.19 (Chemaxon). The monoisotopic masses were in conformity with the nominal molecular weights of the MRM method and also match literature reports. **Figure 5.3.** outlines. ENZ, m/z 465.1 dissociates into the predominant fragment ions, m/z 209.1 which is used for quantitation and m/z 380.2 and m/z 178.2 which were used as confirmation ions. Deuterated standard, [$^2\text{H}_6$]-ENZ, follows the same structural fragmentation pattern, with the precursor m/z 471.1 forming the main ion m/z 215.1 and a confirmation ion, m/z 184.0. The MRM method also included the theoretical molecular mass of the metabolite of ENZ, with a precursor mass of m/z 451.1, which formed the quantitation ion m/z 195.1 and a confirmation ion, 178.2 identical also the ENZ fragment ion. The deuterated analogue, [$^2\text{H}_6$]-desmethylENZ, precursor ion at m/z 457.1 formed the quantitation ion m/z 201.1 and confirmation ions, m/z 184.1 and m/z 158.1.

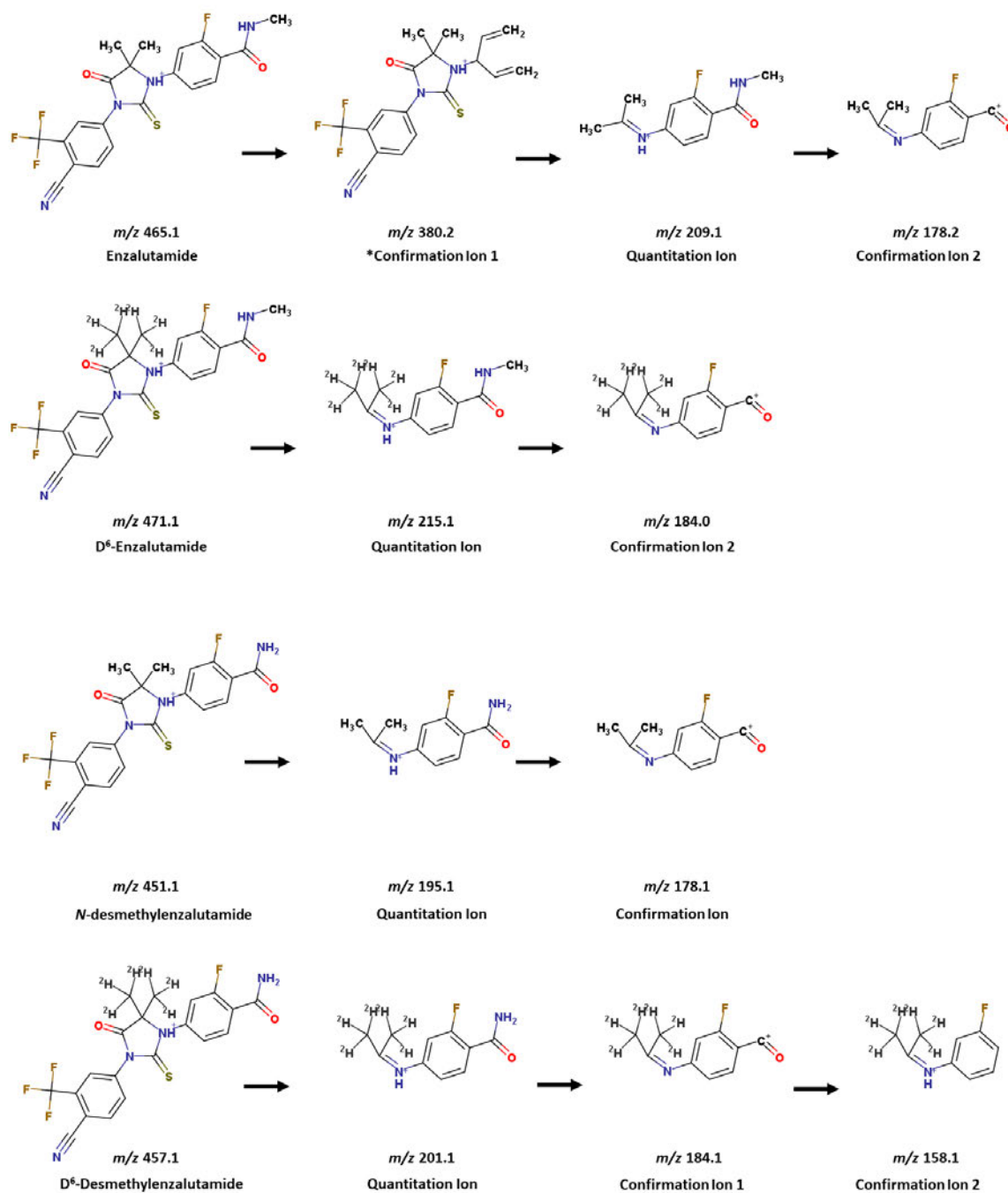


Figure 5.3. Chemical structures of analyte and internal standard ions. Arrow indicated CID fragmentation of precursor (parent) ions selected at Q1 to yield subsequent fragment (daughter) ions detected at Q3 after application of unique CE values in Q2.

5.3.2. LC-MS/MS conditions

Following the optimised ion fragmentation measurements above, an MRM method with 8 pairs of transitions was set to achieve optimum sensitivity. Here, coupling the MS/MS conditions to the established UPLC conditions abundant fragment ions of both enzalutamide and internal standards were obtained as dominantly protonated molecular ions. ENZ and [$^2\text{H}_6$]-ENZ quantitation and confirmation ions eluted at 3.0 min and the monitored [$^2\text{H}_6$]-desmethylENZ fragments eluted at 2.8 min as shown in **Figure 5.4**.

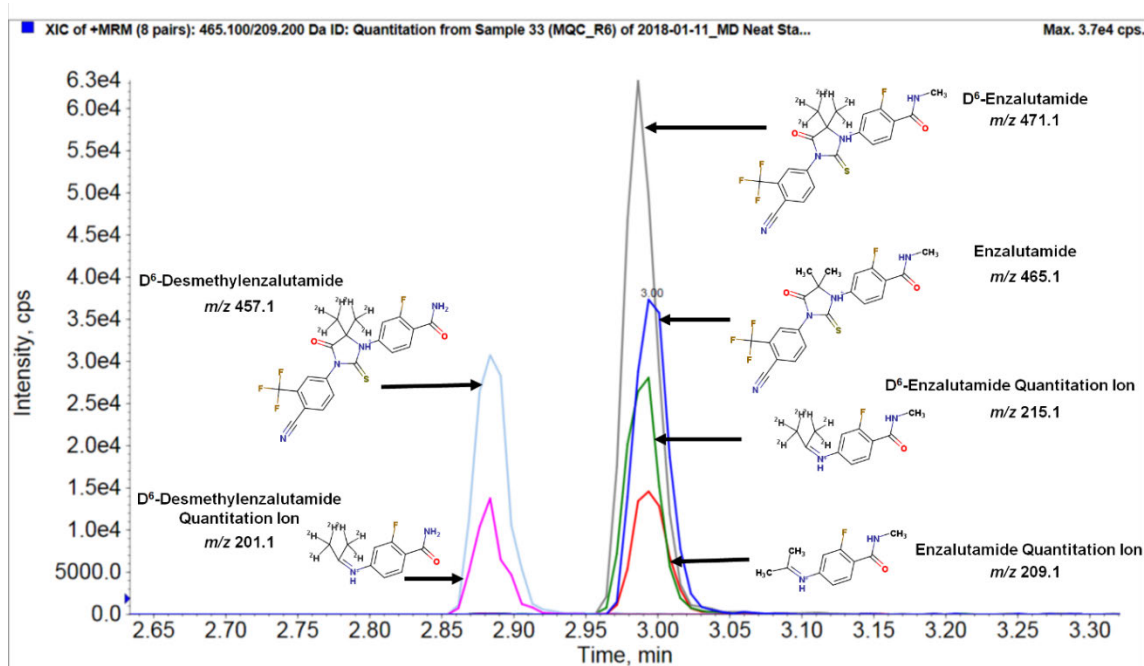


Figure 5.4. Chromatogram of enzalutamide and internal standards.

5.3.3. Establishment of Drug Extraction

The purpose for this method development was test the feasibility of isolating ENZ from biological matrices. Two drug extraction approaches were evaluated. 50 μM of dosed culture medium was subjected crude extraction by protein precipitation versus Folch extraction. In **Table 5.5**, the data indicates that both methods appeared to achieve segregation of the drug from medium, with at least five orders of magnitude in signal difference of the drug samples compared to controls. It was also observed that at least 95% of the drug partitions into the lower hydrophobic phase using the Folch extraction method. The protein precipitation method was more efficient and experimentally more straight-forward compared to the Folch approach.

Samples	Concentration	Intensity (cps)
Blank	-	50
DMSO Crude Extraction_100X	-	275
DMSO Folch Aqueous_100X	-	130
DMSO Folch Hydrophobic_100X	-	115
MDV Crude Extraction_100X	0.5 μM	902,000
MDV Folch Aqueous_100X	0.5 μM	920
MDV Folch Hydrophobic_100X	0.5 μM	212,000

Table 5.5. Method development for drug extraction from cultured medium. Comparison of crude extraction by protein precipitation and Folch extraction in spiked cultured M4 medium samples by LC-MS/MS.

Further method development was then performed using cultured explant tissue incubated for 48 h at a dose of 10 μM treatment. Both protein precipitation and modified Folch extraction were performed as earlier described. **Figure 5.5.** shows a summary of the results. After 48 h of treatment, it was evident that drug amount in medium tended to decline. Importantly, there was appearance of adequate drug in cultured tissue which was well above the baseline level of the

untreated fresh-frozen and control specimens. The apparent decrease in drug amount in medium cannot be judged to be significant given that the accuracy and precision of the method was not tested at this point. The principle of testing the extraction was to ascertain if drug could be isolated and detected following culture and the protein precipitation method was subsequently advanced as it was more conducive.

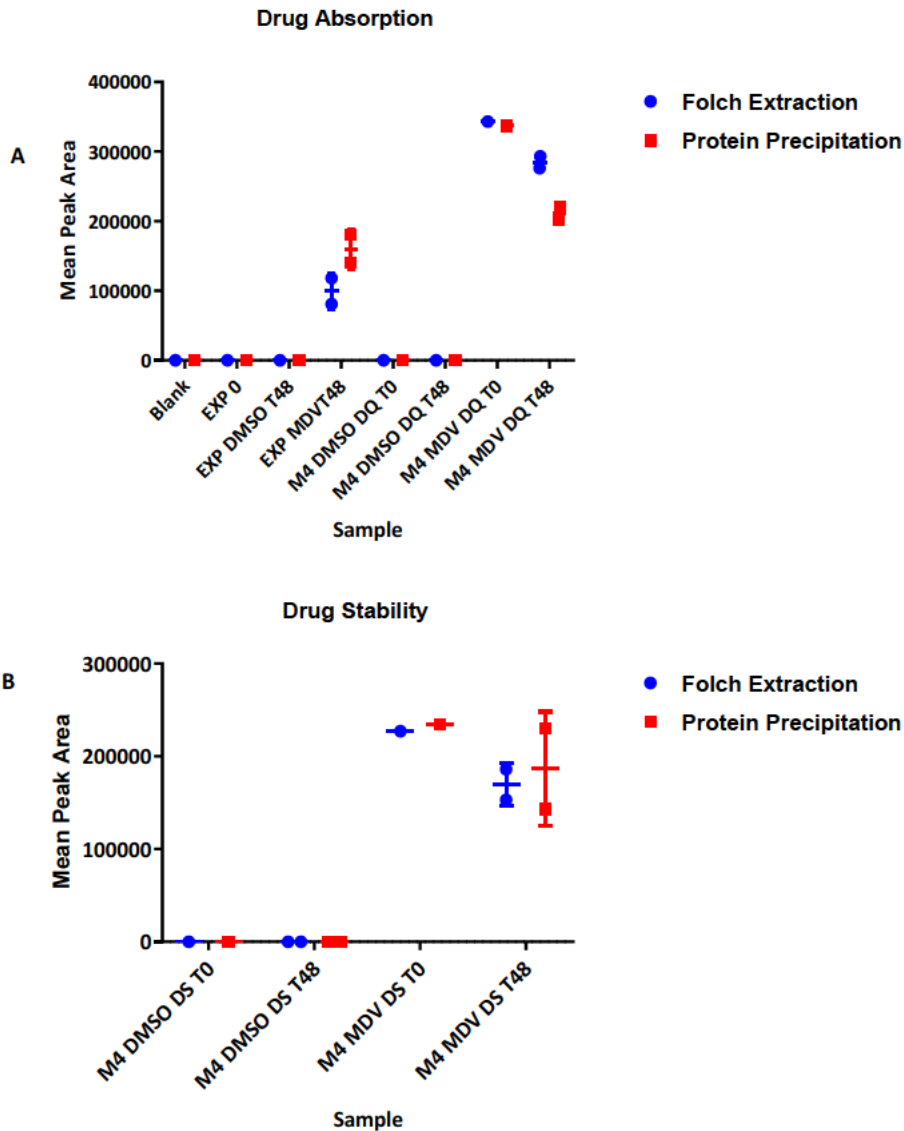


Figure 5.5. Method development for drug extraction from cultured medium and explant tissue. Comparison of protein precipitation and Folch extraction in cultured M4 medium and explant tissue homogenate samples by LC-MS/MS. **A.** Quantitation assay (DQ) to check for detection of absorbed drug int PDE tissue following culture. **B.** Assessment of stability (DS) to check differences between pre- and post-incubation wells without explant tissue. EXP – explant. T- time.

5.3.4. Sample Handling of Prepared Calibration and QC Samples

The stability of the analyte (ENZ) at working QC concentrations in neat solutions was checked at autosampler conditions. Here, sample stability in the plastic 96-well plates was checked.

Autosampler conditions resemble that of a standard laboratory refrigerator (4°C-6°C). Fresh standard and adequate volumes of QC samples of ENZ spiked with internal standards (IS) at a concentration of 100 ng/ml were prepared. 65 µL of fresh neat analyte QC solutions was aliquoted to six separate 96-well plate. 100 µL of QC solutions was aliquoted to three separately sealed wells on the same plate. The autosampler samples resided for the duration of the initial assay and tested after 20 h. The analyte response (peak area) was normalised to the change of the IS response (autosampler/fresh sample) as shown in **Table 5.6**.

Overall, the implications of the autosampler stability measurements was to perform the entire technical procedure from sample preparation, starting with reconstitution of the analyte and IS, up to programming the analytical run within a few of hours to avoid potential analyte/IS loss and to maintain sufficiently reproducible measurements for the bioanalytical method validation procedures. Importantly, this data also demonstrated that it was appropriate to store an already aliquoted sealed 96-well sample plate at 4°C – 6°C (refrigerator) or colder (-20°C freezer) in case, of any technical issues that would delay conducting the LC-MS/MS assay or necessitate re-analysis.

	Fresh Peak Area	Autosampler Peak Area	IS Peak Area Ratio Change	Expected (ng/ml)	Measured (ng/ml)	Back calculated PPS (ng/ml)	Stability
LLOQ	1.812e+03	1.757e+03	9.42e-01	3.0	3.2	3.0	94.2%
MQC	2.715e+04	2.417e+04	8.93e-01	50.0	52.1	46.5	89.3%
HQC	4.067e+05	3.797e+05	9.35e-01	800.0	810.0	757.6	93.5%

Table 5.6. Stability of enzalutamide at post-preparative (autosampler) conditions. Freshly prepared neat solution of analyte (mean of n=6 replicates) were assayed and compared to analyte solution in separate-sealed wells (mean of n=3 replicates). Concentrations of PPS QC samples were back calculated by multiplying the IS response fold change with measured fresh concentrations. Stability is expressed as a percentage of back-calculated PPS values to measured fresh concentrations. PA – peak area measured as cps.

5.3.5. Method Validation Parameters

5.3.5.1. Selectivity and Specificity

There is always potential of crosstalk when measuring the quantification ion analyte of interest by interference of the internal standard quantification ion within the same MRM transmission window. Here, 2 ng/ml and 3 ng/ml neat concentrations of ENZ were tested for this interference by injection of a neat zero solution (IS only) and checking the percentage response of the analyte ion.

The peak area response of m/z 209.1 (ENZ) detected in the deuterated IS channel was 0.5% indicating that the deuterated analogue of the analyte was not completely pure. At 2 ng/ml and 3 ng/ml amounts, the IS interference was 17.1% and 10.7%, respectively as shown in **Table 5.7** below. The highest level of acceptable interference at the LLOQ is 20%. Thus, to sufficiently overcome interference at any given day of the assay, the LLOQ and LQC needed to be marginally adjusted upwards. Following this, the accuracy and precision was verified in three independent experiments, with 3 ng/ml and 8 ng/ml, set as the LLOQ and LQC standard concentrations, respectively. A calibration curve with a standard at the equivalent LLOQ concentration was included in subsequent validation experiments.

	Peak Area Analyte Quantification Ion MRM	Peak Area IS Quantification Ion MRM	Cross- talk
Solvent Blank 1	3.07e+03	4.56e+02	—
Solvent Blank 2	1.54e+02	0.00e+00	—
Solvent Blank 3	7.68e+01	0.00e+00	—
Solvent Blank 4	4.56e+01	0.00e+00	—
Zero*	6.20e+02	1.33e+05	0.5%
2ng/ml [^]	3.63e+03	1.19e+05	17.1%
3 ng/ml [^]	5.78e+03	1.16e+05	10.7%

Table 5.7. Cross talk between a neat solution of zero IS with the analyte MRM channel. [^]values are means of n=10 consecutive injections. *means of n=3 injections.

5.3.5.2. Calibration Curve in Neat Solution

The calibration curve in neat solution was established first using the calibration curve preparation sheet shown in **Table 5.8**. Standard curve fitting was applied, where the reciprocal of the squared concentration as a predictor of the analyte response ($1/x^2$), to yield a model that sufficiently described the concentration-response relationship (calibration curve) with an R-squared (R^2) value of 0.9993 as shown in **Figure 5.6**. Carry over was measured by dividing the peak area of a solvent blank succeeding a standard sample in the analytical run. The carry over at the highest standard (2), 1,000 ng/ml, was 0.22%. and lowest standard (9), 3 ng/ml was 0.95% (**Figure 5.7**).

The limit of detection (LOD) is defined as the lowest concentration of an analyte that can be reliably differentiated from background noise was checked. Many times LOD is regarded as a signal-to-noise ratio of greater than three⁴⁴⁵, but “reliability” is not specifically defined which makes the definition of LOD to be ambiguous as contamination can give rise to false positive and false negative results as argued by Evard *et al.* In this method validation report, the LOD was

set at 10 nM (1 ng/ml) because at this analyte concentration the IS interference (crosstalk) was 30.19%. Furthermore, the accuracy at 1 ng/ml did not consistently satisfy the 20% cut-off. Therefore, the lowest standard (10) 1 ng/ml was excluded from the quantitation (**Figure 5.6**). On the other hand, the upper limit of quantification (ULOQ) defined as the highest concentration of the standard curve that can be measured with acceptable accuracy was established at ~10,800 nM (1,000 ng/ml), which was also the highest standard (2).

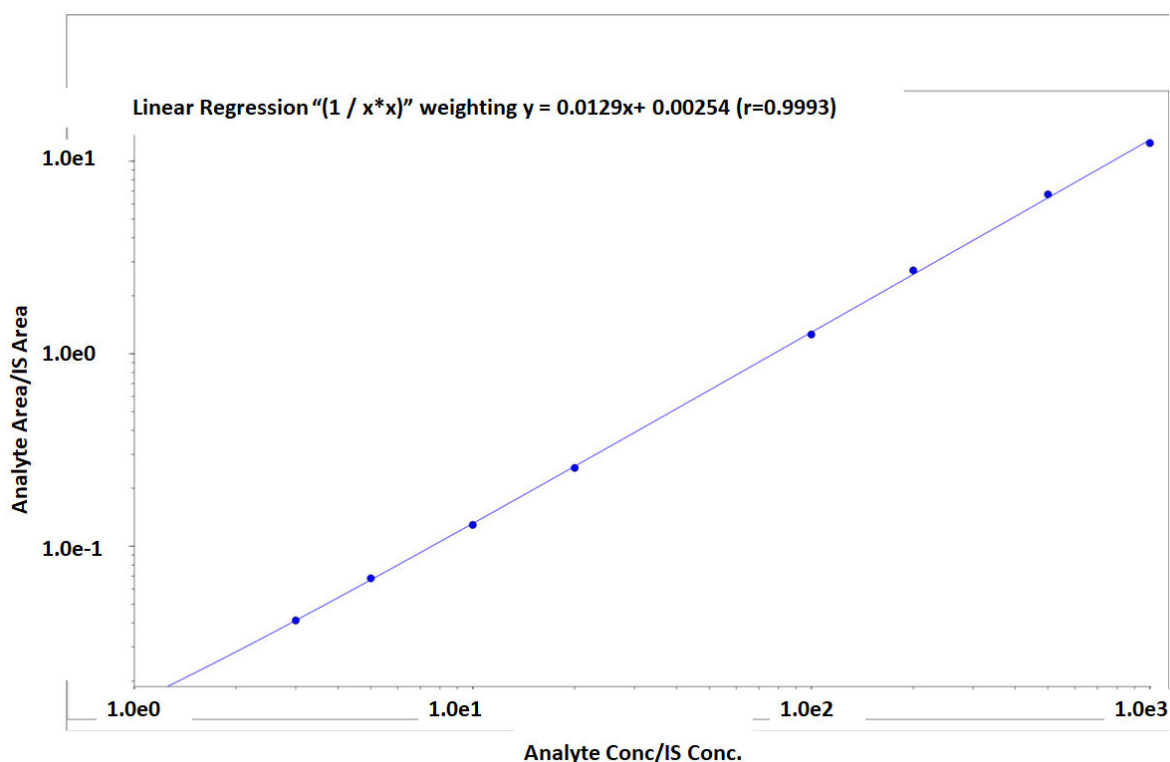


Figure 5.6. Calibration curve in neat solution. The regression coefficient of determination (R^2) = 0.9993.

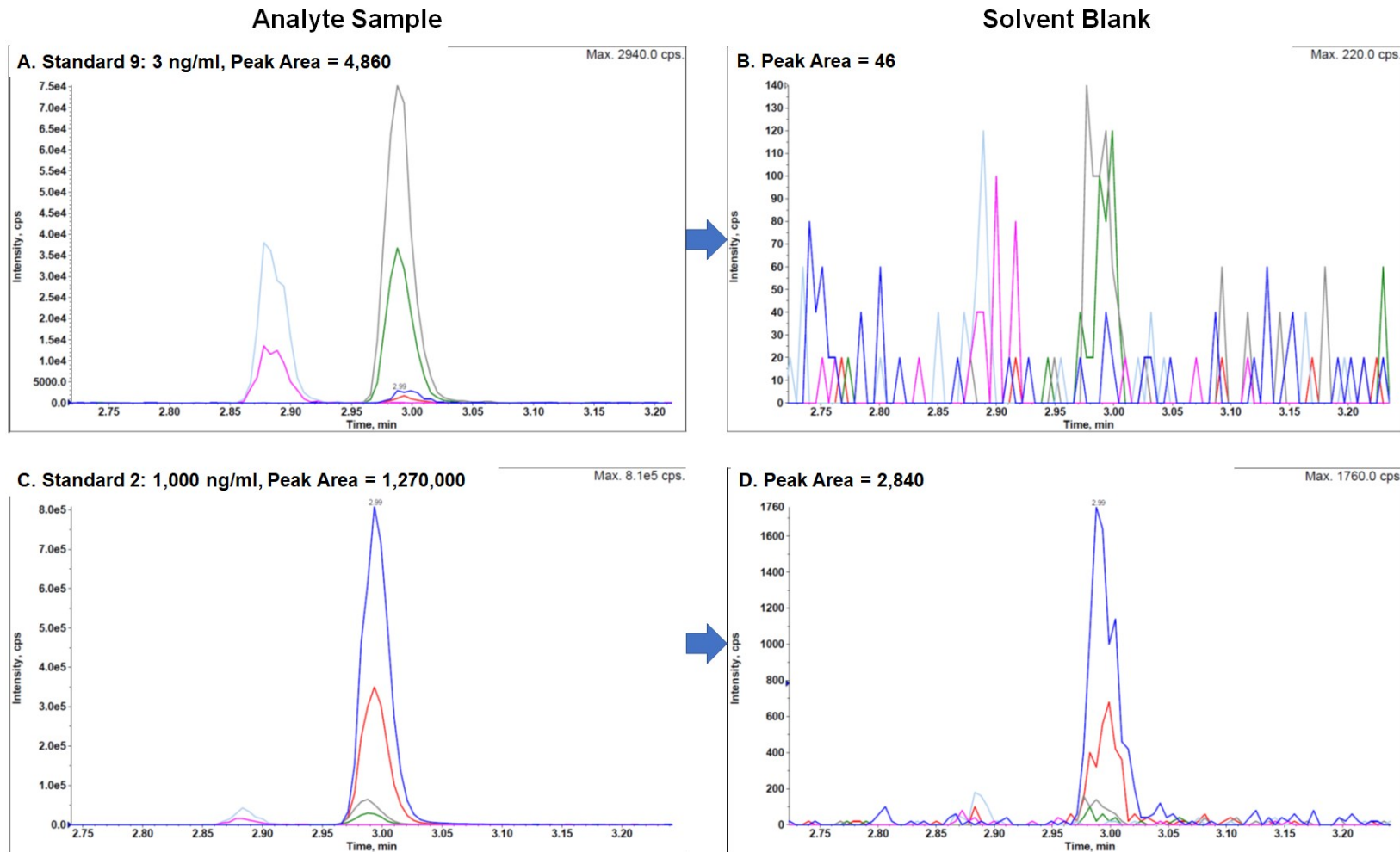


Figure 5.7. Assessment of enzalutamide carryover. The carryover of analyte in neat solution at 3 ng/ml (LLOQ and Standard 9) and 1,000 ng/ml (ULOQ and Standard 2) in comparison to solvent blank was 0.95% and 0.22%, respectively. Chromatograms from Figure 5.7. Arrows indicate successive samples in assay run.

Standard No.	Solution Diluted	Volume Taken (µL)	Volume Diluted to (µL)	Final Conc in Diluent (µM)	Final Conc in Diluent (ng/ml)	ng per ml of matrix*
<i>STD1</i>	<i>STOCK</i>	<i>50</i>	<i>4,640</i>	<i>107.6889</i>	<i>50,015</i>	<i>10,003.01</i>
STD2	STD1	400	4,000	10.7689	5,002	1,000.30
STD3	STD 1	200	4,000	5.3844	2,501	500.15
STD4	STD 1	80	4,000	2.1538	1,000	200.06
STD5	STD 1	10	1,000	1.0769	500	100.03
STD6	STD 5	100	500	0.2154	100.0	20.01
STD7	STD 5	50	500	0.1077	50.0	10.00
STD8	STD 5	50	1,000	0.0538	25.0	5.00
STD9	STD 5	30	1,000	0.0323	15.0	3.00
<i>STD10</i>	<i>STD 6</i>	<i>50</i>	<i>1,000</i>	<i>0.0108</i>	<i>5.0</i>	<i>1.00</i>
High QC (HQC)	MDV-STD 02	800	1,000	8.62	4,001.20	800.24
Medium QC (MQC)	MDV-STD 03	100	1,000	0.54	250.08	50.02
Low QC (LQC)	MDV-STD 04	40	1,000	0.09	40.01	8.00
Lower limit of quantitation (LLOQ)	MDV-STD 05	30	1,000	0.03	15.00	3.00

Table 5.8. Calibration curve preparation sheet for enzalutamide. Values in grey italics not included in calibration curve. STD – standard. QC - quality control. *ng/ml of matrix - 50 µL of diluent spiked into 250 µL of matrix.

5.3.5.3. Accuracy and Precision in Neat Solution

The accuracy of the method was described as the closeness of the average result obtained by the method to the actual value of the analyte. Accuracy was expressed as the percentage of the ratio of the mean measured amount to the expected (nominal) amount. In this case six technical replicates were quantified in three separate runs (separate days). **Figure 5.8.** depicts the calibration curves of the individual runs.

The precision of the method was described as the closeness of the average of individual measures of the analyte when the procedure was evaluated repeatedly to six aliquots of a single neat solution or homogenous volume of biological matrix. Precision was determined at four QC concentrations within the calibration curve (**Table 5.9**). Here, the intra-batch precision was calculated from the mean measured concentration per run whilst inter-batch precision was calculated from the overall means of measured concentrations, both expressed as coefficient of variation (%CV).

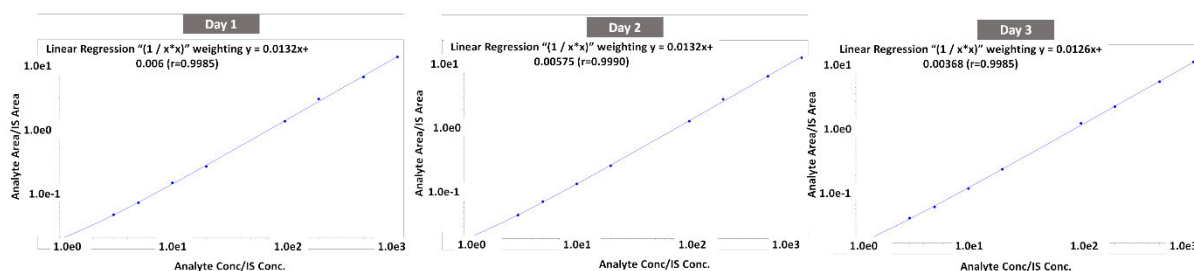


Figure 5.8. Validation of calibration curve in neat solution. On three independent days the regression coefficient was $R^2=0.9985$, $R^2 = 0.9990$ and $R^2 = 0.9990$.

Neat Solution (Analyte in methanol-water 1:1 (v/v))				
Concentration (ng/ml)	Measured	Accuracy (%)	Intra-Batch Precision (%)	Inter-Batch Precision (%)
3 (LLOQ)	2.9	97.3	4.5	7.2
8 (LQC)	7.9	99.8	2.6	4.2
50 (MQC)	50.7	101.1	4.3	4.7
800 (HQC)	800.7	100.0	3.4	4.1

n = 18: Means of 6 technical replicates per concentration in 3 separate runs

Table 5.9. Accuracy and precision of the LC-MS/MS assay for neat solution standards.

5.3.5.4. Extracted Calibration Curve in Biological Matrices

The calibration curve was established in the primary biological matrix – M4 medium. The calibration curve model across three separate days of testing was able to accurately predict more than 99.5% of the concentration-response relationship as shown in **Figure 5.9**.

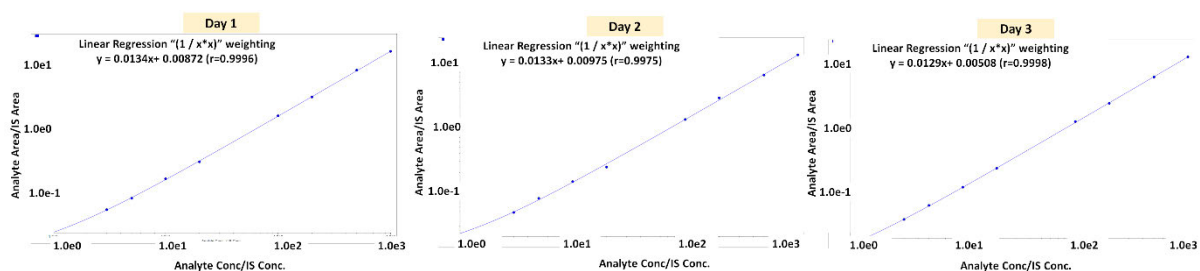


Figure 5.9. Validation of calibration curve in extracted M4 culture medium. On three independent days the regression coefficient was $R^2=0.9996$, $R^2 = 0.9975$ and $R^2 = 0.9998$.

Following this, the calibration curve was also established in the secondary biological matrix – fresh-frozen patient tissue homogenate (TH). Consistent with the extracted calibration curve in culture medium, the calibration curve model in TH samples across three independent test days, was able to satisfactorily explain >99.5% of the concentration-response relationship as presented in **Figure 5.10**.

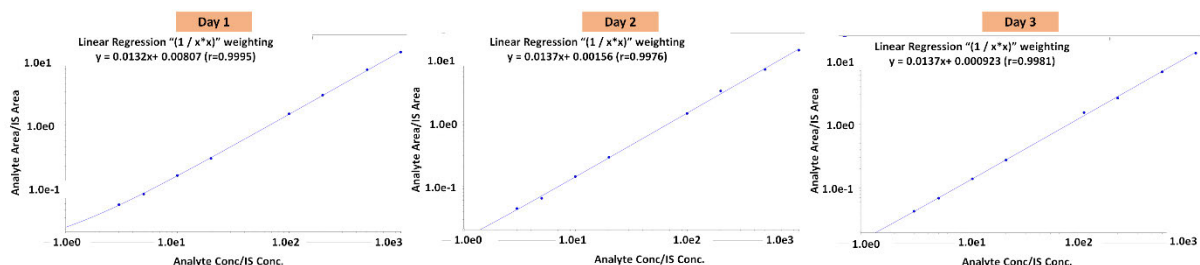


Figure 5.10. Validation of calibration curve in extracted tissue homogenate. On three independent days the regression coefficient was $R^2=0.9995$, $R^2 = 0.9976$ and $R^2 = 0.9981$.

5.3.5.5. Accuracy and Precision in Biological Matrices

The accuracy and precision were established in the primary biological matrix – M4 medium as shown below in **Table 5.10**.

Extracted M4 Medium				
Concentration (ng/ml)	Measured	Accuracy (%)	Intra-Batch Precision (%)	Inter-Batch Precision (%)
3 (LLOQ)	3.0	100.8	9.9	9.4
8 (LQC)	7.9	98.9	2.1	5.9
50 (MQC)	50.1	100.3	5.0	4.8
800 (HQC)	800.0	100.0	2.1	4.8

n = 18: Means of 6 individual replicates per concentration in 3 separate runs

Table 5.10. Accuracy and precision of the LC-MS/MS assay for culture medium samples.

The accuracy and precision were established in the secondary biological matrix – fresh-frozen patient tissue homogenate (TH) as shown below in **Table**

5.11

Extracted Patient Tissue Homogenate				
Concentration (ng/ml)	Measure d	Accuracy (%)	Intra-Batch Precision (%)	Inter-Batch Precision (%)
3 (LLOQ)	3.2	105.0	11.1	11.8
8 (LQC)	8.2	102.8	5.8	6.0
50 (MQC)	52.1	104.3	4.7	5.6
800 (HQC)	794.4	99.4	2.0	3.7

n = 18: Means of 6 individual replicates per concentration in 3 separate runs

Table 5.11. Accuracy and precision of the LC-MS/MS assay for tissue homogenate samples

The accuracy and precision of the assay following drug extraction and reconstitution from both medium and TH samples meet acceptance criteria.

5.3.5.6. Matrix Effects

The influence of the primary biological matrix on analyte extraction was evaluated on three parameters: matrix effect, recovery efficiency and process efficiency. Set 1 was neat solution of analyte, set 2 was spiked with analyte and IS after extraction and set 3 was spiked with analyte and IS before extraction. Matrix effect values <100% indicate ion suppression whereas >100% indicate ionisation enhancement⁴⁴⁴.

The matrix effects assay for M4 medium samples was evaluated with internal standards dissolved DMSO and the results are presented below in **Table**

5.12.

	SET 1 %CV	SET 2 %CV	SET 3 %CV	Matrix Effect	Recovery Efficiency	Process Efficiency
LLOQ	6.5	6.8	3.7	91.0%	100.0%	91.0%
LQC	2.4	4.8	7.8	83.8%	118.8%	99.6%
MQC	4.2	3.8	4.0	84.7%	126.7%	107.4%
HQC	4.3	2.8	6.8	72.7%	131.0%	95.3%

Means of n = 6 individual replicates per concentration

Table 5.12. Matrix effects assay M4 AR antagonist medium IS reconstituted in DMSO.

The matrix effects assay for TH samples was evaluated with internal standards dissolved in acetonitrile and the results are presented below in **Table**

5.13.

	SET 1 %CV	SET 2 %CV	SET 3%CV	Matrix Effect	Recovery Efficiency	Process Efficiency
LLOQ	4.4	7.0	8.0	109.4%	92.2%	100.9%
LQC	4.9	5.1	3.3	97.8%	98.1%	95.9%
MQC	1.6	3.6	2.4	99.4%	89.3%	88.8%
HQC	3.6	6.5	2.1	97.3%	87.8%	85.4%

Mean of n = 6 individual replicates per concentration

Table 5.13. Matrix effects assay tissue homogenate IS reconstituted in acetonitrile.

5.3.5.7. Stability in Biological Matrices

The stability of the drug (ENZ) in biological matrices, M4 medium and patient fresh-frozen biopsy tissue homogenates samples were evaluated for multiple parameters as described earlier.

The short-term and post-preparative stability parameters of ENZ in M4 medium are shown in **Table 5.14**. Across the four QC concentration, it can be seen the stability is within an acceptable 15% threshold. Similarly, the readings obtained from both -20°C and -80°C stored aliquots after three freeze and thaw cycles readings was acceptable (**Table 5.15**). The long-term stability assay indicated that ENZ was stable in culture medium while in -80°C freezer for 225 days as shown in **Table 5.15**. The short-term and post-preparative stability measurements in prostate tissue homogenate were also satisfactory as indicated in **Table 5.16**. Similarly, the freeze and thaw test of both -20°C and -80°C yielded appropriate results (**Table 5.17**). However, the long-term stability reading was intolerable at LLOQ and LQC concentrations marginally exceeding the 15% threshold as demonstrated in **Table 5.17**. It is unlikely to have an increase in drug concentration after long term cold storage. Hence, this may be attributed to a slight dilution/pipetting error during the initial sample preparation. ENZ was discovered to have a long-term stability in tissue homogenate while in -80°C freezer for 82 days.

	Fresh Extraction (ng/ml)	Short Term (ng/ml)	Post Preparative (ng/ml)	Short Term Stability (%)	Post Preparative Stability (%)
LLOQ	3.3	3.3	3.1	99.8	96.1
LQC	9.2	8.9	9.0	96.9	98.2
MQC	54.5	55.3	51.9	101.5	95.1
HQC	807.0	827.3	820.0	102.5	101.6

Table 5.14. Short-term and post preparative stability of enzalutamide in M4 AR antagonist medium. Comparison of short-term stability (18 h 55 min at room temperature) and post-preparative stability (equivalent aliquots of fresh-extraction reconstituted samples in separated sealed well resided in autosampler for 21 h) to freshly extracted spiked drug at four QC concentrations. Values are means of n=3 technical replicates.

	Fresh Extraction (ng/ml)	Freeze Thaw (-20°C) (ng/ml)	Freeze Thaw (-80°C) (ng/ml)	Long Term (-80°C) (ng/ml)	Freeze Thaw (-20°C) Stability (%)	Freeze Thaw (-80°C) Stability (%)	Long Term (-80°C) Stability (%)
LLOQ	2.9	2.9	3.0	2.9	100.8	104.8	101.5
LQC	8.8	8.3	8.5	8.3	94.3	96.5	94.4
MQC	52.5	51.2	49.8	50.9	97.5	94.9	96.8
HQC	799.0	792.7	788.3	783.7	99.2	98.7	98.1

Table 5.15. Freeze-thaw and long-term stability of enzalutamide in M4 AR antagonist medium. Comparison of freeze-thaw cycle stabilities at -20°C and -80°C (at least 12 h at RT and 12 h in respective freeze conditions) and long-term stability at -80°C (225 days) to freshly extracted spiked drug at four QC concentrations. Values are means of n=3 technical replicates.

	Fresh Extraction (ng/ml)	Short Term (ng/ml)	Post Preparative (ng/ml)	Short Term Stability (%)	Post Preparative Stability (%)
LLOQ	3.1	3.2	3.2	103.3	101.9
LQC	8.9	9.0	8.9	101.1	99.0
MQC	47.4	48.5	48.3	102.3	102.0
HQC	741.7	742.3	733.7	100.1	98.9

Table 5.16. Short-term and post preparative stability of enzalutamide in tissue homogenate. Comparison of short-term stability (19 h 30 min at room temperature) and post-preparative stability (equivalent aliquots of fresh-extraction reconstituted samples in separated sealed well resided in autosampler for 21 h) to freshly extracted spiked drug at four QC concentrations. Values are means of n=3 technical replicates.

	Fresh Extraction (ng/ml)	Freeze Thaw (-20°C) (ng/ml)	Freeze Thaw (-80°C) (ng/ml)	Long Term (-80°C) (ng/ml)	Freeze Thaw (-20°C) Stability %	Freeze Thaw (-80°C) Stability %	Long Term (-80°C) Stability %
LLOQ	2.8	3.2	3.1	3.5	113.8%	112.1%	124.4%
LQC	8.9	9.9	10.1	10.3	110.7%	113.2%	116.0%
MQC	54.9	53.4	58.6	59.5	97.3%	106.8%	108.4%
HQC	788.3	802.3	818.3	838.0	101.8%	103.8%	106.3%

Table 5.17. Freeze-thaw and long-term stability of enzalutamide in tissue homogenate. Comparison of freeze-thaw cycle stabilities at -20°C and -80°C (at least 12 h at RT and 12 h in respective freeze conditions) and long-term stability at -80°C (82 days) to freshly extracted spiked drug at four QC concentrations. Values are means of n=3 technical replicates.

5.3.5.8. Stock Solution Stability

The stock solution stability of ENZ was satisfactory. Storage of stocks of ENZ reconstituted in DMSO at both -20°C and -80°C did not lead to compound disintegration. ENZ was found to be stable for 526 days. The assay showed the values of the stored aliquots across the four QC levels was very precise between the cryogenic aliquots compared to a freshly reconstituted powder aliquot as seen in **Table 5.18**.

	-20°C (Old)	-80°C (Old)	New/Fresh Reconstitution	Stability	
				-20°C	-80°C
LLOQ (2 ng/ml)	2.7	2.8	3.0	92.0%	100.2%
	2.5	2.8	2.7		
	2.9	2.7	3.0		
	2.6	2.9	2.7		
	2.7	2.9	3.2		
	2.7	3.1	2.8		
LQC (3 ng/ml)	7.1	7.4	7.5	92.7%	92.7%
	7.5	7.0	8.0		
	7.1	7.6	7.7		
	7.1	7.2	7.5		
	7.4	7.3	7.7		
	7.0	6.8	8.2		
MQC (50 ng/ml)	50.3	48.5	49.3	99.1%	99.9%
	48.0	47.8	50.2		
	49.7	51.0	47.5		
	48.1	50.5	46.7		
	47.5	50.6	52.9		
	49.9	47.4	49.5		
HQC (800 ng/ml)	732.0	818.0	788.0	95.1%	100.2%
	740.0	779.0	731.0		
	702.0	759.0	785.0		
	730.0	771.0	752.0		
	722.0	747.0	768.0		
	783.0	770.0	813.0		

Table 5.18. Stock solution stability testing of enzalutamide. Stock solutions of 10 mM ENZ were diluted to four QC concentrations.

5.4. Discussion

Reliable quantification of drugs and metabolites in biological fluids is important for sound understanding of the pharmacokinetic/pharmacodynamic (PK/PD) properties of a drug²⁷⁶. Here, an LC-MS/MS assay for quantification of enzalutamide (ENZ) and detection of its metabolite *N*-desmethylenzalutamide metabolite was developed and validated according to the US FDA Bioanalytical Method Development and Validation guidelines⁴⁴³. Enzalutamide is a second-generation androgen-receptor antagonist indicated for the treatment of advanced prostate cancer⁴⁴⁶ including metastatic castrate resistant hormone-insensitive disease²².

The physicochemical properties of enzalutamide enable it to be readily soluble in high organic solvents. Bearing this in mind, a Folch extraction approach and crude extraction by protein precipitation were originally evaluated as potential extraction techniques to isolate the drug from M4 medium and tissue from PDEs. As a proof-of-principle experiment, a 100-fold dilution of 50 μ M ENZ cultured without tissue was able to be successfully isolated in the organic phases in both methods. After this, in actual *ex vivo* tissue was cultured in 10 μ M treatments. ENZ was detected readily in the reconstituted organic phases and remarkably extracted from treated explants with marked signal intensity of the characteristic fragment ion, *m/z* 209.1 There was also good selectivity showing hardly any drug present in the vehicle exposed explants.

The calibration/standard curve, accuracy and precision of the assay was established at the outset at four QC levels, LLOQ, LQC, MQC and HQC. The linear quantification range of ENZ was 3 ng/ml – 1000 ng/ml. This was important because subsequent stability testing could only be sound if the method confirmed

to acceptable thresholds. First, in neat solutions of the analyte, the calibration curve had a linearity response of $R^2 \Rightarrow 0.99$ in three independent test day runs. The associated accuracy ranged from 97.2% - 100.0% whilst the intra-batch precision and inter-batch precision ranged from 3.4% - 4.4% and 4.1% - 7.1%, respectively. Subsequently, the calibration curves were established in biological matrices in question. For both M4 culture medium and prostate tissue homogenate the linear relationship was $R^2 \Rightarrow 0.99$ in three separate experiments. In M4 medium, the accuracy was 98.8% - 100.7%, with intra-batch precision and inter-batch precision of 2.0% - 9.8% and 4.8% - 9.3%, respectively. In tissue homogenate, the accuracy was 99.9% - 104.9%, with intra-batch precision and inter-batch precision of 1.9% - 11.0% and 3.6% - 11.8%, respectively. Generally, the accuracy of the assay was constant, but precision improved with increasing QC concentration. These findings are consistent with a validation study conducted by Song and colleagues. They reported accuracy (relative error) and relative precision (standard deviation) of 0.1-3.6% and 1.1-8.9% for the calibration curve at LLOQ 1.0 ng/ml⁴⁴¹. The intra-assay and inter-assay precision that assessed ENZ at four QC levels of 1 ng/ml, 3 ng/ml, 100 ng/ml and 900 ng/ml. was <5.1% with accuracy range of 100.8% - 105.6%⁴⁴¹.

During initial quantification experiments with M4 medium as the biological matrix, it was observed that DMSO underwent slow lyophilisation and tubes were kept in the freeze-dryer for up to 18 h. Therefore, the internal standards were subsequently reconstituted in acetonitrile, which was still a suitable solvent as per manufacturer's certificate of analysis reports. For most of the experiments involving M4 medium the IS working stocks were reconstituted in DMSO whereas tissue homogenate was analysed with IS made up in acetonitrile. The matrix

effect was more pronounced with increasing ENZ concentration, in DMSO compared to acetonitrile, ranging from 72.7% - 91.0% and 97.3%- 109%. Concomitantly, the recovery efficiency in M4 medium was 100.0% - 131.0% for DMSO and in tissue homogenates 87.8% - 92.2% for acetonitrile. This indicated that the interaction between DMSO and biological matrix caused ion suppression during the ESI process of reconstituted extracted analyte. However, the process efficiency was somewhat comparable at 91.0% - 107.4% and 85.4% - 100.9%, for DMSO-M4 medium and acetonitrile-tissue homogenate, respectively. Overall, these data strongly suggest isolation of the analyte by protein precipitation using acetonitrile prior to quantitative analysis is an optimum analytical strategy. It is generally accepted that the analyte should have an extraction recovery of >70%, with no strict specifications for the matrix effects as long as the assay is satisfactorily accurate and precise^{439,443,447,448}.

Enzalutamide was established to be stable at a concentration of 10 mM at freezing conditions of -20°C and -80°C for 526 days well within the precision range of $\pm 15\%$. As with other validated approaches the method described herein satisfactorily met stability requirements. Bennet and colleagues have reported ENZ stock solution stability of have reported of 1,000,000 ng/ml in acetonitrile at 4°C for 359 days in salinised amber glass containers⁴⁴⁹. Kim and colleagues have also described the stock solution stability of ENZ at 1,000,000 ng/ml in DMSO at -80°C to be at 96.7% for 3 months⁴³⁹. Their method used ¹³C₂ isotopologues of the optimally sensitive ENZ and *N*-desmethyl ENZ to attain a 12-factor signal dilution to avoid detector saturation while detecting the less ionisable ¹²C bicalutamide⁴³⁹. This is a reasonable approach which might minimise volume dilution errors. In comparison, to the method described herein the differences in

analyte sensitivities could be attributed to the choice of RP column and chromatographic method, since the MS detection systems are identical.

The LC-MS/MS assay expounded herein can also be used in future tissue culture studies using ENZ as a therapeutic agent. It also has the potential to be amenable to other newer clinical AR antagonists such as darolutamide and apalutamide. The validated method was applied to quantitate uptake of enzalutamide in *ex vivo* culture of human prostate tissue. The output of this is the published work in [Chapter 6](#) of this thesis.

CHAPTER 6:

Evaluation of Small Molecule Drug Uptake in Patient-Derived Prostate Cancer Explants by Mass Spectrometry

Statement of Authorship

Title of Paper	Evaluation of Small Molecule Drug Uptake in Patient-Derived Prostate Cancer Explants by Mass Spectrometry
Publication Status	<input checked="" type="checkbox"/> Published <input type="checkbox"/> Accepted for Publication <input type="checkbox"/> Submitted for Publication <input type="checkbox"/> Unpublished and Unsubmitted work written in manuscript style
Publication Details	Mutuku SM, Trim PJ, Prabhala BK, Irani S, Bremert KL, Logan JM, Brooks DA, Stahl J, Centenera MM, Snel MF, Butler LB. 2019. Evaluation of Small Molecule Drug Uptake in Patient-Derived Prostate Cancer Explants by Mass Spectrometry. Scientific Reports 9:15008. Scientific Reports, 18 October 2019, https://doi.org/10.1038/s41598-019-51549-3

Principal Author

Name of Principal Author (Candidate)	Shadrack Mulinge Mutuku		
Contribution to the Paper	Designed the research, Performed mass spectrometry imaging and chromatography experiments, Generation and analysis of data, Writing and editing of the manuscript		
Overall percentage (%)	75%		
Certification:	This paper reports on original research I conducted during the period of my Higher Degree by Research candidature and is not subject to any obligations or contractual agreements with a third party that would constrain its inclusion in this thesis. I am the primary author of this paper.		
Signature		Date	01 Jun 2020

Co-Author Contributions

By signing the Statement of Authorship, each author certifies that:

- i. the candidate's stated contribution to the publication is accurate (as detailed above);
- ii. permission is granted for the candidate to include the publication in the thesis; and
- iii. the sum of all co-author contributions is equal to 100% less the candidate's stated contribution.

Name of Co-Author	Paul J Trim		
Contribution to the Paper	Designed the research, reviewed the data and edited the manuscript.		
Signature		Date	03/06/20

Name of Co-Author	Bala K. Prabhala		
Contribution to the Paper	Designed the research Experimental and intellectual input		
Signature		Date	01/06/2020

Name of Co-Author	Swati Irani		
Contribution to the Paper	Experimental and intellectual input		
Signature		Date	10.06.2020

Name of Co-Author	Kayla L. Bremert		
Contribution to the Paper	Experimental and intellectual input, provided clinical material		
Signature		Date	2.06.2020

Name of Co-Author	Jessica M. Logan		
Contribution to the Paper	Intellectual input and editing of manuscript.		
Signature		Date	2.06.2020

Name of Co-Author	Douglas A. Brooks		
Contribution to the Paper	Intellectual input and editing of manuscript.		
Signature		Date	2.06.2020

Name of Co-Author	Jürgen Stahl		
Contribution to the Paper	Pathological assessment of clinical material		
Signature		Date	10.06.2020

Name of Co-Author	Margaret M. Centenera		
Contribution to the Paper	Reading and editing of manuscript		
Signature		Date	11.06.2020

Name of Co-Author	Marten F. Snel		
Contribution to the Paper	Data analysis and interpretation of results, reading and editing of manuscript Supervised the research		
Signature		Date	10/6/2020

Name of Co-Author	Lisa M. Butler		
Contribution to the Paper	Conceptualization of study, data analysis and interpretation of results, supervised the research Reading, editing and approval of final manuscript		
Signature		Date	10/6/2020

OPEN Evaluation of Small Molecule Drug Uptake in Patient-Derived Prostate Cancer Explants by Mass Spectrometry

Shadrack M. Mutuku^{1,2}, Paul J. Trim³, Bala K. Prabhala^{3,4}, Swati Irani^{1,2,5}, Kayla L. Bremert^{1,2,5}, Jessica M. Logan⁶, Douglas A. Brooks⁶, Jürgen Stahl⁷, Margaret M. Centenera^{1,2,5}, Marten f. Snel³ & Lisa M. Butler^{1,2,5*}

Patient-derived explant (PDE) culture of solid tumors is increasingly being applied to preclinical evaluation of novel therapeutics and for biomarker discovery. In this technique, treatments are added to culture medium and penetrate the tissue via a gelatin sponge scaffold. However, the penetration profile and final concentrations of small molecule drugs achieved have not been determined to date. Here, we determined the extent of absorption of the clinical androgen receptor antagonist, enzalutamide, into prostate PDEs, using liquid chromatography-tandem mass spectrometry (LC-MS/MS) and matrix-assisted laser/desorption ionisation (MALDI) mass spectrometry imaging (MSI). In a cohort of 11 PDE tissues from eight individual patients, LC-MS/MS quantification of PDE homogenates confirmed enzalutamide (10 μ M) uptake by all PDEs, which reached maximal average tissue concentration of 0.24–0.50 ng/ μ g protein after 48 h culture. Time dependent uptake of enzalutamide (50 μ M) in PDEs was visualized using MALDI MSI over 24–48 h, with complete penetration throughout tissues evident by 6 h of culture. Drug signal intensity was not homogeneous throughout the tissues but had areas of markedly high signal that corresponded to drug target (androgen receptor)-rich epithelial regions of tissue. In conclusion, application of MS-based drug quantification and visualization in PDEs, and potentially other 3-dimensional model systems, can provide a more robust basis for experimental study design and interpretation of pharmacodynamic data.

Prostate cancer is the most commonly diagnosed male cancer and the second leading cause of cancer deaths in Western countries¹. Androgens and their intracellular target, the androgen receptor (AR), are established drivers of prostate cancer initiation, development and progression^{2,3}. As such, blocking androgen action by androgen deprivation therapies or by selective inhibition of the AR with antagonists has been the mainstay of past and current therapeutic interventions for prostate cancer⁴. However, these strategies are not curative and durable tumor responses are currently unattainable⁵. Enzalutamide (ENZ) is a second-generation AR antagonist with additional modes of action compared to first-generation agents, namely suppression of AR nuclear translocation and binding of the androgen-AR complex to DNA⁵. Enzalutamide is currently used for treatment of metastatic castration resistant prostate cancer (CRPC)^{6,7}, and was recently approved for men with high-risk localized disease (HRLD)^{3,8,9}. Unfortunately, enzalutamide treatment is not curative, and intrinsic and acquired resistance are both common, representing critical research priorities in the field³. There is an increasing appreciation that using patient-derived tumor models may reveal more clinically-relevant mechanisms of drug activity and/or resistance¹⁰. However, the interpretation of drug-related endpoints in such models requires an understanding of

¹Adelaide Medical School, University of Adelaide, Adelaide, SA, 5005, Australia. ²Prostate Cancer Research Group, South Australian Health and Medical Research Institute (SAHMRI), Adelaide, SA, 5000, Australia. ³South Australian Health and Medical Research Institute (SAHMRI), Adelaide, SA, 5000, Australia. ⁴Department of Drug Design and Pharmacology, University of Copenhagen, København, Denmark. ⁵Freemasons Foundation Centre for Men's Health, University of Adelaide, Adelaide, SA, 5005, Australia. ⁶Mechanisms in Cell Biology and Disease Research Group, School of Pharmacy and Medical Sciences, Cancer Research Institute, University of South Australia, Adelaide, SA, 5000, Australia. ⁷Clinpath Laboratories, Adelaide, SA, 5000, Australia. *email: lisa.butler@adelaide.edu.au

the penetration of small molecule agents into the tissue structure, and the in-tissue drug concentrations achieved during culture.

Mass spectrometry is used extensively in the characterisation of pharmacokinetic behaviour of compounds in drug development¹¹, for quantification of metabolites¹² and hormones¹³. Orthodox quantification assays typically involve homogenization of the drug-containing tissue or biofluid, sample clean-up, and separation by liquid chromatography followed by absolute quantification using tandem mass spectrometry (LC-MS/MS). Although such approaches yield accurate quantification data, homogenization of tissue samples results in complete loss of spatial information and all measurements represent integrated values for the whole tissue, thereby making it impossible to know whether the molecule of interest is evenly distributed or differentially bio-accumulated, dependent on cell type and tissue penetration. With the advent of mass spectrometry imaging (MSI), it is possible to retain spatial information, allowing detailed mapping of the tissue distribution of molecules of interest such as drugs, metabolites or endogenous compounds such as phospholipids^{14–16}. MALDI MSI involves laser-desorption/ionization of molecules from a thin layer matrix-coated biological sample on a glass slide^{17,18}. An intensity map can be generated to visualize and quantify specific ions based on their *m/z*, resulting in a form of chemical histology¹⁹. MSI currently has two broad applications based on target molecular mass. Large molecule imaging typically encompasses *in situ* proteomic profiling, revealing protein and peptide composition^{16,20}, while small molecule imaging has largely characterized metabolites such as sugars, fatty acids²¹ and lipids^{19,22}. Many pharmacological small molecule agents occupy a similar chemical space (comparable molecular weights, physicochemical properties and functional groups) as endogenous metabolites. Consequently, drug imaging in preclinical and clinical settings constitutes an important emerging area of small molecule imaging²³.

Determination of enzalutamide quantities in human plasma and rat plasma for pharmacokinetics studies has been previously described^{24,25} but has not been attempted in a tissue culture model. Herein, we utilized LC-MS/MS and MALDI MSI to both quantify and visualize the profile of enzalutamide uptake from culture in an *ex vivo* PDE model of clinical prostate cancer. Moreover, we describe the spatial localization of enzalutamide-derived ion signals in tissues with heterogenous histological features and in comparison to immunohistochemical staining of the intracellular drug target, AR.

Results

Enzalutamide is detectable in patient-Derived explant (PDE) culture systems. We developed,

and validated according to US FDA guidelines, a quantitative LC-MS/MS assay capable of measuring enzalutamide levels in both culture media and tissue specimens from our widely used PDE model system^{26,27} (Fig. 1). In a cohort of 11 prostate tissues from 8 patients (3 patients provided cores from the left and right sides of the prostate), enzalutamide (ENZ) was readily detectable above the lower limit of quantitation (LLOQ) in conditioned medium after 48 h of culture with a working dose of 10 μM (4.6 $\mu\text{g/ml}$), and concentrations were within 15% of assay quality control (QC) measurements (Fig. 2, Supplementary Table ST2). Enzalutamide was not detected in medium from vehicle control (DMSO) wells, confirming assay selectivity. For each patient sample, enzalutamide concentration values in media were highly consistent when comparing 0 h versus 48 h of culture (Fig. 2), indicating that the drug remained stable in the medium throughout the culture period.

Next, the concentration of enzalutamide was assessed in conditioned medium from PDEs cultured at two different concentrations of ENZ (10 μM or 50 μM) for time points up to 24 h. Stability of ENZ at both concentrations was evident over the 24 h incubation period (Table 1), while control samples showed nil amounts of drug present in the well at all time points. The integrity of enzalutamide in the cryo-stored samples ($-80\text{ }^{\circ}\text{C}$) was confirmed by including freshly prepared, dilution quality control (DQC), samples at the same concentration as the experimental test samples.

For assessment of ENZ uptake in PDE tissues, initially quadruplicate pieces of tissue were analyzed for each PDE sample ($n = 11$) after 48 h of treatment at 10 μM . ENZ was detected above the LLOQ in all homogenates. While disparity in ENZ content was evident between tissues and patients, the concentrations achieved were comparable in magnitude, 0.24–0.50 ng/ μg of total protein. The drug absorption exhibited an intra- and inter-patient variability of 17.7% and 20.1%, respectively (Fig. 3, Supplementary Table ST3). The major active metabolite of ENZ, *N*-desmethylenzalutamide, was not detectable in any PDE homogenates.

Visualization of enzalutamide uptake in prostate PDE tissues. The spatial kinetics and distribution of ENZ uptake in *ex vivo* cultured PDEs was visualized by MALDI MS/MS imaging of the predominant ENZ fragment ion, *m/z* 209.09. In a pilot study, the penetration of ENZ (50 μM) was assessed in frozen PDE sections cultured for defined times (1, 5, 20 or 48 h). Uptake of drug into the tissues was evident and extended throughout the PDEs by 5 h of culture, confirmed by imaging multiple depth planes in the tissues (Supplementary Fig. S1). The fragment ion of the drug then remained detectable at similar intensity over the remaining incubation period

(Supplementary Fig. S1). Whereas it was possible to map the intensity distribution of ENZ signal by MALDI MS/MS imaging in PDEs cultured at both 10 and 50 μM doses, the relative abundance of *m/z* 209.09 from the 10 μM treatment generated insufficient signal intensity compared to the 50 μM treatment for reliable data generation. This was confirmed by LC-MS/MS quantification of tissue from 10 μm sections in a subset of PDEs, where the level of ENZ quantified at 10 μM was at the limit of detection (LOD) and 50 μM was above the lower limit of quantification (LLOQ) (Supplementary Fig. S2). Accordingly, 50 μM of ENZ was selected for further MALDI MSI studies.

MALDI MSI and LC-MS/MS indicate the kinetics of drug uptake in PDEs. Next, the spatial profile of ENZ uptake was assessed over a 24 h incubation period using 50 μM ENZ treatment in two independent PDEs from another patient. Data for the left core of the prostate in a single patient is shown (Fig. 4). For this experiment, the images of the sections correspond to the planar orientation of the explant such that the bottom

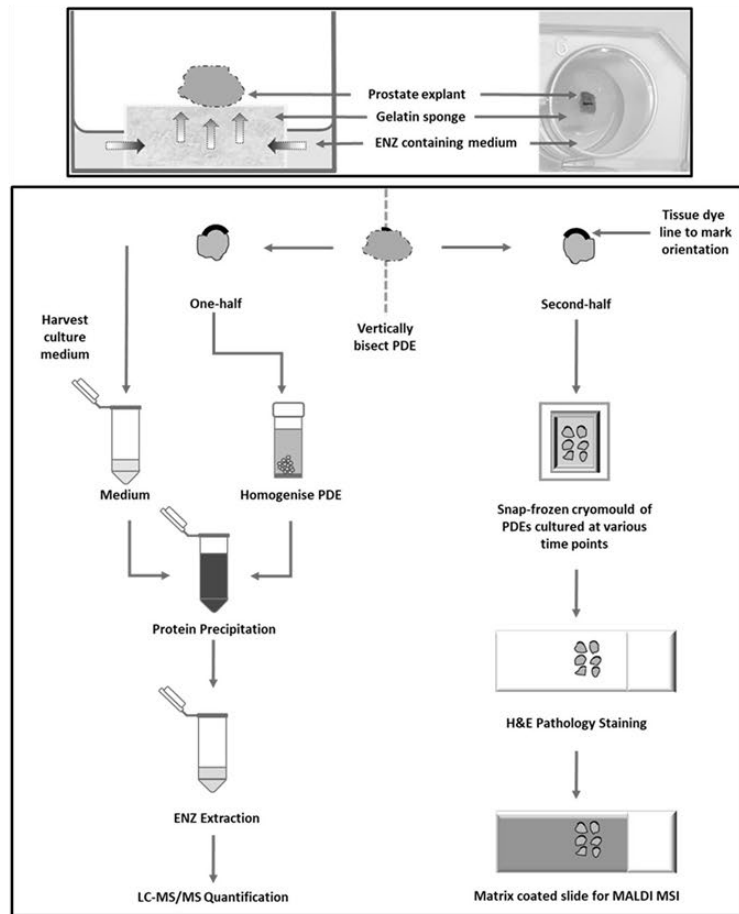


Figure 1. Schematic of drug uptake in *ex vivo* culture of human prostate tumors. Top panel. Schematic and photograph of a PDE on top of a gelatine sponge in a well with 500 μ L medium. Bottom panel. Workflow chart for evaluation of ENZ uptake in human prostate PDEs by mass spectrometry.

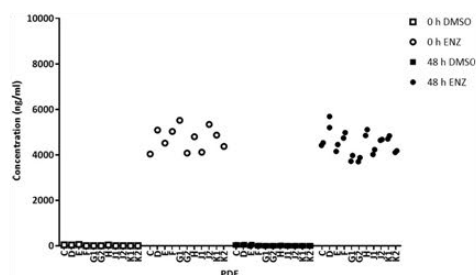


Figure 2. LC-MS/MS quantification of ENZ in conditioned explant media. PDE's were cultured in medium containing 10 μ M ENZ or DMSO control over a 48h period. LC-MS/MS quantification of the predominant ENZ fragment ion, m/z 209.09 is shown. Drug concentration in medium expressed as ng/ml.

of each tissue image indicates the site of contact between the explant and the gelatine sponges in the well (Fig. 1). Cumulative uptake of ENZ from the sponge surface into the PDEs was detected over the 24 h period, and confirmed by quantification of ion signal intensity (Fig. 4). At time 0 h there was no drug signal detected in the tissue. After 1 h of incubation, ENZ was evident at low levels, primarily at the bottom (sponge-contacting) edge of the

Concentration (ng/ml)	Patient A-L [^]	Patient A-R [^]	Patient B-L ⁺	Patient B-R ⁺
DMSO Stability	—	—	0	0
DMSO 0 h	0	0	0	0
DMSO 24 h	0	0	0	0
DQC	4410	4410	23170	23170
DS well	—	—	26200	26200
ENZ 0 h	4620	4220	23600	26100
ENZ 1 h	4700	4420	21700	20200
ENZ 2 h	4070	4280	20500	19300
ENZ 6 h	3450	4560	18500	20100
ENZ 24 h	4130	4470	19900	19100

Table 1. LC-MS/MS quantification of 10 μM [^] and 50 μM ENZ* in culture media. Six PDEs from separate prostate cores left (L) and right (R) of two patients, A and B, were treated at indicated dose of ENZ for 1 h, 2 h, 6 h, 24 h or 24 h control; media from corresponding wells was collected by snap-freezing at respective time points including 0 h and 24 h control. DQC values are an average of triplicate measurements. Values are expressed as ng/ml.

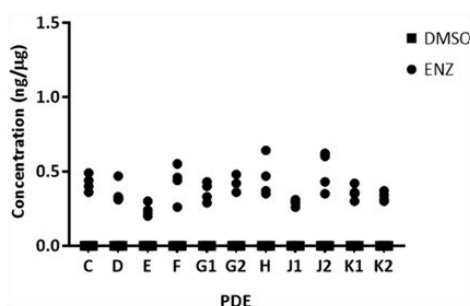


Figure 3. LC-MS/MS quantification of ENZ in PDE homogenates. PDEs were cultured in medium containing 10 μM ENZ or DMSO control over a 48h period. LC-MS/MS quantification of the ENZ MRM transition 465.1 \rightarrow 209.09 is shown. Measured drug concentration in homogenate is normalized to total protein expressed as ng/ μg of total protein. Intra-patient variability of 17.7% and intra-patient variability of 20.1%. n = 4 (two explant pieces per well containing medium with 10 μM ENZ or DMSO vehicle).

PDE, and by 2 h the drug was abundant in the lower areas of the tissue. By 6 h–24 h, there was distribution evident throughout the tissue. The 24 h control treatment had no signal from the ENZ fragment ion, m/z 209.09, similar to the 0 h uncultured tissue (Fig. 4, Supplementary Fig. 1).

In parallel, the amount of ENZ absorbed by PDEs was quantified by LC-MS/MS on the bisected tissue halves of each of the treated PDEs from Fig. 4. This confirmed a time-dependent increase in tissue drug concentrations (Fig. 5, Supplementary Fig. S3). The maximum drug concentration reached after 24 h of culture following 50 μM dose was 0.87–1.18 ng/ μg of total protein. Again, the *N*-desmethylenzalutamide metabolite fragment ion of ENZ (m/z 201.1) was undetectable.

Enzalutamide accumulates in epithelium-rich regions of prostate tissue. Notably, the pattern of enzalutamide signal detected by MALDI MSI in the prostate tissues was not homogenous throughout the tissue sections, but invariably displayed discrete regions of high signal. Comparison of serial sections of MALDI MS/MS images to the tissue histology (H&E staining) revealed that areas of high enzalutamide signal co-localized with histological tissue regions containing high epithelial cell content. (Fig. 6). The co-location of ENZ ion signal with benign or malignant prostate epithelial cells was further confirmed by immunohistochemical staining for AR in consecutive adjacent sections (Fig. 6).

Discussion

There is increasing interest in applying patient-derived tissue model systems such as explants and/or xenografts to preclinical cancer research and drug development^{26–28}. Such systems maintain 3-dimensional tumor structure, which in turn retains important features such as hormone responsiveness in the case of breast and prostate cancers²⁶. A potential advantage of PDEs is the ability to relate drug responses to spatial features of the tissues, thereby allowing consideration of tumor multifocality and histological features of the tumor microenvironment. However, a key knowledge gap has been the accurate measurement of the degree and spatial kinetics of tissue penetration of such models by small molecules, and the effective intra-tissue concentrations achieved. This is

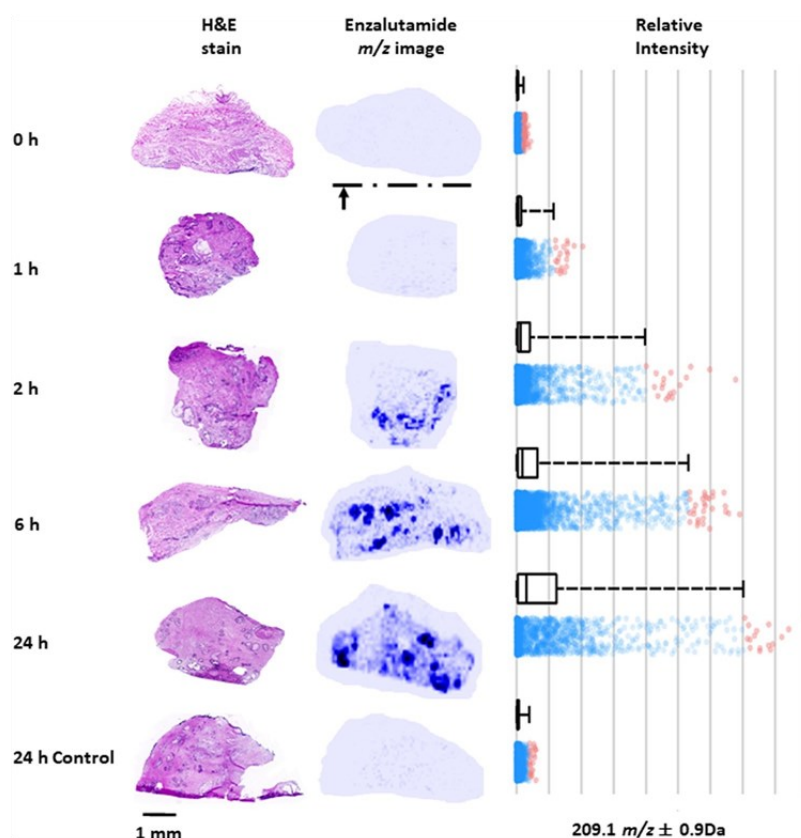


Figure 4. Time profile of ENZ penetration in *ex vivo* prostate tissue culture. Left panel. Six PDE's were cultured in medium containing 50 μ M ENZ over a 24 h period or DMSO control (24 h). MALDI MSI MS/MS images of the predominant ENZ fragment ion, m/z 209.09, are shown with normalization to TIC next to a serial section stained by H&E. The arrow at the bottom of the image at 0 h indicates the contact of the PDE with the gelatin sponge surface. H&E sections are 30 μ m adjacent to the MALDI image tissue section. Right panel. Relative intensity of m/z 209.09 at 0 h, 1 h, 2 h, 6, h and 24 h/24 h control of respective MS/MS images (A) show a time-dependent increase in drug concentration in the tissues during culture. Red dots represent the spectra of enzalutamide outside of the upper quartiles.

the first study to both quantify and visualize uptake of a current clinical agent, enzalutamide, into clinical PDEs during culture. Moreover, by incorporating tissue histology and immunostaining we demonstrate marked accumulation of enzalutamide in the tissue epithelium, which highly expresses the agent's intracellular target, the AR³.

MSI of non-endogenous small compounds has been explored previously in the study of anti-cancer agents in solid tumors, but this is largely confined to *in vivo* animal models. The distribution of the anti-cancer drug vinblastine has been directly performed on rat whole body sections by MALDI MSI²⁹. Kwon and colleagues have reviewed the uptake of various anticancer agents in multiple solid tumors³⁰. They reported localization of the protein kinase inhibitor vemurafenib within tumor regions of human malignant melanoma, where it specifically bound to its targets, BRAF mutated proteins, as opposed to BRAF negative tumor regions. MALDI MSI was also used to elucidate pharmacodynamic/pharmacokinetic properties of the anti-angiogenic small molecules and their metabolites, YCG185 and sunitinib, both targets for VEGFR2³⁰. Specifically, for sunitinib, they demonstrated downregulation of the target receptor in response to treatment in a murine model of colorectal cancer. Thus, MALDI MSI supplemented with immunohistochemistry approaches is a powerful and spatially informative tool to assess drug-target engagement in preclinical studies. MSI of drugs and their metabolites has also been investigated in whole-body murine models^{31,32}. This platform offers a unique advantage of observing drug distribution within pathophysiological areas of organ³³ and tissue microenvironments³³. The pharmaceutical industry has adopted whole body autoradiography (WBA)³⁴ and MALDI MSI for drug imaging, although this has not been as extensive in academic research. Although WBA is a robustly quantitative and sensitive technique, it requires the use of expensive radiolabelled isotopes that yield indistinguishable organ images of the drug analytes from its metabolites of interest. However, MALDI MSI can be used for the direct analysis of a drug and can employ more

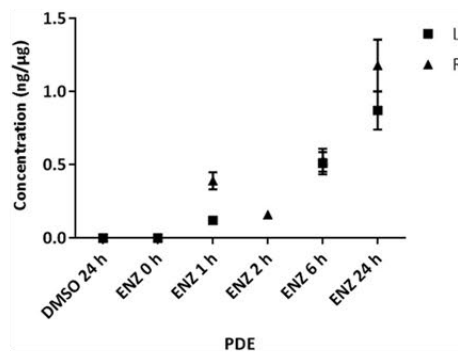


Figure 5. LC-MS/MS quantification of ENZ in PDE homogenates over a time course. Six PDEs from either the left (L) and right (R) prostate cores were cultured in 50 μM ENZ and harvested at 0 h, 1 h, 2 h, 6 h, 24 h (DMSO control) and bisected. One-half was homogenized for LC-MS/MS analysis. Drug concentration is normalized to total protein expressed as ng/ μg . *Note: PDE for L at 2 h lost during sample homogenization. Error bars indicate the 15% CV threshold for accuracy and precision of assay.

relatively affordable deuterated analogues that can be spatially resolved from metabolites with high molecular specificity.

Here, we combined MALDI MSI with a highly sensitive LC-MS/MS assay to assess stability of enzalutamide in explant culture conditions and its uptake and distribution in the tumor tissues. These quantitative results indicate the maintenance of drug stability in PDE culture medium as a biological matrix over the entire culture period, and ensuring its availability in desired concentrations to perfuse viable tissue. The variability in comparative intra-patient drug absorption (measured amount of drug between replicate explants dissected from the same biopsy core) was evident. Nevertheless, the inter-patient drug uptake was still consistent in a diverse range of patient samples including benign tissue or heterogeneous Gleason grades when normalized to total protein content of the tissues. Our results suggest that it is unlikely that the variation in clinical response to enzalutamide is related to its uptake and the clinical features of the tissues. Recently, others have argued at the cellular level that during tumorigenesis prostate cancer cells produce altered lipid membranes^{35,36}, which may reduce the efficacy of enzalutamide and lead to treatment resistance³⁵. Given that our targeted MALDI MSI revealed marked accumulation of enzalutamide in AR-expressing epithelial cells, the positivity and/or expression level of the AR is likely to be another important determinant of enzalutamide content in individual tissues.

The recommended clinical dose of enzalutamide is 160 mg orally once daily for treatment of metastatic CRPC³⁷. The dosage of enzalutamide employed in our *ex vivo* model of human prostate cancer PDE model is 10 μM (4.6 $\mu\text{g}/\text{ml}$) and importantly, this is comparable to plasma concentrations readily achieved systemically in clinical patients³⁸. It is consistent with the clinical dose described by Gibbons and colleagues who analyzed the pharmacokinetics of enzalutamide and *N*-desmethylenzalutamide from five clinical studies³⁹. They also reported after a consecutive multiple oral doses of 160 mg that the pre-dose steady-state mean plasma concentration (C_{trough}) reached was 11.4 $\mu\text{g}/\text{ml}$ ³⁹. Moreover, 10 μM enzalutamide is a routinely employed dosage in pre-clinical models, both cell culture⁴⁰ and *in vivo* studies⁴¹, of prostate cancer for evaluation of its efficacy in combination with other non-AR targeted genome therapies^{41–43}. PDEs often require 5–10-fold higher drug doses than in 2-dimensional cell culture studies to attain equivalent efficacy and the 10 μM dose was primarily evaluated in this study.

MALDI MS/MS imaging experiments of 10 μm sections of PDEs treated with 10 μM enzalutamide yielded low signal intensity close to the limit of detection and consequently the spatial drug visibility during the 24 h time profile was unreliable. Using targeted MALDI MS/MS, we have evaluated a higher dose of 50 μM (~25 $\mu\text{g}/\text{ml}$) enzalutamide that approximates to 360 mg/day administered as multiple oral doses previously reported³⁸. The higher dose provided high quality MSI data, and allowed us to ascertain the drug-target engagement by MSI and revealed its high affinity for epithelial cells that are known to express its intracellular target receptor, AR. The time-dependent increase in *in situ* drug concentration we observed may explain the drugs' reported clinical pharmacokinetic parameters of a half-life of 5.8 days and accumulating at least 8-fold³⁹. The major active metabolite, *N*-desmethylenzalutamide was not detected, likely because enzalutamide primarily undergoes hepatic metabolism³⁸.

In conclusion, understanding the parameters of agent penetration and accumulation is essential to undertake pharmacodynamic experiments using PDE preclinical model systems. Using a mass spectrometry-based experimental approach, we demonstrate for the first time that the current clinical agent enzalutamide fully and rapidly suffuses cultured prostate tissues, thereby identifying optimal endpoints for experimental assays involving ENZ. More broadly, such approaches warrant inclusion in translational research involving not only PDEs but other 3-dimensional model systems such as patient-derived organoids, where penetration rates of various small molecular agents will profoundly influence both study design and interpretation of experimental endpoints.

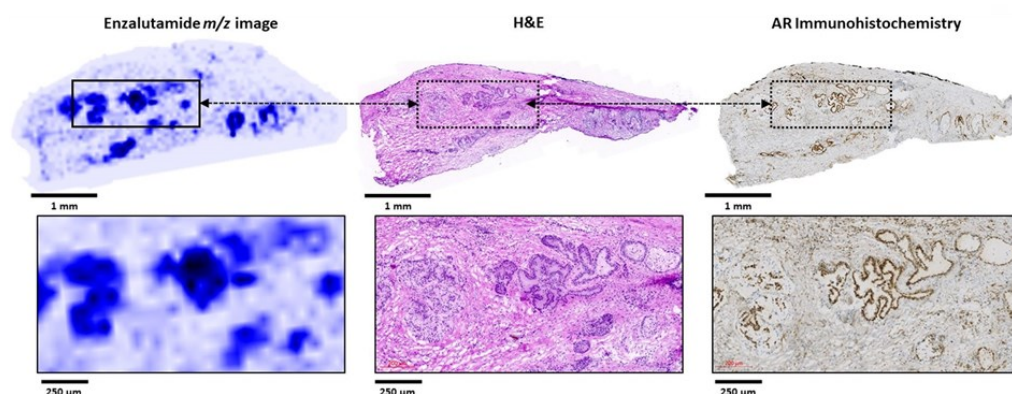


Figure 6. ENZ signal co-localization in prostate tissue epithelium. Comparison of the MS/MS image (ENZ fragment ion, m/z 209.09, left) to an H&E scan (middle) and immunohistochemical detection of the androgen receptor (AR). Lower panels: higher magnification images.

Methods

Chemicals. α -cyano-hydroxycinnamic acid (CHCA), polyethylene glycol (PEG) standards (200, 600, 1000) were obtained from Sigma-Aldrich. Carboxymethylcellulose (CMC) and dimethylsulfoxide (DMSO) were purchased from Sigma-Aldrich (NSW, Australia). Methanol and acetonitrile (all LC-MS hyper grade, Lichrosolv) were purchased from Merck (VIC, Australia). Argon (Catalogue No. 262) for mass spectrometry application was purchased from BOC (NSW, Australia). Formic acid was purchased from Fisher Chemicals (St. Louis, MO, USA). RPMI 1640 phenol free culture medium (Catalogue No. 1185-030) was purchased from Life technologies (USA). Gelatin sponges were purchased from Johnson and Johnson (NC, USA). Water was obtained from a MilliQ system with 0.22 μm filter. Micro Bicinchoninic acid (BCA Catalogue No. 23235) assay kit was purchased from Thermo Scientific (Rockford, IL, USA). Enzalutamide (ENZ) (MDV3100 Catalogue No. S1250 000-09083) was purchased from Selleckchem (Houston, TX, USA). [$^2\text{H}_6$]-enzalutamide and [$^2\text{H}_6$]-desmethylenzalutamide were purchased from Alsachim (Strasbourg, France). Chemical structures are shown in Supplementary Fig. S4.

Ex Vivo culture of human prostate tissue. We employed a well-defined explant model of patient-derived prostate tumor explants (PDEs)^{26,27}. Following radical prostatectomy, 6–8 mm tissue cores from the left and/ or right sides of the prostate were dissected into approximately 1–3 mm³ pieces and cultured in quadruplicate, as described previously²⁶. The pathological information for $n = 8$ patients (yielding 11 separate tissue samples), indicating Gleason grade, clinical stage and prostate specific antigen (PSA) levels, as well as rescored pathology (J.S.) for the PDE-derived tissue samples, is shown in Supplementary Table ST1. For measurement of homogenates, PDEs were cultured for 48 h in the presence and absence of 10 μM ENZ, with samples collected at 0 h and 48 h (Fig. 1). For time course experiments tissues were cultured in the presence or absence of 10 or 50 μM ENZ and samples were harvested at a range of time points as described. Controls included both untreated fresh frozen tissue and DMSO at 24 h, as well as a drug stability (DS) well that included gelatine sponge and medium only without tissue, and a drug quantification (DQ) well of gelatine sponge, medium and explants. The DS well monitored the integrity of ENZ during incubation period.

LC-MS/MS. The LC-MS/MS method was validated according to US FDA guidelines prior to sample analyses⁴⁴. ENZ was extracted from the culture media, snap-frozen PDE tissues and/or PDE frozen tissue sections. Briefly, 250 μL of 1:100 diluted medium was spiked with 50 μL of 1 μM deuterated ($^2\text{H}_6$) ENZ and 50 μL $^2\text{H}_6$ desmethylENZ internal standard (IS) and subjected to protein precipitation using pre-chilled acetonitrile (1:4 v/v) and incubated at -20°C for 1 h. Samples were then centrifuged at ca 16,000 *rcf* at 4°C for 20 min. The supernatant was aliquoted into new tubes, freeze-dried and reconstituted to starting volume of 400 μL with methanol-water 1:1 (v/v). PDE samples from each time point were placed in 2.0 ml tough tubes (Mo Bio Laboratories, CA, USA) with 1,000 μL methanol-water 1:1 (v/v) for homogenisation using a Precellys 24 homogeniser (Bertin Technologies, Australia) set at 6500 rpm for 30 sec twice with a 30 sec rest period in between.

Total protein in tissue homogenates was measured using the Micro BCA protein assay kit following manufacturer's protocol. 250 μL of PDE tissue homogenates were subjected to the same protein precipitation and drug extraction procedure as described above.

LC-MS/MS analysis was performed on an Acquity ultra-performance liquid chromatography (UPLC) system (Waters Corporation, MA, USA) coupled to an API 4000 QTrap (Applied Biosystems MDS Sciex, Ontario, Canada). Chromatography employed a BEH C18 1.7 μm particle size 2.1 mm by 50 mm column (Waters, Corporation, Ireland). Solvent A was 0.1% aqueous formic acid and solvent B was 99.9% acetonitrile with 0.1% formic acid. Other conditions were: column temperature, 30.0°C , sample temperature, 6.0°C and total run time, 7.40 min. An injection volume of 5 μL of reconstituted analyte was used and samples were eluted using a solvent gradient of 1–99% B from 0.2 min to 4.0 min, the column was washed from 4.0 min to 5.8

min with 99% B and re-equilibrated between 5.81 min to 7.40 min at 1% B at 0.35 ml/min flow rate. The mass spectrometer was operated in multiple reaction monitoring (MRM) mode. Transitions of m/z 465.1 to 209.2 (ENZ), m/z 471.1 to 215.1 ($[^2\text{H}_6]$ -ENZ), m/z 451.1 to 201.1 (desmethylENZ) and m/z 457.1 to 195.1 ($[^2\text{H}_6]$ - desmethylENZ) were monitored and the retention times were approximately 3.0 and 2.8 min for the drug and metabolite, together with their corresponding internal standards, respectively.

The assay limit of detection (LOD) was 1 ng/ml and lower limit of quantification (LLOQ) was 3 ng/ml. A freshly prepared stock of 10 μM ENZ (4,640 ng/ml) or 50 μM ENZ (23,200 ng/ml) was spiked into conditioned medium and diluted to a working concentration of 46.4 ng/ml or 232.0 ng/ml for use as a dilution quality control (DQC), to guarantee the integrity and accuracy of the test samples.

Tissue preparation for MALDI imaging. PDEs were cultured in the absence or presence of ENZ for multiple time points as described above. At the time of harvest, explants were bisected along the marked tissue dye line that indicated the planar orientation of the tissue. One-half of the tissue was arranged in a cryo-mould filled with chilled 2% CMC and snap frozen. 10 μm sections of tissues were cut from the frozen block using a Shandon E cryotome (Thermo Scientific, Germany) and consecutive sections collected by thaw mounting on Superfrost glass slides (Thermo Scientific, Hungary) for haematoxylin and eosin (H&E) and drug imaging (MALDI MSI MS/MS). The other tissue halves were snap-frozen and stored at -80°C for LC-MS/MS analysis as described above.

Histology and immunohistochemistry. H&E slides were air-dried briefly (equilibrated to room temperature if frozen), heat-fixed on a heat block at 65°C for 2 h and stained within 24 h according to an in-house protocol. Immunohistochemistry (IHC) slides were rinsed in Tris Buffered Saline (TBS) pH 7.6 and fixed in 4% paraformaldehyde (Sigma-Aldrich, NSW, Australia) at room temperature for 10 minutes. Slides were again rinsed with TBS for 5 minutes before they were placed on to the Discovery Ultra staining platform (Roche, Basel, Switzerland). Routine IHC was performed using the androgen receptor antibody (ab108341, Abcam, Cambridge, UK), anti-Rabbit HQ antibody (760-4815 Roche, Basel, Switzerland), anti-HQ HRP antibody (760-4820, Roche, Basel, Switzerland) and ChromoMap DAB kit (760-159, Roche, Basel, Switzerland) according to manufacturer's instructions. Slides were counterstained with haematoxylin (760-2011, Roche, Basel, Switzerland) and bluing reagent (760-2037, Roche, Basel, Switzerland), dehydrated and mounted in DPX (LabChem, Zelenople, PA). Slides were scanned with an Axio Z.1 Scanner (Carl Zeiss Pty. Ltd., NSW, Australia) using an 40x objective, images were captured using Zen Blue 2.6 (Carl Zeiss Pty. Ltd., NSW, Australia) software.

Matrix application on glass slide tissue sections. Application of matrix on tissue sections for MSI analyses was achieved by sublimation^{15,45}. Slides stored at -80°C were fully equilibrated to room temperature in a dry atmosphere to avoid condensation before processing began. Sublimation entailed depositing 300 μl of 10 mg/ml α -CHCA in methanol on the bottom of the glass chamber of the sublimation apparatus and allowing the solvent to evaporate to achieve a final dry weight of 3 mg of MALDI matrix. The sublimation device (Christ, John Morris Scientific) was connected to a vacuum pump, placed in an oil bath on a heating block and evacuated to a set pressure of 0.03 mbar. 100 ml of water was added to the water cooler of the sublimation apparatus, and a cylindrical ice block was suspended in the water without touching the bottom of the chamber and allowed to cool for 10 min. The heating block was set to 145°C for at least 45 min. The matrix was gradually coated on the glass slide through a solid-gas phase state change because of the low pressure and high temperature difference in the closed system.

MALDI MSI. MALDI MSI analysis was performed on PDEs treated with 10 μM ENZ ($n = 1$ patient) and 50 μM ENZ, ($n = 2$ patients; 3 PDEs). Tissue sections were analyzed on a MALDI SYNAPT HDMS Mass Spectrometer (Waters Corporation, Manchester, UK) operating in MS/MS imaging mode. Prior to analyses, the mass spectrometer was calibrated using a calibration solution of PEG and α -CHCA over the m/z range 50–990 Da in positive ion mode.

The m/z of the protonated precursor ion of ENZ is 465.10 Da. Enhanced duty cycle (EDC) mode was used to optimise the transmission of the dominant ENZ fragment ion m/z 209.09 (Supplementary Fig. S5). Scan time was set at 1.5 sec, 1 scan was recorded per pixel, laser settings used were repetition rate of 200 Hz and laser intensity was attenuated using a variable neutral density filter set to 150 a.u. The laser-raster step-size was set at 60 μm for both x - and y -directions with beam diameter of *ca* 100 μm .

The total ion count (TIC) normalisation method was used to determine intensity of a given m/z feature in the context of the entire dataset.

Data processing and analysis. MALDI raw data files (.raw) were converted to MSI data files using HDImaging v1.4 software (Waters, Manchester, UK). The data processing settings were: resolution 8,000 full-width half-maximum (FWHM) and mass window 0.02 Da. The HDI imaging data was exported in continuum mode to the universal MSI file-sharing format- imzML. The imzML data was compatible for analysis in SciLS Lab MVS (Bruker, Bremen, Germany). The peak of interest was the most abundant ENZ fragment ion of m/z 209.09 and was visualized for the six time points and normalised by TIC.

The LC-MS/MS data were processed using Analyst (Analyst 1.62, AB Sciex). The datafiles (.wiff and scan files) were processed using a quantitation method tuned to measure the analyte and IS peak intensities at the expected elution times. The peak integration parameters were configured to a smoothing radius of 2 and bunching factor of 1–3. Automatic peak integration of all the peaks was manually checked and adjusted when necessary. The tabulated concentration for each QC samples was within 15% threshold (except for the LLOQ which is 20%). Interferences were assessed by including a biological matrix blank, unextracted IS solution and a spiked biological matrix of IS solution.

Ethics approval and informed consent. Human ethics approval for this project was obtained from the Adelaide University Human Research Ethics Committee and the Research Ethics Committee of St Andrew's Hospital (Adelaide, Australia). Fresh prostate cancer specimens were obtained with written informed consent through the Australian Prostate Cancer BioResource collection from men undergoing robotic radical prostatectomy at St Andrew's Hospital. All experiments involving human tissue were performed in accordance with the relevant guidelines and regulations.

Data availability

All data generated or analyzed during this study are either included in this published article (and its Supplementary Information Files) or are available from the Corresponding Authors upon request.

Received: 5 April 2019; Accepted: 1 October 2019;

Published online: 18 October 2019

References

- Merriell, S. W. D., Funston, G. & Hamilton, W. Prostate Cancer in Primary Care. *Adv Ther* **35**, 1285–1294, <https://doi.org/10.1007/s12325-018-0766-1> (2018).
- Barfeld, S. J., Itkonen, H. M., Urbanucci, A. & Mills, I. G. Androgen-regulated metabolism and biosynthesis in prostate cancer. *Endocr Relat Cancer* **21**, T57–66, <https://doi.org/10.1530/ERC-13-0515> (2014).
- Montgomery, B. *et al.* Neoadjuvant Enzalutamide Prior to Prostatectomy. *Clin Cancer Res* **23**, 2169–2176, <https://doi.org/10.1158/1078-0432.CCR-16-1357> (2017).
- Hoda, M. R., Kramer, M. W., Mersberger, A. S. & Cronauer, M. V. Androgen deprivation therapy with Leuprolide acetate for treatment of advanced prostate cancer. *Expert Opin Pharmacother* **18**, 105–113, <https://doi.org/10.1080/14656566.2016.1258058> (2017).
- Schalcken, J. & Fitzpatrick, J. M. Enzalutamide: targeting the androgen signaling pathway in metastatic castration-resistant prostate cancer. *BJU Int* **117**, 215–225, <https://doi.org/10.1111/bju.13123> (2016).
- Kapoor, A., Wu, C., Shayegan, B. & Rybak, A. P. Contemporary agents in the management of metastatic castration-resistant prostate cancer. *Can Urol Assoc J* **10**, E414–E423, <https://doi.org/10.5489/cuaj.4112> (2016).
- Penson, D. F. *et al.* Enzalutamide Versus Bicalutamide in Castration-Resistant Prostate Cancer: The STRIVE Trial. *J Clin Oncol* **34**, 2098–2106, <https://doi.org/10.1200/JCO.2015.64.9285> (2016).
- Davda, R. *et al.* Chemotherapy at First Diagnosis of Advanced Prostate Cancer - Revolution or Evolution? Findings from a British Uro-oncology Group UK Survey to Evaluate Oncologists' Views on First-line Docetaxel in Combination with Androgen Deprivation Therapy in Castrate-sensitive Metastatic and High-risk/locally Advanced Prostate Cancer. *Clin Oncol (R Coll Radiol)* **28**, 376–385, <https://doi.org/10.1016/j.clon.2016.01.006> (2016).
- Williams, S. G. *et al.* Randomised Phase 3 Trial of Enzalutamide In Androgen Deprivation Therapy With Radiation Therapy For High Risk, Clinically Localised, Prostate Cancer: Enzarad (Anzup 1303). *Asia-Pac. J. Clin. Oncol.* **11**, 149–149 (2015).
- Risbridger, G. P., Toivanen, R. & Taylor, R. Preclinical Models of Prostate Cancer: Patient-Derived Xenografts, Organoids, and Other Explant Models. *Cold Spring Harbor Perspect. Biol.* **10**, <https://doi.org/10.1101/cshperspect.a030536> (2018).
- Cole, R. B. & Cole, R. B. *Electrospray and MALDI Mass Spectrometry: Fundamentals, Instrumentation, Practicalities, and Biological Applications.* (John Wiley & Sons, Incorporated, 2009).
- Najdekr, L. *et al.* Influence of Mass Resolving Power in Orbital Ion-Trap Mass Spectrometry-Based Metabolomics. *Analytical Chemistry* **88**, 11429–11435, <https://doi.org/10.1021/acs.analchem.6b02319> (2016).
- Qi, Y., Müller, M., Stokes, C. S. & Volmer, D. A. Rapid Quantification of 25-Hydroxyvitamin D3 in Human Serum by Matrix-Assisted Laser Desorption/Ionization Mass Spectrometry. *Journal of The American Society for Mass Spectrometry*, <https://doi.org/10.1007/s13361-018-1956-4> (2018).
- Ait-Belkacem, R. *et al.* Mass spectrometry imaging is moving toward drug protein co-localization. *Trends Biotechnol* **30**, 466–474, <https://doi.org/10.1016/j.tibtech.2012.05.006> (2012).
- Rohner, T. C., Staab, D. & Stoekli, M. MALDI mass spectrometric imaging of biological tissue sections. *Mech Ageing Dev* **126**, 177–185, <https://doi.org/10.1016/j.mad.2004.09.032> (2005).
- Stoekli, M., Chairand, P., Hallahan, D. E. & Caprioli, R. M. Imaging mass spectrometry: A new technology for the analysis of protein expression in mammalian tissues. *Nature Medicine* **7**, 493, <https://doi.org/10.1038/86573> (2001).
- Hercules, D. M., Hillenkamp, F. & Peter-Katalinic, J. (Eds): MALDI MS. A practical guide to instrumentation, methods and applications. *Analytical and Bioanalytical Chemistry* **392**, 565–566, <https://doi.org/10.1007/s00216-008-2090-0> (2008).
- Stoekli, M., Farmer, T. B. & Caprioli, R. M. Automated mass spectrometry imaging with a matrix-assisted laser desorption ionization time-of-flight instrument. *Journal of the American Society for Mass Spectrometry* **10**, 67–71, [https://doi.org/10.1016/S1044-0305\(98\)00126-3](https://doi.org/10.1016/S1044-0305(98)00126-3) (1999).
- Trim, P. J. & Snel, M. F. Small molecule MALDI MS imaging: Current technologies and future challenges. *Methods* **104**, 127–141, <https://doi.org/10.1016/j.jymeth.2016.01.011> (2016).
- Chait, B. T., Cadene, M., Olinares, P. D., Rout, M. P. & Shi, Y. Revealing Higher Order Protein Structure Using Mass Spectrometry. *J Am Soc Mass Spectrom* **27**, 952–965, <https://doi.org/10.1007/s13361-016-1385-1> (2016).
- Lucarelli, G. *et al.* Metabolomic profiling for the identification of novel diagnostic markers in prostate cancer. *Expert Rev Mol Diagn* **15**, 1211–1224, <https://doi.org/10.1586/14737159.2015.1069711> (2015).
- Pirman, D. A. & Yost, R. A. Quantitative tandem mass spectrometric imaging of endogenous acetyl-L-carnitine from piglet brain tissue using an internal standard. *Anal Chem* **83**, 8575–8581, <https://doi.org/10.1021/ac2019496> (2011).
- He, L. E. *Mass Spectrometry Imaging of Small Molecules.* (Springer New York: Imprint: Humana Press, 2015).
- Kim, K. P. *et al.* Simultaneous quantitation of abiraterone, enzalutamide, N-desmethyl enzalutamide, and bicalutamide in human plasma by LC-MS/MS. *J Pharm Biomed Anal* **138**, 197–205, <https://doi.org/10.1016/j.jpba.2017.02.018> (2017).
- Song, J. H. *et al.* Quantitative determination of enzalutamide, an anti-prostate cancer drug, in rat plasma using liquid chromatography-tandem mass spectrometry, and its application to a pharmacokinetic study. *Biomed Chromatogr* **28**, 1112–1117, <https://doi.org/10.1002/bmc.3127> (2014).
- Centenera, M. M. *et al.* A patient-derived explant (PDE) model of hormone-dependent cancer. *Molecular Oncology* **12**, 1608–1622, <https://doi.org/10.1002/1878-0261.12354> (2018).
- Centenera, M. M., Raj, G. V., Knudsen, K. E., Tilley, W. D. & Butler, L. M. *Ex vivo* culture of human prostate tissue and drug development. *Nat Rev Urol* **10**, 483–487, <https://doi.org/10.1038/nrurol.2013.126> (2013).
- Lawrence, M. G. *et al.* Patient-derived Models of Abiraterone- and Enzalutamide-resistant Prostate Cancer Reveal Sensitivity to Ribosome-directed Therapy. *Eur Urol* **74**, 562–572, <https://doi.org/10.1016/j.eururo.2018.06.020> (2018).

1. Trim, P. J. *et al.* Matrix-Assisted Laser Desorption/Ionization-Ion Mobility Separation-Mass Spectrometry Imaging of Vinblastine in Whole Body Tissue Sections. *Anal. Chem.* **80**, 8628–8634, <https://doi.org/10.1021/ac8015467> (2008).
2. Kwon, H. J. *et al.* Drug compound characterization by mass spectrometry imaging in cancer tissue. *Archives of Pharmacol Research* **38**, 1718–1727, <https://doi.org/10.1007/s12272-015-0627-2> (2015).
3. Sun, N. *et al.* Pharmacokinetic and pharmacometabolic study of pirfenidone in normal mouse tissues using high mass resolution MALDI-FTICR-mass spectrometry imaging. *Histochemistry and Cell Biology* **145**, 201–211, <https://doi.org/10.1007/s00418-0151382-7> (2016).
4. Fan, J., Jones, E. E., Drake, R. R. & Crosson, C. E. Spatial Distribution of Sphingolipids in The Mouse Retina by MALDI Imaging Mass Spectrometry. *Investigative Ophthalmology & Visual Science* **56**, 156–156 (2015).
5. Dilillo, M. *et al.* Ultra-High Mass Resolution MALDI Imaging Mass Spectrometry of Proteins and Metabolites in a Mouse Model of Glioblastoma. *Sci Rep* **7**, 603, <https://doi.org/10.1038/s41598-017-00703-w> (2017).
6. Takai, N., Tanaka, Y. & Saji, H. Quantification of small molecule drugs in biological tissue sections by imaging mass spectrometry using surrogate tissue-based calibration standards. *Mass Spectrom (Tokyo)* **3**, A0025, <https://doi.org/10.5702/massspectrometry.A0025> (2014).
7. Rysman, E. *et al.* De novo lipogenesis protects cancer cells from free radicals and chemotherapeutics by promoting membrane lipid saturation. *Cancer Res* **70**, 8117–8126, <https://doi.org/10.1158/0008-5472.CAN-09-3871> (2010).
8. Talebi, A. *et al.* Sustained SREBP-1-dependent lipogenesis as a key mediator of resistance to BRAF-targeted therapy. *Nature Communications* **9**, 2500, <https://doi.org/10.1038/s41467-018-04664-0> (2018).
9. Efsthathiou, E. *et al.* Molecular Characterization of Enzalutamide-treated Bone Metastatic Castration-resistant Prostate Cancer. *European Urology* **67**, 53–60, <https://doi.org/10.1016/j.eururo.2014.05.005> (2015).
10. Gibbons, J. A. *et al.* Pharmacokinetic Drug Interaction Studies with Enzalutamide. *Clin Pharmacokinet* **54**, 1057–1069, <https://doi.org/10.1007/s40262-015-0283-1> (2015).
11. Gibbons, J. A. *et al.* Clinical Pharmacokinetic Studies of Enzalutamide. *Clin Pharmacokinet* **54**, 1043–1055, <https://doi.org/10.1007/s40262-015-0271-5> (2015).
12. Bader, D. A. *et al.* Mitochondrial pyruvate import is a metabolic vulnerability in androgen receptor-driven prostate cancer. *Nature Metabolism* **1**, 70–85, <https://doi.org/10.1038/s42255-018-0002-y> (2019).
13. Kuruma, H. *et al.* A novel antiandrogen, Compound 30, suppresses castration-resistant and MDV3100-resistant prostate cancer growth *in vitro* and *in vivo*. *Mol Cancer Ther* **12**, 567–576, <https://doi.org/10.1158/1535-7163.MCT-12-0798> (2013).
14. Pal, S. K. *et al.* Identification of mechanisms of resistance to treatment with abiraterone acetate or enzalutamide in patients with castration-resistant prostate cancer (CRPC). *Cancer* **124**, 1216–1224, <https://doi.org/10.1002/cncr.31161> (2018).
15. Luk, I. S. *et al.* BIRC6 Targeting as Potential Therapy for Advanced, Enzalutamide-Resistant Prostate Cancer. *Clin Cancer Res* **23**, 1542–1551, <https://doi.org/10.1158/1078-0432.CCR-16-0718> (2017).
16. FDA, U. S. In *Food and Drug Administration* (ed U.S. Department of Health and Human Services) (U.S. Department of Health and Human Services Food and Drug Administration, Center for Drug Evaluation and Research Center for Veterinary Medicine, 2013).
17. Price, D. M., Bashir, S. & Derrick, P. R. Sublimation properties of x,y-dihydroxybenzoic acid isomers as model matrix assisted laser desorption ionisation (MALDI) matrices. *Thermochimica Acta* **327**, 167–171, [https://doi.org/10.1016/S0040-6031\(98\)00606-6](https://doi.org/10.1016/S0040-6031(98)00606-6) (1999).

Acknowledgements

S.M.M. is supported by a University of Adelaide International Wildcard Scholarship Award at the University of Adelaide; M.M.C. is supported by a Young Investigator Award from the Prostate Cancer Foundation of Australia; L.M.B. is supported by a Future Fellowship from the Australian Research Council (FT130101004), and a Principal Cancer Research Fellowship produced with the financial and other support of Cancer Council SA's Beat Cancer Project on behalf of its donors and the State Government of South Australia through the Department of Health. L.M.B. and M.M.C. acknowledge grant support from Cancer Australia (ID1138766) and from The Movember Foundation/Prostate Cancer Foundation of Australia (MRTA3). We thank Dr Benjamin Ung (School of Pharmacy and Medical Sciences, University of South Australia) for technical guidance on high resolution slide scanning.

Author contributions

S.M.M., B.K.P., P.J.T., M.F.S. and L.M.B. designed the research. S.M.M. performed all experiments with assistance in conducting the research as noted; K.L.B. consented patients and provided clinical specimens. B.K.P. and P.J.T. assisted with tissue set-up for mass spectrometry imaging. S.I. and K.L.B. assisted with *ex vivo* culture of clinical prostate tissue. J.M.L. and D.A.B. assisted with immunohistochemistry and slide scanning. J.S. performed clinical pathological assessment of clinical specimens. S.M.M., P.J.T. and M.F.S. analyzed the results. P.J.T., M.F.S. and L.M.B. supervised the research. M.M.C. edited the manuscript. S.M.M. wrote the manuscript, which was edited and approved by all authors. **competing interests**
The authors declare no competing interests.

Additional information

Supplementary information is available for this paper at <https://doi.org/10.1038/s41598-019-51549-3>.

Correspondence and requests for materials should be addressed to L.M.B.

Reprints and permissions information is available at www.nature.com/reprints.

Publisher's note Springer Nature remains neutral with regard to jurisdictional claims in published maps and institutional affiliations.



Open Access This article is licensed under a Creative Commons Attribution 4.0 International License, which permits use, sharing, adaptation, distribution and reproduction in any medium or format, as long as you give appropriate credit to the original author(s) and the source, provide a link to the Creative Commons license, and indicate if changes were made. The images or other third party material in this article are included in the article's Creative Commons license, unless indicated otherwise in a credit line to the material. If material is not included in the article's Creative Commons license and your intended use is not permitted by statutory regulation or exceeds the permitted use, you will need to obtain permission directly from the copyright holder. To view a copy of this license, visit <http://creativecommons.org/licenses/by/4.0/>.

© The Author(s) 2019

6.2. Supplementary Information

Patient	PDE label	Patient ID	Age RP	Pre RP PSA	P Stage	GI (RP)	GI (1°)	GI (2°)	Core used for Research-Pathologist Rescore
1	C	33042R	72.3	19.7	PT3B	7	4	3	6 (3+3)
2	D	33036R	71	2.24	PT2C	7	3	4	Benign
3	E	33050L	69	18.3	PT3A	8	4	4	8 (4+4)
4	F	33063L	64.6	-	PT3B	9	4	5	9 (4+5)
5	G1	33055R	73.4	18	PT3A	7	4	3	Benign
5	G2	33055L	73.4	18	PT3A	-	-	-	Benign
6	H	33026L	59.6	5.5	PT3A	6	3	3	Benign
7	J1	33061L	69.8	4.6	PT3A	-	-	-	6 (3+3)
7	J2	33061R	69.8	4.6	PT3A	7	4	3	Benign
8	K1	33065L	67.3	17	PT3A	-	-	-	6 (3+3)
8	K2	33065R	67.3	17	PT3A	7	3	4	Benign

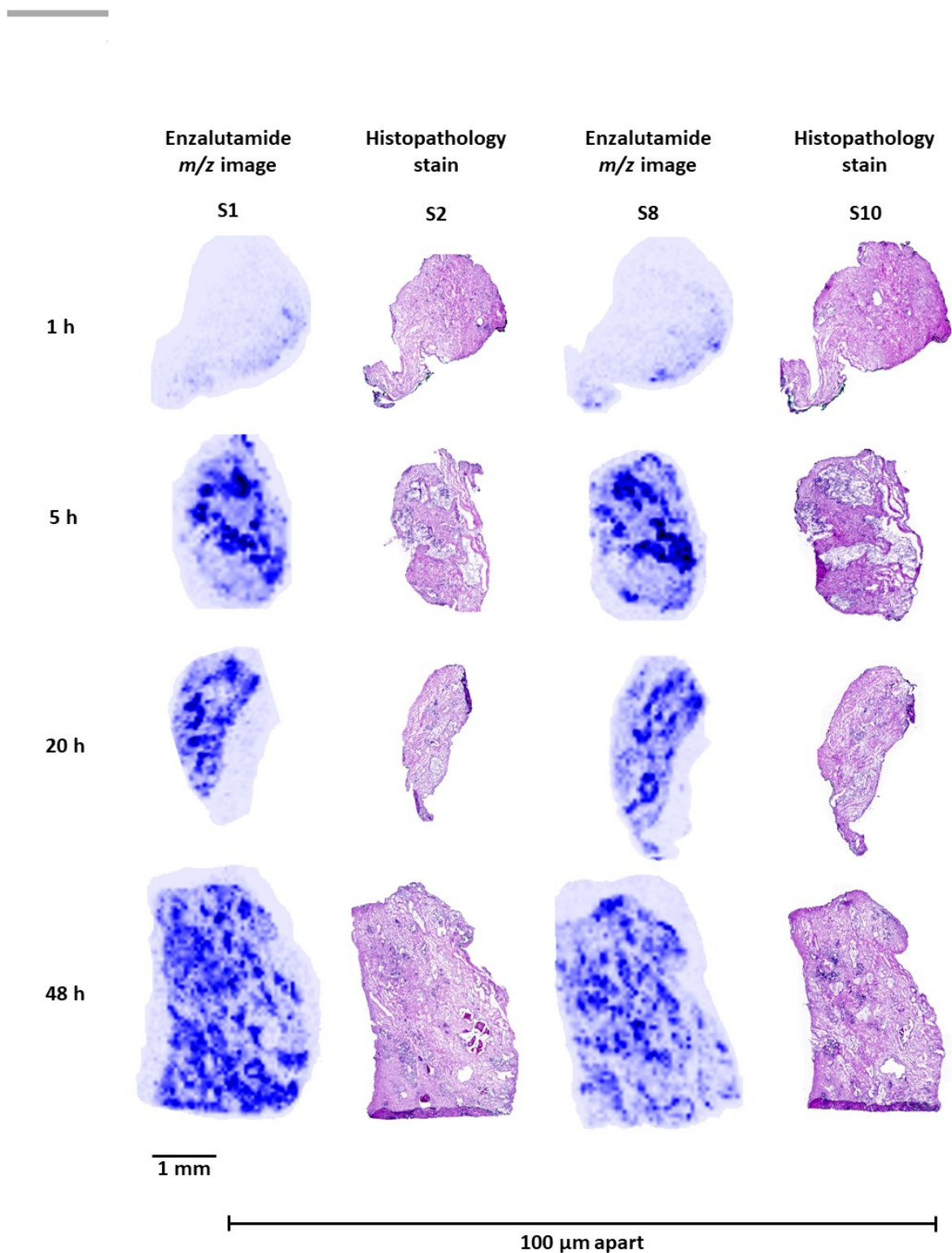
Supplementary Table ST1. Clinical pathological assessment of Day 0 formalin-fixed paraffin-embedded samples of PDE tissues used in LC-MS/MS quantification assay. GI (RP)- represents overall Gleason score for the patient sample at the time of surgery by radical prostatectomy.

				DMSO (ng/ml)										ENZ (ng/ml)										
				0 h		48 h				0 h	48 h	0 h (50µM)	48 h (50µM)	0 h		48 h				0 h	48 h	0 h (50µM)	48 h (50µM)	
Patient	PDE	DQC	Accuracy	DS	DQ	DSS1	DSS2	DQS1	DQS2	MALDI	MALDI	MALDI	MALDI	DS	DQ	DSS1	DSS2	DQS1	DQS2	MALDI	MALDI	MALDI	MALDI	
1.	C	45.8	98.7%	BLOQ	BLOQ	BLOQ	BLOQ	BLOQ	BLOQ	BLOQ	BLOQ	BLOQ	N/A	N/A	5,650	4,040	5,270	5,330	4,420	4,530	4,890	4,640	N/A	N/A
2.	D	45.8	98.7%	BLOQ	BLOQ	BLOQ	BLOQ	BLOQ	BLOQ	BLOQ	BLOQ	BLOQ	N/A	N/A	4,950	5,090	4,240	4,910	5,200	5,690	5,260	5,250	N/A	N/A
3.	E	53.1	114.4%	BLOQ	BLOQ	BLOQ	BLOQ	BLOQ	BLOQ	BLOQ	BLOQ	BLOQ	N/A	N/A	6,230	4,520	5,060	4,800	4,150	4,450	4,240	4,640	N/A	N/A
4.	F	53.1	114.4%	BLOQ	BLOQ	BLOQ	BLOQ	BLOQ	BLOQ	BLOQ	BLOQ	BLOQ	N/A	N/A	4,360	5,030	4,280	4,610	4,740	4,980	4,730	5,250	N/A	N/A
5.	G1	51.3	110.5%	BLOQ	BLOQ	BLOQ	BLOQ	BLOQ	BLOQ	BLOQ	BLOQ	BLOQ	N/A	N/A	5,320	5,520	4,550	4,270	3,970	3,720	5,310	4,510	N/A	N/A
5.	G2	51.3	110.5%	BLOQ	BLOQ	BLOQ	BLOQ	BLOQ	BLOQ	BLOQ	BLOQ	BLOQ	N/A	N/A	4,620	4,080	3,950	4,270	3,700	3,880	5,170	4,010	N/A	N/A
6.	H	51.3	110.5%	BLOQ	BLOQ	BLOQ	BLOQ	BLOQ	BLOQ	BLOQ	BLOQ	BLOQ	BLOQ	BLOQ	4,950	4,800	4,520	4,490	4,850	5,110	5,460	4,400	23,100	22,000
7.	J1	44.7	96.4%	BLOQ	BLOQ	BLOQ	BLOQ	BLOQ	BLOQ	BLOQ	BLOQ	BLOQ	BLOQ	BLOQ	4,740	4,120	4,010	4,410	4,020	4,230	4,890	4,110	20,300	20,700
7.	J2	44.7	96.4%	BLOQ	BLOQ	BLOQ	BLOQ	BLOQ	BLOQ	BLOQ	BLOQ	BLOQ	BLOQ	BLOQ	4,490	5,340	5,000	4,690	4,680	4,640	4,920	4,930	21,600	20,700
8.	K1	42.9	92.4%	BLOQ	BLOQ	BLOQ	BLOQ	BLOQ	BLOQ	BLOQ	BLOQ	BLOQ	BLOQ	BLOQ	4,880	4,870	4,220	4,520	4,700	4,840	4,230	3,820	22,700	20,500
8.	K2	42.9	92.4%	BLOQ	BLOQ	BLOQ	BLOQ	BLOQ	BLOQ	BLOQ	BLOQ	BLOQ	BLOQ	BLOQ	4,720	4,370	4,470	4,440	4,180	4,110	4,170	3,840	20,100	19,500

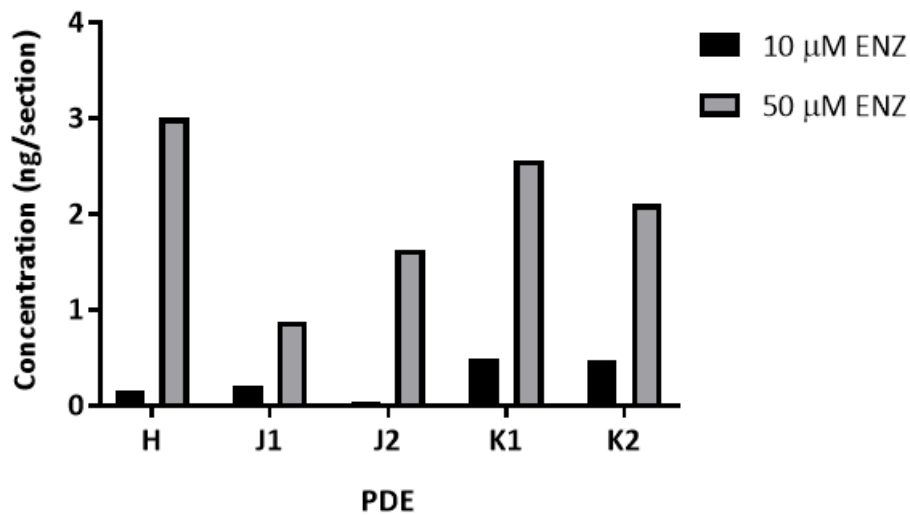
Supplementary Table ST2. Summary data for LC-MS/MS quantification of enzalutamide in M4 media. PDEs from n=8 patients (11 PDEs) were cultured in medium containing 10 µM ENZ or DMSO control over 48 h. Prior to incubation, at 0 h, cultured media was collected for drug stability (DS – medium with gelatin sponge only) and drug quantification (DQ – medium with explant atop of a gelatin sponge). Quadruplicate PDE tissues were placed evenly in separate DQ wells, DQS1 and DQS2 whilst DS wells, DSS1 and DSS2, monitored integrity of ENZ over the 48-h incubation period. An extra subset of tissues from n=3 patients were cultured in medium containing 50 µM ENZ or DMSO control over 48 h for MALDI MSI. Dilution quality control (DQC) indicates a freshly prepared stock of 10 µM ENZ (4,640 ng/ml) or 50 µM ENZ (23,200 ng/ml) was spiked into conditioned medium and diluted to a working concentration of 46.4 ng/ml or 232.0 ng/ml. BLOQ - below LLOQ (3.0 ng/ml).

Patient	Measured Concentration (ng)										Normalised (ng/ μ g) Total Protein									
	Day \emptyset	DMSO, control					ENZ, 10 μ M treatment					Day \emptyset	DMSO, control				ENZ, 10 μ M treatment			
	PDE	QC	QC/1	2	3	4	5	6	7	8	QC	QC/1	2	3	4	5	6	7	8	
1.	C	—	0.00	0.00	0.00	0.00	4.13	3.68	2.62	2.17	—	0.00	0.00	0.00	0.00	0.44	0.36	0.49	0.40	
2.	D	0.14	0.00	0.00	0.00	0.00	5.84	4.78	6.74	6.18	0.01	0.00	0.00	0.00	0.00	0.31	0.33	0.32	0.47	
3.	E	0.00	0.00	0.00	0.00	0.00	3.52	2.89	4.41	7.31	0.00	0.00	0.00	0.00	0.00	0.22	0.30	0.20	0.24	
4.	F	0.01	0.00	0.00	0.00	0.00	4.6	2.21	5.47	4.15	0.00	0.00	0.00	0.00	0.00	0.46	0.55	0.44	0.26	
5.	G1	0.01	0.00	0.00	0.00	0.00	2.09	1.78	2.99	2.18	0.00	0.00	0.00	0.00	0.00	0.33	0.29	0.40	0.43	
5.	G2	0.02	0.00	0.00	0.00	0.00	1.16	3.8	1.24	2.25	0.00	0.00	0.00	0.00	0.00	0.42	*1.39	0.48	0.36	
6.	H	0.00	0.00	0.00	0.00	0.00	5.53	4.77	7.67	7.98	0.00	0.00	0.00	0.00	0.00	0.37	0.35	0.47	0.64	
7.	J1	0.00	0.00	0.00	0.00	0.00	3.48	3.70	4.51	4.22	0.00	0.00	0.00	—	0.00	0.30	0.26	0.31	0.29	
7.	J2	0.00	0.00	0.00	0.00	0.00	5.48	9.51	4.18	8.02	0.00	0.00	0.00	0.00	0.00	0.35	0.62	0.43	0.60	
8.	K1	0.00	0.00	0.00	0.00	0.00	11.7	5.99	9.93	12.5	0.00	0.00	0.00	0.00	0.00	0.36	0.30	0.35	0.42	
8.	K2	0.13	0.00	0.00	0.00	0.00	14.6	6.11	9.08	10.6	0.00	0.00	0.00	0.00	0.00	0.31	0.30	0.37	0.34	

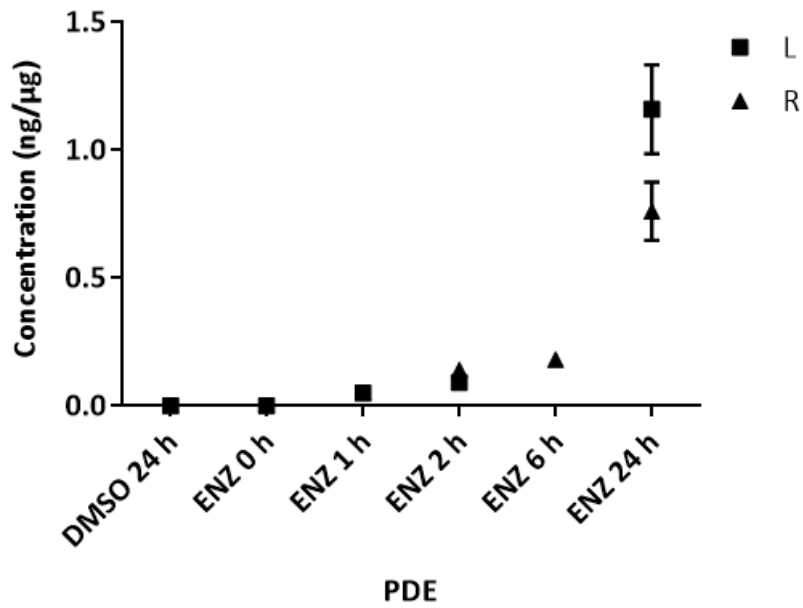
Supplementary Table ST3. Summary data for LC-MS/MS quantification of enzalutamide in PDE homogenates. PDEs from n=8 patients (11 PDEs) were cultured in medium containing 10 μ M ENZ or DMSO control over 48 h as previously outlined ([Supplementary Table ST2](#)). Intra-patient variability is the percent average coefficient of variation (%) of measured drug concentration (ng/ μ g) in replicate PDEs from each patient. Inter-patient variability is the percent average of the mean drug concentration (ng/ μ g) across the entire patients. The drug absorption had an intra- and inter-patient variability of 17.7% and 20.1%, respectively. Values in italics not used in calculation.



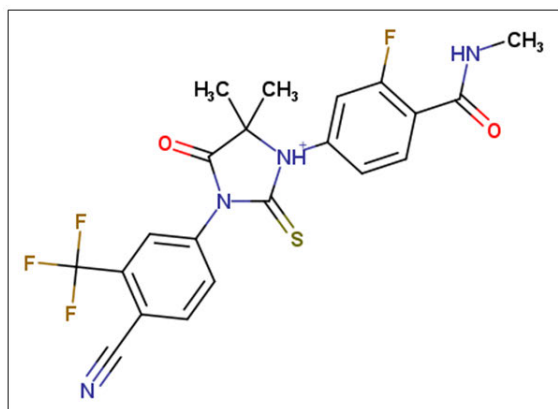
Supplementary Figure S1. Time profile of ENZ penetration in *ex vivo* prostate tissue culture. A. Four PDE's from a single patient were cultured in medium containing 50- μ M ENZ over a 48-h period. MALDI MSI MS/MS images (S1 and S8) normalised to TIC of the predominant ENZ fragment ion, m/z 209.09, next to a H&E stained serial sections (S2 and S10) at 0 h, 5 h, 20 h and 48 h. S1 and S2 are adjacent sections whereas S8 and S10 are 10 μ m apart; S1 and S10 represent a cryo-sectioning depth of 100 μ m into the PDE block.



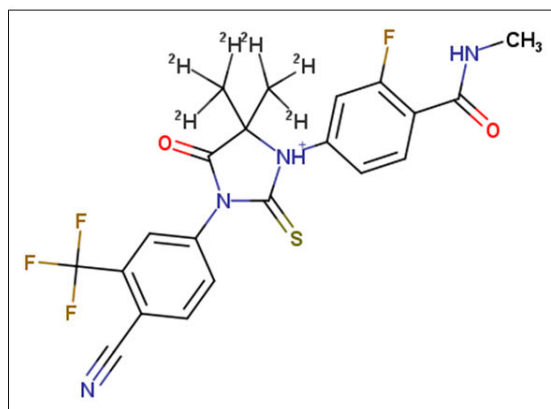
Supplementary Figure S2. LC-MS/MS quantification of ENZ in PDE homogenates derived from thin cryosections. PDEs from different patients were cultured in medium containing 10 μ M ENZ or 50 μ M ENZ over a 48-h period and harvested by embedding in 2% CMC. Samples were cryo-sectioned at a thickness of 10 μ m. For equivalent dosage, n=5 section(s) (10 μ M ENZ), dark grey bar and n=1 section(s) (50 μ M ENZ) light grey bar, were collected and analysed by LC-MS/MS as earlier described. Data displayed as ng per tissue section. Sample volume was insufficient for total protein measurements.



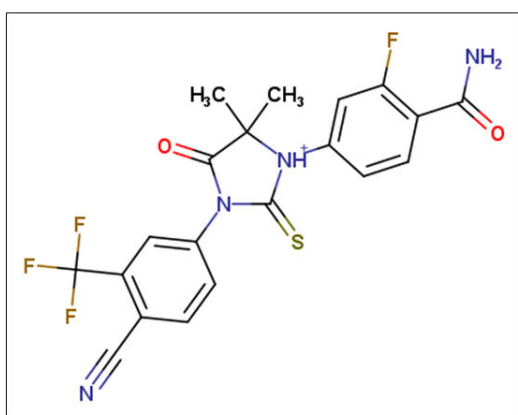
Supplementary Figure S3. LC-MS/MS quantification of ENZ in PDE homogenates over a time course. Six PDEs from either the left (L) and right (R) prostate cores were cultured in 10 µM ENZ and harvested at 0 h, 1 h, 2 h, 6 h, 24 h or 24 h (DMSO control) and bisected into two halves. One-half was homogenised as described for LC-MS/MS analysis. Drug concentration is normalised to total protein expressed as ng/µg. *Note: PDE for L at 6 h lost during sample homogenisation. Error bars indicate the 15% CV threshold allowed for accuracy and precision of assay.



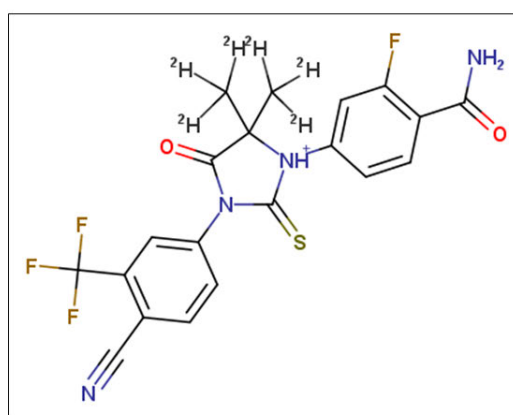
1. Enzalutamide (ENZ)
 $[M+H]^+$ m/z 465.1



2. [²H₆]-Enzalutamide
 $[M+H]^+$ m/z 471.1

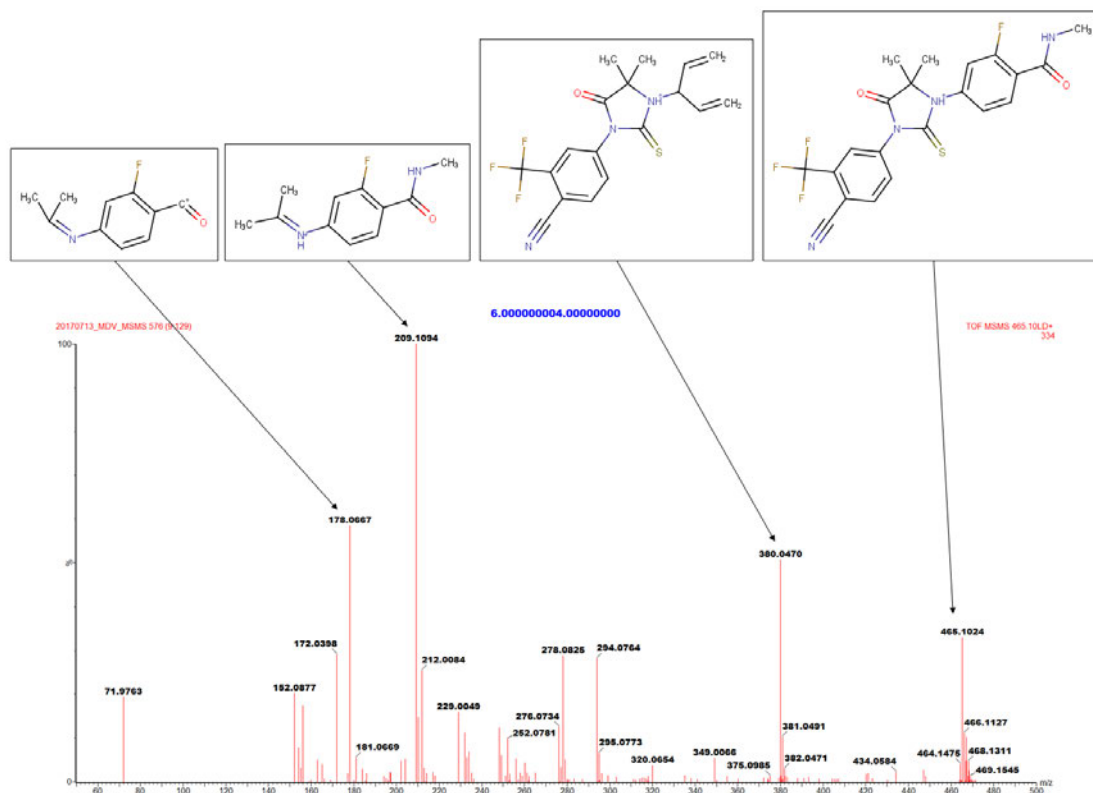


3. Desmethylenzalutamide
 $[M+H]^+$ m/z 451.1



4. [²H₆] - Desmethylenzalutamide
 $[M+H]^+$ m/z 457.1

Supplementary Figure S4. Chemical structures. Molecular structures and exact molecular weights for MRM selection of **1.** enzalutamide (ENZ), **2.** deuterated ENZ, **3.** desmethylENZ and **4.** deuterated desmethylENZ. Structures drawn using MarvinSketch version 18.19.0.



Supplementary Figure S5. MRM transmission of fragment ions of enzalutamide in positive ion mode MALDI MSI. m/z 209.1 is the most dominant fragment ion of the collision induced dissociation (CID) of the precursor m/z 465.1. Other confirmation ions are m/z 380.0 and m/z 178.0.

CHAPTER 7:

Spatial Mapping of the Lipidomics Effects of AR Inhibition by Enzalutamide in Patient-Derived Prostate Cancer Explants

Context

As previous result Chapters in this thesis reported on the use of a different mass spectrometer, the justification of change of instrumentation needs to be pointed out. In comparison to the Waters MALDI SYNAPT HDMS instrument, the Bruker timsTOF Flex, had better laser optics for generation of well-defined square pixels as opposed to oversampled ablated areas, improved mass resolution 40,000 FWHM versus 8,000 FWHM and provided more streamlined data processing workflows without need for commercial-to-vendor neutral file type conversion thereby inherently preserving raw data mass accuracy. Although a parallel evaluation of the two systems was not assessed in the project, an example of comparative mass spectra from automated spray coated unmatched prostate tissues is presented in [Appendix C](#). The main advantage of this system was generation of refined molecular profiles of *ex vivo* human prostate tissues with incredible spatial resolution to drive prudent interrogation of lipid metabolic changes following culture and anti-hormonal treatment.

7.1. Introduction

As PCa development and progression is dependent on AR signalling with a hallmark of increased lipogenesis, several therapies have been put forward to target various aspects of lipid synthesis. These pharmacological interventions seek to hamper substrate flux for lipid anabolism and competitively inhibit lipid synthetic enzymes that are direct AR regulated genes such as FASN, Acetyl-CoA carboxylase (ACC) and Stearoyl-CoA desaturase (SCD). GSK2194069 is one of the early inhibitors of FASN that acts by blocking its β -ketoacyl reductase site¹³⁰. Another novel FASN inhibitor reprogrammed the metabolome of CPRC resulting in down regulation of AR and its AR-V7 variant³⁰⁰ whilst Osajin inhibited FASN activity leading to decreased fatty acid levels, lipid accumulation and PSA downregulation³⁰⁷. In contrast, another group has argued that targeting SREBP1 is more potent than FASN inhibition irrespective of AR status, since it downregulates a host of other SREBP-regulated enzymes including ATP citrate lyase and ACC³⁰⁸. ACC and SCD inhibitors are being developed and re-purposed for PCa²⁹⁸. Blockade of mitochondrial pyruvate import has also been recently implicated in PCa therapy by depriving cells of TCA-derived substrates that support lipogenesis driven proliferation³⁸⁸. ADT is the primary therapy for men with local and advanced PCa as described in the introduction (**Chapter 1 [Section 1.2.5](#)**). Collectively, these anti-hormonal therapies not only bring about morphological changes to prostate tissue but can be expected to induce alterations in lipid content due to suppression of various nodes of androgen-regulated lipid and fatty metabolism pathways³⁷.

The impact of ADT on systemic lipid metabolism has been characterised using serum from men undergoing short-term ADT (baseline versus 3 – 6

months). Metabolomic effects of ADT include decreased gonadal and adrenal steroid synthesis, lower level of acetyl-carnitines and omega oxidation together with moderately increased 3-hydroxybutrate levels, a marker of insulin resistance, but with minor effects on cholesterol^{64,450}. Unfortunately, these physiological changes of ADT can predispose men to develop metabolic syndrome and cardiovascular co-morbidities⁴⁵¹. On a macroscopic level, it has been reported that hormonal therapy may alter glandular structure of the epithelium in both BPH and prostate adenocarcinoma and lead to artefactual Gleason grading³⁷.

Pathological examination of biopsy sections is the mainstay of tumour grading of PCa. Despite this, pathological expertise may not always be available and often not consistent between two or three pathologists. To overcome this challenge, immunohistochemical markers assist with pathological assessment and related to GS and tumour grading. Hence, IHC staining of benign, PIN and malignant markers can be useful to guide ROI selection for multivariate analysis of MSI data. p63 is a homolog of the tumour suppressor p53^{452,453}, a transcription factor that regulates proteins of cell cycle arrest, DNA repair, apoptosis, and senescence^{431,452,454}. p63 has been detected in basal cell nucleoli in normal prostate tissue but not expressed in malignant tumours⁴⁵⁵. Hence p63 is a reliable immunohistochemical marker of normal and benign tissue³⁹⁴. p63 is often employed as a cocktail with high-molecular weight cytokeratin (cytoplasmic) marker, 34 β E12, for normal basal cells⁴⁵⁶. α -methylacyl coenzyme A (AMACR) is a peroxisomal and mitochondrial enzyme critical for bile acid synthesis and β -oxidation of branched chained fatty acids²⁹. AMACR also known as P504S, was first identified from a cDNA library as a gene overexpressed in prostate

adenocarcinoma with very low expression in normal prostate glands^{457,458}. PIN glands have also been found to express AMACR whereas it is undetectable in benign glands, but AMACR is positively expressed only in 80% of PCa cases and may be confounded with atrophy, foamy glands and weakly stained in highly hyperplastic tumours, including mCRPC⁴⁵⁸. In light of the above, it is becoming increasingly common to undertake preliminary pathological assessments on tissues using a cocktail of p63 and AMACR staining, although the results must be interpreted with caution and ideally be confirmed by a pathologist.

Molecular characterisation of histopathological stained tissues by spatial mapping of parallel *in situ* data is the focus of any imaging study. To efficiently achieve this, automated molecular identification programs are increasingly being applied to make the most out of high dimension, information-rich MSI data⁴¹⁶. Various bioinformatics platforms available to researchers employ a false-discovery rate (FDR) feature to correctly assign metabolite identities³⁹¹. For example, METASPACE (<https://metaspace2020.eu/>), is an open-source data repository engine specifically suited for annotation of Orbitrap and FT-ICR MALDI data³⁸⁹. It depends on high mass accuracy (>0.001 ppm) and high resolution (>100,000 FWHM) to designate molecular formulas with incorporation of isotopic pattern distribution. A score is generated utilising spatial, spectral and chaos parameters³⁸⁹. MetaboScape 5.0® used in this Chapter, also has similar annotation scoring parameter known as annotation quality (AQ) score based on spectra acquired at a mass resolving power of 40,000 FWHM. Thus, the annotation information acquired on the integrated timsTOF Flex-SCiLS Lab-MetaboScape platform is still tentative as its only MS only data, but some degree of sureness on measurements can be taken based on the wider lipidomics

literature, matched conventional lipidomics analyses and findings in preceding Chapters of this thesis.

Ex vivo culture of human prostate tissue offers a more clinically-relevant physiological model of cancer compared to cell lines and patient-derived xenografts³⁶². The patient-derived explant (PDE) model retains hormonal signalling and recapitulates better AR action compared to cell lines³⁴⁵. Additionally, genomic features of patient tumours are also reported to be retained in patient-derived xenografts⁴⁵⁹. Enzalutamide (ENZ) is an AR inhibitor used in our explant studies to assess the effect of androgen antagonism on lipid metabolism and cellular proliferation. ENZ has three modes of action in PCa cells: inhibition of androgen binding to AR, inhibition of nuclear transport of androgen-AR complex and inhibition of binding of this complex to DNA **Figure 7.1**. Hence, it was postulated that the lipidome of prostate tissue is modulated by ENZ treatment by mediating the repression of AR regulated lipid metabolic genes.

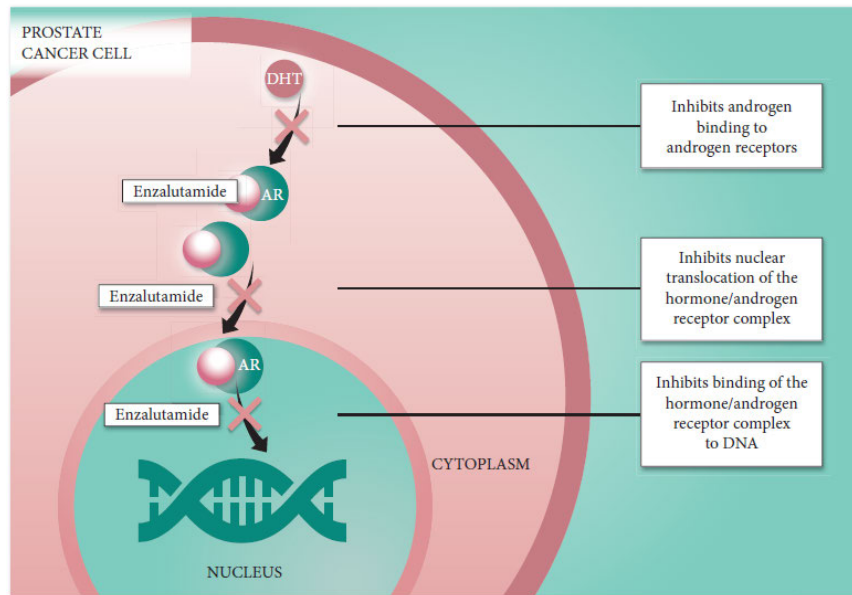


Figure 7.1. Mechanism of action of enzalutamide in prostate cancer. Reproduced with permission from John Wiley and Sons: Schalken *et al.*, 2016 Enzalutamide: targeting the androgen signalling pathway in metastatic castration-resistant prostate cancer BJU International²⁴.

Moreover, prior laboratory data from a PDE study using 10 μM ENZ showed variable response in cellular proliferation signified by ki67 expression between matched control and treated tissue (courtesy of Dr. Margaret Centenera). This is shown in **Figure 7.2** by the IHC staining waterfall plot.

NOTE:

This figure/table/image has been removed to comply with copyright regulations.

Figure 7.2. Ki67 proliferative index to enzalutamide in individual patients.

In [Chapter 3](#) and [Chapter 4](#), MALDI MSI revealed lipid profiles that were spatially associated with PCa aggressiveness. There are no MALDI studies that have interrogated lipid or metabolite profiles in hormonal cancers using an *ex vivo* model. A gap in knowledge is how lipids can respond to AR inhibition therapy using targeted pharmacological agents. To address this deficiency, this project employed a well characterised human *ex vivo* model of human prostate tumours^{362,460} to interrogate lipid changes following ENZ treatment. To fully take advantage of this model, MALDI imaging with high resolution and accurate mass (HRAM) afforded by the availability of a new instrument, Bruker timsTOF fleX™ was conducted.

The objective of this Chapter is to describe the application of lipid imaging to the PDE culture system to spatially map dynamic lipidomic changes in prostate tissue compartments and immunohistochemically defined cell types following AR inhibition.

7.2. Experimental Approach

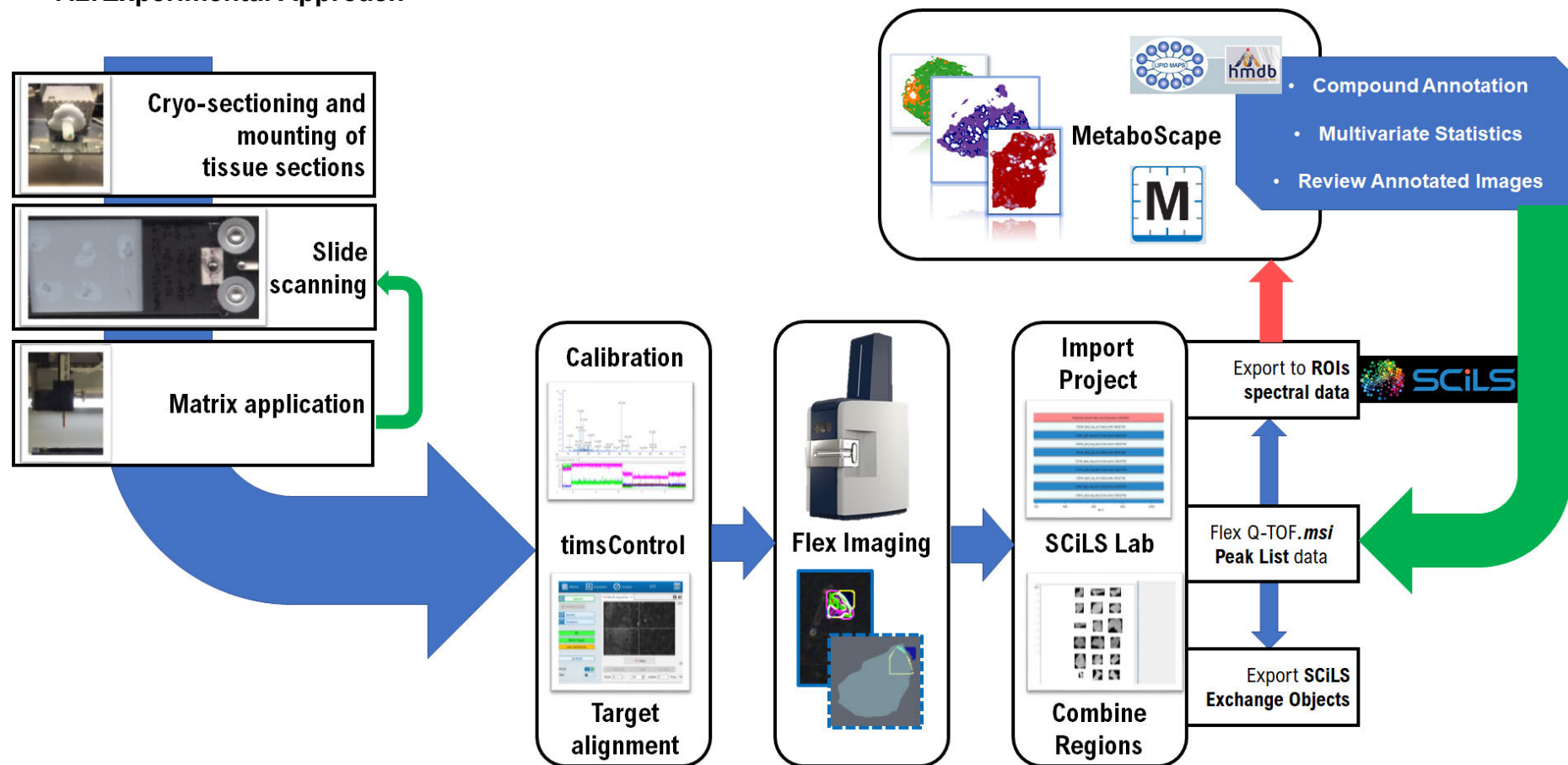


Figure 7.3. Comprehensive molecular imaging workflow. Sample preparation, data acquisition, data processing and automatic molecular annotation.

Sample cryosectioning was performed as described in **Chapter 2 [Section 2.2.1](#)** and **[Section 2.5.1](#)**. For each individual patient biopsy core or explant, 10 μm tissue serial sections were collected as follows. H&E staining, negative ion mode MSI, p63+AMACR IHC staining, positive ion mode MSI, drug MS/MS imaging and triplicate 30 μm sections collected for lipidomics. The clinical pathological features of the patients are shown in **[Supplementary Table 7.1](#)**.

7.3. Results

7.3.1. Enzalutamide Abrogates AR in PDE Tissues

In [Chapter 6](#) of this thesis, MALDI MSI was used to demonstrate that high dose of ENZ (50 μ M) penetrates cultured PDE tissues with an upward orientation over 24 h. By 6 h, ENZ distribution was evident throughout the tissue localised to epithelial cells⁴¹². IHC staining of AR was performed on additional sections from the same tissue block. It appeared to reveal decreasing AR positivity in response to ENZ in a time-dependent manner (**Figure 7.4A**). Quantification of percent (%) AR positive cells was performed using ImageJ as described in [Section 2.5.8](#). At the initial incubation stages, 1 h and 2 h, the bottom areas of the explant in contact with treatment medium (soaked sponge) show weaker staining compared to the top. At 6 h - 24 h, the bottom and top regions of the explants show similar AR detection that is lower compared to 24 h vehicle as shown in **Figure 7.4B**. This indicates that pharmacological inhibition of AR is associated with macroscopically reduced AR levels in ENZ treated explants. Serial sections to the IHC were used for histology and lipid imaging. The spatial distribution of several lipid features distributed in glandular epithelium and stromal tissue compartments is presented in **Figure 7.5**.

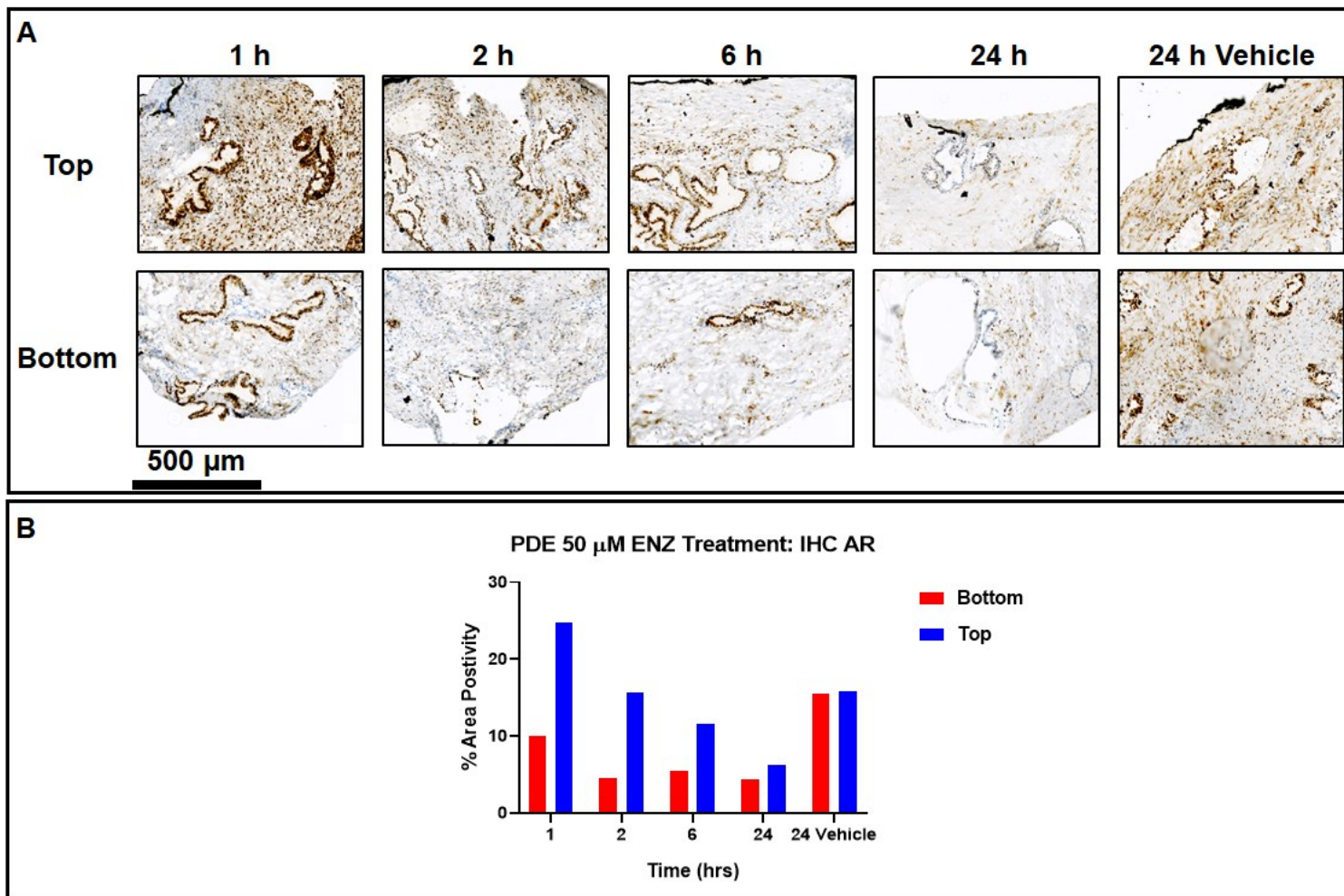


Figure 7.4. IHC staining of AR in a PDEs. A. Explants were treated with 50 μM ENZ for 1 h, 2 h, 6 h and 24 h compared to 24 h vehicle (DMSO control). IHC scans of top regions versus bottom regions (tissue in contact with treatment medium). **B.** Percentage (%) of AR positive areas in tissue were calculated from regions shown in A using ImageJ colour deconvolution tool.

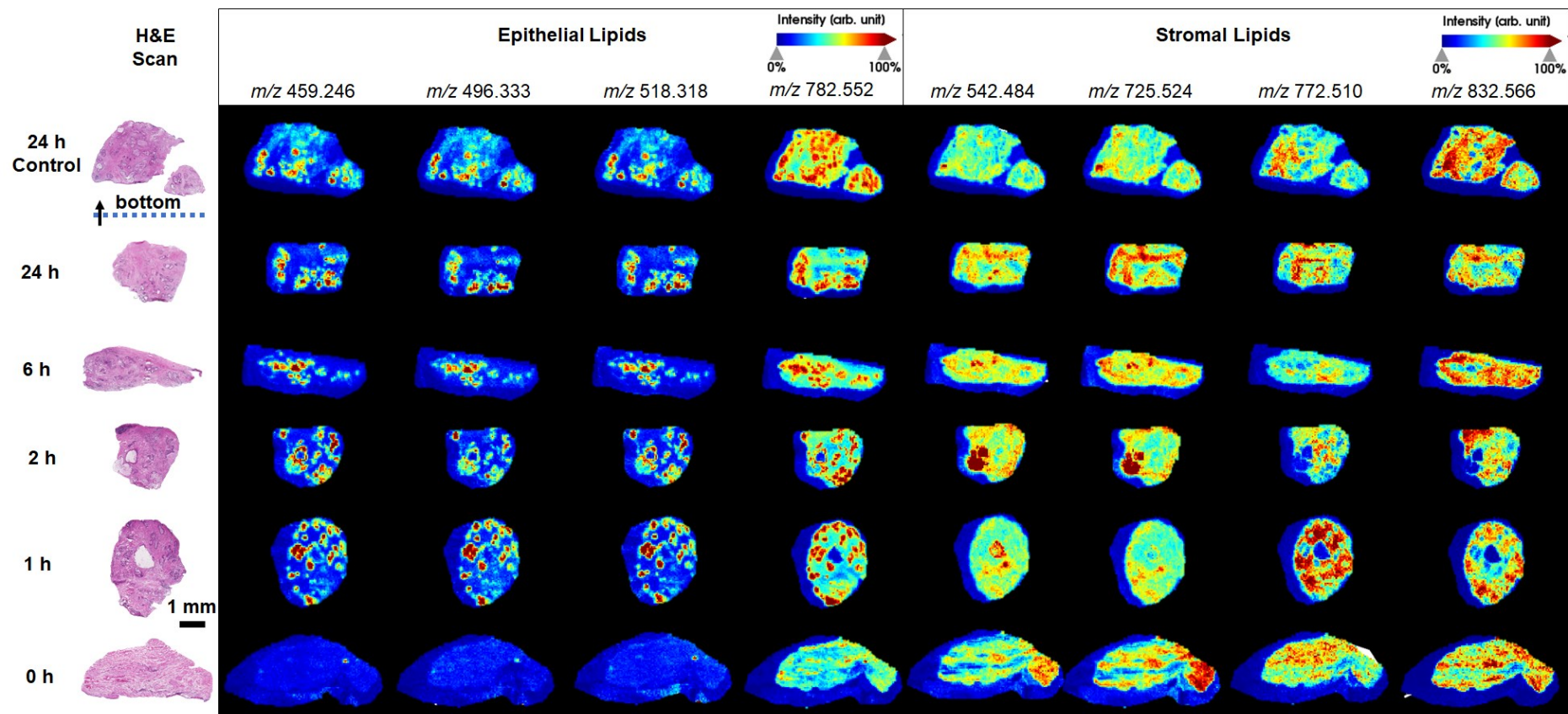


Figure 7.5. MALDI MSI of lipids in ENZ uptake in PDEs over a time course. Six PDEs were cultured in medium and harvested at various time points (50 μ M ENZ at 1 h, 2 h, 6, h and 24 h) and controls (0 h; Day 0 and 24 h DMSO). Consecutive tissues were used for H&E staining and MALDI imaging. Lipid ion images of common lipid masses in epithelium and stroma. Data acquired on SYNAPT Q-TOF in positive ion mode by sampling 60 μ m pixels.

7.3.2. Morphological Changes in Cultured and Drug-Treated PDE Tissues

In the present study, 10 μ M ENZ was used as it is a clinically/therapeutically relevant concentration⁴³⁸. The morphological appearance of tissue was assessed by H&E staining (**Chapter 2 Section 2.2.2**). Culture-related changes were reduced intensity of nuclear staining in glandular epithelium but still with healthy pink stroma like the fresh tissue. Treatment-related changes following ENZ exposure were seemingly reduced glandular prominence, necrosis with and without pyknosis and apoptotic-like cells (**Figure 7.6**). Foci of secretory cells with pyknotic nuclei bearing a similar appearance to immune infiltrate was evident in some cultured explants. Additionally, some tissues showed niches of necrosis as shown (**Figure 7.6**). This is not uncommon given that necrosis can occur because of tissue injury following surgery (radical prostatectomy/transrectal resection of the prostate) or in response to hypoxia²⁹. Insufficient access of nutrients to densely transforming benign glands can also lead to necrosis which is often seen with ductal adenocarcinoma and GS pattern 5 tumours³⁰.

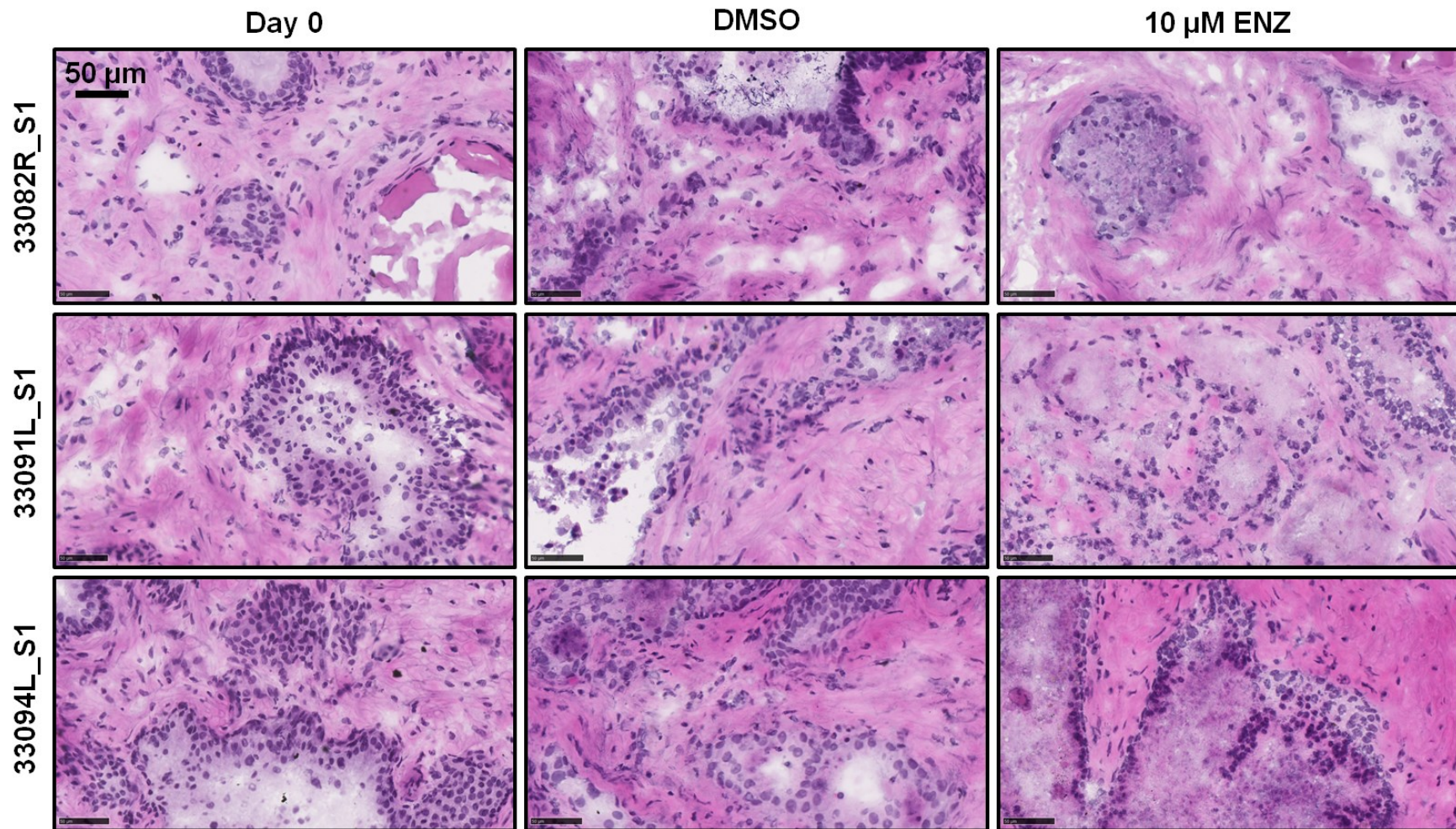


Figure 7.6. Tissue morphology of fresh-frozen and PDE cultured samples. Comparison of H&E scan of 10 μm thick cryosections from Day 0 and cultured samples (DMSO and 10 μM ENZ treatment). n=3 patients' sections are shown stained in a single batch.

7.3.3. MALDI MS/MS Imaging of Enzalutamide

Next, targeted drug imaging was performed by monitoring the mass transition of the precursor m/z 465.10 to the main fragment m/z 209.09. For the high-resolution cohort, preliminary targeted drug imaging in PDE tissues treated with 10 μ M ENZ at 20 μ m resolution yielded unreliable spatial maps. The drug signal was barely above the limit of detection in comparison to control. Hence, ensuing imaging was performed at 40 μ m in two patients ([Supplementary Figure 7.1](#)) and 60 μ m in three patients, with the former setting better showing the spatial intensity of the drug. Consistent with the prior study ([Chapter 6](#)), it was observed that the ENZ fragment ion m/z 209.09 signal was localised to glandular regions. In [Figure 7.7A](#), it is appreciable that the ENZ drug signal is emanating from epithelium. Some luminal epithelia showed morphological changes such as reduced cellularity and nuclear shrinkage possibly due to ENZ treatment ([Figure 7.7B](#)).

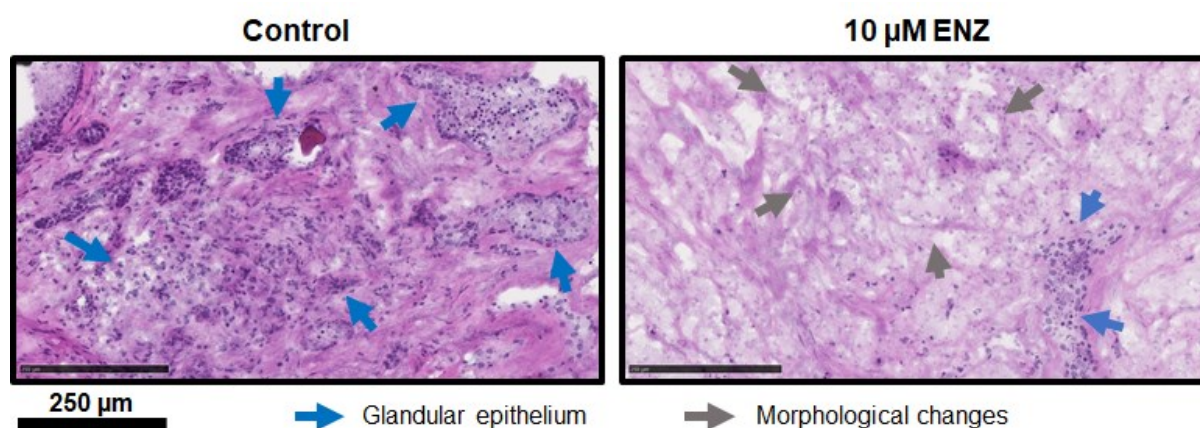


Figure 7.7B. Drug-related morphological changes in PDE samples. Comparison of epithelial architectural features in control (left) DMSO versus 10 μ M ENZ treated explants following 48 h of culture. Hormonal AR inhibition appears to cause overall reduction glandular epithelium prominence.

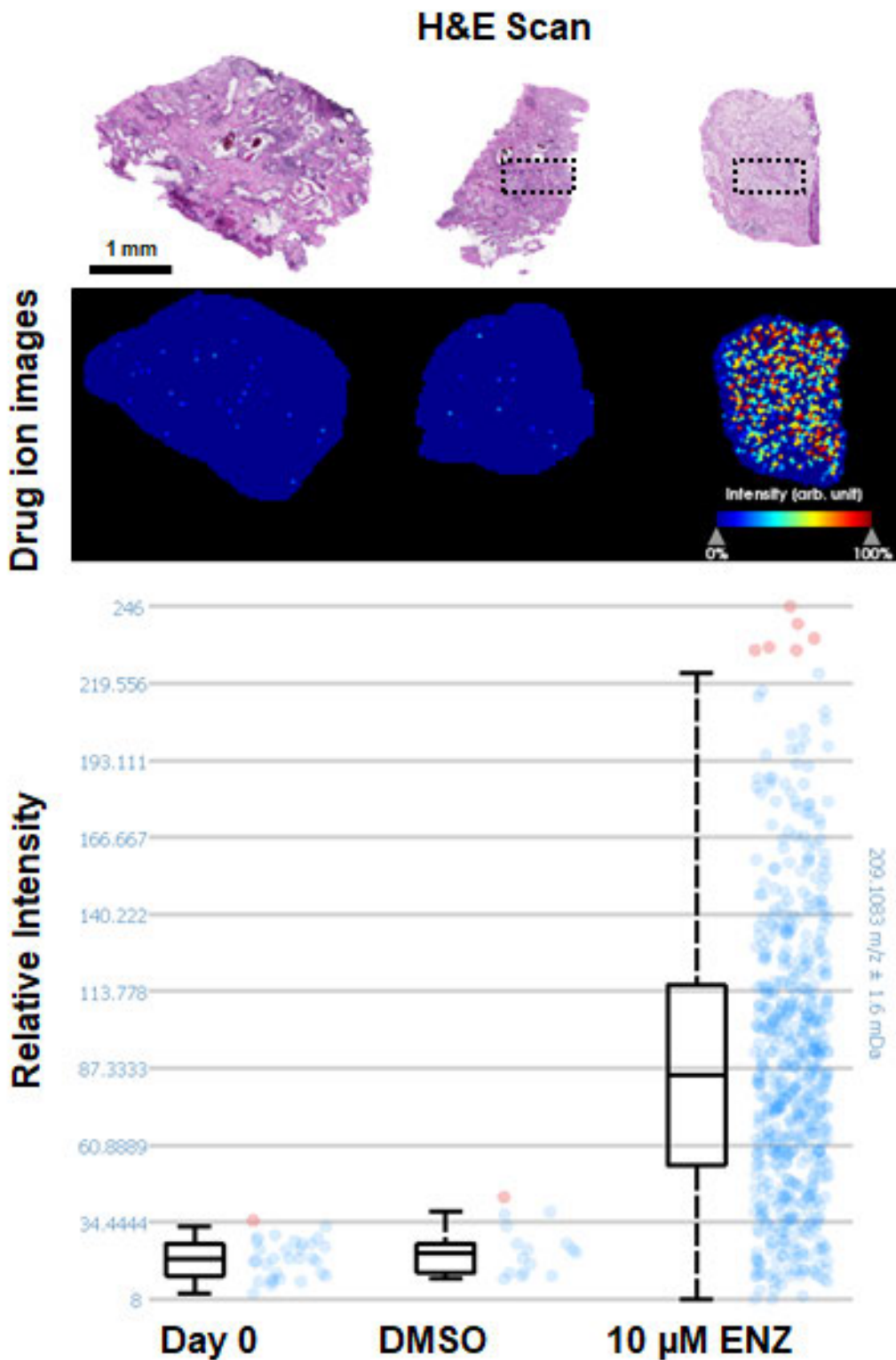


Figure 7.7A. MALDI MS/MS imaging of enzalutamide in PDE. Serial sections of H&E and targeted drug imaging were collected from Day 0, DMSO and 10 μ M ENZ culture treatments. The characteristic ENZ fragment ion, m/z 209.09 data was sampled at 60 μ m pixel sizes. Inset square boxes are shown in **Figure 7.7B**.

7.3.4. Molecular Annotations in MSI Data

Afterwards, automatic molecular identifications in MetaboScape was conducted with reference to LMSD and HMDB. This employed an algorithm for feature identification by peak picking, deadducting and deisotoping. A representative example of the ion deconvolution result is shown (**Figure 7.8**). In negative ion mode imaging, 500 m/z local maxima intervals for the tissue cluster regions were imported into MetaboScape 5.0. This resulted in 78 unique annotated features that were for review and produced 100 named m/z intervals upon re-importation in SCiLS Lab. This greater number of named features is due to deconvolution of seed ions ([Supplementary Table 7.2](#)). Conversely, the positive ion data spectra were more complex. Thus 1,000 m/z features from the tissue segments were processed. This resulted in 127 unique annotated features that were re-imported into SCiLS for review, which produced 200 named m/z intervals ([Supplementary Table 7.3](#)). Noteworthy, un-annotated masses were not precluded from the statistical analysis and still represented chemical species of biological significance. Besides, not all annotated masses are true identities especially at the lower mass range (<200 Da) where many isobaric and isomeric compounds share the same chemical space. In the same regard, a proportion of significantly altered molecular features from the volcano plots was background chemical noise.

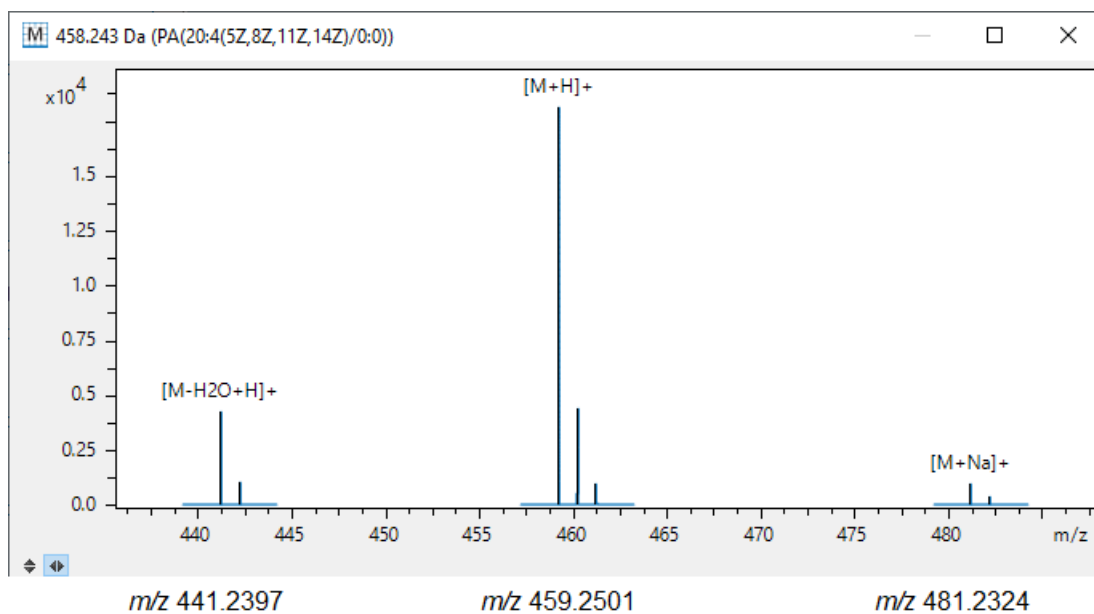


Figure 7.8. Molecular annotation by ion deconvolution. Deisotoping and deadducting of tentative LysoPA(20:4) with a neutral mass (M) of 458.243.

7.3.5. Spatial Segmentation Maps Epithelium and Stroma Cells

The timsTOF Flex platform generated high quality MSI spectra in ~4 mm² prostate sections with impressive spatial resolution for lipid visualisation. A representative example of fatty acids (FA) is given in [Supplementary Figure 7.2](#). The distribution of the possible palmitic acid, FA(16:0) and FA(16:1) varied with the MUFA having inferior peri-glandular localisation. Likewise, the signal intensity of stearic acid, FA(18:0) was localised to epithelia but FA(18:1) was less unique to stroma and in fresh-frozen tissue, and FA(18:2) more pronounced in specific niches of explants. Comparatively, FA(20:4), arachidonic acid, distribution was more stromal suggestive of its paracrine signalling role. Hence, with such highly defined morphological lipid profiles, spatial segmentation of the imaging data was conducted to delineate epithelium and stroma regions stratified according to Day 0, DMSO and 10 µM ENZ treatments. FA, PI, PS and PE lipids were detected in negative ion mode imaging whilst PC, sphingolipids and cations of PA lipids species were measured in positive ion mode.

Clustering analysis of the negative ion mode data was consistent and reproducible, revealing several prominent *m/z* features ([Figure 7.9](#)). On the other hand, the segmentation profile in the positive ion mode data was fairly heterogenous ([Figure 7.10](#)). This was due to acquisition of the first data set on a different date from the rest of the cohort and the high intensity phosphorylcholine, *m/z* 184.073 exhibited a slight mass shift. Individual patient experiment run MSI data had an average data point accuracy of ±3.1 milli Dalton (mDa). To mitigate this challenge, clustering for each patient experiment run was performed separately. The epithelium and stroma clusters were exported as objects and re-imported into the combined file with a data point accuracy of ±8.8

mDa. This effectively resulted in satisfactory peak alignment and peak picking. Subsequently, the tissue clusters in this combined region multi-patient data set were exported for automatic molecular identification as described in **7.3.4**.

In SCiLS Lab, discriminative ROC tool value was generated for six tissue files (n=5 patients). The informative *m/z* features (variables) were above 0.75 threshold. Only a single mass met this criteria, *m/z* 419.217, tentatively identified as cyclic phosphatidic acid (CPA) C18:0, with a mass error of -0.814 ppm. CPA(18:0) was more specific to fresh-frozen tissue and its reduced abundance in explants may herald it is a bioactive lipid. ANOVA of tissue segments between Day 0, control (DMSO) and ENZ detected “interesting” peaks in both polarities. Many features were deemed from the negative MALDI MSI data as “interesting” with examples presented in [Table 7.1](#). There were fewer “interesting” peaks in positive ion mode. In epithelium, LPC(16:0) had a pAD = 0.139 and *m/z* 785.657 pAD = 0.057 in Day 0 tissue, indicative of their pronounced abundance in comparison to cultured explants. Cholesterol sulfate, *m/z* 465.2301, was quite intense in benign glands and suspected tumour lesions ([Figure 7.11A](#), [Figure 7.11B](#)). As exemplified in one patient, PI(36:4) like its choline substituent, PC(36:4), was highly localised within secretory glands but the elongated PI(38:4) was rather ubiquitously distributed areas across tissue. Interestingly, in the ENZ-treated explants, lysophospholipid species, LPA(20:4)/LPA(18:1) and LPC(16:0) which have been previously demonstrated in this project to be specific to benign glands showed a differential spatial distribution compared to the full product PC(36:4)/PC(34:1) as shown in [Supplementary Figure 7.3](#).

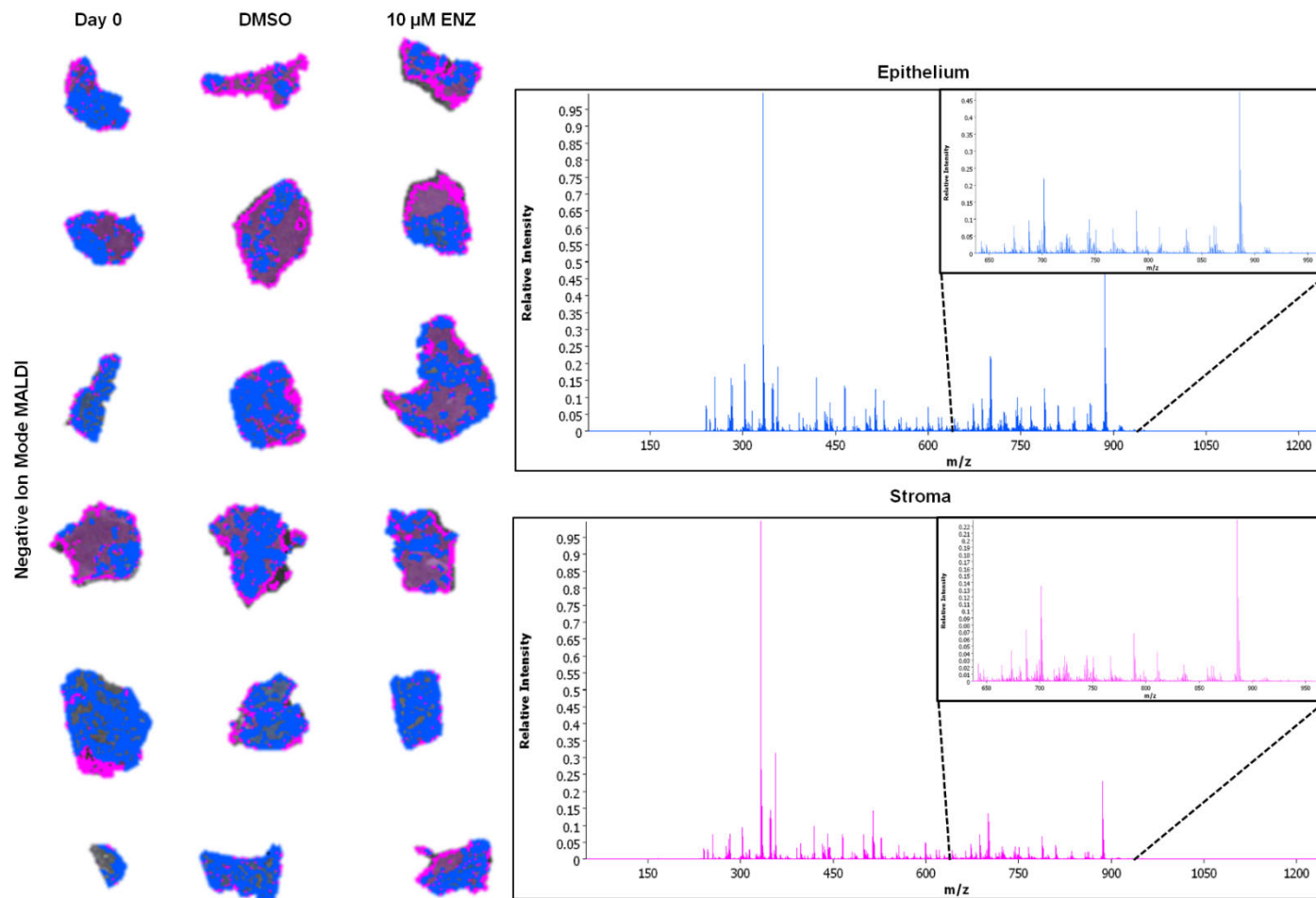


Figure 7.9. Spatial segmentation in negative ion mode. Left. Clusters showing epithelial (blue) and stromal (pink) in six PDEs. **Right.** Mass spectra of epithelial and stromal clusters with inset of m/z 650 - 950 range show lipid ion peaks.

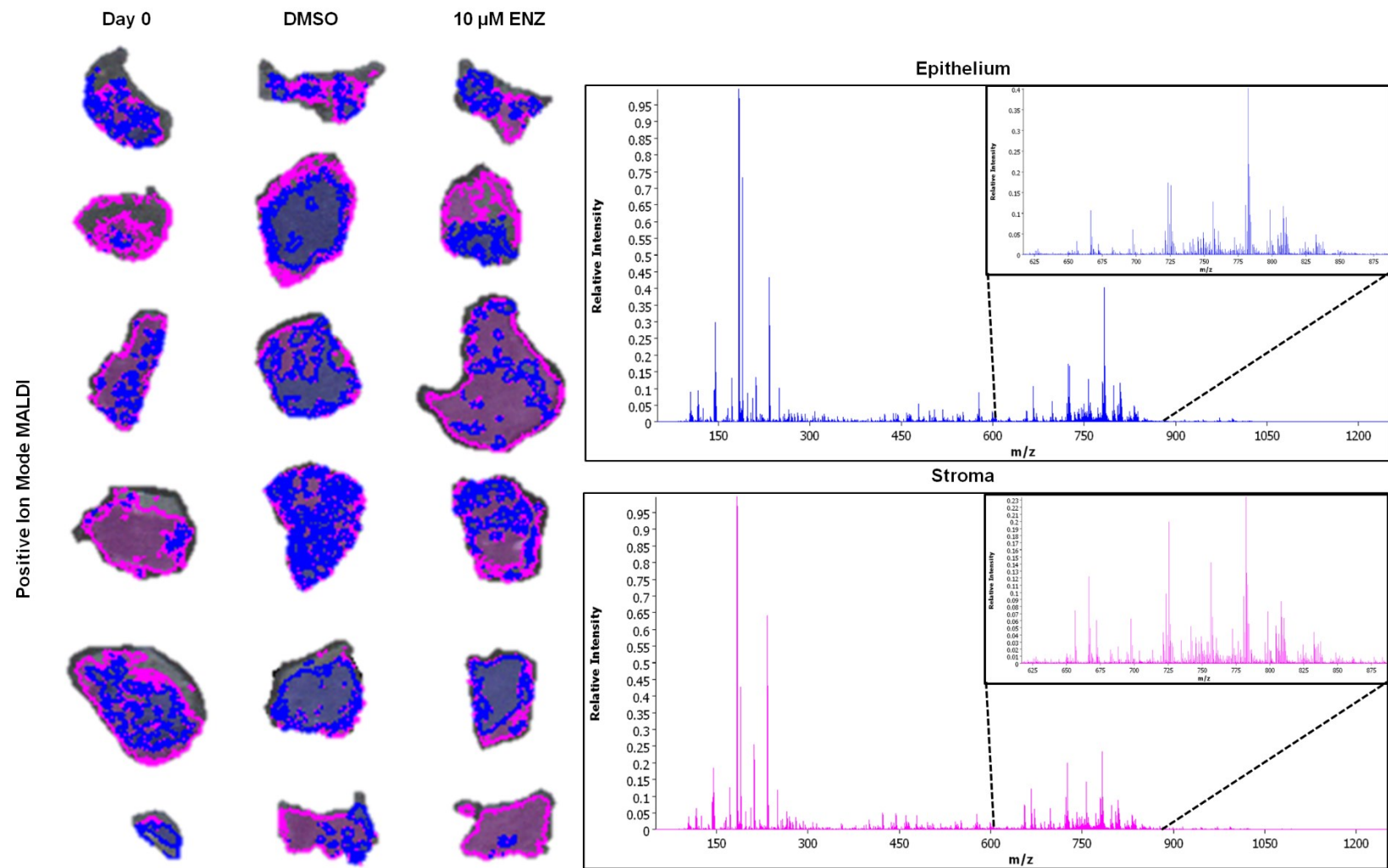


Figure 7.10. Spatial segmentation in positive ion mode. Left. Clusters showing epithelial (blue) and stromal (pink) in six PDEs. **Right.** Mass spectra of epithelial and stromal clusters with inset of m/z 625 - 875 range shows lipid ion peaks.

Bucket (Epithelium)	p-Value	p-Value (Rank)	p-Value (FWER)	p-Value (FDR)	Max. Intensity	pAD "Day0"	pAD "DMSO"	pAD "ENZ"
436.259 M	0.000116	0.003413	0.035038	0.000365	4428	0.365802	0.014616	0.000135
Palmitic acid	0.020536	0.014425	1	0.036697	22029	0.3397	0.028806	0.052971
PI(20:3)	0	0	0	0	5095	0.319401	0.000292	0.326251
486.238 M	0	0	0	0	2253	0.249626	0.510173	0.00023
434.243m/z	0	0	0.000001	0	2973	0.208981	0.005792	0.005588
PS(36:1)	0.000011	0	0.003254	0.000049	25165	0.182136	0.000004	0
PA(32:0)	0.000015	0.000024	0.004398	0.000063	3121	0.176718	0.000224	0.049682
CPA(18:0)	0	0	0	0	16598	0.154437	0	0.019891
LysoPA(16:0)	0	0.000002	0.000004	0	6084	0.133457	0	0.000023
352.132 M	0.000109	0.000056	0.033044	0.000352	94565	0.131972	0.149456	0.000003
737.558 M	0.000243	0.000437	0.073317	0.000673	4443	0.087418	0.018914	0.011744
PE(36:1)	0	0	0	0	16553	0.084449	0.008937	0.000343
Bucket (Stroma)	p-Value	p-Value (Rank)	p-Value (FWER)	p-Value (FDR)	Max. Intensity	pAD "Day0"	pAD "DMSO"	pAD "ENZ"
LysoPA(16:0)	0.000003	0.00026	0.000961	0.000012	5071	0.243714	0.019841	0.000001
LysoPA(18:0)	0.000001	0.000003	0.000383	0.000005	9839	0.166757	0.377255	0
674.489 M	0.670772	0.662644	1	0.733961	8058	0.145371	0	0
698.364 M	0	0	0	0	5531	0.022672	0.121831	0.000799
328.241 M	0	0.000001	0.000136	0.000002	5714	0.005562	0.530919	0.180123
Stearic acid	0	0	0	0	28886	0.004965	0.098109	0.000219
886.556 M	0	0	0	0	39435	0	0.857579	0.014519
358.120 M	0	0	0	0	69652	0	0.547122	0.250262
PA(32:0)	0	0	0	0	3659	0	0.140532	0.000008
486.238 M	0	0	0	0	2218	0	0.135335	0.000001
557.276 M	0	0	0	0	6871	0	0.067232	0.000002

Table 7.1. Negative MALDI data ANOVA of tissue types between treatment groups. “Interesting” peaks are statistically regarded having p-value t-test ≤ 0.05 and p-value Anderson Darling (pAD) test > 0.05 . FWER – family-wise error rate. M – neutral mass.

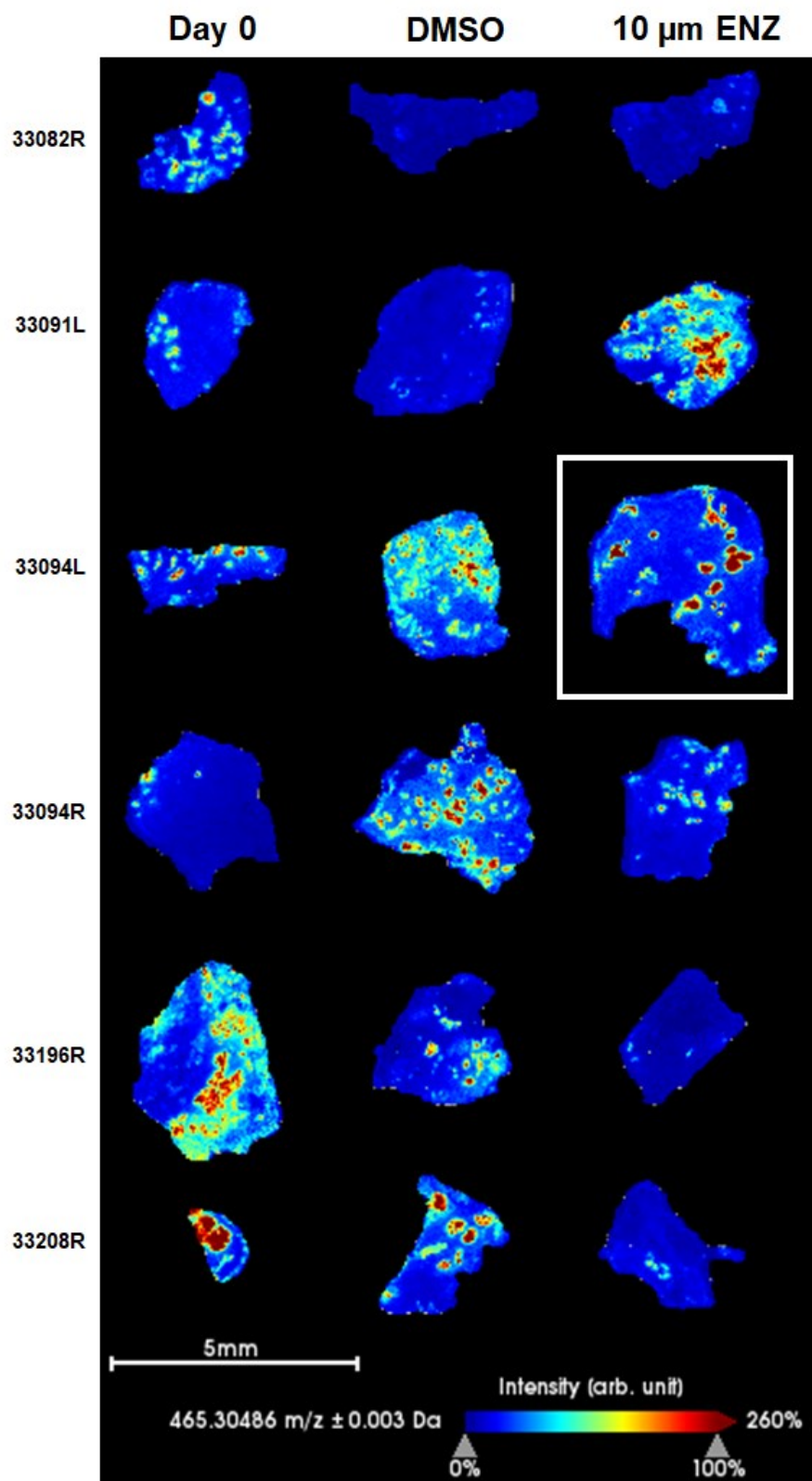


Figure 7.11A. MALDI MSI in negative ion mode in PDE tumours. Ion map of m/z 465.304 spatial distribution in six PDE sample sets ($n=5$ patients). High resolution image of 33094L ENZ (white square) shown in **Figure 7.9B**

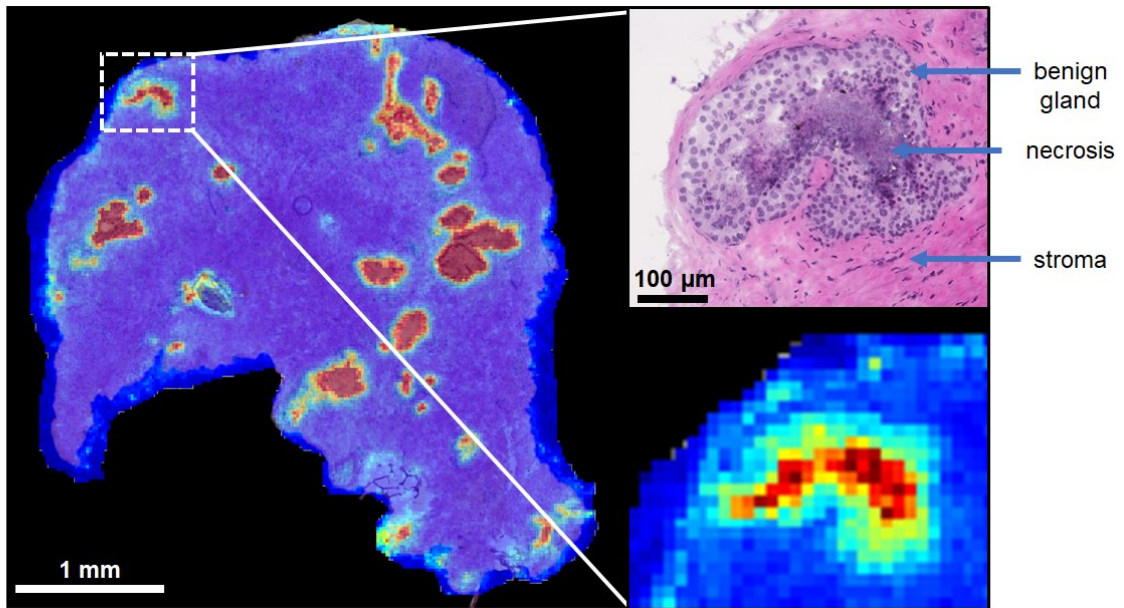


Figure 7.11B. Co-registration of serial H&E scan with MALDI MSI ion map. ENZ treated sample depicting relative intensity of m/z 465.304, tentative cholesterol sulfate. High magnification histology image shows stroma and benign gland with necrotic lesions matched to high resolution pixel m/z image. Lateral resolution at 20 μm (x, y).

Subsequent analysis focused on teasing out culture- and treatment-related changes in lipid composition using the spatial clusters of the two main tissue types. The culture effect was described as the lipidomics changes in control tissues compared to fresh-frozen (DMSO/Day 0) and the treatment effect was described as the lipidomic changes that occurred after 48 h culture with drug treatment at 10 μ M dose (ENZ/DMSO). **Table 7.2.** below outlines the approximate proportions of culture- and treatment-related effects on lipid profile of PDEs. The overall culture effect is marginally higher than treatment effect.

MALDI mode	Culture Effect		Treatment Effect	
	Negative	Positive	Negative	Positive
Epithelium	3.9%	4.2%	2.1%	2.0%
Stroma	6.8%	3.4%	0.9%	1.0%

Table 7.2. Estimated lipidomic composition changes in PDE tissues. Comparison of culture effect and drug treatments effect in epithelium versus stroma for both MALDI ionisation modes. Percent (%) values were calculated by sum of m/z features in a bucket with fold change >2.0 and fold change <-2.0 divided by total m/z features excluding intervals with below the LOD (missing intensity values in sampled regions) with a projected 50% on-tissue lipid signal.

7.3.6. Culture Effects on PDE Lipid Profiles

7.3.6.1. Negative Ion Mode MALDI

Volcano plots were employed to highlight significant changes (FDR <0.05) in metabolomic features in distinguished cluster regions of epithelium and stroma with upregulated features exhibiting a \log_2 fold change (FC) >1 and downregulated features \log_2 FC < -1. 18 features were found to be downregulated and 17 were upregulated in epithelium. Tentative m/z 751.532 PA(40:4), m/z 699.497 PA(34:2)[M-H]⁻, m/z 747.500 PA(40:6)[M-H]⁻ and m/z 452.278 LysoPE(16:0)[M-H]⁻ were enriched after DMSO treatment whereas m/z 889.574 PA(38:2)[M-H]⁻, m/z 865.577 PI(36:0)[M-H]⁻ and m/z 835.533 PA(34:1)[M-H]⁻ were downregulated in Day 0. ([Figure 7.12A](#), [Supplementary Table 7.4](#)). 25 and 48 features were upregulated and downregulated in stroma, respectively. An uncommon LysoPC(15:0), m/z 837.546 PI(34:0)[M-H]⁻, m/z 452.279 LysoPE(16:0)[M-H]⁻, m/z 809.517 PI(32:0)[M-H]⁻ and m/z 887.560 PI(38:3)[M-H]⁻ were enhanced after culture whilst m/z 865.577 PI(36:0)[M-H]⁻, m/z 750.544 PE(O-36:5)[M-H]⁻, m/z 835.533 PA(34:1)[M-H]⁻ and tentative m/z 621.303 PI(20:3)[M-H]⁻ were diminished in fresh-frozen samples ([Figure 7.12B](#), [Supplementary Table 7.6](#)).

7.3.6.2. Positive Ion Mode MALDI

Results indicated the presence of 39 downregulated and 29 upregulated significant features with respect to epithelial changes. Only a few of these, were lipid masses in consideration of their mass defect. These included potential PC species m/z 784.581 PC(34:0)[M+Na]⁺, m/z 758.567 PC(34:2)[M+H]⁺ and m/z

756.552 PC(32:0)[M+Na]⁺, possible fatty acid amides *m/z* 304.302 NAE(18:3)[M+H-H₂O]⁺, *m/z* 332.333 NAE(20:3)[M+H-H₂O]⁺, as well as *m/z* 773.515 a potential PA(42:8)[M+H]⁺/PG(O-34:1)[M+K]⁺ which were upregulated in epithelium. There was downregulation of the tentative LPA(20:4) and *m/z* 774.603 PC(38:1)[M+H]⁺ in DMSO treated tissues as shown in **Figure 7.13A** ([Supplementary Table 7.8](#)). On the other hand, for the stroma, 25 downregulated features and 26 upregulated features were detected as the ratio of DMSO to Day 0 intensities. The enhanced lipid species were *m/z* 332.333, *m/z* 304.302 and *m/z* 914.602 PC(43:6)[M+K]⁺. However, only a few diminished metabolites were lipids, associated to potential carnitine species, but this may be due to their localisation to only some tissue sections (**Figure 7.13B**, [Supplementary Table 7.10](#)).

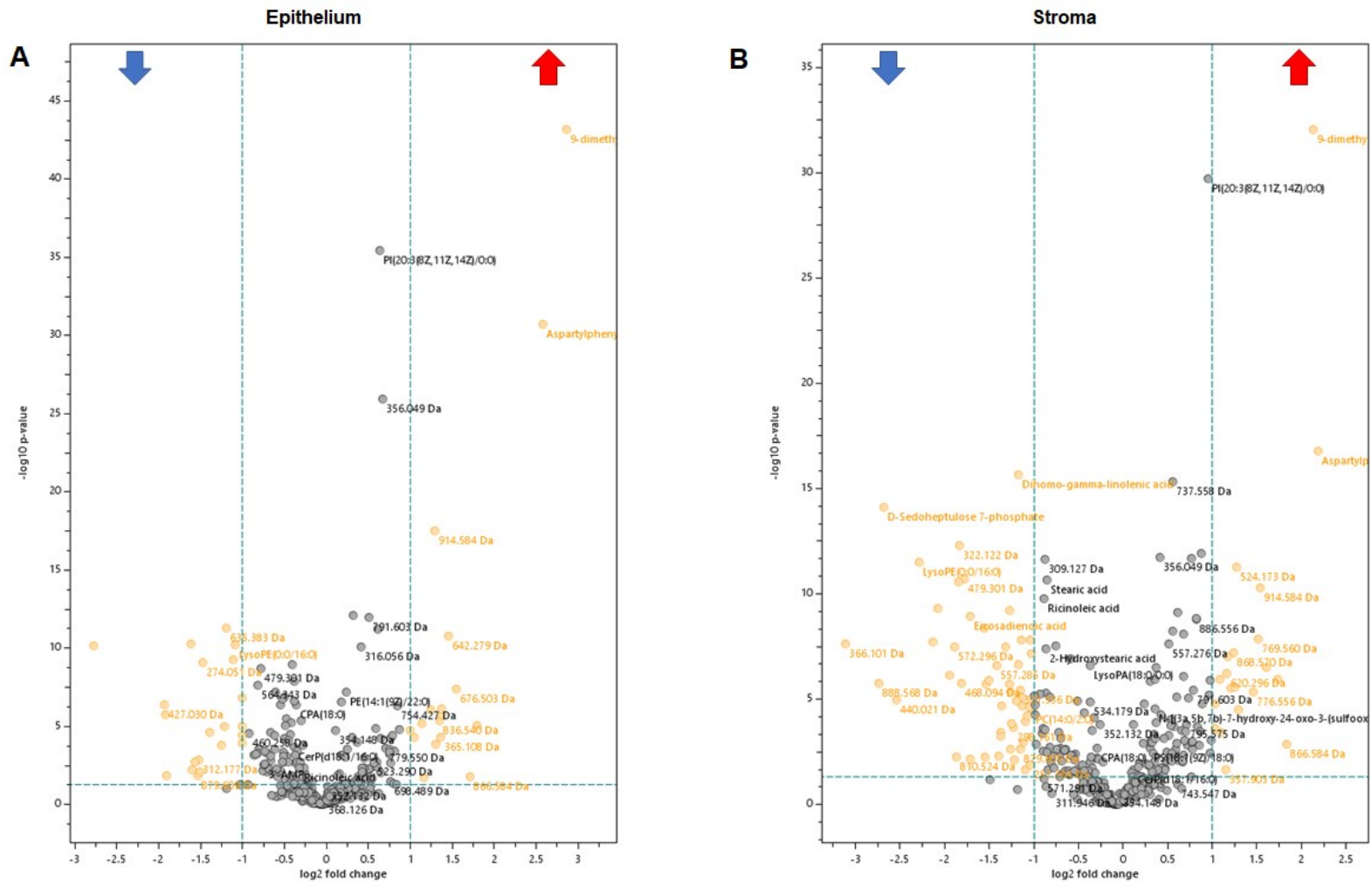


Figure 7.12. Culture effect in prostate tissue segments of negative ion MALDI data. Lipidomic changes in A. Epithelium. B. Stroma. Bottom facing blue arrow indicates downregulation \log_2 FC < -1 and FDR < 0.05 ; grey dots unaltered features; Up facing red arrow indicates downregulation \log_2 FC > 1 and FDR < 0.05

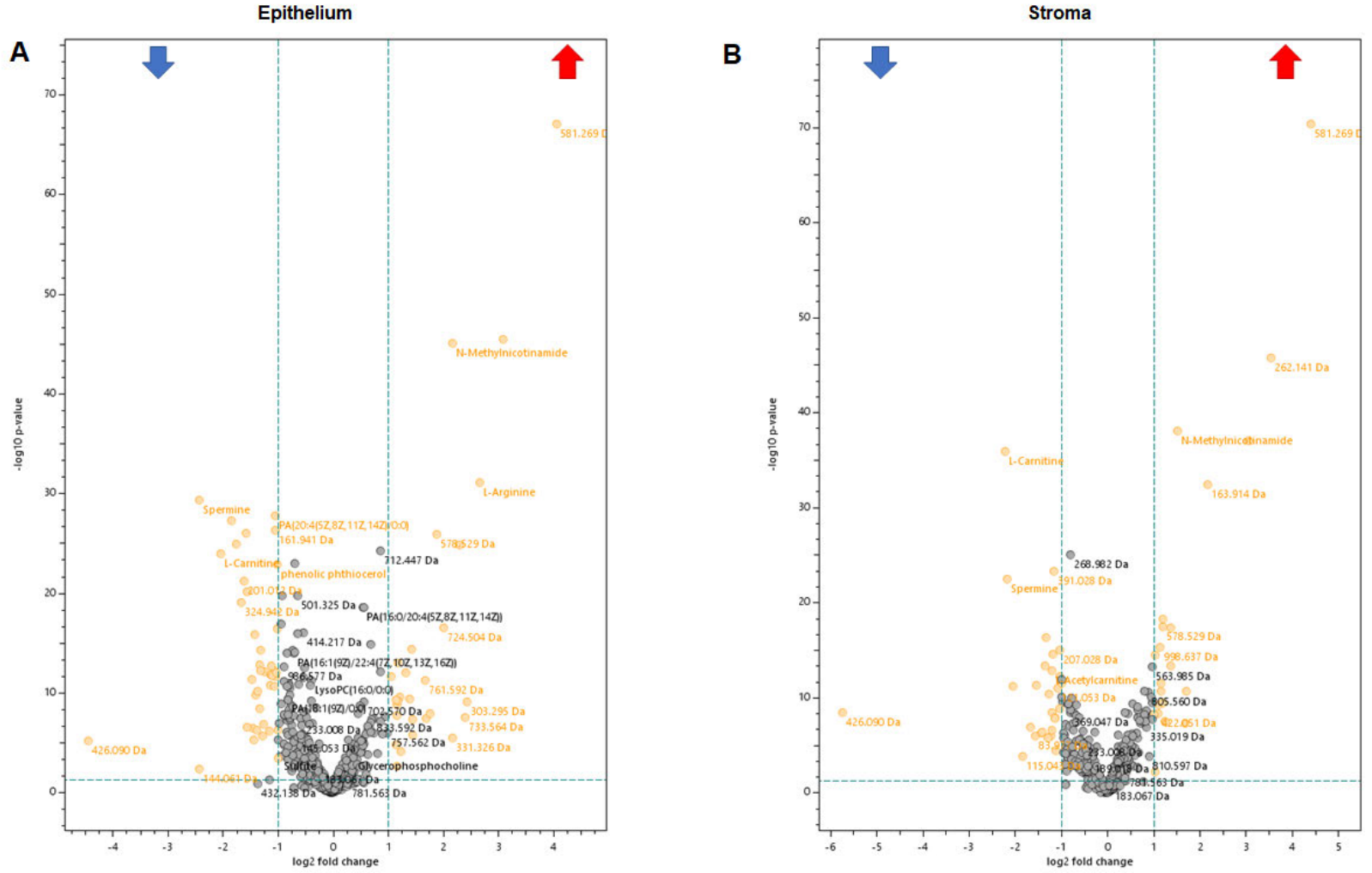


Figure 7.13. Culture effect in prostate tissue segments of positive ion MALDI data. Lipidomic changes in **A. Epithelium. B. Stroma.** Bottom facing blue arrow indicates downregulation \log_2 FC <-1 and FDR <0.05 ; grey dots unaltered features; Up facing red arrow indicates downregulation \log_2 FC >1 and FDR <0.05 .

7.3.7. Treatment Effects on PDE Lipid Profiles

7.3.7.1. Negative Ion Mode MALDI

There appeared to be differences in treatment effect in segmented clusters, with a higher degree of metabolite shift in epithelium compared to stroma as shown in [Figure 7.14](#). Not a single metabolite feature was downregulated in glandular regions while 19 features were upregulated. In the epithelium, m/z 889.574 PA(38:2)[M-H]⁻, m/z 716.524 PE(34:1)[M-H]⁻, m/z 699.497 PA(34:2)[M-H]⁻, m/z 722.513 PE(O-36:5)[M-H]⁻ and LysoPE(P-16:0) exhibited increased abundance following challenge by ENZ treatment but in comparison to DMSO, only a trend in reduction of m/z 675.494 PA(34:0)[M-H]⁻ and m/z 887.560 PI(38:3)[M-H]⁻ ([Figure 7.14A](#), [Supplementary Table 7.5](#)). In the stroma, three features were downregulated and six were upregulated with neither being significant perturbations for probable lipid masses. However, m/z 865.577 PI(36:0)[M-H]⁻ and m/z 753.419 PA(38:7)[M+Cl]⁻ were marginally below the threshold of upregulation with ENZ treatment ([Figure 7.14B](#), [Supplementary Table 7.7](#)). Cholesterol sulfate was unaffected by ENZ treatment.

7.3.7.2. Positive Ion Mode MALDI

A volcano plot of lipidomics effects showed that five downregulated features and 29 upregulated features when comparing changes between ENZ and DMSO epithelial regions ([Supplementary Table 7.9](#)). The enhanced masses were tentative PC(36:1) and m/z 426.360 CAR(18:0)[M+H]⁺ whilst the reduced masses were m/z 565.353 possible LPG(22:2)[M+H]⁺ or PA(25:1;O)[M+H]⁺ and fatty ester, m/z 453.441 FA(30:0)[M+H]⁺. In the stroma,

there were only 15 significantly altered features but they had substantially lower relative intensity ([Figure 7.15](#), [Supplementary Table 7.11](#)). This observation indicates that PC may play localised functions within the confines of prostate epithelium as opposed to stroma.

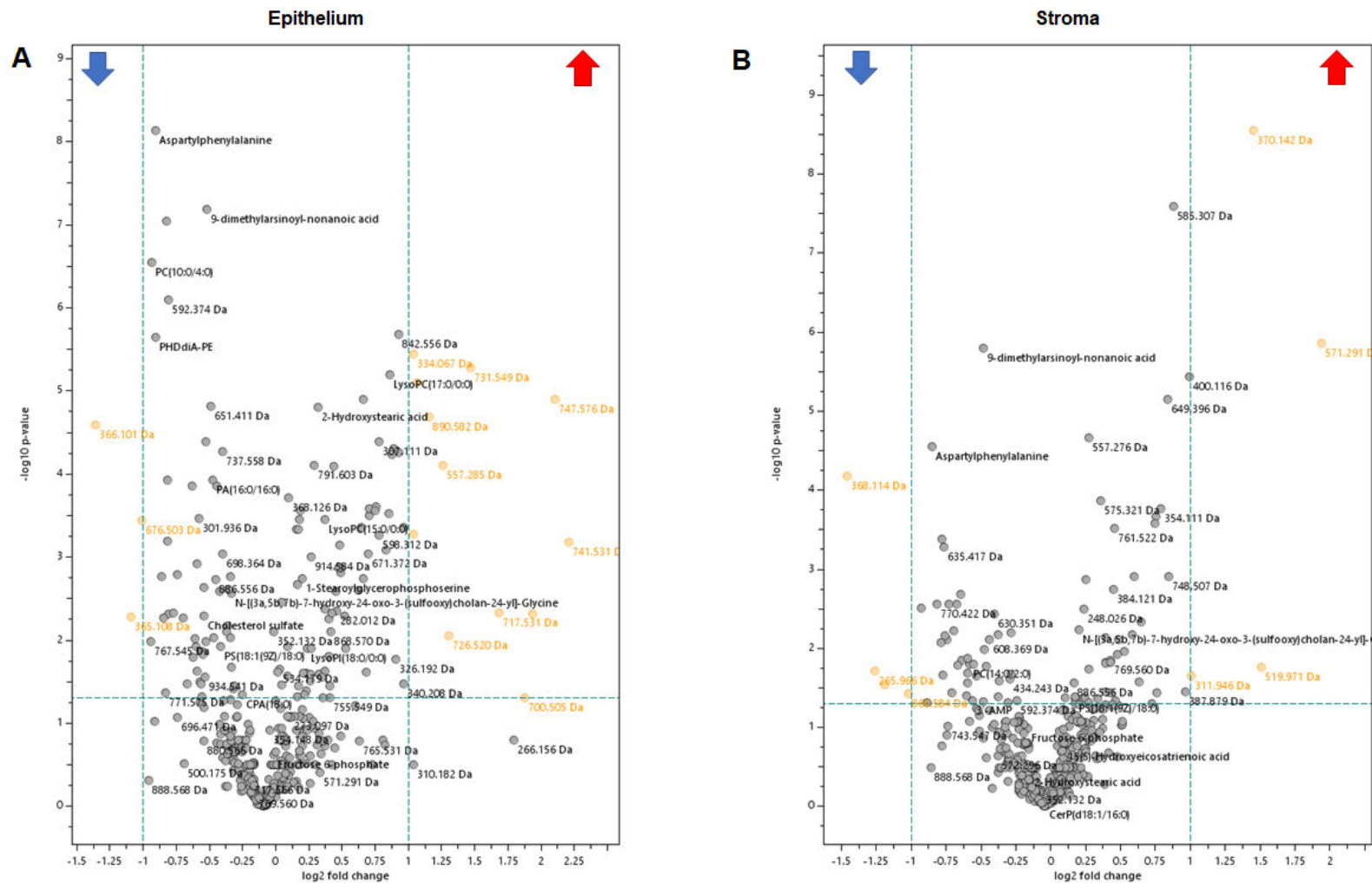


Figure 7.14. Treatment effect in prostate tissue segments of negative ion MALDI data. Lipidomic changes in **A.** Epithelium. **B.** Stroma. Bottom facing blue arrow indicates downregulation \log_2 FC < -1 and FDR < 0.05; grey dots unaltered features; Up facing red arrow indicates downregulation \log_2 FC > 1 and FDR < 0.05.

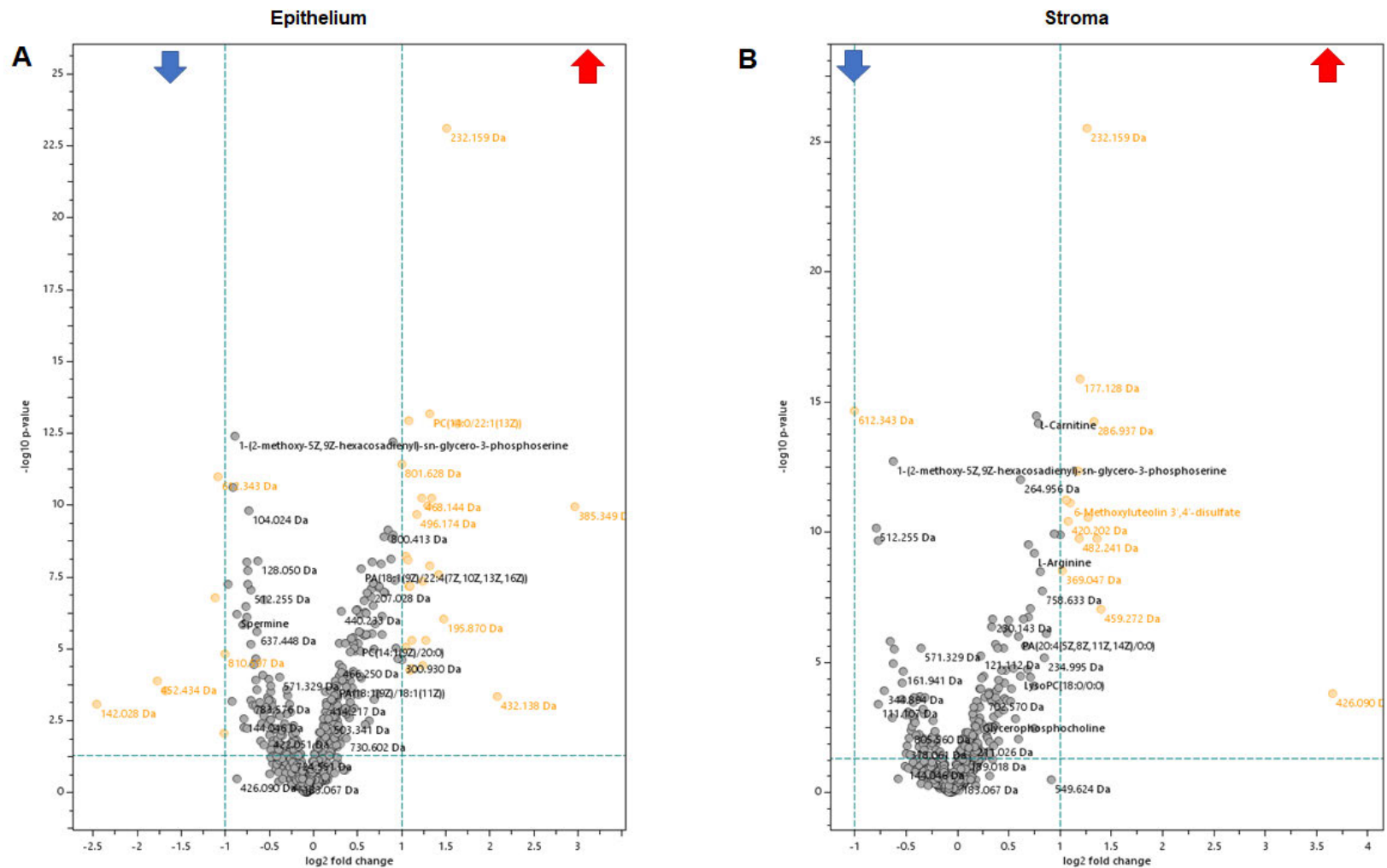


Figure 7.15. Treatment effect in prostate tissue segments of positive ion MALDI data. Lipidomic changes in **A.** Epithelium. **B.** Stroma. Bottom facing blue arrow indicates downregulation \log_2 FC < -1 and FDR < 0.05; grey dots unaltered features; Up facing red arrow indicates downregulation \log_2 FC > 1 and FDR < 0.05.

7.3.8. LC-ESI-MS/MS Lipidomics

Conventional lipidomics by LC-ESI-MS/MS (see Chapter 2 [Methods 2.2.8](#)) was also undertaken to investigate changes following culture and ENZ treatment. Here, 30 μm triplicate sections were pooled and analysed for each patient specimen. For the culture effect, there was variation in lipid species. Numerous TAG species and a handful of Cer and PG species were upregulated following culture while PE(18:1/20:3) was downregulated as seen in **Figure 7.16**. However, this lipid upregulation should be interpreted with caution because particularly for most TAGs, their absolute quantitative amounts signalled they were lowly abundant metabolites. Nonetheless, analysis with exclusion of TAGs also showed no significant lipid alterations. For the treatment effect, there were no significant changes in lipid perturbations.

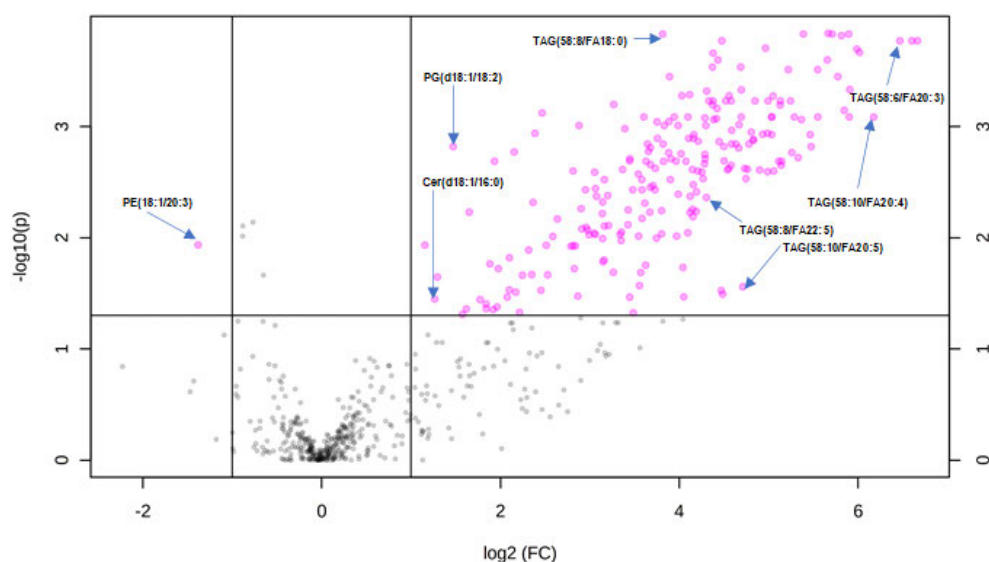


Figure 7.16. Conventional lipidomics analysis of culture effects. Tissue homogenates were analysed by LC-ESI-MS/MS. Quantitative lipid species amounts (nmol/mg DNA) normalised to total DNA data was subjected to volcano plot analysis in MetaboAnalyst 4.0.

7.3.9. Co-registration of IHC and Spatial Lipid Profiles

To further explore pathology-based biomarker defined tissues, IHC staining of p63+AMACR was attempted. Due to unforeseeable technical issues only one patient set yielded acceptable staining criteria, and this is illustrated in **Figure 7.17**. The IHC scan was co-registered and compared to MALDI imaging spatial profiles in both positive and negative ion mode. p63 positive secretory epithelia show benign tissue and transforming PIN glands and absence of p63 staining within glandular structures may indicate malignancy.

Typically, IHC staining works well on formalin-fixed paraffin-embedded (FFPE) processed sections. p63+AMACR labelling has been demonstrated on fresh-frozen tissue samples in this project ([Appendix D](#)). Further method optimisation for automated staining of fresh-frozen tissue cryosections of PDEs is proposed for future work. This is because cultured explants are usually smaller compared to biopsy cores and are more delicate. Changes in cellular properties of PDEs may affect the retention or adhesiveness of cryosections on positively charged glass slides during IHC procedures.

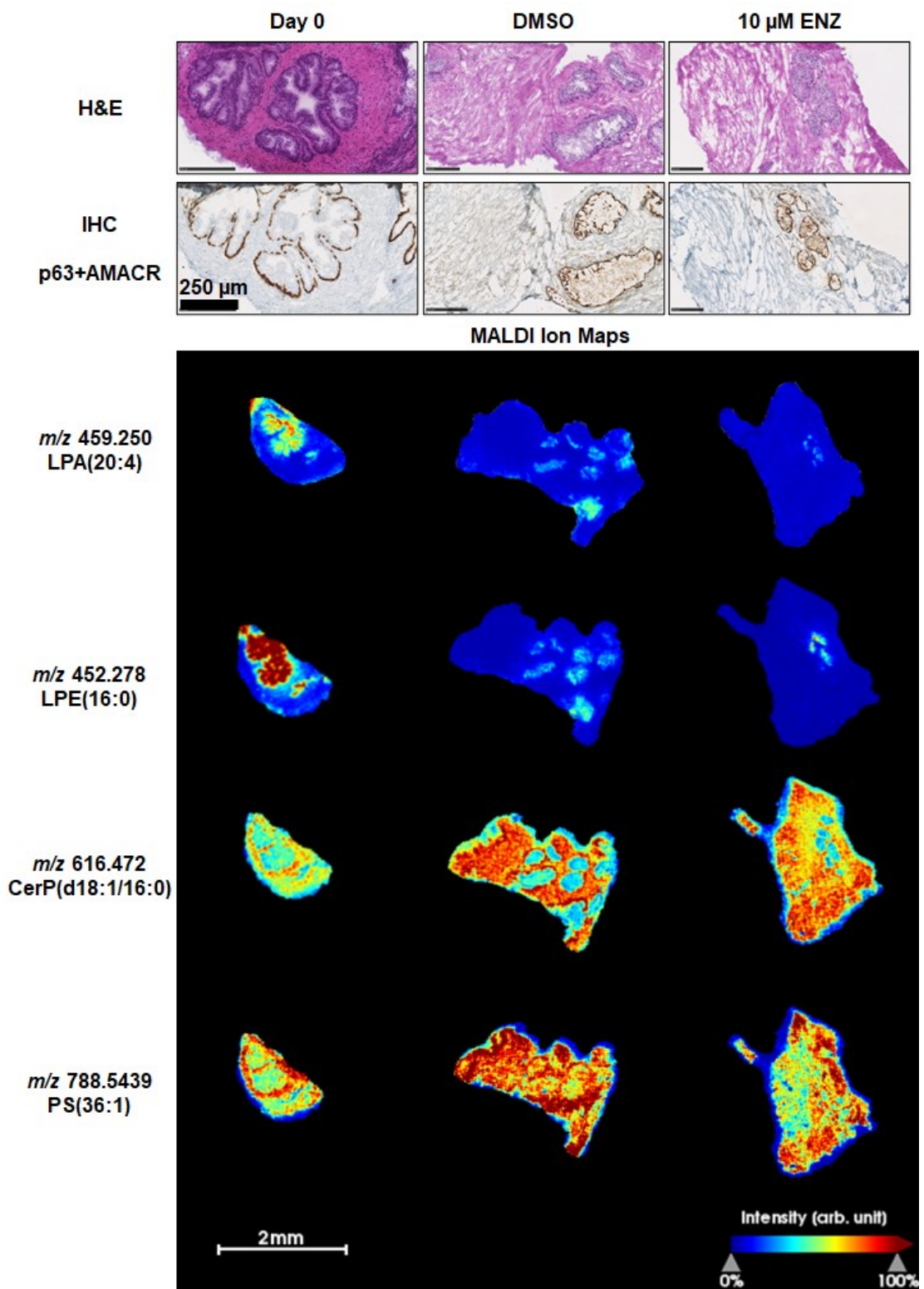


Figure 7.17. Comparison of histopathological H&E and p63+AMACR IHC staining to spatial lipid ion maps. Top panel. Serial sections of higher magnification of H&E scans and p63 positive areas indicative of benign glands. **Bottom panel.** MALDI images depicting examples of key epithelial and stromal lipids PDE data set from a single patient.

7.4. Discussion

In this Chapter, MALDI MSI was used as a proof-of-principle technique to explore the lipidomic effects of tissue culture and AR inhibition treatment in *ex vivo* human prostate tumours. IHC staining of AR in the 50 μM ENZ treated explants showed a decrease in AR positive staining with increased drug uptake in a time-dependent manner over a 24-h period. This observation lends credence to pharmacological inhibition of AR in prostate PDE resulting in changes in lipid composition. Another conceptual basis for this work is that pre-existing laboratory data showed heterogenous changes in the ki67 proliferation index at individual level but largely pointing to inhibition of tumour cell multiplication.

To begin with, targeted drug imaging was performed on adjacent sections for MALDI lipid imaging to establish whether ENZ uptake occurred during 48 h of culture. In comparison to matched H&E scans, visualization of the drug signal showed that m/z 209.09 was co-localised to heterogenous glandular regions. Critically, this experiment illustrated it is possible to image ENZ at 10 μM . Hence, the Bruker timsTOF Flex delivered an important technical improvement for targeted ENZ imaging given that the initial study used five-times the current dose to be able to generate reliable drug ion maps³²⁹. Many MALDI MSI studies on quantitative drug imaging have embraced lateral resolutions which are inadequate to sufficiently resolve localised drug concentrations⁴⁶¹. For example, salmeterol has been analysed in 10 μm thick rat lung tissue sections at 70 μm resolution⁴⁶² and rifampicin in 12 μm thick rat kidney sections at 100 μm ²⁶⁴ resolution, as well as separately at 12 μm thick rat liver sections at 200 μm resolution⁴⁶³. Only with adaptation of MALDI-2 technology it seems that drug imaging can be performed at much improved sensitivity at marginally improved

resolution, as was shown by Barre and colleagues who analysed a series of common pharmaceutical agents at 50 μm step sizes³⁹⁶.

Spatial segmentation of high-resolution lipid imaging data of PDE sections in SCiLS Lab was used to create tissue regions for automated metabolite annotations in MetaboScape. Unlike, LC-ESI-MS/MS, spatial metabolomics and lipidomics suffer from the impracticality of online tandem MS/MS imaging as each data point pixel generates at least hundreds of relevant lipid features. Hence, the lipid information is putative MS-only data and validation of lipid identity can be mined from the conventional lipidomics. A solution for this has been developed by Ellis *et al*, where data dependent imaging combined an Orbitrap for MS imaging on one pixel and an ion trap for CID MS/MS on a parallel pixel to resolve lipid isomers³³⁸. Spatial lipidomics profiling of the PDEs illustrated that the most predominant peak in the negative ion mode data was m/z 465.304, cholesterol sulfate. This observation underpins the fact that cholesterol is a component of plasma membrane which plays the role of regulating membrane fluidity⁴⁶⁴ and integrates cell signalling in association with sphingolipids in lipid raft domains^{127,376,465}. The heterogenous spatial distribution of cholesterol sulfate makes it tempting to speculate that it is indicative of potentially transforming benign glands. Moreover, cholesterol is a precursor for androgen biosynthesis via the adrenal and steroidogenic pathways where cells prefer to use it an alternate source for testosterone in CPRC^{82,364}. Clinically, cholesterol is associated with increased risk of developing aggressive PCa^{134,376}. Cell line and xenograft models have shown cholesterol fuels tumour activity²⁸⁸. Consequently, some clinical studies have sought to re-purpose statins which are conventional agents for management of cardiovascular disease to tackle advanced PCa^{305,466}.

Statins are cholesterol synthesis inhibitors that target HMG-CoA reductase. Their use is proposed to improve outcomes of men with PCa, with most benefit in overweight/obese patients who tend to have high risk lipid profile in CRPC³⁷⁰. Therefore, data in this project provides strong rationale and support for further mechanistic studies for using clinically relevant PDE models to target cholesterol metabolism in prostate tumours.

Using a combination of segmentation and univariate analysis, lipidomic effects in the explant culture system were explored in five patients for two discerned tissue types, epithelium (largely benign glands) and stroma. There was heterogeneity of distribution of phospholipids in PDE's which appeared to vary depending on FA chain length and degree of unsaturation, suggestive of tissue and cancer-specific lipid metabolic activity. Analysis of the culture effects uncovered complex perturbations in multiple lipid species, particularly in PI and PA subclasses with variable changes in lipid distribution either way between fresh tissue and control. Generally, enhanced lysophospholipid species were observed following culture with increase of LPE(16:0) but decrease of LPA(20:4). Likewise, analysis of the treatment effects revealed upregulation of PA and PI lipids with more pronounced alterations in the epithelium but with no significant downregulation of lipids. A tentative PI(38:3) tended to undergo reduction following AR inhibition. Nevertheless, PC(36:1) was the clearest indicator of response ENZ treatment as it exhibited significant downregulation. In [Chapter 4](#), it was evidenced that m/z 826.562 PC(36:1) was a lipid marker of tumour aggressiveness and now is also apparently sensitive to hormonal (ADT) therapy. Indeed, the spatial data analyses in this report demonstrates substantial heterogeneity in lipidomics changes in PDEs.

Contrastingly, interrogation of lipidomic effects by conventional chromatography lipidomics analysis of tissue shavings uncovered different results. There was only upregulation of TAG lipids following 48 h culture although these were subtle differences. Such TAG enhancements may imply sustained fatty acid metabolism for cellular energy storage, but remarkably, there were no significant changes with ENZ treatment. Normally, LC-ESI-MS/MS analysis uses larger specimen sizes (several mg of tissue or ~ 1-2 millions of cells for *in vitro* assays). These observation does not only yet again highlight the advantage of retention of spatial information MALDI MSI over conventional lipidomics but emphasises that single-cell measurements pertaining treatment interventions are probably better revealed with imaging which samples a greater number of data points. Collectively, the findings from the spatial and conventional lipidomics strategies, reported herein need to be authenticated in a larger cohort of carefully pathologically and/or IHC marker stratified patients. In this regard, dual p63+AMACR labelling would provide more valuable information for supervised spatial lipidomic segmentation analyses.

Certainty in annotation of MSI data can be further confirmed by incorporating retention time, structural MS/MS fragment information, and CCS values from ion mobility separation ideally from accompanying lipidomics analysis in adjacent samples¹⁹⁸. At the time of data analysis, there was one key limitation with the MetaboScape software package. The selection of sampling data points for the tissue segments could not be expanded beyond 50 speckles which impinged on computational times on the already exceedingly large three-dimensional data files which would otherwise have enhanced the quality of the univariate statistical analysis. Incorporating other measures of annotation

confidence with the spatial lipidomics data would improve m/z identification paving the way for pathway analysis. Recently, augmentation of trapped ion mobility (TIMS) and parallel-accumulation serial fragmentation (PASEF) to tandem MS has been touted to produce multi-dimensional annotated lipidomics data¹⁹⁷. Implementation of PASEF-TIMS on MSI analyses of PDE tissues, together development of metabolomics and lipidomics data workflow methods on the Bruker timsTOF Flex-MetaboScape platform, has the potential to reveal alterations in fatty acid and glycerophospholipid metabolism in following targeted AR inhibition making pathophysiological and pharmacotherapeutics interpretations more meaningful.

7.5. Supplementary Information

	Patient ID	Age at RP	PSA prior to RP	P Stage	Total GS (RP)	1° GG (RP)	2° GG (RP)	Core	Biopsy Core GS
1	33082	86.8	5.6	PT3A	7	4	3	R mid	4+4=8
2	33091	62.4	3.7	PT3A	8	4	4	L post base	4+4=8
3	33094	60.2	7.15	PT3B	9	5	4	L post	4+5=9
4	33094	60.2	7.15	PT3B	9	5	4	R post	4+5=9
5	33196	83.7	14.5	PT3A	9	4	5	R post	4+4=8
6	33208	63.5	4.38	PT3B	9	4	5	R mid	5+4=9

Supplementary Table 7.1. Clinical pathology of PDE tissues used for HR-MALDI MSI.

CHAPTER 8:

Conclusion and Future Directions

8.1. Introduction

Omic technologies have come a long way in elucidating the biological mechanisms of disease causality, screening of druggable molecular targets and understanding mechanisms of therapeutic resistance. These omic modalities have largely encompassed proteomics and genomics leaving lipidomics as an emerging and relatively understudied area. Given the complexity and functionality of lipids, the cellular lipidome is increasingly gaining attention in health and disease⁴⁶⁷. Importantly, with the recognitions of the energetics hallmark of cancer, lipidomics has become an attractive area of research for the discovery of biomarkers and therapeutic vulnerabilities^{149,297,468}. By and large the development of electrospray ionisation (ESI) sources has greatly advanced lipidomics research along with technological enhancements of mass analysers, undoubtedly making conventional lipid analytics high-throughput, robust and reproducible³¹². However, this comes with the loss of three-dimensional spatial localisation of molecules (metabolites, drugs, xenobiotics). Mass spectrometry imaging bridges this gap to provide knowledge of the distribution of molecules with respect to anatomical and physiological context. In prostate cancer, research has shown that the androgen receptor regulates expression of lipogenic enzymes that provide fatty acid and lipid substrates to support cell proliferation, survival and metastasis^{137,138}. This dysregulated phenotype along with the known multifocality of clinical prostate tumours provided strong rationale for the application of spatial lipidomics techniques to characterise the lipid composition of highly heterogeneous tissue and solid tumours of the prostate gland.

While [Chapter 1 \(Introduction\)](#) focused on how prostate cancer is hormonally driven by androgen receptor signalling and the concepts of mass spectrometry instrumentation for lipid analysis, the [Review Article](#) examined key studies where multiple lipidomics strategies have shown strong translational potential for the discovery of lipid-based biomarkers for prostate cancer disease prognostication.

The original aims of these research project were:

1. To determine the spatial location of lipid species across prostate tissue using MALDI MSI and correlate to histopathological evaluation in individual PCa patients, including the use of LC-MS/MS and MALDI MS/MS to validate lipid species.
2. To quantitate the uptake of enzalutamide in human prostate patient-derived explant cultures using LC-MS/MS and evaluate enzalutamide penetration in prostate tissues by MALDI MS/MS imaging together with AR immunohistochemistry.
3. To explore the lipidomic changes in patient-derived explant cultures following enzalutamide antagonism of AR using high resolution MALDI MSI.

The results of this PhD research project in light of these objectives are discussed forthwith.

8.2. Thesis Findings

8.2.1. MALDI MSI Offers Precise Tissue-Specific Lipid Profiles

The first objective was addressed in [Chapter 3](#). MALDI MSI offered an insight into the lipidomic composition of prostate tissue. Generally, the lipid profiles reflected changes in tissue heterogeneity with imaged sections collected at multiple interspersed depths within individual tissue blocks. These spatial lipid profiles were further mirrored and detail added with lipidomics analysis on matched samples. Here the data showed the glandular epithelium to be composed of predominantly phosphatidylcholines such as PC(34:1) with a subset of patients having enriched Cer lipids. A limitation in this component of the project was the matrix application protocol using sublimation, as this approach did not yield reliable signal intensity of lipids present in the stroma. There was some loss of data quality where multiple sections from the same patient data set could not be combined let alone across individuals to facilitate integrated patient statistical comparisons.

The subsequent availability of the SunChrom SunCollect automated sprayer at the mass spectrometry core facility offered a more reproducible and robust matrix deposition method later in the project. This was combined with a rigorous MALDI MS optimisation protocol that saw an overall improved lipid ion signal intensity from organic prostate tissue extracts with satisfactory signal-to-noise ratios ([Appendix B](#)). Spatially, the lipid ion signals in the glandular epithelium (secretory lumen) had at least 10-fold improvement whilst enhancing the detection of lipids in the stroma ([Appendix B3](#)). Moreover, combined data analysis was possible even for separate patient samples.

8.2.2. MALDI MSI Revealed Spatially Informative Lipid Changes in Prostate Tumours

Further to the attainment of the first objective, the works in [Chapter 4](#) (*prepared for submission to an invited special issue of Frontiers Endocrinology*) also describe the spatial lipid composition of prostate tissues. This was achieved by MALDI imaging on automated spray coated sections from a separate patient cohort (n=10). Again, at individual patient level it was evidenced that the lipid profiles were distinct between multiple cell types (epithelium versus tumour versus stroma). Enrichment of specific lipids in the stroma was seen and their relative intensity was more pronounced with influx of inflammatory cells. From a biological standpoint this may help delineate immune response from other mimickers of prostate adenocarcinoma. These lipidomic signatures of the reactive stroma highlight a role of lipids within the tumour microenvironment that requires further research. Critically, this work demonstrated that the lipid composition in benign tissue was conserved and consisted primarily of lysophospholipids. This work demonstrated that a novel m/z 459.246, a possible LPA(18:1)+Na]⁺ or LPA(20:4)+H]⁺ species was also enriched in non-cancerous tissue. It was also evidenced m/z 496.337 LPC(16:0)+H]⁺ and m/z 518.318 LPC(16:0)+Na]⁺ were also abundant in benign tissues consistent with a prior study by Goto *et al* that linked low lysophosphatidylcholine levels to increased risk of biochemical recurrence of prostate cancer following surgery²⁸⁴. Whether the reduced abundance of LPA and LPC lipids in tumour regions indicates altered phospholipid remodelling pathways remains unknown. On the other hand, though the tumour lipid profile was not quite as pronounced ostensibly due to the

metabolic heterogeneity in prostate cancer but a small number of unique lipids signified adenocarcinoma at individual patient level, thereby supporting the project hypothesis that specific lipid species are indicative of prostate malignancy. Further research in larger patient cohorts with a greater range of malignant features is the next logical step to more rigorously link lipid profiles to prostate cancer and give insight into the underlying biology driving such profiles.

8.2.3. Robust Drug Quantification and Targeted Enzalutamide Imaging in Patient-Derived Explants (PDE) Culture System

The second objective was tackled in [Chapter 5](#) and [Chapter 6](#). Initially, the development of a method for quantification of enzalutamide according to the US FDA guidelines for bioanalytical method validation is documented in [Chapter 5](#). Linearity, accuracy, precision, selectivity, and stability of the drug assay was evidenced in the laboratory settings at SAHMRI using the available mass spectrometry platforms. This work served as a prelude to the published work in [Chapter 6](#). Combined mass spectrometry approaches showed that enzalutamide was fully penetrated viable tissues in PDE cultures within 6 h, which was the first available evidence for complete drug penetration – a key knowledge gap in the field that had only been inferred previously. Automated antibody staining for the AR showed drug localisation specific to epithelial cells in glandular niches of tissue. Importantly, this method for antibody labelling was specifically designed for fresh-frozen tissue sections and applied in [Chapter 4](#). It appeared that abrogation of AR occurred primarily due enzalutamide antagonism. The outcomes of this work can significantly inform design of *ex vivo* experiments,

including drug concentrations and culture timepoints, and interpretation of therapeutic readouts.

8.2.4. High Resolution MALDI Q-TOF Imaging Shows Refined Insights into Lipidomic Compositions of *Ex Vivo* Cultured Prostate Tissues

The third objective was explored in [Chapter 7](#) where the ethos was to converge the technical gains made in the previous Chapters. First, to use a high-resolution high mass accuracy MALDI-TOF system, the Bruker timsTOF Flex, to generate the most resolved and spatial intense signals yet in fresh prostate and *ex vivo* PDE model tissues³⁵⁹. This instrument was commercially launched in the third quarter of 2019. Again, here the matrix application protocol was re-optimised for this system, with norhamane being suitable for negative ion mode MALDI MS imaging ([Appendix C](#)). This enabled the detection of multiple lipid species including, but not limited to fatty acids, phosphatidylinositols, phosphatidic acids and cholesterol sulphate. Importantly, this Chapter underlined the advantage of spatial MALDI MS imaging to unravel lipidomic fingerprints as opposed to LC-ESI-MS/MS, where cell-type specific alterations in lipid content were observed following AR inhibition therapy, which were not discernible from the conventional lipidomics. Unequivocally, some of the tentative lipid species revealed here point out in [Chapter 7](#) metabolic markers of disease aggressiveness that need to be interrogated in the wider context of androgen deprivation therapy induced metabolic syndrome.

8.3. Future Work

There were several limitations in the MALDI MS imaging work explicated in [Chapter 3](#) and [Chapter 4](#). First, MALDI imaging at 60 μ m spatial resolution is not specific enough to resolve single cell biomolecular information but rather an average population of the same cell type or close by different cells which may have slightly diminished the discernment of chemical tissue margins. Second, the study sample size was small. A larger patient cohort size would have very likely improved the robustness statistical analysis and revealed more unique lipid signatures of prostate tumours. During the execution of this PhD project time and instrument constraints prohibited data generation for more patients. Even with higher repetition rate lasers, MALDI imaging is expensive as the machine laser of such systems have limited life cycles which makes spatial analyses not as scalable compared to conventional lipidomics. However, with latest state-of-the-art MALDI and MALDI-2 Q-TOF technology in the form of the timsTOF Flex platform, the future is promising for this emerging space of spatial profiling of lipid metabolism changes in prostate cancer.

The work presented in this thesis portends new projects for characterisation of lipid-based spatially resolved biomarkers. The following opportunities can give rise to further exciting research projects.

- **Spatial Imaging with Lipid Isomer Resolution**

The identification and validation of key lipid species following histopathological data driven analysis of MALDI imaging data is not always feasible. In one single MALDI experiment, tens of interesting lipidomic features can be detected in different morphological foci with several isomeric and isobaric

masses. It is not practical to perform MALDI MS/MS imaging on each of these potential lipids for unambiguous identification. Conventional lipidomics on matched serial sections was employed in an attempt to inform lipid identification, but comparison of MALDI and LC-ESI-MS/MS lipid ions is not always direct. This challenge can be practically surmounted, in part, by coupling ion mobility separation (IMS) to MALDI mass spectrometry separation where each lipid is isolated based on accurate mass and separated by distinctive collisional cross-sectional areas. Investigations with MALDI-IMS-MSI was not possible in the scope of the current thesis. An example of a prostate tissue section analysed by MALDI-IMS-MSI is provided in the review article ([Chapter 1](#)).

▪ **MALDI MS Imaging Data Processing and Analyses**

With each technological advancement in mass spectrometry, new challenges arise. The spatial profiling in this project was initially conducted on an older generation MALDI-SYNAPT Q-TOF (Waters Corporation, Manchester, UK) platform. The timsTOF flex (Bruker Daltonics, Bremen, Germany) generated larger data sets due to improved lateral resolution and better signal intensity at a wider dynamic m/z range.

- Waters: 0.8 – 1.5 GB for a 4 mm² at 60 μm pixels, 50 – 990 Da
- timsTOF Flex 10 – 15 GB for a 4 mm² at 20 μm pixels, 50 – 1250 Da

This required SCiLS Lab to be housed on a computer with interlinked high-end processors for efficient data processing. Moreover, coupling IMS to MSI creates 4-dimensional data cubes from 3-dimensional matrix arrays. Upgrading of the proprietary software (SCiLS Lab) to handle accurate/exact mass measurements, CID MS/MS fragmentation and ion mobility data will be of benefit. Such inputs,

together with an amenable database with KEGG identifiers will truly actualise pathway analysis. The multi-parametric data generated will need customised hardware platforms to carry on wholistic analysis of integrated large patient cohort data. Finally, any change in instrumentation should be met with head-to-head experimental comparisons to ascertain suitability of method transfer. Evaluation of lipid coverage is important because ionisation sources differ in gas pressure, laser optics, laser emission and beam profile etc. Robinson and colleagues have demonstrated changes in absolute ion yields using two matrix systems by varying UV-MALDI parameters of laser repetition rate and raster modes under different pulse energies²⁶⁶. Given these technical parameters influence desorption/ionisation yield of MALDI imaging, how they may likely lead to variation in the number of detectable lipid subclasses should be checked.

- **Immunohistochemical driven MALDI Data Analysis**

To complement expert pathology advice, IHC markers can be used to stain for benign, PIN and malignant tumours in prostate tissue and select regions of interest in MSI data for multivariate analyses. In this project, the application of a dual-antibody detection kit was demonstrated on fresh-frozen tissue for the p63 staining of basal cells indicative of normal tissue and AMACR for cancerous lesions ([Appendix D](#)). This method was attempted on cultured PDE samples but did not achieve satisfactory staining due to smaller tissue sections that are more prone to physical damage during the procedure. Further optimisation of this method for PDEs is recommended. If this achieved, it would enable more precise spatial stratification of lipid profiles based on diagnostic protein level changes which will potentially offer more accurate metabolic readouts of AR inhibition.

Already, the performance of IHC on tissue sections analyzed by MSI has been uniquely reported. Kriegsmann *et al.*, showed positive detection of multiple biomarkers of multiple myeloma after imaging bone marrow specimens on a MALDI-TOF mass spectrometer⁴⁶⁹. Hence, supplementing and incorporation of IHC into pathological H&E grading of prostate tissue sections is one step closer towards a systems biology driven approach to MALDI MSI lipidomics data analyses. Additionally, correlation of spatial lipid profiles with current clinical endpoints such as PSA and TNM stage should be considered in future work.

- **DESI Imaging of Poorly Ionisable Lipid Classes**

Independent of biological sample matrix effects and ion suppression, most lipids are readily ionizable and detectable by shotgun, LC-MS/MS and MALDI MSI analysis. Still, some lipids belonging to the sterol and prenol categories are not readily measurable. Generally, cholesterol, androgens, Vitamin D metabolites and ubiquinone suffer from poor ionisation efficiency due to the unconjugated aromatic structure, rapid metabolic flux and/or physiologically low concentrations⁴⁷⁰. To overcome this, mass spectrometrists have incorporated silver in experiments by DESI. Silver (Ag^+) creates strong coordinate bonds with alkene containing moieties resulting in reliable detection of PUFAs, FA esters, TAGs, eicosanoids and prostaglandins that are normally detected in negative ion mode^{331,471}. Ag^+ cationisation approaches are also be amenable for MALDI MSI.

- **Chemical Strategies to Improve Characterisation of Lipids**

Several MS studies have investigated the use of salt additives to improve detection of lipid classes or washing with buffers to reduce cation salt adducts or

enhance protonated species^{472,473}. Usually, CID alone of a phospholipid generates the headgroup, diacyl FA chains and/or naturally occurring ions that form $[M+H]^+$, $[M+Na]^+$ and $[M+K]^+$ adducts. To improve structural elucidation of interesting lipid m/z peaks, lithium hydroxide was first used in the infusion mixture of the ESI solvent⁴⁷³. Lithium chelates to carbonyl groups of fatty esters. Lithiated adducts $[M+Li]^+$ of glycerophospholipid species generate tandem mass spectra with identifiable acyl substituent locations³¹². Similarly, formal lithium solution for the *in situ* fixation of liver tissue has been adopted to acquire MALDI MS images from sections with spatially matched characteristic lipid fragment ions⁴⁷⁴. Furthermore, brief washing of tissue sections of a *Myc* lung tumour model by lithium nitrate improved fragmentation yields²⁸⁵. Overall, Li^+ displace the H^+ ion and reduces the proportion of Na^+ and K^+ lipid ions. These approaches and other on-tissue chemical derivatization techniques⁴⁷⁵ will shed deeper insight into the role of other interesting lipid components in healthy prostate tissue and cancer. Perhaps to draw physiological interpretation of lipid distribution in MSI data probably only the endogenous electrolyte ions and their adducts should be considered, and extra sample treatment procedures of tissue sections such as additive coating or washing with buffered salts may be used for careful identification of lipids of interest. Although, such approaches may confer better signal, they may not always be conducive or necessary for routine interrogation of tissue lipid profiles for *in situ* discovery of cancer-related lipid markers, and risk of potentially re-distributing analytes.

- **Quantitative Small Molecule Imaging**

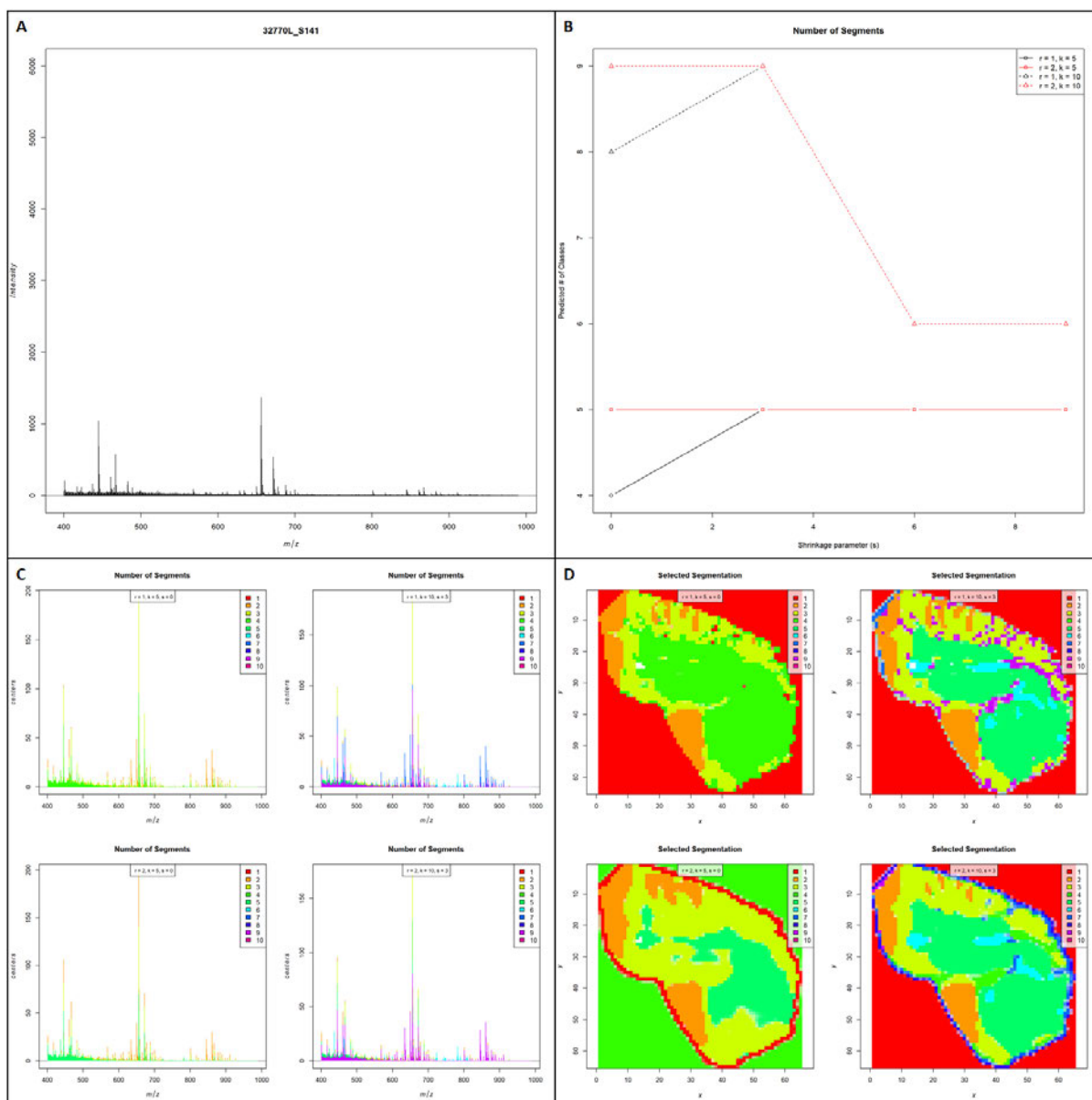
The work contained in [Chapter 7](#) demonstrates that it is quite feasible to image enzalutamide at the clinical dose of 10 μM . Additional work is recommended to gain insight into the efficiency of desorption of enzalutamide by sublimation and automated spray coating. Further research could focus on development of quantitative mass spectrometry imaging (Q-MSI) not only on ENZ but also other anti-prostate cancer pharmacological agents. Thin sections of a tissue mimetic model consisting of known standard curves alongside test sample, can be used to create a calibration curve to establish unknown concentrations of the drug treated tissues⁴⁷⁶. The drug signal can also be potentially normalised to a homogenous spray coated layer of internal standard deposited before, along with or after the matrix. The Q-MSI data can be subsequently validated against already proven LC-MS/MS method(s).

8.4. Conclusion

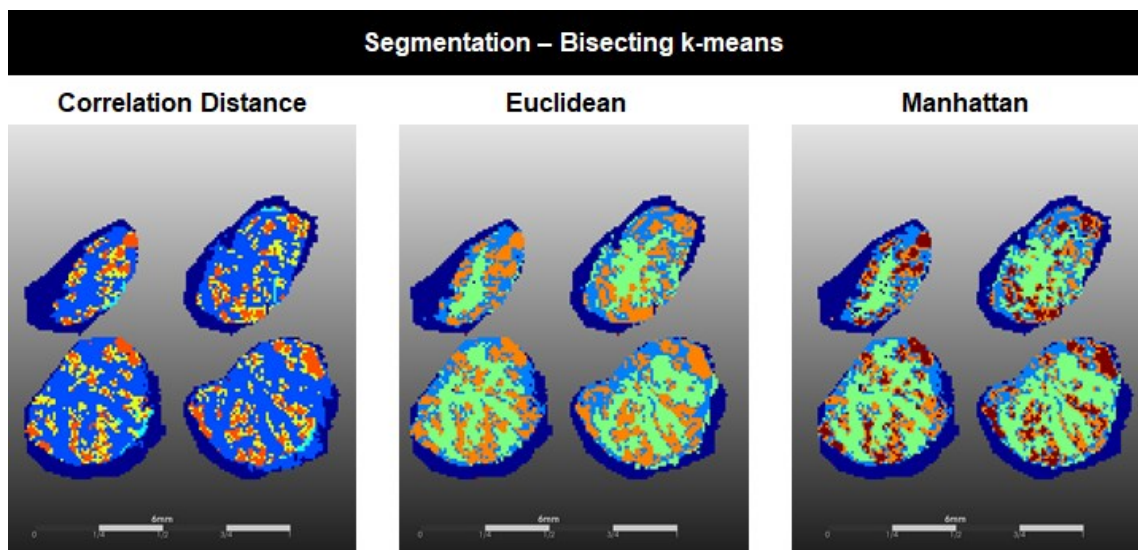
The research conducted in this thesis has showcased the ability of MALDI MSI to provide *in situ* chemical information of highly multi-heterogenous clinical prostate tissues with accompanying data analysis by spatial segmentation uncovering lipidomic profiles consistent with their native tissue morphology. Further work using an optimised MALDI MSI sample preparation by automated spray coating enabled the delineation of tissue-type specific lipid profiles with better sensitivity. The application of a multivariate supervised analysis model on histopathology guided *m/z* clustering data established lipid classifiers for main tissue compartments of the prostate. Collectively, not only do these findings provide novel insights into deregulated prostate cancer lipid metabolism, but they also highlight how it leaves a fingerprint on tissue architecture. This work should underpin further research that can be accomplished with the application of advanced MALDI MSI systems on clinical tissues and/or a clinically relevant models to characterise lipids with unprecedented spatial definition and illuminate metabolic changes in response to targeted hormonal therapy. Ultimately, cell-type resolved lipid signatures, coupled with long-term clinical follow-up are hoped to significantly influence our capability to accurately stratify prostate patients with indolent and aggressive cancers for improved disease management.

APPENDICES

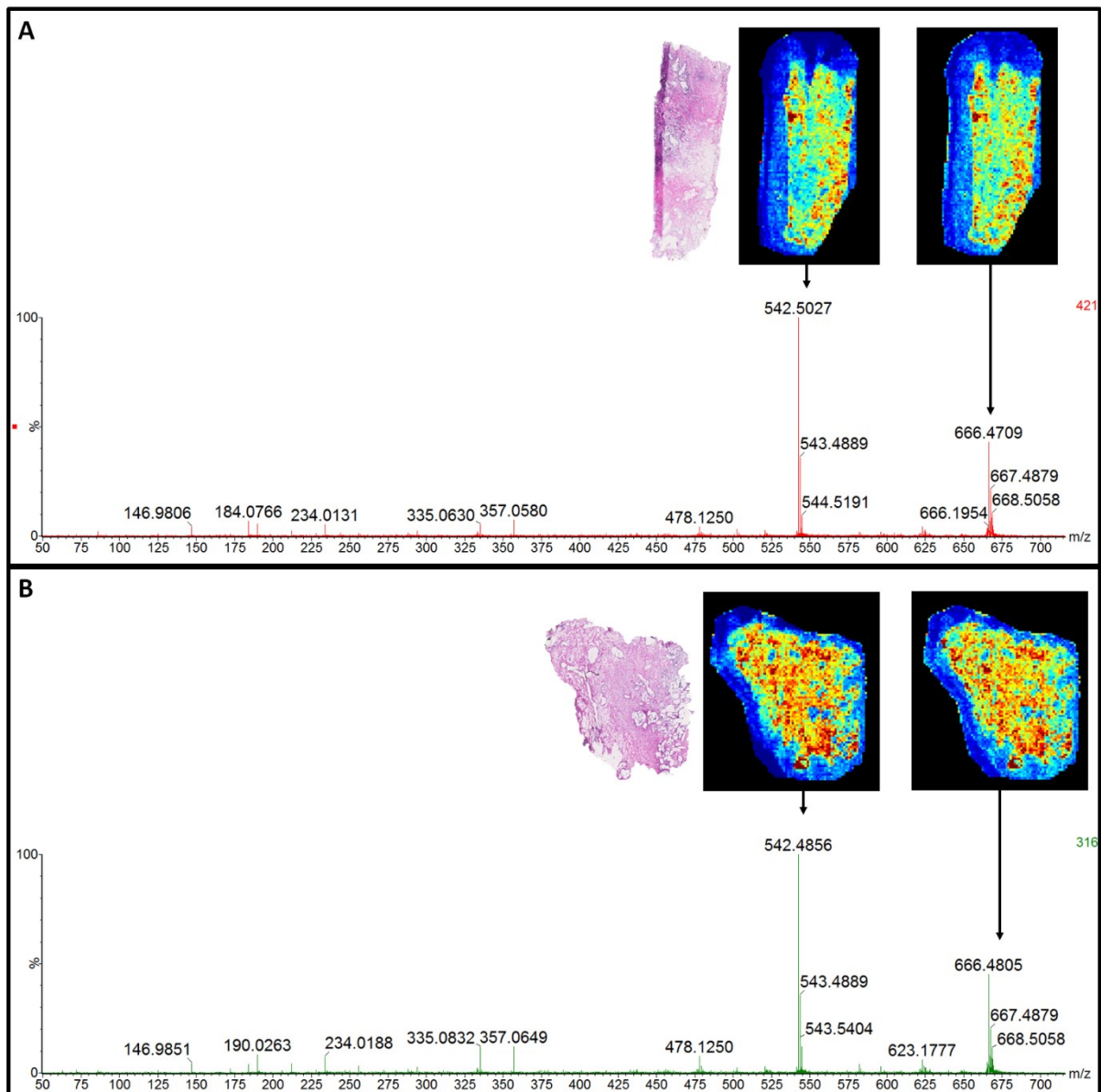
9.1. Appendix 1: Supplementary Information Chapter 3



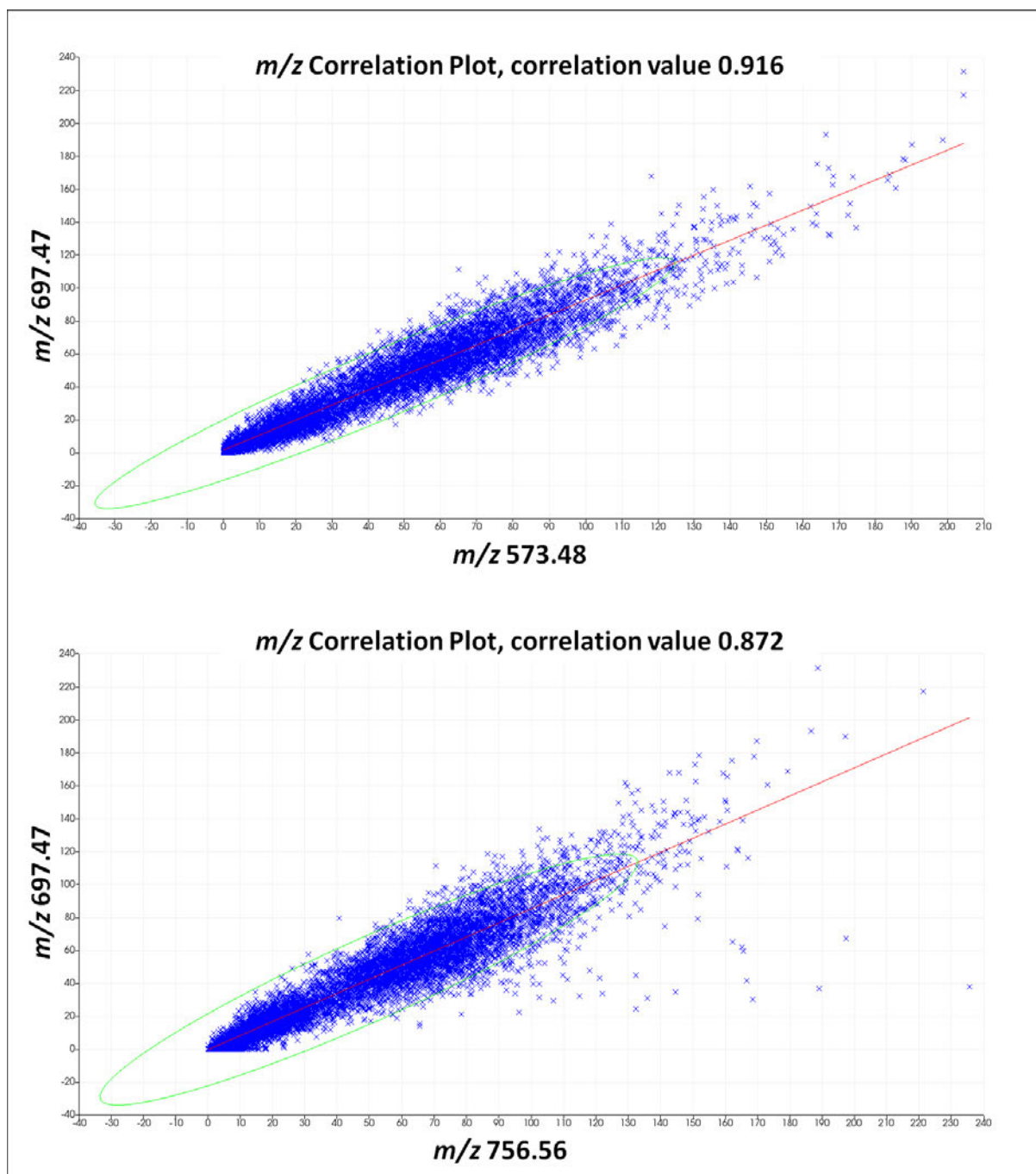
Supplementary Figure 3.1. Determination of number of segments for SSCG clustering. **A.** Data for patient 32770L_S141 was imported over m/z 400-990 and batch processed. **B.** Summary plot of SSCG comparing $r = 1$ and $r = 2$ for $k = 5$ vs $k = 10$ initial segments. **C.** Plot of peak centres of spectra for respective smoothing radii and segments shown. **D.** Plot of SSCG segmentation shows that $r = 1$, $s = 3$, $k = 9$ as the most suitable spatial segmentation settings chosen for subsequent analyses.



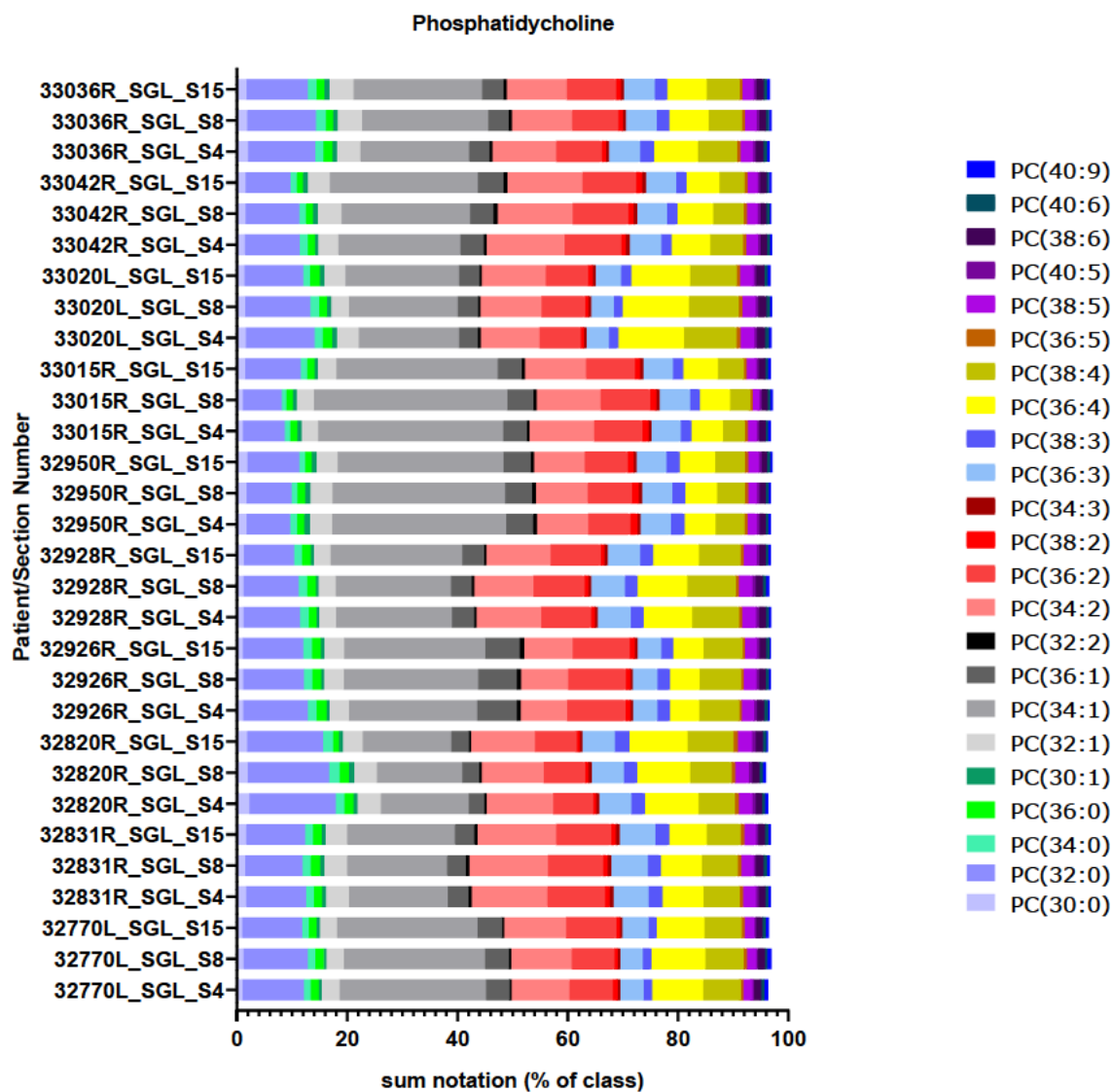
Supplementary Figure 3.2. Comparison of different segmentation metrics of the bisecting k-means algorithm. MSI data from four interspersed prostate tissue sections from a single biopsy analysed in SCiLS Lab.



Supplementary Figure 3.3. Validation of lipid ions in stromal regions of prostate tissue. A. MS/MS spectrum of m/z 666.48 in patient 33042R shows co-localized distribution of predominant fragment ion m/z 542.49 **B.** MS/MS spectrum of m/z 666.48 in patient 33036R.



Supplementary Figure 3.4. Correlation of distribution of lipid fragment ions in stromal regions of prostate tissue. Predominant fragment ions of PC(32:0)[M+Na]⁺ *m/z* 756.56 (**Figure 3.10**), *m/z* 697.47 and *m/z* 573.47 are highly co-localised with a correlation of 0.916 whereas the precursor *m/z* 756.55 and *m/z* 697.47 have a correlation of 0.872. Line of best fit in red and ellipse in green signifies error at 95% confidence interval.



Supplementary Figure 3.5. Sum notation of PC species. Composition of lipid species by the percentage of total carbons and degree of unsaturation. Top 25% of n=69 PC species are shown.

Sample	Patient_ID Section Number	Fluorescence Units		Concentration		Mean ng/125 µL	Corrected Dilution Factor ng/125 µL	DNA ng/125 µL	0.5 µg	H ₂ O to 700 µL
		1	2	1	2					
1	32770L_SGL_S4	8.157	8.037	3.5	0.7	2.13	6.66	0.05	9388.6	-8688.6
2	32770L_SGL_S8	8.071	7.811	1.5	-4.5	-1.50	-4.68	-0.04	-13354.0	14054.0
3	32770L_SGL_S15	8.519	8.851	11.9	19.7	15.80	49.39	0.40	1265.5	-565.5
4	32831R_SGL_S4	12.63	12.98	107.5	115.7	111.62	348.81	2.79	179.2	520.8
5	32831R_SGL_S8	12.61	11.62	107.1	84.1	95.57	298.66	2.39	209.3	490.7
6	32831R_SGL_S15	13.87	13.88	136.4	136.6	136.50	426.57	3.41	146.5	553.5
7	32820R_SGL_S4	10.19	9.387	50.8	32.1	41.47	129.59	1.04	482.3	217.7
8	32820R_SGL_S8	8.919	9.207	21.2	27.9	24.60	76.86	0.61	813.2	-113.2
9	32820R_SGL_S15	10.15	9.69	49.9	39.2	44.53	139.14	1.11	449.2	250.8
10	32926R_SGL_S4	12.7	12.5	109.2	104.5	106.85	333.91	2.67	187.2	512.8
11	32926R_SGL_S8	10.93	10.56	68.0	59.4	63.71	199.10	1.59	313.9	386.1
12	32926R_SGL_S15	9.678	9.096	38.9	25.4	32.13	100.41	0.80	622.5	77.5
13	32928R_SGL_S4	17.04	16.93	210.1	207.5	208.83	652.59	5.22	95.8	604.2
14	32928R_SGL_S8	15.81	15.18	181.5	166.9	174.18	544.30	4.35	114.8	585.2
15	32928R_SGL_S15	14.94	14.52	161.3	151.5	156.39	488.71	3.91	127.9	572.1
16	32950R_SGL_S4	9.845	9.722	42.8	39.9	41.35	129.22	1.03	483.7	216.3
17	32950R_SGL_S8	11.52	11.49	81.7	81.0	81.39	254.33	2.03	245.7	454.3
18	32950R_SGL_S15	13.16	13.53	119.9	128.5	124.18	388.05	3.10	161.1	538.9
19	33015R_SGL_S4	10.52	10.36	58.5	54.8	56.62	176.93	1.42	353.2	346.8
20	33015R_SGL_S8	11.57	11.4	82.9	78.9	80.92	252.88	2.02	247.2	452.8
21	33015R_SGL_S15	15.05	14.83	163.8	158.7	161.27	503.97	4.03	124.0	576.0
22	33020L_SGL_S4	9.315	9.743	30.5	40.4	35.43	110.73	0.89	564.5	135.5

23	33020L_SGL_S8	11.39	11.2	78.7	74.3	76.50	239.07	1.91	261.4	438.6
24	33020L_SGL_S15	10.25	10.03	52.2	47.1	49.64	155.13	1.24	402.9	297.1
25	33042R_SGL_S4	13.22	12.96	121.3	115.2	118.25	369.52	2.96	169.1	530.9
26	33042R_SGL_S8	10.52	10.43	58.5	56.4	57.43	179.48	1.44	348.2	351.8
27	33042R_SGL_S15	11.05	10.66	70.8	61.7	66.27	207.09	1.66	301.8	398.2
28	33036R_SGL_S4	12.49	12.4	104.3	102.2	103.25	322.65	2.58	193.7	506.3
29	33036R_SGL_S8	9.448	9.655	33.5	38.4	35.96	112.36	0.90	556.2	143.8
30	33036R_SGL_S15	9.11	9.343	25.7	31.1	28.40	88.74	0.71	704.3	-4.3

Supplementary Table 3.1. Total DNA measurement results for lipidomics analyses.

9.2. Appendix 2: Supplementary Information Chapter 5

Procedure for Testing Matrix Parameters

Set 1: Neat		
Solution	Solutions/Concentration	Volume
MDV	LQC, MQC & HQC * 6 r	50 µL
D6-MDV	IS 1,000 nM	50 µL
D6M-MDV	IS 1,000 nM	50 µL
Solvent blank	CH ₃ OH-H ₂ O 1:1 (v/v)	250 µL
		400 µL Total Volume
Set 2: Spike after Extraction		
Solution	Solutions/Concentration	Volume
M4 Media/Tissue Homogenate	Absolute	250 µL for protein precipitation
MDV	LQC, MQC & HQC * 6 r	50 µL
D6-MDV	IS 1,000 nM	50 µL
D6M-MDV	IS 1,000 nM	50 µL
Solvent blank	CH ₃ OH-H ₂ O 1:1 (v/v)	250 µL
		100 µL + 50 µL spiked into 250 µL of reconstituted extract = 400 µL total assay volume.
Control (Blank of M4 Media)		<u>250 µL media for protein precipitation</u> followed by 400 µL solvent reconstitution
Set 3: Spike before Extraction		
Solution	Solutions/Concentration	Volume
M4 Media/Tissue Homogenate	Absolute	250 µL + 100 µL + 50 µL = 400 µL for protein precipitation followed by 400 µL solvent reconstitution = 400 µL total assay vol
Solvent blank	CH ₃ OH-H ₂ O 1:1 (v/v)	0 µL
D6M-MDV	IS 1,000 nM	50 µL
D6-MDV	IS 1,000 nM	50 µL
MDV	LQC, MQC & HQC* 6 r	50 µL
Control (Blank of M4) Media		<u>250 µL media + 150 µL solvent</u> for protein precipitation followed by 400 µL solvent reconstitution
<ul style="list-style-type: none"> Inject 5 µL into LC-MS/MS system 		

Supplementary Table 5.1. Summary procedure for assessment of matrix effects and recovery efficiency parameters.

Procedure for Drug Stability Testing of Enzalutamide

i. Freeze and Thaw Stability (FTS)

1. Prepare three aliquots enzalutamide in M4 culture medium/tissue homogenate at LQC and HQC concentrations are stored both at -20°C and at -80°C. LQC and MQC may be tested as well.
2. Thaw unassisted at room temperature and re-frozen.
3. Repeat two more times
4. Add internal standard (IS) mix i.e. 50 µL each of 1,000 nM d6-enzalutamide and d6-desmethylenzalutamide
5. Extract as previously described and analyse after the third cycle.
6. Perform analysis together with freshly extracted QC-standards and compare results

ii. Short-Term Temperature Stability (STS)

1. Prepare six aliquots of M4 culture medium/tissue homogenate at LLOQ, LQC, MQC and HQC.
2. Extract three aliquots within 2 h on same day - fresh extraction (**FE**)
3. Perform extraction as previously described.
4. Place remaining three aliquots at room temperature for at least 4 h and up to 24 h.
5. Add internal standard (IS) mix i.e. 50 µL each of 1,000 nM d6-enzalutamide and d6-desmethylenzalutamide
6. Extract as previously described.
7. Compare results of **FE** to **STS**

iii. Long-Term Stability (LTS)

1. Prepare nine aliquots enzalutamide in M4 culture medium/tissue homogenate at LQC and HQC concentrations are stored at -80°C. LQC and MQC may be tested as well.
2. Split samples into three aliquots per cycle
3. Analyse each cycle after every two-three months or as scheduled
4. For each cycle set, thaw unassisted at room temperature.

-
5. Add internal standard (IS) mix i.e. 50 μ L each of 1,000 nM d6-enzalutamide and d6-desmethylenzalutamide
 6. Extract as previously described together with a **FE** set.

iv. Stock Solution Stability (STS)

1. Prepare from frozen stock (DMSO) solution of enzalutamide and internal standards in solvent at LLOQ, LQC, MQC and HQC.
2. Prepare from fresh/new un-reconstituted compound stocks of enzalutamide and internal standards in DMSO.
3. Prepare three aliquots working solution in methanol-water 1:1 (v/v) at LLOQ, LQC, MQC and HQC.
4. Compare mean analyte response/concentrations of refrigerated/frozen to freshly prepared ones.
5. The mean analyte responses standard deviation between frozen stock samples and fresh reconstituted stocks should not exceed >15%.

v. Post-Preparative Stability (PPS)

1. Prepare six aliquots of M4 culture medium/tissue homogenate at LLOQ, LQC, MQC and HQC.
2. Extract three aliquots within 2 h on same day - fresh extraction (**FE**)
3. Perform extraction as previously described
4. Reconstitute freeze-dried extract with 400 μ L solvent blank.
5. Split samples equally and aliquot into separate sealed wells, one set **FE** and other set **PPS**
6. **PPS** aliquots will reside in autosampler for 12 - 24 h at 6°C during the FE analytical run.
7. Analyse **PPS** samples at the end of **FE** run and compare results to both **FE** and **STS**.

Note: Run stability samples in this sequence: FE, PPS and STS samples on the same data file.

9.3. Appendix 3: Supplementary Information Chapter 7

Supplementary Table 7.2. Bucket list for annotation for negative ion mode data.

m/z meas.	M meas.	Ions	Name	Molecular Formula	$\Delta m/z$ [ppm]	$\Delta m/z$ [mDa]	m-Sigma
167.062	168.069	[M-H]-	beta-Carboline	C11H8N2	4.814	0.804	4.2
239.083	240.09	[M-H]-	3-Carboxy-4-methyl-5-propyl-2-furanpropionic acid	C12H16O5	-39.211	-9.375	11.3
241.012	260.03	[M-H ₂ O-H]-, [M-H]-	Fructose 6-phosphate	C6H13O9P	2.75	0.663	1.4
242.08	243.088	[M-H]-	Cytidine	C9H13N3O5			∞
243.105	244.112	[M-H]-	Batatasin IV	C15H16O3	8.409	2.044	∞
253.218	254.225	[M-H]-	Hypogeic acid	C16H30O2	1.899	0.481	15.1
255.233	256.241	[M-H]-	Palmitic acid	C16H32O2			∞
267.074	268.081	[M-H]-	Allopurinol riboside	C10H12N4O5	2.188	0.584	11.9
269.249	270.256	[M-H]-	Heptadecanoic acid	C17H34O2	1.332	0.359	13.3
277.074	278.082	[M-H]-, [M-H ₂ O-H]-	9-dimethylarsinoyl-nonanoic acid	C11H23AsO3	-18.204	-5.044	9.7
277.185	278.192	[M-H]-	7-hydroxy-10E,16-heptadecadien-8-ynoic acid	C17H26O3	14.336	3.974	18.1
279.09	280.097	[M-H]-	Aspartylphenylalanine	C13H16N2O5	-32.635	-9.108	14.4
279.127	280.134	[M-H]-	Tyrosyl-Valine	C14H20N2O4	-28.412	-7.931	12.2
279.234	298.251	[M-H ₂ O-H]-, [M+Cl]-, [M-H]-	Ricinoleic acid	C18H34O3	1.792	0.5	13.3
281.144	282.151	[M-H]-	3,4-dimethyl-5-carboxyethyl-2-furanhexanoic acid	C15H22O5	15.296	4.3	13.5
281.249	300.267	[M-H ₂ O-H]-, [M-H]-	2-Hydroxystearic acid	C18H36O3	1.765	0.497	14.2
283.016	284.021	[M-H]-, [M+Cl]-	Repensol3,7,9-Trihydroxycoumestan	C15H8O6	-31.75	-8.986	18.5
283.265	284.272	[M-H]-	Stearic acid	C18H36O2	1.152	0.326	8.7
289.038	290.045	[M-H]-	D-Sedoheptulose 7-phosphate	C7H15O10P	17.368	5.02	12.6
297.28	298.288	[M-H]-	Pristanic acid	C19H38O2	1.362	0.405	15.1
299.054	300.062	[M-H]-	beta-D-3-Ribofuranosyluric acid	C10H12N4O7	-30.183	-9.026	12.6

301.218	302.225	[M-H]-	Retinyl ester	C20H30O2	1.373	0.414	17.8
303.234	322.252	[M-H2O-H]-, [M+Cl]-	15(S)-Hydroxyeicosatrienoic acid	C20H34O3	1.8	0.546	16
305.249	306.256	[M-H]-	Dihomo-gamma-linolenic acid	C20H34O2	0.853	0.26	15.9
307.265	308.272	[M-H]-	Eicosadienoic acid	C20H36O2	1.994	0.613	15.9
309.281	310.288	[M-H]-	11Z-Eicosenoic acid	C20H38O2	2.062	0.638	18.2
311.296	312.303	[M-H]-	Phytanic acid	C20H40O2	0.134	0.042	15.9
323.029	324.036	[M-H]-	Uridine 5'-monophosphate	C9H13N2O9P	1.956	0.632	16.6
337.109	338.117	[M-H]-	Psoralenol	C20H18O5	4.966	1.674	19.3
337.146	338.153	[M-H]-	Hildgardtol A	C21H22O4	3.864	1.303	16
337.206	338.213	[M-H]-	LMST02020108	C19H30O5	11.117	3.749	19.5
338.989	339.996	[M-H]-	alpha-D-Glucose 1,6-bisphosphate	C6H14O12P2	1.098	0.372	17.2
346.056	347.064	[M-H]-	3'-AMP	C10H14N5O7P	1.868	0.647	3.5
357.059	358.067	[M-H]-	LMPK12050420	C18H14O8	-6.231	-2.225	5.1
377.094	378.101	[M-H]-	Isojamaicin	C22H18O6	-21.539	-8.122	8.8
391.226	410.243	[M-H2O-H]-, [M-H]-	LysoPA(0:0/16:0)	C19H39O7P	0.318	0.125	13.1
393.241	394.248	[M-H]-	LysoPA(P-16:0/0:0)	C19H39O6P	0.664	0.261	4.1
403.262	422.279	[M-H2O-H]-, [M-H]-	Volicitin	C23H38N2O5	3.855	1.554	10.4
419.257	420.264	[M-H]-, [M-H2O-H]-	CPA(18:0)	C21H41O6P	-0.814	-0.341	4.4
436.283	437.291	[M-H]-	LysoPE(P-16:0/0:0)	C21H44NO6P	-0.412	-0.18	5.9
437.267	438.275	[M-H]-	LysoPA(18:0/0:0)	C21H43O7P	1.215	0.531	8
452.279	453.286	[M-H]-	LysoPE(0:0/16:0)	C21H44NO7P	0.431	0.195	8.8
465.305	466.31	[M-H]-, [M-H2O-H]-	Cholesterol sulfate	C27H46O4S	0.319	0.149	13.9
480.274	481.282	[M-H]-	PC(10:0/4:0)	C22H44NO8P	-0.397	-0.19	18.1
480.31	481.317	[M-H]-, [M-H2O-H]-	LysoPC(15:0/0:0)	C23H48NO7P	0.165	0.079	1.8
505.989	506.996	[M-H]-	Adenosine triphosphate	C10H16N5O13P3	-0.069	-0.035	4.5
506.289	525.307	[M-H2O-H]-, [M-H]-	1-Stearoylglycerophosphoserine	C24H48NO9P	0.814	0.412	8.4
508.269	509.276	[M-H]-	PS(17:1(9Z)/0:0)	C23H44NO9P	0.834	0.424	15.4
508.304	509.312	[M-H]-, [M-H2O-H]-	PC(14:0/2:0)	C24H48NO8P	-0.486	-0.247	12.2
508.341	509.348	[M-H]-	LysoPC(17:0/0:0)	C25H52NO7P	0.458	0.233	12.1

511.248	512.255	[M-H]-	TMC-1A	C28H36N2O7	5.18	2.648	17.5
528.273	529.28	[M-H]-, [M+Cl]-	N-[(3a,5b,7b)-7-hydroxy-24-oxo-3-(sulfooxy)cholan-24-yl]-Glycine	C26H43NO8S	17.796	9.401	4.5
536.372	537.379	[M-H]-	PC(O-16:0/3:0)	C27H56NO7P	0.091	0.049	13.6
580.363	581.37	[M-H]-	PS(22:0/0:0)	C28H56NO9P	1.307	0.759	14
599.321	600.328	[M-H]-, [M-H2O-H]-	LysoPI(18:0/0:0)	C27H53O12P	1.077	0.645	1.8
616.472	617.479	[M-H]-, [M-H2O-H]-	CerP(d18:1/16:0)	C34H68NO6P	0.603	0.372	15.2
621.303	622.31	[M-H]-, [M+Cl]-	PI(20:3(8Z,11Z,14Z)/0:0)	C29H51O12P	-3.048	-1.894	16.6
625.187	626.194	[M-H]-	5-O-Methylerythrodiol 7-glucosyl-(1->4)-galactoside	C28H34O16	14.411	9.009	17.6
647.466	648.473	[M-H]-	PA(16:0/16:0)	C35H69O8P	-0.123	-0.08	6.5
664.42	665.427	[M-H]-	PS(12:0/15:0)	C33H64NO10P	0.057	0.038	7.9
673.231	674.239	[M-H]-	(N-acetylneuraminosyl(a2-6)lactosamine)	C25H42N2O19	0.517	0.348	18.6
678.4	679.407	[M-H]-, [M-H2O-H]-	PHDdiA-PE	C33H62NO11P	-1.676	-1.137	14.6
678.434	679.441	[M-H]-	PS(14:0/14:0)	C34H66NO10P	-1.918	-1.301	19.7
683.343	684.35	[M-H]-	PG-PI	C31H57O14P	0.603	0.412	5
687.5	688.507	[M-H]-	DG(20:5(5Z,8Z,11Z,14Z,17Z)/22:5(7Z,10Z,13Z,16Z,19Z)/0:0)[iso2]	C45H68O5	-0.402	-0.276	19.9
687.545	688.552	[M-H]-	SM(d16:1/17:0)	C38H77N2O6P	0.054	0.037	13.6
701.513	702.52	[M-H]-	PA(18:0/18:1(9Z))	C39H75O8P	0.139	0.098	12.8
735.334	736.342	[M-H]-	OKOHA-PI	C34H57O15P	-5.21	-3.831	19.2
744.554	745.562	[M-H]-	PE(14:1(9Z)/22:0)	C41H80NO8P	-0.573	-0.426	15.2
751.532	752.539	[M-H]-	PA(18:2(9Z,12Z)/22:2(13Z,16Z))	C43H77O8P	3.014	2.265	14.8
754.611	755.618	[M-H]-	PC(P-18:0/P-18:1(11Z))	C44H86NO6P	-0.84	-0.634	18.4
771.638	772.646	[M-H]-	SM(d16:1/23:0)	C44H89N2O6P	-1.244	-0.96	14.4
788.544	789.553	[M-H]-, [M-H2O-H]-	PS(18:1(9Z)/18:0)	C42H80NO10P	-0.598	-0.471	12.4
816.574	817.581	[M-H]-	PS(16:0/22:1(11Z))	C44H84NO10P	-1.037	-0.847	8.5
837.546	838.553	[M-H]-	PI(16:0/18:0)	C43H83O13P	-1.96	-1.641	19.5
843.518	844.525	[M-H]-	PG(20:3(8Z,11Z,14Z)/22:6(4Z,7Z,10Z,13Z,16Z,19Z))	C48H77O10P	-0.385	-0.324	16.8

865.503	866.511	[M-H]-	PG(22:6(4Z,7Z,10Z,13Z,16Z,19Z)/22:6(4Z,7Z,10Z,13Z,16Z,19Z))	C50H75O10P	1.678	1.452	13.1
871.534	872.542	[M-H]-	PI(17:0/20:4(5Z,8Z,11Z,14Z))	C46H81O13P	-0.339	-0.295	17.1

Supplementary Table 7.3. Bucket list for annotation for positive ion mode data.

m/z meas.	M meas.	Ions	Name	Molecular Formula	$\Delta m/z$ [ppm]	$\Delta m/z$ [mDa]	mSigma
89.039	176.063	[M+H+H] ²⁺	2-Isopropylmalic acid	C7H12O5	-31.141	-2.773	∞
90.046	178.078	[M+H+H] ²⁺	4-Methoxycinnamic acid	C10H10O3	83.913	7.556	∞
98.984	195.954	[M+H+H] ²⁺	bromosuccinic acid	C4H5BrO4	87.858	8.697	∞
102.047	202.079	[M+H+H] ²⁺	Serylproline	C8H14N2O4	-79.179	-8.08	∞
104.05	206.085	[M+H+H] ²⁺	Diethyl tartrate	C8H14O6	27.905	2.904	∞
104.972	81.981	[M+Na] ⁺ , [M+K] ⁺	Sulfite	H2O3S	94.063	9.874	∞
106.98	105.972	[M+H] ⁺	2-chloroacrylic acid	C3H3ClO2	-92.295	-9.874	∞
107.05	124.054	[M-H2O+H] ⁺ , [M+Na] ⁺ , [M+K] ⁺	4-Methylcatechol	C7H8O2	4.374	0.468	12.7
113.001	223.986	[M+H+H] ²⁺ , [M+K] ⁺	4-thiodimethylarsenobutanoic acid	C6H13AsO2S	10.572	1.195	∞
113.001	111.993	[M+H] ⁺	Methylphosphate	CH5O4P	8.758	0.99	∞
114.034	226.054	[M+H+H] ²⁺	3-Nitrotyrosine	C9H10N2O5	-21.625	-2.466	∞
114.903	113.896	[M+H] ⁺	Cadmium	Cd	-71.437	-8.208	∞
115.042	228.07	[M+H+H] ²⁺	Deoxyuridine	C9H12N2O5	-23.683	-2.724	∞
115.055	228.095	[M+H+H] ²⁺	Prolylhydroxyproline	C10H16N2O4	71.735	8.254	∞
116.05	230.086	[M+H+H] ²⁺	Naproxen	C14H14O3	-37.713	-4.377	∞
117.058	232.101	[M+H+H] ²⁺	Valylaspartic acid	C9H16N2O5	-19.007	-2.225	∞
117.071	134.075	[M-H2O+H] ⁺ , [M+Na] ⁺	1-Phenyl-1-propanone	C9H10O	10.371	1.214	∞
117.071	232.127	[M+H+H] ²⁺	Melatonin	C13H16N2O2	24.784	2.901	∞
117.12	116.113	[M+H] ⁺	(\hat{A} \pm)-2-Heptanol	C7H16O	-59.486	-6.967	∞
118.087	117.08	[M+H] ⁺	Betaine	C5H11NO2	7.973	0.942	8.9
119.086	236.158	[M+H+H] ²⁺	Procaine	C13H20N2O2	23.483	2.797	∞
121.029	138.031	[M-H2O+H] ⁺ , [M+K] ⁺	3-Hydroxybenzoic acid	C7H6O3	4.247	0.514	6.4
123.045	122.037	[M+H] ⁺	4-Hydroxybenzaldehyde	C7H6O2	4.573	0.563	8.7
128.05	254.084	[M+H+H] ²⁺ , [M-H2O+H] ⁺	Ketoprofen	C16H14O3	-35.114	-4.496	∞

129.058	256.101	[M+H+H] ²⁺	Pyrimidine, 2,4- bis[(trimethylsilyl)oxy]-	C10H20N2O2Si2	-21.293	-2.748	∞
129.071	256.127	[M+H+H] ²⁺	LMPK12020230	C16H16O3	63.083	8.142	∞
130.066	258.117	[M+H+H] ²⁺	3'-O-methylbatatasin III	C16H18O3	-35.33	-4.595	∞
131.05	260.085	[M+H+H] ²⁺	Khellin	C14H12O5	62.288	8.163	∞
131.061	130.054	[M+H] ⁺	Mevalonolactone	C6H10O3	-71.65	-9.391	13.2
131.086	260.158	[M+H+H] ²⁺	Cyclo(Leu-Phe)	C15H20N2O2	20.877	2.737	∞
132.045	262.076	[M+H+H] ²⁺	LMPK12130001	C17H10O3	46.982	6.204	∞
132.081	262.148	[M+H+H] ²⁺	Isoleucyl-Methionine	C11H22N2O3S	62.645	8.274	∞
133.053	264.093	[M+H+H] ²⁺ , [M+Na] ⁺	N-Acetylcystathionine	C9H16N2O5S	50.303	6.693	∞
133.102	264.189	[M+H+H] ²⁺	3,5-Bis(1,1-dimethylethyl)-4-hydroxy-benzoic acid ethyl ester	C16H24O3	62.965	8.381	∞
134.097	266.18	[M+H+H] ²⁺	Tetranor 12-HETE	C16H26O3	64.032	8.587	∞
136.063	270.111	[M+H+H] ²⁺	LMPK12020231	C17H18O3	-55.751	-7.586	∞
137.047	136.039	[M+H] ⁺	Hypoxanthine	C5H4N4O	6.921	0.948	∞
137.072	136.065	[M+H] ⁺ , [M+Na] ⁺	N-Methylnicotinamide	C7H8N2O	7.681	1.053	4.5
144.045	161.048	[M-H2O+H] ⁺ , [M+H] ⁺	2-Indolecarboxylic acid	C9H7NO2	1.737	0.25	∞
146.076	145.067	[M+H] ⁺ , [M-H2O+H] ⁺	Allysine	C6H11NO3	-32.882	-4.803	13.2
146.162	145.155	[M+H] ⁺	Spermidine	C7H19N3	-21.758	-3.18	∞
159.029	158.022	[M+H] ⁺	2-methylene-4-oxo-pentanedioic acid	C6H6O5	1.803	0.287	∞
161.048	160.041	[M+H] ⁺	Oxoadipic acid	C6H8O5	21.456	3.456	∞
161.109	160.101	[M+H] ⁺	Tryptamine	C10H12N2	7.585	1.222	∞
162.113	161.106	[M+H] ⁺ , [M-H2O+H] ⁺	L-Carnitine	C7H15NO3	5.807	0.941	6.6
169.077	168.069	[M+H] ⁺	beta-Carboline	C11H8N2	7.654	1.294	4.2
172.04	189.043	[M-H2O+H] ⁺ , [M+K] ⁺ , [M+H] ⁺	Kynurenic acid	C10H7NO3	8.908	1.533	1.4
173.031	190.034	[M-H2O+H] ⁺ , [M+H] ⁺	Deca-2,4,6-triynedioic acid	C10H6O4	46.309	8.013	∞
173.133	172.126	[M+H] ⁺	1,2-Dihydro-1,1,6-trimethylnaphthalene	C13H16	4.311	0.746	∞
175.12	174.113	[M+H] ⁺ , [M+Na] ⁺	L-Arginine	C6H14N4O2	8.252	1.445	8.7
176.093	175.086	[M+H] ⁺	hydroxyvalerylglycine	C7H13NO4	5.723	1.008	7
180.96	179.953	[M+H] ⁺	Hafnium	Hf	50.577	9.152	∞

183.09	182.083	[M+H] ⁺	Harman	C12H10N2	-8.013	-1.467	∞
187.124	186.117	[M+H] ⁺	10-hydroxy-2E-decenoic acid	C10H18O3	-46.563	-8.713	7.9
189.015	188.008	[M+H] ⁺	p-Cresol sulfate	C7H8O4S	-38.007	-7.184	∞
189.123	188.115	[M+H] ⁺	N6-Acetyl-L-lysine	C8H16N2O3	-3.314	-0.627	10.3
189.162	188.155	[M+H] ⁺	N6,N6,N6-Trimethyl-L-lysine	C9H20N2O2	15.479	2.928	10.4
190.105	189.098	[M+H] ⁺	4-hydroxyhexanoylglycine	C8H15NO4	-8.715	-1.657	∞
198.09	197.083	[M+H] ⁺ , [M+Na] ⁺	N-Acetylhistidine	C8H11N3O3	16.377	3.244	13.4
203.154	202.147	[M+H] ⁺	Symmetric dimethylarginine	C8H18N4O2	23.491	4.772	14.6
203.224	202.217	[M+H] ⁺ , [M+Na] ⁺	Spermine	C10H26N4	6.993	1.421	9.6
204.099	203.092	[M+H] ⁺	Methyl indole-3-propanoate	C12H13NO2	-12.943	-2.642	∞
204.124	203.117	[M+H] ⁺	L-Acetylcarnitine	C9H17NO4	4.933	1.007	5.9
206.14	205.133	[M+H] ⁺	Pantothenol	C9H19NO4	8.863	1.827	∞
214.005	212.998	[M+H] ⁺ , [M+Na] ⁺	L-Aspartyl-4-phosphate	C4H8NO7P	-27.751	-5.939	8.8
218.14	217.132	[M+H] ⁺	Propionylcarnitine	C10H19NO4	4.237	0.924	∞
219.085	218.077	[M+H] ⁺	Triacetin	C9H14O6	-7.773	-1.703	∞
221.02	220.012	[M+H] ⁺ , [M-H2O+H] ⁺	2-hydroxy-4-oxobutane-1,2,4-tricarboxylic acid	C7H8O8	-40.286	-8.904	∞
226.085	225.078	[M+H] ⁺ , [M+Na] ⁺	(E)-4-Nitrostilbene	C14H11NO2	-4.349	-0.983	∞
229.009	228.002	[M+H] ⁺	Thiorubrine A	C13H8S2	-19.77	-4.528	∞
234.034	211.045	[M+Na] ⁺ , [M+K] ⁺ , [M+H] ⁺	Phosphocreatine	C4H10N3O5P	39.822	9.32	19.7
234.126	233.118	[M+H] ⁺	Hydroxypropionylcarnitine	C10H19NO5	-33.303	-7.797	∞
246.121	245.114	[M+H] ⁺	N-Phenylacetyl pyroglutamic acid	C14H15NO3	35.601	8.762	19.5
247.02	264.023	[M-H2O+H] ⁺ , [M+H] ⁺	3-Methoxy-4-Hydroxyphenylglycol sulfate	C9H12O7S	-27.353	-6.757	19.5
249.08	248.073	[M+H] ⁺	methyl 10-acetoxy-8,9-epoxy-2Z-decen-4,6-diynoate	C13H12O5	17.018	4.239	∞
250.085	249.078	[M+H] ⁺	S-Acetyldihydrolipoamide	C10H19NO2S2	-30.714	-7.681	∞
262.166	261.159	[M+H] ⁺	3-Hydroxyisovaleryl carnitine	C12H23NO5	6.484	1.7	10.4
263.239	262.231	[M+H] ⁺	6-[3]-ladderane-1-hexanol	C18H30O	4.557	1.2	15.2
265.254	264.247	[M+H] ⁺ , [M-H2O+H] ⁺	9,12,15-Octadecatrien-1-ol	C18H32O	7.633	2.025	12.4

277.099	254.111	[M+Na] ⁺ , [M+H+H] ²⁺	methyl 4-[2-(2-formyl-vinyl)-3-hydroxy-5-oxo-cyclopentyl]-butanoate	C13H18O5	-17.883	-4.956	18.3
278.056	239.094	[M+K] ⁺ , [M-H ₂ O+H] ⁺	Dihydrobiopterin	C9H13N5O3	-31.961	-8.887	10.6
279.27	278.263	[M+H] ⁺	6Z,9Z-Nonadecadien-3-one	C19H34O	7.938	2.217	16.3
280.094	257.104	[M+Na] ⁺ , [M+H] ⁺ , [M+K] ⁺ , [M-H ₂ O+H] ⁺	Glycerophosphocholine	C8H20NO6P	6.806	1.906	4.2
283.266	282.258	[M+H] ⁺	Oleic acid	C18H34O2	9.501	2.691	18
288.291	287.284	[M+H] ⁺ , [M-H ₂ O+H] ⁺	C17 Sphinganine	C17H37NO2	4.348	1.253	7.4
301.213	300.206	[M+H] ⁺	all-trans-Retinoic acid	C20H28O2	-9.42	-2.837	5.4
304.094	281.106	[M+Na] ⁺ , [M+H] ⁺ , [M+K] ⁺	1-Methyladenosine	C11H15N5O4	-26.371	-8.019	3.3
313.276	330.28	[M-H ₂ O+H] ⁺ , [M+H] ⁺	MG(0:0/16:0/0:0)	C19H38O4	6.647	2.082	9
321.055	320.048	[M+H] ⁺	Amaronol A	C15H12O8	-18.672	-5.995	18.6
325.052	324.045	[M+H] ⁺	Uridine 5'-monophosphate	C9H13N2O9P	19.565	6.36	6.3
329.244	328.237	[M+H] ⁺	Malyngic acid	C18H32O5	28.61	9.42	17.5
335.079	312.089	[M+Na] ⁺ , [M+K] ⁺	Cabreuvin	C18H16O5	-29.142	-9.765	12.9
339.07	338.062	[M+H] ⁺	AICAR	C9H15N4O8P	-16.212	-5.497	13.1
341.307	340.3	[M+H] ⁺	2-oxo-heneicosanoic acid	C21H40O3	7.349	2.508	19.5
355.043	332.053	[M+Na] ⁺ , [M+K] ⁺	3',4',5'-Trihydroxywogonin	C16H12O8	-1.794	-0.637	18.3
355.107	354.1	[M+H] ⁺ , [M+K] ⁺ , [M+Na] ⁺	Chlorogenic acid	C16H18O9	14.074	4.998	6.8
369.352	368.344	[M+H] ⁺	3-Deoxyvitamin D3	C27H44	0.125	0.046	14.9
373.06	334.097	[M+K] ⁺ , [M+H] ⁺	Mesquitol-4beta-ol 3,8-dimethyl ether	C17H18O7	-22.539	-8.408	17.4
400.345	399.337	[M+H] ⁺	L-Palmitoylcarnitine	C23H45NO4	6.13	2.454	16.6
401.077	400.069	[M+H] ⁺ , [M+K] ⁺ , [M-H ₂ O+H] ⁺	LMPK12111983	C20H16O9	-24.906	-9.989	4.1
428.376	427.369	[M+H] ⁺	Stearoylcarnitine	C25H49NO4	5.998	2.569	3.9
445.273	444.266	[M+H] ⁺	sn-3-O-(geranylgeranyl)glycerol 1-phosphate	C23H41O6P	6.202	2.761	11.3
459.25	458.243	[M+H] ⁺ , [M-H ₂ O+H] ⁺ , [M+Na] ⁺	PA(20:4(5Z,8Z,11Z,14Z)/0:0)	C23H39O7P	0.463	0.213	9.1
463.108	462.101	[M+H] ⁺	farnesyl triphosphate	C15H29O10P3	8.104	3.753	17

475.224	436.261	[M+K] ⁺ , [M-H ₂ O+H] ⁺	PA(18:1(9Z)/0:0)	C21H41O7P	4.536	2.156	11.2
476.986	475.979	[M+H] ⁺	6-Methoxyluteolin 3',4'-disulfate	C16H12O13S2	19.948	9.515	15.8
478.331	495.335	[M-H ₂ O+H] ⁺ , [M+H] ⁺ , [M+Na] ⁺ , [M+K] ⁺	LysoPC(16:0/0:0)	C24H50NO7P	4.445	2.126	3.5
487.282	486.274	[M+H] ⁺ , [M-H ₂ O+H] ⁺	PA(22:4(7Z,10Z,13Z,16Z)/0:0)	C25H43O7P	-7.722	-3.763	14.7
510.292	509.284	[M+H] ⁺	PS(17:1(9Z)/0:0)	C23H44NO9P	18.886	9.637	9.7
510.358	509.351	[M+H] ⁺	LysoPC(17:0/0:0)	C25H52NO7P	6.424	3.278	19.5
526.289	525.281	[M+H] ⁺ , [M-H ₂ O+H] ⁺	LysoPE(22:6(4Z,7Z,10Z,13Z,16Z,19Z)/0:0)	C27H44NO7P	-11.895	-6.26	17.5
546.319	523.33	[M+Na] ⁺ , [M+K] ⁺ , [M+H] ⁺	PE(10:0/10:0)	C25H50NO8P	4.065	2.221	4.4
546.355	523.366	[M+Na] ⁺ , [M+H] ⁺ , [M+K] ⁺ , [M-H ₂ O+H] ⁺	LysoPC(18:0/0:0)	C26H54NO7P	-2.494	-1.362	1.6
551.506	550.499	[M+H] ⁺ , [M+Na] ⁺	DG(P-14:0/18:1(9Z))	C35H66O4	4.361	2.405	10
577.521	576.514	[M+H] ⁺ , [M+Na] ⁺	phenolic phthiocerol	C37H68O4	6.447	3.723	4.6
649.52	648.513	[M+H] ⁺	PA(O-18:0/15:0)	C36H73O7P	4.599	2.987	19
672.424	649.435	[M+Na] ⁺ , [M+K] ⁺ , [M+H] ⁺	1-(2-methoxy-5Z,9Z-hexacosadienyl)-sn-glycero-3-phosphoserine	C33H64NO9P	4.408	2.964	7.8
697.48	696.473	[M+H] ⁺ , [M+K] ⁺ , [M+Na] ⁺	PA(16:0/20:4(5Z,8Z,11Z,14Z))	C39H69O8P	0.435	0.303	17.5
706.542	705.535	[M+H] ⁺	PC(15:0/15:0)	C38H76NO8P	3.909	2.762	18.8
709.482	708.475	[M+H] ⁺	LMGP00000052	C37H73O8PS	-2.433	-1.726	5.7
723.496	722.488	[M+H] ⁺ , [M+K] ⁺ , [M+Na] ⁺	PA(16:1(9Z)/22:4(7Z,10Z,13Z,16Z))	C41H71O8P	2.628	1.901	17.7
739.471	700.505	[M+K] ⁺ , [M-H ₂ O+H] ⁺	PA(18:1(9Z)/18:1(11Z))	C39H73O8P	3.067	2.268	0.6
749.506	726.519	[M+Na] ⁺ , [M-H ₂ O+H] ⁺	PA(16:1(9Z)/22:2(13Z,16Z))	C41H75O8P	2.453	1.839	15
750.581	767.584	[M-H ₂ O+H] ⁺ , [M+H] ⁺ , [M+Na] ⁺	PC(18:2(9Z,12Z)/P-18:1(9Z))	C44H82NO7P	-5.968	-4.48	10
751.526	750.52	[M+H] ⁺ , [M+K] ⁺	PA(18:1(9Z)/22:4(7Z,10Z,13Z,16Z))	C43H75O8P	1.451	1.091	0.6
782.569	759.578	[M+Na] ⁺ , [M-H ₂ O+H] ⁺ , [M+H] ⁺ , [M+K] ⁺	PC(14:1(9Z)/20:0)	C42H82NO8P	5.417	4.239	12.8
810.599	787.608	[M+Na] ⁺ , [M-H ₂ O+H] ⁺ , [M+K] ⁺ , [M+H] ⁺	PC(14:0/22:1(13Z))	C44H86NO8P	4.46	3.615	15.4

Supplementary Table 7.4. Culture effects in MALDI negative ion mode data - epithelium. Selected mass features for volcano plot analyses in six PDE samples (n=5 patients). Buckets features are annotated neutral masses for tentative identified compounds. Blue and red highlighted cells signify downregulation and upregulation, respectively. FWER – family wise error rate. FDR – false discovery rate. Max. – maximum.

NB: Subsequent supplementary tables for volcano plot also show select chemical features.

Bucket	p-Value	p-Value(Rank)	Average Ratio "Epithelium_DM SO"/"Epitheliu m_Day0"	Fold Change "Epithelium_DM SO"/"Epitheliu m_Day0"	p-Value(FWER)	p-Value(FDR)	Max. Intensity
PA(18:2(9Z,12Z)/ 22:2(13Z,16Z))	0.000002	0.000613	0.266	-3.613	0.00084	0.000024	5628
266.156m/z	0.013915	0.134822	0.267	-3.598	1	0.047145	8953
298.161m/z	0.005727	0.142639	0.33	-2.906	1	0.021848	5047
326.192m/z	0.002008	0.004956	0.339	-2.834	0.911654	0.009026	14146
312.177m/z	0.00142	0.001412	0.35	-2.747	0.64472	0.007008	15214
340.208m/z	0.007857	0.213166	0.352	-2.725	1	0.029002	9904
366.101m/z	0.000023	0.071162	0.38	-2.525	0.010513	0.00021	6613
700.505m/z	0.091272	0.713986	0.439	-2.186	1	0.20928	4704
LysoPE(0:0/16:0)	0	0	0.473	-2.032	0	0	3115
889.573m/z	0.02006	0.212269	2.24	2.332	1	0.064134	8146
836.540m/z	0.000004	0.000463	2.547	2.652	0.001907	0.00005	13388
866.584m/z	0.015684	0.266249	3.275	3.41	1	0.052355	8034
890.582m/z	0.000009	0.000057	3.474	3.618	0.004116	0.000098	7425
9- dimethylarsinoyl -nonanoic acid	0	0	7.265	7.566	0	0	9159

Supplementary Table 7.5. Treatment effects in MALDI negative ion mode data – epithelium for volcano plot analyses.

Bucket	p-Value	p-Value(Rank)	Average Ratio "Epithelium_EN Z"/"Epithelium _DMSO"	Fold Change "Epithelium_EN Z"/"Epithelium _DMSO"	p-Value(FWER)	p-Value(FDR)	Max. Intensity
366.101m/z	0.000025	0.000578	0.39	-2.398	0.01224	0.00072	2302
365.108m/z	0.005252	0.084302	0.471	-1.984	1	0.03081	2367
676.503m/z	0.000366	0.004975	0.498	-1.877	0.175918	0.004291	1844
888.568m/z	0.49154	0.90083	0.517	-1.808	1	0.654932	17928
326.192m/z	0.017248	0.000454	1.87	2.002	1	0.078265	12521
340.208m/z	0.033273	0.006442	1.951	2.089	1	0.130117	9857
310.182m/z	0.319748	0.902765	2.058	2.202	1	0.459102	11408
890.582m/z	0.000021	0.011929	2.232	2.388	0.010042	0.000628	7912
717.531m/z	0.004764	0.2498	3.215	3.441	1	0.029208	7531
266.156m/z	0.160162	0.177417	3.48	3.725	1	0.372699	20084
700.505m/z	0.04993	0.62507	3.666	3.923	1	0.17278	9161
LysoPE(P- 16:0/0:0)	0.004797	0.217692	3.831	4.1	1	0.029208	6936
741.531m/z	0.000667	0.134186	4.629	4.954	0.320727	0.006545	6407

Supplementary Table 7.6. Culture effects in MALDI negative ion mode data – stroma for volcano plot analyses.

Bucket	p-Value	p-Value(Rank)	Average Ratio "Stroma_DMSO "/"Stroma_Day 0"	Fold Change "Stroma_DMSO "/"Stroma_Day 0"	p-Value(FWER)	p-Value(FDR)	Max. Intensity
366.101m/z	0	0.001963	0.115	-8.223	0.000013	0	13618
888.568m/z	0.000002	0.000178	0.15	-6.322	0.000993	0.000017	7308
LysoPE(0:0/16:0)	0	0	0.205	-4.62	0	0	5135
810.524m/z	0.00585	0.268357	0.274	-3.459	1	0.018768	5223
PI(16:0/18:0)	0.002388	0.010374	0.419	-2.265	1	0.008875	6701
929.847m/z	0.185826	0.804131	0.442	-2.145	1	0.309137	7153
Dihomo- gamma- linolenic acid	0	0	0.445	-2.131	0	0	5553
LysoPC(15:0/0:0)	0	0.000898	0.453	-2.095	0.000009	0	13279
PI(20:3(8Z,11Z,1 4Z)/0:0)	0	0	1.94	2.046	0	0	4084
836.540m/z	0.003511	0.01105	1.97	2.077	1	0.012287	11393
604.173m/z	0.000003	0.000006	2.305	2.431	0.001586	0.000026	5914
554.196m/z	0.000031	0.006538	2.464	2.598	0.016664	0.000192	3278
769.560m/z	0	0	2.865	3.021	0.000008	0	9561
866.584m/z	0.001327	0.037813	3.562	3.756	0.715458	0.00542	4825
9- dimethylarsinoy l-nonanoic acid	0	0	4.393	4.633	0	0	10293

Supplementary Table 7.7. Treatment effects in MALDI negative ion mode data – stroma for volcano plot analyses.

Bucket	p-Value	p-Value(Rank)	Average Ratio "Stroma_ENZ"/ "Stroma_DMSO "	Fold Change "Stroma_ENZ"/ "Stroma_DMSO "	p-Value(FWER)	p-Value(FDR)	Max. Intensity
368.114m/z	0.000067	0.003876	0.363	-2.679	0.035021	0.003891	2252
265.966m/z	0.019238	0.003014	0.417	-2.333	1	0.178642	21098
357.903m/z	0.029413	0.457609	0.44	-2.214	1	0.228277	3235
866.584m/z	0.0374	0.475555	0.494	-1.97	1	0.266412	4825
754.427m/z	0.003071	0.007995	0.526	-1.852	1	0.063028	3432
257.002m/z	0.049086	0.62507	0.541	-1.798	1	0.287729	2428
888.568m/z	0.319748	0.902765	0.551	-1.767	1	0.464439	7308
387.879m/z	0.03559	0.463548	1.953	2.006	1	0.266412	3668
400.116m/z	0.000004	0.000135	1.996	2.05	0.001904	0.000381	1806
311.946m/z	0.022504	0.151844	2.012	2.066	1	0.191842	2834
370.142m/z	0	0.000152	2.744	2.818	0.000001	0.000001	894
519.971m/z	0.017555	0.328393	2.842	2.919	1	0.169046	4628
571.291m/z	0.000001	0.001822	3.837	3.942	0.000721	0.000209	3543

Supplementary Table 7.8. Culture effects in MALDI positive ion mode data - epithelium for volcano plot analyses.

Bucket	p-Value	p-Value(Rank)	Average Ratio "Epithelium_D MSO"/"Epitheli um_Day0"	Fold Change "Epithelium_D MSO"/"Epitheli um_Day0"	p-Value(FWER)	p-Value(FDR)	Max. Intensity
Spermine	0	0	0.185	-5.284	0	0	4247
L-Carnitine	0	0	0.244	-4.017	0	0	7761
103.977m/z	0	0.072412	0.364	-2.686	0.000295	0.000002	5947
83.977m/z	0.000005	0.16427	0.37	-2.647	0.004257	0.000027	12762
773.596m/z	0	0	0.474	-2.066	0	0	5351
PA(20:4(5Z,8Z,1 1Z,14Z)/0:0)	0	0	0.481	-2.033	0	0	13092
757.562m/z	0.000001	0.000481	1.973	2.016	0.000879	0.000007	5898
747.580m/z	0	0.000001	2.073	2.118	0	0	1740
115.043m/z	0.002184	0.13578	2.228	2.277	1	0.007317	9724
163.923m/z	0.000076	0.007821	2.349	2.4	0.062095	0.00033	10406
772.505m/z	0	0	2.478	2.532	0	0	6538
783.576m/z	0	0	2.606	2.663	0	0	10563
217.852m/z	0	0.006443	3.378	3.452	0.00001	0	5520
331.326m/z	0.000003	0.000013	4.482	4.58	0.002314	0.000016	23244
N- Methylnicotina mide	0	0	4.504	4.603	0	0	7324
163.914m/z	0	0	4.914	5.022	0	0	3514
733.564m/z	0	0.000002	5.278	5.394	0.000022	0	26948
303.295m/z	0	0.000004	5.36	5.477	0.000001	0	13337
L-Arginine	0	0	6.355	6.494	0	0	3305
262.141m/z	0	0	8.506	8.693	0	0	3417
581.269m/z	0	0	16.643	17.008	0	0	7305

Supplementary Table 7.9. Treatment effects in MALDI positive ion mode data - epithelium for volcano plot analyses.

Bucket	p-Value	p-Value(Rank)	Average Ratio "Epithelium_EN Z"/"Epithelium _DMSO"	Fold Change "Epithelium_EN Z"/"Epithelium _DMSO"	p-Value(FWER)	p-Value(FDR)	Max. Intensity
142.028m/z	0.000844	0.384871	0.181	-5.229	0.7072	0.004822	23764
452.434m/z	0.000134	0.092246	0.294	-3.225	0.112165	0.00101	12648
564.346m/z	0.000286	0.377141	0.312	-3.038	0.239668	0.001964	5764
752.536m/z	0	0.00569	0.461	-2.055	0.000142	0.000003	2192
612.343m/z	0	0.000002	0.471	-2.014	0	0	2116
837.625m/z	0	0.017794	1.907	2.011	0.000036	0.000001	1443
L- Palmitoylcarniti ne	0.000009	0.043091	1.91	2.015	0.007812	0.000095	2640
217.852m/z	0.000055	0.268978	2.13	2.247	0.046318	0.000482	11721
812.680m/z	0.000005	0.003399	2.165	2.283	0.004373	0.000059	4550
Stearoylcarnitin e	0.000047	0.079796	2.176	2.295	0.039287	0.000414	4587
425.353m/z	0.000038	0.040037	2.365	2.494	0.031751	0.000341	5039
776.536m/z	0	0.032589	2.369	2.499	0.000037	0.000001	2883
211.843m/z	0.000005	0.332273	2.429	2.562	0.004123	0.000056	7291
781.796m/z	0	0.001033	2.452	2.586	0	0	1715
PC(14:0/22:1(13 Z))	0	0	2.5	2.637	0	0	30776
794.630m/z	0	0.000006	3.114	3.285	0	0	2428
432.138m/z	0.000463	0.177933	4.251	4.484	0.388338	0.00292	110605
385.349m/z	0	0.033063	7.819	8.247	0	0	14915

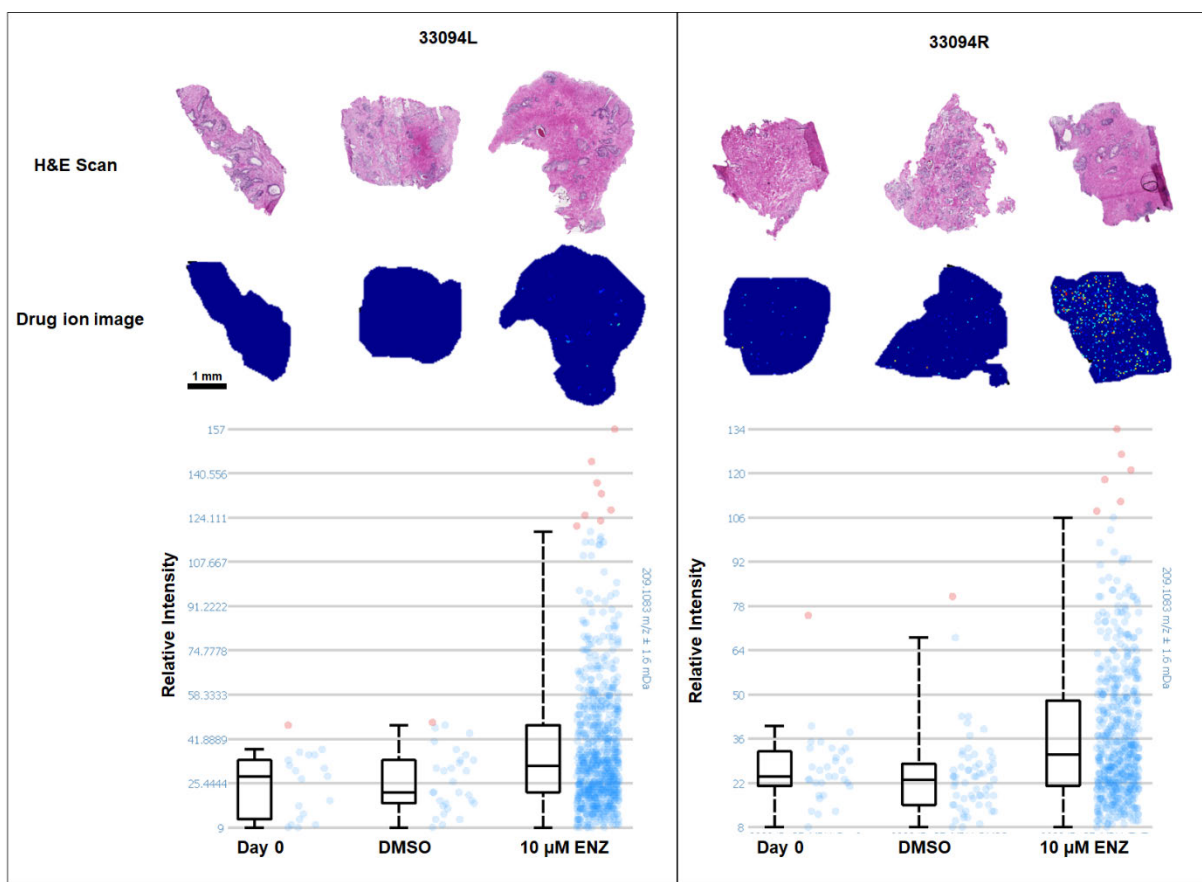
Supplementary Table 7.10. Culture effects in MALDI positive ion mode data – stroma for volcano plot analyses.

Bucket	p-Value	p-Value(Rank)	Average Ratio "Stroma_DMSO "/"Stroma_Day 0"	Fold Change "Stroma_DMSO "/"Stroma_Day 0"	p-Value(FWER)	p-Value(FDR)	Max. Intensity
L-Carnitine	0	0	0.214	-4.548	0	0	10435
205.961m/z	0	0.20713	0.312	-3.126	0.000088	0.000001	10419
83.977m/z	0.000001	0.28211	0.339	-2.876	0.000854	0.000009	17294
103.977m/z	0.000001	0.242587	0.368	-2.654	0.000375	0.000004	5920
128.960m/z	0	0.20713	0.374	-2.611	0.000289	0.000003	7717
144.046m/z	0.000001	0.001381	0.428	-2.279	0.000781	0.000008	173454
L-Acetylcarnitine	0	0	0.434	-2.247	0	0	6760
2-Indolecarboxylic acid	0	0.000072	0.436	-2.237	0.000003	0	20326
822.112m/z	0	0.000003	0.452	-2.158	0.000008	0	5334
163.923m/z	0.000038	0.885755	0.462	-2.11	0.028249	0.00021	18548
913.595m/z	0	0.000004	1.981	2.031	0.000004	0	5685
944.591m/z	0	0.000033	2.019	2.07	0.000005	0	4546
704.583m/z	0.006006	0.542192	2.042	2.094	1	0.017641	7108
PE(10:0/10:0)	0	0	2.292	2.35	0	0	1401
761.592m/z	0	0.012545	2.358	2.418	0.000024	0	3584
303.295m/z	0	0.002837	2.409	2.469	0.000031	0	6155
N-Methylnicotinamide	0	0	2.862	2.934	0	0	5451
331.326m/z	0	0.000006	3.212	3.292	0.000039	0.000001	10952
163.914m/z	0	0	4.471	4.583	0	0	5651
262.141m/z	0	0	11.534	11.824	0	0	5046

581.269m/z	0	0	21.143	21.674	0	0	7556
------------	---	---	--------	--------	---	---	------

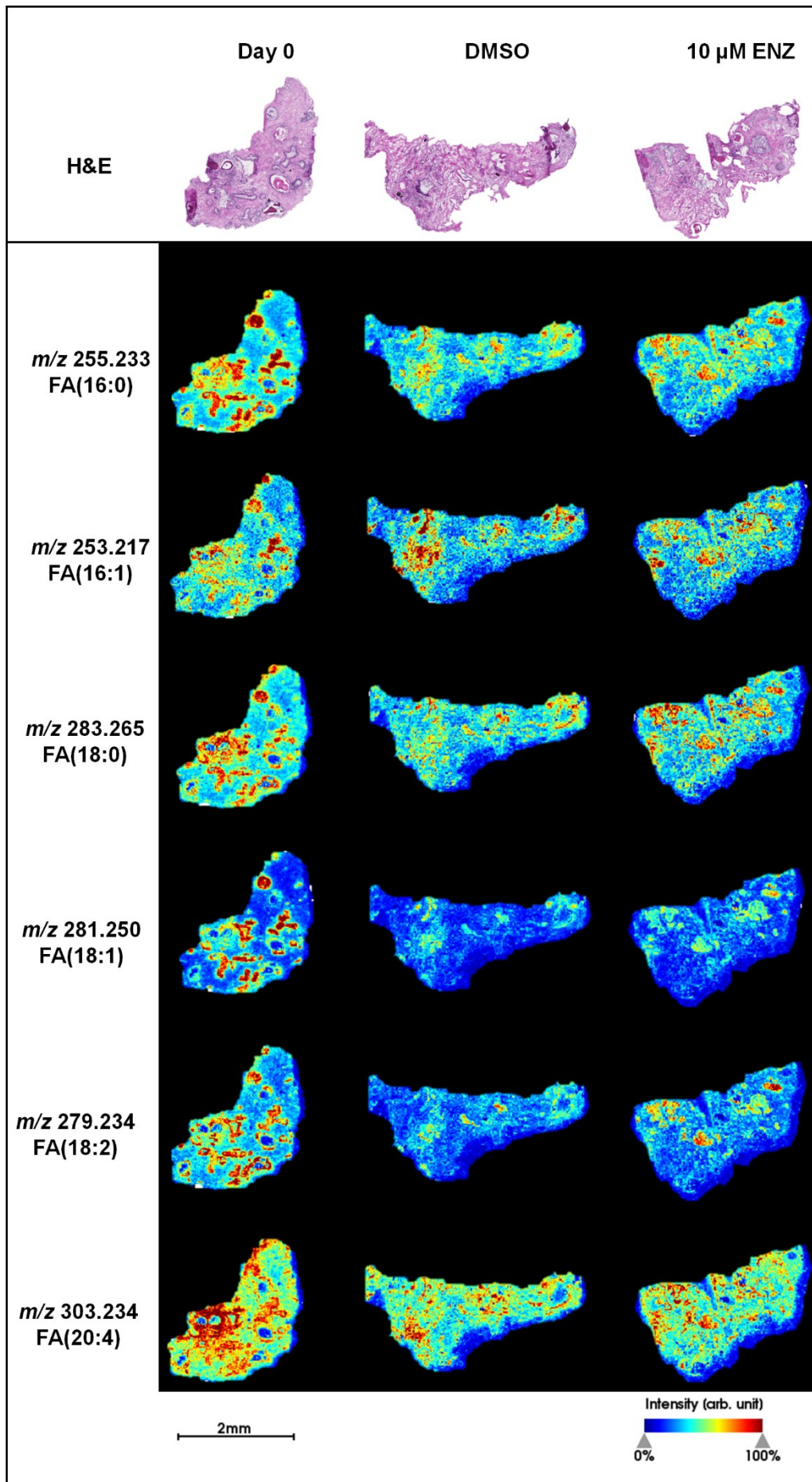
Supplementary Table 7.11. Treatment effects in MALDI positive ion mode data – stroma for volcano plot analyses.

Bucket	p-Value	p-Value(Rank)	Average Ratio "Stroma_ENZ"/ "Stroma_DMSO "	Fold Change "Stroma_ENZ"/ "Stroma_DMSO "	p-Value(FWER)	p-Value(FDR)	Max. Intensity
PS(17:1(9Z)/0:0)	0	0.001154	2.424	2.538	0	0	2123
LysoPE(22:6(4Z, 7Z,10Z,13Z,16Z, 19Z)/0:0)	0	0.00137	2.567	2.687	0	0	2772
459.272m/z	0	0.028509	2.645	2.769	0.000071	0.000003	3645
426.090m/z	0.000161	0.322602	12.612	13.205	0.121639	0.001816	30687

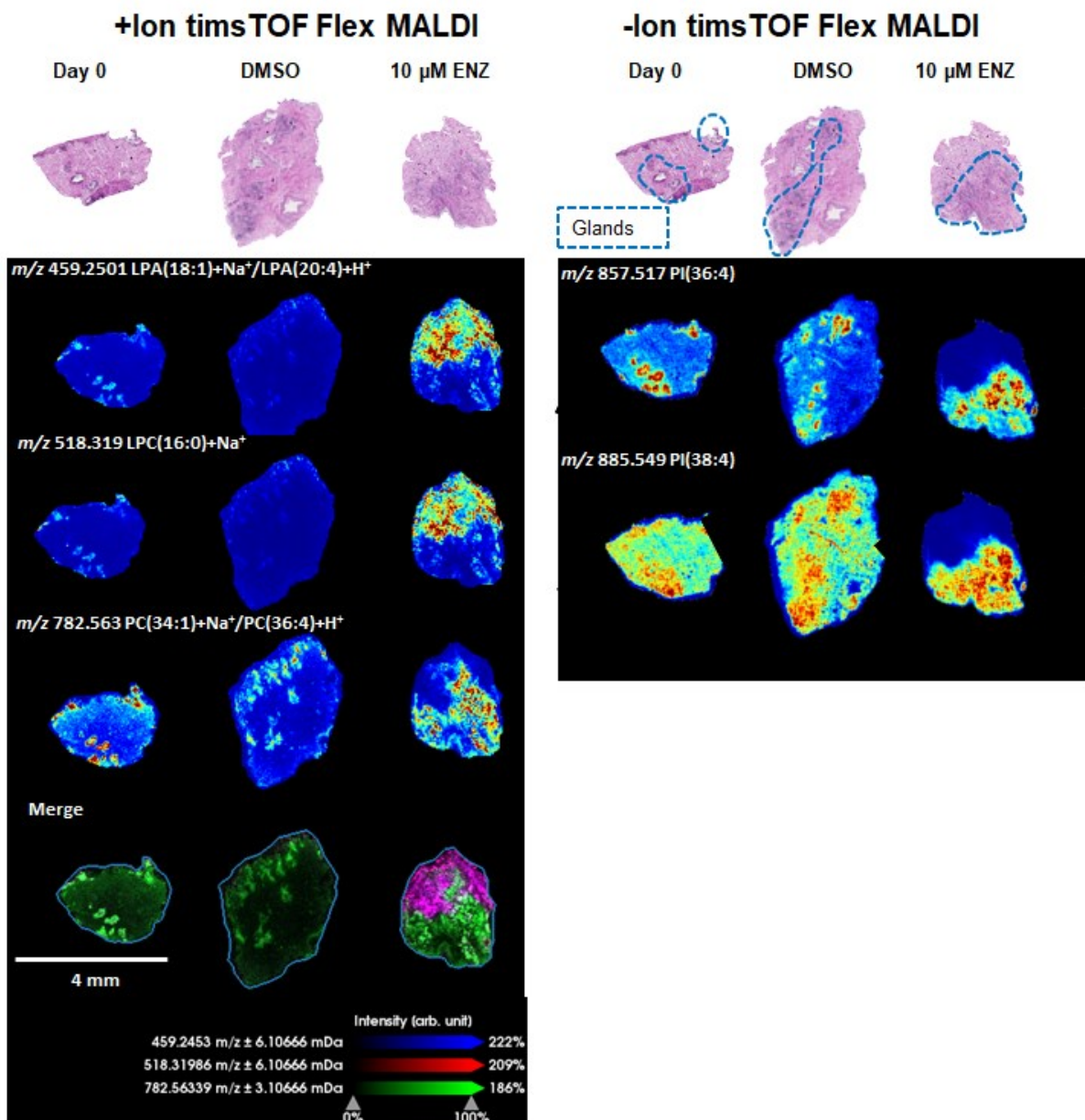


Supplementary Figure 7.1. MALDI MS/MS imaging of enzalutamide in PDE.

Serial sections of H&E and targeted drug imaging were collected from Day 0, DMSO and 10 μ M ENZ culture treatments. Characteristic ENZ fragment ion, m/z 209.1083 \pm 1.6 mDa data acquired by MRM with imaging performed at 40 μ m pixel sizes.



Supplementary Figure 7.2. Fatty acid distribution in PDE tissues. Histopathological scans of tissue sections from Day 0, DMSO and ENZ treated explants co-registered to serial sections analysed by MALDI MSI. Visualisation of putatively identified *m/z* features shows different spatial distribution of FA in stroma and epithelium.



Supplementary Figure 7.3. Phospholipid distribution in PDE tissue. Left. Positive ion mode imaging showing distribution of tentative LPA(18:1/20:4) and LPC(16:0) that constitute predominant isobaric PC(34:1) / PC(36:4) species. **Right.** Predominant putative PI species in prostate tissue showing PI(36:4) to be more localised in glandular regions whilst PI(38:4) to be more abundant in stromal areas with suspected tumour areas.

9.4. Appendix A: Cardinal R Markdown Script

Data analysis for sections at different depths in Day 0 frozen prostate tissue - 32928.R post mid 3+3

Shadrack Mutuku

10 Jul 2019

Executive Summary

Data acquired on a SYNAPT HDMS system for prostate tissue sections prepared with a sublimated layer of CHCA. The following analysis makes use of R, rmarkdown and Cardinal to report on the pre-processing of this data and the delineation of tissue-specific sub-regions using a combination of PCA and SSCG.

This analysis combines four MSI files of interspersed cut sections of fresh-frozen prostate tissue to explore their common lipid signature between different tissue types i.e. epithelium, stroma, and potentially tumour margin areas, the so called “microenvironment”.

```
knitr::opts_chunk$set(echo = TRUE, cache=TRUE, message=FALSE, autod
ep=TRUE)
```

Data Import

Data selected for import was Analyze7.5 format. Here, data was read in for the following data sets:

1. 32928R_S31_003_001
2. 32928R_S71_003_001
3. 32928R_S111_003_001
4. 32928R_S141_003_001

```
#libraries required
library(Cardinal)

#data import
data1 <- readMSIData("./32928R_S31_003/32928R_S31_003_001.img")
data2 <- readMSIData("./32928R_S71_003/32928R_S71_003_001.img")
data3 <- readMSIData("./32928R_S111_003/32928R_S111_003_001.img")
data4 <- readMSIData("./32928R_S141_003/32928R_S141_003_001.img")

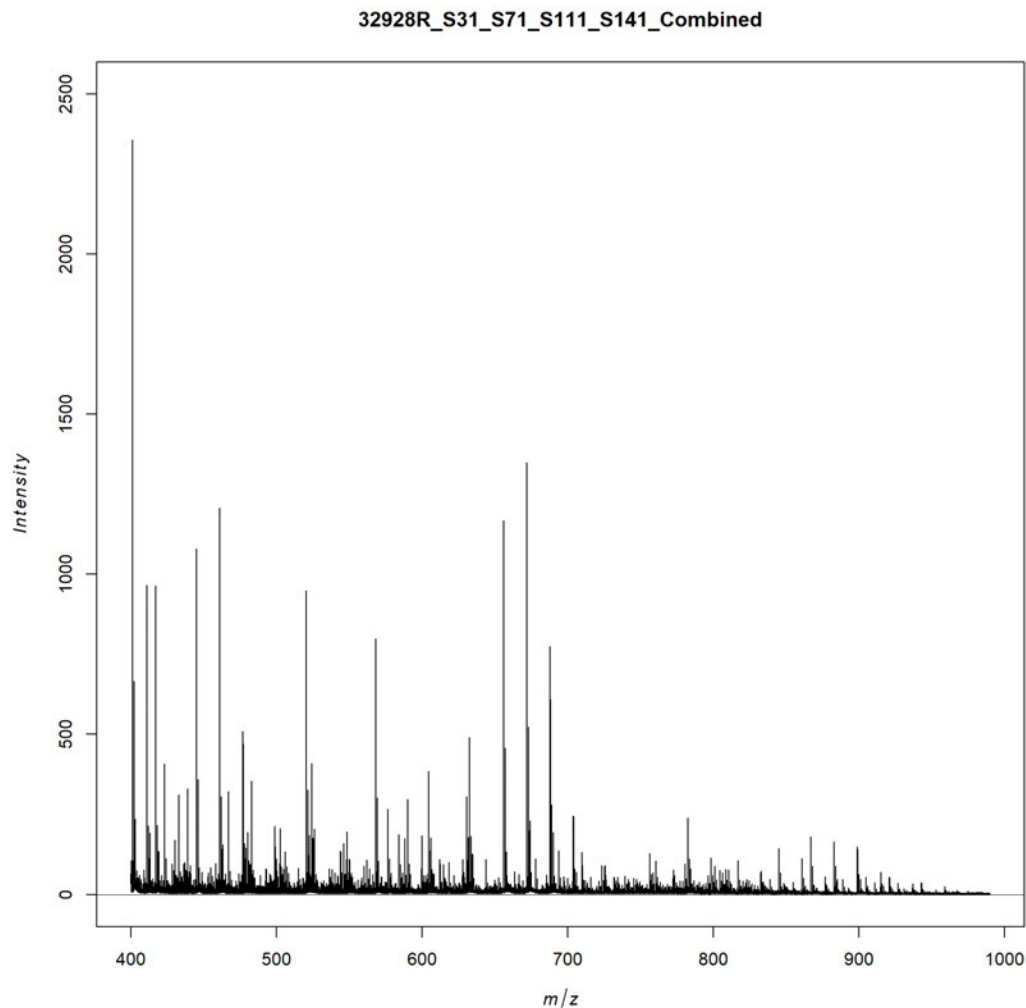
#subset m/z range
data1 <- data1[400 < mz(data1) & mz(data1) < 990,]
data2 <- data2[400 < mz(data2) & mz(data2) < 990,]
data3 <- data3[400 < mz(data3) & mz(data3) < 990,]
data4 <- data4[400 < mz(data4) & mz(data4) < 990,]
```

Combine datasets

```
comb <- combine(data1,data2,data3,data4)
```

Mean spectra for 32928R_Four MSI files Combined

```
plot(comb, pixel=1:ncol(comb), ylim=c(0,2500), main = "32928R_S31_S71_S111_S141_Combined")
```



Data batch processing

```
datacomb_processed <- batchProcess(comb, normalize=TRUE, smoothSignal=TRUE, reduceBaseline=list(blocks=200), peakPick=list(SNR=5), peakAlign=TRUE)
```

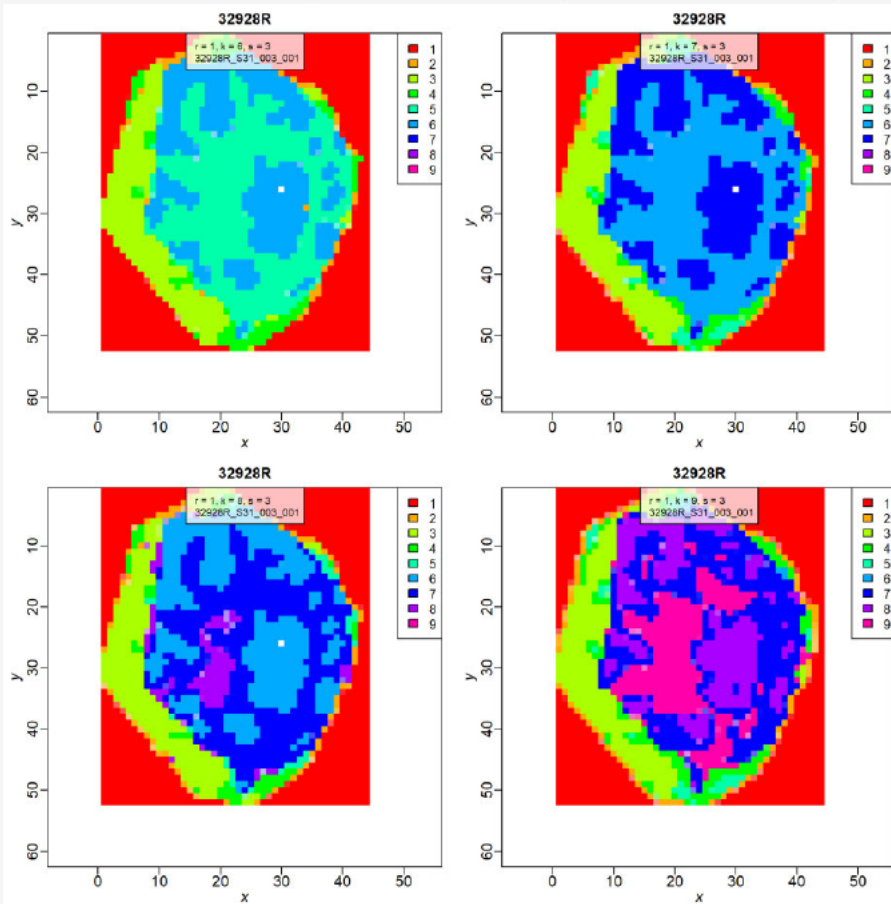
Spatial shrunken centroids (GAUSSIAN) - 32928R_Combined

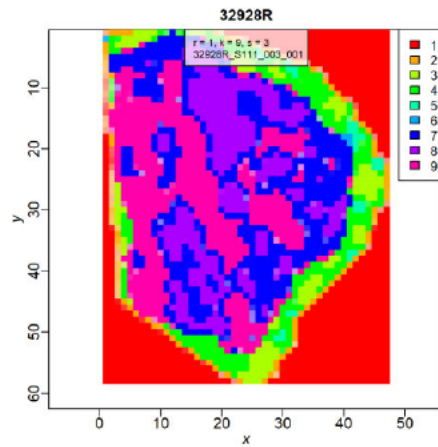
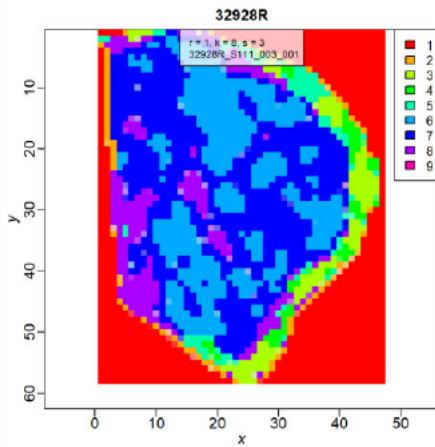
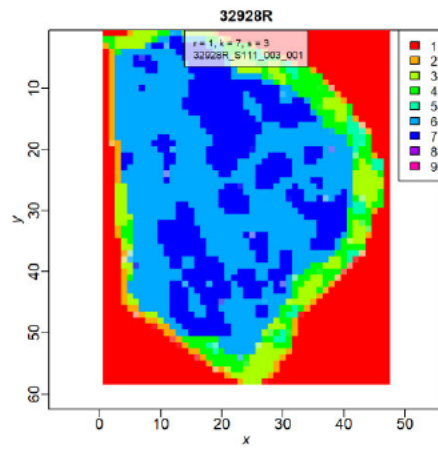
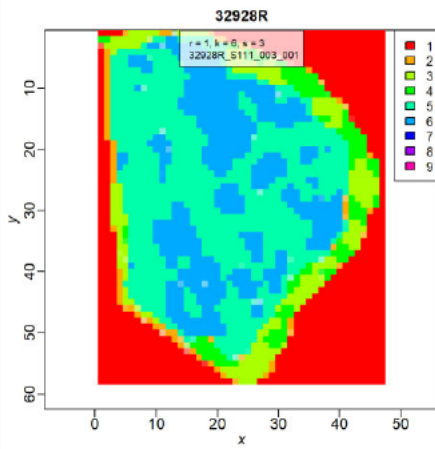
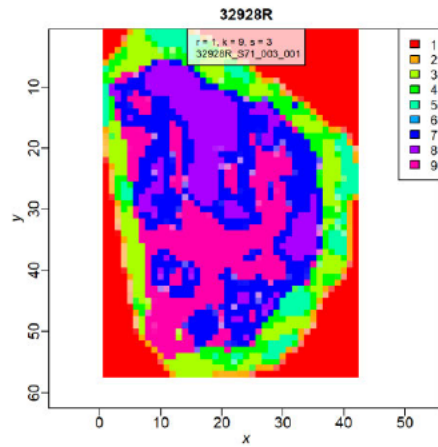
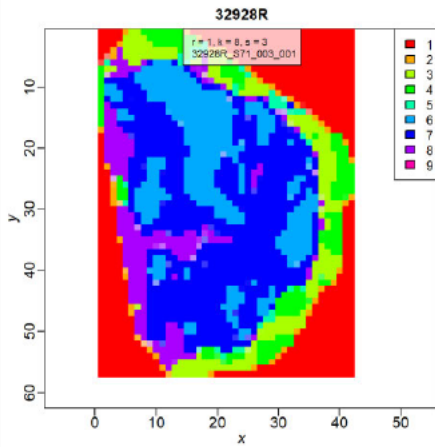
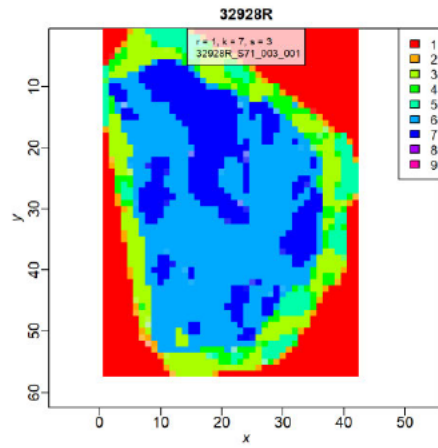
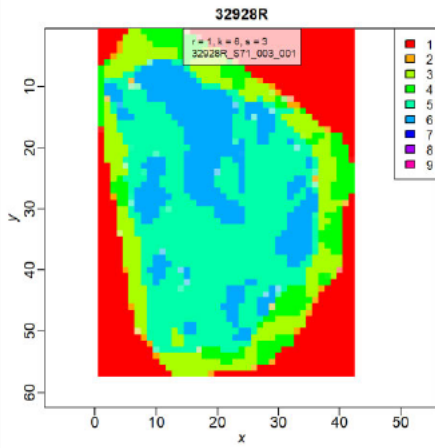
```
set.seed(5)  
data.sscg5 <- spatialShrunkenCentroids(datacomb_processed, r = 1, k = c(6,7,8,9), s = 3, method = "gaussian")  
#image of sscg segmentation
```

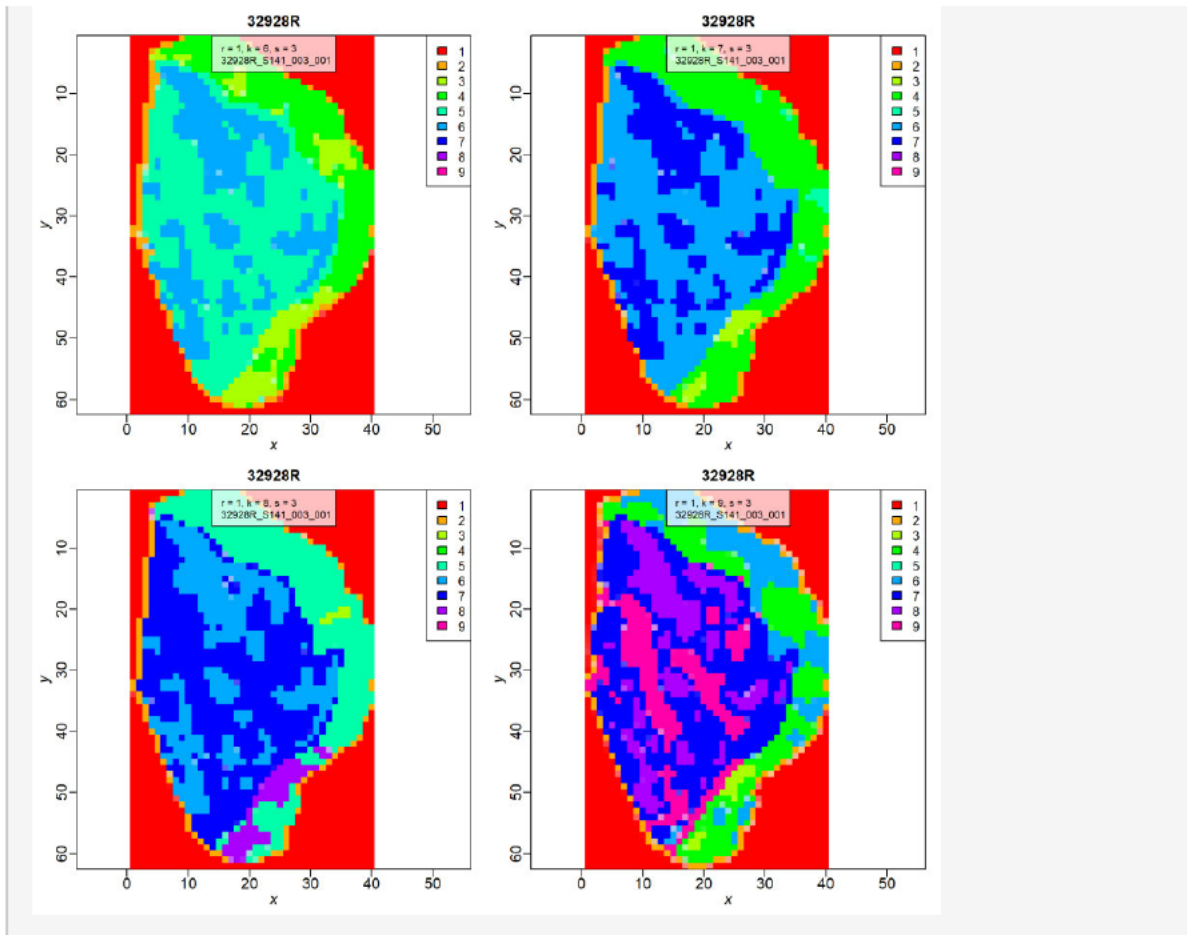
```

image(data.sscg5, key = TRUE, layout = c(2,2), main = "32928R", fam
ily = "sans", font.main = 2,
      font.lab = 2, cex.lab = 1.2, cex.axis = 1.2, cex.main = 1.2)

```







Top labels 32928R_Combined

```

data.frame17<- (topLabels (data.sscg5, model = list(r = 1, s = 3, k =
9), filter = list(classes = 6), n=20))
write.csv (data.frame17, "./32928R comb 003 001 k9c6.csv")

data.frame18<- (topLabels (data.sscg5, model = list(r = 1, s = 3, k =
9), filter = list(classes = 7), n=20))
write.csv (data.frame18, "./32928R_comb_003_001_k9c7.csv")

data.frame19<- (topLabels (data.sscg5, model = list(r = 1, s = 3, k =
9), filter = list(classes = 8), n=20))
write.csv (data.frame19, "./32928R_comb_003_001_k9c8.csv")

data.frame20<- (topLabels (data.sscg5, model = list(r = 1, s = 3, k =
9), filter = list(classes = 9), n=20))
write.csv (data.frame20, "./32928R_comb_003_001_k9c9.csv")

total.labels 32928R comb <- rbind (data.frame17, data.frame18, data
.frame19, data.frame20)
write.csv (total.labels 32928R comb, "./total.labels 329
28R comb.csv")

summaryPlots5 <- function(data.sscg5, results, model, segment, name
, col) {
image (results, model = model, key = FALSE, column = segment, main
= name, layout = c(3, 4), col = col)

```

```

plot(results, model = model, key = FALSE, column = segment, mode
= "centers",main = "Shrunken mean spectrum", col = col)
plot(results, model = model, key = FALSE, column = segment, mode
= "tstatistics",main = "Shrunken t-statistics", col = col)
top <- topLabels(results, n = 9, model = model, filter = list(cla
sses = segment))
image(data.sscg5, mz = top$mz, normalize.image = "linear", contra
st.enhance = "histogram", main = "32928R")
  #smooth.image = "gaussian")
}

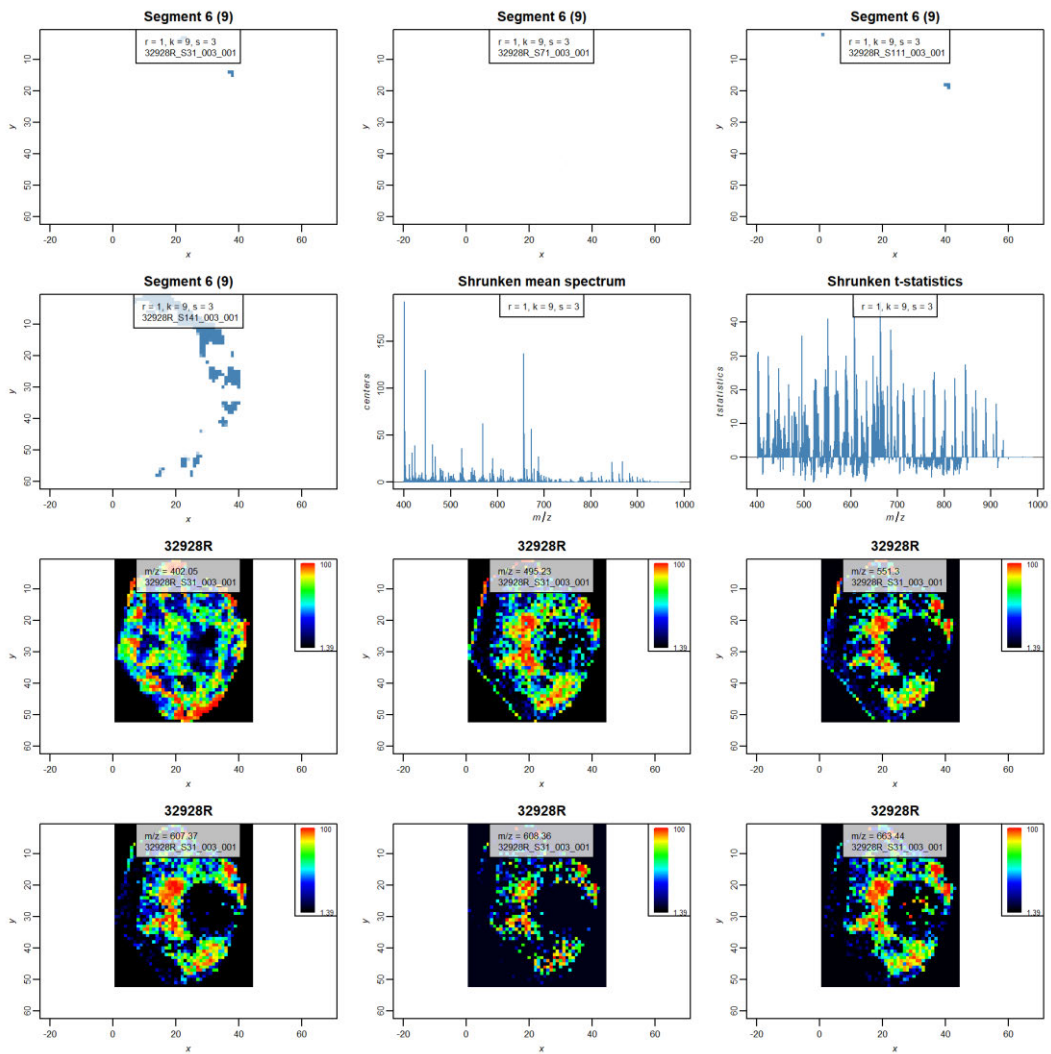
```

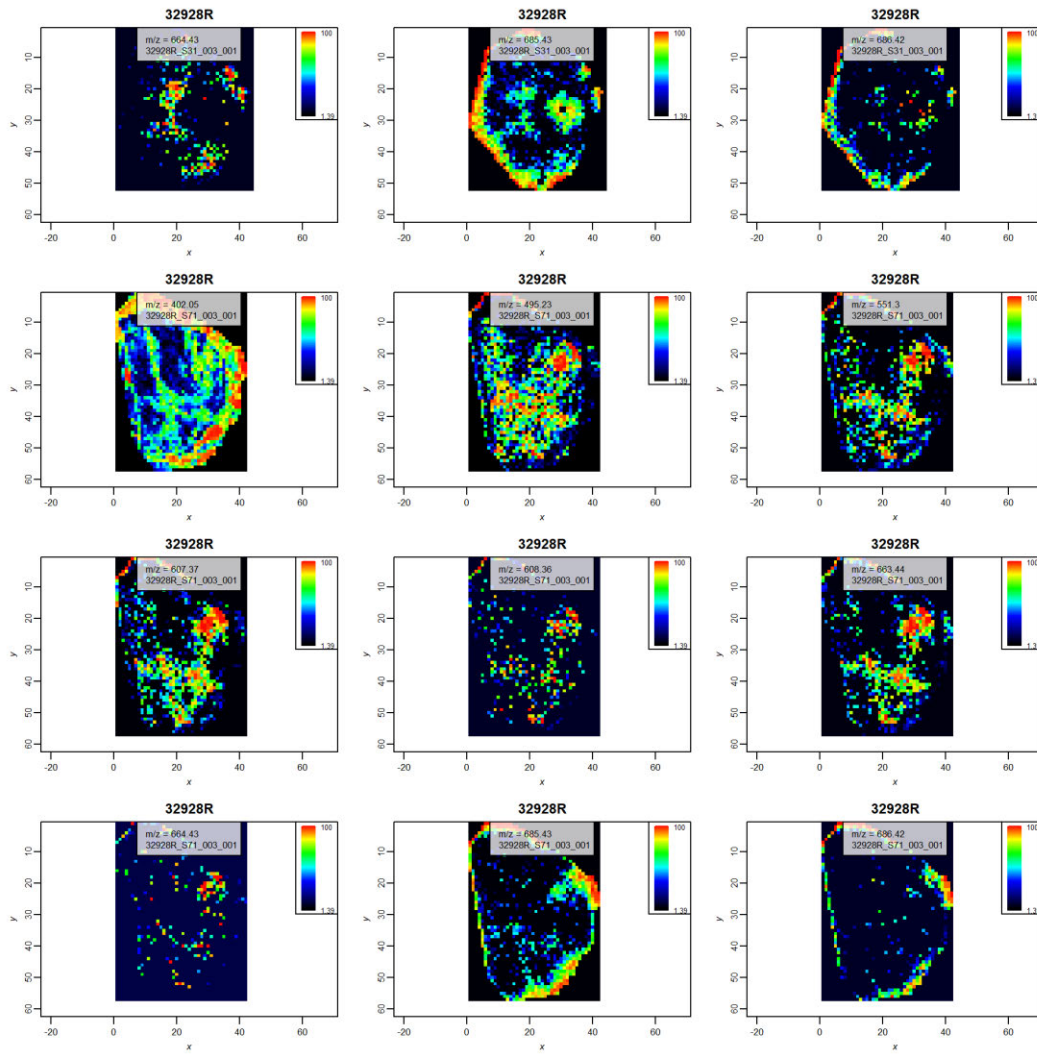
Summary plots 32928R_Combined

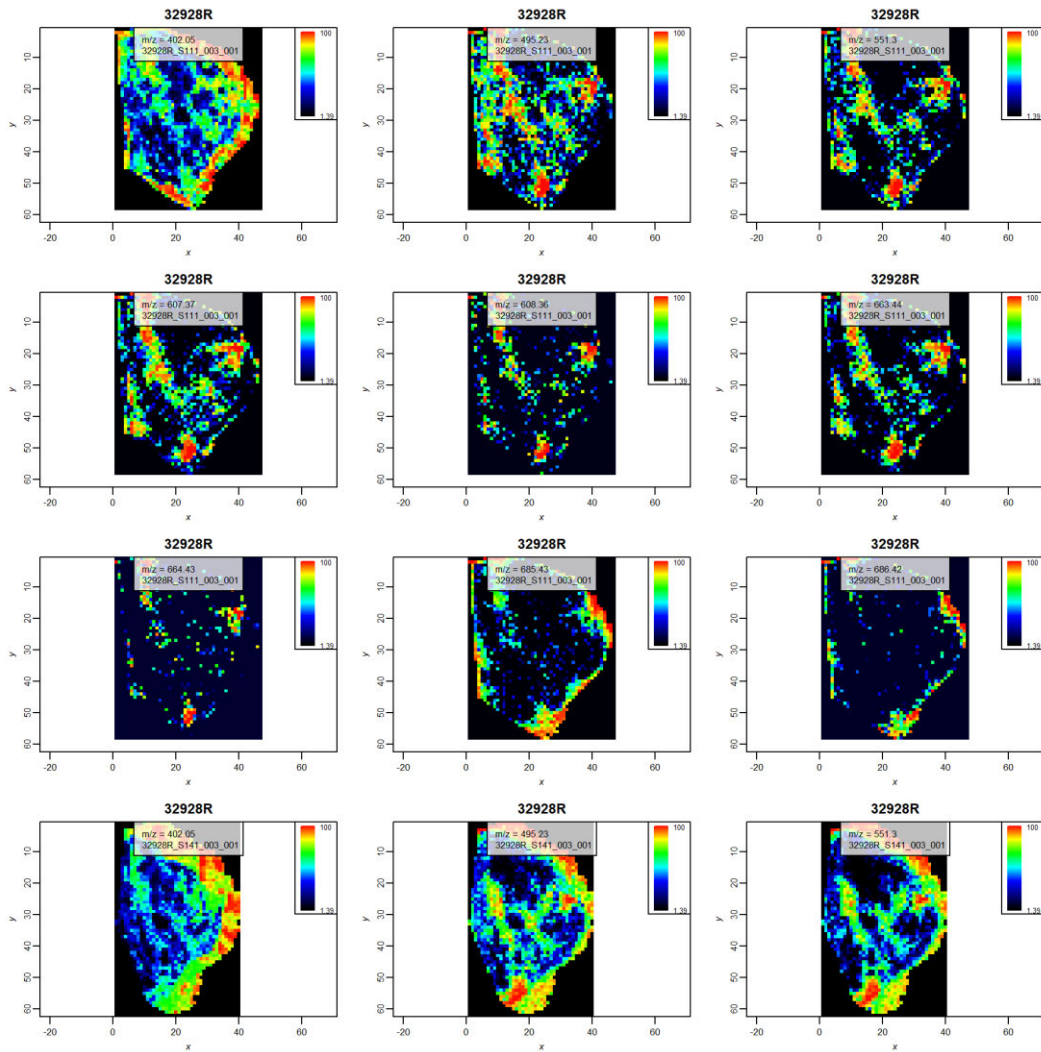
```

### Summary plots 32928R S71 003 001
mycol=c("red", "orange", "yellow", "green" , "turquoise" , "steelbl
ue" , "blue", "purple" , "magenta")
main="32928R Comb"
summaryPlots5(datacomb_processed, data.sscg5, model = list(r = 1, s
= 3, k = 9), segment = 6,name = "Segment 6 (9)", col = mycol)

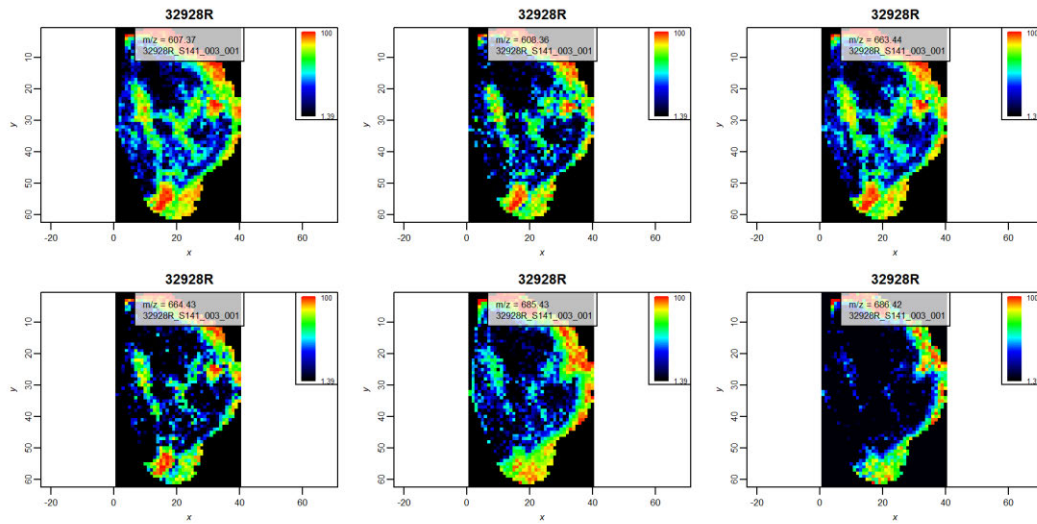
```

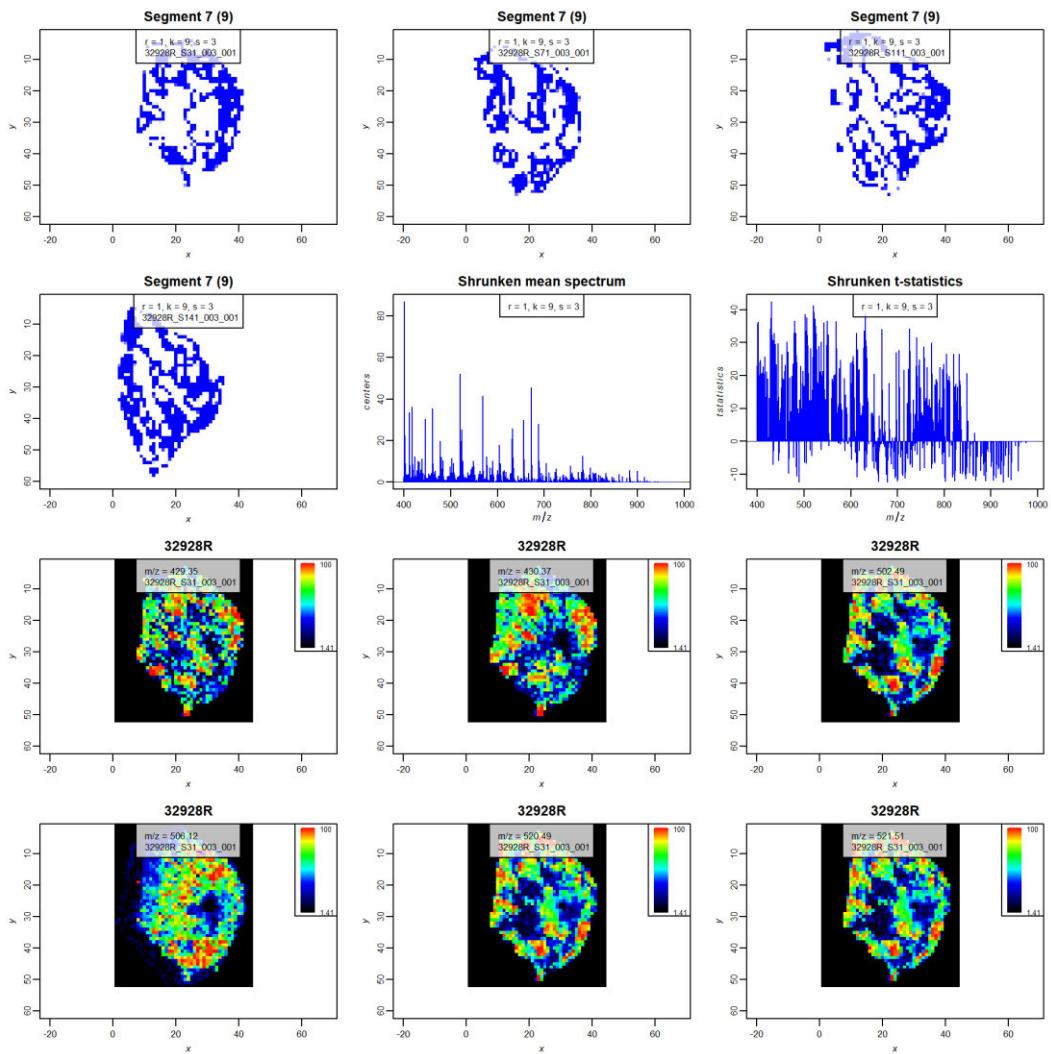


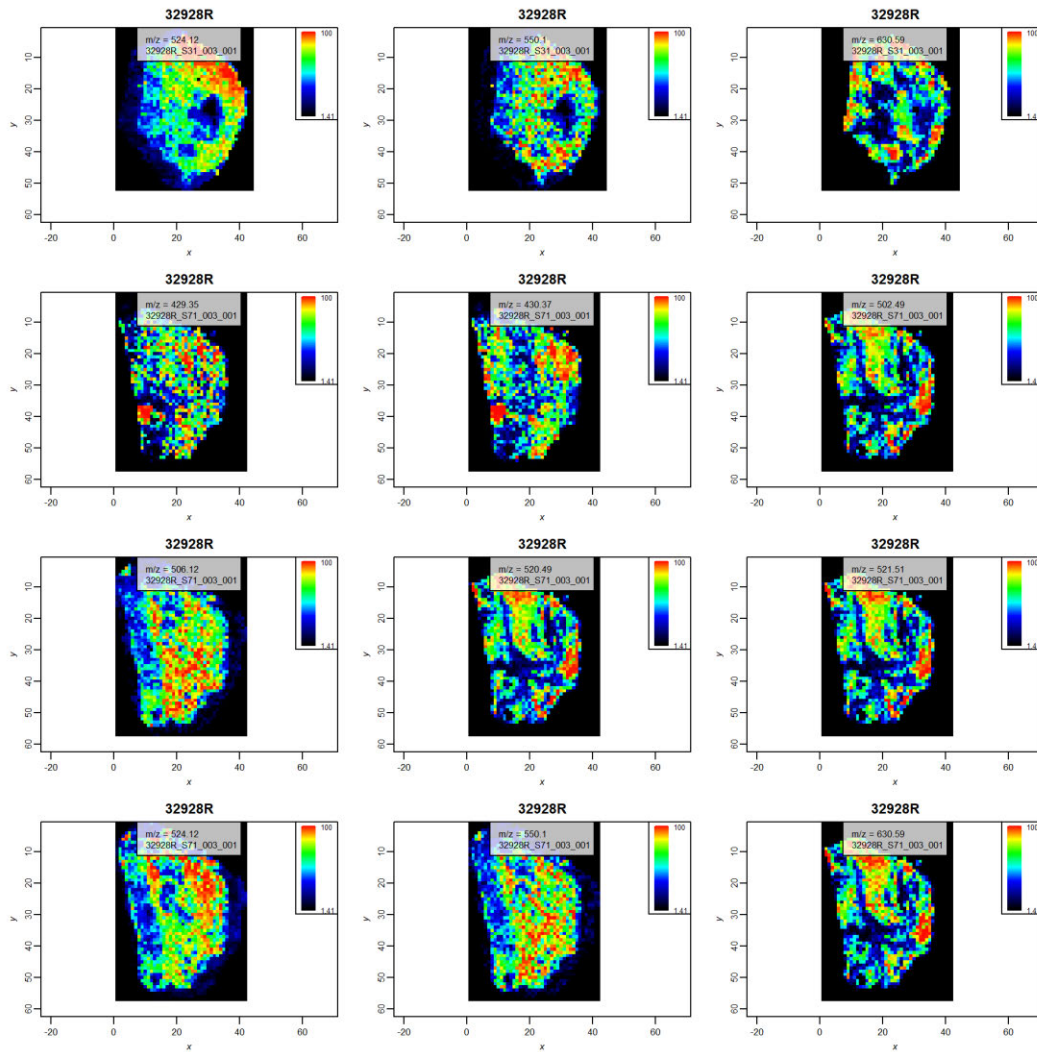


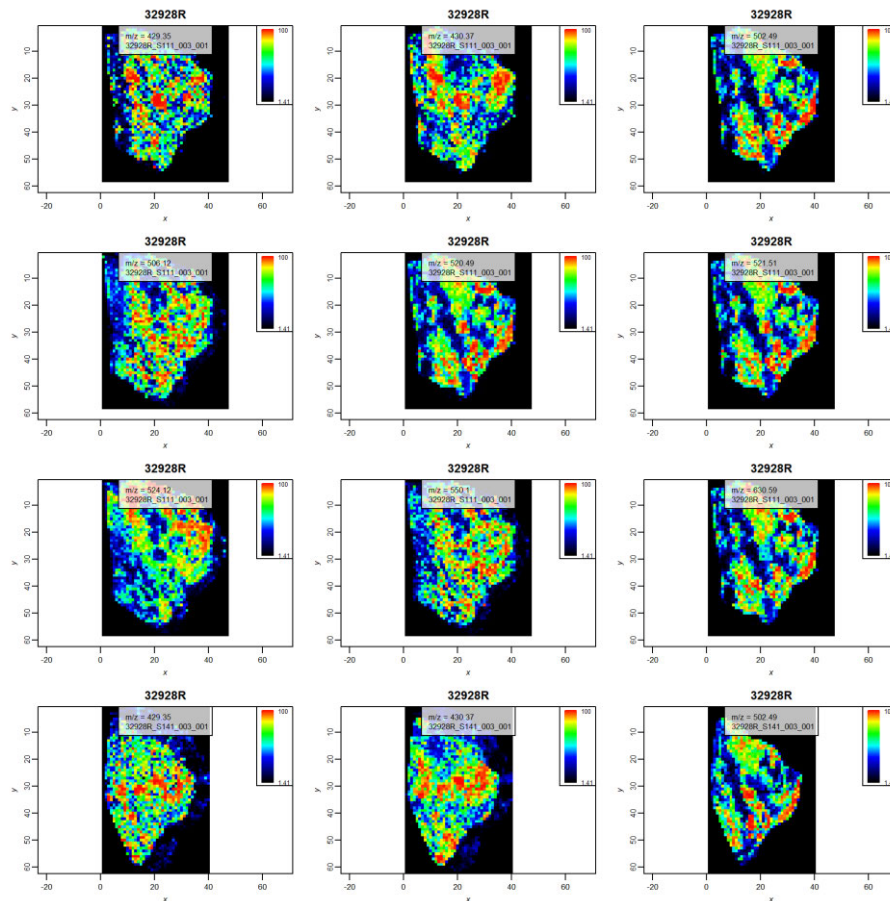


```
summaryPlots5(datacomb_processed, data.sscg5, model = list(r = 1, s
= 3, k = 9), segment = 7, name = "Segment 7 (9)", col = mycol)
```

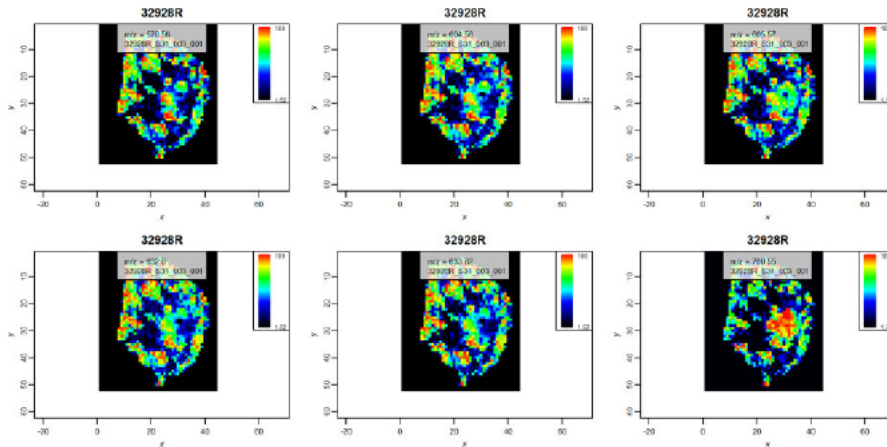
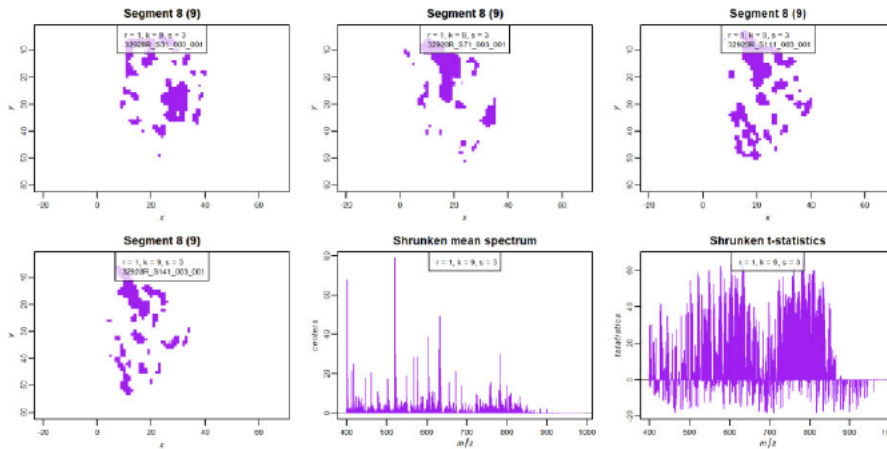
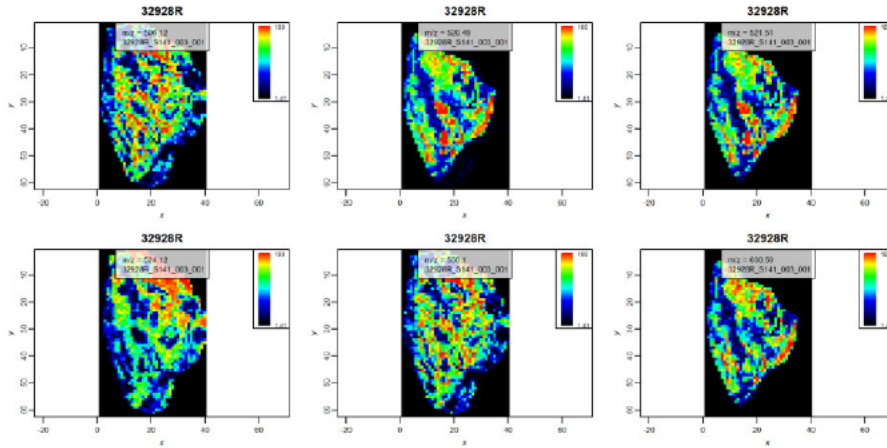


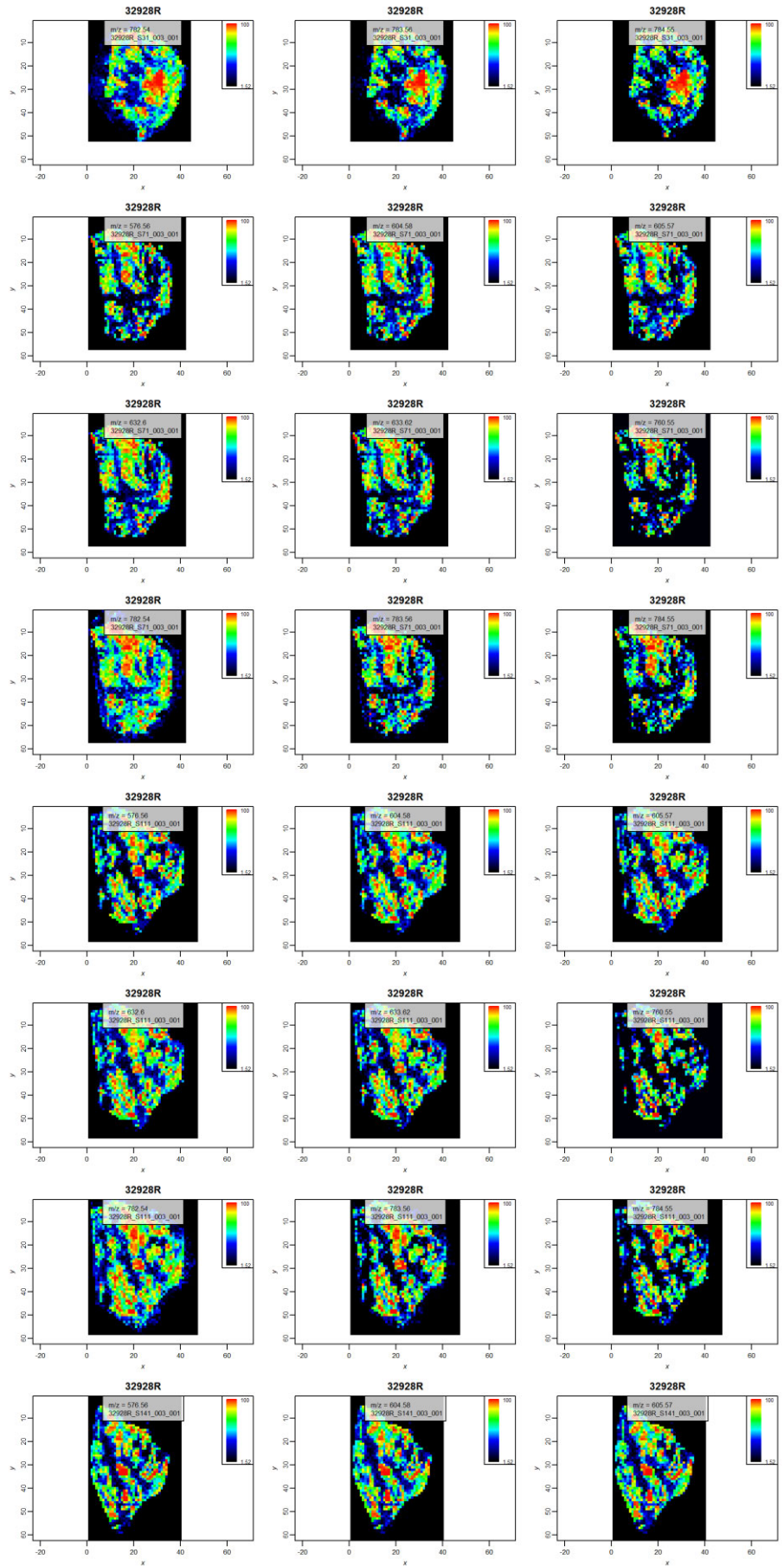




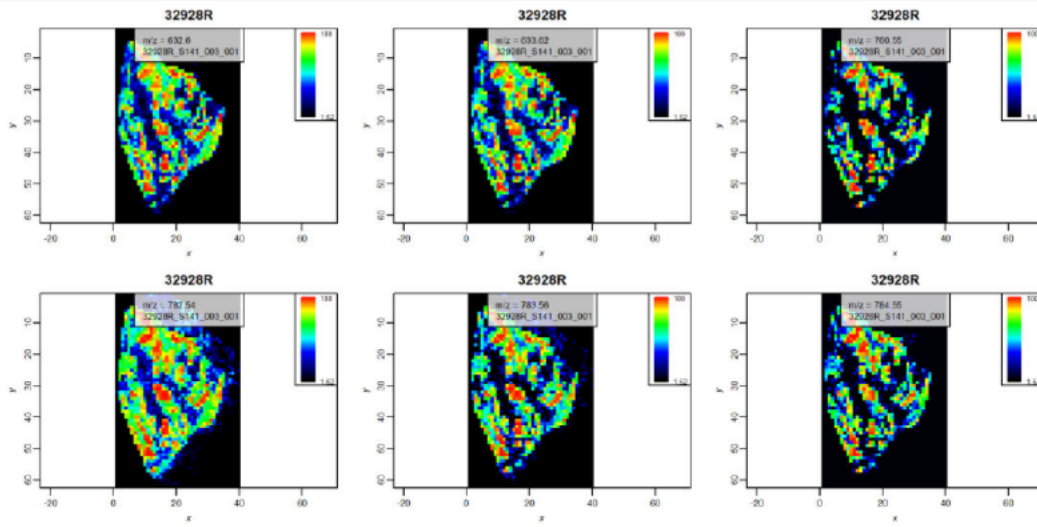


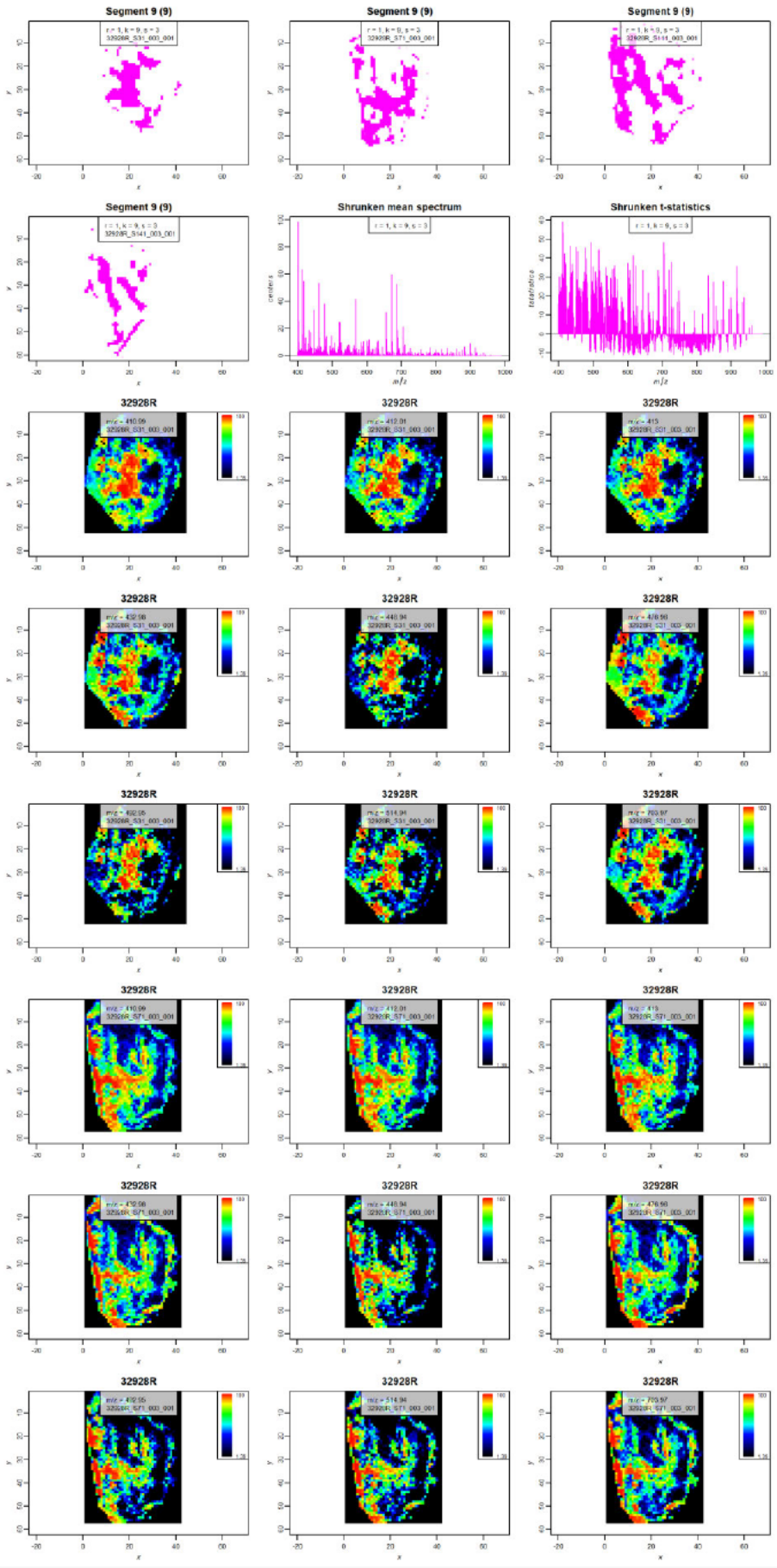
```
summaryPlots5(datacomb_processed, data.sscg5, model = list(r = 1, s = 3, k = 9), segment = 8, name = "Segment 8 (9)", col = mycol)
```

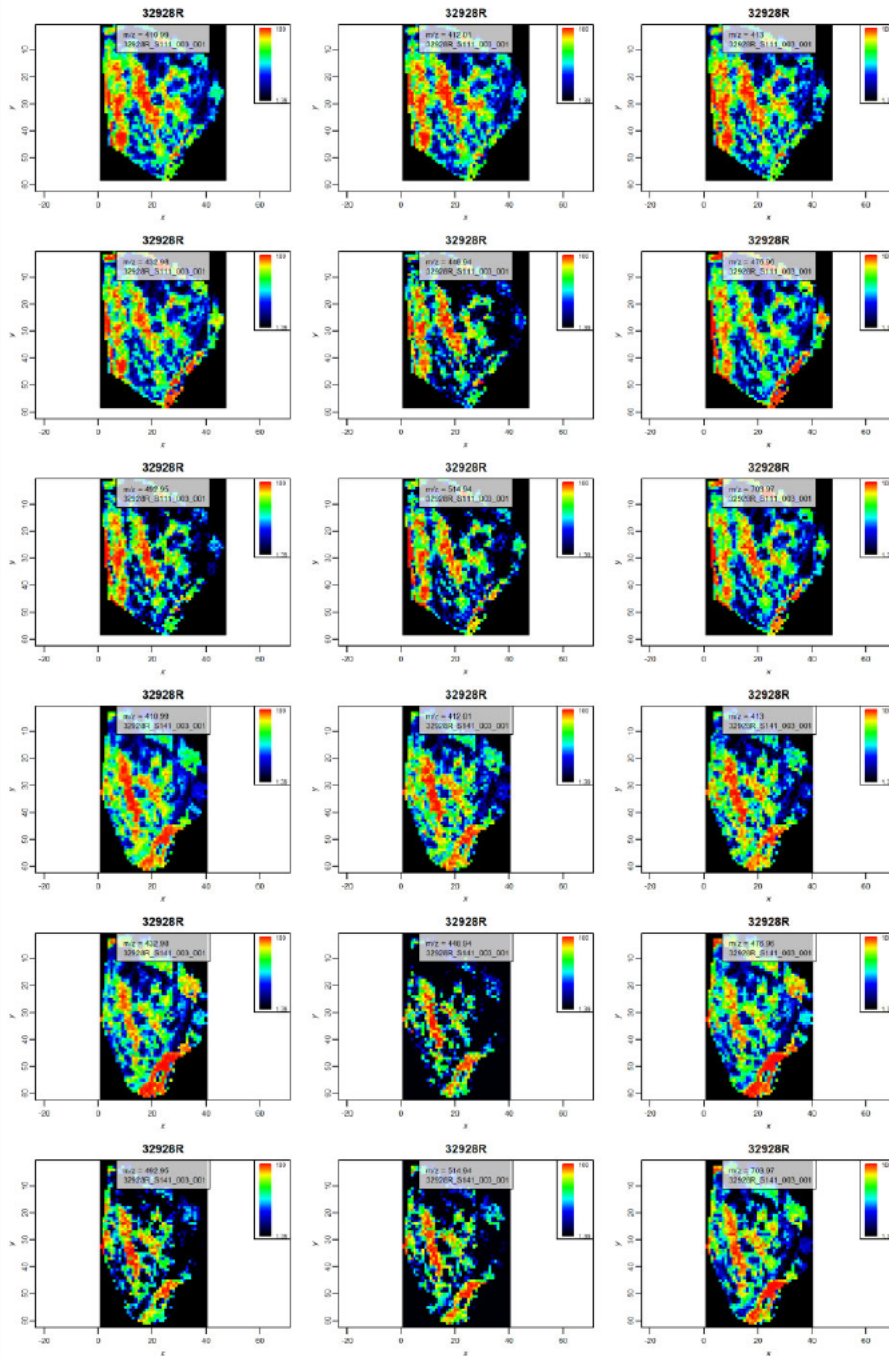




```
summaryPlots5(datacomb processed, data.sscg5, model = list(r = 1, s = 3, k = 9), segment = 9, name = "Segment 9 (9)", col = mycol)
```





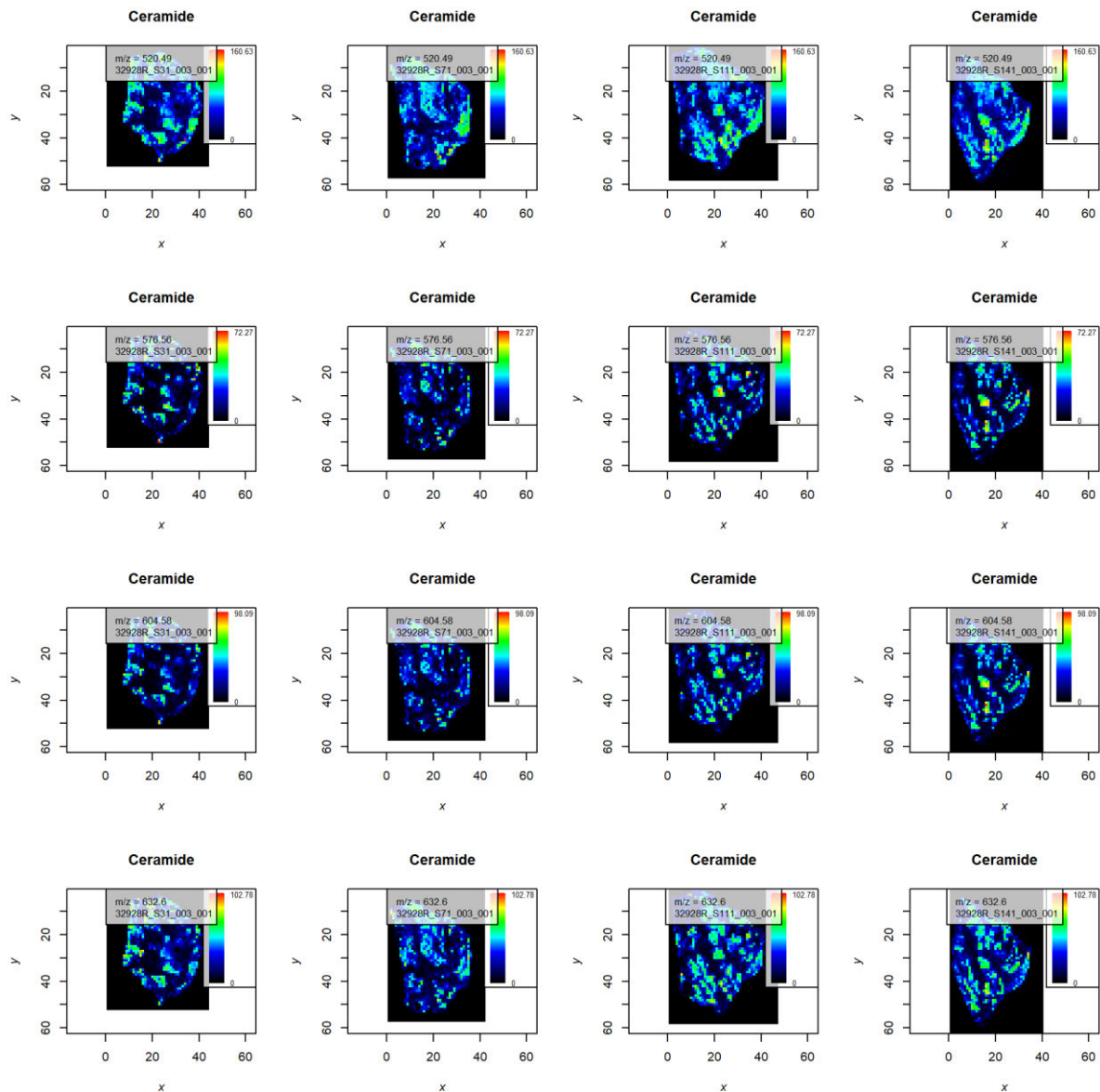


Plot of Combined SSCG Segmentation 32928R

```
#image of sscg segmentation
tiff("./32928R_sscg_Comb_poster.tiff", width = 768, height = 1024)
par(mfrow=c(4,4))
plot
## standardGeneric for "plot" defined from package "graphics"
##
## function (x, y, ...)
## standardGeneric("plot")
## <environment: 0x00000000230513a8>
## Methods may be defined for arguments: x, y
## Use showMethods("plot") for currently available ones.
image(data.sscg5, superpose = TRUE, key = TRUE, main = "32928R Comb"
, family = "sans", font.main = 2, font.lab = 2, cex.lab = 1.2, cex.
axis = 1.2, cex.main = 1.2)
```

Plots of MS/MS Validated Lipid Subclasses

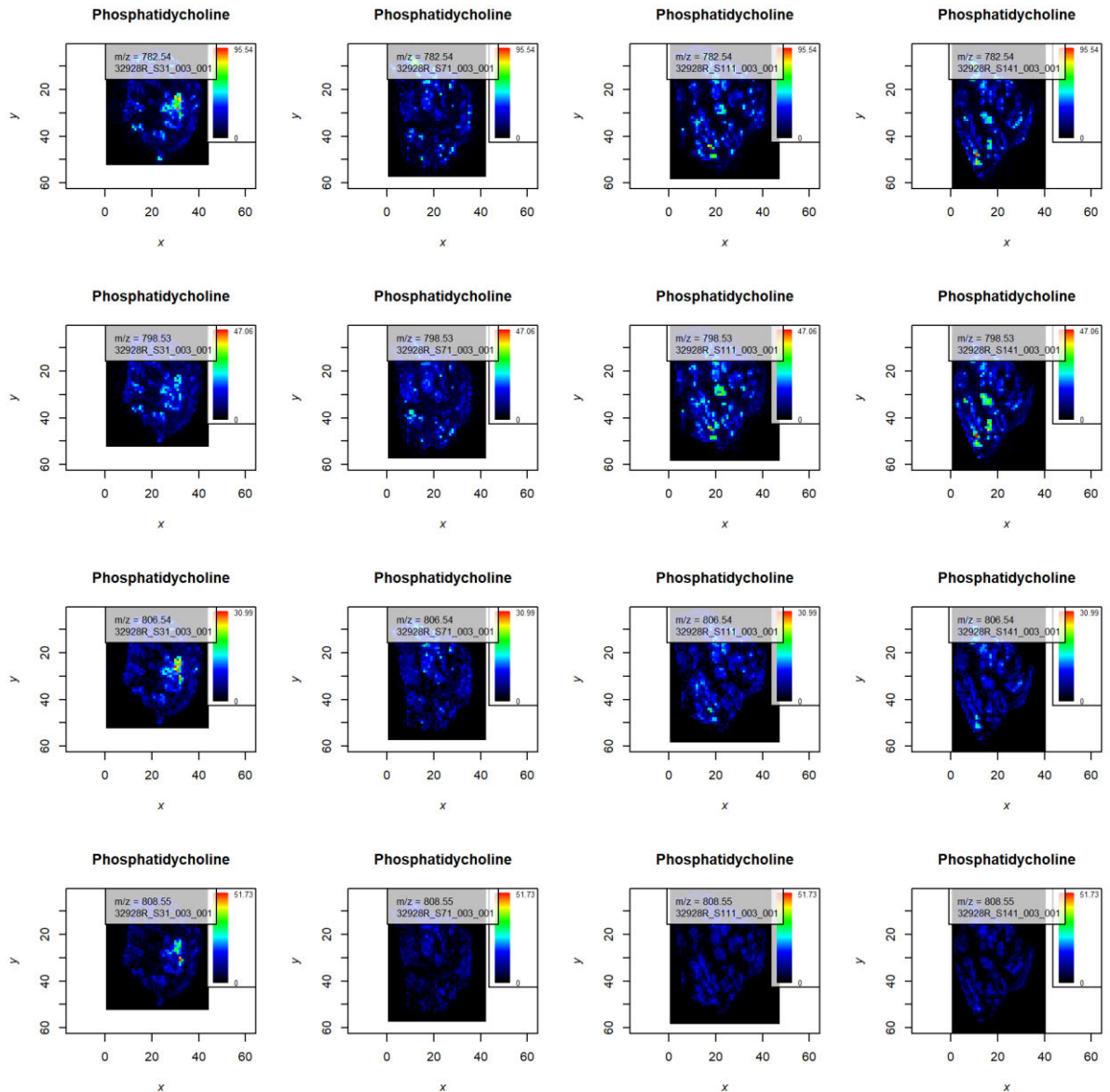
```
par(mfrow=c(4,4))
plot
## standardGeneric for "plot" defined from package "graphics"
##
## function (x, y, ...)
## standardGeneric("plot")
## <environment: 0x00000000204848e8>
## Methods may be defined for arguments: x, y
## Use showMethods("plot") for currently available ones.
image(datacomb_processed, main = "Ceramide", mz=520.49, plusminus=0
.05)
image(datacomb_processed, main = "Ceramide", mz=576.56, plusminus=0
.05)
image(datacomb_processed, main = "Ceramide", mz=604.58, plusminus=0
.05)
image(datacomb_processed, main = "Ceramide", mz=632.60, plusminus=0
.05)
```



```

image(datacomb_processed, main = "Phosphatidycholine", mz=782.56, p
lusminus=0.05)
image(datacomb_processed, main = "Phosphatidycholine", mz=798.54, p
lusminus=0.05)
image(datacomb_processed, main = "Phosphatidycholine", mz=806.54, p
lusminus=0.05)
image(datacomb_processed, main = "Phosphatidycholine", mz=808.55, p
lusminus=0.05)

```

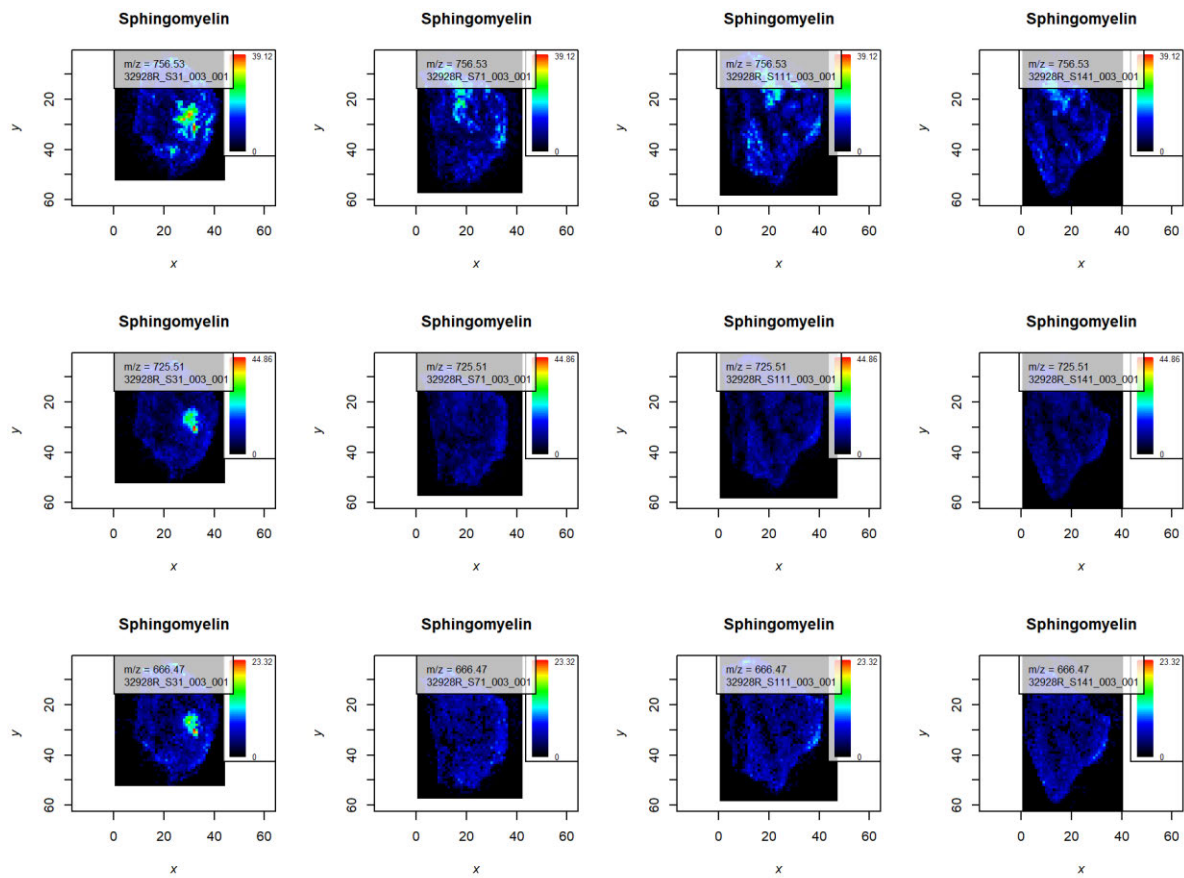


```

par(mfrow=c(4,4))
plot
## standardGeneric for "plot" defined from package "graphics"
##
## function (x, y, ...)
## standardGeneric("plot")
## <environment: 0x0000000204983e8>
## Methods may be defined for arguments: x, y
## Use showMethods("plot") for currently available ones.
image(datacomb_processed, main = "Sphingomyelin", mz=756.56, plusminus=0.05)
image(datacomb_processed, main = "Sphingomyelin", mz=725.55, plusminus=0.05)

```

```
image(datacomb processed, main = "Sphingomyelin", mz=666.47, plusmi  
nus=0.05)
```



Session Information

```
sessionInfo()  
## R version 3.4.4 (2018-03-15)  
## Platform: x86_64-w64-mingw32/x64 (64-bit)  
## Running under: Windows 10 x64 (build 18362)  
##  
## Matrix products: default  
##  
## locale:
```

```

## [1] LC_COLLATE=English_Australia.1252 LC_CTYPE=English_Australia.1252

## [3] LC_MONETARY=English_Australia.1252 LC_NUMERIC=C

## [5] LC_TIME=English_Australia.1252

##

## attached base packages:

## [1] parallel stats graphics grDevices utils datasets
methods

## [8] base

##

## other attached packages:

## [1] Cardinal_1.10.0 ProtGenerics_1.10.0 matter_1.4.1
## [4] biglm_0.9-1 DBI_1.0.0 Biobase_2.38.0
## [7] BiocGenerics_0.24.0

##

## loaded via a namespace (and not attached):

## [1] Rcpp 1.0.1 knitr 1.26 magrittr 1.5 MASS 7.3
-49
## [5] lattice 0.20-35 stringr 1.4.0 tools 3.4.4 grid 3.4
.4
## [9] xfun 0.11 irlba 2.3.3 htmltools 0.3.6 yaml 2.2
.0
## [13] digest 0.6.18 Matrix 1.2-12 codetools 0.2-15 signal 0
.7-6
## [17] evaluate 0.14 rmarkdown 1.17 sp 1.3-1 stringi
1.4.3
## [21] compiler_3.4.4 stats4_3.4.4

```

9.5. Appendix B: SYNAPT Q-TOF HDMS MALDI MSI Optimisation

B.1. Optimisation of Solvent Composition and Matrix Concentration

As highlighted in the introduction ([Chapter 1 of this thesis](#)), the method of matrix deposition is crucial to the quality of MALDI data generated.

α -CHCA was the matrix of choice for the MALDI SYNAPT Q-TOF HDMS system (Waters Corporation, Manchester, UK) due to its high vacuum stability. In addition, it was efficiently coated by sublimation. The automated spray coating method on the SunChrom (SunChrom GmbH, Friedrichsdorf, Germany) has multiple variables such as spray head distance (Z-position), flow rate, number of layers, step rate and gas pressure parameters. Altering each variable propagate adjustments of the others. Briefly, the closer the spray head is to the glass slide the more damp the tissue will be which can cause physical damage. Z-distance should therefore be kept at a bare minimum. Similarly, a higher flow rate can cause the tissue to be wetter, leading to analyte delocalization. So, this should probably be maintained on the lower side and the matrix slide may be allowed to dry in between passes. The spray speed also affects the amount of matrix deposited and should be adjusted considering the flow rate. Therefore, an amenable approach was to focus on the solvent composition and matrix concentration whilst keeping the settings of the SunCollect sprayer constant as shown in the screen shot below (**Figure B1**).

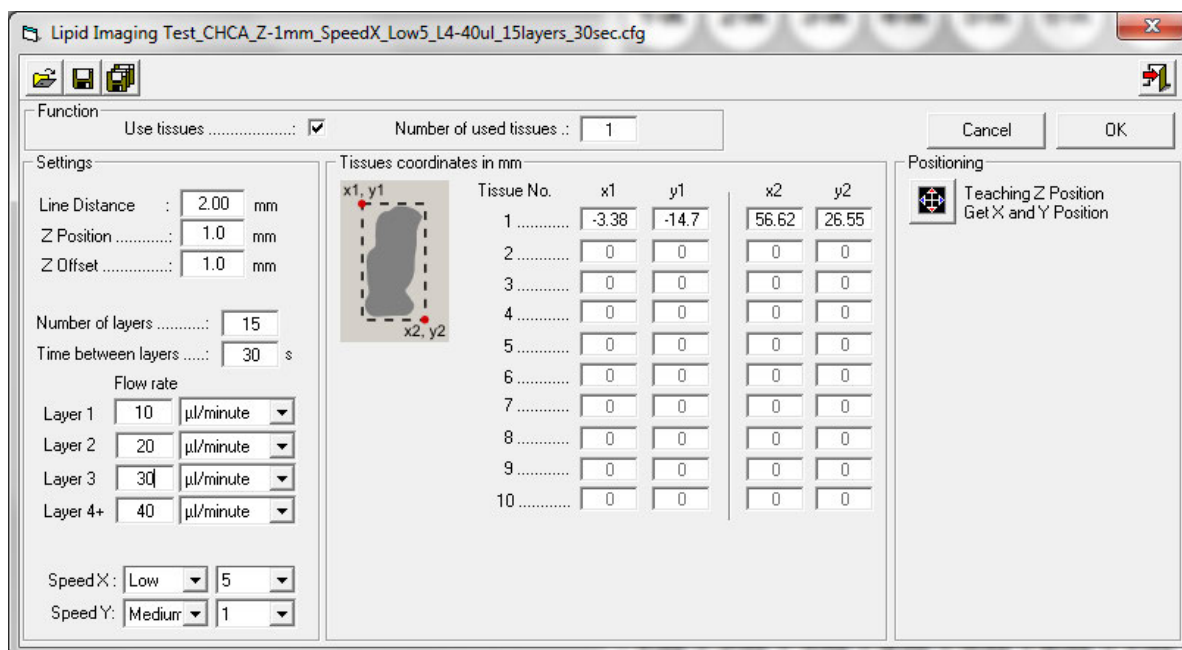


Figure B1. SunCollect SunChrom spray settings.

Automated spray coating of the matrix was achieved by deposition of α -CHCA solution using a SunCollect MALDI sprayer (SunChrom GmbH, Friedrichsdorf, Germany). 15 passes of matrix were used at an increasing flow rate of 10-40 μ L/min and 30 sec pause between passes. The first four layers are important for formation of very minute “seeding” matrix crystals; 1st pass 10 μ L/min, 2nd pass 20 μ L/min. 3rd pass 10 μ L/min and 4th pass 40 μ L/min 10. The horizontal track (X) speed was 350 mm/min, line distance of 2.00 mm, Z-position of 1.00 mm, and nitrogen gas at room temperature set and nebulizing pressure at 2.0 Bar.

Initially the lipid signal obtained by sublimation was inferior both in terms of signal-to-noise ratio on tissue areas and intensity of ions found in the lipid mass range. This necessitated the development of an optimised matrix application method.

13 mg of tissue from a patient prostate (33036R) biopsy was homogenised in a 2.0 ml tough tube in 1:1 acetonitrile-water (V/V). Precellys homogeniser was set at 6,500 rpm for 30 sec twice with a rest of 30 sec. Five 1 μ L droplets were spotted at a space of approximately 10 mm on two glass slides. 1 μ L of blue tissue dye was also applied on the slides as a control. The first slide (Set 1) was spray coated with 5 mg/l α -CHCA at increasing composition of organic content and the second slide (Set 2) was spray coated similarly with 7 mg/ml α -CHCA as shown in **Figure B2**. Two rectangular areas were ablated from both slides' sets. Data for the top area was acquired at m/z 50-990 whereas the bottom at m/z 400-990. 60 sec worth of data in the base peak intensity (BPI) chromatogram was summed in both the on-tissue and off-tissue areas. The best signal intensity over the lipid mass range was checked.

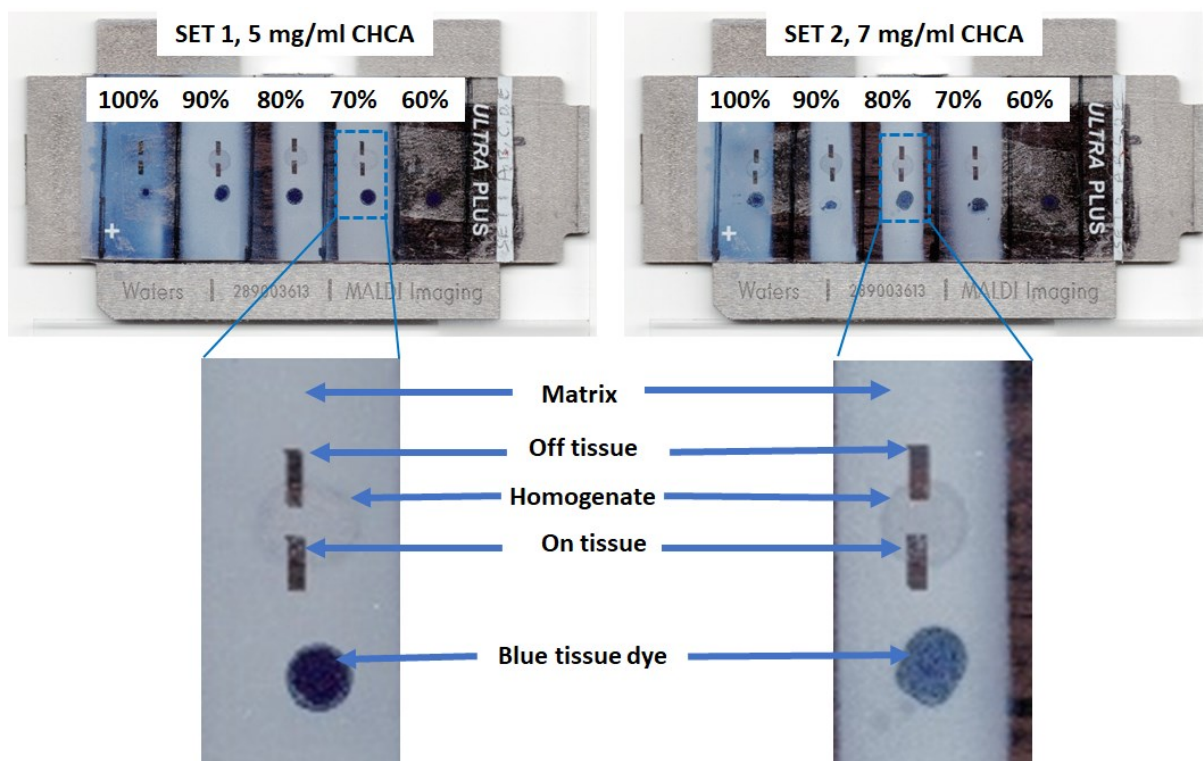


Figure B2. Optimization of lipid imaging in positive ion mode. Dried droplets of Tissue homogenate were spray coated with increasing organic solution of matrix. **Left panel.** 5 mg/ml CHCA. **Right Panel.** 7 mg/ml CHCA.

B.2. Effect of Solvent and Matrix Content on Lipid Ion Signal

Matrix deposition by sublimation achieved to a great extent the elucidation of lipids localised in glandular/epithelial regions of prostate tissue as revealed by unsupervised clustering analyses using both R *Cardinal* and SCiLS Lab in [Chapter 3](#). However, the detection of lowly abundant lipid species that constitute stromal cells may be masked by excessive chemical noise of the matrix. To mitigate this, automated spray coating was evaluated in a separate cohort and resulted in improved signal intensity and revealed a distinctly richer lipid spectral composition as highlighted in **Table B1** and **Figure B3**.

CHCA amount	Ablated area	<i>m/z</i> range	70% MeOH	80% MeOH	90% MeOH	100% MeOH	BPI
5 mg/ml	On-Tissue	50-990	49,800	36,300	25,800	12,200	184.07
	Off-Tissue	50-990	46,300	40,500	44,400	27,000	Matrix
	Off-Tissue	400-990	31,100	27,300	26,300	11,100	Matrix
	On-Tissue	400-990	22,700	14,900	11,400	6,060	782.57
7 mg/ml	On-Tissue	50-990	39,800	64,300	60,200	47,600	*184.07
	Off-Tissue	50-990	37,600	72,500	79,900	79,600	Matrix
	Off-Tissue	400-990	26,100	41,700	40,200	48,300	Matrix
	On-Tissue	400-990	16,600	32,500	27,200	30,000	782.57

Table B1. Total ion chromatograms of matrix and lipid masses. Note α -CHCA at 60% methanol aq. was not fully soluble. Values are summed from a width of ~ 60 sec in the TIC. Highlighted cells are exemplified in **Figure 4.4**

In comparison, to the other solvent compositions at 5 mg/ml, 70% methanol (MeOH) produced a BPI of 2.27e4 and 4.98e4 for the PC and its respective headgroup. On the other hand, at 7 mg/ml, 80% methanol yielded the best BPI with 3.25e4 and 6.43e4, for the PC and its respective headgroup.

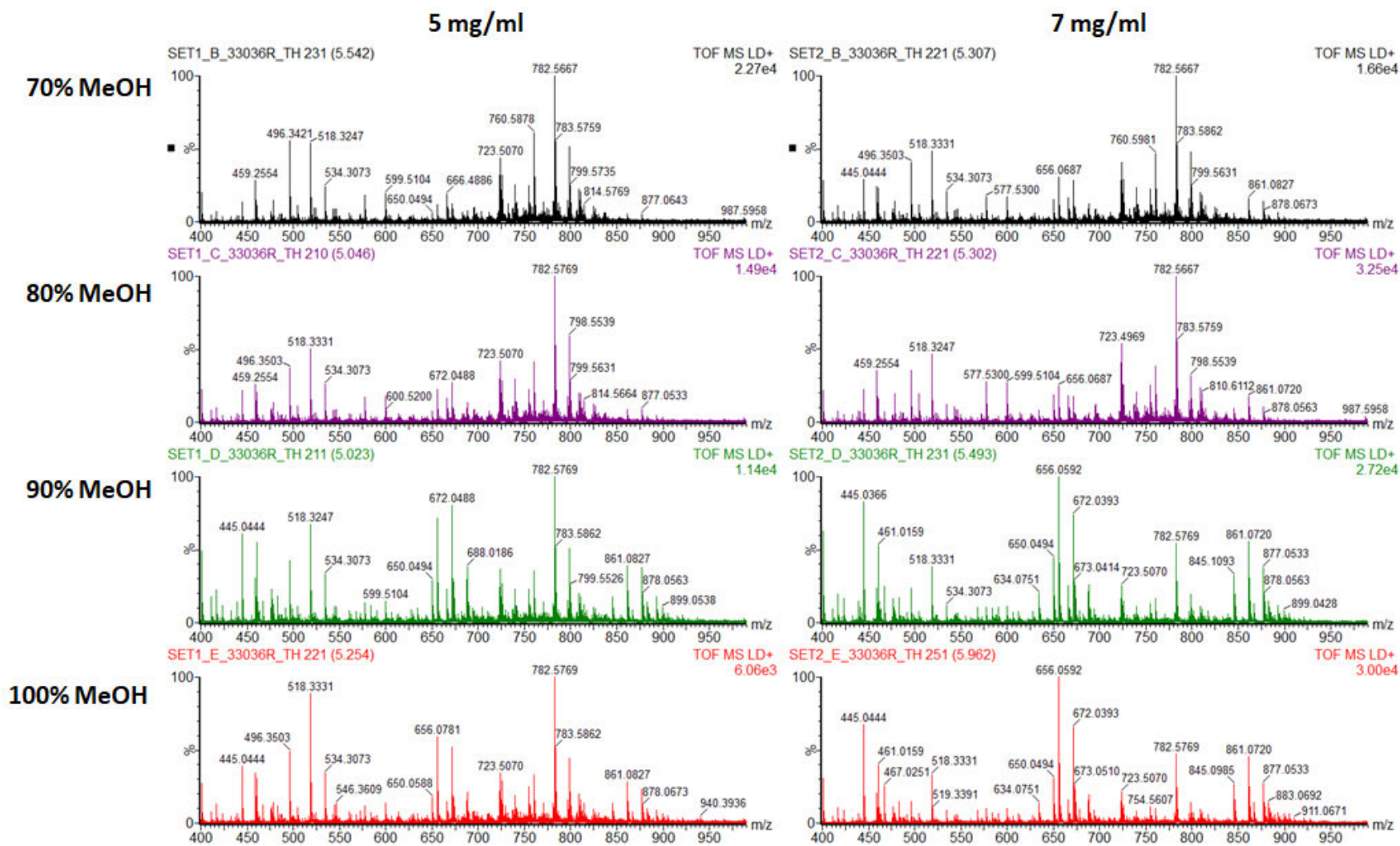


Figure B3. Comparison of automated spray coating at varying solvent composition and matrix concentration.

B.3. Comparison of Matrix Deposition Techniques for Lipid Imaging

Next, the spatial intensity and quality of lateral resolution was evaluated with the best two solvent composition parameters. Three consecutive sections of a single patient biopsy were deposited with matrix. 3 mg sublimation was compared to 5 mg/ml CHCA 70% methanol aq. and 7 mg/ml 80% methanol aq. with incorporation of 0.1% TFA to enhance ionisation as shown below in **Figure B4**.

B4.

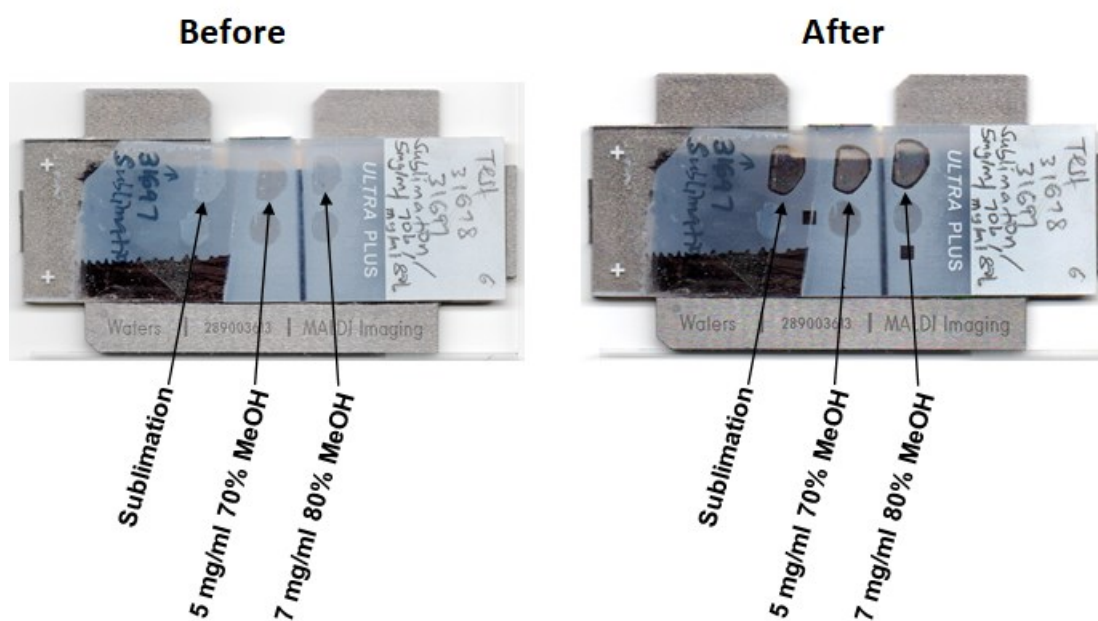


Figure B4. Matrix deposition on consecutive section of a single prostate tissue.

MALDI MSI of three serial sections from the single patient revealed interesting signal intensity and distribution. Visualisation of matrix and a common phospholipid ion is shown in **Figure B5**. Using the banded colour scheme, it is quite evident from the ion map sublimation yielded more noise on tissue, compared to 5 mg/ml 70% methanol aq. and 7 mg/ml 80% methanol aq. CHCA. In the case of m/z 417.05 as a representative ion for matrix, the level of spatial interference in the sublimated tissue was at 50% whereas for the two respective spray coated sections is around 10% (**Figure B5 top panel**) Conversely, the signal from m/z 798.54 which is a tentative PC(34.1)[M+K]⁺ based on MALDI lipid imaging literature was quite low for the sublimated tissue, but its relative intensity in glandular regions was much higher for both spray coated sections. Moreover, it was apparent that 7 mg/ml (80% methanol aq.) was better than 5 mg/ml (70% methanol aq.) given the markedly higher signal from the epithelium. The localisation of the signal in the luminal regions was better defined at the higher matrix-higher organic matrix solution. Practically, the lower water content yielded a slightly lower ion re-distribution (**Figure B5 top panel**). Remarkably, the stromal-derived signal in the spray coated section is comparable to the epithelial lipid signature in the sublimated tissue.

PCA bi-plot of the entire data sets showed that the noise level was 50% for the sublimation, 22% for 5 mg/ml CHCA and 20% for 7 mg/ml CHCA. A single spectrum selected from the same data point/pixel for the respective tissue which further expounds on the improved sensitivity of lipids with the spray coating approach in comparison to sublimation as depicted in **Figure B5 bottom panel**.

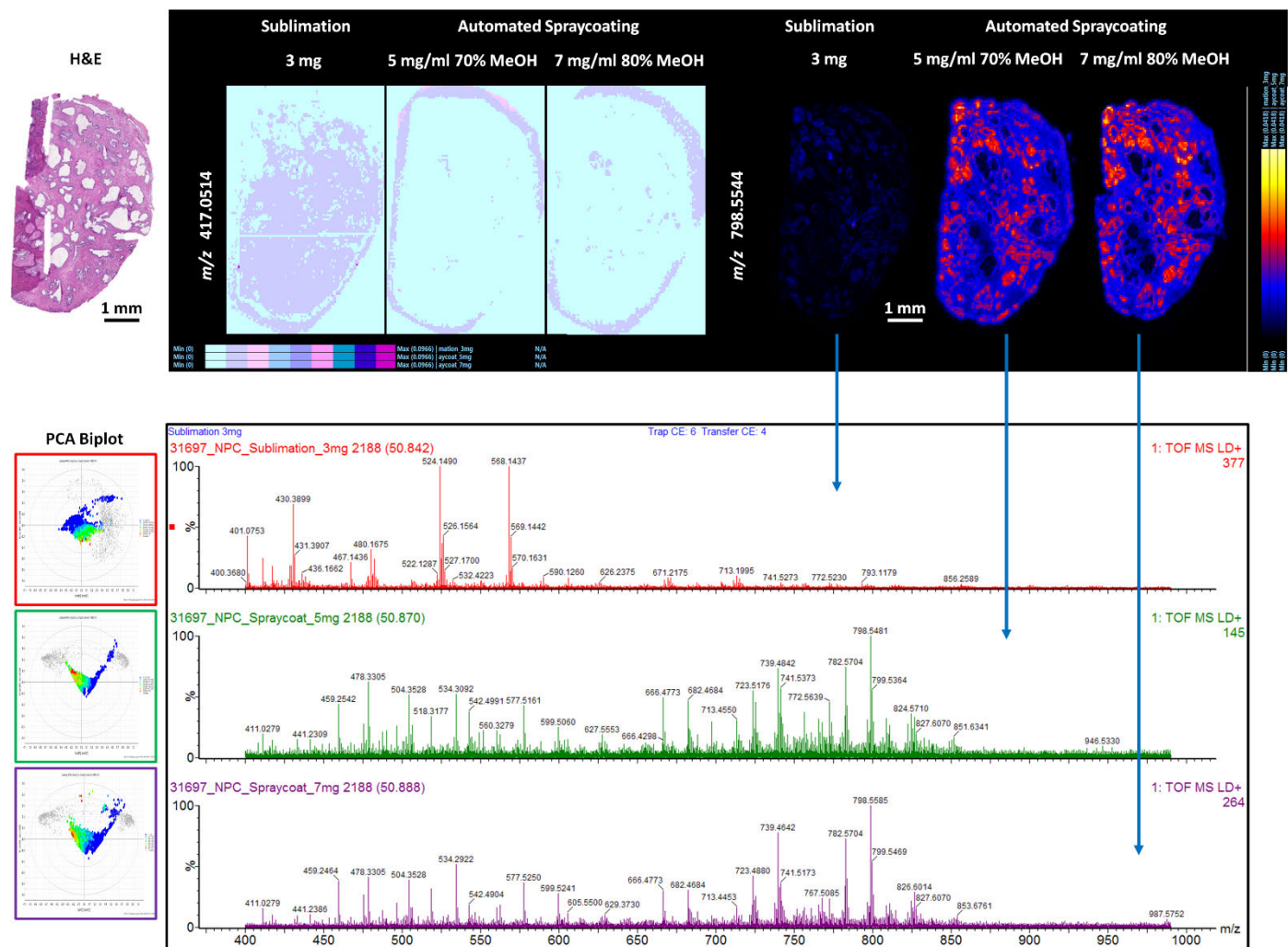


Figure B5. Spatial ion maps of different matrix deposition protocols. Three serials section were coated with matrix: 3 mg sublimation, 5 mg/ml 70%- and 7 mg/ml 80%- methanol. **Top panel.** Visualisation of matrix ion, m/z 417.05 and phospholipid ion m/z 798.54. **Bottom panel.** PCA biplot of entire data sets together with a single spectrum from matched data points/pixels.

Thus, spray coating was subsequently used for experiments in a separate cohort of patient sections. Automated spray coating of the matrix was achieved by deposition of 7.0 mg/ml (80% aqueous methanol-0.1% TFA v/v) α -CHCA using a SunCollect MALDI sprayer (SunChrom GmbH, Friedrichsdorf, Germany). The optimised method was used for the work submitted for publication in [Chapter 4](#) of this thesis.

Besides improvement in spectral quality and improved detection of the regional distribution of lipids in prostate tissue, the other benefit of matrix application by automated spray coating versus sublimation is the consolidation of data processing and analysis. **Figure B6** illustrates the data quality upon importation of multiple data sets generated by positive ion mode MALDI MSI in SCiLS Lab. The sublimated tissue sections (n=4) are from interspersed depths of the same patient biopsy whilst the spray coated tissue sections (n=11) are from different patients with data acquired on a MALDI SNYAPT instrument. There are also QC areas on the glass slides constituted of ablated CHCA matrix before and after the tissue imaging experiments. The preservation of data quality may be, in part, because automated spray coating attains deposition of a highly consistent and homogenous matrix layer across the entire glass slide. Interestingly, sublimation has also been documented to produce reproducible matrix coatings^{477,478}. Furthermore, with sublimation it is likely to encounter day-to-day variables (apparatus temperature, glass chamber pressure, distribution of final dry matrix). On the contrary, there is more experimental control with automated matrix application ultimately resulting in identical mass spectra indices that allow combined data importation, multiple file merging and statistical analyses.

Sublimation

Automated Spray Coating

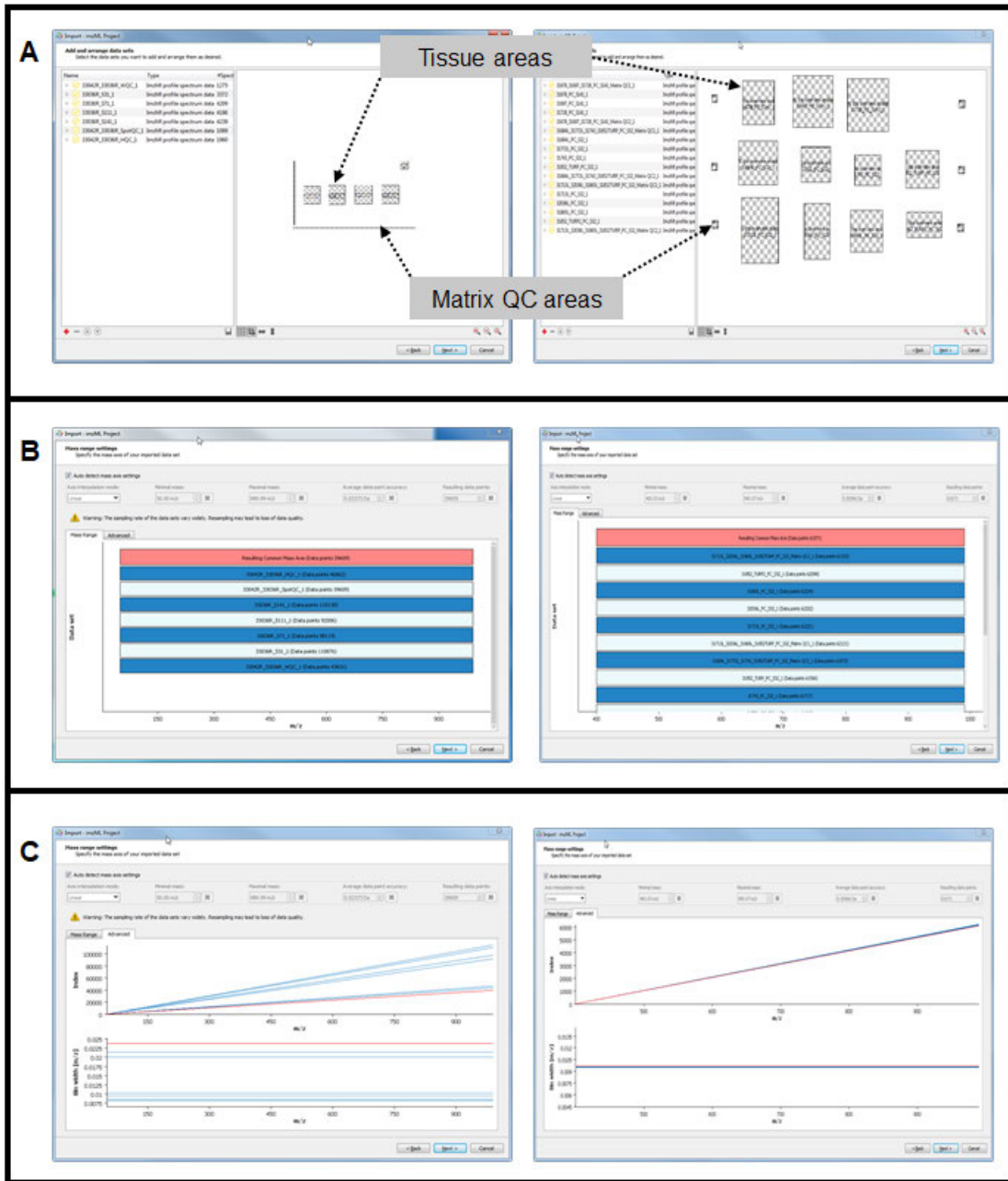


Figure B6. Importation data quality in SCiLS Lab between different matrix application technologies. Comparison of sublimation and automated spray coating of CHCA for generation of positive ion mode MALDI MSI data sets acquired on a Waters SYNAPT HDMS mass spectrometer. **A.** Addition and arrangement of data sets in the imzML project. **B.** Mass range settings showing sampling rate and average data point accuracy **C.** Data quality in the form mass spectra index as a function m/z interval. Note the different bin widths for sublimation, ± 0.02373 Da and automated spray coating, ± 0.00966 Da.

9.6. Appendix C: timsTOF Flex MALDI MSI Optimisation

C.1. Optimisation of Solvent Composition and Matrix Concentration

This Appendix describes the protocol for method optimisation for negative ion mode MALDI imaging using norhamane matrix on the timsTOF Flex (Bruker Daltonics, Bremen, Germany). The solvent composition and matrix concentration were optimised using a similar approach for CHCA in positive ion mode imaging ([Appendix B](#)). Briefly, 1 μ L droplet of tissue homogenate 1:1 acetonitrile-water (v/v) was deposited on ITO slides and allowed to air dry. Glass slides were further desiccated under vacuum for 30 min. Two matrix concentrations, 5 mg/ml and 10 mg/ml were assessed at increasing organic content of 60%, 70%, 80%, 90% and 100% methanol. The spatial resolution was 40 μ m (x, y). The results are shown in **Figure C1**.

At the lower matrix concentration, 5 mg/ml, the relative abundance of m/z 255.233, a tentative fatty acid, and m/z 863.562, a phosphatidylinositol species, was constant with rising solvent composition. However, with doubling of the matrix content, it was observed the lipid signal varied. There was general trend of enhancement of relative intensity with increase in water content. Interestingly, 80% methanol 10 mg/ml matrix produced the optimum lipid ion signal intensity with a marked difference of the phospholipid compared to the fatty acid species. Importantly, there was hardly any delocalisation of lipid features in the “off-tissue” area for most ions.

First, these data showed that the molar matrix content is an important factor for the ionisation efficiency of the lipids. As previously highlighted in the Introduction ([Chapter 1](#)), the MALDI process requires 5,000 - 10,000 matrix-

analyte ratio for efficient ion generation. Second, a balance in the water content in the matrix composition may influence crystal formation for optimum laser desorption process. Water constituting approximately 20% of the mixture formed the best crystal lattices with norhamane. Given that 5 mg/ml did not show differences in signal intensity across the four solvent compositions, 10 mg/ml 80% methanol was chosen to be compared with 98% methanol on cryo-cut prostate tissue sections.

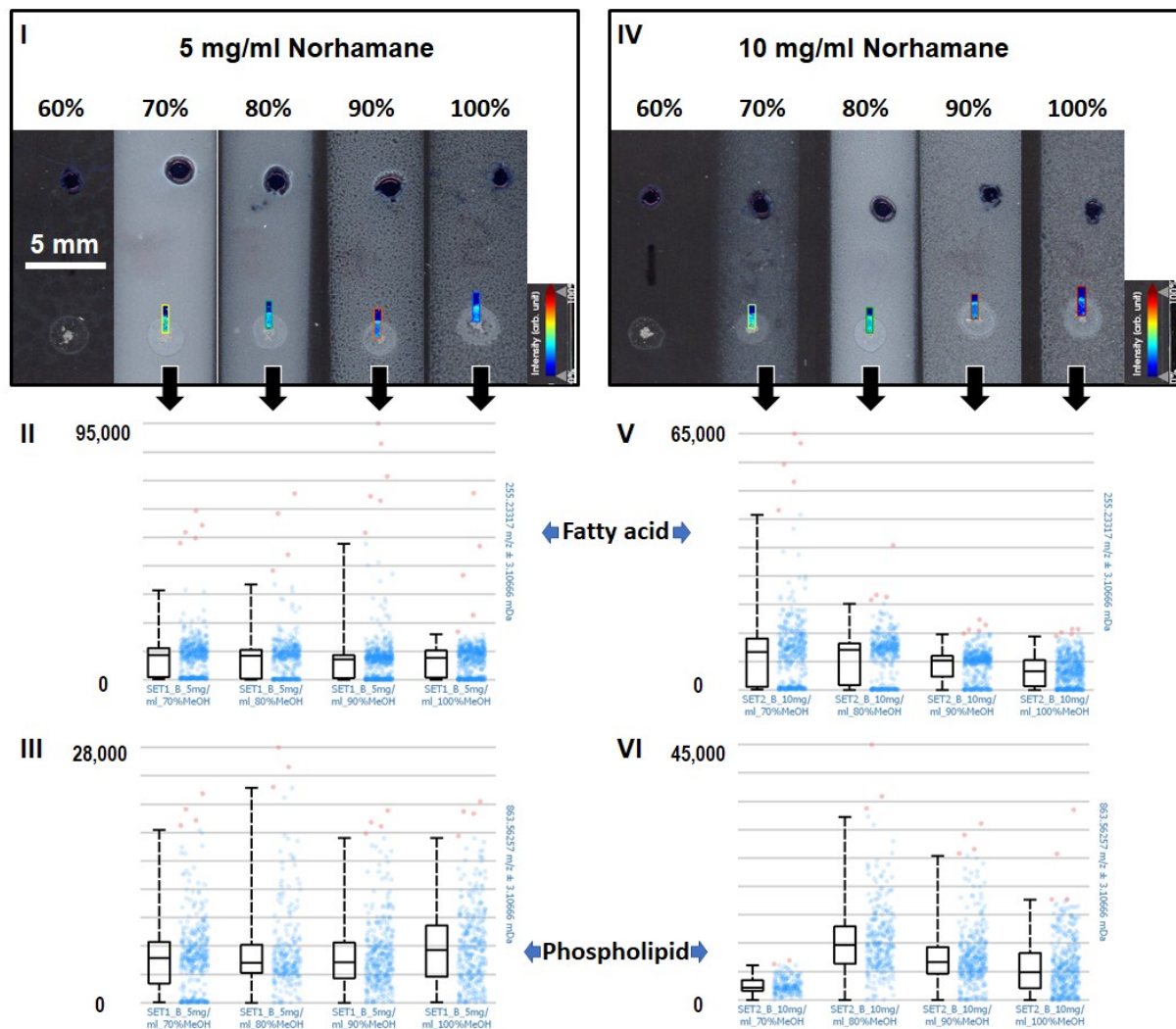


Figure C1. Optimisation of the solvent composition and matrix concentration. Tissue homogenate spots were spray coated and imaged at a lateral resolution of 40 μm pixel. **(I)** 5 mg/ml and **(IV)**; 10 mg/ml norhamane at increasing solvent composition, 70% aq.- 100% methanol. **(II)** and **(V)**; m/z 255.233. **(III)** and **(VI)**; m/z 863.562.

C.2. Optimisation of Solvent Composition for Imaging

For this experiment, serial tissue sections were collected on a single ITO slide. The two tissue sections were spray coated as previously described (**Chapter 2 Materials and Methods [Section 2.3.2.](#) and [Appendix B.1](#)**) except at 10 passes of norhamane matrix at 98% and 80% aqueous methanol compositions both at 10 mg/ml. A subsection of the tissue was imaged at 20 μm lateral resolution in both x and y.

Photos of whole sections were taken using a Smartphone down a 10X objective lens microscope as illustrated in **Figure C2**. 98% methanol yielded smaller crystal formation on tissue but with a more honeycomb like pattern on the slide of larger coarse crystal aggregates. On the other hand, 80% methanol exhibited seemingly finer crystal appearance on the glass slide with the tissue blending with the rest of the background margin and on tissue glandular structures appearing to be better resolved. Notably, it was observed that 98% methanol section has a darker tone compared to the 80% methanol, perhaps indicating different chemical induced changes to tissue appearance.

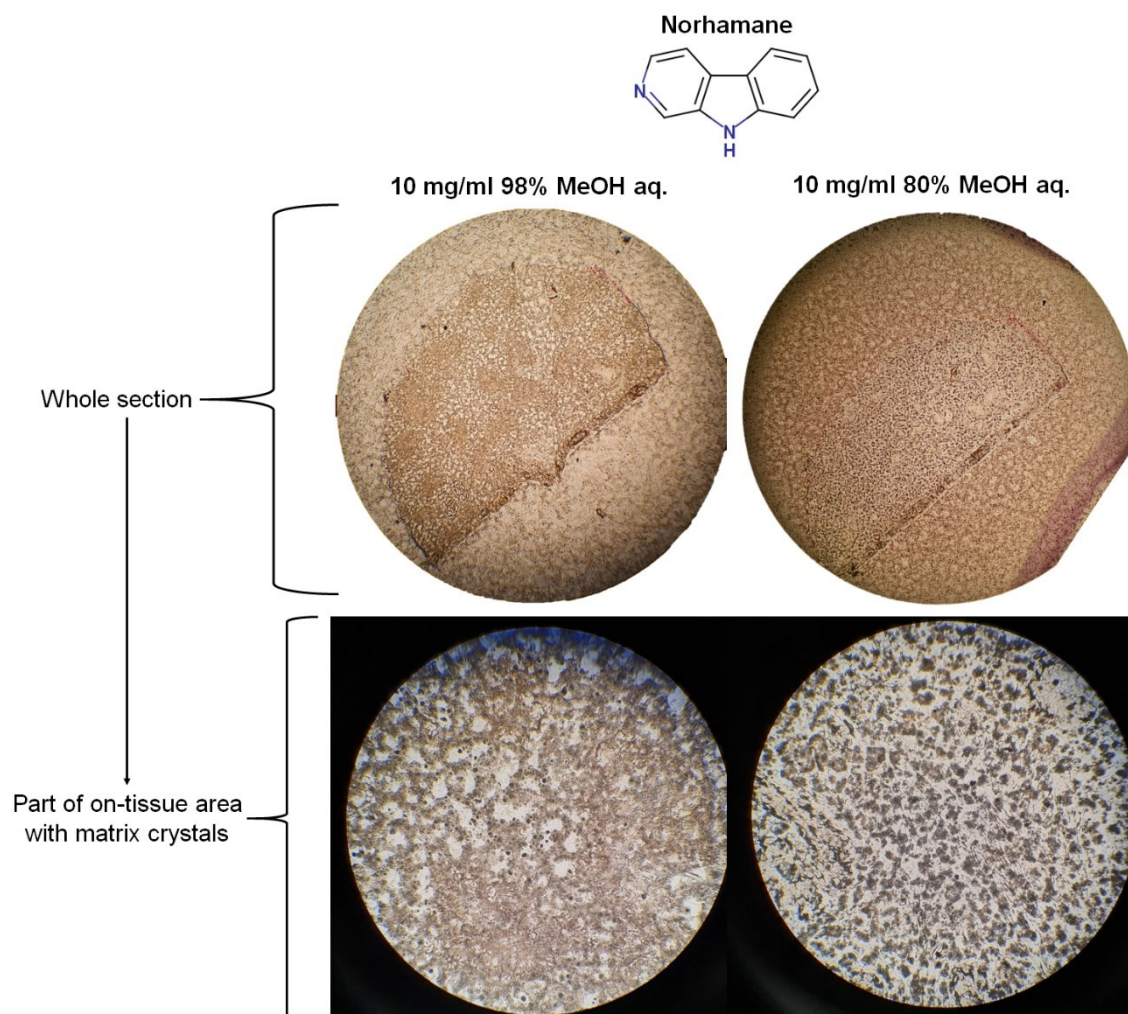


Figure C2. Optimisation of the solvent composition for imaging. 10 mg/ml Norhamane was spray coated at a solvent composition of 98% methanol aq. and 80% methanol aq. **Top panel.** Photos of whole section depicting matrix coating on glass slide **Bottom panel.** Photo of on tissue area.

A sub-area of both solvent coated sections was visualised for ions in the m/z 200-320 range. These masses were potentially deprotonated adducts of fatty acid. The ion maps were compared to the light microscope micrograph captured images as demonstrated in **Figure C3**.

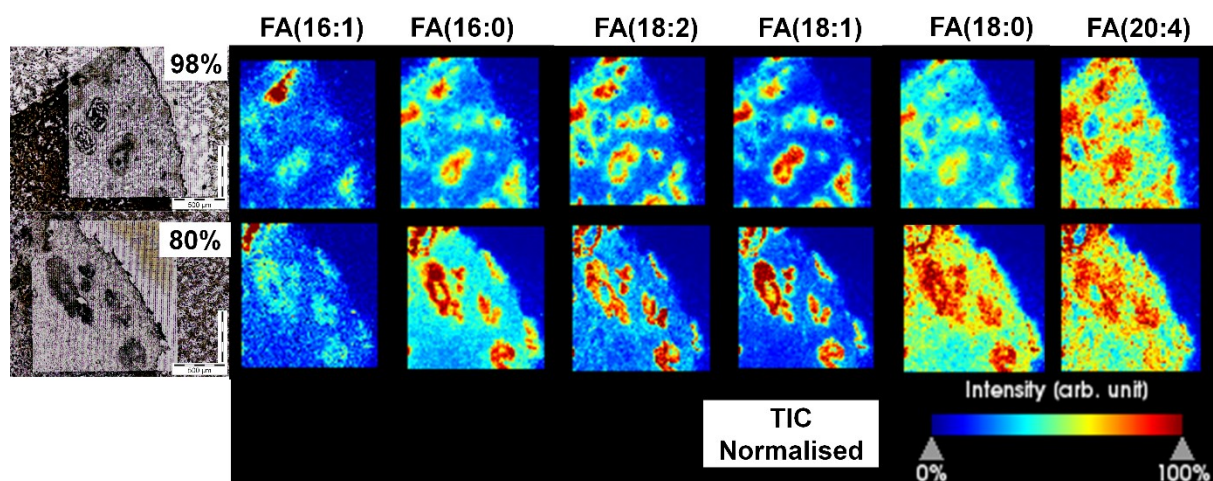


Figure C3. Optimisation of the solvent composition for MALDI MSI. Microscope capture images of 10 mg/ml norhamane 98% methanol aq. and 80% methanol aq. are shown on the left with corresponding MALDI ion map images of tentatively identified fatty acid species.

Notably, 98% methanol compared to 80% methanol showed an inferior spatial resolution of secretory glandular structures. This observation was intriguing as one would expect delocalization of ions with more H₂O content. Quite the reverse, the minute water content in the 98% composition possibly caused slightly leaching of membrane-bound structural lipids and lead to their minor extracellular re-distribution. A slight spread of lipids from the glandular areas into the surrounding stroma is seen. Therefore, to confirm that spatial specificity of lipid ions at 20 μm raster imaging, the automated spray coating was repeated on two consecutive sections that were fully imaged. A closer investigation of the photomicrographs is illustrated in **Figure C4**. It is appreciable the instruments' focused laser settings offers "dynamic pixel imaging" that exhibited little oversampling.

98% MeOH aq. ← 10 mg/ml Norhamane → 80% MeOH aq.

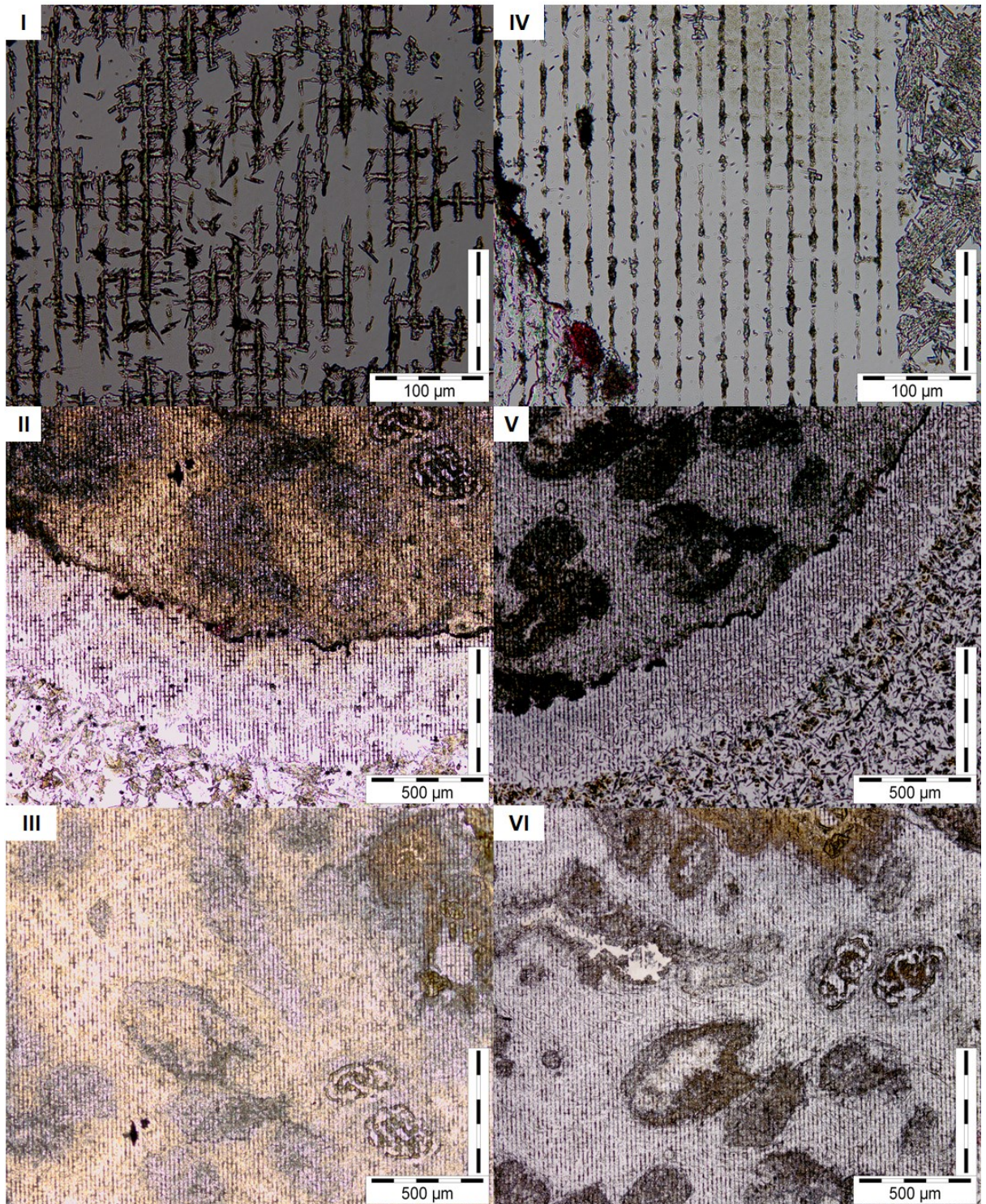


Figure C4. Comparison of the solvent composition for MALDI MSI. Microscope capture images of 10 mg/ml norhamane 98% methanol aq. and 80% methanol aq. are shown. (I) and (IV); aftermath of raster imaging showing each pixel $\sim 20 \mu\text{m}$ by $\sim 20 \mu\text{m}$. (II) and (V); tissue margin appearance. (III) and (VI); physical appearance of matched glandular epithelium and stromal structures.

C.3. High Resolution MALDI MS Imaging in Negative Ion Mode

Spray coating whole tissue areas was achieved with 5 additional passes/layers of matrix using the same SunCollect parameters mentioned above. The comparison of H&E scans and lipid ion masses is shown in [Figure C5](#).

These results strongly suggest that the volume of water affects the quality of the MSI spatial resolution. Spray coating 98% methanol leads to deposition of more organic content with drier matrix coating. Therefore, it can be conceived that this high organic content (98% methanol) repulses the 2% H₂O to effect partitioning of lipophilic molecules with a rapid co-crystallisation (~ 1 msec) with adjacent matrix molecules. Conceivably, at 80% methanol lipids are more efficiently extracted from the tissue microdomains with 20% H₂O. Proteins are basically fixed at this composition and allowing the lipids to slowly form well-defined fused matrix-analyte structures. This can account for the improved spatial resolution that resonates highly with the histological tissue architecture and morphology.

C.4. Method Transfer Between MALDI Q-TOF Systems

The rationale of the change of instrumentation from the MALDI SYNAPT HDMS to the timsTOF Flex is demonstrated in [Figure C6](#). Two unmatched prostate tissue sections are shown deposited with CHCA for positive ion mode imaging as described in [Section 2.5.4](#). However, this is not a direct comparison because of different laser, ion transmission and *m/z* acquisition parameters. The benefits of switching to the new instrument are ease of calibration, better spatial resolution and an apparent enhancement in relative sensitivity, although the SYNAPT data was binned and converted to .imzML to be compatible in SCiLS Lab.

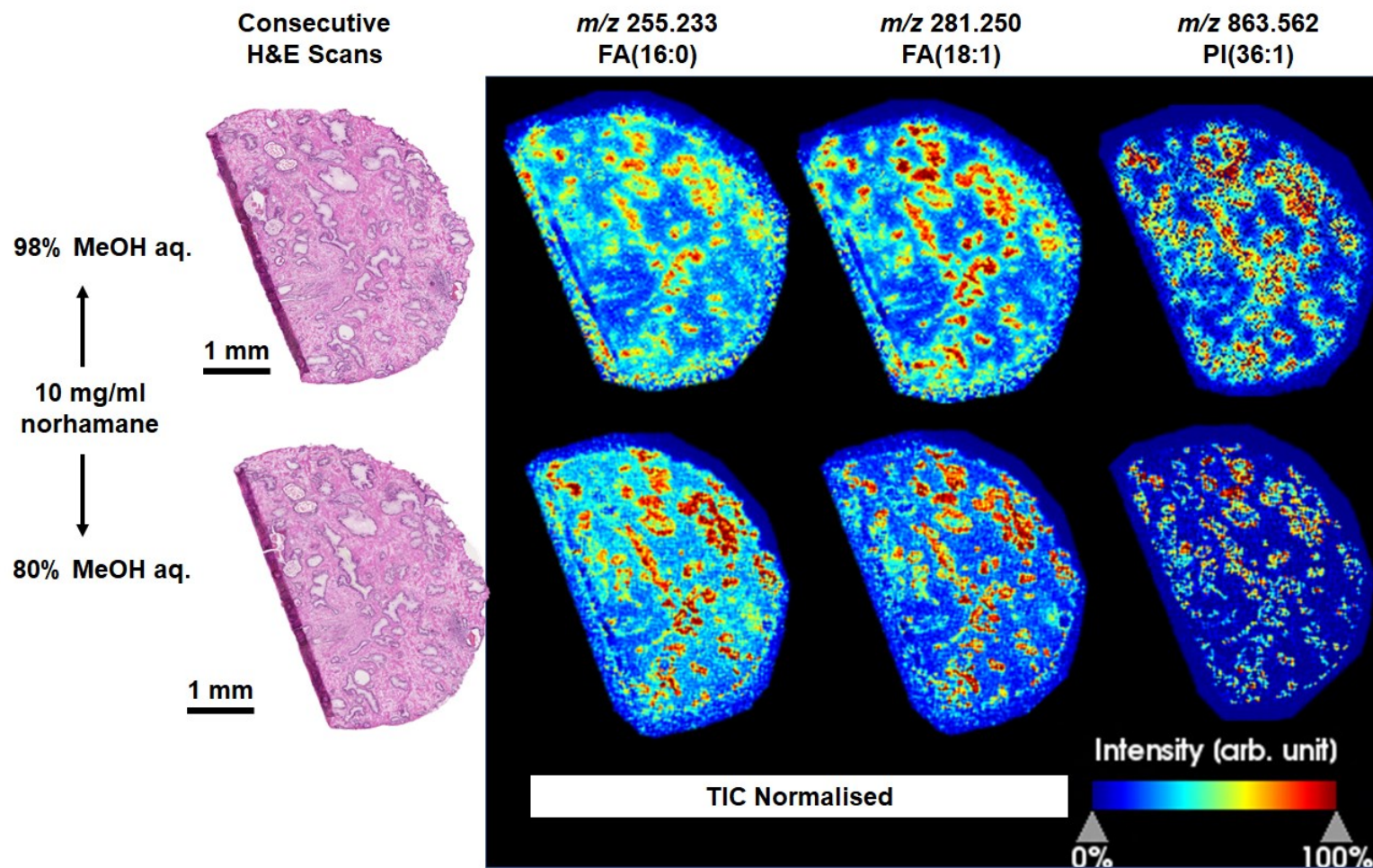


Figure C5. Comparison of histology and MALDI MSI ion maps. **Top panel.** 10 mg/ml norhamane solution of 98% methanol aq. with slight migration of periglandular epithelial lipids into the tissue stroma. **Bottom panel.** 80% methanol aq. shows there is improved signal localisation in morphological niches.

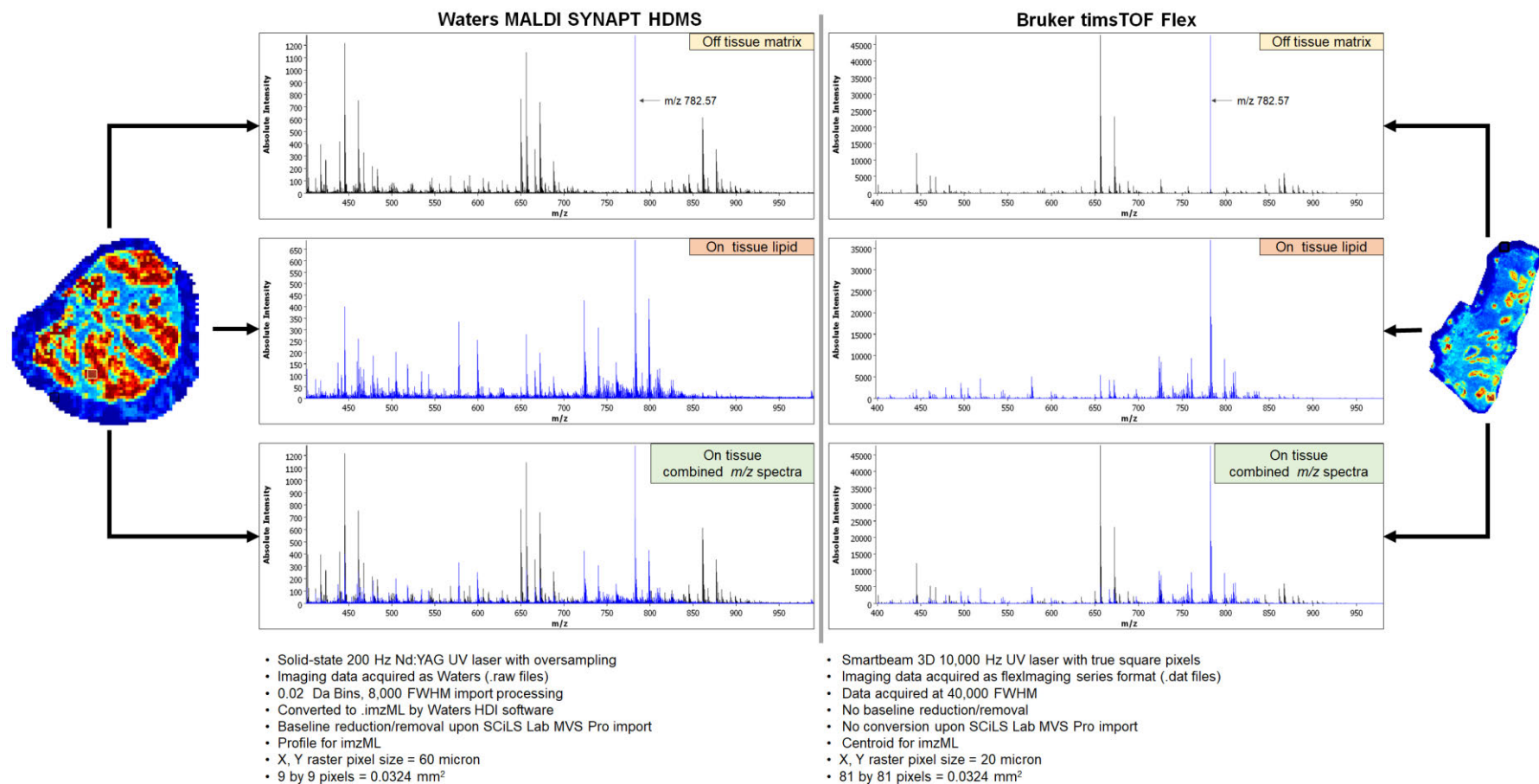


Figure C6. Comparison of two MALDI Q-TOF MS imaging data sets. Left panel. Waters MALDI SYNAPT HDMS, data acquired at m/z 400-990*. **Right panel.** Bruker timsTOF Flex, data acquired at m/z 50-1250. Matrix application by automated spray coating of fresh-frozen prostate tissue sections on ITO slides for positive ion MALDI. Data normalised to TIC and distribution of m/z 782.57 PC(34.1) is shown. Equivalent ROIs selected. *sample previously sublimated with 3 mg of α -CHCA.

9.7. Appendix D: Experimental Optimisation for Frozen Section IHC Staining

D.1. Optimisation of Sample Fixation for IHC p63+AMACR Staining

One of the drawbacks with applying the diagnostic staining protocol of p63+AMACR for immunohistochemical (IHC) of fresh-frozen Day 0 tissue sections is the issue of tissue remaining on the glass slide during the whole procedure. This is because the protocol is designed for FFPE sections that can withstand the rigours of antigen retrieval at high temperatures of >95°C for approximately 60 min. To mitigate tissue affixation strategies were tested to ensure that cryosections (10 µm thick) adhered to tissue and still retained enough morphological detail for antigen detection. Briefly, serial section from three different patients underwent different fixation procedures as outlined in **Figure D1**. All samples were then rinsed twice in 1X TBS pH 8.4, re-applied with buffer and placed in a humid chamber at room temperature for 12 hours. Subsequently, samples were histologically stained as described in **Chapter 2 (Materials and Methods [Section 2.2.2](#))**.

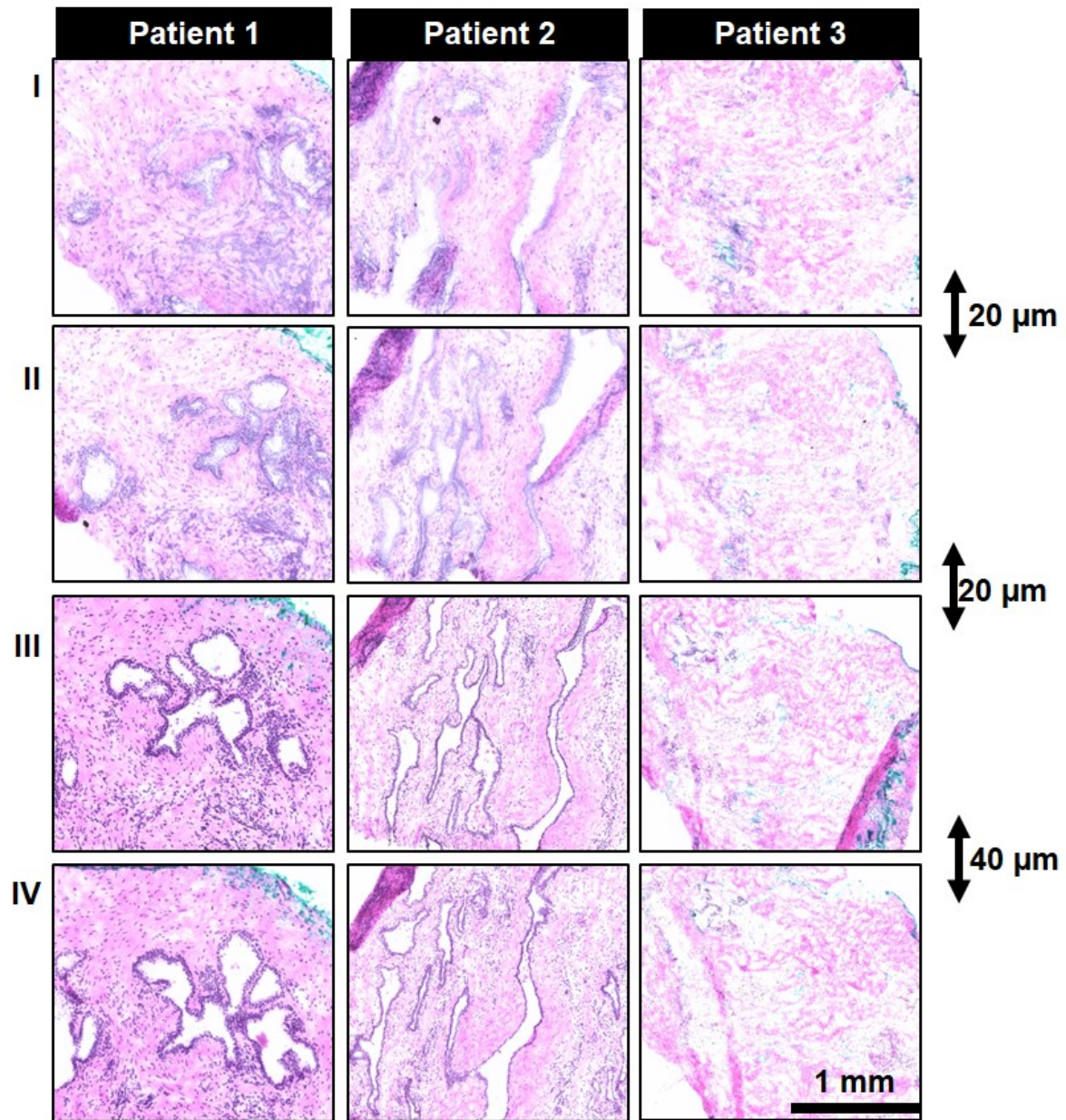


Figure D1. Optimisation of sample preparation for IHC staining. Serial cryosection from individual patient prostate biopsy cores were collected on individual glass slides and stained by H&E. (I); No chemical or heat fixation. (II); Heat fixation at 45°C for 2 min on a slide warmer. (III); 4% PFA fixation for 10 min (IV); Heat fixation at 45°C for 2 min on a slide warmer followed by 4% PFA fixation for 10 min.

D.2. Evaluation of IHC p63+AMACR Staining in Day 0 Tissues

After successful optimisation of the sample fixation (preparation), p63+AMACR immunohistochemical labelling was trialled in another set of three separate patients. The procedure for p63+AMACR immunostaining is described in **Chapter 2 (Methods [Section 2.5.9](#))**.

The results of p63+AMACR IHC staining are depicted in **Figure D2**. Detection of p63 and cytokeratin marker 34 β E12 was indicated by a brown colour of basal cells signifying benign glands or normal epithelial cells. Positive AMACR staining was indicated by a pink colour signifying malignant glands or tumour cells. The appearance of intraluminal pink staining within brown stained basal epithelium was suggestive of prostatic intraepithelial neoplasia (PIN). Two out of three patients had almost completely benign tissue, of which one had pockets of possibly PIN glands. The last patient had the most cancerous tissue with $\geq 40\%$ malignant tissue.

A higher magnification of the above results is provided in **Figure D3**. The typical stages of prostate cancer progression (aggressiveness) are represented across the three individual patients.

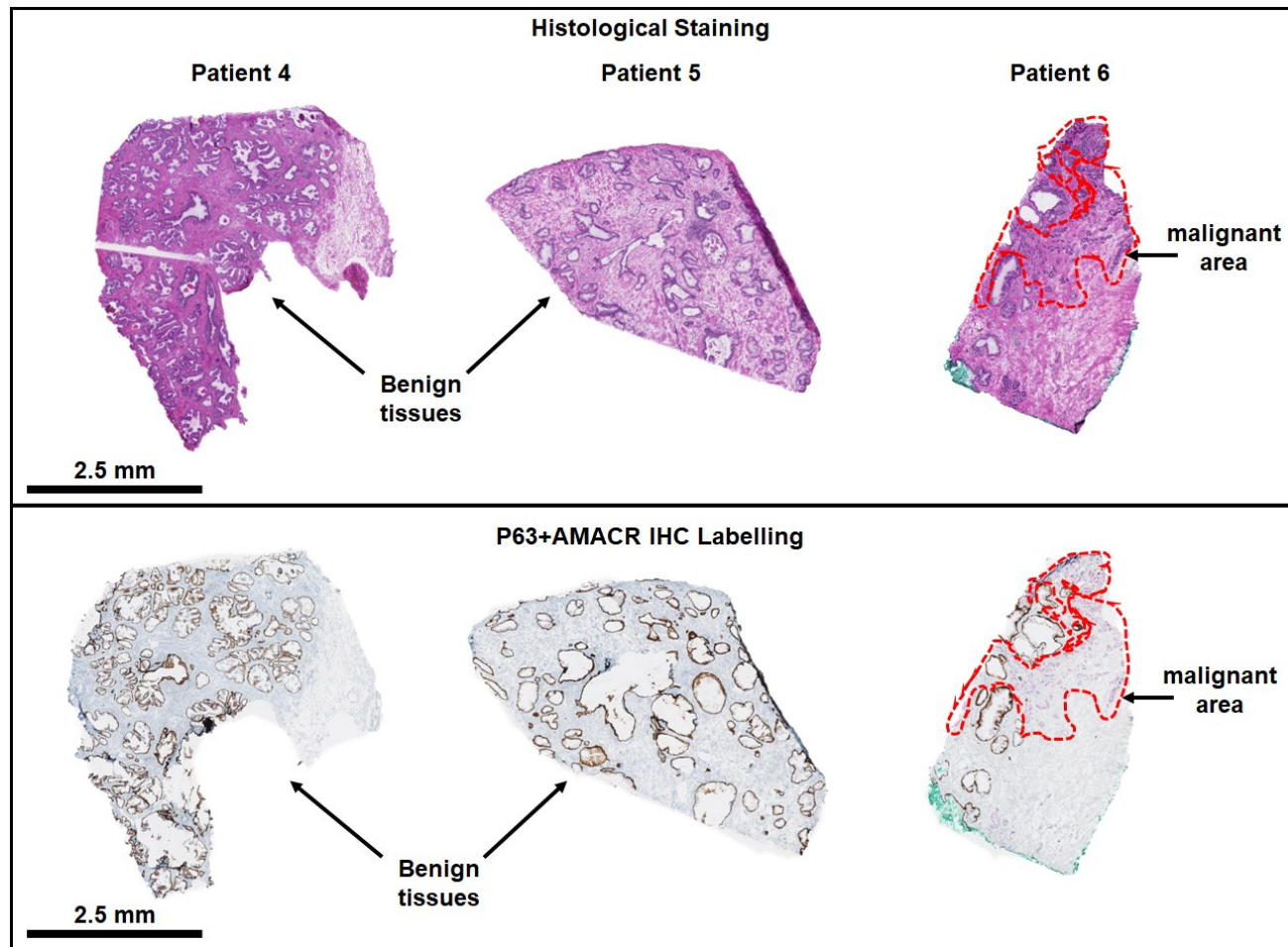


Figure D2. Comparison of histological staining to p63+AMACR IHC staining. Top panel. H&E scan. Bottom panel. IHC scan. Adjacent cryosections from individual patients (n=3) depicting heterogenous tissues. Patient 6 has malignant tissue shown in red outline.

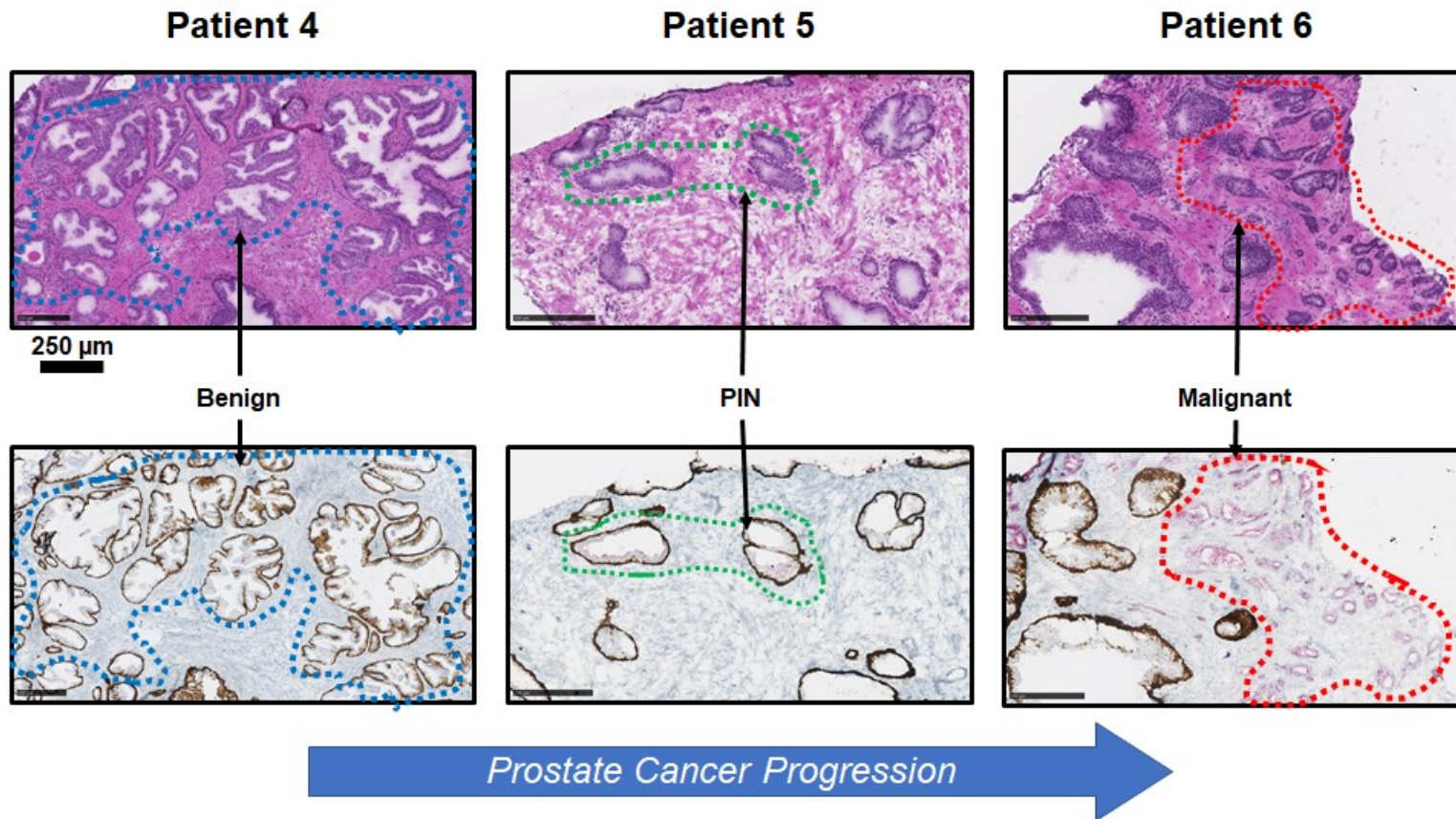


Figure D3. Higher magnification images of co-registered histological staining and p63+AMACR IHC staining scans. Top panel. Inset zoom from top panel Figure D2. Bottom panel. Inset zoom from bottom panel Figure D2. Patient 4 - blue outline had benign glands. Patient 5 - green outline had foci of potential PIN glands. Patient 6 - red outline had at least 40% malignant glands.

THIS PAGE IS INTENTIONALLY LEFT BLANK.

REFERENCES

1. Uhlen, M., *et al.* Proteomics. Tissue-based map of the human proteome. *Science* **347**, 1260419 (2015).
2. Thul, P.J., *et al.* A subcellular map of the human proteome. *Science* **356**, eaal3321 (2017).
3. Magi-Galluzzi, C. *Genitourinary Pathology Practical Advances*, (Springer New York, New York, NY, 2015).
4. Uhlen, M., *et al.* A pathology atlas of the human cancer transcriptome. *Science* **357**, eaan2507 (2017).
5. Culp, M.B., Soerjomataram, I., Efstathiou, J.A., Bray, F. & Jemal, A. Recent Global Patterns in Prostate Cancer Incidence and Mortality Rates. *Eur Urol* **77**, 38-52 (2020).
6. Stangelberger, A., Waldert, M. & Djavan, B. Prostate cancer in elderly men. *Rev Urol* **10**, 111-119 (2008).
7. Merglen, A., *et al.* Short- and long-term mortality with localized prostate cancer. *Arch Intern Med* **167**, 1944-1950 (2007).
8. Lu-Yao, G.L. & Yao, S.L. Population-based study of long-term survival in patients with clinically localised prostate cancer. *Lancet* **349**, 906-910 (1997).
9. Rider, J.R., *et al.* Long-term outcomes among noncuratively treated men according to prostate cancer risk category in a nationwide, population-based study. *Eur Urol* **63**, 88-96 (2013).
10. Pettaway, C.A., *et al.* Benign prostatic hyperplasia: racial differences in treatment patterns and prostate cancer prevalence. *BJU Int* **108**, 1302-1308 (2011).
11. Ogino, Y., Miyagawa, S. & Iguchi, T. Testosterone/Dihydrotestosterone. in *Handbook of Hormones* (eds. Takei, Y., Ando, H. & Tsutsui, K.) 515-e594E-513 (Academic Press, San Diego, 2016).
12. Wiren, K.M. & Orwoll, E.S. Androgens and Bone. in *Osteoporosis in Men* (eds. Orwoll, E.S., Bilezikian, J.P. & Vanderschueren, D.) 295-317 (Academic Press, San Diego, 2010).
13. Li, J. & Al-Azzawi, F. Mechanism of androgen receptor action. *Maturitas* **63**, 142-148 (2009).
14. Berry, P.A., Maitland, N.J. & Collins, A.T. Androgen receptor signalling in prostate: effects of stromal factors on normal and cancer stem cells. *Mol Cell Endocrinol* **288**, 30-37 (2008).
15. Tan, M.H., Li, J., Xu, H.E., Melcher, K. & Yong, E.L. Androgen receptor: structure, role in prostate cancer and drug discovery. *Acta Pharmacol Sin* **36**, 3-23 (2015).
16. Huggins, C. & Hodges, C.V. Studies on Prostatic Cancer. I. The Effect of Castration, of Estrogen and of Androgen Injection on Serum Phosphatases in Metastatic Carcinoma of the Prostate. *Cancer Research* **1**, 293 (1941).
17. Brendler, H. Adrenalectomy and hypophysectomy for prostatic cancer. *Urology* **2**, 99-102 (1973).
18. Kyprianou, N., English, H.F. & Isaacs, J.T. Programmed cell death during regression of PC-82 human prostate cancer following androgen ablation. *Cancer Res* **50**, 3748-3753 (1990).
19. Taplin, M.E., *et al.* Mutation of the androgen-receptor gene in metastatic androgen-independent prostate cancer. *N Engl J Med* **332**, 1393-1398 (1995).
20. Sun, C., *et al.* Androgen receptor mutation (T877A) promotes prostate cancer cell growth and cell survival. *Oncogene* **25**, 3905-3913 (2006).

-
21. Edwards, J., Krishna, N.S., Grigor, K.M. & Bartlett, J.M. Androgen receptor gene amplification and protein expression in hormone refractory prostate cancer. *Br J Cancer* **89**, 552-556 (2003).
 22. Graham, L. & Schweizer, M.T. Targeting persistent androgen receptor signaling in castration-resistant prostate cancer. *Med Oncol* **33**, 44 (2016).
 23. Bennett, N.C., Gardiner, R.A., Hooper, J.D., Johnson, D.W. & Gobe, G.C. Molecular cell biology of androgen receptor signalling. *Int J Biochem Cell Biol* **42**, 813-827 (2010).
 24. Schalken, J. & Fitzpatrick, J.M. Enzalutamide: targeting the androgen signalling pathway in metastatic castration-resistant prostate cancer. *BJU Int* **117**, 215-225 (2016).
 25. Edlind, M.P. & Hsieh, A.C. PI3K-AKT-mTOR signaling in prostate cancer progression and androgen deprivation therapy resistance. *Asian J Androl* **16**, 378-386 (2014).
 26. Carver, B.S., *et al.* Reciprocal feedback regulation of PI3K and androgen receptor signaling in PTEN-deficient prostate cancer. *Cancer Cell* **19**, 575-586 (2011).
 27. Zynger, D., Parwani, A. & Suster, S. *Prostate Pathology*, (Demos Medical Publishing, New York, UNITED STATES, 2014).
 28. Bostwick, D.G. & Cheng, L. Neoplasms of the Prostate. in *Urologic Surgical Pathology* (eds. Cheng, L.M.D., MacLennan, G.T.M.D. & Bostwick, D.G.M.D.M.B.A.) 415-525.e442 (2020).
 29. Bostwick, D.G. Nonneoplastic Diseases of the Prostate. in *Urologic Surgical Pathology* (eds. Cheng, L.M.D., MacLennan, G.T.M.D. & Bostwick, D.G.M.D.M.B.A.) 358-414.e313 (2020).
 30. Zhou, M. & Srigley, J.R. Benign mimickers and potential precursors of prostatic adenocarcinoma. *Diagnostic Histopathology* **17**, 434-446 (2011).
 31. Wallig, M.A. & Janovitz, E.B. *Morphologic Manifestations of Toxic Cell Injury*, (2013).
 32. Haschek, W.M., Rousseaux, C.G. & Wallig, M.A. Manifestations of Toxic Cell Injury. in *Fundamentals of Toxicologic Pathology* (eds. Haschek, W.M., Rousseaux, C.G. & Wallig, M.A.) 9-42 (Academic Press, San Diego, 2010).
 33. Lee, C.H., Akin-Olugbade, O. & Kirschenbaum, A. Overview of prostate anatomy, histology, and pathology. *Endocrinol Metab Clin North Am* **40**, 565-575, viii-ix (2011).
 34. Lee, S.W.H., Chan, E.M.C. & Lai, Y.K. The global burden of lower urinary tract symptoms suggestive of benign prostatic hyperplasia: A systematic review and meta-analysis. *Sci Rep* **7**, 7984 (2017).
 35. Kaplan, S.A. Re: Prevalence of Inflammation and Benign Prostatic Hyperplasia on Autopsy in Asian and Caucasian Men. *J Urol* **195**, 1042-1044 (2016).
 36. Bullock, M.J., Srigley, J.R., Klotz, L.H. & Goldenberg, S.L. Pathologic effects of neoadjuvant cyproterone acetate on nonneoplastic prostate, prostatic intraepithelial neoplasia, and adenocarcinoma: a detailed analysis of radical prostatectomy specimens from a randomized trial. *Am J Surg Pathol* **26**, 1400-1413 (2002).
 37. Tetu, B. Morphological changes induced by androgen blockade in normal prostate and prostatic carcinoma. *Best Pract Res Clin Endocrinol Metab* **22**, 271-283 (2008).
 38. Guinan, P., *et al.* The effect of androgen deprivation on malignant and benign prostate tissue. *Med Oncol* **14**, 145-152 (1997).
 39. Smith, D.M. & Murphy, W.M. Histologic changes in prostate carcinomas treated with leuprolide (luteinizing hormone--releasing hormone effect). Distinction from poor tumor differentiation. *Cancer* **73**, 1472-1477 (1994).
 40. Yang, X.J., *et al.* Does long-term finasteride therapy affect the histologic features of benign prostatic tissue and prostate cancer on needle biopsy? *Urology* **53**, 696-700 (1999).
 41. Kiess, A.P., Cho, S.Y. & Pomper, M.G. Translational Molecular Imaging of Prostate Cancer. *Curr Radiol Rep* **1**, 216-226 (2013).

-
42. Welch, H.G. & Albertsen, P.C. Prostate cancer diagnosis and treatment after the introduction of prostate-specific antigen screening: 1986-2005. *J Natl Cancer Inst* **101**, 1325-1329 (2009).
 43. Catalona, W.J., *et al.* Comparison of Digital Rectal Examination and Serum Prostate Specific Antigen in the Early Detection of Prostate Cancer: Results of a Multicenter Clinical Trial of 6,630 Men. *J Urol* **197**, S200-S207 (2017).
 44. Hayes, J.H. & Barry, M.J. Screening for prostate cancer with the prostate-specific antigen test: a review of current evidence. *JAMA* **311**, 1143-1149 (2014).
 45. Van der Meer, S., *et al.* Impact of the European Randomized Study of Screening for Prostate Cancer (ERSPC) on prostate-specific antigen (PSA) testing by Dutch general practitioners. *BJU Int* **112**, 26-31 (2013).
 46. Moyer, V.A. & Force, U.S.P.S.T. Screening for prostate cancer: U.S. Preventive Services Task Force recommendation statement. *Ann Intern Med* **157**, 120-134 (2012).
 47. Mottet, N., *et al.* EAU-ESTRO-SIOG Guidelines on Prostate Cancer. Part 1: Screening, Diagnosis, and Local Treatment with Curative Intent. *Eur Urol* **71**, 618-629 (2017).
 48. Carter, H.B., *et al.* Early detection of prostate cancer: AUA Guideline. *J Urol* **190**, 419-426 (2013).
 49. Dale, W. Prostate cancer: PSA testing in older men--are we following the guidelines? *Nat Rev Urol* **9**, 357-358 (2012).
 50. Buyyounouski, M.K., *et al.* Prostate cancer - major changes in the American Joint Committee on Cancer eighth edition cancer staging manual. *CA: a cancer journal for clinicians* **67**, 245-253 (2017).
 51. Schroder, F.H., *et al.* The TNM classification of prostate cancer. *Prostate Suppl* **4**, 129-138 (1992).
 52. Bostwick, D.G. & Qian, J. High-grade prostatic intraepithelial neoplasia. *Mod Pathol* **17**, 360-379 (2004).
 53. Trpkov, K. Contemporary Gleason Grading System. in *Genitourinary Pathology* (eds. Magi-Galluzzi, C. & Przybycin, C.G.) 13-32 (Springer New York, New York, NY, 2015).
 54. DuPre, N.C., *et al.* Corpora amylacea in prostatectomy tissue and associations with molecular, histological, and lifestyle factors. *Prostate* **78**, 1172-1180 (2018).
 55. Gleason, D.F., Mellinger, G.T. & Veterans Administration Cooperative Urological Research, G. Prediction of Prognosis for Prostatic Adenocarcinoma by Combined Histological Grading and Clinical Staging. *J Urol* **197**, S134-S139 (2017).
 56. Gordetsky, J. & Epstein, J. Grading of prostatic adenocarcinoma: current state and prognostic implications. *Diagn Pathol* **11**, 25 (2016).
 57. Epstein, J.I., *et al.* The 2014 International Society of Urological Pathology (ISUP) Consensus Conference on Gleason Grading of Prostatic Carcinoma: Definition of Grading Patterns and Proposal for a New Grading System. *Am J Surg Pathol* **40**, 244-252 (2016).
 58. Merriel, S.W.D., Funston, G. & Hamilton, W. Prostate Cancer in Primary Care. *Adv Ther* **35**, 1285-1294 (2018).
 59. Davis, B.J., *et al.* ACR appropriateness criteria: Permanent source brachytherapy for prostate cancer. *Brachytherapy* **16**, 266-276 (2017).
 60. Laing, R., *et al.* Low-dose-rate brachytherapy for the treatment of localised prostate cancer in men with a high risk of disease relapse. *BJU Int* **122**, 610-617 (2018).
 61. Ehdai, B. & Scardino, P.T. Decade in review-prostate cancer: a decade of progress in detection and treatment. *Nat Rev Urol* **11**, 618-620 (2014).
 62. Evans, A.J. Treatment effects in prostate cancer. *Mod Pathol* **31**, S110-121 (2018).
 63. Pal, S.K., *et al.* Identification of mechanisms of resistance to treatment with abiraterone acetate or enzalutamide in patients with castration-resistant prostate cancer (CRPC). *Cancer* **124**, 1216-1224 (2018).

-
64. Chi, J.T., *et al.* Metabolomic effects of androgen deprivation therapy treatment for prostate cancer. *Cancer Med* **9**, 3691-3702 (2020).
 65. Hoda, M.R., Kramer, M.W., Merseburger, A.S. & Cronauer, M.V. Androgen deprivation therapy with Leuprolide acetate for treatment of advanced prostate cancer. *Expert Opin Pharmacother* **18**, 105-113 (2017).
 66. Chandrasekar, T., Yang, J.C., Gao, A.C. & Evans, C.P. Mechanisms of resistance in castration-resistant prostate cancer (CRPC). *Transl Androl Urol* **4**, 365-380 (2015).
 67. Kapoor, A., Wu, C., Shayegan, B. & Rybak, A.P. Contemporary agents in the management of metastatic castration-resistant prostate cancer. *Can Urol Assoc J* **10**, E414-E423 (2016).
 68. Azarenko, O., Smiyun, G., Mah, J., Wilson, L. & Jordan, M.A. Antiproliferative mechanism of action of the novel taxane cabazitaxel as compared with the parent compound docetaxel in MCF7 breast cancer cells. *Mol Cancer Ther* **13**, 2092-2103 (2014).
 69. Oudard, S. TROPIC: Phase III trial of cabazitaxel for the treatment of metastatic castration-resistant prostate cancer. *Future Oncol* **7**, 497-506 (2011).
 70. Mellado, W., *et al.* Preparation and biological activity of taxol acetates. *Biochem Biophys Res Commun* **124**, 329-336 (1984).
 71. Fitzpatrick, J.M. & de Wit, R. Taxane mechanisms of action: potential implications for treatment sequencing in metastatic castration-resistant prostate cancer. *Eur Urol* **65**, 1198-1204 (2014).
 72. Lowe, F.C. & Bamberger, M.H. Indications for use of ketoconazole in management of metastatic prostate cancer. *Urology* **36**, 541-545 (1990).
 73. de Bono, J., *et al.* ABIRATERONE ACETATE (AA) PLUS LOW DOSE PREDNISONE (P) IMPROVES OVERALL SURVIVAL (OS) IN PATIENTS (PTS) WITH METASTATIC CASTRATION-RESISTANT PROSTATE CANCER (MCRPC) WHO HAVE PROGRESSED AFTER DOCETAXEL-BASED CHEMOTHERAPY (CHEMO): RESULTS OF COU-AA-301, A RANDOMIZED DOUBLE-BLIND PLACEBO-CONTROLLED PHASE III STUDY. *Annals Of Oncology* **21**, 3-3 (2010).
 74. Scher, H.I., *et al.* Bicalutamide for advanced prostate cancer: the natural versus treated history of disease. *J Clin Oncol* **15**, 2928-2938 (1997).
 75. Scher, H.I., *et al.* Antitumour activity of MDV3100 in castration-resistant prostate cancer: a phase 1–2 study. *The Lancet* **375**, 1437-1446 (2010).
 76. Scher, H.I., *et al.* Increased survival with enzalutamide in prostate cancer after chemotherapy. *N Engl J Med* **367**, 1187-1197 (2012).
 77. Armstrong, A.J., *et al.* Clinical outcomes and survival surrogacy studies of prostate-specific antigen declines following enzalutamide in men with metastatic castration-resistant prostate cancer previously treated with docetaxel. *Cancer* **123**, 2303-2311 (2017).
 78. Efstathiou, E., *et al.* Molecular characterization of enzalutamide-treated bone metastatic castration-resistant prostate cancer. *Eur Urol* **67**, 53-60 (2015).
 79. Markham, A. & Duggan, S. Darolutamide: First Approval. *Drugs* **79**, 1813-1818 (2019).
 80. Fizazi, K., Smith, M.R. & Tombal, B. Clinical Development of Darolutamide: A Novel Androgen Receptor Antagonist for the Treatment of Prostate Cancer. *Clin Genitourin Cancer* **16**, 332-340 (2018).
 81. Rice, M.A., Malhotra, S.V. & Stoyanova, T. Second-Generation Antiandrogens: From Discovery to Standard of Care in Castration Resistant Prostate Cancer. *Front Oncol* **9**, 801 (2019).
 82. Massard, C. & Fizazi, K. Targeting continued androgen receptor signaling in prostate cancer. *Clin Cancer Res* **17**, 3876-3883 (2011).

-
83. Wilt, T.J. & Thompson, I.M. Clinically localised prostate cancer. *BMJ* **333**, 1102-1106 (2006).
 84. Nagel, K.N.A., *et al.* Differentiation of Prostatitis and Prostate Cancer by Using Diffusion-weighted MR Imaging and MR-guided Biopsy at 3 T. *Radiology* **267**, 164-172 (2013).
 85. Filella, X. & Foj, L. Prostate Cancer Detection and Prognosis: From Prostate Specific Antigen (PSA) to Exosomal Biomarkers. *International journal of molecular sciences* **17**, 1784 (2016).
 86. Schroder, F.H., *et al.* Screening and prostate-cancer mortality in a randomized European study. *N Engl J Med* **360**, 1320-1328 (2009).
 87. Schröder, F.H., *et al.* Screening and prostate cancer mortality: results of the European Randomised Study of Screening for Prostate Cancer (ERSPC) at 13 years of follow-up. *The Lancet* **384**, 2027-2035 (2014).
 88. Andriole, G.L., *et al.* Mortality results from a randomized prostate-cancer screening trial. *N Engl J Med* **360**, 1310-1319 (2009).
 89. Andriole, G.L., *et al.* Prostate cancer screening in the randomized Prostate, Lung, Colorectal, and Ovarian Cancer Screening Trial: mortality results after 13 years of follow-up. *J Natl Cancer Inst* **104**, 125-132 (2012).
 90. Hoeh, M.P. & Deane, L.A. PSA Screening: A Discussion Based on the USPSTF Recommendations and the AUA and EAU Guidelines. *Journal of Men's Health* **11**, 10-17 (2014).
 91. Bell, N., *et al.* Recommendations on screening for prostate cancer with the prostate-specific antigen test. *CMAJ* **186**, 1225-1234 (2014).
 92. Shen, M.M. & Abate-Shen, C. Molecular genetics of prostate cancer: new prospects for old challenges. *Genes Dev* **24**, 1967-2000 (2010).
 93. Yard, D. PSA Testing: Why the U.S. and Europe Differ. *Renal & Urology News* **10**, 18 (2011).
 94. Felgueiras, J., Silva, J.V. & Fardilha, M. Prostate cancer: the need for biomarkers and new therapeutic targets. *J Zhejiang Univ Sci B* **15**, 16-42 (2014).
 95. Egevad, L., Allsbrook, W.C., Jr. & Epstein, J.I. Current practice of Gleason grading among genitourinary pathologists. *Hum Pathol* **36**, 5-9 (2005).
 96. Hanahan, D. & Weinberg, Robert A. Hallmarks of Cancer: The Next Generation. *Cell* **144**, 646-674 (2011).
 97. Antoun, S., *et al.* High subcutaneous adipose tissue predicts the prognosis in metastatic castration-resistant prostate cancer patients in post chemotherapy setting. *Eur J Cancer* **51**, 2570-2577 (2015).
 98. Kolonel, L.N., Nomura, A.M. & Cooney, R.V. Dietary fat and prostate cancer: current status. *J Natl Cancer Inst* **91**, 414-428 (1999).
 99. Di Sebastiano, K.M. & Mourtzakis, M. The role of dietary fat throughout the prostate cancer trajectory. *Nutrients* **6**, 6095-6109 (2014).
 100. Voelker, D.R. Lipid assembly into cell membranes. in *Biochemistry of Lipids, Lipoproteins and Membranes*, Vol. Volume 31 (eds. Dennis, E.V. & Jean, E.V.) 391-423 (Elsevier, 1996).
 101. Zhou, X., *et al.* Identification of plasma lipid biomarkers for prostate cancer by lipidomics and bioinformatics. *PLoS One* **7**, e48889 (2012).
 102. Lambeth, J.D. & Ryu, S.H. Glycerolipids in signal transduction. in *Biochemistry of Lipids, Lipoproteins and Membranes*, Vol. Volume 31 (eds. Dennis, E.V. & Jean, E.V.) 237-255 (Elsevier, 1996).
 103. Han, X., Yang, K. & Gross, R.W. Multi-dimensional mass spectrometry-based shotgun lipidomics and novel strategies for lipidomic analyses. *Mass Spectrom Rev* **31**, 134-178 (2012).

-
104. Fahy, E., *et al.* Update of the LIPID MAPS comprehensive classification system for lipids. *J Lipid Res* **50 Suppl**, S9-14 (2009).
 105. Spector, L.B. 12 Citrate Cleavage and Related Enzymes. in *The Enzymes*, Vol. 7 (ed. Boyer, P.D.) 357-389 (Academic Press, 1972).
 106. Brownsey, R.W. & Denton, R.M. 5 Acetyl-Coenzyme A Carboxylase. in *Control by Phosphorylation Part B - Specific Enzymes (II) Biological Processes*, Vol. 18 (eds. Boyer, P.D. & Krebs, E.G.) 123-146 (Academic Press, 1987).
 107. Wakil, S.J. & Stoops, J.K. 1 Structure and Mechanism of Fatty Acid Synthetase. in *Lipid Enzymology*, Vol. 16 (ed. Boyer, P.D.) 3-61 (Academic Press, 1983).
 108. Salati, L.M. & Goodridge, A.G. Fatty acid synthesis in eukaryotes. in *Biochemistry of Lipids, Lipoproteins and Membranes*, Vol. Volume 31 (eds. Dennis, E.V. & Jean, E.V.) 101-127 (Elsevier, 1996).
 109. Ferro, M., *et al.* The emerging role of obesity, diet and lipid metabolism in prostate cancer. *Future Oncol* **13**, 285-293 (2017).
 110. Holloway, P.W. 2 Fatty Acid Desaturation. in *Lipid Enzymology*, Vol. 16 (ed. Boyer, P.D.) 63-83 (Academic Press, 1983).
 111. Rodriguez-Cuenca, S., Whyte, L., Hagen, R., Vidal-Puig, A. & Fuller, M. Stearoyl-CoA Desaturase 1 Is a Key Determinant of Membrane Lipid Composition in 3T3-L1 Adipocytes. *PLoS One* **11**, e0162047 (2016).
 112. Pace-Asciak, C.R. & Smith, W.L. 16 Enzymes in the Biosynthesis and Catabolism of the Eicosanoids: Prostaglandins, Thromboxanes, Leukotrienes and Hydroxy Fatty Acids. in *Lipid Enzymology*, Vol. 16 (ed. Boyer, P.D.) 543-603 (Academic Press, 1983).
 113. Bell, R.M. & Coleman, R.A. 3 Enzymes of Triacylglycerol Formation in Mammals. in *Lipid Enzymology*, Vol. 16 (ed. Boyer, P.D.) 87-111 (Academic Press, 1983).
 114. Vance, D.E. Glycerolipid biosynthesis in eukaryotes. in *Biochemistry of Lipids, Lipoproteins and Membranes*, Vol. Volume 31 (eds. Dennis, E.V. & Jean, E.V.) 153-181 (Elsevier, 1996).
 115. Berry, K.A., *et al.* MALDI imaging of lipid biochemistry in tissues by mass spectrometry. *Chem Rev* **111**, 6491-6512 (2011).
 116. Christie, W.W. *Lipid analysis : isolation, separation, identification and lipidomic analysis*, (Oily Press, an imprint of PJ Barnes & Associates, Bridgwater, England, 2010).
 117. Reynolds, C.P., Maurer, B.J. & Kolesnick, R.N. Ceramide synthesis and metabolism as a target for cancer therapy. *Cancer Lett* **206**, 169-180 (2004).
 118. Lands, W.E. Metabolism of glycerolipides; a comparison of lecithin and triglyceride synthesis. *J Biol Chem* **231**, 883-888 (1958).
 119. Benesch, M.G.K., MacIntyre, I.T.K., McMullen, T.P.W. & Brindley, D.N. Coming of Age for Autotaxin and Lysophosphatidate Signaling: Clinical Applications for Preventing, Detecting and Targeting Tumor-Promoting Inflammation. *Cancers (Basel)* **10**(2018).
 120. McDermott, M.I., Wang, Y., Wakelam, M.J.O. & Bankaitis, V.A. Mammalian phospholipase D: Function, and therapeutics. *Prog Lipid Res* **78**, 101018 (2020).
 121. Smith, S.K.S. Milo, Ron: Cell biology by the numbers.(Brief article)(Book review). Vol. 53 1494 (American Library Association CHOICE, 2016).
 122. Nelson, D.L. *Lehninger principles of biochemistry*, (W.H. Freeman, New York, 2013).
 123. Suburu, J. & Chen, Y.Q. Lipids and prostate cancer. *Prostaglandins Other Lipid Mediat* **98**, 1-10 (2012).
 124. Balaban, S., *et al.* Extracellular Fatty Acids Are the Major Contributor to Lipid Synthesis in Prostate Cancer. *Mol Cancer Res* **17**, 949-962 (2019).
 125. Oh, H.Y., Leem, J., Yoon, S.J., Yoon, S. & Hong, S.J. Lipid raft cholesterol and genistein inhibit the cell viability of prostate cancer cells via the partial contribution of EGFR-Akt/p70S6k pathway and down-regulation of androgen receptor. *Biochem Biophys Res Commun* **393**, 319-324 (2010).

-
126. Simons, K. & Toomre, D. Lipid rafts and signal transduction. *Nat Rev Mol Cell Biol* **1**, 31-39 (2000).
 127. Freeman, M.R., Cinar, B. & Lu, M.L. Membrane rafts as potential sites of nongenomic hormonal signaling in prostate cancer. *Trends Endocrinol Metab* **16**, 273-279 (2005).
 128. Schlaepfer, I.R., *et al.* Lipid catabolism via CPT1 as a therapeutic target for prostate cancer. *Mol Cancer Ther* **13**, 2361-2371 (2014).
 129. Benedettini, E., Nguyen, P. & Loda, M. The pathogenesis of prostate cancer: from molecular to metabolic alterations. *Diagn Histopathol (Oxf)* **14**, 195-201 (2008).
 130. Hardwicke, M.A., *et al.* A human fatty acid synthase inhibitor binds beta-ketoacyl reductase in the keto-substrate site. *Nat Chem Biol* **10**, 774-779 (2014).
 131. Swinnen, J.V., Esquenet, M., Goossens, K., Heyns, W. & Verhoeven, G. Androgens stimulate fatty acid synthase in the human prostate cancer cell line LNCaP. *Cancer Res* **57**, 1086-1090 (1997).
 132. Schug, Z., *et al.* Acetyl-coA synthetase 2 promotes acetate utilization and maintains cell growth under metabolic stress. *Cancer & Metabolism* **2**, 09 (2014).
 133. Monaco, M.E., *et al.* Expression of Long-chain Fatty Acyl-CoA Synthetase 4 in Breast and Prostate Cancers Is Associated with Sex Steroid Hormone Receptor Negativity. *Translational oncology* **3**, 91-98 (2010).
 134. Al Kadhi, O., *et al.* Increased transcriptional and metabolic capacity for lipid metabolism in the peripheral zone of the prostate may underpin its increased susceptibility to cancer. *Oncotarget* **8**, 84902-84916 (2017).
 135. Heemers, H., *et al.* Androgens stimulate coordinated lipogenic gene expression in normal target tissues in vivo. *Mol Cell Endocrinol* **205**, 21-31 (2003).
 136. Deep, G. & Schlaepfer, I.R. Aberrant Lipid Metabolism Promotes Prostate Cancer: Role in Cell Survival under Hypoxia and Extracellular Vesicles Biogenesis. *Int J Mol Sci* **17**(2016).
 137. Swinnen, J.V., *et al.* Androgens, lipogenesis and prostate cancer. *J Steroid Biochem Mol Biol* **92**, 273-279 (2004).
 138. Butler, L.M., Centenera, M.M. & Swinnen, J.V. Androgen control of lipid metabolism in prostate cancer: novel insights and future applications. *Endocr Relat Cancer* **23**, R219-227 (2016).
 139. Baron, A., Migita, T., Tang, D. & Loda, M. Fatty acid synthase: a metabolic oncogene in prostate cancer? *J Cell Biochem* **91**, 47-53 (2004).
 140. Ranasinghe, W.K., *et al.* The role of hypoxia-inducible factor 1alpha in determining the properties of castrate-resistant prostate cancers. *PLoS One* **8**, e54251 (2013).
 141. Ranasinghe, W.K., *et al.* HIF1alpha expression under normoxia in prostate cancer--which pathways to target? *J Urol* **193**, 763-770 (2015).
 142. Furuta, E., *et al.* Fatty acid synthase gene is up-regulated by hypoxia via activation of Akt and sterol regulatory element binding protein-1. *Cancer Res* **68**, 1003-1011 (2008).
 143. Fukuchi, J., *et al.* Androgenic suppression of ATP-binding cassette transporter A1 expression in LNCaP human prostate cancer cells. *Cancer Res* **64**, 7682-7685 (2004).
 144. Swinnen, J.V., Van Veldhoven, P.P., Esquenet, M., Heyns, W. & Verhoeven, G. Androgens markedly stimulate the accumulation of neutral lipids in the human prostatic adenocarcinoma cell line LNCaP. *Endocrinology* **137**, 4468-4474 (1996).
 145. Heemers, H., *et al.* Identification of an androgen response element in intron 8 of the sterol regulatory element-binding protein cleavage-activating protein gene allowing direct regulation by the androgen receptor. *J Biol Chem* **279**, 30880-30887 (2004).
 146. Mah, C.Y., Nassar, Z.D., Swinnen, J.V. & Butler, L.M. Lipogenic effects of androgen signaling in normal and malignant prostate. *Asian J Urol* **7**, 258-270 (2020).

-
147. Huang, W.C., Li, X., Liu, J., Lin, J. & Chung, L.W. Activation of androgen receptor, lipogenesis, and oxidative stress converged by SREBP-1 is responsible for regulating growth and progression of prostate cancer cells. *Mol Cancer Res* **10**, 133-142 (2012).
 148. Poulou, N., *et al.* Genetics of lipid metabolism in prostate cancer. *Nat Genet* **50**, 169-171 (2018).
 149. Snaebjornsson, M.T., Janaki-Raman, S. & Schulze, A. Greasing the Wheels of the Cancer Machine: The Role of Lipid Metabolism in Cancer. *Cell Metab* **31**, 62-76 (2020).
 150. Vander Heiden, M.G. & DeBerardinis, R.J. Understanding the Intersections between Metabolism and Cancer Biology. *Cell* **168**, 657-669 (2017).
 151. Scupakova, K., *et al.* Spatial Systems Lipidomics Reveals Nonalcoholic Fatty Liver Disease Heterogeneity. *Anal Chem* **90**, 5130-5138 (2018).
 152. Huizing, L.R.S., *et al.* Development and evaluation of matrix application techniques for high throughput mass spectrometry imaging of tissues in the clinic. *Clinical Mass Spectrometry* **12**, 7-15 (2019).
 153. Ho, C.S., *et al.* Electrospray ionisation mass spectrometry: principles and clinical applications. *Clin Biochem Rev* **24**, 3-12 (2003).
 154. Morris, H.R., *et al.* High sensitivity collisionally-activated decomposition tandem mass spectrometry on a novel quadrupole/orthogonal-acceleration time-of-flight mass spectrometer. *Rapid Commun Mass Spectrom* **10**, 889-896 (1996).
 155. Griffiths, J. Secondary ion mass spectrometry. *Anal Chem* **80**, 7194-7197 (2008).
 156. Pottiez, G. Introduction to Mass Spectrometry. 1-7 (2015).
 157. Grant, R.P. High throughput automated LC-MS/MS analysis of endogenous small molecule biomarkers. *Clin Lab Med* **31**, 429-441 (2011).
 158. Klampfl, C.W. & Himmelsbach, M. Direct ionization methods in mass spectrometry: An overview. *Anal Chim Acta* **890**, 44-59 (2015).
 159. Agar, N.Y., Yang, H.W., Carroll, R.S., Black, P.M. & Agar, J.N. Matrix solution fixation: histology-compatible tissue preparation for MALDI mass spectrometry imaging. *Anal Chem* **79**, 7416-7423 (2007).
 160. Beckey, H.D. Field desorption mass spectrometry: A technique for the study of thermally unstable substances of low volatility. *International Journal of Mass Spectrometry and Ion Physics* **2**, 500-502 (1969).
 161. Posthumus, M.A., Kistemaker, P.G., Meuzelaar, H.L.C. & Ten Noever de Brauw, M.C. Laser desorption-mass spectrometry of polar nonvolatile bio-organic molecules. *Analytical Chemistry* **50**, 985-991 (2002).
 162. Hillenkamp, F., Unsöld, E., Kaufmann, R. & Nitsche, R. A high-sensitivity laser microprobe mass analyzer. *Applied Physics* **8**, 341-348 (1975).
 163. Karas, M., Bachmann, D. & Hillenkamp, F. Influence of the wavelength in high-irradiance ultraviolet laser desorption mass spectrometry of organic molecules. *Analytical Chemistry* **57**, 2935-2939 (2002).
 164. Karas, M., Bachmann, D., Bahr, U. & Hillenkamp, F. Matrix-assisted ultraviolet laser desorption of non-volatile compounds. *International Journal of Mass Spectrometry and Ion Processes* **78**, 53-68 (1987).
 165. Tanaka, K., *et al.* Protein and polymer analyses up to m/z 100 000 by laser ionization time-of-flight mass spectrometry. *Rapid Communications in Mass Spectrometry* **2**, 151-153 (1988).
 166. Dreisewerd, K. The desorption process in MALDI. *Chem Rev* **103**, 395-426 (2003).
 167. Harvey, D.J. Quantitative aspects of the matrix-assisted laser desorption mass spectrometry of complex oligosaccharides. *Rapid Commun Mass Spectrom* **7**, 614-619 (1993).

-
168. Knochenmuss, R. MALDI ionization mechanisms: the coupled photophysical and chemical dynamics model correctly predicts 'temperature'-selected spectra. *J Mass Spectrom* **48**, 998-1004 (2013).
169. Ehring, H., Karas, M. & Hillenkamp, F. Role of photoionization and photochemistry in ionization processes of organic molecules and relevance for matrix-assisted laser desorption ionization mass spectrometry. *Organic Mass Spectrometry* **27**, 472-480 (1992).
170. Karas, M., Gluckmann, M. & Schafer, J. Ionization in matrix-assisted laser desorption/ionization: singly charged molecular ions are the lucky survivors. *J Mass Spectrom* **35**, 1-12 (2000).
171. Karas, M. & Kruger, R. Ion formation in MALDI: the cluster ionization mechanism.(matrix-assisted laser desorption ionization). *Chemical Reviews* **103**, 427-439 (2003).
172. Knochenmuss, R. Ion formation mechanisms in UV-MALDI. *Analyst* **131**, 966-986 (2006).
173. Fenn, J.B., Mann, M., Meng, C.K., Wong, S.F. & Whitehouse, C.M. Electrospray ionization for mass spectrometry of large biomolecules. *Science* **246**, 64-71 (1989).
174. Yamashita, M. & Fenn, J.B. Electrospray ion source. Another variation on the free-jet theme. *The Journal of Physical Chemistry* **88**, 4451-4459 (1984).
175. Cole, R.B. & Cole, R.B. *Electrospray and MALDI Mass Spectrometry : Fundamentals, Instrumentation, Practicalities, and Biological Applications*, (John Wiley & Sons, Incorporated, Hoboken, UNITED STATES, 2009).
176. Dole, M., *et al.* Molecular Beams of Macroions. *The Journal of Chemical Physics* **49**, 2240-2249 (1968).
177. Iribarne, J.V. On the evaporation of small ions from charged droplets. *The Journal of Chemical Physics* **64**, 2287-2294 (1976).
178. Takats, Z., Wiseman, J.M., Gologan, B. & Cooks, R.G. Mass spectrometry sampling under ambient conditions with desorption electrospray ionization. *Science* **306**, 471-473 (2004).
179. Feider, C.L., *et al.* DESI Spray Stability in the Negative Ion Mode Is Dependent on Relative Humidity. *J Am Soc Mass Spectrom* **30**, 376-380 (2019).
180. van Meer, G., Voelker, D.R. & Feigenson, G.W. Membrane lipids: where they are and how they behave. *Nat Rev Mol Cell Biol* **9**, 112-124 (2008).
181. Leopold, J., Popkova, Y., Engel, K.M. & Schiller, J. Recent Developments of Useful MALDI Matrices for the Mass Spectrometric Characterization of Lipids. *Biomolecules* **8**(2018).
182. Betancourt, S.K., *et al.* Trimethylation Enhancement Using (13)C-Diazomethane: Gas-Phase Charge Inversion of Modified Phospholipid Cations for Enhanced Structural Characterization. *Anal Chem* **89**, 9452-9458 (2017).
183. Sun, G., *et al.* Matrix-assisted laser desorption/ionization time-of-flight mass spectrometric analysis of cellular glycerophospholipids enabled by multiplexed solvent dependent analyte--matrix interactions.(Author abstract)(Report). *Analytical Chemistry* **80**, 7576 (2008).
184. Shanta, S.R., *et al.* Binary matrix for MALDI imaging mass spectrometry of phospholipids in both ion modes. *Anal Chem* **83**, 1252-1259 (2011).
185. Zemski Berry, K.A., Murphy, R.C., Kosmider, B. & Mason, R.J. Lipidomic characterization and localization of phospholipids in the human lung. *J Lipid Res* **58**, 926-933 (2017).
186. March, R.E. An Introduction to Quadrupole Ion Trap Mass Spectrometry. *Journal of Mass Spectrometry* **32**, 351-369 (1997).

-
187. Haag, A.M. Mass Analyzers and Mass Spectrometers. in *Modern Proteomics – Sample Preparation, Analysis and Practical Applications* (eds. Mirzaei, H. & Carrasco, M.) 157-169 (Springer International Publishing, Cham, 2016).
 188. Xia, Y.Q., Miller, J.D., Bakhtiar, R., Franklin, R.B. & Liu, D.Q. Use of a quadrupole linear ion trap mass spectrometer in metabolite identification and bioanalysis. *Rapid Commun Mass Spectrom* **17**, 1137-1145 (2003).
 189. Van De Steene, J.C. & Lambert, W.E. Comparison of matrix effects in HPLC-MS/MS and UPLC-MS/MS analysis of nine basic pharmaceuticals in surface waters. *J Am Soc Mass Spectrom* **19**, 713-718 (2008).
 190. Zhang, L., Zhang, Y.D., Zhao, P. & Huang, S.M. Predicting drug-drug interactions: an FDA perspective. *AAPS J* **11**, 300-306 (2009).
 191. Beavis, R.C. & Chait, B.T. High-accuracy molecular mass determination of proteins using matrix-assisted laser desorption mass spectrometry. *Anal Chem* **62**, 1836-1840 (1990).
 192. Hercules, D.M. Franz Hillenkamp and Jasna Peter-Katalinic (Eds.): MALDI MS. A practical guide to instrumentation, methods and applications. *Analytical and Bioanalytical Chemistry* **392**, 565-566 (2008).
 193. Li, L. *MALDI Mass Spectrometry for Synthetic Polymer Analysis : Mass Spectrometry for Synthetic Polymer Analysis*, (John Wiley & Sons, Incorporated, Hoboken, UNITED STATES, 2009).
 194. Dodds, J.N. & Baker, E.S. Ion Mobility Spectrometry: Fundamental Concepts, Instrumentation, Applications, and the Road Ahead. *J Am Soc Mass Spectrom* **30**, 2185-2195 (2019).
 195. Morris, C.B., May, J.C., Leaptrot, K.L. & McLean, J.A. Evaluating Separation Selectivity and Collision Cross Section Measurement Reproducibility in Helium, Nitrogen, Argon, and Carbon Dioxide Drift Gases for Drift Tube Ion Mobility-Mass Spectrometry. *J Am Soc Mass Spectrom* **30**, 1059-1068 (2019).
 196. Zang, X., Monge, M.E., Gaul, D.A. & Fernandez, F.M. Flow Injection-Traveling-Wave Ion Mobility-Mass Spectrometry for Prostate-Cancer Metabolomics. *Anal Chem* **90**, 13767-13774 (2018).
 197. Vasilopoulou, C.G., *et al.* Trapped ion mobility spectrometry and PASEF enable in-depth lipidomics from minimal sample amounts. *Nat Commun* **11**, 331 (2020).
 198. Kliman, M., May, J.C. & McLean, J.A. Lipid analysis and lipidomics by structurally selective ion mobility-mass spectrometry. *Biochim Biophys Acta* **1811**, 935-945 (2011).
 199. Maccarone, A.T., *et al.* Characterization of acyl chain position in unsaturated phosphatidylcholines using differential mobility-mass spectrometry. *J Lipid Res* **55**, 1668-1677 (2014).
 200. Rohner, T.C., Staab, D. & Stoeckli, M. MALDI mass spectrometric imaging of biological tissue sections. *Mech Ageing Dev* **126**, 177-185 (2005).
 201. Song, X., *et al.* Virtual Calibration Quantitative Mass Spectrometry Imaging for Accurately Mapping Analytes across Heterogenous Biotissue. *Anal Chem* **91**, 2838-2846 (2019).
 202. Aichler, M. & Walch, A. MALDI Imaging mass spectrometry: current frontiers and perspectives in pathology research and practice. *Lab Invest* **95**, 422-431 (2015).
 203. Prideaux, B. & Stoeckli, M. Mass spectrometry imaging for drug distribution studies. *J Proteomics* **75**, 4999-5013 (2012).
 204. Spengler, B. PSD-MALDI Analysis of Peptides. in *Selected Topics in Mass Spectrometry in the Biomolecular Sciences* (eds. Caprioli, R.M., Malorni, A. & Sindona, G.) 377-398 (Springer Netherlands, Dordrecht, 1997).

-
205. Caprioli, R.M., Farmer, T.B. & Gile, J. Molecular imaging of biological samples: localization of peptides and proteins using MALDI-TOF MS. *Anal Chem* **69**, 4751-4760 (1997).
 206. Stoeckli, M., Farmer, T.B. & Caprioli, R.M. Automated mass spectrometry imaging with a matrix-assisted laser desorption ionization time-of-flight instrument. *J Am Soc Mass Spectrom* **10**, 67-71 (1999).
 207. Stoeckli, M., Staab, D., Staufenbiel, M., Wiederhold, K.-H. & Signor, L. Molecular imaging of amyloid β peptides in mouse brain sections using mass spectrometry. *Analytical Biochemistry* **311**, 33-39 (2002).
 208. McCombie, G., Staab, D., Stoeckli, M. & Knochenmuss, R. Spatial and spectral correlations in MALDI mass spectrometry images by clustering and multivariate analysis. *Anal Chem* **77**, 6118-6124 (2005).
 209. Klerk, L.A., Broersen, A., Fletcher, I.W., van Liere, R. & Heeren, R.M.A. Extended data analysis strategies for high resolution imaging MS: New methods to deal with extremely large image hyperspectral datasets. *International Journal of Mass Spectrometry* **260**, 222-236 (2007).
 210. Alexandrov, T., *et al.* Spatial segmentation of imaging mass spectrometry data with edge-preserving image denoising and clustering. *J Proteome Res* **9**, 6535-6546 (2010).
 211. Klerk, L.A., Altaalar, A.F.M., Froesch, M., McDonnell, L.A. & Heeren, R.M.A. Fast and automated large-area imaging MALDI mass spectrometry in microprobe and microscope mode. *International Journal of Mass Spectrometry* **285**, 19-25 (2009).
 212. Soltwisch, J., *et al.* MALDI mass spectrometry imaging in microscope mode with infrared lasers: bypassing the diffraction limits. *Anal Chem* **86**, 321-325 (2014).
 213. Snel, M.F. & Fuller, M. High-spatial resolution matrix-assisted laser desorption ionization imaging analysis of glucosylceramide in spleen sections from a mouse model of Gaucher disease. *Anal Chem* **82**, 3664-3670 (2010).
 214. Trim, P.J. & Snel, M.F. Small molecule MALDI MS imaging: Current technologies and future challenges. *Methods* **104**, 127-141 (2016).
 215. Angel, P.M., Spraggins, J.M., Baldwin, H.S. & Caprioli, R. Enhanced sensitivity for high spatial resolution lipid analysis by negative ion mode matrix assisted laser desorption ionization imaging mass spectrometry. *Anal Chem* **84**, 1557-1564 (2012).
 216. Schwamborn, K. & Caprioli, R.M. MALDI imaging mass spectrometry--painting molecular pictures. *Mol Oncol* **4**, 529-538 (2010).
 217. Campanella, G., *et al.* Clinical-grade computational pathology using weakly supervised deep learning on whole slide images. *Nat Med* **25**, 1301-1309 (2019).
 218. Gustafsson, J.O., Oehler, M.K., Ruskiewicz, A., McColl, S.R. & Hoffmann, P. MALDI Imaging Mass Spectrometry (MALDI-IMS)-application of spatial proteomics for ovarian cancer classification and diagnosis. *Int J Mol Sci* **12**, 773-794 (2011).
 219. Buck, A., *et al.* High-resolution MALDI-FT-ICR MS imaging for the analysis of metabolites from formalin-fixed, paraffin-embedded clinical tissue samples. *J Pathol* **237**, 123-132 (2015).
 220. Chaurand, P., *et al.* Imaging mass spectrometry of intact proteins from alcohol-preserved tissue specimens: bypassing formalin fixation. *J Proteome Res* **7**, 3543-3555 (2008).
 221. Haukaas, T.H., *et al.* Impact of Freezing Delay Time on Tissue Samples for Metabolomic Studies. *Front Oncol* **6**, 17 (2016).
 222. Fox, J.M., *et al.* Methodology for reliable and reproducible cryopreservation of human cervical tissue. *Cryobiology* **77**, 14-18 (2017).
 223. Shabihkhani, M., *et al.* The procurement, storage, and quality assurance of frozen blood and tissue biospecimens in pathology, biorepository, and biobank settings. *Clin Biochem* **47**, 258-266 (2014).

-
224. Dong, Y., *et al.* Sample Preparation for Mass Spectrometry Imaging of Plant Tissues: A Review. *Front Plant Sci* **7**, 60 (2016).
225. Enthaler, B., *et al.* Improved sample preparation for MALDI-MSI of endogenous compounds in skin tissue sections and mapping of exogenous active compounds subsequent to ex-vivo skin penetration. *Anal Bioanal Chem* **402**, 1159-1167 (2012).
226. Scupakova, K., *et al.* Cellular resolution in clinical MALDI mass spectrometry imaging: the latest advancements and current challenges. *Clin Chem Lab Med* **58**, 914-929 (2020).
227. Shimma, S. & Sugiura, Y. Effective Sample Preparations in Imaging Mass Spectrometry. *Mass Spectrom (Tokyo)* **3**, S0029 (2014).
228. Sugiura, Y., Shimma, S. & Setou, M. Thin Sectioning Improves the Peak Intensity and Signal-to-Noise Ratio in Direct Tissue Mass Spectrometry. *Journal of the Mass Spectrometry Society of Japan* **54**, 45-48 (2006).
229. Cazares, L.H., *et al.* Heat fixation inactivates viral and bacterial pathogens and is compatible with downstream MALDI mass spectrometry tissue imaging. *BMC Microbiol* **15**, 101 (2015).
230. Pirman, D.A. & Yost, R.A. Quantitative tandem mass spectrometric imaging of endogenous acetyl-L-carnitine from piglet brain tissue using an internal standard. *Anal Chem* **83**, 8575-8581 (2011).
231. Takai, N., Tanaka, Y. & Saji, H. Quantification of small molecule drugs in biological tissue sections by imaging mass spectrometry using surrogate tissue-based calibration standards. *Mass Spectrom (Tokyo)* **3**, A0025 (2014).
232. Zhou, J. & Lee, T.D. Charge state distribution shifting of protein ions observed in matrix-assisted laser desorption ionization mass spectrometry. *J Am Soc Mass Spectrom* **6**, 1183-1189 (1995).
233. Castro, J.A., Koster, C. & Wilkins, C. Matrix-assisted laser desorption/ionization of high-mass molecules by Fourier-transform mass spectrometry. *Rapid Commun Mass Spectrom* **6**, 239-241 (1992).
234. Perry, W.J., *et al.* Uncovering matrix effects on lipid analyses in MALDI imaging mass spectrometry experiments. *J Mass Spectrom* **55**, e4491 (2020).
235. Edwards, J.L. & Kennedy, R.T. Metabolomic analysis of eukaryotic tissue and prokaryotes using negative mode MALDI time-of-flight mass spectrometry. (Author Abstract). *Analytical Chemistry* **77**, 2201 (2005).
236. Billeci, T.M. & Stults, J.T. Tryptic mapping of recombinant proteins by matrix-assisted laser desorption/ionization mass spectrometry. *Anal Chem* **65**, 1709-1716 (1993).
237. Tsarbopoulos, A., *et al.* Comparative mapping of recombinant proteins and glycoproteins by plasma desorption and matrix-assisted laser desorption/ionization mass spectrometry. *Anal Chem* **66**, 2062-2070 (1994).
238. Guo, L., *et al.* Regulation of lipid A modifications by Salmonella typhimurium virulence genes phoP-phoQ. *Science* **276**, 250-253 (1997).
239. Gorman, J.J., Ferguson, B.L. & Nguyen, T.B. Use of 2,6-Dihydroxyacetophenone for Analysis of Fragile Peptides, Disulphide Bonding and Small Proteins by Matrix-assisted Laser Desorption/Ionization. *Rapid Communications in Mass Spectrometry* **10**, 529-536 (1996).
240. Lichtenwalter, K.G., *et al.* Approaches to functional genomics: potential of matrix-assisted laser desorption ionization–time of flight mass spectrometry combined with separation methods for the analysis of DNA in biological samples. *Journal of Chromatography B: Biomedical Sciences and Applications* **745**, 231-241 (2000).
241. Fischer, W.H., Rivier, J.E. & Craig, A.G. In situ reduction suitable for matrix-assisted laser desorption/ionization and liquid secondary ionization using tris(2-carboxyethyl)phosphine. *Rapid Commun Mass Spectrom* **7**, 225-228 (1993).

-
242. Inutan, E.D., Wager-Miller, J., Mackie, K. & Trimpin, S. Laserspray ionization imaging of multiply charged ions using a commercial vacuum MALDI ion source. *Anal Chem* **84**, 9079-9084 (2012).
243. Trimpin, S., *et al.* Extending the laserspray ionization concept to produce highly charged ions at high vacuum on a time-of-flight mass analyzer. *Analytical Chemistry* **83**, 5469 (2011).
244. Heudt, L., *et al.* Raman spectroscopy and laser desorption mass spectrometry for minimal destructive forensic analysis of black and color inkjet printed documents. *Forensic Sci Int* **219**, 64-75 (2012).
245. Yamagaki, T. & Nakanishi, H. A new technique distinguishing alpha2-3 sialyl linkage from alpha2-6 linkage in sialyllactoses and sialyl-N-acetyllactosamines by post-source decay fragmentation method of MALDI-TOF mass spectrometry. *Glycoconj J* **16**, 385-389 (1999).
246. Scott, A.J., *et al.* Norharmine Matrix Enhances Detection of Endotoxin by MALDI-MS for Simultaneous Profiling of Pathogen, Host, and Vector Systems. *Pathog Dis* **74**(2016).
247. Nonami, H., Tanaka, K., Fukuyama, Y. & Erra-Balsells, R. β -Carboline alkaloids as matrices for UV-matrix-assisted laser desorption/ionization time-of-flight mass spectrometry in positive and negative ion modes. Analysis of proteins of high molecular mass, and of cyclic and acyclic oligosaccharides. *Rapid Communications in Mass Spectrometry* **12**, 285-296 (1998).
248. Wiegelmann, M., Dreisewerd, K. & Soltwisch, J. Influence of the Laser Spot Size, Focal Beam Profile, and Tissue Type on the Lipid Signals Obtained by MALDI-MS Imaging in Oversampling Mode. *J Am Soc Mass Spectrom* **27**, 1952-1964 (2016).
249. Gemperline, E., Rawson, S. & Li, L. Optimization and comparison of multiple MALDI matrix application methods for small molecule mass spectrometric imaging. *Anal Chem* **86**, 10030-10035 (2014).
250. Caughlin, S., Park, D.H., Yeung, K.K., Cechetto, D.F. & Whitehead, S.N. Sublimation of DAN Matrix for the Detection and Visualization of Gangliosides in Rat Brain Tissue for MALDI Imaging Mass Spectrometry. *J Vis Exp*, 55254 (2017).
251. Price, D.M., Bashir, S. & Derrick, P.R. Sublimation properties of x,y-dihydroxybenzoic acid isomers as model matrix assisted laser desorption ionisation (MALDI) matrices. *Thermochimica Acta* **327**, 167-171 (1999).
252. Mounfield, W.P., 3rd & Garrett, T.J. Automated MALDI matrix coating system for multiple tissue samples for imaging mass spectrometry. *J Am Soc Mass Spectrom* **23**, 563-569 (2012).
253. Mounfield, W.P. & Garrett, T.J. Automated MALDI Matrix Coating System for Multiple Tissue Samples for Imaging Mass Spectrometry. *Journal of the American Society for Mass Spectrometry* **23**, 563-569 (2012).
254. Poncelet, L., Ait-Belkacem, R., Marillier, R., Gomes, B. & Stauber, J. Target exposure and pharmacodynamics study of the indoleamine 2,3-dioxygenase-1 (IDO-1) inhibitor epacadostat in the CT26 mouse tumor model. *J Pharm Biomed Anal* **170**, 220-227 (2019).
255. Randall, E.C., *et al.* Integrated mapping of pharmacokinetics and pharmacodynamics in a patient-derived xenograft model of glioblastoma. *Nat Commun* **9**, 4904 (2018).
256. Bakker, B., *et al.* Oxygen regulates lipid profiles in human primary chondrocyte cultures. *Osteoarthritis and Cartilage* **24**, S456-S457 (2016).
257. Dilillo, M., *et al.* Ultra-High Mass Resolution MALDI Imaging Mass Spectrometry of Proteins and Metabolites in a Mouse Model of Glioblastoma. *Sci Rep* **7**, 603 (2017).
258. Webb, C. History of Gas Lasers, Part 2: Pulsed Gas Lasers. *Optics and Photonics News* **21**(2010).

-
259. Horning, E.C., *et al.* Development and use of analytical systems based on mass spectrometry. *Clinical Chemistry* **23**, 13 (1977).
260. Abramczyk, H. *Introduction to Laser Spectroscopy*, (Elsevier Science & Technology, Oxford, NETHERLANDS, THE, 2005).
261. Trim, P.J., *et al.* Introduction of a 20 kHz Nd:YVO₄ laser into a hybrid quadrupole time-of-flight mass spectrometer for MALDI-MS imaging. *Anal Bioanal Chem* **397**, 3409-3419 (2010).
262. Byer, R.L. Diode laser--pumped solid-state lasers. *Science* **239**, 742-747 (1988).
263. Kondo, K., *et al.* Demonstration of long-term reliability of a 266-nm, continuous-wave, frequency-quadrupled solid-state laser using beta-BaB(2)O(4). *Opt Lett* **23**, 195-197 (1998).
264. Prentice, B.M., Chumbley, C.W. & Caprioli, R.M. High-speed MALDI MS/MS imaging mass spectrometry using continuous raster sampling. *J Mass Spectrom* **50**, 703-710 (2015).
265. Steven, R.T., Palmer, A.D. & Bunch, J. Fluorometric beam profiling of UV MALDI lasers. *J Am Soc Mass Spectrom* **24**, 1146-1152 (2013).
266. Robinson, K.N., Steven, R.T., Race, A.M. & Bunch, J. The Influence of MS Imaging Parameters on UV-MALDI Desorption and Ion Yield. *J Am Soc Mass Spectrom* **30**, 1284-1293 (2019).
267. Holle, A., Haase, A., Kayser, M. & Hohndorf, J. Optimizing UV laser focus profiles for improved MALDI performance. *J Mass Spectrom* **41**, 705-716 (2006).
268. Gross, R.W. The evolution of lipidomics through space and time. *Biochim Biophys Acta Mol Cell Biol Lipids* **1862**, 731-739 (2017).
269. Zullig, T. & Kofeler, H.C. High Resolution Mass Spectrometry in Lipidomics. *Mass Spectrom Rev* (2020).
270. Li, A., Hines, K.M. & Xu, L. Lipidomics by HILIC-Ion Mobility-Mass Spectrometry. in *Ion Mobility-Mass Spectrometry : Methods and Protocols* (eds. Paglia, G. & Astarita, G.) 119-132 (Springer US, New York, NY, 2020).
271. Folch, J., Lees, M. & Sloane Stanley, G.H. A simple method for the isolation and purification of total lipides from animal tissues. *J Biol Chem* **226**, 497-509 (1957).
272. Bligh, E.G. & Dyer, W.J. A rapid method of total lipid extraction and purification. *Can J Biochem Physiol* **37**, 911-917 (1959).
273. Zangarini, M., *et al.* Development and validation of LC-MS/MS with in-source collision-induced dissociation for the quantification of pegcantratinib in human skin tumors. *Bioanalysis* **9**, 279-288 (2017).
274. Yang, S., Yang, Z. & Wang, P.G. Bioanalysis for precision medicine. *Bioanalysis* **11**, 1039-1043 (2019).
275. Obach, R.S., *et al.* The prediction of human pharmacokinetic parameters from preclinical and in vitro metabolism data. *J Pharmacol Exp Ther* **283**, 46-58 (1997).
276. Grime, K.H., Barton, P. & McGinnity, D.F. Application of in silico, in vitro and preclinical pharmacokinetic data for the effective and efficient prediction of human pharmacokinetics. *Mol Pharm* **10**, 1191-1206 (2013).
277. Yang, W., Freeman, M.R. & Kyprianou, N. Personalization of prostate cancer therapy through phosphoproteomics. *Nat Rev Urol* **15**, 483-497 (2018).
278. Becher, F., *et al.* A simple and rapid LC-MS/MS method for therapeutic drug monitoring of cetuximab: a GPCO-UNICANCER proof of concept study in head-and-neck cancer patients. *Sci Rep* **7**, 2714 (2017).
279. Eberlin, L.S., *et al.* Cholesterol sulfate imaging in human prostate cancer tissue by desorption electrospray ionization mass spectrometry. *Anal Chem* **82**, 3430-3434 (2010).

-
280. Cimino, J., *et al.* Towards lipidomics of low-abundant species for exploring tumor heterogeneity guided by high-resolution mass spectrometry imaging. *Int J Mol Sci* **14**, 24560-24580 (2013).
 281. Pirman, D.A., *et al.* Changes in cancer cell metabolism revealed by direct sample analysis with MALDI mass spectrometry. *PLoS One* **8**, e61379 (2013).
 282. Mirnezami, R., *et al.* Chemical mapping of the colorectal cancer microenvironment via MALDI imaging mass spectrometry (MALDI-MSI) reveals novel cancer-associated field effects. *Mol Oncol* **8**, 39-49 (2014).
 283. Goto, T., *et al.* The expression profile of phosphatidylinositol in high spatial resolution imaging mass spectrometry as a potential biomarker for prostate cancer. *PLoS One* **9**, e90242 (2014).
 284. Goto, T., *et al.* Decreased expression of lysophosphatidylcholine (16:0/OH) in high resolution imaging mass spectrometry independently predicts biochemical recurrence after surgical treatment for prostate cancer. *Prostate* **75**, 1821-1830 (2015).
 285. Hall, Z., *et al.* Myc Expression Drives Aberrant Lipid Metabolism in Lung Cancer. *Cancer Res* **76**, 4608-4618 (2016).
 286. Sans, M., *et al.* Metabolic Markers and Statistical Prediction of Serous Ovarian Cancer Aggressiveness by Ambient Ionization Mass Spectrometry Imaging. *Cancer Res* **77**, 2903-2913 (2017).
 287. Sun, C., *et al.* Spatially resolved metabolomics to discover tumor-associated metabolic alterations. *Proc Natl Acad Sci U S A* **116**, 52-57 (2019).
 288. Tousignant, K.D., *et al.* Lipid Uptake Is an Androgen-Enhanced Lipid Supply Pathway Associated with Prostate Cancer Disease Progression and Bone Metastasis. *Mol Cancer Res* **17**, 1166-1179 (2019).
 289. Cucchi, D., *et al.* Fatty acids - from energy substrates to key regulators of cell survival, proliferation and effector function. *Cell Stress* **4**, 9-23 (2019).
 290. Bandu, R., Mok, H.J. & Kim, K.P. Phospholipids as cancer biomarkers: Mass spectrometry-based analysis. *Mass Spectrom Rev* **37**, 107-138 (2018).
 291. Perrotti, F., *et al.* Advances in Lipidomics for Cancer Biomarkers Discovery. *Int J Mol Sci* **17**(2016).
 292. Baade, P.D., Youlden, D.R. & Krnjacki, L.J. International epidemiology of prostate cancer: geographical distribution and secular trends. *Mol Nutr Food Res* **53**, 171-184 (2009).
 293. Jemal, A., Siegel, R., Xu, J. & Ward, E. Cancer statistics, 2010. *CA: a cancer journal for clinicians* **60**, 277-300 (2010).
 294. Barfeld, S.J., Itkonen, H.M., Urbanucci, A. & Mills, I.G. Androgen-regulated metabolism and biosynthesis in prostate cancer. *Endocr Relat Cancer* **21**, T57-66 (2014).
 295. Corona, G., Baldi, E. & Maggi, M. Androgen regulation of prostate cancer: where are we now? *J Endocrinol Invest* **34**, 232-243 (2011).
 296. Swinnen, J.V., *et al.* Selective activation of the fatty acid synthesis pathway in human prostate cancer. *Int J Cancer* **88**, 176-179 (2000).
 297. Hanahan, D. & Weinberg, R.A. Hallmarks of cancer: the next generation. *Cell* **144**, 646-674 (2011).
 298. Fritz, V., *et al.* Abrogation of de novo lipogenesis by stearoyl-CoA desaturase 1 inhibition interferes with oncogenic signaling and blocks prostate cancer progression in mice. *Mol Cancer Ther* **9**, 1740-1754 (2010).
 299. Semenas, J., *et al.* The role of PI3K/AKT-related PIP5K1alpha and the discovery of its selective inhibitor for treatment of advanced prostate cancer. *Proc Natl Acad Sci U S A* **111**, E3689-3698 (2014).
 300. Zadra, G., *et al.* Inhibition of de novo lipogenesis targets androgen receptor signaling in castration-resistant prostate cancer. *Proc Natl Acad Sci U S A* **116**, 631-640 (2019).

-
301. Dai, C., *et al.* Direct Metabolic Interrogation of Dihydrotestosterone Biosynthesis from Adrenal Precursors in Primary Prostatectomy Tissues. *Clin Cancer Res* **23**, 6351-6362 (2017).
302. Paton, C.M. & Ntambi, J.M. Biochemical and physiological function of stearyl-CoA desaturase. *Am J Physiol Endocrinol Metab* **297**, E28-37 (2009).
303. Marien, E., *et al.* Phospholipid profiling identifies acyl chain elongation as a ubiquitous trait and potential target for the treatment of lung squamous cell carcinoma. *Oncotarget* **7**, 12582-12597 (2016).
304. Moon, J.S., *et al.* Androgen stimulates glycolysis for de novo lipid synthesis by increasing the activities of hexokinase 2 and 6-phosphofructo-2-kinase/fructose-2,6-bisphosphatase 2 in prostate cancer cells. *Biochem J* **433**, 225-233 (2011).
305. Li, X., Chen, Y.T., Hu, P. & Huang, W.C. Fatostatin displays high antitumor activity in prostate cancer by blocking SREBP-regulated metabolic pathways and androgen receptor signaling. *Mol Cancer Ther* **13**, 855-866 (2014).
306. Rysman, E., *et al.* De novo lipogenesis protects cancer cells from free radicals and chemotherapeutics by promoting membrane lipid saturation. *Cancer Res* **70**, 8117-8126 (2010).
307. Huang, S.Y., Huang, G.J., Hsieh, P.F., Wu, H.C. & Huang, W.C. Osajin displays potential antiprostata cancer efficacy via impairment of fatty acid synthase and androgen receptor expression. *Prostate* **79**, 1543-1552 (2019).
308. Singh, K.B., Hahm, E.R., Pore, S.K. & Singh, S.V. Leelamine Is a Novel Lipogenesis Inhibitor in Prostate Cancer Cells In Vitro and In Vivo. *Mol Cancer Ther* **18**, 1800-1810 (2019).
309. Chen, M., *et al.* An aberrant SREBP-dependent lipogenic program promotes metastatic prostate cancer. *Nat Genet* **50**, 206-218 (2018).
310. Ashcroft, A.E. Fast atom/ion bombardment ionization, continuous flow fast atom/ion bombardment ionization. 97-121 (1997).
311. Han, X. & Gross, R.W. Electrospray ionization mass spectroscopic analysis of human erythrocyte plasma membrane phospholipids. *Proc Natl Acad Sci U S A* **91**, 10635-10639 (1994).
312. Han, X. & Gross, R.W. Global analyses of cellular lipidomes directly from crude extracts of biological samples by ESI mass spectrometry: a bridge to lipidomics. *J Lipid Res* **44**, 1071-1079 (2003).
313. Hsu, F.F. Mass spectrometry-based shotgun lipidomics - a critical review from the technical point of view. *Anal Bioanal Chem* **410**, 6387-6409 (2018).
314. Chen, J., Green, K.B. & Nichols, K.K. Quantitative profiling of major neutral lipid classes in human meibum by direct infusion electrospray ionization mass spectrometry. *Invest Ophthalmol Vis Sci* **54**, 5730-5753 (2013).
315. Najdekr, L., *et al.* Influence of Mass Resolving Power in Orbital Ion-Trap Mass Spectrometry-Based Metabolomics. *Anal Chem* **88**, 11429-11435 (2016).
316. Southam, A.D., Weber, R.J., Engel, J., Jones, M.R. & Viant, M.R. A complete workflow for high-resolution spectral-stitching nanoelectrospray direct-infusion mass-spectrometry-based metabolomics and lipidomics. *Nat Protoc* **12**, 310-328 (2016).
317. Rojas-Betancourt, S., Stutzman, J.R., Londry, F.A., Blanksby, S.J. & McLuckey, S.A. Gas-Phase Chemical Separation of Phosphatidylcholine and Phosphatidylethanolamine Cations via Charge Inversion Ion/Ion Chemistry. *Anal Chem* **87**, 11255-11262 (2015).
318. Glaser, P.E. & Gross, R.W. Plasmenylethanolamine facilitates rapid membrane fusion: a stopped-flow kinetic investigation correlating the propensity of a major plasma membrane constituent to adopt an HII phase with its ability to promote membrane fusion. *Biochemistry* **33**, 5805-5812 (1994).

-
319. Williams, P.E., Klein, D.R., Greer, S.M. & Brodbelt, J.S. Pinpointing Double Bond and sn-Positions in Glycerophospholipids via Hybrid 193 nm Ultraviolet Photodissociation (UVPD) Mass Spectrometry. *J Am Chem Soc* **139**, 15681-15690 (2017).
320. Murphy, R.C., Okuno, T., Johnson, C.A. & Barkley, R.M. Determination of Double Bond Positions in Polyunsaturated Fatty Acids Using the Photochemical Paterno-Buchi Reaction with Acetone and Tandem Mass Spectrometry. *Anal Chem* **89**, 8545-8553 (2017).
321. Marshall, D.L., *et al.* Sequential Collision- and Ozone-Induced Dissociation Enables Assignment of Relative Acyl Chain Position in Triacylglycerols. *Anal Chem* **88**, 2685-2692 (2016).
322. Sun, Y., Saito, K. & Saito, Y. Lipid Profile Characterization and Lipoprotein Comparison of Extracellular Vesicles from Human Plasma and Serum. *Metabolites* **9**(2019).
323. Porta Siegel, T., Ekroos, K. & Ellis, S.R. Reshaping Lipid Biochemistry by Pushing Barriers in Structural Lipidomics. *Angew Chem Int Ed Engl* **58**, 6492-6501 (2019).
324. Deutsch, M.J., Schriever, S.C., Roscher, A.A. & Ensenuer, R. Digital image analysis approach for lipid droplet size quantitation of Oil Red O-stained cultured cells. *Anal Biochem* **445**, 87-89 (2014).
325. Mehlem, A., Hagberg, C.E., Muhl, L., Eriksson, U. & Falkevall, A. Imaging of neutral lipids by oil red O for analyzing the metabolic status in health and disease. *Nat Protoc* **8**, 1149-1154 (2013).
326. Gessel, M.M., Norris, J.L. & Caprioli, R.M. MALDI imaging mass spectrometry: spatial molecular analysis to enable a new age of discovery. *J Proteomics* **107**, 71-82 (2014).
327. Spengler, B. & Cotter, R.J. Ultraviolet laser desorption/ionization mass spectrometry of proteins above 100,000 daltons by pulsed ion extraction time-of-flight analysis. *Anal Chem* **62**, 793-796 (1990).
328. Trim, P.J., *et al.* Matrix-assisted laser desorption/ionization-ion mobility separation-mass spectrometry imaging of vinblastine in whole body tissue sections. *Anal Chem* **80**, 8628-8634 (2008).
329. Mutuku, S.M., *et al.* Evaluation of Small Molecule Drug Uptake in Patient-Derived Prostate Cancer Explants by Mass Spectrometry. *Sci Rep* **9**, 15008 (2019).
330. Girod, M., Shi, Y., Cheng, J.X. & Cooks, R.G. Desorption electrospray ionization imaging mass spectrometry of lipids in rat spinal cord. *J Am Soc Mass Spectrom* **21**, 1177-1189 (2010).
331. Duncan, K.D., *et al.* Quantitative Mass Spectrometry Imaging of Prostaglandins as Silver Ion Adducts with Nanospray Desorption Electrospray Ionization. *Anal Chem* **90**, 7246-7252 (2018).
332. Nemes, P., Barton, A.A., Li, Y. & Vertes, A. Ambient molecular imaging and depth profiling of live tissue by infrared laser ablation electrospray ionization mass spectrometry. *Anal Chem* **80**, 4575-4582 (2008).
333. Piehowski, P.D., *et al.* Time-of-flight secondary ion mass spectrometry imaging of subcellular lipid heterogeneity: Poisson counting and spatial resolution. *Anal Chem* **81**, 5593-5602 (2009).
334. Frame, F.M., *et al.* Tumor heterogeneity and therapy resistance - implications for future treatments of prostate cancer. *Journal of Cancer Metastasis and Treatment; Vol 3, No 12 (2017)* (2017).
335. Schrimpe-Rutledge, A.C., Codreanu, S.G., Sherrod, S.D. & McLean, J.A. Untargeted Metabolomics Strategies-Challenges and Emerging Directions. *J Am Soc Mass Spectrom* **27**, 1897-1905 (2016).
336. Randall, E.C., *et al.* Molecular Characterization of Prostate Cancer with Associated Gleason Score Using Mass Spectrometry Imaging. *Mol Cancer Res* **17**, 1155-1165 (2019).

-
337. Bowman, A.P., *et al.* Ultra-High Mass Resolving Power, Mass Accuracy, and Dynamic Range MALDI Mass Spectrometry Imaging by 21-T FT-ICR MS. *Anal Chem* **92**, 3133-3142 (2020).
338. Ellis, S.R., *et al.* Automated, parallel mass spectrometry imaging and structural identification of lipids. *Nat Methods* **15**, 515-518 (2018).
339. Leaptrot, K.L., May, J.C., Dodds, J.N. & McLean, J.A. Ion mobility conformational lipid atlas for high confidence lipidomics. *Nat Commun* **10**, 985 (2019).
340. Culig, Z., Hobisch, A., Bartsch, G. & Klocker, H. Expression and function of androgen receptor in carcinoma of the prostate. *Microscopy research and technique* **51**, 447-455 (2000).
341. Sieh, S., *et al.* Phenotypic characterization of prostate cancer LNCaP cells cultured within a bioengineered microenvironment. *PLoS One* **7**, e40217 (2012).
342. Huang, W.C., Zhau, H.E. & Chung, L.W. Androgen receptor survival signaling is blocked by anti-beta2-microglobulin monoclonal antibody via a MAPK/lipogenic pathway in human prostate cancer cells. *J Biol Chem* **285**, 7947-7956 (2010).
343. Li, X., *et al.* MicroRNA-185 and 342 inhibit tumorigenicity and induce apoptosis through blockade of the SREBP metabolic pathway in prostate cancer cells. *PLoS One* **8**, e70987 (2013).
344. Cunningham, D. & You, Z. In vitro and in vivo model systems used in prostate cancer research. *Journal of Biological Methods; Vol 2, No 1 (2015)* (2015).
345. Risbridger, G.P., Toivanen, R. & Taylor, R.A. Preclinical Models of Prostate Cancer: Patient-Derived Xenografts, Organoids, and Other Explant Models. *Cold Spring Harb Perspect Med* **8**(2018).
346. Zhou, X., *et al.* Effect of PTEN loss on metabolic reprogramming in prostate cancer cells. *Oncol Lett* **17**, 2856-2866 (2019).
347. Burch, T.C., *et al.* Comparative Metabolomic and Lipidomic Analysis of Phenotype Stratified Prostate Cells. *PLoS One* **10**, e0134206 (2015).
348. Sorvina, A., *et al.* Lipid profiles of prostate cancer cells. *Oncotarget* **9**, 35541-35552 (2018).
349. Gasper, R., Vandenbussche, G. & Goormaghtigh, E. Ouabain-induced modifications of prostate cancer cell lipidome investigated with mass spectrometry and FTIR spectroscopy. *Biochim Biophys Acta* **1808**, 597-605 (2011).
350. Jeong, R.U., Lim, S., Kim, M.O. & Moon, M.H. Effect of D-allose on prostate cancer cell lines: phospholipid profiling by nanoflow liquid chromatography-tandem mass spectrometry. *Anal Bioanal Chem* **401**, 689-698 (2011).
351. Li, J. & Cheng, J.X. Direct visualization of de novo lipogenesis in single living cells. *Sci Rep* **4**, 6807 (2014).
352. Duscharla, D., *et al.* Prostate Cancer Associated Lipid Signatures in Serum Studied by ESI-Tandem Mass Spectrometry as Potential New Biomarkers. *PLoS One* **11**, e0150253 (2016).
353. Lih, F.B., Titus, M.A., Mohler, J.L. & Tomer, K.B. Atmospheric pressure photoionization tandem mass spectrometry of androgens in prostate cancer. *Anal Chem* **82**, 6000-6007 (2010).
354. Dalmau, N., Jaumot, J., Tauler, R. & Bedia, C. Epithelial-to-mesenchymal transition involves triacylglycerol accumulation in DU145 prostate cancer cells. *Mol Biosyst* **11**, 3397-3406 (2015).
355. Peak, T.C., *et al.* Exosomes secreted by placental stem cells selectively inhibit growth of aggressive prostate cancer cells. *Biochem Biophys Res Commun* **499**, 1004-1010 (2018).
356. Brzozowski, J.S., *et al.* Lipidomic profiling of extracellular vesicles derived from prostate and prostate cancer cell lines. *Lipids Health Dis* **17**, 211 (2018).

-
357. Skotland, T., *et al.* Molecular lipid species in urinary exosomes as potential prostate cancer biomarkers. *Eur J Cancer* **70**, 122-132 (2017).
358. Gieniec, K.A., Butler, L.M., Worthley, D.L. & Woods, S.L. Cancer-associated fibroblasts-heroes or villains? *Br J Cancer* **121**, 293-302 (2019).
359. Centenera, M.M., Raj, G.V., Knudsen, K.E., Tilley, W.D. & Butler, L.M. Ex vivo culture of human prostate tissue and drug development. *Nat Rev Urol* **10**, 483-487 (2013).
360. Okada, S., Vaeteewoottacharn, K. & Kariya, R. Application of Highly Immunocompromised Mice for the Establishment of Patient-Derived Xenograft (PDX) Models. *Cells* **8**(2019).
361. Lin, D., *et al.* Next generation patient-derived prostate cancer xenograft models. *Asian J Androl* **16**, 407-412 (2014).
362. Centenera, M.M., *et al.* A patient-derived explant (PDE) model of hormone-dependent cancer. *Mol Oncol* **12**, 1608-1622 (2018).
363. Choi, Y., *et al.* Studying cancer immunotherapy using patient-derived xenografts (PDXs) in humanized mice. *Exp Mol Med* **50**, 99 (2018).
364. Longo, J., *et al.* An actionable sterol-regulated feedback loop modulates statin sensitivity in prostate cancer. *Mol Metab* **25**, 119-130 (2019).
365. Gwinn, D.M. & Shaw, R.J. AMPK Control of mTOR Signaling and Growth. in *Structure, Function and Regulation of Tor Complexes from Yeasts to Mammals Part B*, Vol. 28 (eds. Tamanoi, F. & Hall, M.N.) 49-75 (Academic Press, 2010).
366. Yue, S., *et al.* Cholesteryl ester accumulation induced by PTEN loss and PI3K/AKT activation underlies human prostate cancer aggressiveness. *Cell Metab* **19**, 393-406 (2014).
367. Li, J., *et al.* Integration of lipidomics and transcriptomics unravels aberrant lipid metabolism and defines cholesteryl oleate as potential biomarker of prostate cancer. *Sci Rep* **6**, 20984 (2016).
368. Sapandowski, A., *et al.* Cardiolipin composition correlates with prostate cancer cell proliferation. *Mol Cell Biochem* **410**, 175-185 (2015).
369. Adada, M., Luberto, C. & Canals, D. Inhibitors of the sphingomyelin cycle: Sphingomyelin synthases and sphingomyelinases. *Chem Phys Lipids* **197**, 45-59 (2016).
370. Lin, H.M., *et al.* A distinct plasma lipid signature associated with poor prognosis in castration-resistant prostate cancer. *Int J Cancer* **141**, 2112-2120 (2017).
371. Harvald, E.B., Olsen, A.S. & Faergeman, N.J. Autophagy in the light of sphingolipid metabolism. *Apoptosis* **20**, 658-670 (2015).
372. Gault, C.R., Obeid, L.M. & Hannun, Y.A. An overview of sphingolipid metabolism: from synthesis to breakdown. *Advances in experimental medicine and biology* **688**, 1-23 (2010).
373. Turner, L.S., *et al.* Autophagy is increased in prostate cancer cells overexpressing acid ceramidase and enhances resistance to C6 ceramide. *Prostate Cancer Prostatic Dis* **14**, 30-37 (2011).
374. Kus, G., Kabadere, S., Uyar, R. & Kutlu, H.M. Induction of apoptosis in prostate cancer cells by the novel ceramidase inhibitor ceranib-2. *In Vitro Cell Dev Biol Anim* **51**, 1056-1063 (2015).
375. Kiebish, M.A., *et al.* Multi-omic serum biomarkers for prognosis of disease progression in prostate cancer. *J Transl Med* **18**, 10 (2020).
376. Pelton, K., Freeman, M.R. & Solomon, K.R. Cholesterol and prostate cancer. *Curr Opin Pharmacol* **12**, 751-759 (2012).
377. Jiang, S.Y., *et al.* Discovery of a potent HMG-CoA reductase degrader that eliminates statin-induced reductase accumulation and lowers cholesterol. *Nat Commun* **9**, 5138 (2018).

-
378. Cinar, B., Mukhopadhyay, N.K., Meng, G. & Freeman, M.R. Phosphoinositide 3-kinase-independent non-genomic signals transit from the androgen receptor to Akt1 in membrane raft microdomains. *J Biol Chem* **282**, 29584-29593 (2007).
379. Schnoeller, T.J., Jentzmik, F., Schrader, A.J. & Steinestel, J. Influence of serum cholesterol level and statin treatment on prostate cancer aggressiveness. *Oncotarget* **8**, 47110-47120 (2017).
380. Knobeler, M. & Wanczek, K.P. In-cell matrix-assisted laser desorption-ionization fourier transform ion cyclotron resonance mass spectrometry. *J Am Soc Mass Spectrom* **7**, 1026-1033 (1996).
381. Juhasz, P., Costello, C.E. & Biemann, K. Matrix-assisted laser desorption ionization mass spectrometry with 2-(4-hydroxyphenylazo)benzoic acid matrix. *J Am Soc Mass Spectrom* **4**, 399-409 (1993).
382. Baenke, F., Peck, B., Miess, H. & Schulze, A. Hooked on fat: the role of lipid synthesis in cancer metabolism and tumour development. *Dis Model Mech* **6**, 1353-1363 (2013).
383. Wang, X., *et al.* Metabolomic profiling of prostate cancer by matrix assisted laser desorption/ionization-Fourier transform ion cyclotron resonance mass spectrometry imaging using Matrix Coating Assisted by an Electric Field (MCAEF). *Biochim Biophys Acta Proteins Proteom* **1865**, 755-767 (2017).
384. Iglesias-Gato, D., *et al.* The Proteome of Primary Prostate Cancer. *Eur Urol* **69**, 942-952 (2016).
385. Morse, N., *et al.* Reliable identification of prostate cancer using mass spectrometry metabolomic imaging in needle core biopsies. *Lab Invest* **99**, 1561-1571 (2019).
386. Banerjee, S., *et al.* Diagnosis of prostate cancer by desorption electrospray ionization mass spectrometric imaging of small metabolites and lipids. *Proc Natl Acad Sci U S A* **114**, 3334-3339 (2017).
387. Costello, L.C. & Franklin, R.B. Prostatic fluid electrolyte composition for the screening of prostate cancer: a potential solution to a major problem. *Prostate Cancer Prostatic Dis* **12**, 17-24 (2009).
388. Bader, D.A., *et al.* Mitochondrial pyruvate import is a metabolic vulnerability in androgen receptor-driven prostate cancer. *Nat Metab* **1**, 70-85 (2019).
389. Palmer, A., *et al.* FDR-controlled metabolite annotation for high-resolution imaging mass spectrometry. *Nat Methods* **14**, 57-60 (2017).
390. Race, A.M. & Bunch, J. Optimisation of colour schemes to accurately display mass spectrometry imaging data based on human colour perception. *Anal Bioanal Chem* **407**, 2047-2054 (2015).
391. Tortorella, S., *et al.* LipostarMSI: Comprehensive, Vendor-Neutral Software for Visualization, Data Analysis, and Automated Molecular Identification in Mass Spectrometry Imaging. *J Am Soc Mass Spectrom* **31**, 155-163 (2020).
392. Kaushik, A.K., *et al.* Metabolomic profiling identifies biochemical pathways associated with castration-resistant prostate cancer. *J Proteome Res* **13**, 1088-1100 (2014).
393. Pinto, F.G., Mahmud, I., Harmon, T.A., Rubio, V.Y. & Garrett, T.J. Rapid Prostate Cancer Noninvasive Biomarker Screening Using Segmented Flow Mass Spectrometry-Based Untargeted Metabolomics. *J Proteome Res* **19**, 2080-2091 (2020).
394. Kerian, K.S., *et al.* Differentiation of prostate cancer from normal tissue in radical prostatectomy specimens by desorption electrospray ionization and touch spray ionization mass spectrometry. *Analyst* **140**, 1090-1098 (2015).
395. Bowman, A.P., *et al.* Evaluation of lipid coverage and high spatial resolution MALDI-imaging capabilities of oversampling combined with laser post-ionisation. *Anal Bioanal Chem* **412**, 2277-2289 (2020).

-
396. Barre, F.P.Y., *et al.* Enhanced Sensitivity Using MALDI Imaging Coupled with Laser Postionization (MALDI-2) for Pharmaceutical Research. *Anal Chem* **91**, 10840-10848 (2019).
397. Niehaus, M., Soltwisch, J., Belov, M.E. & Dreisewerd, K. Transmission-mode MALDI-2 mass spectrometry imaging of cells and tissues at subcellular resolution. *Nat Methods* **16**, 925-931 (2019).
398. Ujma, J., *et al.* Cyclic Ion Mobility Mass Spectrometry Distinguishes Anomers and Open-Ring Forms of Pentasaccharides. *J Am Soc Mass Spectrom* **30**, 1028-1037 (2019).
399. Mascini, N.E., *et al.* The use of mass spectrometry imaging to predict treatment response of patient-derived xenograft models of triple-negative breast cancer. *J Proteome Res* **14**, 1069-1075 (2015).
400. Patterson, N.H., *et al.* Assessment of pathological response to therapy using lipid mass spectrometry imaging. *Sci Rep* **6**, 36814 (2016).
401. Spick, C., Herrmann, K. & Czernin, J. Evaluation of Prostate Cancer with ¹¹C-Acetate PET/CT. *J Nucl Med* **57**, 30S-37S (2016).
402. Kwee, S.A. & Lim, J. Metabolic positron emission tomography imaging of cancer: Pairing lipid metabolism with glycolysis. *World J Radiol* **8**, 851-856 (2016).
403. Wetter, A., *et al.* Choline-based imaging of prostate cancer with combined [(18)F] fluorocholine PET and (1)H MR spectroscopy by means of integrated PET/MRI. *Clin Imaging* **42**, 198-202 (2017).
404. Maines, F., *et al.* Serial ¹⁸F-choline-PET imaging in patients receiving enzalutamide for metastatic castration-resistant prostate cancer: response assessment and imaging biomarkers. *Future Oncol* **12**, 333-342 (2016).
405. Schlaepfer, I.R., *et al.* Abstract 107: Lipid metabolism inhibitors enhance glycolysis and FDG-PET imaging of prostate cancer tumors. *Cancer Research* **74**, 107 (2014).
406. Liu, I.J., Zafar, M.B., Lai, Y.H., Segall, G.M. & Terris, M.K. Fluorodeoxyglucose positron emission tomography studies in diagnosis and staging of clinically organ-confined prostate cancer. *Urology* **57**, 108-111 (2001).
407. Kang, P.M., *et al.* Incidental abnormal FDG uptake in the prostate on ¹⁸-fluoro-2-deoxyglucose positron emission tomography-computed tomography scans. *Asian Pac J Cancer Prev* **15**, 8699-8703 (2014).
408. Han, E.J., H, O.J., Choi, W.H., Yoo, I.R. & Chung, S.K. Significance of incidental focal uptake in prostate on ¹⁸-fluoro-2-deoxyglucose positron emission tomography CT images. *Br J Radiol* **83**, 915-920 (2010).
409. Hodolic, M. Imaging of Prostate Cancer Using (18)F-Choline PET/Computed Tomography. *PET Clin* **12**, 173-184 (2017).
410. Chong, J. & Xia, J. MetaboAnalystR: an R package for flexible and reproducible analysis of metabolomics data. *Bioinformatics* **34**, 4313-4314 (2018).
411. Bemis, K.D., *et al.* Probabilistic Segmentation of Mass Spectrometry (MS) Images Helps Select Important Ions and Characterize Confidence in the Resulting Segments. *Mol Cell Proteomics* **15**, 1761-1772 (2016).
412. Mutuku, S.M., *et al.* Evaluation of Small Molecule Drug Uptake in Patient-Derived Prostate Cancer Explants by Mass Spectrometry. *Scientific Reports* **9**(2019).
413. Wishart, D.S., *et al.* HMDB 4.0: the human metabolome database for 2018. *Nucleic Acids Res* **46**, D608-D617 (2018).
414. Sud, M., *et al.* LMSD: LIPID MAPS structure database. *Nucleic Acids Res* **35**, D527-532 (2007).
415. Criswell, S., Lazar, C. & Lewis, P. Troubleshooting on the Roche Ventana BenchMark ULTRA IHC/ISH automated staining system. *Journal of Histotechnology* **42**, 19-30 (2018).

-
416. Fonville, J.M., *et al.* Hyperspectral visualization of mass spectrometry imaging data. *Anal Chem* **85**, 1415-1423 (2013).
417. Hageman, J.A., *et al.* Robust and Confident Predictor Selection in Metabolomics. in *Statistical Analysis of Proteomics, Metabolomics, and Lipidomics Data Using Mass Spectrometry* (eds. Datta, S. & Mertens, B.J.A.) 239-257 (Springer International Publishing, Cham, 2017).
418. Hanselmann, M., *et al.* Concise representation of mass spectrometry images by probabilistic latent semantic analysis. *Anal Chem* **80**, 9649-9658 (2008).
419. Krasny, L., *et al.* Spatial segmentation of MALDI FT-ICR MSI data: a powerful tool to explore the head and neck tumor in situ lipidome. *J Am Soc Mass Spectrom* **26**, 36-43 (2015).
420. Wu, X., *et al.* Top 10 algorithms in data mining. *Knowledge and Information Systems* **14**, 1-37 (2007).
421. Franck, J., *et al.* MALDI imaging mass spectrometry: state of the art technology in clinical proteomics. *Mol Cell Proteomics* **8**, 2023-2033 (2009).
422. Konicek, A.R., Lefman, J. & Szakal, C. Automated correlation and classification of secondary ion mass spectrometry images using a k-means cluster method. *Analyst* **137**, 3479-3487 (2012).
423. Long, F.H. Multivariate Analysis for Metabolomics and Proteomics Data. in *Proteomic and Metabolomic Approaches to Biomarker Discovery* (eds. Issaq, H.J. & Veenstra, T.D.) 299-311 (Academic Press, Boston, 2013).
424. Talebi, A., *et al.* Sustained SREBP-1-dependent lipogenesis as a key mediator of resistance to BRAF-targeted therapy. *Nat Commun* **9**, 2500 (2018).
425. Basu, S.S., *et al.* Rapid MALDI mass spectrometry imaging for surgical pathology. *NPJ Precis Oncol* **3**, 17 (2019).
426. Koundouros, N. & Poulogiannis, G. Reprogramming of fatty acid metabolism in cancer. *Br J Cancer* **122**, 4-22 (2020).
427. D'Angelo, G., Moorthi, S. & Luberto, C. Chapter Three - Role and Function of Sphingomyelin Biosynthesis in the Development of Cancer. in *Advances in Cancer Research*, Vol. 140 (eds. Chalfant, C.E. & Fisher, P.B.) 61-96 (Academic Press, 2018).
428. Shah, S., *et al.* Targeting ACLY sensitizes castration-resistant prostate cancer cells to AR antagonism by impinging on an ACLY-AMPK-AR feedback mechanism. *Oncotarget* **7**, 43713-43730 (2016).
429. Cai, C., *et al.* Androgen receptor gene expression in prostate cancer is directly suppressed by the androgen receptor through recruitment of lysine-specific demethylase 1. *Cancer Cell* **20**, 457-471 (2011).
430. Centenera, M.M., *et al.* Co-targeting AR and HSP90 suppresses prostate cancer cell growth and prevents resistance mechanisms. *Endocr Relat Cancer* **22**, 805-818 (2015).
431. Parrales, A. & Iwakuma, T. p53 as a Regulator of Lipid Metabolism in Cancer. *Int J Mol Sci* **17**(2016).
432. Berglund, E., *et al.* Spatial maps of prostate cancer transcriptomes reveal an unexplored landscape of heterogeneity. *Nat Commun* **9**, 2419 (2018).
433. Pedregosa, F., *et al.* Scikit-learn: Machine Learning in Python. *Journal Of Machine Learning Research* **12**, 2825-2830 (2011).
434. Dang, Q., Chen, Y.A. & Hsieh, J.T. The dysfunctional lipids in prostate cancer. *Am J Clin Exp Urol* **7**, 273-280 (2019).
435. Nielsen, M.M., *et al.* Mass spectrometry imaging of biomarker lipids for phagocytosis and signalling during focal cerebral ischaemia. *Sci Rep* **6**, 39571 (2016).
436. Wang, Y., Ma, S. & Ruzzo, W.L. Spatial modeling of prostate cancer metabolic gene expression reveals extensive heterogeneity and selective vulnerabilities. (2019).

-
437. Guerrero, J., Alfaro, I.E., Gomez, F., Protter, A.A. & Bernales, S. Enzalutamide, an androgen receptor signaling inhibitor, induces tumor regression in a mouse model of castration-resistant prostate cancer. *Prostate* **73**, 1291-1305 (2013).
438. Gibbons, J.A., *et al.* Pharmacokinetic Drug Interaction Studies with Enzalutamide. *Clin Pharmacokinet* **54**, 1057-1069 (2015).
439. Kim, K.P., *et al.* Simultaneous quantitation of abiraterone, enzalutamide, N-desmethyl enzalutamide, and bicalutamide in human plasma by LC-MS/MS. *J Pharm Biomed Anal* **138**, 197-205 (2017).
440. Zang, T., *et al.* Simultaneous quantitation of nine hydroxy-androgens and their conjugates in human serum by stable isotope dilution liquid chromatography electrospray ionization tandem mass spectrometry. *J Steroid Biochem Mol Biol* **165**, 342-355 (2017).
441. Song, J.H., *et al.* Quantitative determination of enzalutamide, an anti-prostate cancer drug, in rat plasma using liquid chromatography-tandem mass spectrometry, and its application to a pharmacokinetic study. *Biomed Chromatogr* **28**, 1112-1117 (2014).
442. Sulochana, S.P., Saini, N.K., Daram, P., Polina, S.B. & Mullangi, R. Validation of an LC-MS/MS method for simultaneous quantitation of enzalutamide, N-desmethylenzalutamide, apalutamide, darolutamide and ORM-15341 in mice plasma and its application to a mice pharmacokinetic study. *J Pharm Biomed Anal* **156**, 170-180 (2018).
443. FDA, U.S. Guidance for Industry-Bioanalytical Method Validation in *Food and Drug Administration* (ed. Services, U.S.D.o.H.a.H.) (U.S. Department of Health and Human Services Food and Drug Administration, Center for Drug Evaluation and Research Center for Veterinary Medicine, 2013).
444. Matuszewski, B.K., Constanzer, M.L. & Chavez-Eng, C.M. Strategies for the assessment of matrix effect in quantitative bioanalytical methods based on HPLC-MS/MS. *Anal Chem* **75**, 3019-3030 (2003).
445. Evard, H., Krueve, A. & Leito, I. Tutorial on estimating the limit of detection using LC-MS analysis, part I: Theoretical review. *Anal Chim Acta* **942**, 23-39 (2016).
446. Williams, S.G., *et al.* Randomised Phase 3 Trial of Enzalutamide In Androgen Deprivation Therapy With Radiation Therapy For High Risk, Clinically Localised, Prostate Cancer: Enzarad (Anzup 1303). *Asia-Pac. J. Clin. Oncol.* **11**, 149-149 (2015).
447. Administration, U.S.D.o.H.a.H.S.F.a.D. Guidance for Industry-Bioanalytical Method Validation. in *Food and Drug Administration* (ed. Services, U.S.D.o.H.a.H.) (Center for Drug Evaluation and Research Center for Veterinary Medicine, 2001).
448. van Nuland, M., Hillebrand, M.J.X., Rosing, H., Schellens, J.H.M. & Beijnen, J.H. Development and Validation of an LC-MS/MS Method for the Simultaneous Quantification of Abiraterone, Enzalutamide, and Their Major Metabolites in Human Plasma. *Ther Drug Monit* **39**, 243-251 (2017).
449. Bennett, D., Gibbons, J.A., Mol, R., Ohtsu, Y. & Williard, C. Validation of a method for quantifying enzalutamide and its major metabolites in human plasma by LC-MS/MS. *Bioanalysis* **6**, 737-744 (2014).
450. Saylor, P.J., Karoly, E.D. & Smith, M.R. Prospective study of changes in the metabolomic profiles of men during their first three months of androgen deprivation therapy for prostate cancer. *Clin Cancer Res* **18**, 3677-3685 (2012).
451. Basaria, S. Androgen deprivation therapy, insulin resistance, and cardiovascular mortality: an inconvenient truth. *Journal of andrology* **29**, 534-539 (2008).
452. Chen, Z., *et al.* Crucial role of p53-dependent cellular senescence in suppression of Pten-deficient tumorigenesis. *Nature* **436**, 725-730 (2005).
453. Khoo, K.H., Verma, C.S. & Lane, D.P. Drugging the p53 pathway: understanding the route to clinical efficacy. *Nat Rev Drug Discov* **13**, 217-236 (2014).

-
454. Singh, S.K., Banerjee, S., Acosta, E.P., Lillard, J.W. & Singh, R. Resveratrol induces cell cycle arrest and apoptosis with docetaxel in prostate cancer cells via a p53/p21WAF1/CIP1 and p27KIP1 pathway. *Oncotarget* **8**, 17216-17228 (2017).
455. Eymerit-Morin, C., *et al.* Histopathology of prostate tissue after vascular-targeted photodynamic therapy for localized prostate cancer. *Virchows Arch* **463**, 547-552 (2013).
456. Paner, G.P., Luthringer, D.J. & Amin, M.B. Best practice in diagnostic immunohistochemistry: prostate carcinoma and its mimics in needle core biopsies. *Arch Pathol Lab Med* **132**, 1388-1396 (2008).
457. Luo, J., *et al.* Alpha-methylacyl-CoA racemase: a new molecular marker for prostate cancer. *Cancer Res* **62**, 2220-2226 (2002).
458. Rubin, M.A., *et al.* alpha-Methylacyl coenzyme A racemase as a tissue biomarker for prostate cancer. *JAMA* **287**, 1662-1670 (2002).
459. Lawrence, M.G., *et al.* Patient-derived Models of Abiraterone- and Enzalutamide-resistant Prostate Cancer Reveal Sensitivity to Ribosome-directed Therapy. *Eur Urol* **74**, 562-572 (2018).
460. Centenera, M.M., *et al.* Evidence for efficacy of new Hsp90 inhibitors revealed by ex vivo culture of human prostate tumors. *Clin Cancer Res* **18**, 3562-3570 (2012).
461. Ellis, S.R., Bruinen, A.L. & Heeren, R.M. A critical evaluation of the current state-of-the-art in quantitative imaging mass spectrometry. *Anal Bioanal Chem* **406**, 1275-1289 (2014).
462. Backstrom, E., *et al.* Uncovering the regional localization of inhaled salmeterol retention in the lung. *Drug delivery* **25**, 838-845 (2018).
463. Chumbley, C.W., *et al.* Absolute Quantitative MALDI Imaging Mass Spectrometry: A Case of Rifampicin in Liver Tissues. *Anal Chem* **88**, 2392-2398 (2016).
464. Cullis, P.R., Fenske, D.B. & Hope, M.J. Physical properties and functional roles of lipids in membranes. in *Biochemistry of Lipids, Lipoproteins and Membranes*, Vol. Volume 31 (eds. Dennis, E.V. & Jean, E.V.) 1-33 (Elsevier, 1996).
465. Freeman, M.R., Yang, W. & Di Vizio, D. Caveolin-1 and prostate cancer progression. *Advances in experimental medicine and biology* **729**, 95-110 (2012).
466. Raval, A.D., Thakker, D., Negi, H., Vyas, A. & Salkini, M.W. Association between statins and clinical outcomes among men with prostate cancer: a systematic review and meta-analysis. *Prostate Cancer Prostatic Dis* **19**, 222 (2016).
467. Shevchenko, A. & Simons, K. Lipidomics: coming to grips with lipid diversity. *Nat Rev Mol Cell Biol* **11**, 593-598 (2010).
468. Cha, J.Y. & Lee, H.J. Targeting Lipid Metabolic Reprogramming as Anticancer Therapeutics. *J Cancer Prev* **21**, 209-215 (2016).
469. Kriegsmann, K., *et al.* Combined Immunohistochemistry after Mass Spectrometry Imaging for Superior Spatial Information. *Proteomics Clin Appl* **13**, e1800035 (2019).
470. Li, L.H., Dutkiewicz, E.P., Huang, Y.C., Zhou, H.B. & Hsu, C.C. Analytical methods for cholesterol quantification. *J Food Drug Anal* **27**, 375-386 (2019).
471. Jackson, A.U., Shum, T., Sokol, E., Dill, A. & Cooks, R.G. Enhanced detection of olefins using ambient ionization mass spectrometry: Ag⁺ adducts of biologically relevant alkenes. *Anal Bioanal Chem* **399**, 367-376 (2011).
472. Griffiths, R.L. & Bunch, J. A survey of useful salt additives in matrix-assisted laser desorption/ionization mass spectrometry and tandem mass spectrometry of lipids: introducing nitrates for improved analysis. *Rapid Commun Mass Spectrom* **26**, 1557-1566 (2012).
473. Hsu, F.-F., Bohrer, A. & Turk, J. Formation of lithiated adducts of glycerophosphocholine lipids facilitates their identification by electrospray ionization

-
- tandem mass spectrometry. *Journal of the American Society for Mass Spectrometry* **9**, 516-526 (1998).
474. Griffiths, R.L., *et al.* Formal lithium fixation improves direct analysis of lipids in tissue by mass spectrometry. *Anal Chem* **85**, 7146-7153 (2013).
475. Smith, K.W., *et al.* Spatial Localization of Vitamin D Metabolites in Mouse Kidney by Mass Spectrometry Imaging. *ACS Omega* **5**, 13430-13437 (2020).
476. Groseclose, M.R. & Castellino, S. A mimetic tissue model for the quantification of drug distributions by MALDI imaging mass spectrometry. *Anal Chem* **85**, 10099-10106 (2013).
477. Murphy, R.C., Hankin, J.A., Barkley, R.M. & Zemski Berry, K.A. MALDI imaging of lipids after matrix sublimation/deposition. *Biochim Biophys Acta* **1811**, 970-975 (2011).
478. Hankin, J.A., Barkley, R.M. & Murphy, R.C. Sublimation as a method of matrix application for mass spectrometric imaging. *J Am Soc Mass Spectrom* **18**, 1646-1652 (2007).
479. The LIPID MAPS® Lipidomics Gateway, <https://www.lipidmaps.org/>
480. The Human Metabolome Database, <https://hmdb.ca/>